An Analysis of the Sources and Sinks for Criegee Intermediates: An Extended Computational Study

A thesis submitted in partial fulfilment of the requirements for the award of

Doctor of Philosophy.

Submitted: March 2021

By

Nathan Anthony Isaac Watson

Summary (no more than 300 words)

This thesis is centred around a common theme of using computational chemistry to investigate reactions that either produce or deplete atmospheric Criegee intermediates (CIs). The computational work investigates many novel reaction mechanisms and generates kinetic and product branching data for these reactions which is then reviewed in the context of their impact on local tropospheric environments.

Firstly, the ozonolysis of a large array of alkenes is examined, as known sources of CIs. The results of this study indicate that factors including the number of α-H atoms in the alkene substituents and others besides all have a significant influence on the ozonolysis rate constants and the fractional distribution of different CI yields.

Assessments of bimolecular CI sinks are also examined, particularly via reaction with gaseous alcohols. The high reactivity of many CI + alcohol reactions shows that in geographical areas such as Sao Paulo, where biofuel use is prevalent, that alcohols are likely a significant sink of CIs. The bimolecular chemistry of a series of CIs derived from a new range of synthetic hydrofluoroolefin refrigerants are also examined, because their refrigerant precursors are being emitted in ever larger quantities, and their fluorinated substituents make their CI chemistry distinctive.

Both the CIs and their alkene precursors are classified into several sets of taxonomic groups on the basis of common structural features and similar bimolecular chemistries. By linking computational ozonolysis chemistry to the structural alkene features, this classification allows the author to generate a new theoretical "FESP" model designed to predict the ozonolysis chemistry of lengthy, conformationally flexible alkenes. This model is used to determine the reaction rate and branching fractions of the O_3 + *Z*-2-hexene reaction, but could be applied to many other alkenes, and perhaps even adapted to explore the bimolecular reactivity of lengthy CIs.

Acknowledgments

Above all others I would like to acknowledge the support of my God and saviour Jesus Christ, who has given me continual support throughout good and challenging times.

I am overwhelmingly thankful to Dr Joseph Beames, my PhD supervisor at Cardiff University for his continual support and input throughout my time as PhD student. He always encouraged me with work and was enthusiastic at giving me great opportunities. The support from the other members of the Beames group, particularly Dr Thomas Stonelake was invaluable and enjoyable.

I would also like to thank my parents, Keith and Tara Watson for their support and prayer during my PhD writing. My siblings, Natasha, Joel and Tanya Watson, who have always been there for me during my time as a PhD student and I am deeply grateful.

I would like to thank the sponsor of my degree programme, the Engineering and Physical Sciences Research Council (EPSRC).

I would also like to acknowledge supported given by Advanced Research Computing at Cardiff and High-Performance Computing Wales and the Marie Skłodowska Curie Individual Fellowship

I am appreciative of the Orr-Ewing group at Bristol University and again Dr Thomas Stonelake for their contribution to my work on sCI reactions with gaseous alcohols.

I am grateful to Dr Joshua A. Black and Professor Peter Knowles for their input into my work on unimolecular fragmentation of Criegee intermediates.

Furthermore, I would also like to thank the group led by Dr Andrew Rickard, whom I collaborated with at University of York in order to produce my work on the ozonolysis of alkenes.

Lastly, I would like to thank my friends in Cardiff and around the country as well as my Bible study group for both spiritual and emotional support during my time as a PhD student.

Preface

Chapter 4 consists of my work in two previously published papers:

'Criegee Intermediate–Alcohol Reactions, A Potential Source of Functionalized Hydroperoxides in the Atmosphere' by McGillen *et al.*, published by *ACS Earth* and *Space Chemistry*, DOI: 10.1021/acsearthspacechem.7b00108

'An Extended Computational Study of Criegee Intermediate–Alcohol Reactions' by Watson *et al.*, published in Journal of Physical Chemistry A, DOI: 10.1021/acs.jpca.8b09349

It is anticipated that the work in this Chapter will produce up to four other publications. At least two publications, consisting from the data and text in Chapter 3. It is anticipated that this work will produce at least one publication, from the data and text in Chapter 5. It is anticipated that this work will produce at least one publication, from the data and text in Chapter 6.

Contents

Table of Figures:

Glossary and Abbreviations:

General Terms:

TS	Transition state
CI	Criegee intermediate
POZ	Primary Ozonide
sCI	Stabilised Criegee intermediate
HFO	Hydrofluoroolefin (used to describe hydrochlorofluoroolefins too)
HFO-sCI	Hydrofluoroolefin derived stabilised Criegee intermediate
Enals	an alkene with a conjugated ketone substituent
FO	Formaldehyde oxide (CH_2OO)
DMFO	Dimethyl Formaldehyde oxide ($(CH_3)_2COO$)
AAAH	α-alkyloxyalkyl hydroperoxide
VHP	Vinyl Hydroperoxide
HHP	Hydro
MeOH/EtOH/iPrOH	Methanol/Ethanol/isopropanol
SAR	Structure-activity relationship
FESP model	Free Energy Structural Projection Model
α- ß- or γ-H atom	a H atom in the α- ß- or γ-position on an alkyl substituent group
VOC	volatile organic compound
Channels	A series of similar TS structures that produce the same products
Subchannel	One TS structure within a channel

General Thermochemical Terms:

ΔE	Relative Energy
ΔG	Relative Gibbs Free Energy
k_{THEO}	Theoretical Rate Constant

k_{ME}	Master Equation Rate Constant
k_{CAN}	Canonical Rate Constant
k_{TST}	Conventional Transition State Theory Rate Constant
k_{EXP}	Experimental Rate Constant
Γ_{THEO}	Theoretical Product Branching Ratio
Γ_{EXP}	Experimental Product Branching Ratio
α_{THEO}	collective theoretical rate constant

Abbreviations used in to describe FESP model in Chapter 6:

ΔG_{THEO}	Computationally derived relative Gibbs Free energy
$\Delta G_{TS\text{-}POZ}$	Difference in ΔG_{THEO} values between a POZ and a TS structure
ΔG_{PROJ}	Projected relative Gibbs Free energy using FESP model 1
$\delta\Delta G$	Deviation of Gibbs Free energy and ΔG_{THEO} values
ΔE_{THEO}	Computationally derived relative energy
Δ_{ADJ}	Difference between the ΔG_{THEO} values
ΔE_{ADJ}	Adjusted relative energy for FESP model 1
k_{TEST}	Test Rate Constant for MESMER projection technique
Γ_{TEST}	Test Product Branching Ratio for MESMER projection technique
δk	Deviation of calculated rate constant from k_{THEO}
$\delta\Gamma$	Deviation of calculated Product Branching Ratio from Γ_{THEO}
k_{PROJ}	Projected Rate Constant for FESP model 1
Γ_{PROJ}	Projected Product Branching Ratio for FESP model 1
Δ_{STERIC}	Steric adjustment factor
Δ_{ROT}	Hindered-internal-rotation adjustment factor
ΔG_{STERIC}	Sterically adjusted relative Gibbs Free energy used for FESP model 2
k_{STERIC}	Sterically adjusted Rate Constant for FESP model 2

Γ_{STERIC}	Sterically adjusted Product Branching Ratio for FESP model 2
Δ_{EMP}	Empirical adjustment factor
ΔG_{EMP}	Empirically adjusted relative Gibbs Free energy for FESP model 3
k_{EMP}	Empirically adjusted Rate Constant for FESP model 3
Γ_{EMP}	Empirically adjusted Product Branching Ratio for FESP model 3

Abbreviations and structures of Alkenes and Criegee intermediates used in this Thesis:

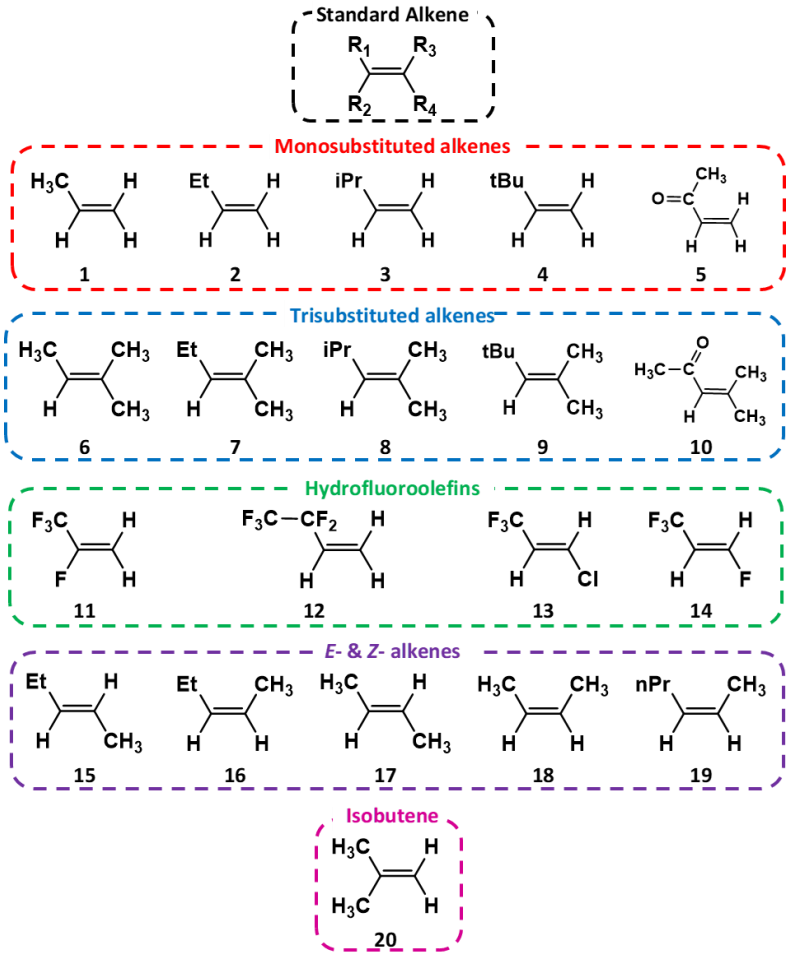

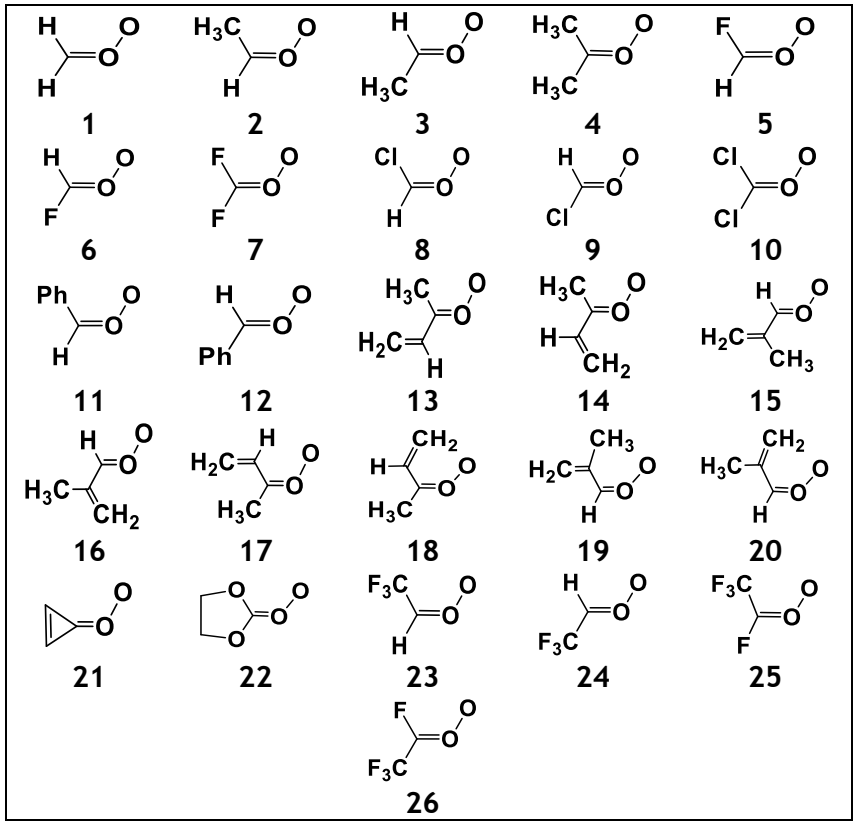

1. Introduction

1.1 The Origins of Atmospheric Chemistry

Throughout history, discoveries made in atmospheric sciences have been shown to have a considerable impact on human life, whether it be informing the authorities about deleterious tropospheric emissions on a local level (e.g. toxic volcanic H_2S gas) or demonstrating the effect that carbon dioxide (CO_2) emissions have on global atmospheric temperatures.[1,2] One of the first landmark discoveries in atmospheric chemistry was the reaction between limewater and CO_2. Joseph Black showed both that CO_2 gas exists and identified its presence in human breath, by observing the precipitation of calcium carbonate in limewater (see in Equation 1.1).[3]

$$Ca(OH)_{2(aq)} + CO_{2(g)} \rightarrow CaCO_{3(s)} + H_2O_{(l)} \qquad \textit{Equation 1.1}$$

The 18th century contains many such important atmospheric chemistry discoveries, for example by the chemist Henry Cavendish, who observed that adding iron or zinc to hydrochloric or sulphuric acid produced hydrogen, or "inflammable air" (see Equations 1.2 and 1.3).[4]

$$Fe_{(s)} + 2\ HCl_{(aq)} \rightarrow FeCl_{2(aq)} + H_{2(g)} \qquad \textit{Equation 1.2}$$

$$Zn_{(s)} + H_2SO_{4(aq)} \rightarrow ZnSO_{4(aq)} + H_{2(g)} \qquad \textit{Equation 1.3}$$

Joseph Priestley, another 18th century chemist, identified dioxygen (O_2) by focusing the sun's rays on mercuric oxide (see Equation 1.4).[5] But O_2 was originally identified as *dephlogisticated air* under the now superseded *phlogiston theory*.

$$2\ HgO_{(s)} + hv \rightarrow 2\ Hg_{(s)} + O_{2(g)} \qquad \textit{Equation 1.4}$$

Antoine Lavoisier helped to disprove this *phlogiston theory* and documented a series of elements and reactions using a new chemical nomenclature. This involved identifying some gaseous elements including: dihydrogen (H_2), by reacting water (H_2O) and iron, producing H_2 and iron oxide (Equation 1.5); and CO_2, as a gas emitted by the reaction of charcoal and mercury oxide (Equation 1.6).[6]

$$Fe_{(S)} + H_2O_{(l)} \rightarrow FeO_{(S)} + H_{2(g)} \qquad \textit{Equation 1.5}$$

$$2\ HgO_{(s)} + C_{(s)} \rightarrow 2\ Hg_{(s)} + CO_{2(g)} \qquad \textit{Equation 1.6}$$

These discoveries continued throughout the 19th and 20th centuries including the important discovery of the noble gases, helium in 1895, and neon, krypton and xenon in 1898-1900.[7]

In 1840—44, C.F. Schönbein discovered that the electrolysis of water produced a "new odour" which he identified as O_3, or ozone (see Equation 1.7).[8,9]

$$H_2O_{(aq)} + O_{2(g)} \rightarrow H_{2(g)} + O_{3(g)} \qquad \textit{Equation 1.7}$$

Schönbein also discovered the production of gaseous O_3 in lightning storms, which is characterized by ozone's distinctive smell. These discoveries, along with subsequent measurements of ozone concentrations within various strata of the atmosphere have identified O_3 as a tropospheric species vital to the survival of life on earth.

1.2 The Role of Ozone in Different Atmosphere Strata

The atmosphere, the small layer of gas that surrounds planet Earth, is divided up into regions, or *strata*, for the purposes of scientific classification (see Figure 1.1). These strata are so classified by their altitude range, because each stratum has a different altitude-temperature relationship. These different altitude—temperature profiles emerge from each stratum having a different proximity to the earth, molecular composition, and degree of transmission of electromagnetic solar radiation. Within a stratum there is often good horizontal chemical transport and therefore uniformity with longitude and latitude, but lack of vertical transportation between strata (often a matter of years) significantly reduces mixing and leads to a more distinct molecular composition for each stratum.[10]

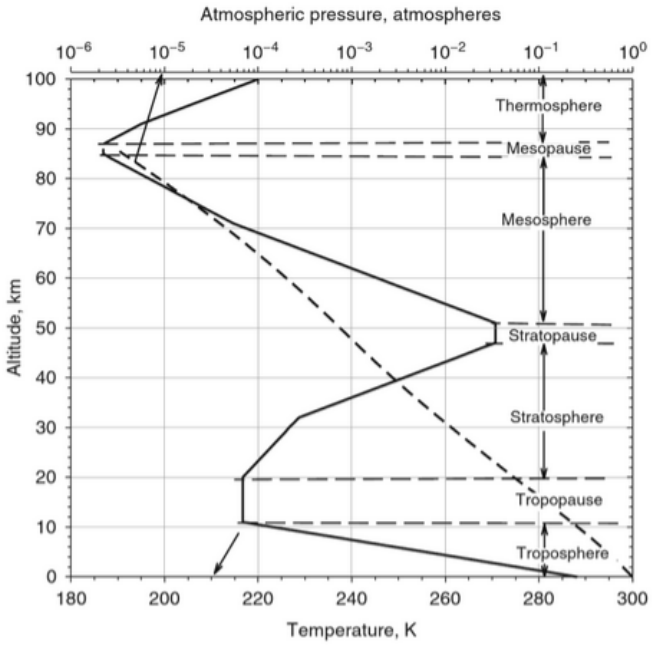

Figure 1.1: A vertical profile of the temperature (solid line), and pressure (short-dashed line) of the Earth's atmospheric strata. The boundaries of these atmospheric strata are defined by the altitudes at which the temperature trend inverts, which are denoted by the horizontal long-dashed lines. The source of this graphic is in Clark et al. (2015) pg 12.[10]

An example of the differing altitude—temperature profiles between strata is observed at ~ 85 km in Figure 1.1, known as the mesopause, which is a span of temperature inflection between the thermosphere and the mesosphere. As molecules descend through the thermosphere their average temperature decreases until the altitude approaches ca. 85 km. High in the thermosphere, higher energy solar radiation being is absorbed by these molecules (typically N_2 and O_2), which increases the thermal temperature. However, the temperature increases as the altitude reduces from here because there is improved energy transfer from a photoactive ozone layer in the stratosphere. There is little change in the chemical composition of the mesosphere and thermosphere.

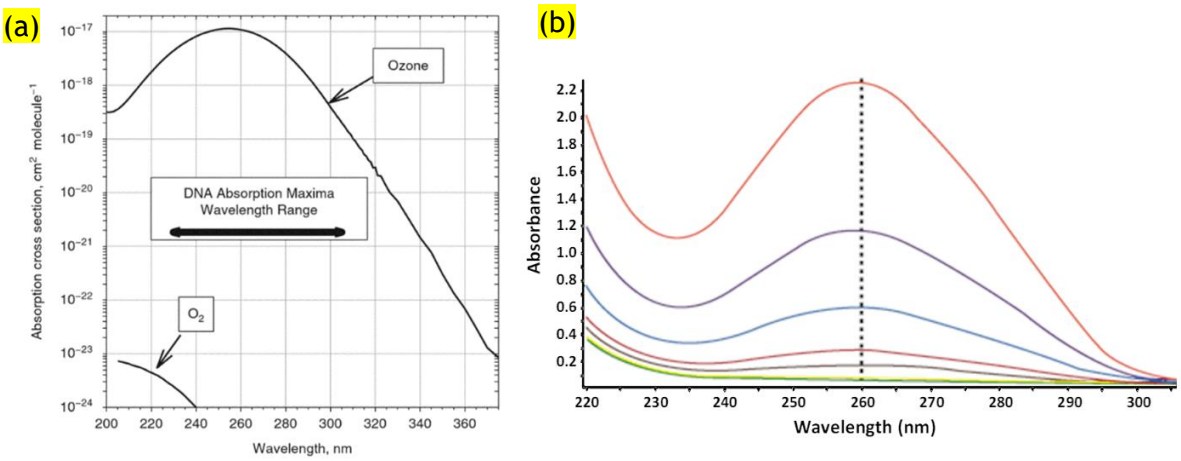

Figure 1.2: Absorption spectra of diatomic oxygen [O_2] and of ozone [O_3] within the key DNA spectral ranges (Figure 1.2a);[10] and absorption spectrum of calfthymus DNA molecule (Figure 1.2b).[11]

Within the stratosphere, there is an increase in the complexity of the chemistry present, and a largely positive temperature gradient with altitude. As seen in the thermosphere, this profile is due to increased solar radiation absorption: photochemistry caused by UV electromagnetic radiation interaction with the ozone layer. As shown in Figure 1.2a, O_3 acts as a very effective screen for much of the high frequency UV ranges, as the stratospheric abundance of O_3 causes only ~5 % of the UVB radiation (280—315 nm) to reach the earth surface, and absorption by either O_3 or O_2 sees almost total elimination of surface level UVC radiation (100—280 nm).[12,13] Figure 1.2b shows that DNA is photoactive at both UVC and UVB frequency ranges and so absorption of UV light by O_3 prevents DNA damage caused by exposure to high-frequency radiation, which could otherwise lead to cataracts and skin cancer. [10,13] As shown in Figures 1.2a & 1.2b, UVA radiation (315–400nm) is much less efficiently absorbed by O_3 and DNA than UVB & UVC, which means that, whilst 95% of UV energy that reaches the earth surface is of UVA frequency, this has a much less deleterious impact on DNA.

The absorption of UV radiation that we are benefiting from is the electronic excitation of stratospheric O_3 molecules, causing homolytic O-O bond fission to produce an O_2 molecule and an excited singlet O atom, $O(^1D)$. Many of the resulting radical reactions are exothermic, the energy from which can be transferred by collision with buffer gases, such as O_2 and dinitrogen (N_2), but which is predominantly non-radiative. O_3, as a greenhouse gas, (GHG) can also absorb IR radiation, and this energy can also be transferred to surrounding molecules, either by IR re-emission and absorption or through collisional energy transfer (see Section 1.3.1 for more details). As 90% of atmospheric O_3 is in the stratosphere, this is observed as a temperature increase in this stratum as the heat is retained rather than transferred by vertical transport.[14] At lower altitudes within the

stratosphere (50—20 km) the number of UVB & UVC photons reduces, triggering fewer photochemical reactions and thus affording a slower temperature decrease to ca. 220 K.

The altitude—temperature profile seen over the stratosphere then inverts within in the tropopause (20—12 km), within the troposphere there is reduced photochemical activity, and increased proximity to the heat emitted from the Earth at lower altitudes causes a negative temperature gradient with altitude.[10] The troposphere contains roughly 85% of all atmospheric mass, and with >50% of atmospheric gases populating the altitude below 5.5 km.[15] Most anthropogenic (human-sourced) activity takes place in the troposphere, as even Mount Everest, the world's highest mountain, at 8.8 km; Burj Khalifa, the highest building, at 829.8 m; and the cruising altitude for most long-haul flights, 10—13 km, are all within this stratum.[16] Most gases produced by human activity are found in the troposphere, with tropospheric lifetimes too short to support vertical transport into the stratosphere.[15] The troposphere retains the vast majority of H_2O evaporated from the Earth's surfaces because as H_2O vapour rises the tropospheric temperature drops towards the tropopause, and the water vapour freezes before it reaches the stratosphere, causing precipitation.

The importance of the distinction between the different strata is seen for gaseous O_3, where in the troposphere it is problematic to human health as it is a strong oxidant, that if inhaled can cause or trigger severe respiratory problems.[17] Tropospheric O_3 caused an estimated 14,000 premature deaths in the EU in 2016 and it has a harmful impact as a GHG, which is in stark contrast to the beneficial impact of stratospheric O_3 in preventing cataracts and skin cancer.[10,13,18] Sources of tropospheric O_3 include: car exhaust fumes, such as nitrous oxides (NO_X), volatile organic compounds (VOCs), and carbon monoxide (CO); vertical transport from the stratosphere; and the photolysis of NO_2 in the presence of O_2.[10,19] When there is a localised temperature inversion in urban environments (when the ground level air is cooler than the troposphere above it), O_3 and NO_X, sulphur oxide (SO_X), smoke and other particulates, can become trapped because they cannot rise or circulate.[16] This localised trapped pollution produces a fog called photochemical smog, which is harmful to those populating the urban zone because these pollutants can oxidise both biogenic and human tissue.[2,19,20] Tropospheric O_3 also provides an important sink for other pollutants, for example it globally removes ~10% of the alkene isoprene.[21]

The fact that the presence of gaseous ozone in the atmosphere has both beneficial and detrimental effects on human health depending on its distribution, makes it an archetypal illustration of the importance of understanding the distribution of an atmospheric species.

This study focuses on ozone—alkene reactions (alkene ozonolysis), and their reaction products. Alkenes are emitted from many sources at the Earth's surface including foliage

and automobile fuel burning, meaning that the focus of this report is tropospheric chemistry. This is consistent with the short atmospheric lifetimes of both non-halogenated alkenes (0.37 hrs — 1.4 days) and of alkene ozonolysis products, Criegee intermediates (<1 s).[22-25] This makes penetration into the stratosphere much more difficult because the time scales for inter-strata mixing often is months to years.[26] These lifetimes are short relative to their alkane equivalents (10 days — 12 years), while halogenated alkenes can last up to ca. 1 month, making the scope for vertical transport into other atmospheric strata greater.

1.3 The Chemical Composition of the Atmosphere

Most of the atmosphere is predominantly composed of two gases N_2 and O_2 (see Figure 1.3). However, accurate atmospheric modelling requires extended information about a variety of non-negligible atmospheric species for example the monitoring of GHG abundance and its effects on global temperature, or more localised hydrogen sulphide (H_2S) emissions from volcanos.[2] Biogenic and anthropogenic species with more marginal atmospheric abundances, such as H_2O (~0—40,000 ppm) and CO_2; or even with trace presence, such as sulphur dioxide (SO_2) and chlorofluorocarbons (CFCs) have been shown to affect human life, health and prosperity.[15]

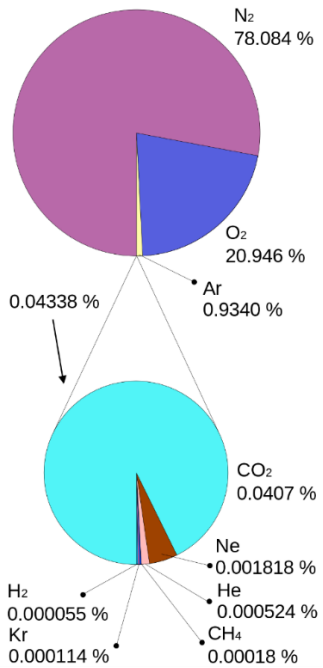

Figure 1.3: Atmospheric composition of the Earth (obtained from NASA data).[27]

The monitoring of trace atmospheric species depends on their *fluxes*, which are made up of two components: their *sources*, which are the processes that produce or release the species involved (e.g. volcanic eruptions); and their *sinks*, which refers to their removal by

decomposition mechanisms, precipitation and/or solvation in oceans. These sources and sinks flow in and out of the gases' *reservoirs*, where atmospheric species accumulate for significant periods of time, such as the methane (CH_4) reservoirs in shale formations and Siberian permafrost.[28,29] Tropospheric chemistry can often vary between different local ecosystems, for example emission local to individual towns or cities. Biogenic emissions, meaning atmospheric processes that emerge naturally without human input, often have the greatest impact upon rural or pristine environments such as rainforests, conservation areas and more remote countryside.

1.3.1 Major Atmospheric Species

The largest component (~78%) of the atmosphere, the inert gas N_2, is involved in some atmospheric processes, such as the nitrogen cycle (a process by which various bacteria convert N_2 into nutrients before being converted back to N_2 by *denitrifying* bacteria), and are also used to synthesize fertilizers and explosives. [30-34] O_2 gas constitutes most of the remaining atmospheric composition (21%), which is required for combustion of fossil fuels and a key component in many biological functions, such as respiration, building deoxyribose nucleic acids (DNA) and synthesis of amino acids.[2,35-41]

Many of the reactions that involve O_2, are also either significant sources of CO_2, such as respiration or fossil fuel combustion, or important sinks, such as photosynthesis.[39-41] Since the beginning of the industrial revolution in the 17th — 19th century, the increased combustion of wood, then coal and finally oil and natural gas for fuel on mass scale has led to a significant increase in atmospheric CO_2.[2,42] During the combustion of fossil fuel, *incomplete combustion* processes like the burning of impurities or burning in O_2-poor environments, produce pollutants such as SO_2, NO_X and CO (see Section 1.3.2). The low efficiency *incomplete combustion* process is more prevalent when burning coal, a fossil fuel that is rich in impurities compared to natural gas.[2]

This increase in atmospheric CO_2 between 1960—2019, seen in Figure 1.4a, appears marginal, with respect to N_2 or O_2 abundance. However, the importance of both understanding the chemistry of how pollutants breakdown and monitoring their abundance in the atmosphere is brought into sharp focus by the impact that increasing CO_2 concentrations along with other GHGs are causing to the global climate. As demonstrated in Figure 1.4, the increase in the concentration of CO_2 in the atmosphere correlates with rising global temperatures. GHGs absorb infrared (IR) radiation either emitted directly from the sun, solar emissions reflected off the earth surface, or from visible solar radiation absorbed by the earth and re-emitted as IR radiation, that would otherwise

escape into space.[2] This excess energy in the GHGs, is then transferred to other species either by collision or re-emission causing net global warming. The increase in global temperature is a strong contributing factor to glacial melting, droughts, and flooding from rising sea levels.[2]

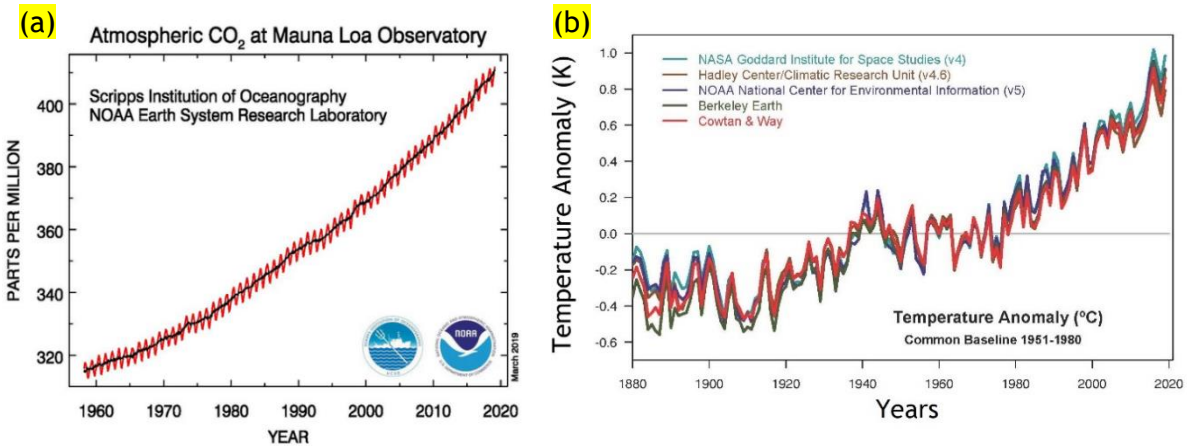

Figure 1.4: CO_2 concentrations over 60 years observed at NOAA's Mauna Loa Observatory in Hawaii (Figure 1.4a);[27] Figure 1.4b shows yearly temperature anomalies from 1880 to 2019 (obtained from NASA data).[43]

Other deleterious impacts of the increase in atmospheric CO_2 includes acidifying of the oceans (through the processes outlined in Equations 1.8—1.11), and contributing to human health problems, particularly increasing blood pressure, respiratory problems and lowering cognitive ability.[44] As shown in Equation 1.8, the atmospheric CO_2 ($CO_{2(g)}$) is in dynamic equilibrium with the aqueous CO_2 ($CO_{2(aq)}$) in sea water, meaning as atmospheric CO_2 levels increased, according to *Le Chatelier principles*, the equilibrium moves to the right and more $CO_{2(aq)}$ is produced.[45]

$$CO_{2\,(g)} \rightleftharpoons CO_{2\,(aq)} \qquad \textit{Equation 1.8}$$

$$CO_{2\,(aq)} + H_2O_{\,(l)} \rightleftharpoons H_2CO_{3\,(aq)} \qquad \textit{Equation 1.9}$$

$$H_2CO_{3\,(aq)} \rightleftharpoons HCO_3^-{}_{(aq)} + H^+{}_{(aq)} \qquad \textit{Equation 1.10}$$

$$HCO_3^-{}_{(aq)} \rightleftharpoons CO_3^{2-}{}_{(aq)} + H^+{}_{(aq)} \qquad \textit{Equation 1.11}$$

This has some benefits as the decrease in $CO_{2(g)}$ reduces the impact of CO_2 emissions on climate change, but this aqueous CO_2 contributes to acidification of oceans. Equation 1.9 shows that $CO_{2(aq)}$, with the excess $H_2O_{(l)}$, is also in equilibrium with dihydrogen carbonate (carbonic acid or $H_2CO_{3(aq)}$), so this increase in CO_2 drives the equilibrium to produce more $H_2CO_{3(aq)}$.

Sea water is an effective pH buffer solution, where the dissolved salt containing a hydrogen carbonate ion ($HCO_3^-{}_{(aq)}$) can act as either a H-acceptor or a H-donor, in

equilibrium with $H_2CO_{3(aq)}$ or the carbonate ion ($CO_3^{2-}{}_{(aq)}$) respectively, as seen in Equation 1.10 & 1.11. This increase in $H_2CO_{3(aq)}$ drives the equilibrium in Equation 1.10 to produce more $HCO_3^-{}_{(aq)}$ and $H^+{}_{(aq)}$, but these species appear on opposite sides of the equilibrium in Equation 1.11. This mildly alkaline "sea water buffer" also has a significant population of basic $CO_3^{2-}{}_{(aq)}$ ions, the additional $H^+{}_{(aq)}$ ions pushing the equilibrium towards producing $HCO_3^-{}_{(aq)}$, overcoming the forward reaction and moderating the increase in acidity. This means the overall effects of additional $CO_{2(aq)}$ in sea water are: an increase in $HCO_3^-{}_{(aq)}$ and H^+ availability. This additional H^+ availability, also known as acidity, has lowered the pH from ~8.20 to ~8.07, between 1766 and 2007, and has contributed to the degradation of calcifying organisms, which has led to bleaching of the coral reefs.[46-48]

The main source of H_2O in the atmosphere is evaporation from large bodies of salt and fresh water but there is also a contribution from biological respiration. Gaseous H_2O or atmospheric droplets are used to facilitate photosynthesis by landing or colliding with plant leaves, although the main source of water for photosynthesis is precipitation and uptake through roots.[49,50] Tropospheric $H_2O_{(g)}$ abundance (referred to as relative humidity) can vary significantly, ~0—40,000 ppm, depending on factors like proximity to bodies of water and time of day.[15] Absorption of solar UV radiation by $O_{3(g)}$ up to ~310 nm, via the *Hartley band*, or within the 320—360 nm range, via the *Huggins band*, induces photolysis to produce $O_{2(g)}$ and an excited singlet $O(^1D)$ atom. This $O(^1D)$ species can react with H_2O, producing a significant source of the atmospheric detergent, OH radicals (sometimes referred to as $HO^{\bullet}{}_{(g)}$).[10,15] Alternatively, as part of the Chapman cycle, excited $O(^1D)$ atoms stabilises down to ground-state triplet $O(^3P)$ atoms, through collisions with $N_{2(g)}$ and $O_{2(g)}$, and this $O(^3P)$ reacts with $O_{2(g)}$ to produce $O_{3(g)}$.[10,15] For more details on OH radicals, please see Section 1.5.1.[51-54]

The atmosphere also has a trace population of *noble gases*, like helium (He), argon (Ar), neon (Ne), and krypton (Kr), which are inert and act as buffer gases or collisional energy quenchers (such as the collisional stabilisation of Criegee intermediates examined in Section 1.5) in gas-phase process.[2,55]

1.3.2 Minor Atmospheric Gases and Other Trace Species

The minor trace gases, such as carbon monoxide (CO) or NO_X to HCl & alkanes, are important, because, although they are frequently described as trace, they have large enough abundances to impact human health and take part in the rich chemistry of the troposphere. Though many of these gases are considered anthropogenic pollutants, even in an environment that has much reduced exposure to human populations, such as in the

countryside, toxic gases and substances can be inhaled or ingested by animal and plant matter, which can subsequently be consumed by humans in the process of bioaccumulation. This process has been demonstrated with the consumption of micro-plastics in aquatic environments by fish. Micro-plastics accumulating in the oceans have been consumed by fish which are then consumed by humans. This has led to toxic trace impurities in human food products and is speculated to have a serious impact on human health.[56–58] CH_4 emissions from natural gas pipelines or permafrost in Siberia are similar examples of process with these kinds of *externalities*, except that these processes cause harm through contributing to climate change.[59,60] Nominally biogenic CH_4 emissions from Siberia permafrost has been accelerated by global warming, which makes it an example of both natural and anthropogenic *externalities*.[2,61]

Nitric oxide and nitrogen dioxide (collectively known as NO_X) are trace gases that are toxic to human health because long term exposure can contribute to lung cancer and other serious respiratory illnesses, leading to hospitalisation or even death.[62–66] One example of the importance in studying trace tropospheric gases, like NO_X, would be the 2015 *Volkswagen emissions scandal*, where the Environmental Protection Agency (EPA) of the United States of America (USA) determined that the car manufacturers, like Volkswagen, had programmed their turbocharged direct injection (TDI) diesel engines to activate their emissions controls only during laboratory testing.[67,68] These TDIs had been installed in 11 million cars worldwide and this lack of emissions controls meant NO_X emissions were much larger than expected.[69] Between 2008—2015, it is estimated that due to the use of the "defeat device" designed to lower the lab-based emissions, the US experienced 59 premature deaths and $450 million in social costs, with Germany experiencing 1200 premature deaths and €1.9 billion in excess health costs over the same time period.[70,71]

NO_X gases emitted from vehicle exhaust emissions has also been shown to be harmful in other ways, such as its role in generating photochemical smog and acid rain.[20,72] NO_X is a precursor of other pollutants too, such as: O_3, which is known to cause respiratory problems; nitrates in microscopic pollutants suspended in the air, called particulate matter (PM); and aerosols, an airborne solid, liquid or multiphase suspension of that particulate matter. These pollutants all contribute to serious respiratory problems and in fact it is estimated that in 2010, there were 13,162 short-term premature deaths in China from exposure to PM2.5, particulate matter with an in aerodynamic diameter <2.5 μm.[19,73–75] Additional evidence has shown that smoking tobacco has not only led to serious health problems and often smoker deaths (~439,000 in the USA in 2019), but it affects those

around them through “passive smoking” (~41,000 in the USA in 2019), much of which can be attributed to the detrimental effect of particulate matter.[76-78]

Pollutant emissions can also emerge from wetlands and bogs (~40% of the global CH_4 budget), livestock farming and Rice paddy fields (~30% and ~11% of CH_4 emissions respectively).[2,79-81]

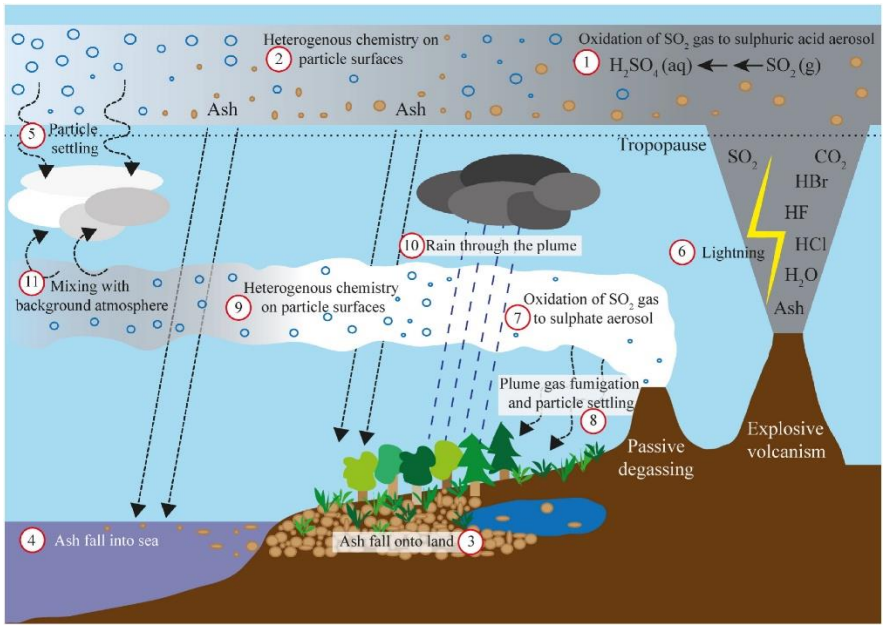

Figure 1.5: Diagram of gaseous emissions from volcanoes and their effects on the atmosphere and environment from study by Mather et al..[82]

Anthropogenic exploitation of geothermal energy for electricity and heating, as well as natural volcanic eruptions, leads to toxic particulate emissions and increased emissions of H_2S, which is deadly at 700 mg/m^3, CO_2 (1% of global budget), SO_2, hydrochloric acid (HCl), bromine monoxide and chlorine dioxide (Figure 1.5).[2,81,83-90]

Other natural products that are harmful pollutants are: CO_2, CO and particulate matter from forest fires; and evaporation off or droplet formation from sea-water which emit significant levels of dissolved gases (such as HCl), sea salt aerosols and hydrochlorocarbons.[91,92]

1.4. The Thermochemistry and Kinetics of Key Tropospheric Species

After these trace gases or precursors are emitted into the atmosphere, they undergo a broad range of chemical reactions for example those with Criegee intermediates (described further in Section 1.6, and a focus of this thesis). While atmospheric reactions are often thermodynamically favourable, these reactions frequently have kinetic barriers that make the reaction less favourable than can be inferred from the thermodynamics alone. This is observed in the contrasting atmospheric processes: $H_2 + ½ O_2 \rightarrow H_2O$, which, while thermodynamically favourable, is a *very* slow reaction (unless there is an ignition) due to a large kinetic barrier; $CH_2OO + CH_3OH$, where the reaction goes to completion due to a low kinetic barrier;[51,93] and $CO_{2(g)} \rightleftharpoons CO_{2\,(aq)}$, where the ongoing forward and reverse processes put the reaction in equilibrium. These types of systems are generalised in Equations 1.12 & 1.13:

$$W + X \rightarrow WX \qquad \textit{Equation 1.12}$$

$$W + X \rightleftharpoons Y + Z \qquad \textit{Equation 1.13}$$

With respect to atmospheric models, the main purpose of measuring experimental information or calculating kinetic information about the irreversible reactions is to see the effect these reactions will have on (W and/or X) species depletion or WX product formation, determined using the rate equation (Equation 1.14). In order to determine the rate of a reaction (rate v_0), either the rate of consumption of the reactant(s) or production of the product(s), at any given time during the reaction process, the rate law of that reaction must also be known. This rate law or rate equation express v_0 as a function of all the concentrations of all the reactants, as shown in Equation 1.14, and these rely on three factors: the reactants' concentrations, referred to as *[W]* & *[X]*; the reaction orders, *w* & *x*; and the thermal rate constant, *k(T)*, the key kinetic descriptor. The order of the reactants refers to how many stoichiometric units of that reactant take part in the rate determining step, and these reaction orders dictate the relationship between reactant concentration and rate. Examples of this includes where the rate is: first-order with respect to reactant *W*, where the decline of *[W]* is in a linear relationship with the decreases in rate; second-order with respect to reactant *W*, where a decline of *[W]* causes a decrease in rate that is exponential; or zero-order with respect to all reactants, where the rate is not determined by reactant concentration, where the important species may be a catalyst. Often each reactant can have a different order (i.e. first-order with respect to reactant *W* and second-order with respect to reactant *X*) and the sum of these individual orders are collectively the *overall order of the reaction*.[94]

$$\text{rate } v_0 = k(T) \times [W]^w \times [X]^x \qquad \textit{Equation 1.14}$$

$$k(T) = A/c^0 \times e^{-Ea/RT} \qquad \text{Equation 1.15}$$

As shown in Equation 1.15, the rate constant, is the key kinetic descriptor of the relationship between rate and the *activation energy* (E_a), also referred to as the energy barrier. This rate constant also includes a *pre-exponential factor* (A), which is dictated by entropic factors and collision orientation. One crucial point here is that the *pressure* or *concentration function* (c^0) in Equation 1.15 does not produce pressure-dependence for bimolecular rate constants, due to the presence of the exponential component ($e^{-Ea/RT}$), which is also pressure-dependent (as displayed in greater detail in the derivation of the computational rate constant in Equations 1.19—1.34). This cancels out any pressure-dependence caused by the c^0 component. For this reason, the c^0 function is often integrated into the pre-exponential, when Equation 1.15 is displayed in the literature.[95] However, the author has separated them here to show that, when analysing a bimolecular gas-phase process, the inverse pressure ($1/c^0$) component of the pre-exponential causes the rate constant to be expressed in cm^3 molec.$^{-1}$ s^{-1} units (often shortened to cm^3 s^{-1}).

This link between energy barriers and rate constants shows that if a theoretical rate constant is to be calculated, at a minimum one requires the one-dimensional potential energy surface (PES) along the reaction coordinate. To calculate this PES, the structures and the energies of key stationary points (minima and transition states) on the PES need to be computed. An example PES for OH + NO_3 is provided:

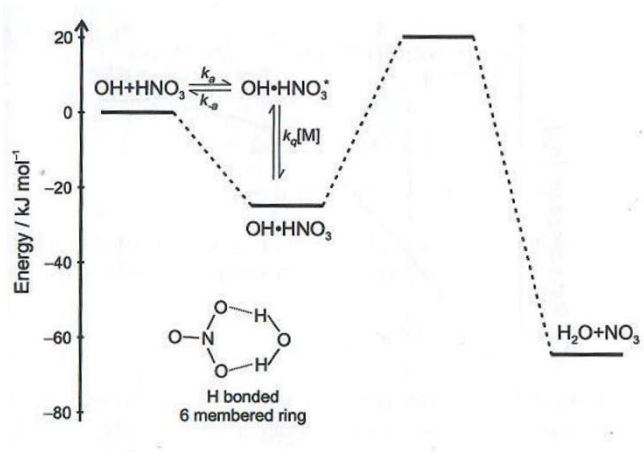

Figure 1.6: Example one-dimensional potential energy surface (PES) for the OH + NO_3 reaction involving stages from left to right of: raw reactants; pre-reaction complex; transition state; and products.[96]

This PES displays an important contrast between the reversible formation of a pre-reaction complex (PRC) and the irreversible nature of product formation, where the reverse reaction would involve overcoming a very large positive-going *transition state* (TS) energetic barrier. The degree of preference for the forward reaction (r_1) over the backward reaction (r_{-1}) is expressed in the PRC equilibrium constant, K_{EQ}, in Equation 1.18:

$$rate\ (W+X \rightarrow PRC) = rate\ (PRC \rightarrow W+X) \qquad \textit{Equation 1.16}$$

$$k_1 \times [W] \times [X] = k_{-1} \times [PRC] \qquad \textit{Equation 1.17}$$

$$K_{EQ} = \frac{[PRC]}{[W] \times [X]} = \frac{k_1}{k_{-1}} \qquad \textit{Equation 1.18}$$

K_{EQ} for the formation of these PRCs is derived from the rate equations at the point of equilibrium, where the rate of forward reaction and backward reaction are equal (shown in Equations 1.16 & 1.17). This generalised concept is referred to as steady state theory. Re-arrangement of this equation to Equation 1.18 uses the PRC in place of the original reactants, W & X, and is derived by using the *k(T)* for forward PRC formation reaction, k_1, divided by that of the reverse PRC decomposition reaction, k_{-1}.

This thesis relies on computed kinetic and thermodynamic properties for the systems under investigation, therefore the relative energies of all stationary points on the PES need to be identified. This total energy can be artificially broken up into several different sets of contributions, such as total electronic energy (ε_0), which is the energy of formation of that single fixed geometry at the stationary point. Vibrational contributions can be incorporated into the total energy to produce the energy of the system at 0 K, known as the *zero-point energy* (ZPE): the lowest harmonic energy level at the bottom of the internuclear potential energy well. This ZPE does not take into consideration the thermal energy from molecular movement along translational (E_t), rotational (E_r), vibrational (E_v), and electronic (E_e) degrees of freedom, shown in Equation 1.19, referred to as *internal thermal energy* (E_{tot}).[97,98] As seen in Equation 1.20, internal thermal energy (ε_{tot}) at 298 K and the total electronic energy (ε_0) makes up the *total thermal energy* at 298 K (U_{298K}).

$$\varepsilon_{tot} = E_t + E_r + E_v + E_e \qquad \textit{Equation 1.19}$$

$$U = \varepsilon_0 + \varepsilon_{tot} \qquad \textit{Equation 1.20}$$

One of the important components to determining the rate constant is the enthalpy of both the reactants and the transition state, which is a description of the internal energy of the system maintained at a constant pressure and volume adjusted (see Equation 1.21).[94]

$$H_{298K} = U_{298K} - p_0V \qquad \textit{Equation 1.21}$$

Another important contributor to the rate constant is the entropy of the system: a measure of the distribution of the energy between the translational (S_t), rotational (S_r), vibrational (S_v), and electronic (S_e) modes of motion of the system (see Equation 1.22). The entropy is low if the motion involved is distributed over a small number of modes as that makes the reaction more likely to occur spontaneously. The *Gibbs free energy*, G, is a comprehensive thermodynamic term to describe the maximum energy stored in the

system, that is free for work, and it is composed of the entropy and thermal enthalpy of the system as shown in Equation 1.23.

$$S_{tot} = S_t + S_r + S_v + S_e \qquad \textit{Equation 1.22}$$

$$G = H - TS \qquad \textit{Equation 1.23}$$

This Gibbs Free energy links the thermochemistry of these molecules to the Arrhenius equation (see Equation 1.15). The Arrhenius equation combines the concepts of the Boltzmann distribution and the activation energy, to produce the rate constant but which also incorporates a pre-exponential (*A*) factor accounting for the likelihood of reaction based on collisional orientation probabilities. The activation energy and the pre-exponential factors also account for the enthalpy and entropy changes within the reaction. The relative enthalpy (ΔH) is assigned to be the activation energy, whereas the pre-exponential incorporates a natural exponential of the relative entropy (ΔS), and how these factors impact the rate constant (k(T)) and are described in Equations 1.24—1.25. [99]

$$k(T) = A \times e^{-\Delta H/RT} \qquad \textit{Equation 1.24}$$

$$A = \frac{k_B T}{h} \times e^{-\Delta S/RT} \qquad \textit{Equation 1.25}$$

Because of the nature of enthalpy and entropy factors this can all be displayed as a function of Gibbs free energy in producing the unimolecular rate equation (Equation 1.26). In this thesis, calculations are performed to determine two key parameters of any reaction: the theoretical rate constant, or k_{THEO}, used to ascertain the reactivity of the reaction; and the product branching ratio (Γ), which measures the proportional yield of competing reaction rate constants.

$$k_2 = \frac{k_B T}{h} e^{-(\Delta G_{TS} - \Delta G_{PRC})/RT} \qquad \textit{Equation 1.26}$$

To determine these rate constants for unimolecular reactions this is sufficient, however if the reactions are like OH + NO_3 seen in Figure 1.6, Equation 1.26 does not fully satisfy these requirements. This is because Equation 1.26 does not take into consideration the impact of pressure or the K_{EQ} of pre-reaction complex (PRC) formation. PRC formation must be considered because it can impact the degree of pressure or temperature dependence in the rate constant or product formation in many gas-phase reactions.

If the TS barrier is high in energy (large positive-going E_a), hotter conditions produce larger rate constants. This is because the thermal contributions to the collision energy are more significant. If the TS is lower in energy, the reactants already possess much of the energy required to react, even at lower temperatures, and excess energy facilitates PRC decomposition, so colder conditions produce larger rate constants. In addition, colder

temperatures can assist in stabilising pre-reactant complexes, orienting the system towards reaction – giving rise to a more favourable Arrhenius pre-factor.

The rate constant Equation 1.26 contains a constant c^0, a function of concentration, which is set to 1 for all unimolecular reactions, such as r_{-1} and r_2, and is unitless because they are not a function of concentration. However, for bimolecular reactions, such as many studied in this thesis, the pre-reaction complex formation reaction (k_1) is caused by the reactant colliding with the excess co-reactant (pseudo first order kinetic conditions), and therefore the c^0 is concentration of gas in the system (units = molec./cm^3). This therefore makes the concentration of gas in the forward reaction ($c^0_{r_1}$) a component of the K_{eq} equation. This is important as gas phase reactions require collisions with co-reactants.

$$K_{eq} = \frac{k_1}{k_{-1}} = \left(\frac{k_B T}{h c^0_{r_1}}\, e^{-\Delta G_{r_1}/RT}\right) \Big/ \left(\frac{k_B T}{h c^0_{r_{-1}}}\, e^{-\Delta G_{r_2}/RT}\right) = \frac{1}{c^0_{r_1}} e^{(-\Delta G_{r_1} + \Delta G_{r2})/RT} = \frac{1}{c^0_{r_1}} e^{-(\Delta G_{r_1})/RT}$$

Equation 1.27

For bimolecular systems, $c^0_{r_1}$ value is determined using the ideal gas law, which is derived from Boyle's law, Charles Law's and Avogadro's law.[100] This ideal gas law describes the thermodynamic behaviour of gases using a monoatomic *ideal* gas with no possible designated polarity, and therefore only undergoes elastic collision. This ideal gas law uses the universal gas constant (R = 8.3145 J K^{-1}) to describe the relationship between pressure (P_0) and temperature (T) of the system, with the volume provided (V) and the number of gas molecules (n) within the system. This is rearranged from Equation 1.28 to 1.29 to find the concentration of gas determined in number of molecule per cm^3, as a function of pressure and temperature, which in this thesis is assumed to be standard (P_0 = 1 atm and T = 298 K), unless otherwise stated. This can then be incorporated into the K_{eq} equation as shown in Equation 1.30.

$$P_0 V = nRT$$

Equation 1.28

$$c^0_{r_1} = \frac{n}{v} = \frac{P_0}{RT}$$

Equation 1.29

$$K_{eq} = \frac{RT}{P_0}\, e^{-\Delta G/RT}$$

Equation 1.30

To derive an accurate K_{EQ} value, the reversible *reactants* ⇌ *PRC* reaction is understood to be in equilibrium, with a PRC population remaining effectively unchanged. The PRC also progresses through an irreversible "unimolecular" reaction to the final product(s), where the rate constant for this pathway, k_2, is derived using Equation 1.34. However, the rate of PRC reaction to product is generally small enough not to affect equilibrium or consequentially K_{EQ} value, throughout. This is the *steady state approximation*. This means that the full bimolecular rate constant from reactants to products for that transition state barrier (k_{TS}), can be determined using a composite rate constant, as seen in Equations

1.32—1.34. If there are multiple TS barriers for a reaction, these k_{TS} are grouped into one rate constant (Equation 1.31).

$$k_{total} = \sum k_{TS}$$

Equation 1.31

$$k_{TS} = K_{eq} \times k_2$$

Equation 1.32

$$K_{eq} = \frac{RT}{P_0} e^{-\Delta G_{PRC}/RT}$$

Equation 1.33

$$k_2 = \frac{k_B T}{h} e^{-(\Delta G_{TS} - \Delta G_{PRC})/RT}$$

Equation 1.34

These rate constant equations are used in this study to calculate the theoretical rate constants for the reactions computed.

1.5 The Importance of Alkene Ozonolysis in the Troposphere

Both the unimolecular and bimolecular rate constants described above are critical to understanding how quickly tropospheric species are generated or breakdown in the troposphere and in differentiating between which of the numerous production and depletion mechanisms contribute most considerably to the abundance of those species. The key reactions undertaken in this thesis are major depletion processes for harmful pollutants, such as O_3 and SO_2; and/or they generate species that perform this function, such as OH radicals or Criegee intermediates (CIs). In the following sections a background to the *main* species studied in this thesis, common alkenes (Sections 1.5.1—1.5.5), Criegee intermediates (Sections 1.5.3 and 1.6) and hydrofluoroolefins (Section 1.7) is provided.

1.5.1 Sources and Sinks of OH radicals in the Atmosphere.

Tropospheric pollutant removal can proceed through *physiological* sinks, which include: dissolving in lakes and oceans, such as with CO_2 dissolving into sea water; atmospheric escape into space by low mass species (~50 g/s of helium is lost from earth); and through molecules and particulates being removed by water droplets and being rained out.[2,101,102] Water droplet adsorption usually occurs via diffusional collision, a mechanism that benefits small diameter species (<0.1 μm), or via initial collision that favours large diameter species (>1 μm). This leaves a group of species with a range of medial diameters (referred to as the "Greenfield" gap), that are less likely to be rained out and therefore are prone to have longer atmospheric residence times.[103,104]

As well as providing a pathway for physiological removal, pollutant collision with, and adsorption by, a water droplet can also facilitate another type of removal process, through chemical reaction. The surface of the droplet can either provide a viable co-reactant for the pollutant or facilitate a reaction with another atmospheric species by providing a catalytic surface.[105]

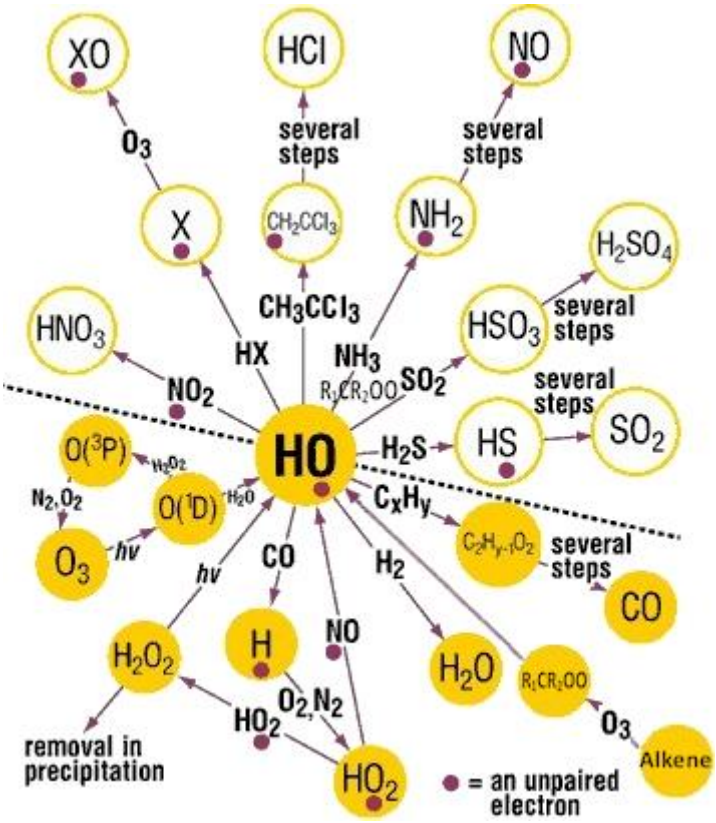

Figure 1.7: A diagram of OH radicals (represented by HO• in this diagram only) with their sources and sinks.[106]

OH radicals are known as an *atmospheric detergent*, as their oxidative capacity and tropospheric abundance, means they play a very significant role in cleansing the atmosphere of various pollutants, including SO_2, NO_2, alkanes and many other species (see Figure 1.7).[2] The oxidative capacity of OH radicals comes from the oxygen's radical lone electron and small molecular structure. The reaction of OH radicals with other pollutants has a strong propensity to form more stable, less toxic products than their precursors, such as CO_2 from CO and HNO_3 from NO_2.[107,108] OH radicals reactions can also produce hydroperoxyl and alkylperoxy radicals (HO_2 & RO_2), both also sinks for toxic pollutants, such as NO_x.[15]

This *detergent* role demonstrates the importance of OH radicals in the troposphere, however, as the main source is photolysis of O_3 in the presence of water vapour, their abundance is significantly diminished by the lack of UV radiation at night-time or in shaded areas. On the other hand, while night-time OH radicals are significantly less abundant (~1.85×10^5 molec./cm^3) than during daytime (~1×10^6 molec./cm^3), they are not depleted to a negligible level, due to non-photolytic OH yield from the gas-phase ozonolysis of alkenes.[10,109-111] This production of OH radicals from alkene ozonolysis has been verified experimentally for a range of alkenes and the OH yield can vary

significantly, for example from ozonolysis of styrene (~0.07) compared to limonene (~0.86).

The prior literature investigating O_3 + alkene reactions shows that these reactions have experimental rate constants (k_{EXP}) large enough to be very atmospherically significant (~10^{-18}—10^{-14} cm^3 s^{-1}).[10] Similarly large literature k_{EXP} values shown for ozonolysis of propene, methyl vinyl ketone (MVK) and styrene (1.0×10^{-17}, 4.5×10^{-18} & 1.2×10^{-17} cm^3 s^{-1}, respectively) show that ozonolysis is viable for alkenes with a range of functional groups, not just those that contain straight chain substituents. [112] This importance of the O_3 + alkene reaction is significant enough to be responsible ~10% of isoprene depletion, the most prevalent VOC in the troposphere.[21]

Alkene ozonolysis contrasts with the O_3 reactions with saturated alkanes, such as CH_4 and n-butane, which have very low experimental rate constants (k_{EXP} ~1.4×10^{-24} & 9.8×10^{-24} cm^3 s^{-1}).[10,113,114] The importance of a double bond in ozonolysis reactions, inferred from this contrast, is confirmed by the low rate constants for the ozonolysis of substituted alkanes with functional groups including: aromatic alcohols, such as phenol and o-cresol (<10^{-21} & <2.6×10^{-19} cm^3 s^{-1}) and ketones, like 3-methyl butanone (6.3×10^{-21} cm^3 s^{-1}).[10] These low rate constants for alkanes make them less likely to produce OH radicals during ozonolysis compared to the ozonolysis of alkenes.

1.5.2 Ozonolysis of Alkenes

Ozonolysis of alkenes was first hypothesised for the liquid phase reaction in 1949 by Rudolph Criegee and later verified in 1975.[115-117] This led him to postulate the mechanism for the gas-phase ozonolysis of various alkenes, shown in Figure 1.8, which has subsequently been verified for such alkenes as: 2,3-dimethyl-2-butene, *cis*-2-hexene and ethene.[10,118,119] Computational studies of the ozonolysis of 1,3-butadiene, isoprene and carene all show the same reaction pathway.[120-122] O_3 + alkenes can also react via an "epoxidation" channel (<1% for mono-alkenes and <5% for dienes) which produces O_2 and an epoxide (explored further in Appendix Section 1.7).[120-122]

Figure 1.8 shows a sample ozonolysis mechanism. The first step is a concerted electrophilic addition from the two terminal O atoms in O_3. This produces a heteroatomic 5-membered ring called a primary ozonide (POZ), with internal torsional strain and ~200—250 kJ mol^{-1} of excess energy, almost guaranteeing instantaneous POZ fragmentation.[123] The short-lived POZ fragments along the C-C bond and one of the two O-O bonds, subsequently forming a carbonyl compound, such as an aldehyde or ketone, and a Criegee intermediate (CI). Due to the excess energy produced by the exothermic reactions of both

the ozonolysis and POZ decomposition steps, a large proportion of the CIs are produced with significant internal excitation often referred to as a *hot* or *excited* CI. However, several factors that increase the stabilisation fraction of the CI population include: formation from the less exothermic ozonolysis processes; the internal electronic stability of the CI; and larger substituent groups on the carbonyl co-product.[10,124,125]

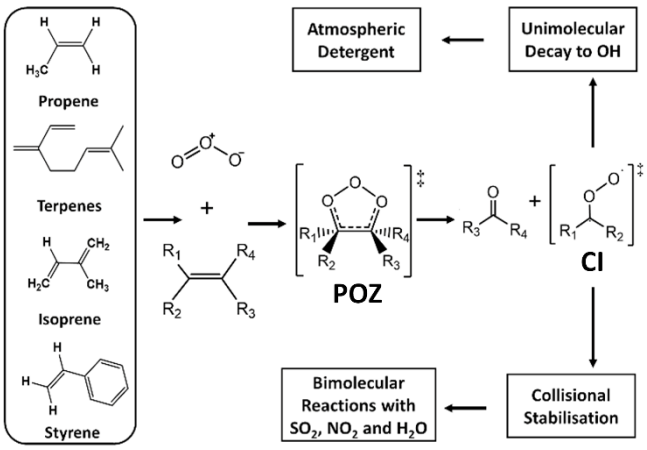

Figure 1.8: Reaction schematic for the ozonolysis of atmospheric alkenes and subsequent Criegee intermediates processes.

About 37%—50% of the tropospheric *excited* CI yield undergoes rapid unimolecular decomposition due to their initial internal energy. [123,126-135] The remaining CIs are collisionally quenched producing stabilised Criegee intermediates (sCIs). These can break down through pathways such as slower, thermal unimolecular decomposition, bimolecular reactions with other trace gases or UV photolysis.[123,126,132,134,135] One important experimentally verified observation from the literature is that these CIs generated from alkene ozonolysis are a major source of OH radicals.[136-138]

1.5.3 Key Characteristics of Criegee Intermediates (CIs)

Key to these CI species, featured in Figure 1.9, is the carbonyl oxide functional group ($C{=}O^{+}{-}O^{-}$). Carbonyl oxides are frequently described in the literature as having both zwitterionic and biradical character related to each other as resonance structures, although recent computational examinations of the CI electronic structure suggests the systems have greater zwitterionic character.[139,140] It is worth noting that the degree of zwitterionic or biradical character affects the CO bond length, R_{CO}, in the CI, as the average C=O bond (zwitterionic representation) is shorter than a single C-O bond (the biradical depiction). The greater unsaturated character of the C=O bond in the zwitterionic CI leads to a more electron rich C=O bond with a highly electronegative central oxygen. This then leads to increased repulsion from a highly electronegative

terminal oxygen and an increased O-O bond length, R_{OO}, compared to the biradical CI. So, the degree of biradical/zwitterionic character can be measured by the R_{OO}/R_{CO} bond ratio.

The two R groups attached to the carbonyl oxide can be composed of substituents with a wide range of size and complexity, for example from phenyl (Ph) to fluorine groups (-F) and from —H to dodecalkyl (—$(CH_2)_{11}CH_3$) groups. The interaction between the substituents and the core carbonyl oxide group can alter the sCI chemistry with respect to both unimolecular decomposition and bimolecular reactions with other atmospheric species (discussed in Chapters 4—5). If the R_1 and R_2 substituents differ, there will be two chemically distinct conformers: the *syn*-CI, where the largest R substituent is *syn* to the terminal O; and the *anti*-CI, which has the largest R substituent *anti* to the terminal O. They typically exhibit a high barrier to interconversion (~160 kJ mol^{-1} for CH_3CHOO) and have different reactivities.[141,142] If the CI has an unsaturated bond in one of the substituents in the α-carbon position, there will be two conformers, the *cis* and *trans* conformer, where the unsaturated bond is either perpendicular or opposite to the C=O-O bond respectively. Both these phenomena are exhibited for the four conformers for the MACROO sCIs as shown in Figure 1.9.

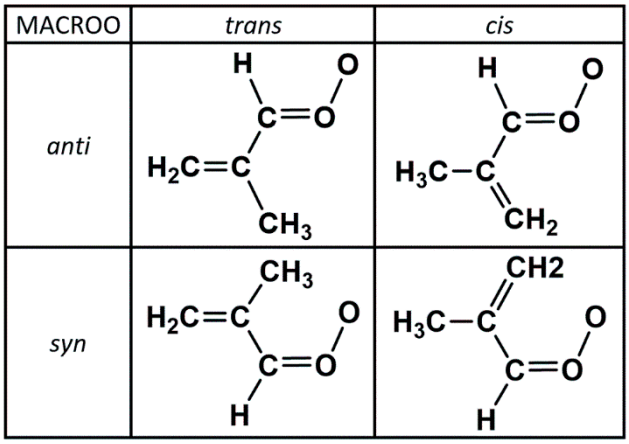

Figure 1.9: MACROO sCI conformers based by characteristics.

This categorisation system divides the various sCIs into: *syn*-sCIs, *anti*-sCIs, and disubstituted sCIs, such as *syn*-CH_3CHOO, *anti*-CH_3CHOO & $(CH_3)_2COO$ respectively; this notation is used throughout this thesis. Despite having two identical substituents (—H), CH_2OO is often categorised separately from any of these groups. This is because it has a reactivity that does not involve the electrochemical impacts of the *syn*-/*anti*-substituted groups. The —H groups are also small and so they only have a limited steric impact. Throughout this thesis these categorisations are important in the analysis of sCIs both in terms of bimolecular reactions and unimolecular decomposition.

The excess energy produced by the highly exothermic ozonolysis reaction has led to challenges in experimentally generating sCIs in a laboratory environment.[143] The first direct detection and assignment of an sCI was executed by Taatjes *et al.*, where formaldehyde oxide, CH_2OO, was produced from reacting dimethyl sulfoxide (DMSO) with Cl radicals in the presence of gaseous O_2 (Equations 1.35 & 1.36).[144]

$$CH_3SOCH_3 + Cl \rightarrow CH_3SOCH_2 + HCl \qquad \textit{Equation 1.35}$$

$$CH_3SOCH_2 + O_2 \rightarrow CH_3SO + CH_2OO \qquad \textit{Equation 1.36}$$

Another method for sCI production was used by both Welz *et al.* and Huang *et al.* where a diiodoalkane, like CH_2I_2, is photolyzed and the resultant photofragment reacted with oxygen: $CH_2I + O_2$ (Equations 1.37 & 1.38).[145,146]

$$CH_2I_2 + h\nu \rightarrow CH_2I + I \qquad \textit{Equation 1.37}$$

$$CH_2I + O_2 \rightarrow CH_2OO + I \qquad \textit{Equation 1.38}$$

This method does have significant drawbacks including that diiodoalkanes are: expensive, toxic and reactive, making their storage difficult; and it does not directly correlate with the branching fractions of the CIs from alkene ozonolysis [143,147] While, these methods were initially utilised to obtain CH_2OO, they can also be used to obtain other CIs, such as the "mono-substituted" methyl formaldehyde oxide conformers, *syn*-/*anti*-CH_3CHOO (Equations 1.39 & 1.40) and "disubstituted" dimethyl formaldehyde oxide, $(CH_3)_2COO$.[148,149]

$$CH_3CHI_2 + h\nu \rightarrow CH_3CHI + I \qquad \textit{Equation 1.39}$$

$$CH_3CHI + O_2 \rightarrow \textit{syn}\text{-}/\textit{anti}\text{-}CH_3CHOO + I \qquad \textit{Equation 1.40}$$

1.5.4 The Importance of a Taxonomic Classification System for Alkenes

As these alkene ozonolysis reactions are known to be effective tropospheric sinks for the important pollutants, alkenes and ozone, as well as a non-photolytic source for "atmospheric detergent" OH radicals, knowledge of their reaction rate constants and product branching ratios are particularly important in modelling the atmosphere. As seen previously, it is alkene reactions with gaseous O_3 that produces secondary OH radicals. As the ozonolysis chemistry changes depending on the size and composition of the >C=C< substituent groups, the OH yields for this vast number of alkenes become difficult to model without a form of taxonomic classification.

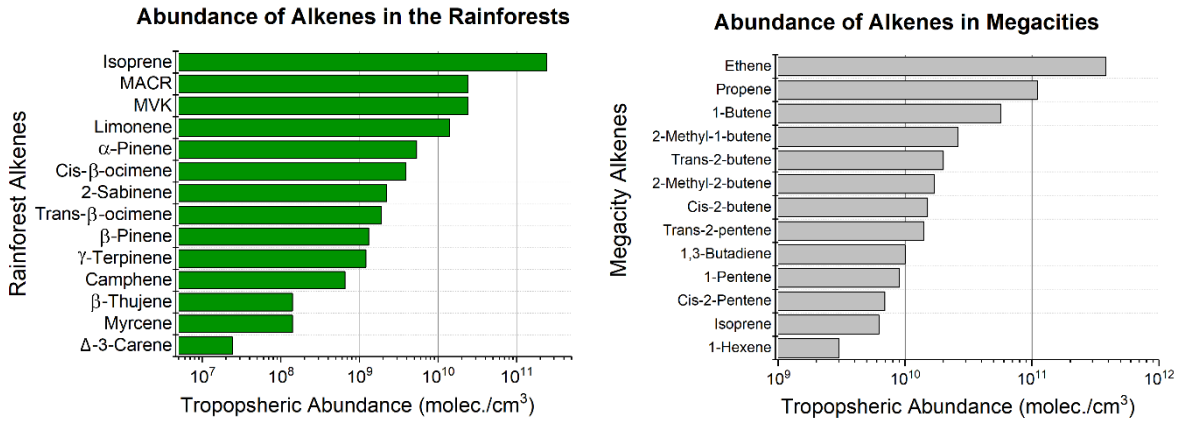

Figure 1.10: Fractional prevalence of different alkenes in example natural and anthropogenic environments.

Often atmospheric chemists divide alkenes into two groups based on a structural and source classification (see Figure 1.10): larger structures that predominate in natural environments, like styrene, isoprene and α-pinene; and the smaller structures, that predominate in anthropogenic environments, such as propene and isobutene.[81,150-153] This natural/anthropogenic classification of alkenes can work well in very local atmospheric models, but the rate constants and OH yields show significant cross-over between groups and large diversity within these classifications. This implies that a much more rigorous analysis of literature trends is vital to understand any relationship between the structure and functionality of the alkene substituent groups, and the ozonolysis reaction chemistry.

1.5.4 Literature Experimental Trends in Alkene Ozonolysis

Comparison of computational data generated in this thesis with existing experimental data is vital for benchmarking the computational work and for comparing trends across molecular systems. Developing accurate trends in structure compared to reactivity is vital, because it is not possible to study every potential tropospheric alkene ozonolysis reaction to their fullest extents. One way this can be performed is through the generation of taxonomic classifications, grouping like-alkene structures and their corresponding k(T) value & product branching ratio (Γ). These taxonomic groups can reduce the number of computational calculations required and represent the chemistry of this group of O_3 + alkene reactions to a single equation or group of equations. These classifications can be used at the *ab initio* level, but can also be used in atmospheric models. The *AtChem 2* software uses a similar taxonomic group, RO_2, to simulate the reactions of a large variety of similar alkyl peroxide radicals, reducing the number of separate calculations that need to be undertaken considerably.[154]

There is some literature precedence for alkene taxonomic classification in this area. One example of this was a structure-activity relationship (SAR) analysis by McGillen *et al.*, which linked the alkene structure and the experimental rate constant (k_{EXP}) value.[118,155] k_{EXP} was linked with structure using an inductive and a steric impact of substituent groups.[118,155] The *inductive factor* is deduced from the number of alkyl substituent groups on the >C=C< bond, creating an electron donating impact and therefore *inducing* a destabilisation of the alkene bond, allowing it to become more reactive. This is verified by the increased k_{EXP} value for 2,3-dimethyl-2-butene over ethene (1.24×10^{-15} & 1.68×10^{-18} $cm^3\ s^{-1}$).[109] This is counterbalanced with a *steric factor* which is a sum of the different steric interferences anticipated depending on proximity of extra alkyl groups to the >C=C< bond.[118]

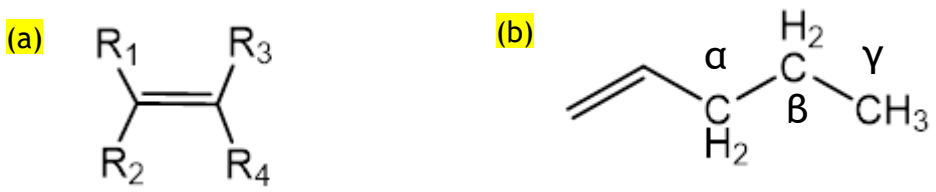

Figure 1.11: Comparison of Alkene substituent positions (Figure 1.11a); and a, β & γ branching positions (Figure 1.11b).

The effect of branched substituent alkyl chains on rate constants is reduced to negligible when additional alkyl groups are attached to the γ-positions or beyond (for greater explanation of this see Appendix Section 1.6.4).[156,157] This approximation is used by McGillen *et al.*, who estimate that additional alkyl branching on γ- carbons and beyond has no effect on the k_{EXP} value.[118] Heteroatom substitution also alters rate constants and is explored in a later SAR.[155]

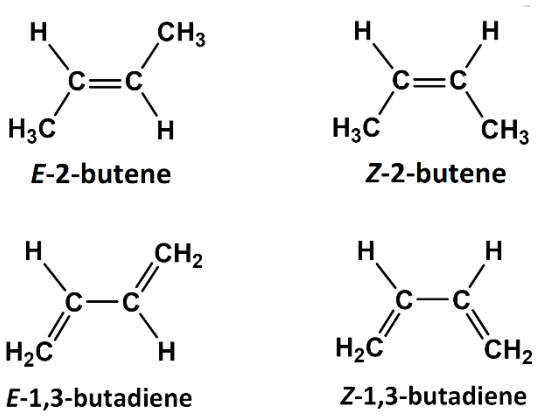

Figure 1.12: Example of E-and Z-butene conformers and E-and Z-1,3-butadiene conformers

The SAR model initially created by McGillen *et al.*, does not include the effect of different conformeric orientations. As shown in Figure 1.12, alkenes like 2-butene can have the two alkyl substituent groups either in the *trans* (or *E*) orientation, where the CH_3 groups are in opposite positions to each other; or the *cis* (or *Z*) position, where they are orthogonal to each other. This separates these alkenes into two distinct taxonomic groups, *cis*- & *trans*-alkenes, that frequently display markedly different bimolecular reaction rates. These groups have a high degree of *internal coherence* in the experimental literature, meaning that when comparing the ozonolysis of 2-pentene and 2-butene, the *cis* stereoisomers see a similarly lower k_{EXP} value and OH yield compared to their *trans* counterpart.[10,118] Alkenes which have two C=C bonds, known as dienes, also exhibit *cis*-/*trans*-isomerisation. Shown in Figure 1.12 is an example of a diene, 1,3-butadiene ($H_2C{=}CH{-}CH{=}CH_2$), where the *trans*-isomer has the two C=C bonds in opposite positions to each other. The *cis*-isomer has the two C=C bonds in orthogonal positions to each other.[121] As the C-C bond that would rotate between the two conformers has delocalised π-electron overlap between the two C=C double bonds, the C-C bond gains some double-bonded character. This conjugation lowers the energy of the overall molecule and provides a higher barrier to internal rotation than a typical C-C single bond. Despite this conjugative effect, dienes typically react with ozone in a manner identical to 'monoenes'.

Ozonolysis studies of various alkenes have included the unsaturated oxygenates such as unsaturated alcohols, aldehydes, ketones and esters. It has been found that they exhibit the same stages of the ozonolysis reaction profile, principally reacting along the >C=C< bond rather than along the C=O unsaturated bond.[109,155] By-products of these reactions include hydroxy-aldehydes and hydroxy-ketones alongside their Criegee intermediate equivalent. One distinct set of reactions is the ozonolysis of cyclic alkenes like 1,2-dimethyl-1-cyclohexene or heteroatomic cyclic alkenes, such as furans.[158,159] These differ from typical alkene ozonolysis reactions because the cyclic nature of the alkene reactant means that only one final product is formed, a long chain with an aldehyde/ketone group at one end and a carbonyl oxide (COO) group on other end. The nature of a cyclic alkene is a reduced ability for internal rotation which produces steric hindrance/ring strain when the O_3 + cycloalkene reaction occurs.

Experimental product branching ratio (Γ_{EXP}) values are less available within the current literature than k_{EXP} values for two major reasons. The CIs produced from alkenes ozonolysis often undergo rapid unimolecular decomposition meaning that detection of these CIs is often very challenging. This can be overcome by the observation of either the sCI yields in conjunction with unimolecular decomposition products, or by recording the

yield of the aldehyde/ketone by-product. The measurement of the aldehyde/ketone by-product is an imperfect tool for measuring CI yield because the high OH yield may have an impact on the aldehyde/ketone by-product concentration present and because it is difficult to determine a yield that discriminates between CI conformer yields, as these high energy CI conformers may interconvert. Until very recently, the difference in yields of the different sCI conformers was inferred using OH yield.[109,160–162] This inability to accurately discriminate between CI conformers at point of production is problematic because these indirect measurements in the literature infer that changes in the alkene structure, e.g. *cis*-/*trans*-isomerisation, can alter the CI yield but without quantification.[109,163] The effect of alkene substituents on the rate constants and Γ_{THEO} of ozonolysis is studied in Chapters 3 and 6.

1.5.5 Criegee Intermediates as a Source of OH Radicals

The unimolecular decomposition of CIs falls into two groupings: rapid fragmentation of internally energetic CIs that are formed upon initial ozonolysis, which often produces OH radicals; and sCI unimolecular decomposition through cyclisation or H-transfer after this initial energy has been collisionally dissipated. The prompt fragmentation can lead to various atmospheric species including CO, CO_2, HCO and CH_3OH.[108,133,135,164–167] The identity and the Γ_{THEO} of CIs produced is critical to understanding the overall OH yield of an alkene ozonolysis, demonstrated by the fact that $CH_2OO^{\ddagger}$ has a smaller OH yield (~0.12) than $CH_3CHOO^{\ddagger}$ (~0.23±0.18).[108,133,135,164–167]

1.5.6 The Atmospheric Impact of Aldehydes and Ketones

Also of interest in this study are the carbonyl co-products of the O_3 + alkene reactions: aldehydes and ketones. Both folic emissions of isoprene and alkene evaporation from fuels have been shown to be notable sources of formaldehyde (HCHO). The production of gaseous HCHO from oxidation of terpenes and other alkenes, by O_3 and OH radicals, and the subsequent increased HCHO tropospheric abundance is harmful to human health.[168,169] Often emitted from smoking cigarettes, HCHO is chemically harmful to humans because it can cause skin irritation and is carcinogenic and toxic if inhaled.[16,170,171] HCHO is identified by the US environment protection agency to be the most important carcinogen found outdoors, after PM and O_3.[172]

Although a tropospheric pollutant, significant proportions of these aldehyde/ketone emissions are removed by photolysis, by being dissolved in the oceans or via reactions with OH radicals.[54,173] Photolysis of HCHO and other aldehydes are known to produce H +

HCO/RCO.[15] These HCO or RCO then react with O_2 to produce CO alongside gaseous HO_2 and RO_2 radicals.[15] This photochemical process is known to contribute tropospheric abundances of HO_2 and RO_2 radicals, throughout the year.[174] Formaldehyde is emitted from many building materials found indoors, like plywood, glues, and paints and are removed by reaction with OH radicals also producing HO_2 & RO_2 radicals.[174,175] The problems that arise from the increases in formaldehyde emissions that build up inside the house can be mitigated with increased air flow and specially chosen houseplants.[176]

sCIs can also react with the carbonyl species co-products, and studies of these reactions can be found in both computational and experimental literature. These analyses show a potentially significant role for these carbonyl species as CH_2OO reactions with CH_3CHO and $(CF_3)_2CO$ have large k_{EXP} values (10^{-13} — 10^{-12} cm^3 s^{-1}).[177-180] The theoretical analysis by Ma Qiao *et al.* shows that final products of reactions between aldehydes/ketones with the sCIs, CH_2OO and PhCHOO may include noteworthy products like formic and benzoic acid.[181] In Chapter 5, some sCI reactions with aldehydes like HCHO, CF_3CHO and CF_3CFO are analysed. This is due to their significance in local atmospheric concentrations and that they may have an enhanced role as sCI sinks due to their status as co-products of the same O_3 reaction.

1.6 Criegee intermediates (CI) Chemistry

1.6.1 Unimolecular sCI Reactions

As mentioned briefly above, prior to collisional stabilisation, the CIs produced from ozonolysis may undergo molecular fragmentation processes to produce a variety of different products. After collisional stabilisation, unimolecular decomposition is still viable, energy constraints mean that there are fewer available fragmentation pathways and the sCIs decompose at much slower rates. The main unimolecular reactions involved in the decay of sCIs, whether it be via *ring-closure*, *H-migration* or *internal rotation*, all of which feature in Figure 1.13, varies depending on the substituents on the sCI and their orientation.[182] The unimolecular decomposition and therefore the atmospheric lifetime depends fundamentally on these unimolecular reaction mechanisms. For example, the slower *1,3-ring closure* mechanism of CH_2OO produces a longer lifetime (τ_{uni}~3s) than sCIs with *syn*-CH_3 groups (τ_{uni}~0.002s), which have a more swift *1,4-alkyl H-migration* sCI breakdown mechanism.[183-185]

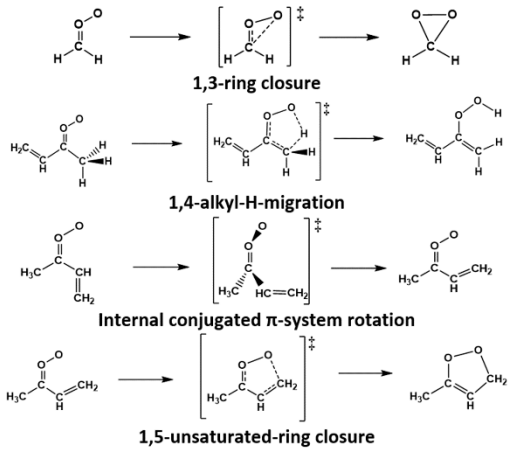

Figure 1.13: Common unimolecular reactions involved in the sCI decay process.[182]

CH_2OO, the most exhaustively investigated sCI, is also the simplest and most abundant sCI, with a relatively high concentration in environments like the amazon rainforest (~10^5 molec. cm^{-3}).[182] Nevertheless, measuring sCI abundance at this low level is extremely difficult, especially considering the short sCI lifetimes. So, in a Novelli *et al.* study, the steady-state concentrations of sCIs in the lower troposphere are estimated using two methods.[186] Firstly, as the inlet pre-injector laser-induced fluorescence assay by gas expansion (IPI-LIF-FAGE) technique is sensitive to OH formed from unimolecular sCI decomposition, Novelli *et al.* used this technique in conjunction with rates for the sCI ⟶ OH reaction, to indirectly measure sCI concentrations.[186] A second method, used by Novelli

et al. and other studies, involves: measuring tropospheric alkene abundances and, using known alkene ozonolysis chemistry, to generate an sCI production rate; using unexplained production rates of OH (likely generated from the sCI ⟶ OH reaction) and H_2SO_4 (likely generated from sCI + SO_2) to estimate sCI depletion rates; and using these production and depletion rates to estimate an overall steady-state sCI abundance.[182,186] Vereecken *et al.* reported that the primary unimolecular decomposition mechanism for CH_2OO is *1,3-ring closure*, where the terminal O undergoes bond formation to the carbon atom with a relatively low rate constant (k_{UNI} ~ 0.3 s^{-1}).[111,182] However, other sCIs that react via *1,3-ring closure*, like *anti*-CH_3CHOO and *anti*-EtCHOO, do have larger k_{UNI} values (53 & 74 s^{-1}).[182]

sCIs with a *syn*-alkyl group and available α-Hs, such as *syn*-CH_3CHOO, $(CH_3)_2COO$ and *syn*-$H_2C{=}CH{-}C(CH_3)OO$, have a more rapid accessible unimolecular reaction channel: *1,4-alkyl-H-migration*. This process involves a H-transfer from the *syn*-CH_3 group to the terminal O to produce a vinyl hydroperoxide (VHP). This gives a moderately high overall k_{UNI} (~350—650 s^{-1}) that usually has a larger k_{UNI} than *1,3-ring closure*.[182] For example, the k_{UNI} for this pathway is ~136 s^{-1}, larger than the k_{UNI} for *anti*-CH_3CHOO (~53 s^{-1}), which can only react via the *1,3-ring closure* pathway.[111,182]

If there is a >C=C< bond in the α-position with respect to the carbonyl oxide, the sCI forms separate *cis* and *trans* conformers. The high interconversion TS_{ISO} barrier of this *internal conjugated π-system rotation* is more important for CIs with unsaturated groups in the *syn*-position, such as *anti*-$H_2C{=}CH{-}C(CH_3)OO$ (see Figure 1.13). Without this TS_{ISO} pathway, *anti*-$H_2C{=}CH{-}C(CH_3)OO$ would have to fragment via the *1,3-ring closure* pathway, but by effectively linking the *trans* and *cis* conformer via TS_{ISO}, the system can still access the *1,4-alkyl-H-migration* channel.

That swift unimolecular decomposition reaction of the *cis*-sCI conformer of *anti*-$H_2C{=}CH{-}C(CH_3)OO$ is referred to as a *1,5-unsaturated-ring closure*, which, as seen in Figure 1.13, involves the terminal oxygen attacking the *β*-carbon. This produces a very large k_{UNI} value (~10^5 -10^7 s^{-1}).[182] This *1,5-unsaturated-ring closure* mechanism is not observed for sCIs like *syn*-$H_2C{=}CH{-}C(CH_3)OO$ where the conjugated group in the *anti*-position.[182]

Other sCI reaction channels can exist but are of limited consequence for the sCIs in this work. Unimolecular reaction studies have been performed for the *1,4-alkyl-H-migration* unimolecular decomposition of *syn*-CH_3CHOO, $(CH_3)_2COO$ and both *cis* and *trans* conformers of *syn*-$CH_2{=}CHC(CH_3)OO$, in Section 4.6.

1.6.2 Bimolecular Depletion Mechanisms for sCIs

If the carbonyl oxide group is predominantly zwitterionic, then the moiety is also polar and thus likely to be highly reactive, even with systems that have weak polarities. sCIs are involved in many important bimolecular reactions with other trace atmospheric species, particularly those that are polar, maximising dipole-dipole interactions. As an example, OH radicals are normally thought of as the "atmospheric detergent" but CH_2OO competes with OH as a sink for polar pollutants, like HNO_3 and NO_2, especially in environments like boreal forests where the [CH_2OO] is high (~1-5 × 10^4 molec. cm^{-3}).[111]

An example of a tropospherically important bimolecular sCI reaction is that of sCI + SO_2. This involves not only the removal of SO_2, a toxic substance known to cause respiratory problems, but these reactions have important secondary products too, such as SO_3.[187–190] SO_3 is implicated in the production of both acid rain and atmospheric aerosols, making them vital to include in atmospheric models.[184,191,192] Bimolecular sCI reactions with H_2O, $(H_2O)_2$ and alcohols have also been shown to be crucial because they are important sources of α-hydroxy-hydroperoxides (HHP) and α-alkyoxyalkyl hydroperoxides (AAAH), which are significant sources of OH radicals.[51,55,105,193–195] sCIs also readily reacts with gaseous tropospheric species including aldehydes, oxidants and acids (both organic and inorganic), such as CH_3CHO, NO_2, HNO_3 and HCl respectively.[111,105,184,191,192,196]

Given the breadth of sCI bimolecular tropospheric reactions, and the abundance of CIs in both urban and pristine environments, it is clear that sCI chemistry is of great atmospheric importance. However, the scientific community is still lacking a great deal of information on many of the sCI reactions likely to be tropospherically relevant, particularly given the challenges associated with experimentally studying sCIs directly. For this reason, this thesis interrogates sCIs reactions with several trace atmospheric co-reactants for which little or no experimental data exists. Chapter 4 features the reactions between various sCIs and the common atmospheric alcohols, methanol, ethanol and isopropanol. Chapter 5 studies the reaction of various important atmospheric species with the hydrofluoroolefin-derived sCIs (HFO-sCIs): CH_2OO, *syn*-/*anti*-CF_3CHOO and *syn*-/*anti*-CF_3CFOO. The HFO-sCIs are becoming more important atmospherically over time because of the increase in the use of anthropogenic HFOs which are discussed in the next section.

1.7. The Importance of Hydrofluoroolefins (HFOs)

HFOs are alkenes that contain halogenated substituent groups such as $-CF_3$, -F and -Cl. HFOs are currently being introduced as refrigerants in various markets, such as the United States of America (USA), the European Union (EU) and China.[197–199] HFOs can also undergo ozonolysis to produce CIs, and these HFO derived CIs, once collisionally stabilised, can subsequently go on to react with trace tropospheric species. However, HFOs and HFO-sCIs are likely to have very different chemistry to typical alkenes and sCIs, due to the halogenated substituent groups. This introduction to the HFO refrigerants provides the context for the further exploration of HFO ozonolysis chemistry and its tropospheric implications in Chapters 3 & 5 of this thesis.

1.7.1 The Impact of Chlorofluorocarbons (CFCs) on the Atmosphere

Various groups of chemicals have been used as refrigerants throughout the 19th — 21st centuries. Prior to refrigeration technology, other methods of food preservation were used such as the addition of salt or the dehydration of meat, to prevent spoiling.[200-202] Milk and other foods that spoiled relatively quickly were kept fresh by packing alongside snow and ice. It was not until the mid-18th century that the first artificial refrigeration machine was invented by the Scottish chemist William Cullen.[203] This involved using pumps within a liquid diethyl ether mechanical container to create a partial vacuum. This caused the ether to boil resulting in the absorption of heat from the air, and cooling the environment. The pursuit of more commercially applicable refrigerators involved devices that used water vapour compression and liquified gases such as NH_3 at low temperatures and high pressures.[204] This culminated, in 1834, with Jacob Perkins, the *father of the refrigerator*, inventing the first continually operating refrigerator, which used a vapour-compression system.[204]

The following commercially viable refrigerators were industrial scale to preserve agricultural products at places of production, processing, transport, and distribution. This resulted in the lowering of the price of these goods globally, and reduced wastage. After gas absorption technology was applied to refrigeration systems and ice machines by Ferdinand Carré, they operated using various gases as coolants including methyl formate (CH_3OCHO), methyl chloride (CH_3Cl), SO_2 and NH_3.[204-206] These refrigerators contributed to society in many ways because, while most food previously had to be produced close to places of consumption, these inventions, alongside innovations in the expansion of fertiliser use, communications, and shipping, meant food could be imported from cheaper and more efficient producers.[207,208] This also had a secondary effect: food production was

made more efficient and waste was reduced meaning more of the working population could work in other economic areas, such as heavy industry.

Despite this major advancement, the *first generation* of refrigerants, NH_3, SO_2, CH_3OCHO and CH_3Cl were all harmful if they leaked and were also potentially explosive meaning they were unsafe for home storage.[209] A new *second generation* of refrigerants were designed in the 1930s by Thomas Midgely Jr. and co-workers, which were called chlorofluorocarbons (CFCs). Examples of CFCs include freon-11 and -12 (CF_2Cl_2 & $CFCl_3$) and these were beneficial because they were inert, non-toxic, and exhibited the high volatility of the *first generation*.[12,210] As shown in Figure 1.14a, between the 1950s-70s, refrigerators were increasingly used and CFC atmospheric emissions from factory production, home use over a long duration and disposal in landfills, all increased.[10]

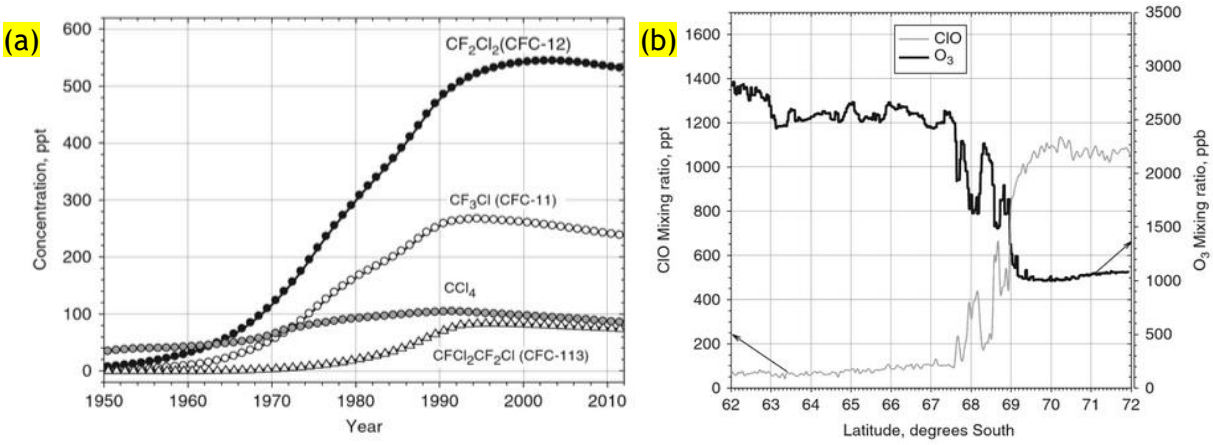

Figure 1.14: Graphical representation of the concentration of CFCs over time (Figure 1.14a)[10] and how this the effect of increased ClO presence on O_3 in the stratosphere on 16th September 1987 (Figure 1.14b).[10,211] Images obtained from Calvert et al., 2015.[10]

These emissions led to a significant build-up of CFCs in the atmosphere, as one of the only significant sinks for CFCs is photolysis by UV radiation below 255 nm which gives these species long atmospheric lifetimes (45—100 yrs).[2] As CFC abundance increased, they were observed to be able to traverse the low temperatures of the tropopause and rise into the stratosphere. In the stratosphere CFCs undergo photolysis forming chlorine radicals which catalytically deplete stratospheric O_3.[12] This was found to be especially important at the poles, where every winter a strong circumpolar vortex in the stratosphere is formed that not only prevents latitudinal transport of most species but the temperature drops below 180 K. The HNO_3 and H_2O condense on sulphate aerosols to form polar stratospheric clouds, which provide surfaces to convert reservoirs of HCl and $ClONO_2$, from the CFC breakdown, into Cl radicals. This increased level of Cl radicals proceeds to react with O_3 leading to higher local mixing ratios of oxychloryl (ClO) radicals, as shown in Figure 1.14b, and degradation of O_3 was so large that it led to "holes" in the ozone layer.[10] This also led

to a subsequent increase in people's level of skin damage, and increased cases of cataracts, and skin cancer, as mentioned in Section 1.2.[212]

Other damage caused by CFCs comes from their high global warming potential (GWP). Due to the large absorption of IR light at many different frequencies, the GWP_{100} of CFC-11 (4660), and other such CFCs, are much higher than CO_2. This means that despite the very low atmospheric concentration of CFC-11 (~600 ppt), the impact on atmospheric temperatures are significant.

These adverse effects led to global concerted commitment and action to reduce CFC usage. The Montreal Protocol, signed in 1987, committed to reduce CFC emissions to zero over the next few decades. All major countries in the world signed the treaty.[213-215] This was achieved by substituting the CFCs with a *third generation* of refrigerants, hydrofluorocarbons and hydrochlorofluorocarbons (HFCs & HCFCs), which had a much lower ozone depletion potential (ODP).[2,24,216] Due to this international action and HFC substitution, CFCs have been reduced significantly since the 1980s and with each major CFC seeing a reduction in atmospheric concentration of between 4 and 15% over the 6 years between 2005-2011.[2]

Without the implementation of the Montreal Protocol, it is estimated there would be an extra 1.5 million skin cancer deaths and 45 million additional cases of cataracts.[212] While the recovery of the O_3 layer is underway, there are still occasional countries and companies that break the Montreal protocol, which subsequently reduces the rate of recovery of the O_3 layer.[217,218] Despite CFC abundance decreasing, global temperatures are continuing to increase due to the increase in emissions of other GHGs, such as HFCs.[2,212]

1.7.2 The Impact of Hydrofluorocarbons and Hydrochlorofluorocarbons (HFCs & HCFCs) on the Atmosphere

HFCs and HCFCs, the CFC refrigerant replacements, are synthesised using chloroalkanes/chloroalkenes, such as chloroform, trichloroethene, and HF gas.[219,220] These *third generation* refrigerants are used in various parts of the manufacturing sector including for the production of electronics, air-conditioning and automobile engine coolants.[221]

Whilst they have low ODP values, like CFCs, HFCs and HCFCs are significance GHGs. As seen in table 1.1, as HFC and HCFC emissions have increased so have global temperatures.[24,216] HFCs and HCFCs, such as HFC-134a and HCFC-22, have high absorption of IR radiation at many frequencies and similarly long atmospheric lifetimes (13.4 and 11.9

yrs respectively), leading to high GWP_{100} values (1300 and 1760 respectively).[2] On the other hand, these species have significantly lower GWPs than the most prevalent CFCs (4000 — 14,000).[2] By curbing the use of HFCs, the world could avoid a subsequent global temperature rise of 0.4^{O}C by 2100.[2,222] There is a small contribution to ozone depletion from HCFC-22 and HFC-134a, but this is minor compared to that of CFCs.[223]

Table 1.1: Comparison of CFCs, HFCs and HFOs as refrigerants in Global Warming Potential over 100 years (GWP_{100}); Ozone Depletion Potential (ODP), atmospheric lifetime and sCIs emitted from reaction with O_3

Name	Structure	GWP_{100}	ODP	Lifetime (yr)	HFO-sCIs	ref
HFO-1234yf	$CF_3CF{=}CH_2$	4	0	10.5 days	CH_2OO	2,24,224
HCFO-1233zd	*E*-$ClCH{=}CHCF_3$	14	0.0005	26 days	*Syn-/Anti*-CF_3CFOO *Syn-/Anti*-ClCHOO	2,225,226
HFO-1234ze	*E*-$FCH{=}CHCF_3$	<1	0	16.4 days	*Syn-/Anti*-CF_3CHOO *Syn-/Anti*-FCHOO	2,24,227
CFC-11	$CFCl_3$	4660	1	45	*Syn-/Anti*-CF_3CHOO N/A	2,24
CFC-12	CCl_2F_2	10,200	0.82	100	N/A	2
HFC-134a	CH_2FCF_3	3710	0.0013	13.4	N/A	2,216
HFC-245fa	$CHF_2CH_2CF_3$	858	0	7.7	N/A	2,24

The need to curb HFC and HCFC emissions led to an amendment to the Montreal protocol, called the Kigali amendment. This favoured the phasing out of these gases in favour of hydrofluoroolefin (HFO) substitutes.[228] These HFOs have a much shorter lifetime (10 — 30 days) than HFCs/HCFCs, yielding much lower GWP_{100} values (~1—14).[2,24,224,225,227] As shown in Table 1.1, compared to both CFCs and HFCs, HFOs have an insignificant impact on the stratospheric ozone and climate change, however, the swift decomposition channel means that their reactive tropospheric chemistry may well be more important.

1.7.3 The Impact of HFO emissions on the Atmosphere

These *fourth-generation* refrigerants can be divided into hydrochlorofluoroolefins (HCFOs) and hydrofluoroolefins (HFOs) but, for the purposes of this thesis, they are grouped together as HFOs. There are several main HFOs that are used in commercial circulation including: HFO-1234yf ($CF_3CF{=}CH_2$), HCFO-1233zd(*E*) (*E*-$ClCH{=}CHCF_3$) and HFO-1234ze(*E*) (*E*-$FCH{=}CHCF_3$).[227,229,230] In the USA, HFO-1234yf, produced by manufacturers like *Chemours* and *Honeywell*, is being used as a viable replacement for the automobile engine coolant, HFC-134a.[231-235] The EU has stated its intention of replacing all HFCs with GWP_{100} >150 with HFOs.[197,198] HFO-1234yf is very difficult to ignite with an electrical spark, only igniting when mixed with PAG oil and temperatures > 900°C.[236] With the restriction on HFCs coming into force in 2020, other HFOs such as HFO-1345yf ($CF_3CF_2CH{=}CH_2$), HFO-1336mzz-

E (*E*-$CF_3CH{=}CHCF_3$) and HFO-1336mzz-Z (*Z*-$CF_3CH{=}CHCF_3$), may also be used as future refrigerants.[231-235]

HFOs have several atmospheric decomposition pathways, including reactions with Cl, NO_3 or OH radicals. HFO-1234yf, HCFO-1233zd(*E*) and HFO-1234ze(*E*) exhibit large k_{EXP} values with OH radicals (~10^{-12} — 10^{-13} cm^3 s^{-1}), with slightly smaller k_{EXP} values for Cl radicals (~10^{-11} — 10^{-10} cm^3 s^{-1}).[237-239] There are some computational chemistry studies on these reactions in literature and these are important to explore further as HFO decomposition pathways have been shown to increase the abundance of important species like tropospheric trifluoroacetic acid (TFA).[199,224,226,237,240,241] An exhaustive study of these O_3 + HFO reactions exploring all pathways as a full understanding of the bimolecular reaction rate constant, determines the effectiveness of O_3 as a HFO sink, and the CI branching ratios demonstrate the ability of a reaction to act as a source of hydrofluoroolefin-derived sCIs (HFO-sCIs).

The HFOs of interest in this thesis (HFO-1234yf, HCFO-1233zd, HFO-1234ze and HFO-1345yf) have small ozonolysis rate constants (≤ 10^{-19} cm^3 s^{-1}), but they are still found locally at atmospheric concentrations high enough to be considered important, especially near cities that have elevated levels of O_3.[10,226,227,241] The fact that the k_{O_3} for HFOs is lower than the $k_{OH}/k_{NO_3}/k_{Cl}$ equivalents does not exclude the importance of these ozonolysis processes for HFOs. For example, many alkenes, including isoprene, have a k_{O_3} smaller than k_{OH} and, due to the much higher concentration of O_3 over OH radicals, ozonolysis is still very competitive with OH radicals as an important alkene sink.[242,243]

Knowing the major tropospheric sinks of HFOs, producing more accurate ozonolysis rate constant values, in this case k_{THEO}, for bimolecular sinks and applying them into both local and global atmospheric models is becoming more vital with increased HFO use. Chapter 3 examines the k_{THEO} values of several HFOs; which CIs are produced from these reactions and relative branching fractions; and places these values in the context of the ozonolysis of other non-halogenated alkenes.

Finally, the existing experimental and computational literature of sCIs has very little analysis of these new HFO derived sCIs (HFO-sCIs). Reactions involving HFO-sCIs, such as *syn*-/*anti*-FCHOO, *syn*-/*anti*-ClCHOO, *syn*-/*anti*-CF_3CHOO, are examined but are sparsely distributed amongst many different computational studies. These studies generally involve these sCIs as part of a greater computational examination of sCI reactions with a low reactivity species, like CO_2, H_2, CH_4, or low abundance tropospheric species, like $CF_3CH{=}CH_2$. This means that the analysis of HFO-sCIs in Chapter 5, is amongst the first extensive computational analysis of HFO-sCIs.

1.8. The role of Computational Chemistry in the Study of Atmospheric Chemistry

One self-evident truism used to be that "chemistry is an experimental subject", but this has come into question more recently.[244] With the development and increasing application of more advanced computer processing, software product development and large-scale data storage, huge volumes of chemistry research is now being performed *in silico*. The application of computational chemistry can now not only be used to complement experimental analysis of chemical properties, reaction mechanisms and reaction outcomes but it can also be used to forecast reactions that are either too expensive to perform in a laboratory setting or are simply beyond current experimental capabilities. As such, computational models are applied to investigate everything from the unimolecular decomposition of small species to the interactions of large macrostructures, such as enzymes bonding with pharmaceutical products.[93,182,245,246] Computational chemistry has been used to model reactions in a diverse set of environments including quantum tunneling in gas-phase reactions, the effect of changing solvents on the speed of a liquid-phase reaction, and the effect of solid surfaces as reaction catalysts. [93,247–250]

1.8.1 Foundations of Theoretical Chemistry and the Construction of Basis Sets.

To perform computational models of chemical reactions, an understanding of each component of the atom is required. Atoms contain protons, neutrons, and electrons which have *elementary charges* (q_e) of +1, 0 and -1 respectively (1 q_e ~ 1.602×10^{-19} Coulomb). The number of protons in the atomic nucleus, referred to as the *atomic number*, defines what element the atom is on the periodic table. The number of neutrons in the nucleus dictates the element's isotope, but this has no effect on the total charge of the atom. For example, a carbon atom must have 6 protons, but it can have 6, 7 or 8 neutrons in its nucleus depending on whether the atom is a Carbon-12, -13 or -14 isotope respectively. Electrons, unlike protons and neutrons, are not found within the nucleus but have their greatest locational probability in the area surrounding the nucleus. They are lighter in mass (5.489×10^{-4} amu) than protons or neutrons (~1 amu). The number and distribution of electrons associated with the atom/molecule relative to the number of protons dictates the molecules total charge and polarity.

In purely classical mechanics, there is a clear distinction between a particle, like a neutron, and a wave, such as electromagnetic radiation. But the later discovery that both crystals and gold foil could cause the diffraction of beams of electrons, defined as particles under classical mechanics, led to Louis de Broglie's wave-particle duality

principle: that matter has a joint wave and particle character.[94,251] This meant that classical mechanics was superseded by quantum mechanics which dictates that the larger the mass of the matter involved and the slower the movements of that body, the less wave-like properties are exhibited. (It is favourable for an electron to exhibit the properties of a wave due to its small mass, and the information determining the behaviour of that wave are mathematically represented in a single term, the *wavefunction* (ψ)).

Nucleus—nucleus, electron—electron and electron—nucleus interactions are all critical to understanding the chemistry of a system but determining the exact behaviour of any given electron is difficult due to the *Heisenberg uncertainty principle*. This theory dictates that the location and momentum of any given subatomic particle, including an electron, cannot be known exactly at any given point in time. This gives rise instead to a probabilistic treatment of electronic structure and this probabilistic distribution can be derived from the integral of the radial wavefunction ($|\psi|^2$) as shown in Figure 1.15:

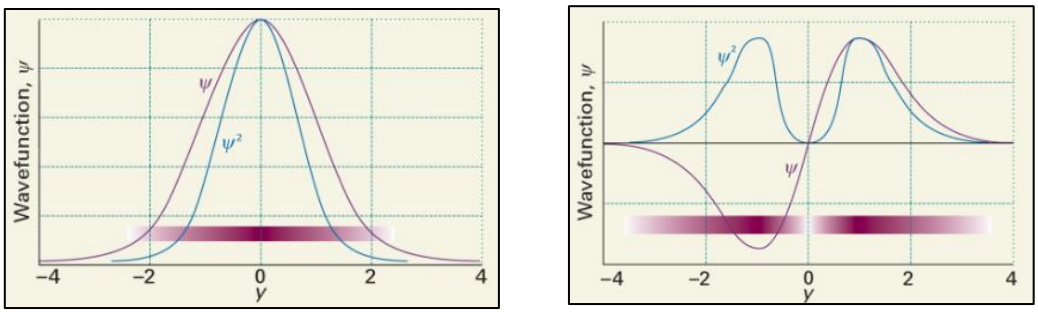

Figure 1.15: The relationship between probability distribution and a normalized wavefunctions.[94]

The *atomic orbital*, made up of angular and radial wavefunction components, are the basis of *atomic orbital theory* (AO theory). This calculation of the electron radial distribution for hydrogen atoms is dependent on the Born-Oppenheimer (BO) approximation: that the electrons respond almost instantaneously to external perturbations, compared to the nucleus, due to the larger mass of the proton and neutron components. The BO approximation contributes considerably to producing an accurate representation of a one-electron system, such as a hydrogen atom, and even multi-nuclear systems such as H_2^+, because both hydrogen atoms are effectively stationary compared to the electron movement. However, AO theory produces an incomplete interpretation of multi-electron systems, such as helium, because electron—electron repulsion cannot be modelled effectively in conjunction with the two nucleus-electron interactions, referred to as the multibody problem.

Despite this, AO theory still maps the behaviour of electrons with a significant amount of precision and therefore the orbital wavefunction can be useful in determining the overall

electronic energy of the system. For example, the computational Hartree-Fock (HF) approach involves determining the electronic energy and probability distribution of an orbital, ψ, based off the assumption that each electron has uncoupled motion. The relationship between the ψ of a particle (such as an electron) with fixed mass and moving in one direction, and the energy of the electron (*E*) is described by the time-independent Schrödinger equation:

$$H\psi = E\psi \qquad \text{Equation 1.41}$$

where *H* is the shorthand for the Hamiltonian operator, which is the function that gives the value of the energy (*E*). The wave function, ψ, is a normal mathematical function that contains information determining the character of the wavefunction depending on nucleus/nuclei (*R*) and electronic (*r*) coordinates of the atom/molecule described for an isolated system. Not only is the number of orbitals vital in determining the electronic energy of an atom, but the behaviour of an atomic/molecular system can differ depending on the type of orbitals involved.

Each orbital wavefunction associated with an atom can contain up to two electrons and each orbital has a unique quantum mechanical description based on the quantum features referred to as: orbital shell number, orbital subshell, and orbital angular momentum. The orbital shell number, also known as the principal quantum number, referred to by the symbol *n*, is used to describe all electrons that have the same ground state energy or "orbital shell". The orbital subshell (l) dictates the type of orbital wavefunction that the electron(s) occupies and therefore the shape of its probability distribution, referred to by their labels (s, p, d, f, g etc.). The orbital angular momentum (m_l) describes the orbital angular direction, which have multiple degenerate orientations, often referred to by using cartesian axis labels (x, y & z). Because "*s*" orbitals are singularly degenerate, the simplest example of orbitals displaying all these features are the $2p_x$, $2p_y$ and $2p_z$ orbitals, which are shown to be p orbitals in the second electronic shell with orientations along the x, y and z axes respectively. In a two—electron orbital wavefunction, referred to as paired electrons, each electron is distinguished from the other by adopting opposite spin angular momentum (m_s [α]), an intrinsic quantum mechanical property which can exhibit two anti-symmetric orientations, m_s [α] = +½ and m_s [α] = —½.

Most atomic/molecular systems include both "Coulombic" attraction, such as the attraction between electrons and nuclei, and Coulombic repulsion, interelectron repulsions or internuclear repulsion, but as shown within the HF ansatz, internuclear electron interaction is more difficult to model. There are two types of Coulombic interelectron interactions, *electron exchange* and *electron correlation*, both exhibited in

all multi-electron systems. The *electron exchange* term relies on the Pauli exclusion principle, which requires two fermions, such as electrons, to be antisymmetric to each other whilst in the same orbital (demonstrated by the m_s [α] property). Electron exchange, which is included in HF modelling, takes into consideration the tendency of electrons of the same spin state to stay away from each other, leading to a subsequent reduction in Coulomb repulsion.

One method of calculating the motion of electron pairs is by means of an *electron correlation* term, which combines using an electrostatic field to model the interactions between electron pairs and determining the impact of lower orbital electrons on higher orbital electrons using a collective Coulombic repulsion.[252] This term approximates the Coulombic attraction between the higher orbital electrons and nucleus, also known as nuclear "shielding", arising from either dynamic or static correlations. The electron exchange contribution and the small correlation contribution in the wavefunction by the fact that two electrons cannot be in the same location at the same time are incorporated in the Slater determinant of the Hartree-Fock molecular wavefunction. The Slater determinant is a shorthand explanatory $N \times N$ rectangular array representing the occupied spin orbitals (the product of spatial and spin components of the orbital) and its expansion give a full HF wavefunction polynomial, then used to determine the HF energy level.[252] If a single molecular structure has two singly occupied molecular orbitals with near degenerate electron configurations, then they may produce overlapping but not identical interactions and excitations. This *static electron correlation* means that using only single determinant generates inadequate energies, especially if the calculations involve multi-radical species or bond dissociation.[253] In contrast, *dynamic electron correlation*, is the effect of the spontaneous motion of single electrons drawing close enough to other electrons to cause short-range electron—electron interactions and how this adjusts the electron's motion.[254] Whereas static electron correlation is partially accounted for by imported *Coulomb repulsion factors*, dynamic correlation is not accounted for at all in HF methods.[252] The Coulomb factor applies "self-consistent" repulsions and exchange interactions to the electron consistent with the average position of the other electrons. Other computational chemistry approaches, such as DFT, and in higher level *ab initio* methods, such as coupled cluster and MP2, do incorporate electron exchange and correlation using other techniques with various degrees of accuracy.

In molecular systems, covalent σ-bonds are formed when an unpaired atomic spin electron pairs with another electron associated with a different atom, forming a single molecular orbital rather than two atomic orbitals. According to molecular orbital theory (MO theory),

rather than each orbital being described separately, bonds are constructed with a *linear combinations of atomic orbitals—molecular orbitals* (LCAO-MO), adopting a wavefunction that is a superposition of the two atomic orbitals. The σ-bond is formed by overlapping orthogonal orbitals along the internuclear axis and has cylindrical symmetry. Multiple bonds can be formed between the same atoms but creating a second or third bond that is π-bonding in nature. This π-bond cannot be formed using *s*-orbitals and involves overlapping *p*-orbitals (or higher) that are parallel to each other rather than orthogonal and, unlike a σ-bond, exhibits electron density above and below the internuclear axis, with the intermolecular axis a nodal plane of symmetry.

The reason why the bonded atom system is lower in energy than the separate atoms is that the wavefunction contains *constructive interference* of this *in-phase* molecular orbital represented by the greatly enhanced electron density along that internuclear bond. The equilibrium bond length is the internuclear separation minimum of the energy curve and the probability density is greatly enhanced along that internuclear bond lowering the energy of the bonding orbitals. The addition of π-bonds decreases the bond length and increases the overall bond dissociation energy. The capacity of each of the atomic orbitals is two electrons, so the LCAO-MO generates an analogous *antibonding MO*. The antibonding MO can be occupied by either the additional electrons in electron rich systems, such as F_2; by ionisation, such as with O_2^-; or by electron excitation. The occupation of antibonding orbitals generates *destructive interference* increasing the length of the bond and, if the antibonding orbitals becomes partially or fully occupied, the highest occupied molecular orbital is then *out-of-phase*. This combination of energy of electrons in all the antibonding and bonding orbitals is greater than the individual fragments, which means it is energetically favourable for the respective σ-/π-bond to break if all antibonding orbitals are occupied.

Most computational representations of these atomic and molecular orbitals are approximations, and require the use of *basis functions* to model electron densities: Slater-type orbital (STO) or cartesian Gaussian-type orbitals (GTO). These functions differ significantly in probability-radial dependence, both seen in Figure 1.16.

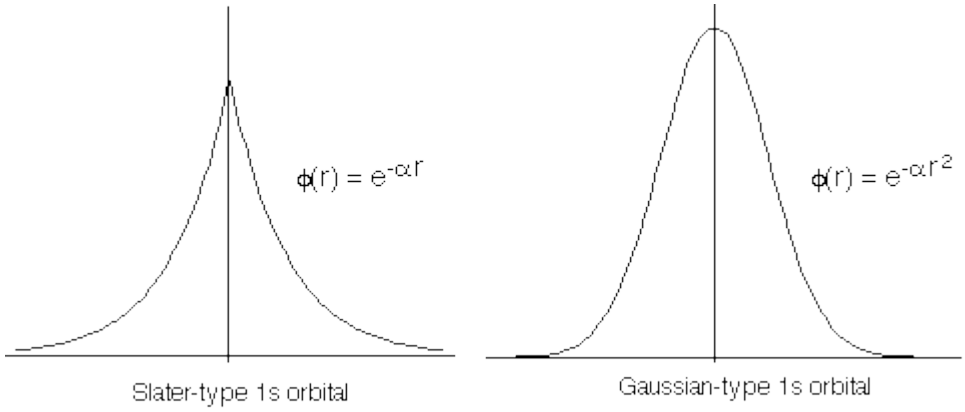

Figure 1.16: Graphical Representation of Slater and Gaussian-type orbitals.[255]

The Slater-type 1s orbital shows a steep incline at the peak of the distribution (r=0) and slower declines of probability distribution at the larger radii, contrasting significantly with the Gaussian-type 1s orbital, which has a flatter peak at r=0 and a steeper incline probability distribution further away from the nucleus.[255] However, STOs see a swift exponential increase in computational power required to undertake calculations, whereas GTOs are much more efficient to calculate, due to the complexity of the Slater-type radial component in the calculation.[256,257] The integration of individual Gaussian functions, referred to as Gaussian primitives, are much swifter to calculate, so if a linear combination of these Gaussian primitives are overlapped, such as in Figure 1.17, they produce GTOs, with a very similar distribution to the STOs, but at much greater efficiency. A larger number of overlapped Gaussian primitives, referred to as a *basis set*, can be calibrated to produce a more similar basis set to the Slater function by fitting these Gaussian shapes to a Slater exponential, referred to as STO-3G or STO-4G, depending on the number of Gaussians.[258]

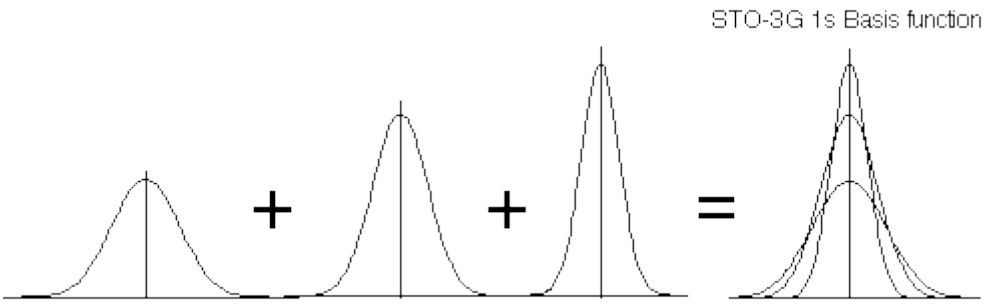

Figure 1.17: Graphical Representation fitting Gaussian primitives to Slater exponentials.[255]

In contrast to these *minimal basis sets*, which involve using one type of basis function for each separate atom, various other types of basis sets have been derived, the *Pople* and the *Dunning* basis sets, using other more intensive approaches. The higher-level *double* or *triple zeta* basis sets involve using multiple atomic GTOs in linear combination to

represent *one* atomic orbital's input into a molecular orbital, to account for distortions in the charge distribution brought about by heteroatomic bonding.[259,260] This is important as identical atoms in different environments may be treated as stereochemically similar under simple basis sets. However as these different zeta functions can produce broader or more diffuse wavefunctions by incorporating the character of other atomic orbitals into their molecular orbitals, a more accurate representation of the character is more likely, in terms of the polarity or reactivity of certain functional groups and the molecule as a whole.[261]

Another way of increasing the accuracy of the wavefunction and the corresponding electronic energy is to use *polarisation* functions on the valent set of electrons. This is where valent orbitals can incorporate character from other orbitals with higher angular momentum, because that character is seen in the valence orbitals other bonding atom(s).[262,263] Polarization functions allow the expansion of the basis set into different spherical harmonic functions, because polarization within a molecule would distort electron density away from typical atomic orbital distributions. An example of this would be the addition of *p*- or *d*-orbital gaussian primitives of *s*-atomic orbital or *d*- or *f*-orbital character to a *p*-orbital for the purpose of mapping the distorting in a LCAO-MO representation.[252] In a homoatomic bond the significant proportion of electron density shift from each atom would be even shared along the interatomic axis. However, along a polar bond, electron density may be so drawn away from a *p*-orbital on one atom that the asymmetric electron distribution maybe better represented with some *d*-orbital character in that *p*-orbital. The inclusion of polarisation functions is necessary and proper when modelling Criegee intermediates, as the COO group sees significant changes in the electron distribution, and therefore unimolecular and bimolecular reactivity, depending on what substituent groups are attached.

Diffuse or *augmentation functions* are particularly important for basis sets representing broad electron distributions, such as in hydrogen bonds or conjugated systems, and are therefore another important component to denoting the intermolecular interactions in pre-reaction complexes and transition states.[252] To represent the electron density spread over a large region in these environments, additional Gaussian primitives included into the GTOs are very broad but shallow, to replicate this wider distribution of electron density.

Pople basis sets involves treating valence electrons with higher level basis sets, but the core electrons are treated with minimal basis sets, which is referred to as *split valence*, to reduce CPU time.[259,264] The construction of this split basis set is indicated by a hyphen using the abbreviation N-MPG: where N is used to describe the number of gaussian

primitives to construct the minimal GTO for the core orbitals; M and P representing the number of gaussian primitives for two or three basis GTOs representing the multi-zeta basis sets.[265] An asterisk, *, is used to incorporate polarisation, with two asterisks, **, included to add this polarisation to the low mass atoms in the molecule as well. Unspecified diffuse functions are included by a plus sign, +, or specified diffuse function by including terms in parentheses.[252]

Dunning correlation-consistent basis sets are often used to describe the wavefunction for correlated approaches, such as DFT and MP2, but it differs from *Pople*-type basis sets because it uses correlation-consistent (cc) basis functions modelled for HF and DFT calculations.[266] The different components that construct the *Pople* basis set are the same as those that construct the *aug-cc-pVnZ* basis set describing: augmentation (or diffuse), *aug*; correlation-consistent, *cc*; polarisation, *p*; with *n* of zeta functions, *nZ* (*n* = D, T, Q, and 5 etc ≡ double, triple, quadruple, five zeta). While *Pople* basis sets, sometimes have shorter job run times than their equivalent *Dunning* basis set calculations, the Dunning approach does have a few significant advantages including that it has been found to produce accurate spectroscopic and molecular energy calculations, particularly for small molecular reactions.[252,266,267] However, the main advantage that Dunning cc basis sets have is that, as the addition of more zeta functions to the aug-cc-pVnZ basis set (*n* = D, T, Q, and 5), the electron correlation energy converges closer to the *complete basis set* value.[266,268,269]

1.8.2 Foundations of Ab Initio Calculations

Alongside the use of basis sets to model electron densities, each computational chemistry calculation involves using one if not multiple methodological approaches, such as *Møller-Plesset* (MP), coupled cluster or density functional theory (DFT) methods. One of the oldest and most common computational chemistry approaches is to use HF theory. Even though MO theory using HF approaches produces mathematical orbital constructs without a true representation of electron correlation and exchange, HF is in widespread use due to its accurate representation of many systems.[252] HF theory is also the basis of all the post-Hartree Fock (post-HF) methods with the inclusion of other coefficients to represent electron correlation to a much greater extent, e.g. as *Møller-Plesset* (MP) and coupled cluster theory. This inaccuracy in electron correlation factors is problematic as every electron—electron repulsion within the molecule can cause perturbations in electron probability distribution, even if many are on a small scale. It is often touted that HF

produces a molecular energy with >99% accuracy, however it is often the remaining 1 % that is the issue.

There are many different computational chemistry approaches but two of the main approaches used most frequently over the last decade are post-HF and DFT methods. One of the main concerns with computational chemistry calculations is the computational cost required to undertake the job, so eliminating "bottlenecks" in the overall approach by selecting an efficient method is particularly important. One of these bottlenecks is the scalability of these calculations, especially where studies involve calculations of a significant size range of molecular systems. Much of the computational literature is devoted to transforming the high intensity post-HF calculation approaches, such as CCSD and CCSDT (with N^6 and N^8 scaling respectively), into more efficient approaches such as the N^4 scaling HF and DFT methods, without seeing a similar reduction in the accuracy of the molecular energies calculated.

Large sources of computational cost within geometric optimisation and vibrational frequency calculations can mean these computations often require using a lower level of theory than that used for molecular energy calculations. However, even using a lower-level post-HF approach, such as MP2, to undertake geometric optimisation and vibrational frequency calculations often produces more costly computations than that of DFT. The *ab initio* method of optimisation proceeds using a cyclical, iterative, *energy only* optimisation method. This involves: inputting distortions at each potential point using every degree of freedom in both potential directions, while freezing all other co-ordinates; determining the steepest descent pathway, undertaking a number of linear distortions down this descent pathway; and this new slightly optimised structure is then tested again for the steepest descent pathway using analysis along every single degree of freedom, beginning the cycle again until the bottom of the energy well is established.[252,270] Whereas analytical approaches, such as those employed by most DFT implementations proceeds by determining an analytical estimate of the second derivative matrix, referred to as the Hessian rather than calculating gradients numerically.[271] Diagonal force constants, derived from the analytical Hessian and empirical rules, are analysed to derive stretches, bends, torsions and out-of-plane deformations and the force and direction of these modes used to identify the driving direction of the steepest descent.[271] The geometric distortions applied to that structure are driven in that direction, repeating the calculation of the Hessian and the primitive modes until the bottom of the energy well is reached.[270] The analytical approach to optimisation and vibration frequencies (as well as some other lower level approaches) has been shown to be excellent at determining the minimum energy or

transition state geometries but not in finding the true energy of that stationary point compared to many post-HF approaches, such as CCSD(T).[194,272-274] This means a mixed approach, of using DFT (see section 1.8.3) for geometry optimisation and vibrational frequencies, and a post-HF approach for the final molecular energy is conceivably an accurate and efficient methodology.

As the *variation theorem* states that the energy derived is always the upper-bound to the *true energy*, the quality of an *ab initio* approach can be found by comparing the energy value to the *true energy* (E_{true}) and that the lower the calculated energy typically the greater the quality of the wavefunction.[94] As shown in Equation 1.42, a significant cause for the energy gap between E_{true} and $E_{Hartree\text{-}Fock}$ is the electron correlation energy ($E_{correlation}$) and relativistic effect energy ($E_{relativistic}$). The $E_{relativistic}$ include effects such as spin-orbital coupling and is mostly only significant for heavy atoms, therefore a negligible contribution in most of atmospheric chemistry.[252] This means to obtain a good representation of the true energy an *ab initio* approach must have good representation of $E_{correlation}$.

$$E_{correlation} = E_{true} - E_{Hartree\text{-}Fock} - E_{relativistic} \qquad \textit{Equation 1.42}$$

One method of measuring this $E_{correlation}$ is using the *Møller-Plesset* (MP) treatment based on many-body perturbation theory.[94] Under MP nomenclature the sum of the one-electron energies and internuclear repulsions (referred to as MP0) is corrected by the exchange and Coulomb integrals (referred to as the $E^{(1)}$ correction), to produce the MP1 energy (E_{MP1}), which is the same as $E_{Hartree\text{-}Fock}$. MP2 is then produced from the E_{MP1} and a perturbation correction, as shown in Equation 1.43.[252]

$$E_{MP2} = E_{MP1} + E^{(2)} \qquad \textit{Equation 1.43}$$

$$E_{MP1} = E_{Hartree\text{-}Fock} = E_{MP0} + E^{(1)} \qquad \textit{Equation 1.44}$$

In perturbation theory the species involved in the system analysed are not all in the ground state, with different proportions in different levels of excitation depending on the temperature of the system. The most common excitation is where, for a small proportion of the molecules per mole, have one pair of electrons move into the unoccupied orbital, referred to as a *doublet excitation*. This is more stable than two unpaired electrons and therefore this transition is more likely to lower the energy, which is known as *Brillouin's theorem*. This *doublet excitation* is a small but significant energy contribution, referred to as $E^{(2)}$ in the total energy, but the size of that contribution depends on the size of the energy gap between occupied and unoccupied orbitals. The increased computational cost of calculating the contribution is significant because it requires calculating the *four-centre*

two-electron integrals, produced by having two electrons and having four "centres", two centres for each bonding or virtual orbital.[252]

What distinguishes *coupled cluster* approaches from MP2 approaches is that the correlation contribution of the **Ψ** is calculated using a summation of determinants or *cluster operators*. To include examination of both the *singlet* and *doublet excitations* contributions in the coupled cluster approach, known as CCSD, is very important because the promotion of a pair of electrons will fill the virtual orbital, like in MP2, but a singlet promotion also has some contribution to the system too.[252] CCSD has a larger scaling factor (N^6) than MP2 (N^4) due to the need to produce a cluster operator for the singlet excitation contribution which still is calculated using a *four-centre two-electron* integral. Whilst the triplet excitation has smaller contributions to the overall wavefunction than that of the doublet, it is still important but calculating using the CCSDT approach has large computational expense. One way to represent the triplet contribution is using coupled—cluster approximation calculations that do not include refining iterations, referred to as the perturbative triplet method, or CCSD(T). Often, CCSD(T) outperforms the other CC methods with accuracy and applicability for medium-sized molecules, but to calculate a larger molecule, the computational power and resources required increase at a rapid pace.[252]

Reduced computational cost can also be achieved by applying a local correlation treatment, based on the knowledge that the correlation energy between electrons in different parts of the molecule reduces rapidly with decreased proximity.[275] Localised approximations often include those derived by Pulay and Saebø, which are that the correlation of these proximate electrons can be confined to a *localised molecular orbital* (LMO). Therefore one can calculate interactions between LMO pairs using accurate methods (full CC calculations), approximated (perturbation theory) or even a neglected, depending on their increasing distance from each other.[276,277] This means the wavefunction calculations of the excitations required for CCSD & CCSD(T) are restricted to the excited states and to co-located LMOs, significantly reducing the number of virtual orbitals that need to be calculated. The impact of localisation approximations on calculation efficiency can be shown by the fact that using a local density-fitted approach has been shown to reduce length of CCSD(T) calculations by 1-2 orders of magnitude.[275] However, one potential source of inaccuracy is that this localisation into finite LMOs may be accurate for a reactant but this impact of correlation on different LMOs may not be contiguous through TS and products, which may lead to less accurate full potential energy surfaces. This could be described as dividing the system into energy-based LMOs or AO bases, or

"fragmentations schemes" and then the final energy is assembled from the summation of these energies.[278]

Much of the computational cost that emerges from the coupled cluster method, such as LCCSD(T), are that as it uses a LCAO-MO approach, incorporating calculations of *four-centre two-electron repulsion integrals*, which provides calculation with N^4 scaling. This emerges from the two-electron electrostatic repulsions, $(\kappa\lambda|\mu\nu)$, from the combination of two atomic orbital measured with one-electron density, $\rho_{\mu\nu}(\boldsymbol{r}_1)$, which have both bonding and anti-bonding contributions, $\chi_\mu(\boldsymbol{r}_1)$ and $\chi_\nu^*(\boldsymbol{r}_1)$. This repulsion factor is also directly proportional to the interelectron distance ($\boldsymbol{r}_{12}$):

$$\rho_{\mu\nu}(\boldsymbol{r}_1) = \chi_\mu(\boldsymbol{r}_1)\chi_\nu^*(\boldsymbol{r}_1) \qquad \text{Equation 1.45} \qquad \rho_{\rho\sigma}(\boldsymbol{r}_2) = \chi_\rho(\boldsymbol{r}_2)\chi_\sigma^*(\boldsymbol{r}_2) \qquad \text{Equation 1.46}$$

$$(\mu\nu|\rho\sigma) = \int d\boldsymbol{r}_1 \int d\boldsymbol{r}_2 \frac{\rho_{\mu\nu}(\boldsymbol{r}_1)\times\rho_{\rho\sigma}(\boldsymbol{r}_2)}{r_{12}} = \int d\boldsymbol{r}_1 \int d\boldsymbol{r}_2 \frac{\chi_\mu(\boldsymbol{r}_1)\chi_\nu^*(\boldsymbol{r}_1)\times\chi_\rho(\boldsymbol{r}_2)\chi_\sigma^*(\boldsymbol{r}_2)}{r_{12}} \qquad \text{Equation 1.47}$$

The *four-centre* refers to, as seen in Equation 1.47, the overall contributions to the electron density of the linear combination of the 2 atomic orbitals, producing both bonding and anti-bonding orbitals with the anti-symmetric contributions of m_s [α] = ±½ (χ_ν, χ_κ^*, χ_λ,and χ_μ^*), which produces the N^4 scaling. This scaling can be altered however by the introduction of *auxiliary basis functions*, which is produced from (Equation 1.48) the $\tilde{\rho}_{\mu\nu}(\boldsymbol{r}_1)$ and $\tilde{\rho}_{\mu\nu}(\boldsymbol{r}_2)$, which include the expansion coefficient, $D_B^{\mu\nu}$, and *auxiliary one-electron integrals*, $\chi_A(\boldsymbol{r}_1)|$, derived from a linear combination of the *auxiliary atomic basis functions*.

$$\rho_{\mu\nu}(\boldsymbol{r}_1) = \chi_\mu(\boldsymbol{r}_1)\chi_\nu^*(\boldsymbol{r}_1) \approx \tilde{\rho}_{\mu\nu}(\boldsymbol{r}_1) = \sum_A C_{\mu A}C_{\nu A} \times (\widetilde{\mu\nu}| = \sum_A D_A^{\mu\nu}\,\chi_A(\boldsymbol{r}_1) \qquad \text{Equation 1.48}$$

To produce an approximation of the *four-centre two-electron repulsion integrals*, three *auxiliary integrals* are required one 2-*centre* 2-*electron repulsion integral* (Equation 1.49) and two 3-*centre* 2-*electron repulsion integrals* (Equations 1.50 & 1.51):

$$(A|B) = \int d\boldsymbol{r}_1 \int d\boldsymbol{r}_2 \frac{\chi_A(\boldsymbol{r}_1)\chi_B(\boldsymbol{r}_2)}{r_{12}} \qquad \text{Equation 1.49}$$

$$(\mu\nu|A) = \int d\boldsymbol{r}_1 \int d\boldsymbol{r}_2 \frac{\chi_\mu(\boldsymbol{r}_1)\chi_\nu^*(\boldsymbol{r}_1)\chi_A(\boldsymbol{r}_2)}{r_{12}} \qquad \text{Equation 1.50}$$

$$(B|\rho\sigma) = \int d\boldsymbol{r}_1 \int d\boldsymbol{r}_2 \frac{\chi_B(\boldsymbol{r}_1)\chi_\rho(\boldsymbol{r}_2)\chi_\sigma^*(\boldsymbol{r}_2)}{r_{12}} \qquad \text{Equation 1.51}$$

These three repulsion integrals are important because they can be incorporated into the full electrostatic repulsion *auxiliary two-electron integrals*, $(\widetilde{\mu\nu}|\widetilde{\rho\sigma})$, from the expansion of these auxiliary basis sets into the following equation:

$$(\widetilde{\mu\nu}|\widetilde{\rho\sigma}) = \frac{(\mu\nu|A) \times (B|\rho\sigma)}{(A|B)} \qquad \textit{Equation 1.52}$$

The combination of this 2 × three-centre and 1 × two-centre approximation that produces these *density fitting* (DF) calculations, have N^3 and N^2 scaling and therefore involves significantly less computational effort to produce the electrostatic repulsion integrals than the N^4 calculation of electrostatic repulsion.[279] These factors produce this *four centre two-electron repulsion integrals* $(rs|pq)$ through the following equation:

$$(rs|pq) = \sum_{\mu\nu\kappa\lambda} C_{\kappa r} C_{\mu p} C_{\lambda s} C_{\nu q} (\widetilde{\mu\nu}|\widetilde{\rho\sigma}) \qquad \textit{Equation 1.53}$$

However, this DF method uses an approximation in the one-electron density functions ($\tilde{\rho}_{\mu\nu}(\boldsymbol{r}_1)$ and $\tilde{\rho}_{\rho\sigma}(\boldsymbol{r}_2)$), which is generated from *matrix elements of the electron density expanded in the atomic orbitals*. These involve bonding and anti-bonding contributions which are standardised to *fitting* (or *auxiliary*) *basis* functions [$\chi_A(\boldsymbol{r}_1)$ and $\chi_B(\boldsymbol{r}_2)$] and their expansion coefficients ($C_{\kappa r}$, $C_{\mu p}$, $C_{\lambda s}$and $C_{\nu q}$). This auxiliary basis function is determined using the products of the atomic orbital gaussian basis functions and the expansion coefficients is fitted to incorporate the factors such as Coulomb and overlap.[280] The expansion coefficients are determined by comparing the full one-electron integrals with those calculated for the auxiliary equivalent and are automatically adjusted, sometimes adjusted by 5 or 10 times, to bring the one-electron coefficient inline.[280]

A significant benefit of using DF approximations is that the reduction in computational cost scaling transfers to the overall LCCSD(T) approach, reducing that cost by a further order of magnitude, and the use of externally designed auxiliary basis sets makes the calculations even more efficient.[281,282] There are some downsides to this method, such as that density fitting involves pre-optimised auxiliary basis sets and this makes it more accurate only for specific quantum chemical methods.[283] While error emerges for both density fitting and to a lesser extent local approximations, these are small compared to effect of variation of the basis set.[279] This is important because the reduction in computational cost by applying both density fitting and localised approximations can provide scope utilising larger basis sets, which leads to more efficient and accurate calculations.

As both localisation and density-fitting of the coulomb electrostatic correlation integrals increases computational efficiency, the electron exchange integrals of the HF step becomes the calculation bottleneck with larger structures.[279,282] To resolve this the density fitting approach can be applied to these HF integrals with a linear combination of these basis functions. This density-fitted Hartree-Fock (DF-HF) method uses localised occupied orbitals to construct an exchange matrix and is therefore much more efficient compared to traditional HF, pure *ab initio* calculations.[279,284]

Another additional factor that can be applied to a LCCSD(T) to make it competitive is the employment of the F12 theory, which uses a Slater-type correlation ansatz to describe dynamic correlation.[285] The linearized F12 theory are mainly incorporated into methods that involve approaches, such as MP2 and CCSD(T), that involve excitations using *virtual orbital* functions and extends the cluster double excitation operator (T_2).[286] This cluster operation includes the studies of both the occupied orbitals factors, denoted as *i*, *j*, *k* & *l* indices, and virtual orbitals, denoted as *a*, *b*, *c* & *d* indices to describe the electron excitation operators ($\hat{E}_{ij}^{ab}$ and $\hat{E}_{ij}^{ab}$).[287]

$$T_2 = \frac{1}{2} T_{ab}^{ij} \hat{E}_{ij}^{ab} + \frac{1}{2} \hat{\mathcal{T}}_{\alpha\beta}^{ij} \hat{E}_{ij}^{\alpha\beta} \qquad \text{Equation 1.54}$$

$$\hat{\mathcal{T}}_{\alpha\beta}^{ij} = \langle mn | F_{12} Q_{12} | \alpha\beta \rangle T_{mn}^{ij} \qquad \text{Equation 1.55}$$

The explicitly correlated terms, t_a^i and T_{ab}^{ij}, are calculated amplitudes with both the singlet excitation and the doublet excitations, which are derived on the accuracy of the *two-centre one-electron repulsion integrals*. Rather than using multiple gaussian determinants ($exp[-\alpha_i\, r_{12}{}^2]$) to derive these *electron repulsion integrals*, the F_{12} coefficient incorporates a Slater determinant to describe the short-range intermolecular distances (r_{12}) for the purpose of producing these doublet integrals (Equation 1.56). The inclusion of a Slater-type function makes this F12 method non-linear and the $\hat{\mathcal{T}}_{\alpha\beta}^{ij}$ also includes a strong-orthogonality projector, Q_{12}, which is a function of the orbital projection operators of the occupied, virtual, and complete orbitals. The Q_{12} is a function of expansion coefficients when the approach involves using the auxiliary basis sets, such as those seen in the density-fitted approach.

$$\sum_i c_i \times exp(-\alpha_i\, r_{12}{}^2) \approx F_{12} = \frac{1}{\gamma} e^{-\gamma r_{12}} \qquad \text{Equation 1.56}$$

There are two F12 approaches: the F12a integral, which neglects contributions from explicitly correlated configurations of double excitations, except for the approximated $\hat{\mathcal{T}}_{\alpha\beta}^{ij}$

amplitude coefficient; or the F12b integral, which also includes greater consideration of explicitly correlated and conventional amplitudes with the use of a new term.[288] However the F12a integral is useful to incorporate into LCCSD(T) methods because the smaller and medium size basis sets, such as the aug-cc-pVDZ and aug-cc-pVTZ adopted in this thesis, estimate the basis set limit well and converge close to that limit.[288,289] The F12b integral is preferred for the largest basis set aug-cc-pVQZ.[288,289]

1.8.3 Foundations of Density Functional Theory (DFT) Approach

While *ab initio* approaches like *DF-LCCSD(T)-F12a*, are strong performing computational methods at analysing the molecular energy, using these types of approaches for analysing vibrational frequency and optimisation calculations are made difficult by the large scaling and the exhaustive numerical technique required, as mentioned in the previous section. The use of analytical techniques of determining the Hessian used in the DFT optimisation method, and the lower scaling ($\sim N^3$), makes DFT excellent for vibrational frequency and optimisation computational analysis. This lower scaling comes from the fact that electronic energy contribution in DFT calculations, $E[\rho]$, is generated from an *electron density* function, ρ, not a wavefunction. This *electron density* function maps electron distribution conceptually as a "cloud" or "gas" around the molecule with that density relative to position in the molecule. The first *Hohenberg-Kohn theorem*, one of the central principles of DFT, is that the electron probability density, $E[\rho]$, is the sum of: contributions to kinetic energy from electron-nucleus and electron-electron potential energy ($E_{\text{classical}}[\rho]$); and exchange-correlation energy ($E_{XC}[\rho]$), as shown in Equation 1.57.[290]

$$E[\rho] = E_{classical}[\rho] + E_{XC}[\rho] \qquad \textit{Equation 1.57}$$

The DFT method has considerable variety in calculating the mathematical $E_{XC}[\rho]$ term, by applying one of many empirically derived *functionals* (a function of a function): equations that converts the electron density into the energy contribution. This functional is particularly critical because the combined treatment of the exchange and correlation contributions reduce computational cost compared to their separate treatment in *ab initio* methods. This universal function $E_{XC}[\rho]$ incorporates spin-based electron—electron effects and nonclassical corrections to the classical electron—electron interactions. Whilst *Hohenberg-Kohn theorem* does justify the existence of the $E_{XC}[\rho]$ term, it does not provide a means for determining it. This generates the central problem of DFT, which is that while the $E_{XC}[\rho]$ term does exist, the functional can be and is calculated using various different approximation mechanisms without a clear theoretical justification for adopting one over

the other, normally ultimately chosen based on empirical performance evidence, and chosen on a system-by-system basis.[252] The second concern is that as functionals are all approximations, DFT calculations can produce molecular energies *below* the true energy of the system and thus do not reliably follow the *variational theorem*.[252]

Nevertheless, the Kohn-Sham (KS) theorems, asserted by W. Kohn and L.J. Sham, state that other molecular properties can be calculated from the electron density and using these molecular properties as a guide a variational approach may yield a more accurate electron density functional.[290,291] This was implemented iteratively and generated the Kohn—Sham equations, the basis of producing an accurate functional, mitigating the effect of not having prior accurate electron density or functional. The first step of this implementation is to determine the electron density (see Equation 1.58) using the *Kohn—Sham equations*.

$$\rho(r) = \sum_{i=1}^{N_e} |\psi_i(r)|^2 \qquad \textit{Equation 1.58}$$

As this modelling of the electron density is designed to measure the impact of the remaining electrons, referred to as an *electron cloud*, on molecular one-electron perturbations, this electron density, *p(r)*, differs significantly from the multi-electron wavefunction distribution, $|\mathbf{\Psi}|^2$, seen in *ab initio* methods. Equation 1.58 shows that density of this electron cloud is modelled by producing an integrated molecular wavefunctions $\psi_i(r)$ of all other electrons (referred to as N_e) in the system, dispersed over all spins and all coordinates, whereas the $|\mathbf{\Psi}|^2$ is the probability of finding electron 1 and electron 2 in a certain cartesian region with specific spins. The electron density is modelled using *Kohn-Sham orbital* (ψ_i), which are non-wavefunction based molecular orbitals, determined iteratively using a *Kohn-Sham equation*, Equation 1.59. This *Kohn-Sham equation* obtains the *Kohn-Sham orbital energies* (ε_i) of a Kohn–Sham two-electron spatial wavefunctions ($\psi_i[1]$) from three factors: a "core" factor (h_1), classical contributions from electron 1 and electron 2 ($j_0 \int \frac{\rho(2)}{r_{12}} d\tau_2$), and ***exchange-correlation potential*** ($V_{XC}[1]$):[94]

$$h_1\psi_i[1] + j_0 \int \frac{\rho(2)}{r_{12}} d\tau_2 \psi_i[1] + V_{XC}[1]\psi_i[1] = \varepsilon_i \psi_i[1] \qquad \textit{Equation 1.59}$$

Kohn and Sham introduced a concept of *non-interacting electrons* which are used to describe electrons in the core of the molecule because their interactions are so negligible, that modelling these electrons as if they have no interactions with outer electrons give a

very similar electron density distribution as the real system.[252,291] This means that the potential and kinetic energy of attraction of each nucleus and the non-interacting electrons can be integrated into one core term. The classical electrostatic potential from electrons 1 & 2 are simply a contribution of the electron density and interelectronic distance.[94] This KS approach mitigates the inaccuracies of DFT by expressing the molecular energy as a sum of terms, with two terms (the core term and the classical electron static contributions) easily calculated if electron density is known, and a smaller less understood term, the $V_{XC}[1]$, meaning that even large errors would have a small impact.[94] This $V_{XC}[1]$, is a functional derivative, and is the only term that needs to be devised, and is referred to as the *DFT functional*. This $V_{XC}[1]$ is defined as the collective deviations in electron correlation and exchange between the true interelectronic repulsion energy and the classical collective repulsion of the electron cloud, seen in Equation 1.60:

$$V_{XC}[\boldsymbol{r}] = \frac{\delta E_{XC}[\rho]}{\delta \rho} \qquad \textit{Equation 1.60}$$

Much of the difficulty in defining a V_{XC} factor for DFT calculations is that $E_{XC}[\rho]$ is a function that is based on multiple values of electron density, $\rho(\boldsymbol{r})$, rather than a single point of electron density. This is because a change in the location of the electron, $\boldsymbol{r}$, will lead to electron perturbations caused by a cumulative array of changes in interelectronic interaction that depend on proximity to different parts of the electron cloud. Therefore, when $\boldsymbol{r}$ goes through small changes, $\delta\boldsymbol{r}$, the corresponding new electron density of $\rho(\boldsymbol{r} + \delta\boldsymbol{r})$ involves an additional change in the electron density at multiple locations in the molecule, referred to as $\delta\rho$. A combination of these $\delta\rho$ changes are applied to the V_{XC} equation and are used to calculate the resultant change in exchange-correlation, $\delta E_{XC}[\rho]$:

$$\delta E_{XC}[\rho] = \int \frac{\delta E_{XC}[\rho]}{\delta \rho} \delta\rho d\boldsymbol{r} = \int V_{XC}(\boldsymbol{r}) \delta\rho d\boldsymbol{r} \qquad \textit{Equation 1.61}$$

An iterative mechanism to determine $V_{XC}[1]$ involving the use of Kohn–Sham orbitals (see in Figure 1.18) is adopted to reduce inaccuracies in DFT. While technically DFT does not involve wavefunctions, a Kohn–Sham approach to calculate noninteracting-system kinetic energy and $E_{XC}[\rho]$ does use Kohn–Sham orbitals in an iterative manner to determine the value and convergence of the electron density.

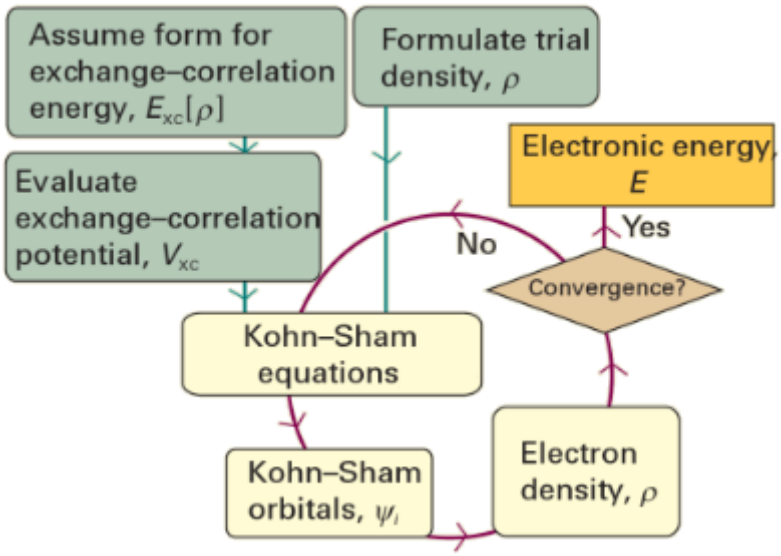

Figure 1.18: The Procedure for implementing the Kohn-Sham equations in DFT.[94]

This Kohn–Sham approach involves a mechanism triggered by inputting a logical trial electron density, such as a Hartree-Fock/experimentally-derived estimate, to calculate KS orbitals and $E_{XC}[\rho]$ values.[94] The second step is to calculate an approximate derivative of the relationship between the exchange-correlation energy and the electron density to derive an approximate $V_{XC}[1]$ (Equation 1.60). The third step is the estimated $V_{XC}[1]$ and the *Kohn-Sham equation* (Equation 1.59) are then used to obtain preliminary *Kohn-Sham orbitals*. The fourth step is that the KS orbitals are then used to determine the electron density (Equation 1.58), which generates an improved estimate of electron probability density. This cycle is repeated for the new approximation of electron density until the newly derived electron density is convergent with the previously calculated one, as shown in figure 1.18. The final KS orbitals are used to determine an accurate electron density and overall $E_{XC}[\rho]$. Finally, using the overall $E_{XC}[\rho]$, alongside the previously calculated classical contribution ($E_{classical}[\rho]$), the overall electrical energy $E[\rho]$ is calculated (Equation 1.57).

Employing the less intensive DFT approach to generate molecular structures also means that using higher accuracy *aug-cc-pVTZ* basis sets instead of the lower–level *cc-pVDZ/cc-pVTZ* is within normal computational cost requirements (for species with < 100 atoms). For these reasons, since the 1990s, DFT has become very widely available and has been increasingly applied throughout computational chemistry literature, as shown by Figure 1.19.[292]

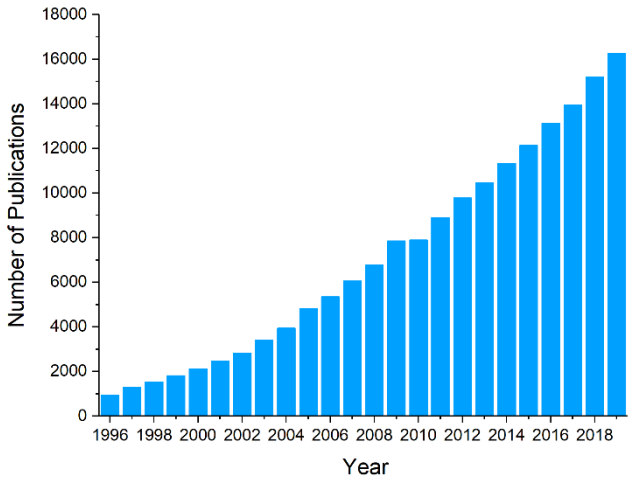

Figure 1.19 Number of publications where the phrase "density functional theory" is found in titles, abstracts and keywords (using Web of Science search functions).[292]

Much research employs the method outlined above, using DFT for optimisation but not single-point energy calculations, so a functional may be adopted to produce accurate geometric structures instead choosing a functional because it adopts a sound theoretical approach towards molecular energy consideration.[224,226,241,272–274,293]

One of the most prevalent functionals in the literature is the hybrid Becke, 3-parameter, and Lee–Yang–Parr (B3LYP) functional.[294-296] This functional is designed to "combine, in variable proportions, local and generalised gradient approximation *[GGA]* treatments of exchange and correlation with HF exchange and are based on the adiabatic connection formula".[297,298] GGA treatment refers to determining exchange and correlation energy dependencies using the gradient of an electron density, $\delta\rho(\boldsymbol{r})$, not only the $\rho(\boldsymbol{r})$ value.[295] The B3LYP equation is displayed below:

$$E_{xc}^{B3LYP} = E_c^{LDA} + E_x^{LDA} + a_c(E_c^{GGA} - E_c^{LDA}) + a_x(E_x^{GGA} - E_x^{LDA}) + a_0(E_x^{HF} - E_x^{LDA})$$

Equation 1.62: B3LYP fitting coefficient equation.

The B3LYP fitting coefficients derived from the fitting of the formulation energies of small molecules, a_0, a_c and a_x are 0.2, 0.81 and 0.72, respectively. Local density approximation functionals for the electron correlation and exchange are the E_c^{LDA} and E_x^{LDA} coefficients, respectively. Generalised gradient approximations, E_c^{GGA} and E_x^{GGA}, are the correlation functional of Lee, Yang and Parr and the exchange functional Becke 1988 (B-88) respectively.[299,300] The HF exchange function is E_x^{HF}.

Selecting a specific functional beyond B3LYP may be difficult as a whole suite of functionals are used in the literature, such as: meta-GGA (or Minnesota) functionals, like M062X; and modified Perdew–Wang 1-parameter model for kinetics functional,

MPW1K.[294,301,302] However, even in full view of this choice, DFT is still widely used, applied in >50% of computational studies, with B3LYP overwhelmingly the most popular functional.[292,295] B3LYP has also been extensively used in the computational literature to determine chemistry of ozonolysis of alkenes and bimolecular chemistry of Criegee intermediates, both of significant interest in this thesis.[131,191,195,293,303–308]

Throughout Chapters 3—6 of this thesis, the computational chemistry data carried out by the author was obtained using state-of-the-art, high-level computational chemistry approaches to determine the tropospheric chemistry of many important gas-phase reactions. The computational chemistry approaches used in this thesis is borne out of much literature precedence both from the author's research group and other studies around the world. One such study by Chhantyal-Pun *et al.* used the same approach seen in this thesis (*DF-HF/DF-LCCSD(T)-F12a/aug-cc-pVTZ//B3LYP/aug-cc-pVTZ*) to produce one-dimensional potential energy surfaces for various sCIs reactions with TFA, which produced theoretical rate constants very similar to those measured experimentally. This study provides a significant computational chemistry precedent for accurate modelling of sCI + TFA reactions, such as those analysed in this thesis (see Section 5.4.2), but also for bimolecular sCI reactions in general.[309] Another such precedent provided for bimolecular sCI reactions, is the studies by the Anglada group, which explore the sCI + H_2O & $(H_2O)_2$ reactions, using a similar computational approach (*CCSD(T)/aug-cc-pVTZ//B3LYP/aug-cc-pVTZ*), as they produce rate constants quite comparable with the experimental literature.[195,293] Similar precedence, where coupled cluster and/or B3LYP methods produce theoretical rate constants similar to those measured experimentally, can be found for alkene ozonolysis in the literature.[121,122,306] These and other similar such examples provide a solid foundation for applying these types of computational approaches to the tropospheric reaction chemistry explored in this thesis.[194,272–274]

[Page is left intentionally blank]

[Page is left intentionally blank]

1.9 Aims and objectives

1.9.1 The Ozonolysis of Alkenes

The first target of this thesis is to produce a computational analysis of the ozonolysis of various alkenes, and to investigate if these alkenes can be divided into taxonomic groups to make them more applicable to atmospheric models. This will involve determining the structure of all stationary points on the potential energy surface and determine, using these structures, the spectroscopic profiles and raw energies using harmonic frequency and molecular energy calculations. The insights from inputting these structures and the information from these calculations into MESMER software allows the production of Master Equation rate constants (k_{ME}) and product branching ratios (Γ_{THEO}). These are then compared with both experimentally determined results (k_{EXP}) and the theoretical canonical rate constants (k_{CAN}).

The common patterns and factors which would make taxonomic classification possible may emerge within the k_{ME} and Γ_{THEO} values when analysed in comparison to the different features within the alkenes studied. These features may include: increasing steric bulk within substituents; hyper-conjugated α-Hs; *E*-/*Z*-conformer; conjugation; and halogenation. An analysis of the epoxide channel and its impact is also undertaken.

1.9.2 Examining Criegee Intermediate–Alcohol Reactions

This is a computational interrogation of the reaction between various atmospheric alcohols and sCIs to determine if these sCIs can also be divided into taxonomic groups. The alcohols of study in this section include methanol, ethanol and isopropanol because they are amongst the most common in the troposphere. The sCI taxonomic groups would be based on if their reactivity correlate with important features such as: *syn* vs *anti* conformers; number of substituent groups; halogenation of substituents; conjugation between unsaturated substituents and sCI group; and a vinyl hydroperoxide channel.

Another aim of this chapter is to validate the author's method of incorporating tunneling rates, by comparing the unimolecular decomposition of various sCIs with high level semi-classical on-the-fly methods.

1.9.3 Bimolecular sinks of Criegee intermediates derived from Hydrofluoroolefins.

The new generation of alkene refrigerants called HFOs undergo ozonolysis to produce HFO-derived sCIs (HFO-sCIs). This study identifies HFO-sCIs that have not been previously investigated (*syn*-/*anti*-CF_3CHOO and *syn*-/*anti*-CF_3CFOO) and compares their reactivity, using computational chemistry, to a benchmark sCI (CH_2OO). The reactivity of these sCIs are computed, generating k_{ME} and the Γ_{THEO} values for their reactions with various atmospheric trace constituents. The focus of this sCI analysis involves investigating the changes in hyperconjugation and hydrogen bonding which emerge from fluorination of the CH_3 substituent group, altering the reactivity of the COO group; and whether a -F substituent group provides inductive effects on both the COO and the $-CF_3$ groups. The co-reactants are examined to see if the reaction is multi-step, with a short-lived intermediate(s) or whether it is one step. This is used to determine if the HFO-sCIs are an effective sink or source of pollutants compared to CH_2OO; and observing the effect of heteroatom tuning of the co-reactants, from the H_2O and HF to H_2S and HCl, has on the reactivity of the sCIs.

1.9.4 Modelling the Ozonolysis of Alkenes With Lengthy Alkyl Substituents

The aim of this section is to determine the k_{THEO} and the Γ_{THEO} values of the ozonolysis of *cis*-2-hexene using a new model based on trends and not direct computational calculations. As a molecule with large amounts of conformeric flexibility, lots of transition states would emerge, putting the system at the very limit for direct calculation. The purpose of these new semi-empirical models is to produce a relative Gibbs free energy (ΔG) for each anticipated transition state and then input these new ΔG into an adapted MESMER file. This MESMER file would then determine the k_{ME} and the Γ_{THEO} values of the ozonolysis for *cis*-2-hexene. These calculated ΔG were determined using already calculated reactants, intermediates, final product ΔG energy, previous relative energy of similar systems and anticipated structural factors on a system-by-system basis. The model is applied to *cis*-2-hexene and on the basis that it produces reliable results, this could be used for other large molecules such as *trans*-2-hexene.

2. Methods

In this thesis, the author seeks to use computational chemistry approaches to determine the kinetics of various gas-phase reactions, such as alkene ozonolysis and bimolecular reactions of stabilised Criegee intermediates (sCIs). This method section fundamentally outlines how to generate two important sets of computational results, the theoretical rate constants (k_{THEO}) and the product branching ratios (Γ_{THEO}). The k_{THEO} constant is a factor that relates the proportional relationship between the rate of reaction and the pressure of the reactants, and so is a measure of reactivity. For reactions with more than one final product, Γ_{THEO} shows the degree of preference for each reaction pathway, through a relative product yield. These thermochemical considerations are important principally because they contribute to understanding the scale and rate of either depletion or generation of important tropospheric species, vital to atmospheric modelling. All raw k_{THEO} & Γ_{THEO} values can be found in the appendix.

Most calculations in this thesis are generated in the following steps: using a computational chemistry programme, such as Gaussian09, to produce geometric structures of the stationary points on a reaction potential energy surface including minima structures (reactants, complexes, intermediate products or final product) and the transition states; the form of these stationary points (the collective term for minima and transition states) are verified by computing harmonic frequencies of their structures and evaluating the number of *imaginary frequencies,* and finally linking these stationary points together with *intrinsic reaction co-ordinate* (IRC) calculations; and using the information obtained by computational calculations to determine k_{THEO} & Γ_{THEO} values, often using interpretive software packages and with high level *ab initio* refined molecular energies. While the backgrounds of thermochemistry and computational chemistry are specified in greater detail in Sections 1.4 & 1.8, the theoretical methods by which these k_{THEO} & Γ_{THEO} values are calculated are delineated in this section.

2.1 Obtaining Stationary Points on a Reaction Surface

All stationary points on the PES need to be identified, including: reactants; all minima (including pre-reaction complexes, intermediate products, post-reaction complexes and final products); and the transition states (TS) between these minima. Identifying every stationary point on the PES is important because the harmonic frequency and molecular energy (ME) calculations of these optimised structures, determine the kinetic data needed to ascertain the k_{THEO} & Γ_{THEO} values. The optimised structures and harmonic frequencies at these stationary points are identified using the computational chemistry suite *Gaussian*

09.[310] These optimisation and harmonic frequency calculations apply the most exhaustively used density functional theory (DFT) hybrid functional: *Becke, 3-parameter, Lee-Yang-Parr*; or B3LYP.[311,312] The high-nonlocality, hybrid meta-exchange DFT functional, M062X, has also been used sparingly, predominantly to verify the reliability of B3LYP as a useful functional for this study (see Section 4.2).[301,313] Dunning's augmented, correlation-consistent, polarised-valence, triplet ζ basis set, or *aug-cc-pVTZ*, was used for all calculated PES structures.[294,300,314,315] Some use is made of the lower level, doublet ζ basis set equivalent, *aug-cc-pVDZ*, for the extensive IRC calculations of large structures. The methods used for geometric optimisation and harmonic frequency calculations, are abbreviated to *B3LYP/aug-cc-pVTZ* and *M062X/aug-cc-pVTZ*.

In this thesis, to simplify understanding of the PES with multiple competing reaction channels, the stationary points are mostly labelled by: the stage of the reaction; the type of reaction undertaken (in subscript); and a number to distinguish it from other channels/subchannels. An example of this nomenclature would be in the ozonolysis of 1-propene, where formaldehyde oxide, or FO, is generated while forming a post-reaction complex with its co-product, labelled as C_{FO} 1 and C_{FO} 2, via the transition states, TS_{FO} 1 and TS_{FO} 2, respectively.

TSs can be obtained using two different types of Synchronous Transit-Guided Quasi-Newton (STQN) methods, referred to as "QST2" and "QST3".[316] The QST2 method uses a "linear synchronous transit or quadratic synchronous transit approach" in finding an initial TS estimate, between the reactant(s) and product(s) geometries; and optimises away from the minimum structure uphill along the minimum energy reaction potential energy curve using a quasi-Newton or eigenvector-following algorithm until the structure converges.[316,317] QST3 operates through the same method, except it requires a third input geometry, an estimated TS suggested by the user, which substitutes for the initial algorithm-estimated TS in QST2. QST2 is often easier to implement and does not require any *a priori* knowledge of the transition state. Alternatively, QST3 can converge more quickly to a solution, and can also converge to the lowest energy solution more readily, assuming the user has some estimation for the transition state geometry. The optimisation precision of both minima and TS structures can be altered by variation of the convergence criteria or the modification of the integration grids.[94,317]

Minima and TS structures can be differentiated by their harmonic frequency calculations, as minima have 0 × imaginary frequencies whereas TSs have only 1 × imaginary frequency. To verify that any given TS is the true inversion point between reactant(s) and product(s), an intrinsic reaction co-ordinate (IRC) calculation is used to map the minimum energy

pathway (MEP) from a TS to the local minima. Each TS requires 2 × IRC calculations to map the MEP in the forward or backward direction of the positive transition vector, referred to as *forward* and *reverse* IRCs respectively.[317] This can be thought of as mapping the reaction from the transition state to the products or reactants.

The IRC calculations involve specification of the size of the gap between points, which is labelled as stepsize (stepsize 1 = 0.01 $amu^{1/2}$/Bohr) and, while the stepsize used for IRCs varies significantly within this thesis, the standard used is a stepsize of ~10.[310] The number of steps provided was 120, referred to by *Gaussian09* as cycles, which is typically sufficient to map out enough of the full reaction curve to optimise a final minimum energy geometry. All IRCs must be calculated using structures derived with the same functional and basis set and all force constants are computed at every point of the IRC.

Under several circumstances, IRCs for reaction pathways cannot be calculated, and so other methods have to be derived to observe the MEP. IRCs require initial forces within the TS to proceed along the MEP, but with low TS barriers, that have small imaginary frequencies, that initial force is much diminished, making IRCs very difficult to ascertain. IRCs also require a TS inversion point to successfully produce a reaction profile, and barrierless reactions have no inversion point to start the IRC. Instead of IRCs, a MEP is obtained using a relaxed PES scan, referred to as the Gaussian09 operation, *modredundant*. This process is described below.

A relaxed PES scan is obtained through a repeating process of: incremental increases/decreases of a specific bond length, bond angle or dihedral angle; freezing that feature; re-optimising the rest of the geometry; and obtaining a molecular energy for the new structure. To obtain an incremental change in that bond length, that maps an MEP from reactant to product, a relaxed PES scan(s) is undertaken using a starting geometry that is either, the reactant(s), product(s) or an anticipated TS. An example of this function in use can be found in Section 5.5.1, for the reaction, between *syn*-CF_3CFOO + CF_3COOH, with many other examples in the appendix. A successful *modredundant* MEP will form an asymptote with no inversion point with respect to the energy of the system, whereas a low TS profile will have a small peak within this same asymptotic MEP.

Molecular orbital calculations were also performed using the *B3LYP/aug-cc-pVTZ* functional and basis set, using the *Gaussian09* software package, and rendered and displayed using the WebMO software. For further details on basis sets, see Section 1.8.1, and for further details on B3LYP and other DFT functionals, see Section 1.8.3.

Single point molecular energies of all stationary points in this thesis are calculated using a coupled cluster (CC) approach, involving single, double and perturbative triple excitations, with additional density fitting approximations to both the correlation correction and the Hartree Fock components.[286] Localisation approximations and a Slater-type correlation "F12a" component are also incorporated into this CC approach.[318] These coupled cluster calculations were also performed using *aug-cc-pVTZ* basis sets. All calculations performed using this *DF-HF/DF-LCCSD(T)-F12a/aug-cc-pVTZ* approach were completed using the *MOLPRO* Quantum Chemistry Software package.[318] For further details on couple cluster approaches, see Section 1.8.2.

2.2 Conventional Transition State Theory (k_{TST}) Rate Constants

To obtain the relative zero-point corrected energy (ΔZPE), enthalpy (ΔH_{298K}) and Gibbs free energy (ΔG_{298K}) (discussed further in section 1.4), appropriate correction factors from the *B3LYP/aug-cc-pVTZ* harmonic frequency calculations are required. These correction factors are then applied to the *DF-HF/DF-LCCSD(T)-F12a/aug-cc-pVTZ* energies. Partition functions (Q) are also obtained from the harmonic frequency calculations. These data are used for the conventional transition state rate constant equations (Equations 2.1—2.6), using either the Q and ΔZPE values or the ΔG_{298K} value, as used in previous studies: [274,319]

$$k_{TST} = \sum k_{TS}$$

Equation 2.1

$$k_{TS} = K_{eq} \times k_2$$

Equation 2.2

$$K_{eq} = \frac{RT}{P_0} \frac{Q_{PRC}}{Q_{R1}Q_{R2}} e^{-(\Delta ZPE_{PRC})/RT}$$

Equation 2.3

$$K_{eq} = \frac{RT}{P_0} e^{-(\Delta G_{PRC})/RT}$$

Equation 2.4

$$k_2 = \boldsymbol{\kappa} \frac{k_B T}{h} \frac{Q_{TS}}{Q_{PRC}} e^{-(\Delta ZPE_{TS} - \Delta ZPE_{PRC})/RT}$$

Equation 2.5

$$k_2 = \boldsymbol{\kappa} \frac{k_B T}{h} e^{-(\Delta G_{TS} - \Delta G_{PRC})/RT}$$

Equation 2.6

The factors in these equations are: $\boldsymbol{\kappa}$ is the tunneling constant (see section 2.6); k_B is Boltzmann constant; T is temperature; h is Planck's constant; R is the gas constant; P_0 is the pressure of the system; Q_{TS}, Q_{PRC}, Q_{R1} and Q_{R2} are the partition functions for transition state, pre-reaction complex, reactant 1 and reactant 2; ΔZPE_{TS} and ΔZPE_{PRC} are the relative zero-point corrected energy of the transition state and pre-reaction complex; ΔG_{TS} and ΔG_{PRC} are the relative molar Gibbs free energy for the transition state and pre-reaction complex, at 298 K. All ΔZPE_{TS} & ΔZPE_{PRC} and ΔG_{TS} & ΔG_{PRC} are relative to the sum of the zero-point corrected energy and the Gibbs free energy of the raw reactants, respectively.

2.3 Dipole-Dipole Capture ($k_{d\text{-}d}$) and Collision Limits (k_{COLL})

The rate constants in this study are fundamentally restrained by the ability for the molecules to collide. If the molecules have no attractive or repulsive forces towards each other, the rate of collision (k_{coll}) only depend on temperature (T), and the mass and the size of the molecules involved, as shown in Equation 2.8. The limits to this collision frequency can be altered somewhat if the molecules are charged or have a significant permanent dipole. In this thesis, there are no charges under consideration, but many reactants have significant dipoles, such that rate constants will increase to the dipole-dipole capture limit ($k_{d\text{-}d}$). The methods for calculating, both the $k_{d\text{-}d}$ and the k_{coll} values, and the reduced mass, μ, (required for both methods), Equations 2.7—2.9, are:

$$k_{d-d} = C\sqrt{\pi/\mu}\ (\mu_{D1}\mu_{D2})^{(2/3)}(k_B T)^{-1/6} \qquad \textit{Equation 2.7}$$

$$k_{COLL} = \left(\frac{8k_B T}{\pi\mu}\right)^{1/2} \pi(r_{R1} + r_{R2})^2 \qquad \textit{Equation 2.8}$$

$$\mu = \left(\frac{m_1 \times m_2}{m_1 + m_2}\right) \qquad \textit{Equation 2.9}$$

Equation 2.7 involves several factors: *C* is a constant dependent on the anisotropy of the capture potential; μ is the reduced mass, calculated using Equation 2.9 and the atomic masses of reactants 1 and 2 (m_1 & m_2); μ_{D1} & μ_{D2} are the dipole moments of reactants 1 and 2 found in the *B3LYP/aug-cc-pVTZ* harmonic frequency file. Equation 2.8 also incorporates the radius of reactants 1 and 2 (r_{R1} & r_{R2}). These calculations have been used to analyse sCI reactions with trifluoracetic, pyric and other organic acids. The *C* value can vary depending on whether the model adopted is isotropic, adiabatic anisotropic or non-adiabatic anisotropic (C= 4.08, 2.68 and 1.953 respectively). In this study, the C value used was the isotropic constant, due to the frequent use of isotropic $k_{d\text{-}d}$ constants in the literature.[309,320] Isotropic $k_{d\text{-}d}$ is referred to as $k_{\text{d-d}}$ for the remainder of the study. All isotropic, adiabatic anisotropic & non-adiabatic anisotropic $k_{\text{d-d}}$ values and all k_{COLL} values for all reactions in the thesis are provided in the appendix.

2.4 *Kinetic and Statistical Thermodynamical Package* (KiSThelP)

Rate constants, as well as both Wigner and Eckart tunneling correction factors, κ_{Wigner} & κ_{Eckart}, (discussed in the next section), can be calculated using the software Kinetic and Statistical Thermodynamical Package (KiSThelP). The *KiSThelP* software uses harmonic vibrational frequencies, in conjunction with the coupled-cluster refined energies to derive

K_{EQ}; k_2; $k_2 + \kappa_{Wigner}$; or $k_2 + \kappa_{Eckart}$. The KiSThelP software only allows for determination of the components of a rate constant and not for the product branching ratios. These components of the rate constant can be used in Equations 2.1 & 2.2 to determine the overall rate constants.

One very useful classification of the different types of reaction in this thesis depends on whether the reaction goes directly through to completion, referred to as a single/one-step reaction; or reacts to produce a short-lived intermediate(s) before decomposing into the final product(s), described as a two-/multi-step reaction. This classification does not refer to pre-/post-reaction complexes as examples of short-lived intermediates and does not refer to the number of different final products. KiSThelP is used for the sCI + alcohol reaction section (Chapter 4), as it is an example of a single-step reaction, without involving any intermediate products. The implications of this are that the component rate-coefficients (k_{TS}) provided by both different channels and subchannels are sufficient to determine the overall k_{THEO} and Γ_{THEO} values.

2.5 *Master Equation Solver for Multi-Energy Well Reactions* (MESMER)

The *Master Equation Solver for Multi-Energy Well Reactions* (MESMER) software was used to compute both k_{THEO} and Γ_{THEO} values for the ozonolysis of alkenes (Chapters 3 & 5) and the HFO-sCIs reactions (Chapter 4) as it can generate product branching ratios for multi-step reactions, which have multiple final products.

Using a MESMER template and the software *OpenBabel*, all raw harmonic frequency Gaussian files for all stationary points on the reaction potential energy surface are compiled into a single ".xml" file. This file requires some key reaction information and parameters to be inserted manually before any MESMER calculations take place. The first of these is the bath gas and that bath gas's collisional transfer factor, which is an N_2 bath gas and an $<\Delta E_{down}>$ factor of 300 cm^{-1} throughout. Standard $<\Delta E_{down}>$ values are 250—500 cm^{-1} for systems with O_2 and N_2 bath gases.[321-324] Each MESMER file requires the input of the relative zero-point corrected energy, not the raw electron energy. Quantum mechanical external rotors (QM rotors) are used instead of classical rotors, which has precedent in the literature for reactions involving Criegee intermediates.[325] Excess reactant concentration is set at 1×10^{16} molec. cm^{-3} and the inverse Laplace transform (ILT) capture rate coefficient is set at 1×10^{-10} cm^3 s^{-1}. An Eckart tunneling factor is used for all reactions with TS barriers but, unlike with the *KiSThelP* software, MESMER incorporates the Eckart factors into its rate constants and does not produce them separately.

All reactions with sizeable barriers use a simple Rice-Ramsperger-Kassel-Marcus (*SimpleRRKM*) method, which specifies the use of the κ_{Eckart} function. If the TS barrier is quite low, with a small imaginary frequency, the κ_{Eckart} function is not applied, as tunneling has little impact on the overall rate. For reactions where the κ_{Eckart} function is not applied, it is noted in the appendix. All barrierless reactions which involve two reactants but form one product, such as the association of a pre-reaction complex, an inverse Laplace transformation, or *MesmerILT,* method is used to calculate K_{eq}. As this MESMER calculation is based on *pseudo-first order rate constant* calculations, all chemical structures in the system must be classified as: a *deficient reactant*, the concentration dependent reactant; *excess reactants*; *modelled* structures, which are the intermediate products; and *sinks*, the final products of the reaction. If there are multiple products to a *SimpleRRKM* pathway these products often initially form a structure referred to as a post-reaction complex, using intermolecular bonds between the multiple products, and the structure of that complex is used as the *sink* rather than the separated products.

If the reaction involves one intermediate product undergoing a barrierless unimolecular dissociation into two products, such as when CH_2OO decomposes into HCO + OH, a reverse inverse Laplace transformation (*reverse ILT*) method is adopted.[326,327] This requires both final products to be set as separate *sink* structures, the pre-exponential factor is assigned to the reverse function with a value equated to the dipole-dipole capture limit ($k_{d\text{-}d}$) of the equivalent forward reaction. This replicates the literature use of the *reverse ILT* method for the HCO + OH and CH_3 + NH exit channels in the unimolecular decompositions of CH_2OO and CH_3NH respectively. [326,327] However, the pre-exponential factors used in these studies are experimental rate constant (k_{EXP}) taken from the literature, instead of the $k_{d\text{-}d}$ values. This can be found in section 5.3.1 in the case of the **sCI 23** + HCHO reaction, where the intermediate HOZ product produces **sCI 1** + CF_3CHO, through a barrierless channel.

MESMER calculates master equation rate constants (k_{ME}), derived through microcanonical rate constants, which use a rigid rotor harmonic oscillator approximation and a stochastic energy-grained master equation (EGME). These EGME calculations depend on “grains” which are a “bundle” of rovibrational states with comparable energies on the PES, and these can be used to approximate the distribution of the deficient reactants across the stages of energy schematic, as a function of time.[321] The accuracy of the micro-canonical rate constants and therefore the whole system, depends on the grain size, which must be selected for each system. The default grain size used herein is 10 cm^{-1}, but many systems are too large or complex to use this small grain size, so larger grain sizes are selected. The highest energy to which the specified energy range spans is dictated by the

energyAboveTheTopHill procedure. This sets that the highest energy as ~x × *kT*, and x is set to 30, in line with prior Criegee intermediate studies.[321,325] The grain size used for each reaction system are found in the appendix.

The software allows the user to specify temperatures over which to compute the rate constants, and in general 200, 275, 298, 325 & 400 K temperatures have been selected herein, all at standard pressure. The temperatures and pressures are modified in those instances where direct comparison with experimental conditions are required. These temperatures have been selected as they span the temperature range of the troposphere.

The MESMER software produces two types of rate constants, the full master equation treatment rate constant (k_{ME}) and the individual canonical rate coefficients which, coupled with the steady state approximation, produce the overall canonical rate constant (k_{CAN}). This use of the steady state approximation to produce the overall canonical rate constant (k_{CAN}), is displayed in Equation 2.10.

$$k_{CAN} = \sum \left(\frac{k_1}{k_{-1}} \times k_2 \right) \qquad \textit{Equation 2.10}$$

Both types of rate constants produced by MESMER are generated from single step reactions or from pseudo-single step simulations of multistep reactions. On the other hand, MESMER calculations of the full reaction cannot only produce the final product branching ratios for both the single-step reactions and two-step reactions but also the fractional species population the whole system as a function of time. This is done in both numerical and graphical representation.

2.6 Tunneling (κ) Constants

One quantum mechanical phenomenon of note is where the quantum shift of particular atoms involved in transition state mechanisms can facilitate the shift or "tunnel" through the classical energy reaction barriers between reactant(s) and product(s). This is referred to as *quantum tunneling* and can have a strong impact on mechanisms involving low mass atom motion, due to the significant capacity for smaller atoms to exhibit the properties of a wave. A computational examination of the *syn*-CH_3CHOO and H_2O reaction by Anglada and Sole, showed that importance of quantum tunneling, not only by this feature increasing the overall rate constant, but by also increasing the product yield of vinyl hydroperoxide from ~ 2% to ~51%. This shows the important impact of quantum tunneling on both overall k_{THEO} and Γ_{THEO} values, which could be replicated in other reactions with significant amount of low mass atom motion, such as the *syn*-CH_3CHOO + MeOH and CH_2OO + $(H_2O)_2$ reactions.

There are several methods for obtaining the tunneling constant ($\boldsymbol{\kappa}$) which are included in this study. One of the simplest $\boldsymbol{\kappa}$ constant is referred to as the Wigner factor, developed by *E. Wigner*.[328] To calculate this simple tunneling correction, this formula is supplied:[329]

$$\boldsymbol{\kappa}_{Wigner} = 1 + \frac{1}{24}\left[\frac{h \times Im(v^{\ddagger})}{k_b T}\right]^2 \qquad \textit{Equation 2.11}$$

This involves several factors including: *T* is temperature; *h* is Planck's constant; k_b is Boltzmann's constant; $Im(v^{\ddagger})$ is the imaginary frequency of the transition state. This method is mainly used as a comparison to the other tunneling methods, found in Section 3.5.1. The main method used throughout this study is the asymmetrical Eckart tunneling correction ($\boldsymbol{\kappa}_{Eckart}$). The $\boldsymbol{\kappa}_{Eckart}$ is calculated using the probability of transmission through the one-dimensional energy barrier (*p(E)*) (Equation 2.12). The α, β, δ, A, B and C factors that are part of the formation of *p(E)*, are formed by Equations 2.13—2.18:

$$p(E) = 1 - \left[\frac{\cosh[2\pi(\alpha - \beta)] + \cosh[2\pi\delta]}{\cosh[2\pi(\alpha + \beta)] + \cosh[2\pi\delta]}\right] \qquad \textit{Equation 2.12}$$

$$\alpha = \frac{1}{2\sqrt{C}}\sqrt{E} \qquad \textit{Equation 2.13} \qquad \beta = \frac{1}{2\sqrt{C}}\sqrt{E - A} \qquad \textit{Equation 2.14}$$

$$\delta = \frac{1}{2\sqrt{C}}\sqrt{B - C} \qquad \textit{Equation 2.15} \qquad A = \Delta H_f^{\ddagger,0K} - \Delta H_r^{\ddagger} \qquad \textit{Equation 2.16}$$

$$B = \sqrt{\Delta H_f^{\ddagger,\mathbf{0K}}} - \sqrt{\Delta H_r^{\ddagger,\mathbf{0K}}} \qquad \textit{Equation 2.17} \qquad C = \left(h.\mathrm{im}(v^{\ddagger})\right)^2 \left[\frac{B^3}{A^2 - B^2}\right]^2 \qquad \textit{Equation 2.18}$$

The three main inputs into these equations are: the zero-point corrected energy barrier between the pre-reaction minima and the TS or the "forward" barrier, $\Delta H_f^{\ddagger,\mathbf{0K}}$; the zero-point corrected energy barrier between the post-reaction minima and TS or the "reverse" barrier, $\Delta H_r^{\ddagger,\mathbf{0K}}$; and the imaginary frequency of the transition state, $Im(v^{\ddagger})$. The Eckart function is then calculated using Equation 2.19.

$$\boldsymbol{\kappa} = \frac{e^{\Delta H_f^{\ddagger,\mathbf{0K}}}}{k_b T} \int_0^{\infty} p(E)\, e^{-\frac{E}{k_b T}} \mathrm{d}E \qquad \textit{Equation 2.19}$$

The *KiSThelP* software uses a 15-point Gauss–Laguerre integration to evaluate Equation 2.19. Both the $\boldsymbol{\kappa}_{Wigner}$ and $\boldsymbol{\kappa}_{Eckart}$ tunneling corrections are non-*ab initio* methods of computing tunneling constants. This $\boldsymbol{\kappa}_{Eckart}$ tunneling constant's main benefit is its accuracy compared to $\boldsymbol{\kappa}_{Wigner}$, combined with its comparative computational cheapness, particularly when compared to the more complex methods such as semiclassical on-the-fly instanton methods.[330] In section 4.5.1, the accuracy of the $\boldsymbol{\kappa}_{Eckart}$ tunneling corrections is benchmarked, by comparing it with these more accurate methods.

This instanton method is based on using ring-polymer beads to map a series of geometries, or "beads", which are on the transition state path close to the TS barrier. The number of beads, *N*, was varied between 16-256 beads depending on the different levels of theory used. Calculations were performed using either *DF-DFT//B3LYP/cc-pVTZ* or *CCSD(T)/cc-pVTZ* to investigate unimolecular decomposition of *syn*-CH_3CHOO and syn-CH_2=CHC(CH_3)OO. As $N \rightarrow \infty$, Eyring & instanton rate constants reach more accurate values, however the computational cost also increases. Higher-level electronic structure methods can also be used to increase the accuracy, as the more precise PES obtained, the smaller the errors of the bead shapes.[330-334] Instanton calculations are carried out using the Molpro computational package.[318] The appendix has a full breakdown of raw data from this work.

2.7 Structure Activity Relationship Rate Constant (k_{SAR})

The accuracy of the theoretical alkene ozonolysis chemistry calculated for this thesis are sometimes compared to values calculated using a *structure-activity relationship* (SAR) model derived by McGillen and co-workers.[118] The equations that produce the SAR rate constant, k_{SAR}, (Equations 2.20—2.22) were derived by fitting a large number of alkene ozonolysis k_{EXP} values to the number of relevant structural features of those alkenes.[118] Therefore, in this thesis, these k_{SAR} values are used as a substitute for k_{EXP} values, where such values are not found in the literature, such as for O_3 + 2,4-dimethyl-2-pentene.[10]

The structural features are key because the number of alkyl substituents do have an inductive effect on the >C=C< bond, but the size and the position of those substituents can inhibit O_3 reaction with that >C=C< group.[118] In this SAR model, the inductive contribution (I) is dictated only by the number of alkyl groups attached to the >C=C< bond (ranging from 0—4). The steric contribution (S), according to Equation 2.20, is derived from a sum of: the obstruction caused by two alkyl substituents at one end of the >C=C< bond (s_0 = 0.20); the obstruction of extra α-alkyl groups (s_1 = 0.033); and the obstruction of extra ß-alkyl groups (s_2 = 0.020). These steric and inductive factors are combined into a single compound inductive steric factor, the "x" value in Equation 2.21.

$$S = \sum s_n \qquad \text{Equation 2.20}$$

$$x = (yS) + I \qquad \text{Equation 2.21}$$

A good example to explain this method is 2,4-dimethyl-1-pentene because the total steric contribution (~0.283) has at least one steric contribution from each factor: 1 × 0.20, for the one set of alkyl groups at the end of an alkene bond; 2 × 0.033 for the two extra α-alkyl groups; 1 × 0.020 for the one extra ß-alkyl group.[118,335] As 2,4-dimethyl-1-pentene has 3 alkyl substituent groups and therefore the total inductive factor (or "*I*") would be 3.

The "x" value in Equation 2.21 is composed of: a total inductive effect, *I*; *y*, a negative constant (-4.04); and the total steric effect (*S*), (Equation 2.20). This "x" value is then the only independent factor to the k_{SAR} value in Equation 2.22:

$$\log k_{SAR}(298\,K) = (1.28 \pm 0.05)x - (18.14 \pm 0.07) \qquad \textit{Equation 2.22}$$

For a full background to this method see appendix.

2.8 Determining the Primary Theoretical Rate Constants (k_{THEO})

In this thesis, the primary theoretical rate constant (k_{THEO}) is usually calculated using either the MESMER master equation rate constant (k_{ME}) or conventional transition state theory (k_{TST}). However, as stated in section 2.3, the main restraint on those reactions, which are either barrierless or with large k_{ME} values (≥ 10^{-10} cm^3 s^{-1}), is the rapidity of collision, calculated using the isotropic dipole-dipole capture limit ($k_{d\text{-}d}$). In situations where $k_{ME} > k_{d\text{-}d}$, $k_{d\text{-}d}$ is employed as the primary k_{THEO} constant because the kinetic barrier is so low that every collision leads to a reaction. The collision limit (k_{COLL}) is also referred to in the main body of the thesis as a comparative tool in situations such as where k_{EXP} is slightly lower than both k_{THEO} and $k_{d\text{-}d}$ constants.

2.9 Defining the Reliability of this Computational Chemistry Approach

As DFT functionals, such as B3LYP in the *DF-HF/DF-LCCSD-F12a//B3LYP/aug-cc-pVTZ* approach (referred to here as the *B3LYP-optimised* approach), are often purposely built and selected because they model the particular target chemical systems well, making an extended error calculations difficult. Instead, here, the author provides a level of confidence for this *B3LYP-optimised* approach by comparing the energies of the TS barriers for sCI + alcohol reactions against both experimentally and other computationally derived barriers.

The first technique used to examine the reliability involves comparing the relative energy (ΔE) of, for instance, the TS_{AAAH} 1 & TS_{AAAH} 2 barriers from CH_2OO + MeOH using the *B3LYP-optimised* approach (-3.8 & 0.1 kJ mol^{-1}) to that of another approach, here the *DF-HF/DF-LCCSD-F12a//M062X/aug-cc-pVTZ* approach (-7.1 & 3.2 kJ mol^{-1}). The energy differences between these approaches for each TS are averaged to determine a *scope of agreeability* factor, (Δ_{AGREE} ~±3.2 kJ mol^{-1}). These small Δ_{AGREE} values provide a rough indicator of a good quality confidence level for the *B3LYP-optimised* approach. Also, when Aroeira *et al.* produced the CH_2OO + MeOH TS_{AAAH} 1 barrier (-6.2 kJ mol^{-1}), using an exhaustive *QCISD(T)/CBS//CCSD(T)/ANO1*-based approach, the Δ_{AGREE} value was also quite small (2.4 kJ mol^{-1}), further authenticating the confidence level for the *B3LYP-optimised* approach.

The second assessment of reliability involves comparing the relative Gibbs free energy of the TS structure, say the ΔG_{THEO} value of the TS_{AAAH} 1 from the CH_2OO + MeOH reaction (42.6 kJ mol^{-1}), to those derived from other experimental or theoretical studies, such as McGillen *et al*. study (ΔG_{EXP} (TS_{AAAH} 1) ~ 37.2 kJ mol^{-1}). This the ΔG_{THEO} value is the key thermodynamic value that characterizes the relationship between the TS, the k_{THEO} values and the product Γ_{THEO} values at a specified temperature and so a *sensitivity variation* (Δ_{SENSI}), derived from difference in ΔG (TS_{AAAH} 1) values, can also indicate a confidence level for the *B3LYP-optimised* approach. The modest size of the Δ_{SENSI} values (~5.3 kJ mol^{-1}) further confirms confidence in this *B3LYP-optimised* approach.

In the extended sensitivity study of many sCI + alcohol reactions, in Appendix Section 2.9, the *B3LYP-optimised* approach mostly yield similarly modest Δ_{AGREE} and Δ_{SENSI} factors when compared to with methodologies in both the experimental and computational literature. For this reason, the Δ_{AGREE} ~±3.2 kJ mol^{-1} seems to be the adequate estimation of the margin of uncertainty in the data. However, this is not a traditional error calculation, and instead the Δ_{AGREE} and Δ_{SENSI} values are derived by evaluating numerical discrepancies between *different* overall approaches. Also of note is that the number of decimal places given in the data presented in this thesis, does not necessarily reflect the Δ_{AGREE} or Δ_{SENSI} values given here.

3.0 The Ozonolysis of Alkenes: A Computational Study

This chapter provides a comprehensive computational chemistry examination of alkene ozonolysis, a natural removal mechanism for alkenes found within the troposphere. This analysis is important because this route, and in turn the formation of a primary ozonide, is a common depletion mechanism for alkenes and O_3, both of which can be harmful to human health. The magnitude or tropospheric significance of these depletion pathways are quantified principally through determining the master equation rate constant (k_{ME}). Identifying the products from fragmentation of the POZ intermediate and determining the branching ratio (Γ_{THEO}) of the subsequent products is also a principle aim of this study. This Γ_{THEO} value is important principally because one of the primary products, Criegee intermediates (CI), are implicated in the depletion of many different toxic pollutants, and contrary to this positive effect are implicated in secondary aerosol formation. Throughout this chapter, the alkenes are grouped by structural and electronic factors such as: the number of >C=C< substituents, steric bulk of or the numbers of inductive α-hydrogen (α-H) atoms within these substituents. If such groupings by substituent characteristics is seen to have a clear relationship with the k_{ME} and/or Γ_{THEO} values, then these taxonomic groupings could be used to produce predictive models of ozonolysis of alkene chemistry, reducing computational cost of such calculations.

3.1 Introduction

3.1.1 The Overall Chemistry and Importance of Alkene Ozonolysis

Tropospheric alkenes are associated with respiratory irritation and occasionally carcinogenic health problems and they also have a significant role in depleting other harmful pollutants (e.g. SO_2 and NO_2). Alkenes, such as 2-butene (seen in Figure 3.1), are distinguished from alkanes by the unsaturated nature of a >C=C< functional group. The four substituent groups attached to the >C=C< bond have a significant influence on alkene chemistry, as shown by the capacity for bulky groups to lower reactivity by hindering the approach of co-reactants to the >C=C< bond. Some substituents can alter electronic character of the alkene, as shown by additional alkene or carbonyl groups in di-alkenes (or dienes) and unsaturated ketones (or enones).

If the >C=C< bond has two different substituents at each end (like with 2-butene in Figure 3.1), the alkene exists in two different isomeric forms: the *E*-isomer and the *Z*-isomer (sometimes also referred to as *trans*- & *cis*-isomers). *E*- & *Z*-alkenes have a high energy barrier to interconversion because the π-component of the >C=C< bond involves a coplanar

overlap of the two singularly-occupied $2p_Z$ orbitals and the 180° spin involved in isomerisation interrupts that overlap.[336] The separate boiling points for *E*- & *Z*-2-butene (3.7 & 0.9 °C) show that *E*- & *Z*-alkenes have their own distinct characteristics.[336]

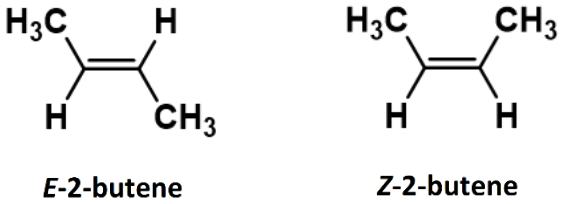

Figure 3.1: Terminology used throughout, E-and Z-2-butene conformers.

It is important to understand alkenes sources and sinks in order to capture changes in their tropospheric concentrations, perhaps as a result of changing pollution levels, which ultimately may have an impact on human health or the biosphere in general. Sources and sinks fall into two main categories: biogenic and anthropogenic. Biogenic sources of alkenes are predominantly from foliar emissions. Biogenic sources generate species including isoprene, emitted from shrubs and boric forests, α- & ß-pinene from pine trees and limonene from orange peels.[81,150-153] Anthropogenic alkenes are produced either by human activity such as ethene and propene evaporation from automobile fuel, or synthetic alkenes produced for human uses such as HFO-1234yf and HFO-1233zd(e), which are used as car refrigerants.[227,337,338]

The differentiation between biogenic and anthropogenic alkene emissions provides a practical example of the different impact between *global* and *local* emissions. *Global* emissions are usually released at such a rate and/or have a long enough lifetime that their presence and impact can be significant on a planetary level, seen with the greenhouse effect caused by large amounts of CO_2 emissions. Many other types of species that are generated are referred to as *local* because, even if they have a negligible effect on a planetary level, they have significant abundances in the region near large emitters. These include species that have strong emissions caused by certain geographic features (e.g. volcanic H_2S), large human populations (e.g. vehicular SO_2), or uncommon conditions of weather restricting or causing an amalgamation of pollutants (e.g. photochemical smog).

Biogenic alkenes dominate the global emission profile, with isoprene emissions totalling ~80% of biogenic volatile organic compound (VOC) emissions.[81,339] Many of the biogenic alkenes have comparably larger molecular weights, such as isoprene, the most tropospherically-emitted alkene at ~600 Tg (C) yr^{-1}.[81]

Localised tropospheric species, on the other hand, are generated at high rates only in certain areas, such as volcanoes or cities, have little planetary impact due to short

lifetimes and/or low global emission rates. While anthropogenic emissions of ethene and propene are small on a global level, 8 Tg (C) yr^{-1} of the 200 Tg (C) yr^{-1} by some studies, the emissions from car fuel has been shown to cause significant concentrations of such gaseous alkenes in Mega Cities.[182,337]

Despite the large variety of sinks (such as those formed in reactions with NO_3 and Cl radicals), reactions with OH radicals and ozone (O_3) (referred to as alkene ozonolysis) are the dominant decay pathways for many gaseous alkenes.[118,224,227] One of the key reasons the alkene ozonolysis, featured in Figure 3.2, is explored in this study is that the process has been implicated as a major source of night-time OH radicals. OH radicals are predominantly produced during the day through the excited singlet $O(^1D)$ atom, generated by the photolysis of O_3 reacting with abundant gaseous H_2O (see Sections 1.3.1 & 1.5.1).[10,15] A night-time abundance of OH radicals (referred to as an *atmospheric detergent*) is important because OH radicals has a significant capacity to remove toxins and radical species, such as NO_2, SO_2 and NO.[2] For further details on OH radicals, see Introduction Section 1.5.1.

Tropospheric O_3, a major reactant in this chapter, has some very harmful effects because it is both a greenhouse gas and a strong oxidant.[2,121,340] This strong oxidising effect means it can cause severe respiratory problems and it is also implicated in the formation of photochemical smog in urban environments.[2,19,20] These health costs of tropospheric O_3 are somewhat offset by their reaction with significant levels of tropospheric alkenes, as the Criegee intermediates (CIs) and secondary OH radicals produced are both implicated with removal of atmospheric toxins.[2,111] While further details on other atmospheric processes involving O_3 can be found in introduction sections 1.3.1 and 1.5, this process of alkene ozonolysis, will be the main subject of further discussion and research in this chapter. The reaction sequence of the ozonolysis of alkenes is found in Figure 3.2:

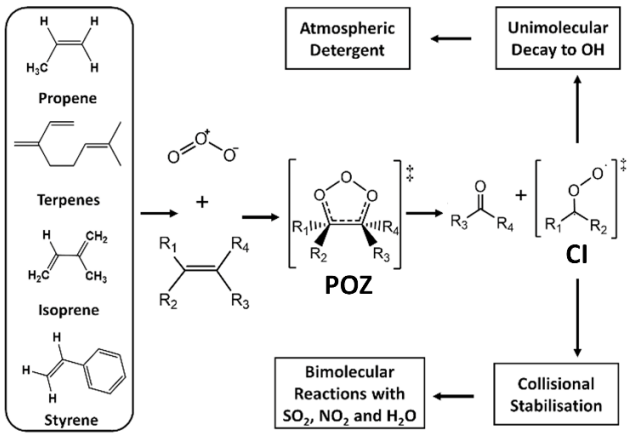

Figure 3.2: Reaction schematic for the ozonolysis of atmospheric alkenes and subsequent Criegee intermediates processes.

The initial 1,3—cycloaddition step in the ozonolysis reaction sequence produces a short-lived 5-membered ring intermediate compound, known as a primary ozonide (POZ), or a 1,2,3-trioxolane adduct. The excess energy produced during the ozonolysis step and the significant amount of tortional strain within the structure, leads to almost instantaneous fragmentation after POZ formation. This fragmentation proceeds via mutual fissures in the original >C=C< bond and one of the O—O—O bonds, after formation into an aldehyde or ketone and a CI, represented by R_3R_4CO and R_1R_2COO respectively in Figure 3.2. There is also some theoretical and experimental evidence that small yields of epoxide products can be produced from the O_3 + alkene reaction.[121,341,342] Conformeric rotation within the ring structure of the POZ is limited to pseudorotation, whereas the R_1 — R_4 groups can freely rotate along the POZ - substituent bond axis.) The energy barriers reported for both pseudorotations (usually ~12.6 kJ mol^{-1}) and alkyl substituent rotations (~9.2—13.4 kJ mol^{-1}) are found in the theoretical literature to be low, meaning these POZ conformers likely freely interconvert.[121,343] This free interconversion between POZs means all cycloaddition pathways can produce all POZ conformers and POZ fragmentation mechanisms do not differentiate between different POZs.

The large amount of internal energy released during O_3 + 2,3-dimethylbutene (ca. 200—250 kJ mol^{-1}), is common across alkene ozonolysis reactions and therefore most CI products will be generated with a high degree of internal energy.[123] This excess energy leads to a significant fraction of the CIs (37—50%) fragmenting before they can undergo stabilising collisions to form what are termed herein as stabilised Criegee intermediates (sCIs).[123,126–135] The degree of rapid unimolecular CI fragmentation and the OH yield changes depending on the CI produced, for example the OH yield of $CH_2OO^{‡}$ is ~0.12 and of $CH_3CHOO^{‡}$ is ~0.23±0.18.[108,133,135,164–167] Previous studies have shown that altering the alkene substituents has a significant impact on the ozonolysis rate constants, CI identity &

branching fraction, which has a knock-on effect on the ensuing yields of OH radical & the sCI species.[10] As both these species are consequential in atmospheric models, the importance of determining the ozonolysis chemistry of each tropospheric alkene is highlighted. As shown in Figure 3.3, the main structure of the CI/sCI is a unsaturated carbonyl oxide (COO) group with two flanking substituent groups attached to the central C atom.

In much of the literature, it has been observed that sCI bimolecular chemistry aligns significantly with certain structural groups (disubstituted sCIs, *syn*-sCIs and *anti*-sCIs) and so examples of each are included in Figure 3.3 as well as the simplest CI (CH_2OO). "Monosubstituted" sCIs, such as CH_3CHOO, form two separate *anti*- & *syn*-sCI conformers, which differ only by the spatial position of the largest substituent by the greatest number of atoms (see Figure 3.3). These conformers are chemically distinct, like *E*- & *Z*-alkenes, due to their significantly different chemistries and high barrier to interconversion (>100 kJ mol^{-1}). For instance, if the $-CH_3$ substituent for CH_3CHOO is in the *anti* position, the hyperconjugative α-H atoms *induce* greater reactivity in, or *activates*, the COO functional group.[93,111,344] Whereas, if the $-CH_3$ substituent is in the *syn* position, these α-H atoms can have a hyperconjugative stabilising effect and can also form an electrostatic force of attraction with the terminal oxygen on the COO group, both of which *reduce* the reactivity of, or *deactivate*, the COO group.[93,195,344] Large *syn* substituents can also have a *reductive* effect by obstructing between with the COO group and the co-reactant.

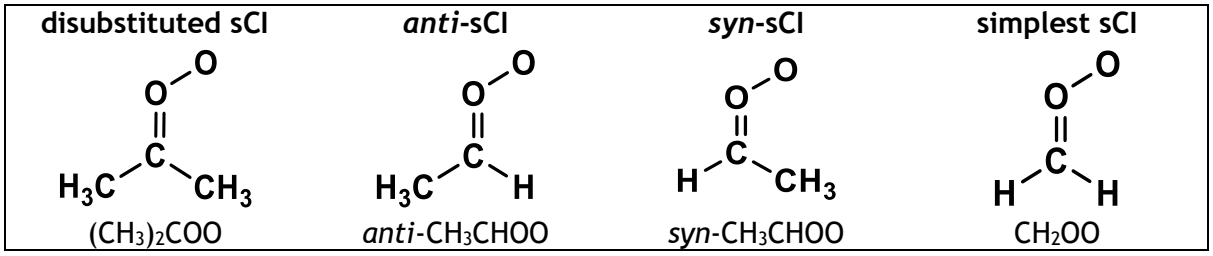

Figure 3.3: Schematic of 3 groups of sCIs (disubstituted, anti- & syn-sCI) with examples of each; and the simplest sCI

Disubstituted sCIs, such as $(CH_3)_2COO$, have substituents in both the *anti*- & *syn*- positions meaning that the impact on the COO groups is a combination of both of these types of *activating* and *deactivating* hyperconjugative factors (referred to collectively as *electronic effects*).[93,111,274] However, CH_2OO is categorised separately, as the —H substituents in the *anti* and *syn* positions do not provide the same the *electronic* effects as other substituents.[51,111]

One of the key hypotheses of this chapter is that factors seen to alter or impact upon sCI chemistry, such as bulky substituents obstructing reactions site, also influence the

ozonolysis chemistry of alkenes. As the presence of hyperconjugative α-H atoms within alkyl substituent groups can alter the character of the COO group in an sCI, adjusting the number of α-H atoms within alkene substituents also tunes the chemistry of the unsaturated >C=C< bond. If these alkene structural features do impact electronic and steric aspects of the ozonolysis chemistry, a taxonomic classification system could be constructed to determine ozonolysis chemistry of a much wider variety of alkenes, without the burden of significant computational cost. As alkene ozonolysis is not just responsible for the reduction of O_3 and alkene populations, but also indirectly responsible for depleting pollutants through secondary reactions with OH radical and sCI species (see Chapters 4—5 for further examples), shows the importance of such a model.[2] A computational chemistry analysis into the ozonolysis of various alkene is undertaken in this chapter to discern whether generating such a taxonomic classification model using factors mentioned above is possible.

3.1.2 Alkene Involved in this Study.

As discussed previously, here the author uses computational chemistry to determine the master equation rate constant (k_{ME}) & branching fractions of alkene ozonolysis products (Γ_{THEO}); assessing how this relates to the common electronic and structural factors; and whether this analysis allows for generating taxonomic alkene groups for a predictive model. The alkenes studied in this chapter, labelled Alkenes **1**—**20**, are grouped in Figure 3.4 on the basis of common structural features. These groups are referred to as: *monosubstituted* alkenes, *trisubstituted* alkenes, hydrofluoroolefins, *E*- & *Z*-alkenes, and 2-methylpropene.

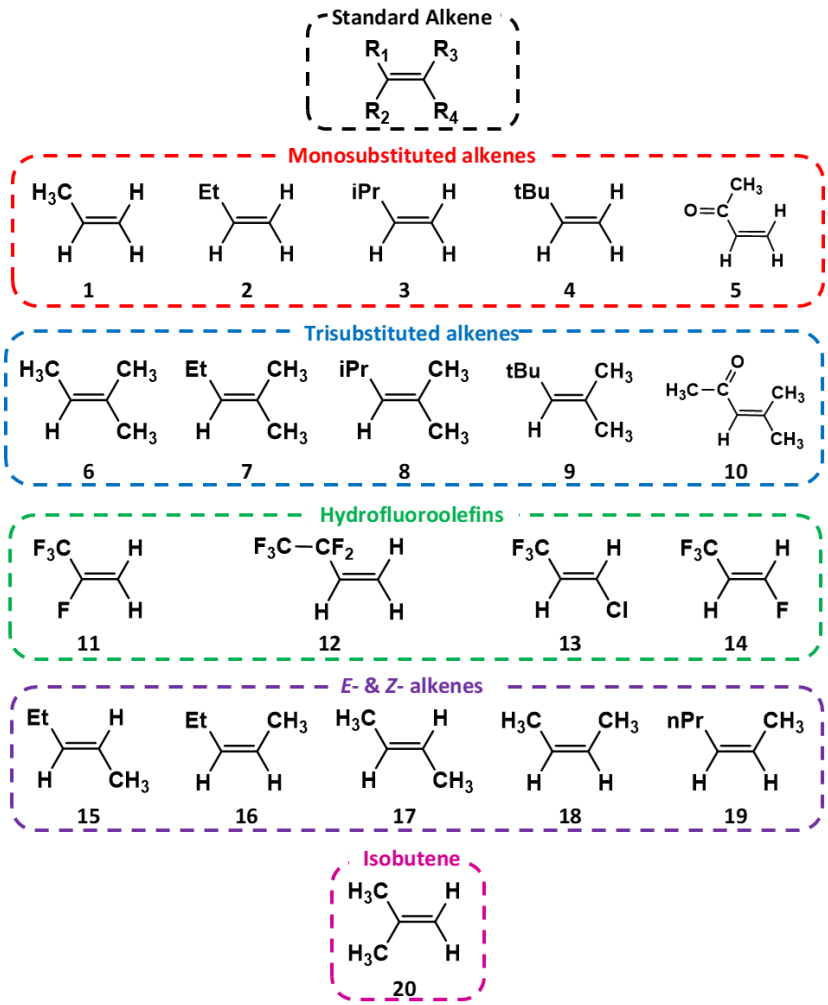

*Figure 3.4: Alkenes, labelled **1**-**20** and delineated by structural factors, modelled for ozonolysis analysis in this chapter.*

Monosubstituted alkenes have the common structure of R_1—CH=CH_2, where the —R_1 position is substituted with increasingly bulky and complex substituents. As seen in Figure 3.4, the chosen group consists of propene, 1-butene, 3-methyl-1-butene, 3,3-dimethyl-1-butene and methyl vinyl ketone, referred to herein as Alkenes **1**—**5**. As there is a stepwise decline in the number of α-H atoms within the —R_1 group across Alkenes **1**—**5**, comparing the different k_{ME} and/or Γ_{THEO} values of these reactions can be used to determine whether altering the number of hyperconjugative α-H atoms does tune the ozonolysis chemistry. The tropospheric importance of the O_3 reaction with Alkenes **1**—**4** are important in urban areas due to the high abundance of Alkenes **1** & **2**, in major cities such as Porto Alegre, Brazil (28.3 & 7.8 ppb respectively).[182,345] The high boiling points of Alkenes **3** & **4** restricts the tropospheric role of their ozonolysis reactions.[345] However, the highest tropospheric levels of Alkene **5** are in the rainforest (~1 ppb) and so the O_3 + Alkene **5** reaction is more important in natural environments.[182,345]

The *trisubstituted* alkenes, 2-methyl-2-butene, 2-methyl-2-pentene, 2,4-dimethyl-2-pentene, 2,4,4-trimethyl-2-pentene and mesityl oxide, are labelled **6**—**10**. The stepwise decline in the number α-H atoms in the $-R_1$ group above is replicated for Alkenes **6**—**10**, affording a direct comparison of reactivity trends. When the ozonolysis of Alkenes **6**—**10** is compared to Alkenes **1**—**5**, the inductive impact of two additional $-CH_3$ groups can be quantified across 5 different reaction sets. Of these *trisubstituted* species, the largest typical urban concentrations are for Alkenes **6** & **7** (~0.1—1 ppb) and even higher abundances in cities like Porto Alegre (17 & 4 ppb respectively).[182,345] Much like with Alkenes **3** & **4**, the greater number of substituent branches, and corresponding increase in boiling point, produces lower tropospheric concentrations for Alkenes **8** & **9** (~0.01 ppb).[345] Another important comparison is that between the enones (Alkenes **5** & **10**), which, as they both have an $-C(O)CH_3$ substituent group, are used to determine whether conjugated carbonyl substituent groups have a comparative inductive or reductive impact on k_{ME} values or CI yields. While determining the impact of ketone substituents, such as the $-C(O)CH_3$ group, is important, the very high boiling point of Alkene **10** (130 ^{o}C) and lack of biogenic or anthropogenic emitters makes significant tropospheric presence unlikely.[346]

The halogenated alkenes, 2,3,3,3-tetrafluoropropene, 3,3,4,4,4-pentfluoro-1-butene, 1-chloro-3,3,3-trifluoropropene and 1,3,3,3-tetrafluoropropene, are labelled **11**—**14**. These hydrochlorofluoroolefins (HCFOs) and hydrofluoroolefins (HFOs) are referred to generically as HFOs throughout this thesis. Studies of HFO ozonolysis have been sparing in the literature, but they are included in this chapter because they are now being phased in to replace older haloalkane refrigerants, with larger ozone depletion potentials (ODPs) and/or high global warming potentials (GWPs).[197,198] Greater HFO sales in the EU, US and China has led to increased HFO emissions from factories and landfills.[240,347] Currently only a small tropospheric HFO concentration has gathered in certain cities (~1 ppq — 1 ppt), but concentrations are projected to grow up to ~0.3 ppb in some cities, increasing the importance of O_3 + Alkenes **11**—**14** reactions.[229,240,347,348] One additional advantage to including Alkenes **11**—**14** in this study, is that by comparing the haloalkyl substituents ($-C_XF_{2x+1}$) to that of equivalent alkyl groups ($-C_XH_{2x+1}$), the impact of hyperconjugative α-H atoms can be further assessed. This is similar to the comparisons made between the different bimolecular sCI chemistry of *syn*-& *anti*-CF_3CHOO with *syn*-& *anti*-CH_3CHOO, in chapters 4 & 5.

The *E*- & *Z*-alkene group, *E*- & *Z*-2-pentene and *E*- & *Z*-2-butene, labelled **15**—**18**, are used to study the effect of decreasing α-H atoms on ozonolysis chemistry. However, of more importance is the study of how *E*- v. *Z*-isomerisation impacts such ozonolysis chemistry.

The calculations for the ozonolysis of *Z*-2-hexene, or Alkene **19**, is studied in much greater detail in chapter 5, as the high conformational flexibility causes a large degree of complexity in calculations. However, the data obtained for the O_3 + alkene **19** reaction is used, when discussing trends in the *E*- & *Z*-alkene group, and so is included on Figure 3.4. O_3 reactions with *E*- & *Z*-alkenes are important because, despite low levels of Alkenes **15**—**18** in rural environments (~0.01 ppb), they are abundant in urban areas like Mexico City (0.37—2.48 ppb).[182,345]

In this chapter, it is anticipated that there may be some significant ozonolysis trends observed by comparing the Γ_{THEO} values of $(CH_3)_2COO$ for Alkenes **6**—**10** with that of CH_2OO from alkenes **1**—**5**, due to the inductive impact of the α-H atoms on alkyl groups have on CI chemistry. So, the analysis of 2-methylpropene, referred to as Alkene **20**, reaction with O_3 may provide additional context to such trends. In addition, this reaction is important due to the significant levels of Alkene **20** seen in cities such as Taipei, Mexico City and Porto Alegre (0.51, 5.28 & 16.5 ppb). For more in-detail tropospheric abundance levels of Alkenes **1**—**20** in various locations, see Appendix Section 1.5.

3.2 General Overview of Alkene Ozonolysis

3.2.1 Ozonolysis of Alkene 1 ($CH_3CH{=}CH_2$)

To compute k_{ME} & Γ_{THEO} values, potential energy surfaces (PES) of all O_3 + alkene reactions must be calculated. The ozonolysis of Alkene **1**, known as propene, is selected to describe the overview of the general reaction because it is both an abundant alkene in many environments and it has a simple structure.[182] A general schematic of the cycloaddition stage of O_3 + Alkene **1** is shown in Figure 3.5.

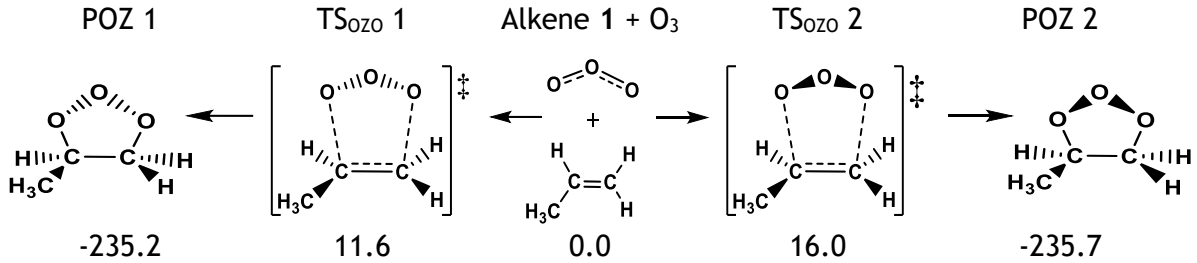

*Figure 3.5: Different Structures in the Cycloaddition Step of O_3 + Alkene **1** reaction with relative energies (kJ mol^{-1})*

O_3 + Alkene **1** react to form POZ conformers 1 & 2 via the two 1,3-cycloaddition channels, TS_{OZO} 1 & 2, that differ mainly on the basis of the orientation of the oxygen at point of reaction. All O_3 + alkene reactions in this study exhibit at least one structure that could be characterised as TS_{OZO} 1 or 2, except for Alkenes **17** & **20**, where any TS_{OZO} 2 is degenerate to TS_{OZO} 1. Very frequently, the raw reactants form a short-lived pre-reaction complex (PRC), prior to cycloaddition. PRCs in these reactions have negligible effects effect on the rate constants in this study, therefore the only reference to PRCs in this chapter are found in the PES figures, and their chemical structures are in the Appendix.

The TS_{OZO} 2 structure in Figure 3.5 has a greater energy barrier than TS_{OZO} 1, because the different orientation of the central oxygen in the O_3 means there is greater steric repulsion with the $-CH_3$ substituent group, which leads to a greater POZ yield from TS_{OZO} 1 (0.842) than TS_{OZO} 2 (0.158). The preference for TS_{OZO} 1 is a common occurrence in this thesis and is often exacerbated when the $-R_1$ substituent is more bulky generating greater repulsion in the TS_{OZO} 2 structure(s). However, the differential in POZ yields is difficult to verify experimentally due to rapid interconversion between these POZs under most conditions, and because of the swift POZ fragmentation pathways. The similarity between the k_{ME} value produced by this study (3.24×10^{-17} cm^3 s^{-1}) and the literature experimental rate constants (k_{EXP} = 0.99—1.01 × 10^{-17} cm^3 s^{-1}) help to substantiate that the computational approach used throughout this thesis produces reliable results for the ozonolysis of alkenes.[349]

As the POZ conformers can often freely interconvert over the low energy isomerisation barrier (TS_{POZ}), displayed in Figure 3.6, all POZ conformers can access all fragmentation pathways. Using this assumption, to reduce computational cost, a different MESMER treatment was assembled, where all cycloadditions and POZ fragmentations of a single O_3 + alkene reaction are channelled through a single POZ structure. An analysis in Appendix Section 1.6.2, found little difference in Γ_{THEO} results between the full MESMER treatment and this new MESMER treatment for any of the ozonolysis of Alkenes **1**, **6**, **11**, **13** & **18**. This new MESMER treatment is applied to all other O_3 + alkene reactions expect for O_3 + Alkenes **1**, **6**, **11**, **13** & **18**.

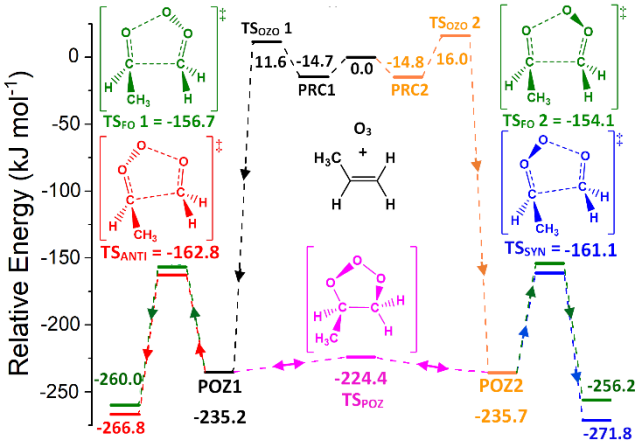

*Figure 3.6: PES of the O_3 + Alkene **1** reaction (Propene). Energies are relative to raw reactants. The POZ 1 & 2 rings are not chemically distinct due to interconversion over the low TS_{POZ} barrier.*

Unlike the ozonolysis of ethene, which only produces one set of final products (CH_2OO + HCHO), the POZ fragmentation process, shown in Figure 3.6, involves multiple reaction pathways generating different products. All fragmentation pathways have a CI product but the proportions of "stabilized" CI to "hot" CIs are unknown and, in this chapter, they are referred to collectively as "CIs", when discussing the Γ_{THEO} of each CI. The final products for POZ fragmentation from O_3 + Alkene **1**, shown in Figure 3.6, are: *anti*-CH_3CHOO + HCHO, via the TS_{ANTI} pathway; *syn*-CH_3CHOO + HCHO, via the TS_{SYN} pathway; and CH_2OO + CH_3CHO, via the TS_{FO} 1 & 2 pathways. Ozonolysis of all alkenes in this study, except for Alkene **20**, form at least one set of *anti*- & *syn*-CI conformers. All TSs are labelled according to the CI conformer that they lead to, i.e. any TS that yields *anti*-CIs are referred to as "TS_{ANTI}". In the aftermath of a POZ fragmentation transition state, such as TS_{FO} 1, the final products may form a post-reaction complex, C_{FO} 1 in this instance. The significant excess of energy of the final products causes the intermolecular bonds, holding the complex together, to break and the products drift apart. Outside of their usefulness in MESMER calculations (see Section 2.6), post-reaction complexes have little impact in this chapter and so they are mainly discussed in the appendix.

As mentioned in Section 1.5.4, comparing these Γ_{THEO} values with experimental branching ratios (Γ_{EXP}) is challenging because of the short CI atmospheric lifetimes (especially "hot" CIs), therefore Γ_{EXP} data is sparing. So, to compare the Γ_{THEO} values in this chapter to the literature, Γ_{EXP} data for CIs must be inferred from the branching ratios of the two aldehyde/ketone co-products.

Although the experimental yields of aldehyde & ketone co-products cannot be used to determine the Γ_{EXP} values of different *anti* & *syn* conformers of the same CI, experimental OH yield can be used to infer a comparative *anti* or *syn* preference. This method is based on the premise that a high OH yield for an O_3 + alkene reaction is often due to the high decay rate constant (k_{UNI}) of the CI produced, and, as displayed in Table 3.1, the k_{UNI} for *syn*- or *anti*-CI often differ significantly.[182] Therefore, an experimental OH yield can be used to infer whether *anti*- or *syn*-CI formation is favoured.

Table 3.1: Unimolecular rate constants (k_{UNI}) of CIs in this study derived by Vereecken et al.[182]

k_{uni} (s^{-1})	CH_3CHOO	EtCHOO	^{i}PrCHOO	^{t}BuCHOO	CH_2OO	Me_2COO
Syn-	136	205	6.7	0.01	0.3	478
Anti-	53	74	102	111		

The literature OH yields and the Γ_{EXP} values of the co-products provide adequate points of comparison to determine the accuracy of the Γ_{THEO} values calculated in this chapter. As seen in the PES of O_3 + Alkene **1** in Figure 3.6, POZ fragmentation via TS_{ANTI} & TS_{SYN} is very favourable and their branching ratios, Γ_{ANTI} (0.452) & Γ_{SYN} (0.276), are not just larger than the individual branching ratios of TS_{FO} 1 & 2 (0.157 & 0.115), but are larger than the total α_{CH_2OO} value of ~0.272 (the α_{CH_2OO} term is used here for the *collective* CH_2OO + CH_3CHO yield, here the sum of the yields from TS_{FO} 1 & 2). The literature on the ozonolysis of Alkene **1** shows a Γ_{EXP} range for CH_2OO + CH_3CHO of ~0.38—0.45, which is somewhat higher than the computational α_{CH_2OO} value above.[10,131,166,350-352] However both Γ_{EXP} and Γ_{THEO} values agree that CH_2OO + CH_3CHO does not comprise the majority of the CI yield.

When considering the OH yield, it must be noted that of the three CIs generated in this reaction two of them, *anti*-CH_3CHOO and CH_2OO have quite low k_{UNI} values, compared to *syn*-CH_3CHOO. This means that as the experimental OH yield range for the ozonolysis of Alkene **1** is quite low (0.32—0.33), a low to medium yield for *syn*-CH_3CHOO can be inferred.[10,131,166,350-352] This experimental trend is in agreement with the theoretical study in this section because it shows O_3 + Alkene **1** has a medium Γ_{THEO} value for *syn*-CH_3CHOO (~0.276) compared to the strong dominance of Γ_{THEO} value for *anti*-CH_3CHOO (~0.452).

There is some probability of O_3 + alkene reactions forming epoxides, but due to low Γ_{THEO} values (≪0.01), analysis of this pathway is restricted to Alkenes **1** & **5** and is explored only in the appendix.

In summary, these calculations for O_3 + Alkene **1**, produce a k_{ME} value that is similar to the k_{EXP} values found in the literature. On top of this, the aldehyde/ketone co-product and the OH yields provide satisfactory substitutes for the Γ_{EXP} values and the Γ_{THEO} values for the O_3 + Alkene **1** appear to be in broad agreement with these "Γ_{EXP} substitute values".

3.2.2 How Multiple Conformers of Alkenes and Intermediate Products Affect Ozonolysis Chemistry using O_3 + Alkene 2 ($EtCH{=}CH_2$)

Like a large number of alkenes in this study, Alkene **2** has multiple conformers and all PESs, rate constants and product branching ratios are calculated under the assumption that the lowest energy conformer found is that of the ground state. With many of the TS_{OZO} structures, the intrinsic reaction co-ordinate (IRC) calculations lead to reactant structures that involve the other, higher energy, alkene conformers. In these situations, it is always possible that the barrier between reactant conformers inhibits reaction via these TSs. This is particularly pertinent in cases where the alkene reactants are either conjugated (Alkenes **5** & **10**) or have very bulky substituents (Alkene **8**). Due to this possibility, in Appendix Section 1.6.1, the ozonolysis of Alkenes **5**, **8** & **10** are analysed with respect to how such conformeric barriers may affect the cycloaddition chemistry. It was found to have negligible effect for these more extreme examples and it is therefore assumed to have very little impact on the other such reactions in this chapter.

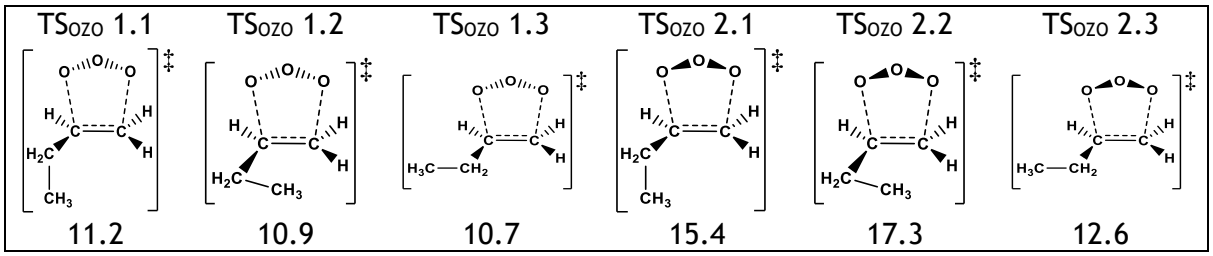

*Figure 3.7: Multiple TS_{OZO} 1 and TS_{OZO} 2 subchannels for O_3 + Alkene **2** reaction with energies (in kJ mol^{-1}) are relative to the raw reactants.*

The ozonolysis of alkenes that have longer and more flexible R_1 groups, such as the —Et group in alkene **2,** often produce multiple TS_{OZO} 1 and TS_{OZO} 2 structures, seen in Figure 3.7. The main difference between these TS_{OZO} 1.1—1.3 and TS_{OZO} 2.1—2.3 "subchannels", is the orientation of the —Et group. These alkenes with longer and more flexible R_1 groups also produce multiple conformers of POZ 1 & 2 (POZ 1.1—1.3 & POZ 2.1—2.3) and multiple

subchannels for each of the TS_{ANTI}, TS_{SYN}, TS_{FO} 1 & TS_{FO} 2 channels, which are labelled in a similar way to the TS_{OZO} 1 & 2 subchannels. However, throughout this chapter, unless otherwise stated, only the lowest energy subchannels for each channel is referenced, although each is included in calculating the k_{ME} & Γ_{THEO} values. Where possible consistent labelling through the ozonolysis reactions has been maintained both within the reaction (PRC 1.1 → TS_{OZO} 1.1 → POZ 1.1 → TS_{FO} 1.1 → C_{FO} 1.1) and between reactions and a full breakdown of all these energies and structures are found in Appendix Section 1.3.

One other particular abbreviation of note is that a yield of the dimethyl formaldehyde oxide is referred to by the abbreviation "DMFO" or by the chemical formula "$(CH_3)_2COO$".

One distinction made in this chapter is between CF_3CFOO structures, where the *syn*- and *anti*- conformers are assigned with reference to the position of largest group by mass (always R_1) in relation to the terminal oxygen, as seen in Figure 3.8. Another degree of complexity comes with systems, such as with Alkenes **15** & **16**, that produce multiple *syn*- and *anti*-CIs via multiple TS_{ANTI} and TS_{SYN} channels. In such reactions, the label of TS_{ANTI} 1.1—1.3 and TS_{SYN} 1.1—1.3 produces *anti*- & *syn*-EtCHOO because it has the substituent with the greatest molecular weight and consequentially TS_{ANTI} 2.1—2.3 and TS_{SYN} 2.1—2.3 produces *anti*- & *syn*-CH_3CHOO (see Figure 3.8).

Alkene 11		**Alkenes 15 & 16**			
TS_{ANTI}	TS_{SYN}	TS_{ANTI} 1.1—1.3	TS_{SYN} 1.1—1.3	TS_{ANTI} 2.1—2.3	TS_{SYN} 2.1—2.3
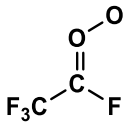	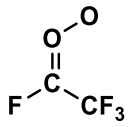	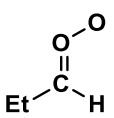	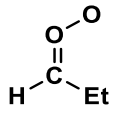	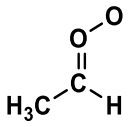	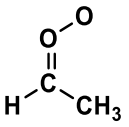
***anti*-CF_3CFOO**	***syn*-CF_3CFOO**	***anti*-EtCHOO**	***syn*-EtCHOO**	***anti*-CH_3CHOO**	***syn*-CH_3CHOO**

*Figure 3.8: Different Structures of some CIs produced in the ozonolysis of Alkenes **11**, **15** & **16**.*

While the aldehyde/ketone co-products do have some significant atmospheric importance, such as formaldehyde, which is a toxic respiratory irritant, the main product of interest discussed in this chapter are the CIs due to the ability of CI secondary reactions to produce OH radicals and deplete pollutants.[16,170,171] This is also because the aldehyde/ketone co-products have longer atmospheric lifetimes and as a result their yields from these reactions are already quite well established.

3.3 Results of the Ozonolysis of Alkenes

When determining the relationship between the electronic and/or steric impact of alkene substituent groups and the ozonolysis k_{ME} & Γ_{THEO} values, a collation of the calculated data into several tables of reference is very useful. The similar fluctuations in relative reactivity between alkenes, represented by the energy barriers (ΔE_{TS}) and k_{ME} values, may be observed to pair with common changes in substituent groups (R_1, R_2, R_3 & R_4), both found in Table 3.2. The collective number of substituent α-H atoms are also suspected to have an impact on ozonolysis chemistry, as mentioned in Section 3.1 and so are also included in Table 3.2. To see if k_{ME} values are accurate and to confirm that observed alkene ozonolysis trends are correct, the experimental (k_{EXP}) rate constants from the literature are also collated in Table 3.2. All ozonolysis k_{ME} values in this section fall significantly <10^{-10} cm^3 s^{-1}, so the $k_{d\text{-}d}$ capture moment is not employed during the entirety of this chapter.

*Table 3.2: The substituent features of Alkenes **1—20** and a collation of the important values of the ozonolysis cycloaddition step of those alkenes: the number label (#no); the number of a-hydrogens (a-H); the identity of alkene substituents (R_1, R_2, R_3 & R_4); the lowest energy TS_{OZO} 1 & 2 cycloaddition barriers (ΔE_{TS}); the Master Equation rate constants (k_{ME}); and the comparative literature experimental rate constants (k_{EXP}).*

#no	*a*-H	Substituent groups				ΔE_{TS} (kJ mol^{-1})		*k* (10^{-18} cm^3 s^{-1})		*Ref*
		R_1	R_2	R_3	R_4	TS_{OZO} 1	TS_{OZO} 2	k_{ME} *	k_{EXP}	
1	3	CH_3	H	H	H	11.6	16.0	32.4	9.9—10.1	349
2	2	Et	H	H	H	10.7	12.6	103	9.65—10.9	353
3	1	^{i}Pr	H	H	H	9.8	11.5	49.6	7.3—9.5	353
4	0	^{t}Bu	H	H	H	10.3	17.3	22.5	3.8—3.9	354
5	0	$C(O)CH_3$	H	H	H	15.2	7.8	69.0	4.5—5.0	10,355
6	9	CH_3	H	CH_3	CH_3	-1.64	2.37	4336	386—797	335
7	8	Et	H	CH_3	CH_3	-0.8	-2.2	5114	406—454	118
8	7	^{i}Pr	H	CH_3	CH_3	3.2	4.8	245.9	(223) SAR	118
9	6	^{t}Bu	H	CH_3	CH_3	3.7	6.3	245.6	125—139	335
10	6	$C(O)CH_3$	H	CH_3	CH_3	12.8	10.4	1.57	8.1±2.8	356
11	0	CF_3	F	H	H	31.3	27.5	0.0114	(2.77±0.21) × 10^{-3}	348
12	0	CF_2CF_3	H	H	H	26.5	27.3	0.0299	0.20—0.234	357,358
13	0	CF_3	H	H	Cl	26.2	28.6	0.0185	(1.46±0.12) × 10^{-3}	239
14	0	CF_3	H	H	F	29.9	29.6	0.0081	(2.81±0.21) × 10^{-3}	359
15	5	Et	H	H	CH_3	2.1	7.6	1127	159.2—315	360
16	5	Et	H	CH_3	H	0.6	4.1	2835	127—128.27	360
17	6	CH_3	H	H	CH_3	6.8		361	127.8—190	360
18	6	CH_3	H	CH_3	H	3.1	10.9	1175	121.5—125	360
19	*5*	*nPr*	*H*	*CH_3*	*H*	*1.4*	*7.2*	*3528 **	*105—114*	360
20	6	CH_3	CH_3	H	H	12.3		30.2	10.8—11.4	109,353,360

** Note 1: Conditions of the used for determination of k_{ME} (such as grain size) are in appendix.*
*** Note 2: Included for comparative purposes only, full analysis of O_3 + alkene **19** in chapter 6.*

In this chapter, the POZ fragmentation in all O_3 + alkenes reactions yield more than two sets of products, meaning extracting any trends from the data and producing taxonomic groups from such reactions may be challenging. For the purpose of data representation these POZ fragmentation Γ_{THEO} values are split into two broad reactant groupings: Alkenes **1—12** & **20** because they yield at least one disubstituted CI (referred to as X_2COO); and Alkenes **1-12** because they yield *only syn* & *anti* conformers of monosubstituted CI. The

comparison between the yields of POZ fragmentation for Alkenes **1**—**12** & **20** group, from the literature (α_{X_2COO} & OH yield) and this chapter (Γ_{ANTI}, Γ_{SYN} & $\Gamma_{X_2COO(1)}$ or $\Gamma_{X_2COO(2)}$) are displayed in Table 3.3. As direct experimental methods of measuring *syn*- & *anti*-CI yields (Γ_{ANTI} & Γ_{SYN}) are used only sparingly in the literature, the *OH yields* (an indirect method of differentiating between such conformers as seen in section 3.2.1) are included instead. This is in contrast to experimental branching ratios (Γ_{EXP}) of X_2COO which are measured directly and so are compared to the collective theoretical X_2COO yield (α_{X_2COO}) calculated in this chapter.

*Table 3.3: The collation of product distributions of O_3 + alkenes **1**—**12** & **20**: alkene label (#no); the number of a-hydrogens (a-H); the lowest energy TS_{OZO} 1 & 2 cycloaddition barriers (ΔE_{TS}); Γ_{THEO} values of* anti- & syn-*R_1CR_2OO (Γ_{ANTI} or Γ_{SYN}); the collective and individual Γ_{THEO} of X_2COO ($\alpha_{X_2COO} = \Gamma_{X_2COO(1)} + \Gamma_{X_2COO(2)}$); and the experimental collective Γ_{EXP} of X_2COO (α_{X_2COO}) and OH yields found in the literature.*

#no	*a*-H	Theoretical					Literature		ref
		Γ_{ANTI}	Γ_{SYN}	$\Gamma_{X_2COO(1)}$	$\Gamma_{X_2COO(2)}$	α_{X_2COO}	α_{X_2COO}	OH Yield	
1	3	0.452	0.276	0.157	0.115	0.272	0.35-0.45	*0.18 -0.39*	10,131,166,350-352
2	2	0.427	0.201	0.199	0.173	0.373	0.36	*0.29 -0.41*	161,352,361,362
3	1	0.431	0.115	0.267	0.187	0.454	0.49	-	352
4	0	0.470	0.059	0.303	0.168	0.471	0.68	-	352
5	0	0.046	0.020	0.588	0.345	0.934	*0.65-0.95*	0.13 -0.16	166,355,363,364
6	9	0.223	0.076	0.495	0.206	0.701	0.68	*0.81-0.98*	10,162,365
7	8	0.152	0.037	0.653	0.158	0.811	-	-	-
8	7	0.117	0.014	0.718	0.151	0.868	0.81	-	352
9	6	0.114	0.010	0.778	0.098	0.876	0.82	-	10
10	6	0.024	0.729	0.243	0.004	0.972	-	-	-
11	0	0.001	0.000	0.499	0.500	0.999	-	-	-
12	0	0.045	0.004	0.524	0.427	0.955	0.261	-	357
20	6	Γ_{CH_2OO}: 0.158		$\Gamma_{(CH_3)_2COO}$: 0.842		0.842	0.75	0.60-0.84	161,361,362,366

*Note: O_3 + alkene **20** yields no anti- & syn-CIs and Γ_{CH_2OO} & $\Gamma_{(CH_3)_2COO}$ values are presented differently herein.*

The branching fractions for O_3 + Alkenes **13**—**19** are displayed in a similar way in Table 3.4, except with new Γ_{THEO} labelling, for *anti*- & *syn*-R_1R_2COO ($\Gamma_{ANTI\text{-}R1}$ & $\Gamma_{SYN\text{-}R1}$) and *anti*- & *syn*-R_3R_4COO ($\Gamma_{ANTI\text{-}R3}$ & $\Gamma_{SYN\text{-}R3}$). One other important difference is that the "α_{X_2COO}" is replaced with a combined $\alpha_{R_1CR_2OO}$ value ($\alpha_{R_1CR_2OO} = \Gamma_{ANTI\text{-}R1} + \Gamma_{SYN\text{-}R1}$) and a combined α_{SYN} value ($\alpha_{SYN} = \Gamma_{SYN\text{-}R1} + \Gamma_{SYN\text{-}R3}$). These combined values provide appropriate values to compare to the experimental "$\alpha_{R_1CR_2OO}$" and OH yield values from the literature.

The identification of the trends seen in these tables and their comparison with experimental trends are found subsequently in Sections 3.4—3.7. The numbers of particular interest are quoted in the text or PES figures.

*Table 3.4: The important features of the product distributions of O_3 + alkenes **13—19**: alkene label (#no); the number of α-hydrogens (α-H); Γ_{THEO} of the anti-/syn-R_1CR_2OO ($\Gamma_{ANTI\text{-}R1}$ or $\Gamma_{SYN\text{-}R1}$) or anti-/syn-R_3CR_4OO ($\Gamma_{ANTI\text{-}R3}$ & $\Gamma_{SYN\text{-}R3}$); combined Γ_{THEO} values for R_1CR_2COO ($\alpha_{R_1CR_2OO}$) and syn-CIs (α_{SYN}); and literature Γ_{EXP} values of both conformers of R_1R_2COO ($\alpha_{R_1CR_2OO}$) and OH radical (OH yield).*

#no	α-H	Theoretical						Literature		ref
		$\Gamma_{ANTI\text{-}R1}$	$\Gamma_{SYN\text{-}R1}$	$\Gamma_{ANTI\text{-}R3}$	$\Gamma_{SYN\text{-}R3}$	$\alpha_{R_1CR_2OO}$	α_{SYN}	$\alpha_{R_1CR_2OO}$	OH Yield	
13	0	0.415	0.312	0.188	0.085	**0.728**	**0.397**	0.63	-	367
14	0	0.473	0.450	0.050	0.027	**0.923**	**0.477**	-	-	-
15	5	0.229	0.203	0.266	0.302	**0.391**	**0.448**	-	0.46	162
16	5	0.378	0.064	0.453	0.104	**0.429**	**0.094**	-	0.27-0.29	162
17	6	*0.520*	*0.480*	-	-	**1**	**0.480**	1	0.19-0.64	10,165,368
18	6	*0.872*	*0.128*	-	-	**1**	**0.225**	1	0.17-0.41	10,131,161
19	*5*	*0.478*	*0.032*	*0.452*	*0.038*	***0.512***	***0.070***	-	-	-

3.4 Discussion of the Ozonolysis of Monosubstituted Alkenes

The purpose of studying the ozonolysis of the *monosubstituted* alkenes (Alkenes **1**—**5** in Figure 3.9), as a group, is that they follow the same $R_1CH{=}CH_2$ structures, except for the increasing complexity of the —R_1 substituent (from —CH_3 & —Et to —iPr & —tBu) so a common trend for the k_{ME} & Γ_{THEO} values may be established. Briefly mentioned in Section 3.1, is that the α-H atoms of a —CH_3 substituent is suggested to have a hyperconjugative impact on the unsaturated COO group, (see Chapter 4 for more details) and this affect could also apply to an unsaturated >C=C< bond.[111] As there is a gradual decline in the number of hyperconjugative α-H atoms between Alkenes **1**—**5** in the —R_1 substituent, the affect this has on the ozonolysis chemistry of alkenes can be examined.

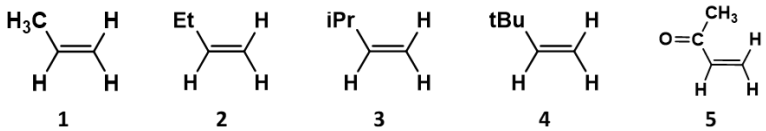

*Figure 3.9: Chemical Structures of Alkenes **1—5***

O_3 + Alkene **5** is important because a —C(O)CH_3 substituent is thought to have a reductive effect on the >C=C< bond and this provides an important contrasting effect to that of the *hyperconjugative effect of* α-H atoms. While O_3 + Alkene **1** is analysed mainly in Section 3.2.1, it is also studied in comparison to the other monosubstituted alkenes here.

3.4.1 The Ozonolysis of Alkene 2 ($EtCH{=}CH_2$)

Of the multiple cycloaddition TSs for the O_3 + Alkene **2** reaction, the lowest energy TS_{OZO} 1 & 2 barriers (TS_{OZO} 1.3 ~ 10.7 kJ mol^{-1} & TS_{OZO} 2.3 ~ 12.6 kJ mol^{-1}) are significantly lower than their Alkene **1** + O_3 equivalents (TS_{OZO} 1 ~ 11.6 kJ mol^{-1} & TS_{OZO} 2 ~ 16.0 kJ mol^{-1}). The resultant k_{ME} value (1.03×10^{-16} cm^3 s^{-1}) is higher but still within an order of magnitude of the literature k_{EXP} value ($0.97—1.09 \times 10^{-17}$ cm^3 s^{-1}). The TS_{OZO} 1 barrier for O_3 reactions with Alkenes **1** & **2** calculated in this chapter are both low compared to the TS_{OZO} barriers

for O_3 + ethene (14.6 kJ mol^{-1}), determined by Olzmann *et al.*, indicating that the —CH_3 & —Et substituents increases the reactivity.[185] This is also reflected in the literature where the k_{EXP} value for O_3 + Alkenes **1** & **2** (~10^{-17} cm^3 s^{-1}) exceeds that of O_3 + ethene (~1.45—1.59 × 10^{-18} cm^3 s^{-1}).[109,349,353] The fact that O_3 + Alkenes **1** & **2** have larger rate constants than ethene indicates that alkene ozonolysis is facilitated by hyperconjugative α-H atoms in substituents, but whether this is the sole contributor to the rate increase is unclear, because Alkene **2** has a larger k_{ME} value than **1**, despite having fewer α-H atoms.

The POZ fragmentation in the Alkene **2** + O_3 reaction shows higher TS barriers for pathways that generate CH_2OO (TS_{FO} 1.3 = -158.5 kJ mol^{-1} & TS_{FO} 2.3 = -156.7 kJ mol^{-1}) than those that produce *anti*- & *syn*-CH_3CHOO (TS_{ANTI} 3 = -164.4 kJ mol^{-1} & TS_{SYN} 3 = -163.3 kJ mol^{-1}). Nevertheless, the reduction in α-H atoms between Alkenes **1** & **2** produces a large increase in the *collective* theoretical yield of CH_2OO (α_{CH_2OO} = 0.373) for Alkene **2**. This theoretical α_{CH_2OO} value for O_3 + Alkene **2** is similar to that of the experimental α_{CH_2OO} value (0.36).[161,352,362] However an experimental α_{CH_2OO} pattern is hard to discern as the experimental α_{CH_2OO} O_3 + alkene **1** has a large range (0.35—0.45).[161,352,361,362]

The greater theoretical α_{CH_2OO} value for O_3 + Alkene **2** leads to a reduced Γ_{THEO} value for *syn*-EtCHOO + HCHO (0.201) compared to that of *syn*-CH_3CHOO + HCHO for Alkene **1** (0.276). As both these *syn*-CIs have significantly larger k_{UNI} values than CH_2OO, this decline in "Γ_{SYN}" might be expected to give a lower OH yield. However, O_3 + Alkene **2** appears to have a larger OH yield (0.29—0.41) than of Alkene **1** (0.18—0.39), although within the margin of uncertainty. Regardless, this observation is difficult to verify as there is no universal strict linear relationship between the two Γ_{SYN} values and the OH yields. This small decline in the Γ_{SYN} value could be compensated for by the greater k_{UNI} value for *syn*-EtCHOO (205 s^{-1}) than *syn*-CH_3CHOO (74 s^{-1}), which could even generate an increase in OH yield. The Γ_{THEO} differences between O_3 + Alkenes **1** & **2** are marginal and produce the same overall trend: $\Gamma_{ANTI} > \Gamma_{SYN} > \Gamma_{CH_2OO\ (1)} > \Gamma_{CH_2OO\ (2)}$.

One important aspect of this Alkene **2** + O_3 reaction is a small reduction in the Γ_{THEO} value for *syn*-EtCHOO, which is caused by an unusually high TS_{SYN} 2 barrier by ~12—13 kJ mol^{-1}. This high barrier is not seen in the TS_{SYN} 1 & 3 structures because the specific orientation of the —Et substituent in the TS_{SYN} 2 structure places the —Et group close enough to an oxygen atom to cause noticeable steric repulsion (see Figure 3.10). Throughout this chapter, steric and rotational distortions like this cause greater energy barriers than anticipated (often by >10 kJ mol^{-1}), including for: TS_{SYN} 2, TS_{SYN} 2.2 & TS_{SYN} 1.2 for O_3 + Alkenes **7**, **15** & **16** reactions. For the purpose of simplicity, the impact of each such distortion is simply integrated into the k_{ME} & Γ_{THEO} values in this chapter. In Chapter 6,

these distortions are explored in detail, to determine the impact on O_3 + Alkene **19** in the new FESP model.

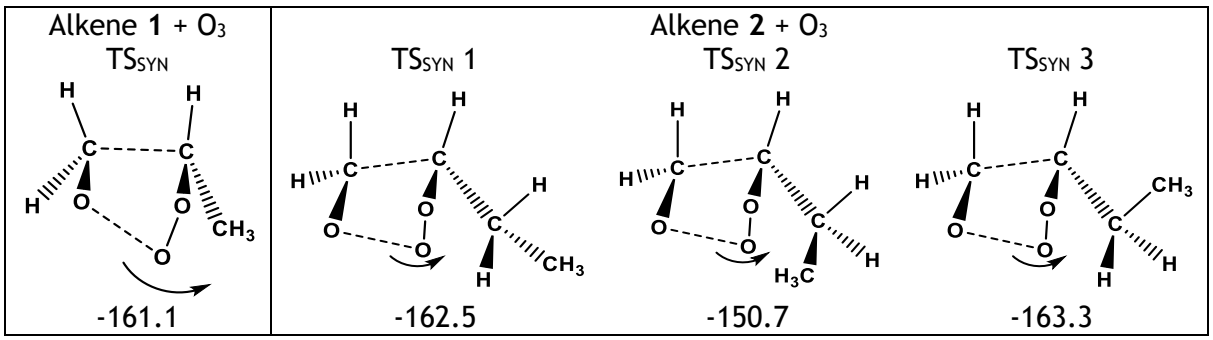

*Figure 3.10: Geometries and energies of the different TS_{SYN} structure of the O_3 reactions with Alkene **1** & **2**. The arrows in the figure show the movement that takes place in as the molecule processes through the relative transition states and indicates what steric interactions might result. Energies (in kJ mol^{-1}) are relative to raw reactants.*

3.4.2 The Ozonolysis of Alkenes 3 & 4 (iPrCH=CH$_2$ & tBuCH=CH$_2$)

Much like with Alkene **2**, the significant conformational flexibility of Alkene **3**, means its reaction with O_3 produces a large number of TS structures on the PES. This is important because the TS_{OZO} 1.1 & TS_{OZO} 2.3 of O_3 + Alkene **3** have lower energy barriers (9.8 & 11.5 kJ mol^{-1}) than their Alkene **2** equivalents. If only the lowest energy barriers for each TS_{OZO} 1 & TS_{OZO} 2 channel were calculated, Alkene **3** would have the larger k_{ME} value. But by using all cycloaddition subchannels (TS_{OZO} 1.1—1.3 & TS_{OZO} 2.1—2.3), O_3 + Alkene **3** generates the smaller of the two k_{ME} values (4.96×10^{-17} cm^3 s^{-1}). This downward trajectory in k_{ME} values between O_3 + Alkenes **2**—**3** continues for Alkene **4** with the lowest k_{ME} value (2.24×10^{-17} cm^3 s^{-1}). This k_{ME} decline is consistent with the k_{EXP} data for both O_3 + Alkene **3** ($7.3—9.5 \times 10^{-18}$ cm^3 s^{-1}) and Alkene **4** ($3.8—3.9 \times 10^{-18}$ cm^3 s^{-1}) reported in the literature.[349,353,354] This reduction in overall k_{ME} values from O_3 + Alkenes **2**—**4** correlates with a stepwise decline in the number of α-H atoms in the —R_1 substituent, which infers that these α-H atoms activate the >C=C< bond.

The increasingly large α_{CH_2OO} values for both O_3 + Alkenes **3** & **4** (0.454 & 0.471) continue the same upward α_{CH_2OO} trajectory seen for Alkenes **1** & **2,** showing that (see Figure 3.11) many Γ_{THEO} trends persist across all O_3 reactions with Alkenes **1**—**4**. The data for O_3 + Alkenes **3** & **4** reactions in the experimental literature also show increasingly large α_{CH_2OO} values of 0.49 to 0.68, respectively. As shown in Figure 3.11, the increased theoretical α_{CH_2OO} values (in purple), have the effect of gradually reducing the Γ_{SYN} values, 0.115 and 0.059, (in green) with the remaining Γ_{ANTI} remaining steady at ~0.45 (in orange).

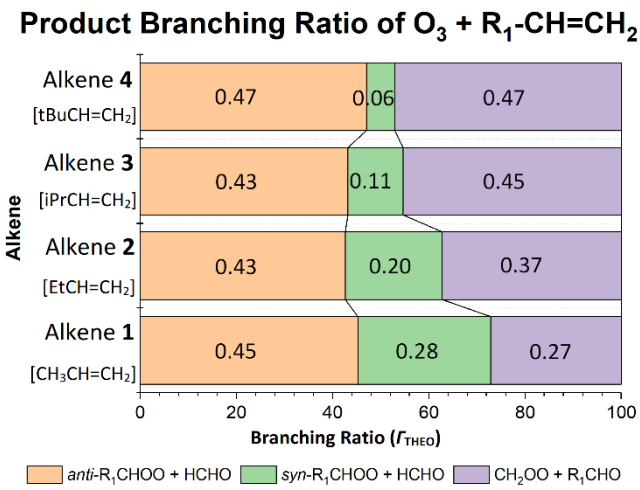

*Figure 3.11: Branching Ratios (Γ_{THEO}) of O_3 + Alkenes **1**, **2**, **3** & **4** reactions (R_1 group refers to CH_3, Et, iPr & tBu respectively).*

Throughout the ozonolysis reactions with Alkenes **1**—**4**, the barrier heights vary very little for any of the following POZ fragmentation channels: TS_{ANTI} (-164 to -161 kJ mol^{-1}), TS_{FO} 1 (-160 to -156 kJ mol^{-1}) & TS_{FO} 2 (-158 to -154 kJ mol^{-1}). The only fragmentation channel, that varies significantly in barrier height is the TS_{SYN} channel (-164 to -149 kJ mol^{-1}) and the dominance of the higher TS_{SYN} barriers increases with the size of the —R_1 substituent.

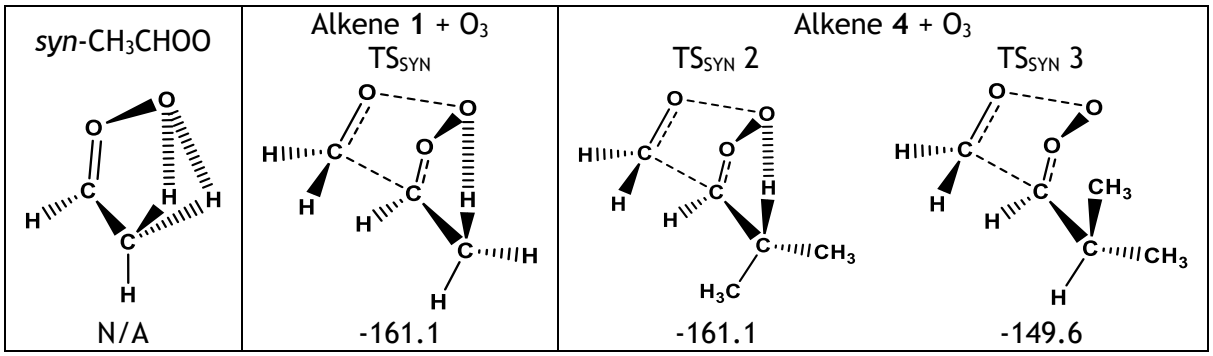

Figure 3.12: Schematic featuring the impact of stabilising intramolecular bonds between a-H atoms in a syn *position with the terminal oxygens in the carbonyl oxide group. Energies (in kJ mol^{-1}) are relative to raw reactants.*

These higher TS_{SYN} barriers appears to be at least partially due to the steric repulsion between one of the O atoms and the increasingly bulky —R_1 substituent (iPr & tBu), also seen in Figure 3.10 for the TS_{SYN} 2 in O_3 + Alkene **2** reaction. These increases in TS_{SYN} barrier heights leads to the stepwise reduction in Γ_{SYN} values across the O_3 reactions with Alkenes **1**—**4** (see Figure 3.11). The low TS_{SYN} barrier heights, seen for O_3 + Alkenes **1**, could be the due to the α-H atoms in the —CH_3 substituent group providing a degree of hyperconjugative stabilising to the newly forming COO group. A further explanation is that those α-H atoms could form intramolecular bonds with the terminal CI oxygen during transition, as shown in Figure 3.12. This same stabilisation caused by α-H atoms in a *syn* position produce a ~14 kJ mol^{-1} lower energy for *syn*-CH_3CHOO, than the *anti*-CH_3CHOO,

which has no α-H atoms in a *syn* position.[93] This degree of stabilisation can change depending on the TS itself, such as for O_3 + Alkene **3** reactions between TS_{SYN} 2, which has this stabilising bond, and TS_{SYN} 3, which has no stabilising bond (see Figure 3.12). The proportion of TSs with such stabilising α-H atoms in the substituent decreases between the O_3 + Alkenes **1**—**4** systems.

3.4.3 The Ozonolysis of Alkene 5 ($CH_3C(O)CH{=}CH_2$)

While these trends, such as decreasing k_{ME} rate constants and a declining Γ_{SYN} branching ratio, well describes the ozonolysis chemistry of the monosubstituted and anthropogenic Alkenes **1**—**4**, many important biogenic alkenes have significantly different ozonolysis chemistry. The O_3 + Alkene **5** reaction is important because it is a biogenic alkene and therefore is abundant in locations like the rainforest (~1 ppb), whereas Alkenes **1**—**4** have largest prevalence in major cities.[182,345] Also, the inclusion of Alkene **5** allows an analysis of how an electron withdrawing —C(O)CH_3 substituent affects the ozonolysis chemistry, compared to the analysis of Alkenes **1**—**4**, which only have electron-donating alkyl substituents (—CH_3, —Et, —iPr & —tBu). This is particularly important because by including this electron-withdrawing group it can be observed whether the decline in both the k_{ME} rate constants and the Γ_{SYN} branching ratio seen for O_3 + Alkenes **1**—**4** is due to the electronic factors reported in previous sections or purely due to steric factors.

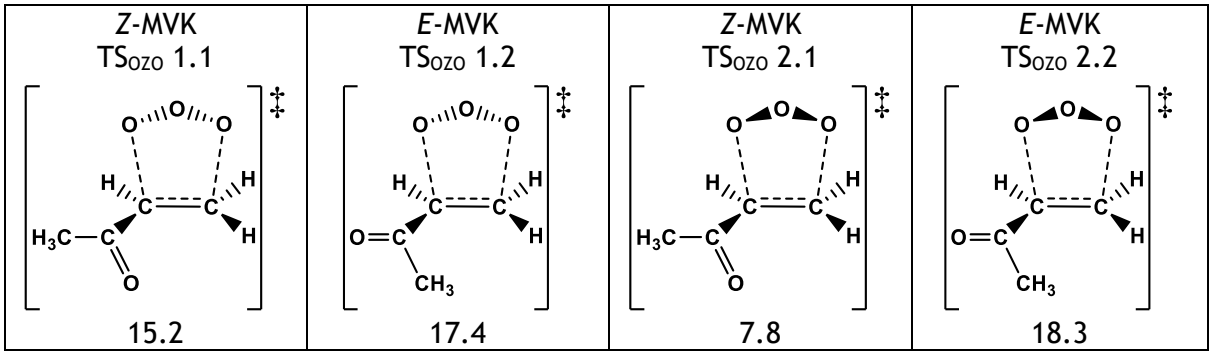

*Figure 3.13: A schematic and the relative energies (kJ mol^{-1}) of the different TS_{OZO} structures of O_3 + Alkene **5** and the E- or Z-isomer of that alkene **5** structures. Energies (in kJ mol^{-1}) are relative to raw reactants.*

One important factor to consider is that the conjugation between the —C(O)CH_3 and the >C=C< means there are two Alkene **5** conformers with a moderately sized isomerisation barrier (TS_{ISO} ~ 20 kJ mol^{-1}) between them. The two minimum energy geometries are designated as either *E*- or *Z*-isomer in line with *Cahn-Ingold-Prelog rules*, and, as shown in Figure 3.13, the cycloaddition structures are also divided by the same *E*- or *Z*-orientation. However, this TS_{ISO} barrier does not inhibit the ground state *E*-isomer reacting via the low energy *Z*-orientated TS_{OZO} 1.1 (15.2 kJ mol^{-1}) and TS_{OZO} 2.1 (7.8 kJ mol^{-1}) structures. As shown in the investigation in Appendix Section 1.6.1, this is because the significant

additional energy the alkene requires to undertake cycloaddition, is in enough excess to make free interconversion between *E*- or *Z*-isomers take place.

One important phenomenon to note here is that the TS_{OZO} 2.1 structure has the lowest cycloaddition pathways for O_3 + Alkene **5**. This is rare because of the steric repulsion between the central oxygen in the O_3 and the R_1 substituent (alkyl groups for Alkenes **1**—**4**) usually increases the barrier height for TS_{OZO} 2 compared to the lower TS_{OZO} 1 energy barrier. This is also unusual because, as seen in Figure 3.13, the TS_{OZO} 2.1 structure places the electronegative ketone oxygen near the central oxygen of the O_3, which would usually coulombically repel each other increasing the barrier height. If it is the inclusion of the *Z*-isomer that causes the low energy of TS_{OZO} 2.1, this only has a minor effect for the other *Z*-orientated cycloaddition TS_{OZO} 1.1 (15.2 kJ mol^{-1}) compared to *E*-orientated TS_{OZO} 1.2 (17.4 kJ mol^{-1}).

The computational analysis of the O_3 + Alkene **5** reaction in this chapter gives a middling k_{ME} value (6.90×10^{-17} cm^3 s^{-1}), with ~92% of this cycloaddition proceeding via the low energy TS_{OZO} 2.1 structure.[10,355] Alkenes **3** & **4** have lower reactivity compared to Alkene **5,** which may be partially explained by the fact that their —iPr & —tBu substituents are bulkier than that of the —C(O)CH_3 group in Alkene **5** and such steric bulk is also known to inhibit reactivity. However, the abrupt decline in reactivity between the highly reactive Alkene **2** and Alkene **5**, without any significant increase in steric bulk, provides evidence that drops in reactivity correlate with decrease in the number of α-H atoms. There is a larger gap between the k_{EXP} value (4.5—5.0×10^{-18} cm^3 s^{-1}) and the k_{ME} value of the O_3 + Alkene **5** reaction than seen for O_3 reactions with Alkenes **1**—**4**.[10,355]

cis-orientation POZ 1.1	*cis*-orientation TS_{ANTI} 1	*trans*-orientation POZ 2.1	*trans*-orientation TS_{ANTI} 2
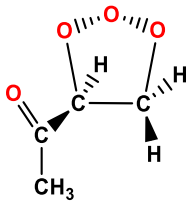	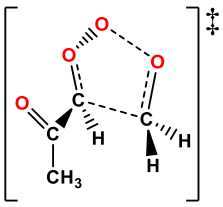	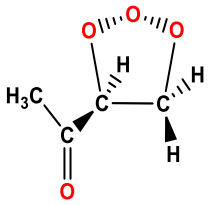	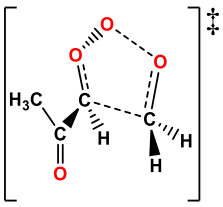
-203.5	-130.8	-220.1	-140.2

*Figure 3.14: A schematic and the relative energies (kJ mol^{-1}) of the different POZ and TS_{ANTI} structures of O_3 + alkene **5** differentiated by the cis or trans orientation. Energies are relative to raw reactants.*

An additional note to the O_3 + Alkene **5** reaction is that where the POZ conformers and POZ fragmentation pathways have the ketone functional group "*cis*" to the O_3 section of the structure (in red), the energies of these geometries are increased by ~15—20 kJ mol^{-1} compared to their "*trans*" equivalents (see Figure 3.14 for examples). This is because the *cis* orientation maximises the repulsive energies between the electronegative oxygens in

ketone and the 1,2,3-trioxolane in the POZs (although all POZ conformers still free interconvert). The higher energy of TSs with *cis* orientations (TS_{ANTI} 1, TS_{SYN} 1, TS_{FO} 1.1 & TS_{FO} 2.1) mean they produce quite low Γ_{THEO} values. Therefore, only TSs with *trans* orientations (TS_{ANTI} 2, TS_{SYN} 2, TS_{FO} 1.2 & TS_{FO} 2.2) are studied herein.

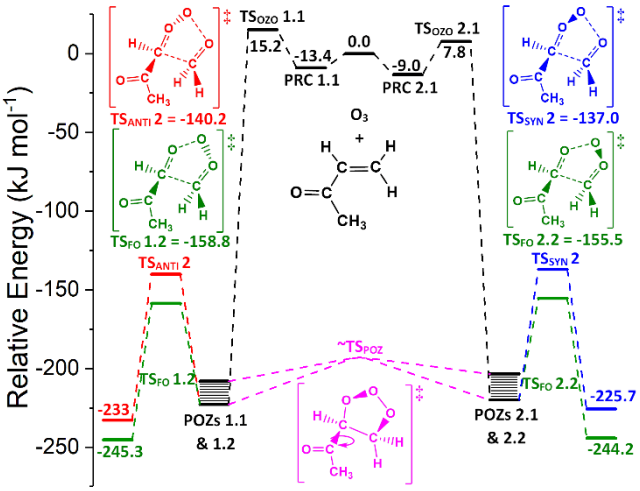

*Figure 3.15: PES of ozonolysis of Alkene **5**, methyl vinyl ketone, showing structures and energies the lowest energy for all major channels. POZs 1.1, 2.2, 2.1 & 2.2 all interconvert via various TS_{POZ} structures (see Appendix Section 1.6.2). Energies are relative to raw reactants.*

Due to the consistently low TS_{FO} barriers, POZ fragmentation in O_3 + Alkene **5** has high Γ_{THEO} values for CH_2OO (~0.934). This is in line with the experimental literature which gives a high collective α_{CH_2OO} branching ratios of 0.65—0.95.[355] An expected repercussion, of the α_{CH_2OO} value is low yield for these CIs from the other TS_{SYN} & TS_{ANTI} channels, *syn*- & *anti*-methylglyoxal oxide (*syn*- & *anti*-$CH_3C(O)CHOO$). Even though the Γ_{SYN} value for O_3 + Alkene **5** (0.020) is the lowest seen for any of the monosubstituted alkenes, it is in fact quite similar to the equivalent Γ_{SYN} value found for O_3 + Alkene **4** (0.059) and is therefore not unprecedented. On the other hand, the high TS_{ANTI} barriers for O_3 + Alkene **5** results in a much lower Γ_{ANTI} (0.046) compared to O_3 + Alkene **1**—**4** (~0.45). The OH yield (0.13—0.16) from the experimental literature is low because CH_2OO is the dominant CI generated in this reaction, and this CI does not have a large k_{UNI} value.[166,364] Usually, the remaining variation in OH yield is indicative of whether Γ_{SYN} or Γ_{ANTI} preferentially generated, however a prerequisite for understanding the validity of this analysis would access to experimental k_{UNI} values for *anti*- & *syn*-$CH_3C(O)CHOO$ which could not be found. The low OH yield may also be due to increased product stability that comes from the increased size and the electron delocalisation of aldehyde, methylglyoxal. The low Γ_{SYN} or Γ_{ANTI} values are likely due to instability of *anti*- & *syn*-$CH_3C(O)CHOO$, which the author proposes is due to two factors: the decline in the number of α-H atoms which stabilise TS_{SYN} structures during ozonolysis of Alkenes **1**—**3**; and the presence of the electron-withdrawing —$C(O)CH_3$ group.

3.4.4 Temperature Dependence for the Ozonolysis of Alkenes 1—5

According to studies by Leather *et al.* and Ren *et al.* respectively, the ozonolysis of Alkene **4** (between 218—288 K) and the ozonolysis of Alkene **5** (between 281—295 K) both display a slow positively correlated k_{EXP}—temperature relationship.[335,355] The author has calculated a similarly positive k_{THEO}—temperature dependency for both O_3 + Alkenes **4** & **5** over the same temperature profile, as seen in Figure 3.16, further authenticating the reliability of this method.[335,355] The k_{THEO}—temperature relationship for O_3 + Alkene **4** calculated here is of such similarity to the slow positive trend to the k_{EXP} temperature dependence measured by Leather *et al.*, a ~1 order of magnitude difference is maintained through every k_{THEO} & k_{EXP} data points, both seen in Figure 3.16. While O_3 + Alkene **5**, is slightly less in agreement because the difference between the k_{THEO} & k_{EXP} values are somewhat larger than 1 order of magnitude, the positive k_{THEO}—temperature inclines are also parallel enough to maintain a similar difference in k_{THEO} & k_{EXP} data points throughout. This implies that if there is an error in the calculation it is consistent throughout and so the reactivity trends are likely to be qualitatively correct.

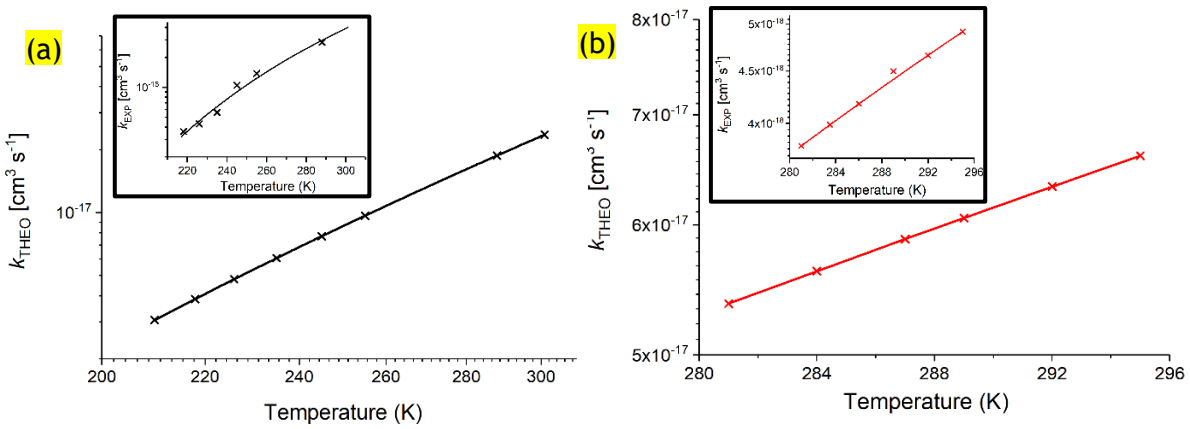

*Figure 3.16: Graphical representations of the theoretical & experimental relationship between temperature with the rate constant (k_{THEO} & k_{EXP}) for the ozonolysis of Alkene **4** (Figure 3.16a) and Alkene **5** (Figure 3.16b) (for full details and numbers check Appendix Section 1.2.1).*[335,355]

Temperature dependencies of the k_{ME} for alkenes **1**, **2** and **3**, have been also reviewed in this study. For those alkenes, to the author's knowledge, there is no literature available which studied these alkenes at the range of temperatures investigated in this paper. O_3 + Alkenes **1**—**3** also have a positive temperature dependence as shown in Table 3.5.

Table 3.5: Temperature dependence of Alkenes 1—3.

Alkene	Rate Constants (10^{-17} cm^3 s^{-1}) at Temperature (K)				
	200	275	298.15	325	400
1	0.263	2.04	3.24	5.23	15.3
2	0.913	6.58	10.3	16.3	45.9
3	0.487	3.21	4.96	7.82	22.1

3.4.5 Summary

In summary, this analysis of the ozonolysis of Alkenes **1**—**5** contains several noteworthy observations including that many of the theoretical trends agree with the experimental data. With the exception of the increases in reactivity form Alkenes **1** to **2**, a general trend is that a decline in the number of α-H atoms for Alkenes **2**—**5** (replaced with either —CH_3 groups or a ketone C=O bond) leads to a drop in k_{ME} values. With respect to Γ_{THEO} values, the preference for *anti*- over *syn*-R_1CHOO increases as the —R_1 substituent increases in complexity. The Γ_{THEO} values of CH_2OO + R_1CHO increases over the course of O_3 reactions with Alkenes **1**—**5**. The gradual increase in α_{CH_2OO} across Alkenes **1**—**4** increases substantially to Alkene **5**, with only minor yields of other CIs, which is attributed to the deactivating effect a —$C(O)CH_3$ on the COO group.

3.5 Discussion of the Ozonolysis of Trisubstituted Alkenes

The common features of Alkenes **6**—**10** are that they have a trisubstituted >C=C< bond and that their —R_3 and —R_4 substituents are —CH_3 groups. The same stepwise variation of the —R_1 substituent groups seen for Alkenes **1**—**5**, is replicated between Alkenes **6**—**10** (see Figure 3.17) and here the author explores similar chemical trends. The analysis of the Alkenes **1**—**5** shows that substituents with α-H atoms have an inductive effect on the >C=C< group during ozonolysis, and so the prospect that additional α-H atoms in **6-10** —CH_3 groups accelerates ozonolysis is also examined in this section. The same decline in Γ_{SYN} values seen for Alkenes **1**—**5**, is likely to occur across the O_3 reactions with Alkenes **6**—**10** as the number of α-H atoms on the —R_1 group decreases. The change in —R_3 and —R_4 substituents to —CH_3 groups means that the POZ fragmentation produces the CI dimethyl-formaldehyde oxide (DMFO or $(CH_3)_2COO$) via TS_{DMFO} structures. These $(CH_3)_2COO$ yields are compared with CH_2OO formation via TS_{FO} structures seen for O_3 + Alkenes **1**—**5** in the previous section. To assist in this comparison, the O_3 + Alkene **20** reaction is also analysed, as it is the only O_3 + monoalkene reaction that produces both CH_2OO and $(CH_3)_2COO$.

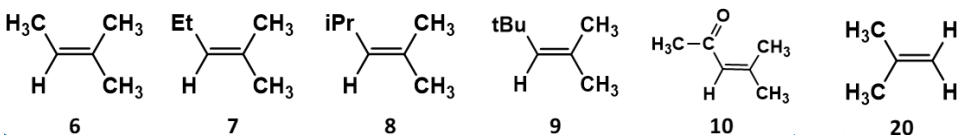

*Figure 3.17: Chemical Structures of Alkenes **6—10** and Alkene **20***

3.5.1 Ozonolysis of Alkenes 6 ($CH_3CH=C(CH_3)_2$)

If the two additional —CH_3 substituents in the R_3 and R_4 positions had no inductive effect on the >C=C< bond then, during the cycloaddition they would act only to sterically hinder

the reactions and therefore O_3 + Alkene **6** would exhibit a lower reactivity than Alkene **1**. However, Alkene **6** has lower TS_{OZO} 1 and 2 barriers (-1.64 and 2.37 kJ mol^{-1}) and reaction via TS_{OZO} 1 dominates cycloaddition (0.901). This produces a larger k_{ME} value for Alkene **6** (4.34×10^{-15} cm^3 s^{-1}) than Alkene **1** by just over two orders of magnitude, indicating that the nine α-H atoms on the three —CH_3 substituents have an inductive effect on the >C=C< bond of Alkene **6**. This larger rate constant agrees with the literature, which also yields larger k_{EXP} values for O_3 + Alkene **6** (~3.86—7.97 × 10^{-16} cm^3 s^{-1}) than for Alkene **1** (~9.9—10.1 × 10^{-18} cm^3 s^{-1}).[10,335,349]

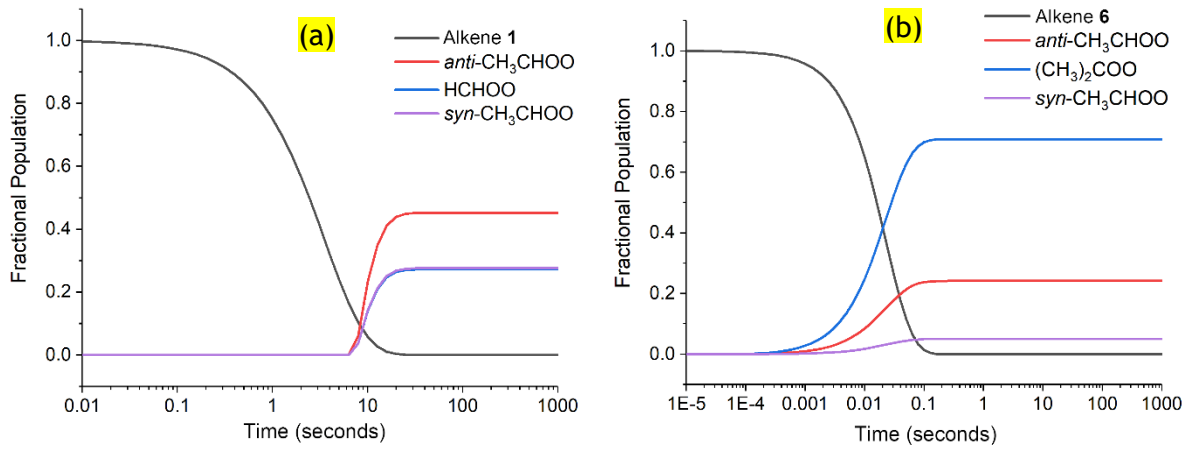

*Figure 3.18: The fractional populations of the reactant and product species over time during O_3 reactions with Alkene **1** on the left (Figure 3.18a) and Alkene **6** on the right (Figure 3.18b). Excess O_3 reagent concentration is ~1.0 × 10^{16} molec./cm^3.*

As mentioned above, the new —CH_3 groups in the R_3 and R_4 positions for Alkene **6**, replacing the —H groups seen in Alkene **1**, changes the R_3R_4COO CI to $(CH_3)_2COO$ from CH_2OO, altering Γ_{THEO} values. The "$\alpha_{(CH_3)_2COO}$" value (a catchall term to describe the collective Γ_{THEO} value for $(CH_3)_2COO$ + CH_3CHO) for O_3 + Alkene **6** in this chapter (0.701) is shown to be accurate compared to the equivalent value in the experimental literature (0.68). Whereas Figure 3.18b displays that the $\alpha_{(CH_3)_2COO}$ value dominates POZ fragmentation in the O_3 + Alkene **6** reaction, Figure 3.18a shows that O_3 + Alkene **1** give a small α_{CH_2OO} value compared to other pathways. This provides evidence that α-H atoms in an alkyl —R substituent induces higher yields for CIs with that —R group as a substituent.

While the preference for *anti*- over *syn*-CIs in POZ fragmentation is maintained for O_3 + Alkene **6**, the high $\alpha_{(CH_3)_2COO}$ value leads to much reduced Γ_{ANTI} (0.241) and Γ_{SYN} (0.005) values compared to O_3 + Alkene **1**, as seen in Figure 3.18. The high experimental OH yield for O_3 + Alkene **6** (0.81—0.98) exceeds that seen for alkenes **1**, **2** & **5** and is in good agreement with the high $\alpha_{(CH_3)_2COO}$ value calculated here.[166,355,363,364] This is because unimolecular fragmentation of $(CH_3)_2COO$ is swift (k_{UNI} ~478 s^{-1}) and it leads to a high yield of vinyl hydroperoxide, which decomposes to form OH radicals.[182]

3.5.2 Ozonolysis of Alkenes 7 ($EtCH=C(CH_3)_2$)

The lengthening of the —R_1 alkyl chain from —CH_3 (Alkene **6**) to—Et (Alkene **7**) is the same change between Alkenes **1** & **2**. Therefore, changes in chemistry due to this longer —R_1 alkyl chain, such as lowering the energy of TS_{OZO} 1.3 & TS_{OZO} 2.3 structures (-2.2 & -0.4 kJ mol^{-1}) compared to the analogous barriers for Alkene **6** (-1.64 and 2.37 kJ mol^{-1}), replicate trends already seen for Alkenes **1** & **2**. It is possible for the —Et substituent to reduce reaction rates by providing steric bulk which inhibit reactions of O_3 + Alkene **7**. However, as shown in Figure 3.19, this is not the case for TS_{OZO} 1.1 & 1.3 for Alkene **2** (in black) or Alkene **7** (in red), where the —Et group adopt analogous low energy orientations. The TS_{OZO} 1.2 structure for O_3 + Alkene **2** has a low barrier because it has no other substituents and consequently the —Et group can adopt a low energy *eclipsed* orientation to the >C=C< bond. However, the additional —CH_3 group in the —R_3 position of Alkene **7** means that a similar eclipsed orientation for —Et group has a significantly higher energy. Alkene **7** therefore has a different orientation where the —Et group is proximate to the O_3 in the TS_{OZO} 1.2 structure causing a steric repulsion that increases the barrier height.

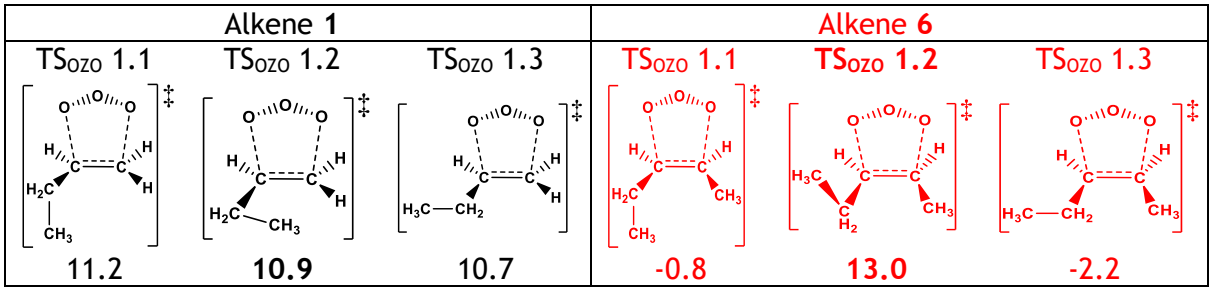

*Figure 3.19: Effect of adjacent extra —CH_3 substituents on TS_{OZO} 1 subpathways by comparing Alkenes **2** (black) and **7** (red). Energies (in kJ mol^{-1}) are relative to raw reactants.*

However, despite the steric repulsions in the TS_{OZO} 1.2 & TS_{OZO} 2.2 structures, Alkene **7** still has a larger ozonolysis k_{ME} value (5.11×10^{-15} cm^3 s^{-1}) than Alkene **2**, due to the activating effect of the α-H atoms in the two additional —CH_3 substituents. While Alkene **6** does feature —CH_3 substituents, it has a lower k_{ME} value than O_3 + Alkene **7** because, as observed with the shift in reactivity between Alkenes **1** & **2**, the lengthening the R_1 group here increases the rate constant. This large k_{ME} value calculated here and the k_{EXP} range (4.06—4.54×10^{-16} cm^3 s^{-1}) for O_3 + Alkene **7** are consistently the highest in this chapter.[10,118]

Although to the author's knowledge the experimental $\alpha_{(CH_3)_2COO}$ value for the reaction of O_3 + Alkene **7** has yet to be determined in the literature, if the POZ fragmentation trend seen for O_3 + Alkenes **1**—**5** continues for Alkenes **6**—**10**, then the $\alpha_{(CH_3)_2COO}$ value for O_3 + Alkene **7** should be between that seen for Alkenes **6** & **8**. As the theoretical $\alpha_{(CH_3)_2COO}$ value

(0.811) exceeds that of Alkene **6** (0.68) and is similar to that of Alkene **8** (0.81), these results seem to be both consistent and relatively accurate. Similarly, the Γ_{THEO} value O_3 + Alkene **7** declines for both *anti*- & *syn*-EtCHOO (0.152 & 0.037) compared to Alkene **6** (0.241 & 0.005). This correlates with a reduction in the number of α-H atoms on the $—R_1$ substituent, while the α-H rich $\alpha_{(CH_3)_2COO}$ values hold. This provides additional evidence for the author's hypothesis that branching fractions from POZ fragmentation favours the CI with more α-H atoms on their alkyl substituents.

3.5.3 Ozonolysis of Alkenes 8 & 9 (iPrCH=C(CH$_3$)$_2$ & tBuCH=C(CH$_3$)$_2$)

While the lengthening of the $—R_1$ substituent from a $—CH_3$ to an —Et group (**6** to **7** - see Figure 3.20) causes an increase in reactivity, the further supplementation of the $—R_1$ group into —iPr & —tBu groups, causes a deactivation of the >C=C< bond in Alkenes **8** & **9**. This inversion in ozonolysis reactivity is seen in the lowest energy TS_{OZO} 1 & 2 barriers of O_3 + Alkene **8** (3.2 & 4.8 kJ mol^{-1}), which is then augmented for Alkene **9** with further increases in barrier heights (3.7 & 6.3 kJ mol^{-1}).

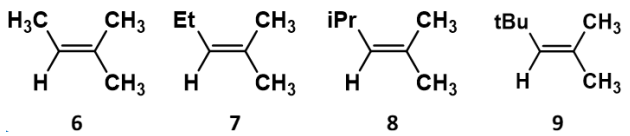

*Figure 3.20: Chemical Structures of Alkenes **6—10** and Alkene **20***

To determine the accuracy of the k_{ME} value of O_3 + Alkene **8**, it is compared to a *structure-activity relationship* rate constant (k_{SAR}), because to the author's knowledge no k_{EXP} value has been measured for this reaction in the literature.[10,118] This method, derived by McGillen et *al.*, uses an equation produced from a correlated pattern of some structural features and literature to project this k_{SAR} constant (further details in Method Section 2.7).[118] Both the k_{SAR} constant (2.2×10^{-16} cm^3 s^{-1}) and the k_{ME} value (2.459×10^{-16} cm^3 s^{-1}) for O_3 + Alkene **8** are both similar and, as shown in Figure 3.21, both much reduced compared to the O_3 + Alkene **7** rate constants.

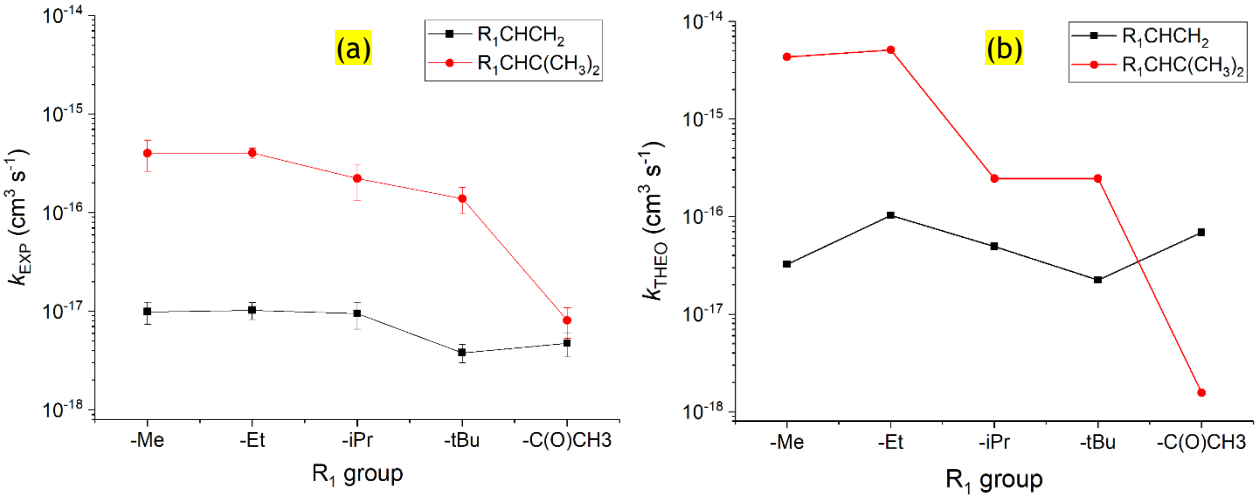

*Figure 3.21: Comparison of ozonolysis for Alkenes **1—10** using experimental rate constants (Figure 3.21a) and theoretical rate constants (Figure 3.21b).[10]*
Note: iPrCHC(CH₃)₂ k_{EXP} rate constant is derived from the k_{SAR} found in the text.

This is followed by a similar reduction for both the k_{ME} value (2.456×10^{-16} cm^3 s^{-1}) and the literature k_{EXP} range ($1.25—1.39 \times 10^{-16}$ cm^3 s^{-1}) for O_3 + Alkene **9**. However, given the degree of computational uncertainty observed in Method Section 2.9, the difference in ozonolysis k_{ME} values for Alkenes **8** & **9** is slight. Not only does Figure 3.21 display how well the computational work here reproduces the trends in k_{EXP} constants, but it also shows how much the trends in k_{ME} values of O_3 + Alkenes **6—10** mirror those of O_3 + Alkenes **1—5**. All O_3 reactions with Alkenes **7—9** have larger rate constants than those of Alkenes **2—4**, once again showing the inductive power of the two additional —CH_3 substituents. However, the trend that a stepwise reduction in the number of α-H atoms in the R_1 group for Alkenes **2—4** leads to a corresponding decline in ozonolysis k_{ME} values, is also clearly reflected here across O_3 + Alkenes **7—9** too.

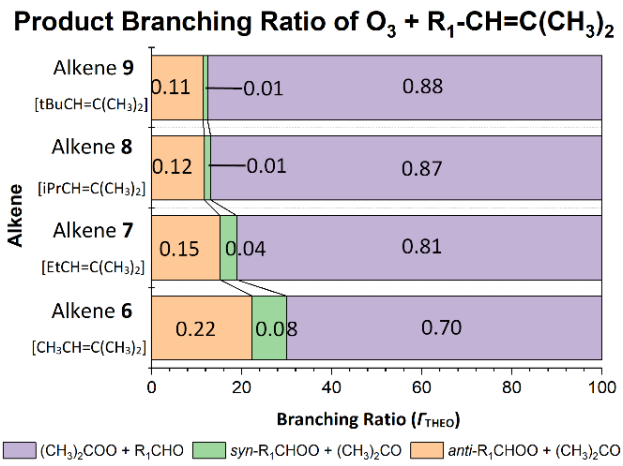

*Figure 3.22: Branching Ratios (Γ_{THEO}) of O_3 + Alkenes **6-9** reactions.*

The gradual increase in $(CH_3)_2COO$ branching ratios ($\alpha_{(CH_3)_2COO}$) seen between O_3 + Alkenes **6** & **7** reactions continues with small incremental increases for O_3 + Alkene **8** ($\alpha_{(CH_3)_2COO}$ ~

0.868) and O_3 + Alkene **9** ($\alpha_{(CH_3)_2COO}$ ~ 0.876). This agrees with the literature which also sees small increases in experimental $\alpha_{(CH_3)_2COO}$ values for O_3 + Alkenes **8** (0.81) and O_3 + alkene **9** (0.82), compared to O_3 + alkene **6**. As displayed in Figure 3.22, these increases in $\alpha_{(CH_3)_2COO}$ values (in purple) across O_3 + Alkenes **6**—**9** lead to a consequential gradual decrease in both Γ_{ANTI} (in orange) & Γ_{SYN} (in green) values, in line with the decline in the number of α-H atoms in the R_1 group of the *anti*- or *syn*-R_1CHOO. This is the same trend seen for O_3 + alkenes **1**—**4**. These trends again indicate that the CI with the large numbers of substituent α-H atoms gain preference in POZ fragmentation. Also shown throughout this analysis of O_3 + alkenes **6**—**9** is that the POZ fragmentation continues the consistent preference for *anti*- over *syn*-CIs.

3.5.4 Ozonolysis of Alkene 10 ($CH_3C(O)CH=C(CH_3)_2$)

The k_{ME} value for O_3 + Alkene **10** (1.57×10^{-18} cm^3 s^{-1}) is lower than that seen for O_3 + Alkene **7** (5.11×10^{-15} cm^3 s^{-1}), which reaffirms that the decline in α-H atoms in substituents and its replacement with a ketone group (the —$C(O)CH_3$) both have deactivating impacts on the >C=C< bond. This is confirmed by the experimental literature where the k_{EXP} of O_3 + Alkene **10** (8.1×10^{-18} cm^3 s^{-1}) is also much lower than that of O_3 + Alkene **7** (4.06—4.54 × 10^{-16} cm^3 s^{-1}).[10,118,356] The deactivating effect of the —$C(O)CH_3$ group can also be observed in the low ozonolysis k_{ME} value of Alkene **5**, which is also an enone when (in Section 3.4.3) it was compared to Alkene **2**.

Alkene **10** also has a lower ozonolysis k_{ME} value than all other trisubstituted Alkenes **6**—**9** (~10^{-16} cm^3 s^{-1}) in this chapter, which, seen in Figure 3.21 in Section 3.5.3, corroborates the experimental literature. However, this k_{ME} value for O_3 + Alkene **10** is also lower than that seen for O_3 + Alkene **5** (6.9×10^{-17} cm^3 s^{-1}), which while not reflected in the average k_{EXP} values in Figure 3.21, it is still within the margin of uncertainty.[10,355] As the reduction in number of α-H atoms does not fully account for this low reactivity for Alkene **10**, the author also proposes that the additional steric bulk of the —$C(O)CH_3$ group in conjunction with the —CH_3 substituent may inhibit reaction.

The POZ fragmentation from the O_3 + Alkene **10** follows the trends observed for Alkenes **1**—**9**, that the inductive impact of the α-H atoms in two —CH_3 substituents leads to very high $\alpha_{(CH_3)COO}$ value (0.972). The subordinate Γ_{THEO} values for *syn*- & *anti*-methylglyoxal oxide (0.004 & 0.024) are similar to those seen for O_3 + Alkene **5** (0.020 & 0.046). This implies that these small Γ_{THEO} values is not just the impact of strong inductive α-H atoms promoting $(CH_3)_2COO$ formation but the steric and electronic repulsion of the —$C(O)CH_3$ group hindering CI formation. Much like with O_3 reactions with Alkenes **8** & **9** no literature

OH yield for O_3 + Alkene **10** is known to the author. However, the high $(CH_3)_2COO$ branching ratio likely produces a high OH yield for O_3 + Alkene **10**, as it does for O_3 + Alkene **6** (OH yield ~ 0.81—0.98).

3.5.5 Comparing O_3 + Alkene 20 ($(CH_3)_2C{=}CH_2$) with other Trisubstituted Alkenes

Observed throughout this section is that systems with two —CH_3 groups in the —R_3 and —R_4 positions, e.g. Alkenes **6**—**9**, inductive effects impact both k_{ME} values and CI formation during ozonolysis, compared—H substituted Alkenes **1**—**4**. To see if $(CH_3)_2COO$ formation is preferred over CH_2OO in absolute terms, rather than just through comparative analysis in different alkenes, the ozonolysis of $(CH_3)_2CCH_2$ (Alkene **20**), which yields both CIs, is explored. This is then then compared to the mono-substituted Alkene **1** and the trisubstituted Alkene **6** (see structures in Figure 3.23).

*Figure 3.23: Chemical Structures of General Alkene and Alkenes **1**, **6** & **20***

The ozonolysis k_{ME} value of Alkene **20** (3.02×10^{-17} cm^3 s^{-1}) is not only well within an order of magnitude of the k_{EXP} range ($1.08—1.14 \times 10^{-17}$ cm^3 s^{-1}), it also agrees with the literature in that it is less reactive than O_3 + Alkene **6** (k_{ME} ~ 4.3×10^{-15} cm^3 s^{-1}). However, unlike in the experimental literature, the k_{ME} value of Alkene **1** (3.24×10^{-17} cm^3 s^{-1}) is smaller than that of Alkene **20**, but it should be noted that since both Alkene **1** and **20** deviate by less than 10% of each other for both the k_{ME} and k_{EXP} values, this discrepancy is not significant. This is not unusual, for example, McGillen *et al.* state that disubstituted —CH_3 groups on one end of a >C=C< bond can steric impede *and* electronically promote alkene ozonolysis.[118]

With respect to POZ fragmentation, the reaction of Alkene **20** confirms the trend inferred during the ozonolyses of Alkenes **1**—**10**, that the inductive α-H atoms in the two —CH_3 groups lower the energy barrier to $(CH_3)_2COO$ formation, (TS_{DMFO} ~ -172.8 kJ mol^{-1}), compared to that of CH_2OO (TS_{FO} -158.4 kJ mol^{-1}). The dominant $\alpha_{(CH_3)_2COO}$ value (0.842) is in good agreement with that seen in experimental yields (~0.75) and, the high decay rate of the dominant $(CH_3)_2COO$ product generates the high experimental OH yield (0.60—0.84). The most important observation is that this $\alpha_{(CH_3)_2COO}$ value exceeds that of O_3 + Alkene **6** (0.701), showing that inductive α-H atoms in 2 × —CH_3 groups do promote CI formation compare to —H substituents. However, the effect of sterically bulky substituents is also

observed, when compared to O_3 reactions with Alkenes **8** & **9** which maximises the size of $\alpha_{(CH_3)_2COO}$ values (~0.868 & 0.876), as —iPr and —tBu substituents inhibit formation of the other CIs.

3.5.6 Summary

In summary, the study of Alkenes **6**—**10** & **20** provides additional evidence of the trends inferred earlier, that the inductive effect of the additional α-H atoms in —CH_3 substituents generally increase the ozonolysis rate constant. The exception to this is the ozonolysis of Alkene **10**, where a reductive effect of a —C(O)CH_3 group, also seen in O_3 + Alkene **5,** diminishes the k_{ME} value considerably. This is best visualised in Figure 3.21 in section 3.5.3.

One very important trend seen in the ozonolysis of Alkenes **6**—**9**, is that the inductive impact of the —CH_3 substituents in —R_3 and —R_4 positions produce sizable $\alpha_{(CH_3)_2COO}$ values (0.6—0.9) during the POZ fragmentation. These are significantly larger than the comparable α_{CH_2OO} values (0.2-0.5) in Alkenes **1**—**4**, which have —H substituents instead. The preference for *anti*-CIs over *syn* equivalence continues due to lack of steric inhibition during the TS_{ANTI} mechanisms. However, as the R_1 substituent group enlarges from the hyperconjugated —CH_3 group to the bulky —tBu and —C(O)CH_3 groups, the Γ_{THEO} values for both *anti* & *syn*-CIs shrink.

3.6 Discussion of the Ozonolysis of *E*- and *Z*-Alkenes

The common features of alkenes in this section is that they have two alkyl substituents (referred to as *disubstituted*) but, unlike with Alkene **20**, the two alkyl substituents in Alkenes **15**—**19** are located at either end of the >C=C< bond. This particular chemical sequencing produces two chemical structures with different spatial arrangements (see Figure 3.24): an *E* isomer, such as Alkenes **15** & **17**, where the two alkyl groups are in the —R_1 and —R_4 positions; and a *Z* isomer, such as Alkenes **16**, **18** & **19**, where the two alkyl groups are in the —R_1 and —R_3 positions. These are also referred to as *trans* & *cis* isomers, respectively and, due to a high barrier to interconversion, are chemically distinct.

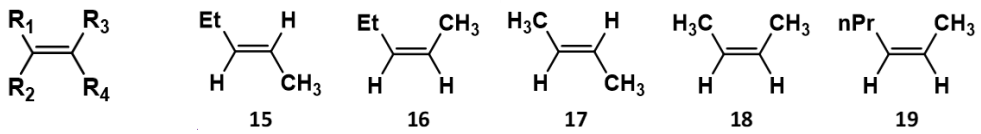

*Figure 3.24: Chemical Structures of Generic Alkene and Alkenes **15**—**19***

By comparing the ozonolysis chemistry of Alkenes **15**—**18**, it can be observed whether the inductive impact of α-H atoms in alkyl groups is affected by *E* or *Z* structural positions of substituents, something which could not be observed in the analysis of Alkenes **1**—**10**. In addition to this, as the identity of the $-R_1$ substituent switches from an —Et group in Alkenes **15** & **16** to a — CH_3 group in Alkenes **17** & **18**, it can be observed whether the consequential depletion in α-H atoms affects the ozonolysis chemistry of *E* & *Z* isomers differently. The theoretical trends of O_3 + Alkene **19** are also mentioned in Subsection 3.6.2 only for comparative purposes, and so for the full analysis see Chapter 6.

To the author's knowledge, unlike with many of the O_3 + Alkenes **1**—**10** reactions, the only literature data for the Γ_{EXP} values for the O_3 + Alkenes **15**—**18** reactions are OH yields. As both *syn*-CH_3CHOO and *syn*-EtCHOO have similar k_{UNI} values that are also much higher than both the *anti*- equivalents, a high OH yield for any of the O_3 + Alkenes **15**—**18** reactions is simply indicative of a high collective yield of both *syn*-CIs (α_{SYN}).

3.6.1 The Ozonolyses of Alkenes 17 & 18 (*E*- & *Z*-$CH_3CH{=}CHCH_3$)

The simplest *E*- or *Z*- hydrocarbon alkenes are Alkenes **17** & **18** and so may provide a basic framework for understanding the ozonolysis chemistry of similar *E*- or *Z*-alkenes. Alkene **17** is similar to Alkene **20** in one key respect, which is that due to the presence of a high degree of symmetry in Alkene **17**, the ozonolysis reaction only has one cycloaddition structure, as shown in Figure 3.25. This degree of symmetry gives the TS_{OZO} a degeneracy of 2, doubling the raw k_{ME} value of O_3 + Alkene **17** to 3.61 × 10^{-16} cm^3 s^{-1}. However, the cycloaddition TS_{OZO} 1 mechanism for O_3 + Alkene **18** has a significantly lower energy barrier (0.6 kJ mol^{-1}), which produces a higher ozonolysis k_{ME} value (1.18 × 10^{-15} cm^3 s^{-1}) than Alkene **17**.

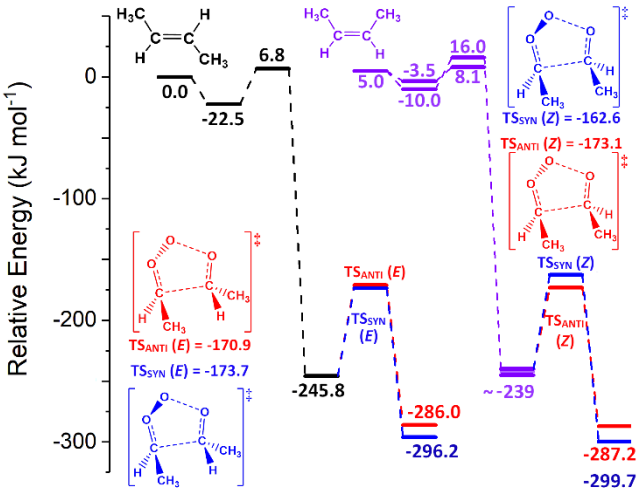

*Figure 3.25: The PESs of the ozonolyses of Alkene **17** (in black) and Alkene **18** (in violet), with the POZ fragmentation transition states labelled according to the E or Z structure of the alkene involved ((*TS_{ANTI} (E) & TS_{SYN} (E) are part of the ozonolysis of Alkene **17** and TS_{ANTI} (Z) & TS_{SYN} (Z) are part of the ozonolysis of Alkene **18**)). The ozonolysis of Alkene **18** produces two POZ conformers, but as they are not chemically distinct they are represented as one POZ at ~-239 kJ mol^{-1}. Energies are relative to the raw energy of O_3 + Alkene **17**.*

Based on limited literature, it appears that the average k_{EXP} values for O_3 + Alkene **18** (1.25 × 10^{-16} cm^3 s^{-1}) does *not* exceed that of Alkene **17** (1.90 × 10^{-16} cm^3 s^{-1}).[360] While this appears to contradict the computational trend observed in this chapter, the difference between such k_{EXP} values is marginal, and the range of k_{EXP} values within the literature are within uncertainty. Crucially, however these k_{ME} values are shown to be within order of magnitude of this literature k_{EXP} range.

The low POZ fragmentation TS_{SYN} barrier (-173.7 kJ mol^{-1}) for O_3 + Alkene **17**, seen in Figure 3.25, indicates a slight preference for *syn*-CH_3CHOO over the *anti*-equivalent (TS_{ANTI} ~ -170.9 kJ mol^{-1}), whereas the TS_{ANTI} structure of O_3 + Alkene **18** is much lower in energy (-178.1 kJ mol^{-1}) than the TS_{SYN} (-167.6 kJ mol^{-1}), following the preference for *anti*-CIs observed for Alkenes **1**—**10**. Although the Γ_{THEO} values for O_3 + Alkene **17** shows a marginal

preference for *anti*-CH_3CHOO (0.520) over the *syn* conformer (0.480), this is much more evenly split than that seen for Alkene **18** (Γ_{ANTI} ~ 0.775 & Γ_{SYN} ~ 0.255). The higher *syn*-CH_3CHOO branching preference for O_3 + Alkene **17** compared to Alkene **18** is in agreement with the literature because a Orzechowska and Paulson study records that O_3 + Alkene **17** has a larger OH yield (0.64) than Alkene **18** (0.33) and high OH yield is indicative of high Γ_{THEO} values for *syn*-CH_3CHOO.[162] While there is a large range of experimental OH yields for the ozonolysis of Alkenes **17** & **18** across many studies, when considering all studies (see Appendix Section 1.4) O_3 + Alkenes **17** usually has a higher OH yield.[162]

3.6.2 The Ozonolyses of Alkenes 15 & 16 (*E*- & *Z*-EtCH=CHCH$_3$)

One important observation here is that the new —Et substituent appears to have increased ozonolysis k_{ME} values for both Alkene **15** (1.13×10^{-15} cm^3 s^{-1}) and Alkene **16** (2.83×10^{-15} cm^3 s^{-1}) above those seen for Alkenes **17** & **18** (3.61 & 11.8 × 10^{-16} cm^3 s^{-1}), which have —CH_3 substituents in the R_1 position instead. The inductive influence of this —Et substituent is consistent with similar trends already observed here between Alkenes **1** & **2** and **6** & **7**. This is also in agreement k_{EXP} values noted by Calvert *et al.*, where O_3 + Alkene **15** (3.15×10^{-16} cm^3 s^{-1}) & Alkene **16** (~1.28×10^{-16} cm^3 s^{-1}) are marginally more reactive than O_3 reactions with Alkene **17** (1.28—1.90 × 10^{-16} cm^3 s^{-1}) and Alkene **18** (~1.25×10^{-16} cm^3 s^{-1}) respectively.[10] The inductive impact of increasing the length of the R_1 substituents from a —CH_3 to an —Et group appears to be supplemented by further lengthening to an —nPr group, as the k_{THEO} value for O_3 + Alkene **19** calculated in Chapter 6, is larger (3.53×10^{-16} cm^3 s^{-1}) than those seen for O_3 + Alkenes **16** & **18**.

Ozonolysis of the *Z*-isomer, Alkene **16**, has a larger k_{ME} value than the *E*-isomer, Alkene **15**, replicating the higher theoretical reactivity seen for the *Z*- over the *E*-isomer, also seen for O_3 + Alkenes **17** & **18**. This is not quite consistent with Calvert *et al.*, which shows a larger k_{EXP} value for *E*-isomer, Alkene **15** rather than the *Z*-isomer, Alkene **16** (both noted above).[10] Given the wide range of k_{EXP} reported in the literature, it is difficult to infer absolute trends in the datasets. With this in mind, the data presented in this report seems entirely plausible, particularly given the consistency of trends in alkene substitution that have already been clearly identified.

Two underlying factors that are important for the O_3 reactions with Alkenes **15** & **16** (*E*- and *Z*-2-pentene), not seen for Alkenes **17** & **18** when considering POZ fragmentation, are that: the greater conformational flexibility of Alkenes **15** & **16** leads to a large number of TS structures; and the new —Et substituent means POZ fragmentation generates of *syn*- & *anti*-EtCHOO, as well as *syn*- & *anti*-CH_3CHOO. This multiplicity of different fragmentation

mechanisms for POZs seen during the ozonolysis of Alkenes **15** & **16** are divided into four different *channels* on the basis of the products they generate: TS_{ANTI} 1 that produces *anti*-EtCHOO + CH_3CHO; TS_{SYN} 1 that produces *syn*-EtCHOO + CH_3CHO; TS_{ANTI} 2 that produces *anti*-CH_3CHOO + EtCHO; and TS_{SYN} 2 that produces *syn*-CH_3CHOO + EtCHO. As with the previous reactions, unless required, only the lowest energy TS (or *subchannel*) of each channel are discussed herein (although the intricacies of individual TSs are discussed further in Chapter 6, to aid determining the reaction chemistry of O_3 + Alkene **19**).

During the O_3 + Alkene **15** reaction, the lowest energy subchannel for each POZ fragmentation channel give very comparable energies: TS_{ANTI} 1.3 (-172.59 kJ mol^{-1}), TS_{SYN} 1.3 (-174.22 kJ mol^{-1}), TS_{ANTI} 2.3 (-172.83 kJ mol^{-1}) and TS_{SYN} 2.3 (-175.23 kJ mol^{-1}). This similarity in energies gives rise to a near-even distribution of products between each channel, as seen in Figure 3.26. The Γ_{THEO} fraction for CIs calculated in this study are compared to literature CI measurements obtained using the indirect approach of inferring branching ratios from two aldehyde/ketone co-products.[10] Such co-product yields would be used to verify the collective CI branching fraction for *anti*- & *syn*-EtCHOO calculated in this chapter (α_{EtCHOO} ~ 0.391). However, to the author's knowledge, this measurement has not been conducted and published in any literature for either the O_3 reactions with Alkenes **15** or **16**, like it has for Alkene **2**.

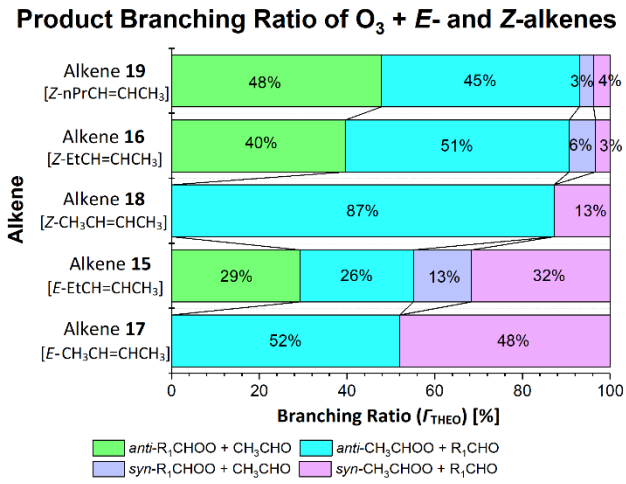

*Figure 3.26: Branching Ratios (Γ_{THEO}) of O_3 + Alkenes **15-19** reactions.*

In contrast to Alkene **15**, the lowest TS barriers for each POZ fragmentation channel of the O_3 + Alkene **16** reaction have larger energy gaps between them: TS_{ANTI} 1.3 (-179.02 kJ mol^{-1}), TS_{SYN} 1.3 (-167.78 kJ mol^{-1}), TS_{ANTI} 2.3 (-179.58 kJ mol^{-1}) and TS_{SYN} 2.3 (-169.13 kJ mol^{-1}). Figure 3.26 shows this gives rise to a much more uneven product distribution, with two CI products *anti*-CH_3CHOO (0.510) and *anti*-EtCHOO (0.395) dominating CI formation yields. During the analysis of the O_3 + Alkenes **1**—**10**, it was determined that a —CH_3 substituent induced a greater preference for CI formation due to the further hyperconjugation

provided by the additional α-H atoms, than in the —Et group. This is reflected here, not only in this preference for *anti*-CH_3CHOO over *anti*-EtCHOO formation, but also in the greater Γ_{THEO} value for *syn*-CH_3CHOO (0.060) than *syn*-EtCHOO (0.034). This disfavour for CIs that have substituents with low numbers of α-H atoms is shown in the low collective theoretical α_{EtCHOO} value for O_3 + Alkene **16** (0.429), and the slightly smaller α_{EtCHOO} for Alkene **15** (0.391). However, as the indirect experimental yield is not available within the current literature, this cannot be fully verified.[10] Yet, also shown in Figure 3.26, this greater preference for CH_3CHOO does not apply to O_3 + Alkene **19**, which shows a slight theoretical preference for nPrCHOO over CH_3CHOO. This change in CI preference is thought to be due to accumulated small changes in steric interaction, rather than hyperconjugative interactions, however this is discussed further in Chapter 6.

One common POZ fragmentation pattern that is seen throughout this section is in that ozonolysis of the *E*-alkenes (Alkenes **15** & **17**) have greater tendency to form *syn*-CIs than do O_3 reactions with *Z*-alkenes (Alkenes **16**, **18** & **19**). One notable example of this is that O_3 + Alkene **15** is a rare example where a *syn*-CI, *syn*-CH_3CHOO, has a plurality of the CI branching fraction although the overall α_{SYN} value for O_3 + Alkene **15** (0.448) is still not dominant over the collective α_{ANTI} branching fraction (0.552). Nevertheless, this is very different to the ozonolysis of the *Z*-orientated Alkene **16**, where *anti*-CIs dominate POZ fragmentation products such that the collective α_{SYN} value is marginal (0.094). Both these *syn*-CIs produced in O_3 + Alkenes **15** & **16** reactions have larger k_{UNI} values and hence are likely to produce greater OH yields compared to their *anti* equivalents. Consequentially, the fact that O_3 + Alkene **15**, both has a larger theoretical propendency to produce *syn*-CIs and a greater experimental OH yield (0.46) than O_3 + Alkene **16** (OH yield ~ 0.27—0.29) shows that this theoretical work is in agreement with the literature. The marginal importance of *syn*-CI formation to ozonolysis of *Z*-alkenes continues for O_3 + Alkene **19**, which, as shown in Figure 3.26, has a Γ_{THEO} distribution dominated by *anti*-CIs though a literature OH yield of this reaction has yet to be found.

3.6.3 Summary of the ozonolysis of *E*- & *Z*-alkenes

In summary, several important computational trends identified for O_3 reactions with Alkenes **1**—**10** continued for the reactions with Alkenes **15**—**18**, including that substituting the —CH_3 group in the R_1 position with an —Et group increased the k_{ME} value. Another noteworthy observation was that, where CI formation competed during the POZ fragmentation step of O_3 + Alkenes **15** & **16** reactions, it was found CH_3CHOO generally

had a larger branching fraction than EtCHOO. This confirmed an observation that could only be made indirectly by comparing different O_3 + Alkenes **1**—**10** reactions.

A new observation that was made during this section, included that the *Z*-alkenes (**16** & **18**) had larger ozonolysis k_{ME} values than their *E*-orientated counterparts. However, both the *E*- & *Z*-alkenes, such as Alkenes **15** & **16** (*E*- & *Z*-EtCHCHCH$_3$), have lower ozonolysis k_{ME} values than their trisubstituted counterpart, Alkene **7** (EtCHC(CH$_3$)$_2$), but higher than their monosubstituted equivalent, Alkene **2** (EtCHCH$_2$). One other noteworthy finding was that comparative to disubstituted alkenes, ozonolysis of *E*-alkenes produce greater quantities of *syn*-CIs than *Z*-alkenes.

3.7 The Ozonolysis of Halogenated Alkenes

The series of halogenated alkenes (Alkenes **11**—**14**) analysed in this section are part of a generation of new refrigerants referred to as hydrofluoroolefins (HFOs).[2,12] They are currently being put into commercial circulation to replace the previous atmospherically detrimental chlorofluorocarbon (CFC), hydrochlorofluorocarbon (HCFC) and hydrofluorocarbon (HFC) refrigerants. HFOs are being introduced because of their relative non-toxicity, short atmospheric lifetimes, low global warming potentials (GWP) and low ozone depletion potentials (ODP).[2,197,347] For further details on the harmful impacts of the CFC, HCFC and HFC refrigerants and the general benefits of HFOs see Introduction Section 1.7. The HFOs explored in this study, and displayed in Figure 3.27, either have halogen substituents, such as —F or —Cl, and/or haloalkyl substituents, such as —CF$_3$ or —CF$_2$CF$_3$.

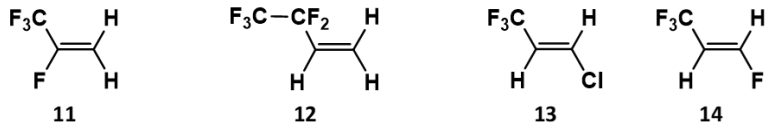

*Figure 3.27: Chemical structures of Alkene **11**—**14** (also referred to as HFOs)*

Alkenes **11**, **13** & **14** are included here as they are already in industrial and commercial use, so it is vital to understand their mechanisms of decomposition and their subsequent products thereby to observe their effect on local and global atmospheric models.[197,198,224,226,347] For example, it is already known that Alkene **11** is breaks down into trifluoracetic acid (TFA), a tropospheric gas known to cause irritation to the respiratory tract.[199] Increased use of HFOs in cities like Beijing has led to an increase in local tropospheric concentrations of TFA and such increases will likely therefore lead to increased respiratory problems.[199]

While Alkene **12** is in limited commercial circulation, the analysis of O_3 + Alkene **12** can be used from a more fundamental perspective to investigate if α-F atoms in the —CF$_2$CF$_3$

substituent have a reductive impact on the >C=C< group, in contrast to the inductive impact that α-H atoms have on Alkene **2**. Such a reductive effect has been found for α-F atoms in —CF_3 substituents on the COO functional group in *anti*-sCIs (discussed further in Chapters 4 & 5) and so such an effect could plausibly be found for unsaturated >C=C< bonds too. Further effects of different halogen and haloalkyl substituents on the ozonolysis chemistry are discussed in this section in the reactions of O_3 with Alkenes **11**, **13** & **14**, which can be compared directly to other non-halogenated alkenes. This includes analysis of how the alternation of -H and alkyl substituents to either halogen and haloalkyl groups affects CI formation yields. Also discussed in this section is the comparative impact of the halogen and haloalkyl substituents on CI formation yields, across all the O_3 reactions with Alkenes **11**—**14**. While, some computational analysis of O_3 + Alkenes **11**, **12** & **13** is present in the literature, the analysis conducted here is much more extensive as it includes previously unidentified TSs and final products in each case.[224,226,241]

Of sCIs produced from these HFO + O_3 reactions (referred to as HFO-sCIs), only CH_2OO and *syn*-/*anti*-ClCHOO, have been experimentally observed.[224,226,369-371] While references to them are sparing in the computational literature, some studies say that HFO-sCIs, like *anti*-/*syn*-CF_3CHOO, can be bimolecular sinks for atmospheric toxins, such as CO_2 and CH_4.[93,273,274,305,325,372] For analysis of "HFO-sCI" reactions with various tropospheric species, see Chapter 5.

3.7.1 Ozonolysis of Alkenes 11 ($CF_3CF{=}CH_2$)

Ozonolysis of Alkene **11** ($CF_3CF{=}CH_2$) is significant because it is the only alkene in this study, excluding Alkene **20**, that has a substituted R_2 group. The ozonolysis reaction PES is similar to Alkene **1**, but has a few significant differences, such as the TS_{OZO} 1 pathway (31.3 kJ mol^{-1}) which has a larger energy barrier than TS_{OZO} 2 (27.5 kJ mol^{-1}). Both these barriers are comparably large which give rise to a small k_{ME} (1.14×10^{-20} cm^3 s^{-1}) compared to O_3 reactions with Alkenes **1**—**10** & **15**—**18** (10^{-18} - 10^{-15} cm^3 s^{-1}). The k_{EXP} is also small, (2.77×10^{-21} cm^3 s^{-1}) showing encouraging reliability for this calculation.[348]

Unlike Alkene **20**, where —R_1 and —R_2 substituents are the same, Alkene **11** has differing —R_1 and —R_2 substituents, a —CF_3 and an —F group. So, for the purposes of this study, as the —CF_3 group is assigned as the primary substituent with the —R_1 position in alkene as it has the larger molecular weight. This is mostly important when discussing the CI orientation because, whether the primary —R_1 substituent (the —CF_3 group) is either *syn*-periplanar or *anti*-periplanar to the terminal oxygen, distinguishing *syn*-CF_3CFOO from *anti*-CF_3CFOO respectively. Furthermore, the two POZ fragmentation barriers TS_{SYN} & TS_{ANTI} are referred

to as such depending on whether they produces the *syn*- or *anti*-CF_3CFOO conformer. All POZ fragmentation mechanisms for O_3 + Alkene **11** are displayed in Figure 3.28.

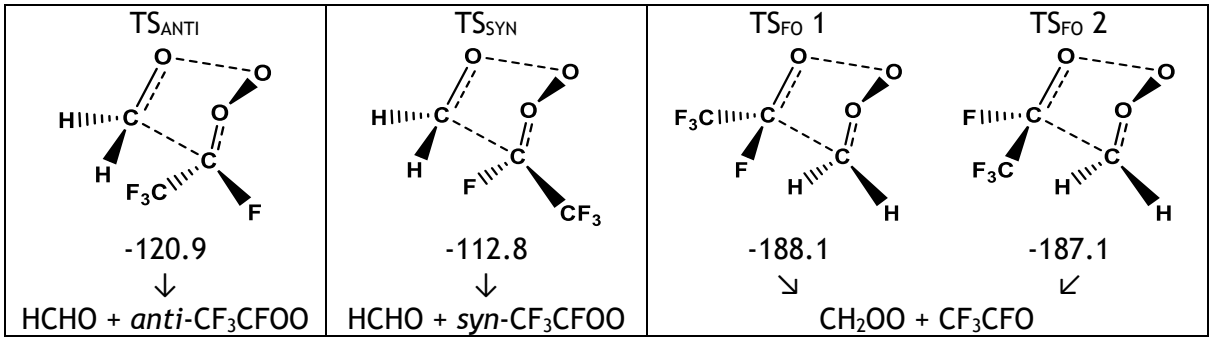

*Figure 3.28: A schematic and the relative energies (kJ mol^{-1}) of the TS_{ANTI} & TS_{SYN} structures of O_3 + alkene **11** in conjunction with the products these mechanisms generate. Energies are relative to raw reactants.*

The POZ fragmentation process of O_3 + Alkene **11**, shown in Figure 3.28, has very low barriers for generating CH_2OO + CF_3CHO (TS_{FO} 1 & 2), whereas the generation of *syn*- & *anti*-CF_3CFOO proceeds via much higher energy TS structures (TS_{ANTI} & TS_{SYN}). To the author's knowledge, the only literature comparison is the less extensive computational analysis of this reaction by Paul *et al.*, and this shows similar sized energy barriers for TS_{ANTI} (-120.5 kJ mol^{-1}) and TS_{FO} 1 (-187.8 kJ mol^{-1}) to those observed in Figure 3.28.[224] This is the largest energy variation in POZ breakdown pathways in the whole alkene ozonolysis study undertaken here, and therefore is responsible for the very large collective CH_2OO branching fraction (α_{CH_2OO} ~ 0.99). However, the Γ_{THEO} value of *anti*-CF_3CFOO (2.49×10^{-6}) still exceeds that of *syn*-CF_3CFOO (3.31×10^{-7}), despite their overall Γ_{THEO} value is $\ll$0.01.

3.7.2 Ozonolysis of Alkenes 12 ($CF_3CF_2CH{=}CH_2$)

The cycloaddition step in the ozonolysis of Alkene **12** ($CF_3CF_2CH{=}CH_2$) is much more energetically demanding than for O_3 + Alkene **2** ($EtCH{=}CH_2$), as shown by the 15.8 kJ mol^{-1} difference in barrier heights for TS_{OZO} 1 (see Figure 3.29). This leads to a much lower ozonolysis k_{ME} value for Alkene **12** (2.99×10^{-20} cm^3 s^{-1}) than Alkene **2** (1.03×10^{-16} cm^3 s^{-1}) and that low k_{ME} value is within an order of magnitude to the literature k_{EXP} value (2.0 - 2.34×10^{-19} cm^3 s^{-1}).[357,358] This demonstrates that the replacement of the α-H atoms in the —Et substituent with α-F atoms does reduce the reactivity of the alkene. This observation could not wholly be vindicated using just the O_3 + Alkene **11** reaction, as the —F substituent in the —R_2 position likely also has a further reductive impact on the reactivity of the >C=C< bond. The substitution of the —Et substituent with a —CF_2CF_3 group also replaces the β-H atoms with β-F atoms, however the effect of a decline β-H atoms on ozonolysis chemistry is explored in Chapter 6 instead.

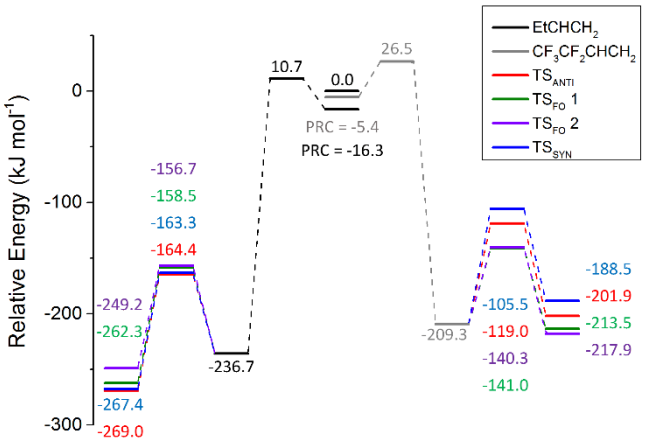

*Figure 3.29: A comparative of the O_3 + Alkenes **2** and **12** PESs using the lowest energy barriers for each channel only. Energies are relative to raw reactants.*

The decline in the number of α-H atoms between O_3 + Alkenes **2** & **12** appears to result in an increase in the energy barrier for each POZ fragmentation mechanism. However, as shown in Figure 3.29, the TS_{ANTI} & TS_{SYN} barriers for O_3 + Alkene **12**, see much greater increases than those of TS_{FO} 1 & TS_{FO} 2 barriers, resulting in a much larger collective α_{CH_2OO} value (0.955) than observed for O_3 + Alkene **2** (0.373). This indicates that replacing the α-H atoms with α-F atoms in the R_1 substituent (and perhaps ß-H atoms with ß-F atoms) marginalises the formation of the CI with that substituent. As the α_{CH_2OO} value for O_3 + Alkene **12** is not as large as that seen for Alkene **11** (≫0.999), this chapter also provides indirect evidence that the —F substituent in Alkene **11** ($CF_3CF{=}CH_2$) further marginalises formation of the CI with that substituent. However the only literature study found of this reaction produces a much lower collective α_{CH_2OO} value (0.261) for O_3 + Alkene **12**.[161,361,362,366]

3.7.3 Ozonolysis of Alkenes 13 (*E*-$CF_3CH{=}CHCl$) and Alkene 14 (*E*-$CF_3CH{=}CHF$)

It is quite plausible that Alkenes **13** & **14** have comparable ozonolysis chemistry, as they share two key common structural features: a —CF_3 group in the —R_1 position and a halogen (either a —Cl or an —F group) in the in the —R_4 position. This similarity is reflected by the fact that the TS_{OZO} 1 & 2 structures for O_3 + Alkene **13** have similar energies (26.2 & 28.6 kJ mol^{-1}) to that of Alkene **14** (29.9 & 29.6 kJ mol^{-1}). This leads to O_3 + Alkene **13** having only a marginally larger k_{ME} value (1.85×10^{-20} cm^3 s^{-1}) than O_3 + Alkene **14** (8.1×10^{-21} cm^3 s^{-1}). These results confirm that an —F group have a greater reductive impact on the >C=C< bond than the —Cl group. Both the k_{ME} values for O_3 + Alkenes **13** & **14** are close to or within an order of magnitude of their k_{EXP} values (1.46 & 2.81×10^{-21} cm^3 s^{-1}).

The POZ fragmentation pathways of O_3 reactions with Alkene **13** & **14** only produce CI products with either a —CF_3 or a halogen substituent and the TSs are labelled accordingly: TS_{ANTI} 1 and TS_{SYN} 1 produce *anti*- & *syn*-CF_3CHOO and TS_{ANTI} 2 & TS_{SYN} 2 produce *anti* & *syn* conformers of either ClCHOO or FCHOO. In the structure of both Alkenes **11** & **12**, only one end of the alkene >C=C< bond includes halogen and/or haloalkyl substituent(s) and as these deactivating groups hinder CI formation the Γ_{THEO} distribution is imbalanced in favour of CH_2OO. However, as the chemical sequencing of Alkene **13** places a deactivating group at either end of the >C=C< bond, all the POZ fragmentation barriers have comparable energies (-148.1 to -136.4 kJ mol^{-1}) and a wide distribution of CI products is generated. O_3 + Alkene **14** also has a similar wide Γ_{THEO} distribution and for the same reasons.

While the theoretical analysis of O_3 + Alkenes **11** & **12**, discussed previously, established that formation of a CI with a —CF_3 (and —CF_2CF_3) substituent were disfavoured compared to those with —H substituents, the analysis of O_3 + Alkenes **13** shows high overall α_{CF_3CHOO} value (0.728). This is a similar α_{CF_3CHOO} value to that found in the experimental literature (0.63) for O_3 + Alkene **13**, but due to the nature of the experimental method a slight Γ_{THEO} preference found for *anti*-CF_3CHOO (0.415) over the *syn* conformer (0.312), seen in this chapter has yet to be experimentally validated.[367] The much lower Γ_{THEO} values for *anti*- & *syn*-ClCHOO (0.188 & 0.085) clearly show that the —CF_3 group is much less of a hindrance to CI formation than a —Cl substituent. The O_3 + alkenes **14** reaction exacerbates this Γ_{THEO} preference for *anti*-& *syn*-CF_3CHOO (0.473 & 0.450), as the new —F substituent appears to diminish the Γ_{THEO} distribution for *anti*-& *syn*-FCHOO (0.050 & 0.027).

3.7.3 Summary of the ozonolysis of HFOs

In summary, there are several trends that are worth observing including that the addition of haloalkyl groups (such as —CF_3 & —CF_2CF_3) and halogen substituents (such as —F or —Cl) to the >C=C< group reduces the alkene ozonolysis k_{ME} value. Furthermore, during POZ fragmentation, CI formation with the haloalkyl substituents, such as —CF_3 & —CF_2CF_3, are diminished compared to purely alkyl substituents, including —CH_3 & —Et. Both these observations agree with one of the central hypotheses in this chapter, that α-H atoms in an alkyl substituent, increase the k_{ME} values and induces a formation preference for CIs with that substituent. This is especially the case if the alkyl substituent, like —Et, is compared to electron withdrawing groups, such as —$C(O)CH_3$ or —CF_2CF_3. This section also shows that overall CI preferences for POZ fragmentation Γ_{THEO} values is CF_3CHOO > ClCHOO > FCHOO, with the usual preference for *anti*-CIs over *syn*-CIs being maintained.

3.8 Atmospheric implications

The research in this chapter has wide tropospheric implications because these O_3 + alkene reactions are attributed with depleting both O_3, which triggers severe respiratory problems, and many prevalent alkenes, such as Alkenes **1** & **5**, in both rural and urban environments (see Propene and MVK concentrations in Figure 3.30). Experimental approaches to determining the ozonolysis chemistry of these tropospheric alkenes has several key hazards & problems including that: ozone is explosive in high concentrations; the exothermicity of the reaction can cause instantaneous decay of the initially formed CIs; and the formaldehyde and other carbonyl products are known to be a skin irritant, carcinogenic and toxic if inhaled.[373,374] A computational approach is therefore quite a suitable cost-effective and low hazard alternative method to determine the ozonolysis chemistry of a variety of tropospheric alkenes.

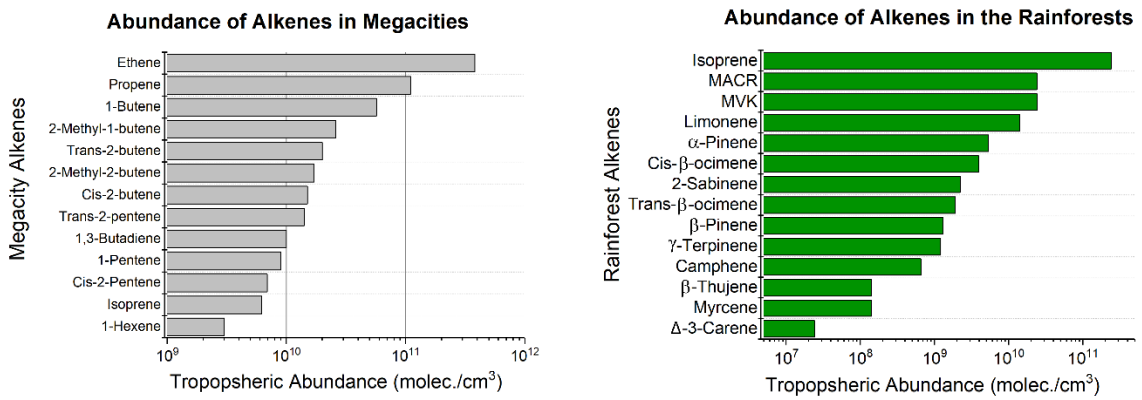

Figure 3.30: Abundance of Different Gaseous Alkenes in Megacities and Rainforests (data obtained from that assembled by Vereecken et al.).[182]

Understanding the ozonolysis chemistry of these alkenes is also vital to atmospheric models because these reactions produce significant primary yields of stabilised CIs and secondary yields of OH radicals, implicated in depleting tropospheric toxins. The experimental data on CI branching fractions in the literature uses the aldehyde or ketone co-product yields to determine the CIs, which has become an important route to confirming the accuracy of the calculations in this chapter. However, the inherent weaknesses of these experimental methods include that these co-product yields cannot distinguish between the *syn*- and *anti*-CI or between hot CIs or stabilised CI yields, both essential to understand the subsequent atmospheric implications of such a reaction. Where experiments are too challenging at present, computational methods such as those used here can determine the yield of excited CIs, including the difference between *syn*- and *anti*- conformers. Stabilisation of these CIs can be predicted based on total system pressure, internal energy during formation and geometric size (which can support stabilising IVR). Computed OH yields can then be added to atmospheric models,

potentially both local and global, which can be used to assist in subsequent determination of various atmospherically important outcomes, e.g. OH co-product yields.

One of the most important ozonolysis reactions in this study comes from predominantly biogenically emitted alkenes such as Alkene **5**, methyl vinyl ketone (MVK). Alkene **5** is a product of the ozonolysis of isoprene and therefore being able to model its ozonolysis rates is important as isoprene accounts for ~80% of VOC emissions.[21,81,339,375] 10% of tropospheric isoprene undergoes by ozonolysis, producing significant levels of both Alkene **5** (10-18%) and methacrolein (MACR, 28-44%).[81,339,355] Alkene **5** has also been shown to have strong abundances in rural environments, including rain and temperate forests and it has been determined by Vereecken *et al.* to therefore be generating a significant portion of the CI in such locations.[182] The O_3 + Alkene **5** (6.9×10^{-17} cm^3 s^{-1}) was found to have a fairly average ozonolysis k_{ME} value compared to that of the other mono-substituted alkenes calculated in this chapter, Alkenes **1**—**4** (~2.2—10.3×10^{-17} cm^3 s^{-1}).

In addition to the above tropospheric implications, MVK reactions are also responsible for ~10% of CI generation in temperate forests (see Figure 3.31). The CH_2OO branching fraction is undeniably dominant in both the theoretical work in this chapter (0.934) and the experimental literature (0.65—0.95), providing a substantial source for CH_2OO in atmospheric models.[10,355] Also, as the literature Γ_{EXP} values for *anti*- & *syn*-$CH_3C(O)CHOO$ have yet to be measured for O_3 + Alkene **5**, these consistent Γ_{THEO} values, generated for the CIs in this chapter, can be used to determine the relative atmospheric significance of these product CIs. Due to the sizeable yields of methyl vinyl ketone oxide and methacrolein oxide found for O_3 + isoprene, much computational and theoretical analysis has been compiled to study the chemistry of such CIs (including by the author in chapter 4).[375–378] Using the data obtained from the research in this chapter it may be that atmospheric models determine a significant role for *anti*- & *syn*-$CH_3C(O)CHOO$ leading to a greater computational and theoretical body of work. A Vereecken *et al.* study suggests ~2% of CIs in temperate forests are $CH_3C(O)CHOO$ conformers.[182] These new computational studies could include unimolecular decomposition of (both hot and stabilised) CIs and bimolecular reactions with species know to react strongly with sCIs, such as H_2O, $(H_2O)_2$ and alcohols.[93,195,293,376,377,379]

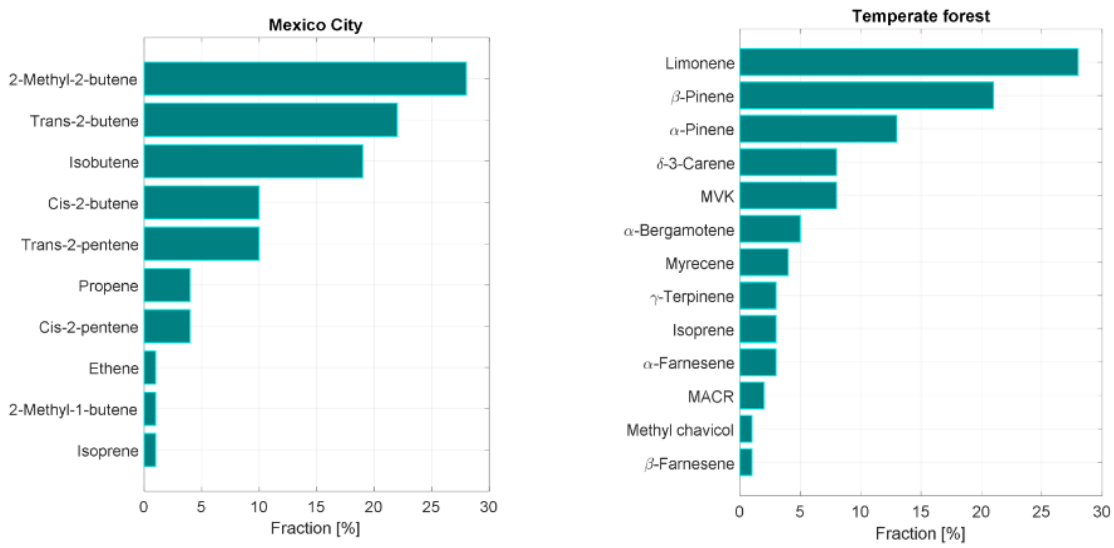

Figure 3.31: Fractional CI population by Alkene Source in both an Example Megacity, Mexico City and a Temperate Forest (diagram obtained from that assembled by Vereecken et al.).[182]

This research is also important with respect to atmospheric models because it can supply a k_{ME} value for the O_3 reaction with Alkene **8**, (2.46×10^{-18} cm^3 s^{-1}), where the literature does not provide a k_{EXP} value,[10] or alternatively provide POZ fragmentation yields of O_3 + Alkene **7**, where the branching fractions of $(CH_3)_2COO$ (0.868), *anti*- (0.117) and *syn*-iPrCHOO (0.014) are unknown.[10] Both these important observations can be added directly to the data sets for atmospheric models if required. These computational values of O_3 + Alkenes **7** & **8** in this chapter are, as explained in previous sections, important to atmospheric models overall because they provide valuable data points in describing ozonolysis chemistry trends between Alkenes **6**—**10** that currently can only be inferred from the literature. Knowledge of these trends is important if an overall taxonomic model is to be produced that is both reliable and cost-effective.

According to a study by Vereecken *et al.*, in megacities like Mexico City, Alkenes **15** & **16** (*E*- & *Z*-2-pentene) have significant abundance and their reactions with O_3 give significant CI yields (see Figure 3.31).[182] However, to the author's knowledge no literature Γ_{EXP} values for O_3 + Alkenes **15** & **16** have been measured, so the Γ_{THEO} values for CI yields provide important data sets for atmospheric models of megacities.[10] In experimental analysis of O_3 reactions with other urban alkenes (Alkenes **1**, **6**, **17** & **18**) this differentiation between the *anti*- & *syn*-CI could be partially inferred by OH yields. However, as O_3 + Alkenes **15** & **16** produces both *syn*-CH_3CHOO and *syn*-EtCHOO, it is unclear which *syn*-CI produces a higher OH yield. As this *anti*- & *syn*-CI differentiation is included in these computational analyses for O_3 + Alkenes **15** & **16**, the author also determines whether *syn*-CH_3CHOO or *syn*-EtCHOO have greater yields. Furthermore, this differentiation between *anti*- & *syn*-CIs supplied in the computational analyses for O_3 reactions with Alkenes **1**, **6**, **15**—**19** is vital

because urban environments have a variety of different pollutants and *anti*- & *syn*-CIs can deplete such pollutants at very different speeds.[182]

When investigating HFOs, it must be considered that the USA, China and the EU have plans to increase HFO (Alkenes **11**—**14**) use as refrigerants and insulation foam so their emissions and their breakdown mechanisms, including via reaction with O_3, have become of greater interest in the literature.[197,198,224,226,347] Preliminary studies show that, as HFOs breakdown via other mechanisms, the O_3 concentrations in the region increase, making these ozonolysis reaction more likely.[199] This study is important to atmospheric models as the current literature computational studies on HFO derived systems are much less extensive and the experimental analysis of such reactions (except for O_3 + Alkene **12**) do not supply CI yields.[10,224,226,241,357] Whilst the k_{ME} values for O_3 + HFO are somewhat lower than those of the other alkenes in this study, yields of "HFO-sCIs" (*anti* & *syn* conformers of ClCHOO, FCHOO & CF_3CHOO) are quite significant. The atmospheric implications of this CI yield is likely to be the greater depletion of many pollutants because, as shown in Section 4.4 and Chapter 5 (as well as previous computational studies), these HFO-sCIs have high bimolecular reactivity.[93,273,372]

Lastly, one very important atmospheric implication is the many observations made in this thesis about how the structure of an alkene affects ozonolysis chemistry, for example the manner and magnitude with which steric hinderance alters branching fractions and reactions rates (by altering transition state energies). The careful notation of how different structural features increase or reduce reactivity helped the author with building the "Free Energy-Structural Projection" model in Chapter 6, which is used to determine the ozonolysis chemistry of larger alkenes. This model significantly reduces the number of calculations required to produce extensive potential energy surfaces and provides accurate descriptions of the ozonolysis chemistry. If they were to provide an accurate set of alkene taxonomic groups, further models of alkene ozonolysis chemistry built either by the author or other computational chemists. These could include: the reducing impact of haloalkyl groups on rate constants, the beneficial effect of substituent α-H atoms (such as in —CH_3 groups) have on CI formation and that enones have very little capacity to generate epoxide yields (compared to dienes for example).[121,342] Once the ozonolysis of alkene model(s) are built there would be a significant reduction of computational power required to process atmospheric simulations, or alternatively with similar computational cost chemical accuracy could be greatly increased.

3.9 Further Study

This ozonolysis study included 20 alkenes which is a particularly large number for the full computational analyses, however, the study could be extended into many different alkenes, essentially *ad infinitum*. Below are assembled groups of further work divided into categories that may be appropriate to follow:

Examination of the effect that decreasing the number of *β*-H atoms on the $-R_1$ substituent (similar to the reduction in the number of α-H atoms examined in this chapter) has on ozonolysis chemistry. This is already pursued in Chapter 6. This involved lengthening $-R_1$ group from an —Et group in *cis*-2-pentene to an —nPr group in *cis*-2-hexene and, using the "Free Energy-Structural Projection" (FESP) model derived in chapter 6, but could be further extended to include 1-pentene, 4-methyl-1-pentene and 4,4-dimethyl-1-pentene. Further research and adaption of the FESP model seen in Chapter 6 could be expanded to include complex $-R_1$ substituents such as a *sec*-butyl or *neo*-pentyl groups. This would develop of substantial new structure-activity relationship (SAR) model, but one that could also determine CI branching fractions.[118]

Secondly, further extension of this study could investigate the effect of substitution of the $-R_2$ substituent (seen for Alkene **20**), including alkenes where R_1=R_2 and R_3=R_4. Examples of this could include $tBu_2C{=}CH_2$ or $tBu_2C{=}C(CH_3)_2$.

Another area of study could include substitution of the $-R_1$ group with other common functional groups to determine their impact on CI formation, such as esters, ketones or other alkene groups. This has already been conducted to some extent with the use of enones, Alkenes **5** and **10**, and HFOs, Alkenes **11**—**14**. Despite this, there are other groups that could be used in the $-R_1$ group, such as aldehydes, which may produce significant differences to their ketone equivalents. Out of possible aldehydes, it is especially important to analyse the ozonolysis of methacrolein, $OHC{-}C(CH_3){=}CH_2$, as it is a significant co-product of isoprene reacting with OH or O_3 and therefore found in many temperate forests and rainforests.[21,182,380] If either aldehydes or dienes were studied, exploration of the epoxide pathway would need to be applied to at least an example alkene each, such as the abundant methacrolein and isoprene compounds. This would need to include an application of a different theoretical method to determine epoxide energies (see appendix for more details).

Cyclic alkenes such as cyclohexene, α-pinene and as well as heteroatomic cyclic alkenes such as furans, thiophenes and pyrroles are all viable targets and may undertake novel ozonolysis pathways worthy of study. As an example, the ozonolysis reaction produces CI

that does not detach fully from the aldehyde or ketone co-product, meaning they may subsequently self-react.[158,381,382] This would require a different method of study to have a full view of the ozonolysis of these cyclic alkenes.

Other pathways of future study include examining the outcomes of the CIs produced from these reactions such as those seen in Chapter 4, in examining sCI + alcohol reactions and Chapter 5, HFO-derived sCIs bimolecular reactions.

3.10 Conclusion

The large number of substituent α-H atoms in the trisubstituted Alkenes **6**—**9** induce greater ozonolysis k_{THEO} values (~10^{-15} cm^3 s^{-1}) than observed for Alkenes **1**—**4** (~10^{-17} cm^3 s^{-1}), which have fewer substituent α-H atoms. This difference in ozonolysis chemistry between these *monosubstituted* and *trisubstituted* sets of alkenes could be the basis of two different taxonomic groupings. The concept of this *monosubstituted* taxonomic group is reinforced by the fact that O_3 + Alkenes **1**—**4** all show a relatively balanced distribution between its CI products: CH_2OO and *anti*-/*syn*-R_1CHOO (R_1 = —CH_3, —Et, —iPr & —tBu). In contrast, the number of hyperconjugated α-H atoms in alkene ozonolysis product $(CH_3)_2COO$ skews the product distribution in its favour, across all Alkenes **6**—**9** ozonolysis, further supporting the concept of creating a *trisubstituted* taxonomic alkene group.

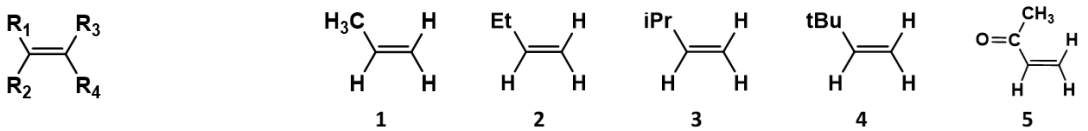

*Figure 3.32: The Spatial Arrangement of Each R group on a Standard Alkene and Structures of Alkenes **1**—**5***

These taxonomic groupings may be made somewhat more flexible if it is deemed important to accommodate more subtle changes such as increasing the number of α-H atoms even further, e.g. moving from —CH_3 sCI substituents to —iPr or —tBu. As α-H atoms are known to increase ozonolysis reactivity and cause changes in CI yields (CH_3CHOO > EtCHOO > iPrCHOO > tBuCHOO), such nuances may be important to incorporate into any classification system where a wide range of alkenes are under consideration.

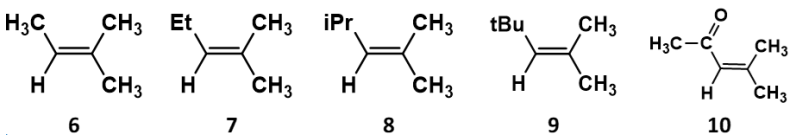

*Figure 3.33: Chemical Structures of Alkenes **6**-**10***

E- & *Z*-alkenes may also form two separate taxonomic groups, despite having similar k_{THEO} values, because the ozonolysis of *Z*-alkenes produces higher Γ_{THEO} values for *anti*-CIs than *syn*-CIs, whereas the *anti*- & *syn*-CI yields for O_3 + *E*-alkenes are more even.

While all alkenes with electron-withdrawing substituents have low k_{THEO} values, they could be generically grouped into two sets: Alkenes **5** & **10**—**12**, where the electron-withdrawing substituents in the adjacent —R_1 and/or —R_2 positions, inducing low Γ_{THEO} values for R_1CR_2OO formation; and Alkenes **13** & **14**, where the opposite position of the electron-withdrawing —R_1 and —R_4 substituents, produces a more even distribution between R_1CHOO & R_3CHOO.

These possible frameworks could be used to produce a comprehensive method for tropospheric models, where the depletion of toxic ozone via reaction with an alkene could be estimated using only the structural features of alkenes.[2,19,20] Furthermore, this all-inclusive method could use alkene structure to project the yields of the different CI products, to reduced computational cost of calculating a large variety of different reactions. One narrow example of such a method is the "FESP" models in Chapter 6, where this electronic and steric taxonomic framework allows previously calculated alkene ozonolysis trends to be projected onto lengthier alkenes (e.g. *Z*-2-hexene) in an accurate and reliable way. Moreover, as these CIs are known to deplete various pollutants at different rates, by accurate modelling CI yields by chemical composition and conformeric form, the depletion of pollutants can also be more accurately estimated.[111] In conclusion, if this electronic and steric taxonomic framework is used in combination with both k_{THEO} and Γ_{THEO} values, an extended and systematic way of determining the ozonolysis chemistry of multi-alkene environments could be devised.

4.0 Chapter 4: An Extended Computational Study of Criegee Intermediate–Alcohol Reactions

The aim of this chapter is to undertake an extended computational analysis of the reactions between tropospheric alcohols and various stabilised Criegee intermediates (sCIs). Both the sCI and alcohol reactants in this study are varied to investigate their effect on reactivity by examining bimolecular rate constants (k_{TST}) and product branching ratios (Γ_{THEO}). Three of the most abundant tropospheric alcohols, methanol, ethanol and isopropanol, are included in this study. The specific sCIs explored in this study are afford interrogation of how the orientation and chemical composition of the CI substituent groups alter their reactivity. This study could contribute directly to atmospheric models, or be combined with other bimolecular sCI reaction analyses to help produce a taxonomic classification system for sCIs. If sCI taxonomic groups can be generated for both unimolecular and bimolecular reactions then they could then be applied to atmospheric models to reduce computational cost. This study also analyses the unimolecular breakdown of various sCIs to produce vinyl hydroperoxides (VHPs).

4.1 Introduction:

4.1.1 The Importance of Stabilised Criegee intermediates (sCIs) Reactions with Tropospheric Alcohols

The stabilised Criegee intermediates (sCIs) analysed in this study are produced from tropospheric alkenes, introduced in section 1.4.2 and explored in a theoretical study Chapter 3.[81,339] The O_3 + tropospheric alkene gaseous reaction is not just a significant alkene sink, (like precipitation, UV photolysis and OH & NO_3 radicals) but also acts as a significant source of Criegee intermediates (CIs). Ozonolysis of alkenes, as the mechanism in Figure 4.1 shows, produces a short-lived primary ozonide (POZ), which subsequently breaks down to produce "excited" Criegee intermediates, which have high amounts of internal energy. [123,126-135] These CIs and sCIs can then undergo unimolecular decomposition, examined further in section 1.5.2. One pathway of particular interest is the *1,4-alkyl-H-migration* decomposition pathway to produce vinyl hydroperoxide (Section 3.5).[182] Once these CIs are stabilised by collision with inert molecules, they are more likely to be removed by reactions with other trace atmospheric species such as alcohols.[123,126,132,134,135]

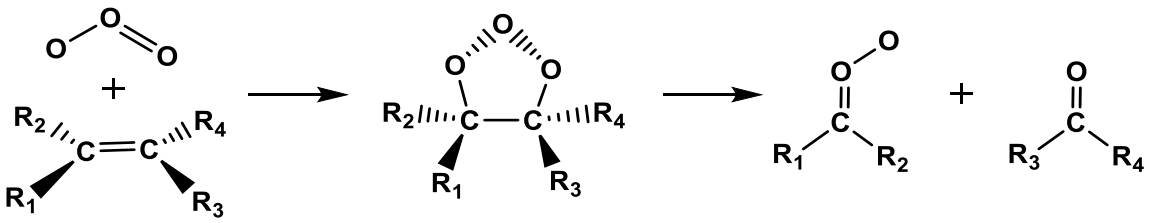

Figure 4.1: The source of atmospheric stabilised Criegee intermediates (sCIs).

sCI + alcohol reactions are worthy of examination because they are not only a potentially significant sink for alcohols but are postulated to be a significant source of α-alkyloxyalkyl hydroperoxide, AAAH.[51] Khan *et al.* identified that Methanol (CH_3OH) and Ethanol (EtOH) reactions with the smallest sCI, CH_2OO, are competitive with OH radicals, the well established "atmospheric detergent".[111] The tropospheric OH abundance ([OH]~10^6 molec. cm^{-3}) is higher than the sCI abundance ([CH_2OO]~10^4 molec. cm^{-3}) but both reactions with the tropospheric alcohols Methanol (CH_3OH) and Ethanol (EtOH) have proximate experimental rate constants (k_{EXP} ~10^{-13} — 10^{-12} cm^3 molec.$^{-1}$ s^{-1}).[111] sCIs may outcompete OH radicals as a sink for other atmospheric co-reactants, such as NO_2, aldehydes, ketones and organic & inorganic acids, but this does not reduce the importance of the sCI + alcohol reaction. This make sCIs very feasible sinks for gaseous alcohols in many different environments and gives the sCI + alcohol reaction increased importance in atmospheric models.

To determine the significance of sCI + alcohol reactions, the co-location of tropospheric sCIs, or their alkene precursors, and alcohols is important to identify. In environments with high alcohol concentrations, these reactions may be a significant sink for both alcohols and sCIs. One known area of high alcohol concentrations is in urban areas that have high biofuel use, such as Sao Paulo, Brazil.[383] The ethanol (EtOH) abundance has been known to reach 400 ppbv in various certain localised areas of Brazillian cities, such as São Paulo, Rio de Janeiro and Porto Allegro, or in excess of 450 ppbv, where industrial and urban emissions mix. While ethanol is the largest contribution to *overall* alcohol abundance in Sao Paulo ([EtOH] ~ 176.3 ppbv), there is still a significant abundance of both methanol and isopropanol ([MeOH] ~ 34.1 ppbv and [iPrOH] ~ 44.2 ppbv).[383] Therefore, all three of these alcohols are important to analyse and are consequentially included in this study.

In Sao Paulo, anthropogenic alkenes have also been found in abundance with ethene (~12.2 ppbv) and propene (~2.77 ppbv) having the greatest contribution to the overall alkene abundance (~24.6 ppbv).[384] Also important is the large abundance of tropospheric O_3 (~160 μg m^{-3}) in Sao Paulo, a significant problem for the city's public health.[384] The

considerable amount of CI precursors and alcohol in the local tropospheric environment of Sao Paulo region makes the sCI + alcohol reaction of increased interest. Also, the city of Sao Paulo has a population of 11 million people and over 20 million in the total metropolitan zone, and if this reaction reduces or indeed generates substances harmful to human health it is of significant impact to the local environment.

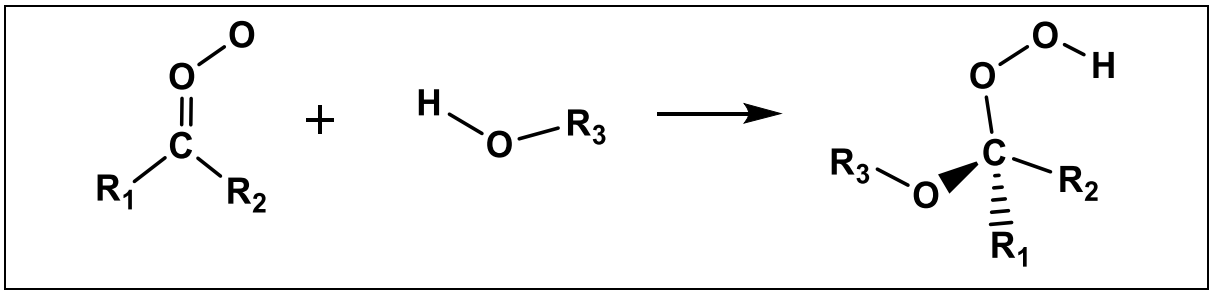

Figure 4.2: Formation of AAAHs from the sCI + alcohol reaction

The sCI + alcohol reaction has been previously investigated but this research provides a more extensive computational analysis of a series of these reactions. As shown in Figure 4.2, the reaction mainly leads to the formation of α-alkyloxyalkyl hydroperoxide, AAAH. This was first demonstrated in 1996 with the experimental analysis of CH_2OO + MeOH reaction by Moorgat and co-workers, who synthesised the AAAH, methoxymethyl hydroperoxide, using methanol and the tropospheric sCI precursors ethene and O_3.[385] This was performed via indirect methods of measuring rate constants, as sCIs had yet to be spectroscopically identified.[144] A study by McGillen *et al.* identified that the alcohol reaction with at least two sCIs, CH_2OO and $(CH_3)_2COO$, have k_{EXP} values of sufficient size and variation (~10^{-14} — 10^{-12} cm^3 s^{-1}) to warrant an extended analysis.

The prior literature in this area has already identified some important trends in reactivity, such as that variation of the alcohol (MeOH, EtOH and iPrOH) in the reaction with CH_2OO shows only small variation in k_{EXP} (~10^{-13} cm^3 s^{-1}). [344] Similarly, changing the alcohol causes only a small change in k_{EXP} in reactions of MeOH & iPrOH with tridecanal oxide which also exhibit very similar k_{EXP} values.[386] Studies by Anglada *et al.* show that both H_2O & $(H_2O)_2$ can catalyse the production of VHP from sCI decomposition. A similar pathway is found for sCI + alcohol reactions, both in this thesis (see appendix) and by Chao *et al.*, whereby alcohols can catalyse the decomposition of sCIs that have a *syn*-CH_3 group to produce VHPs.[194] A full visual representation of both the AAAH and VHP reaction pathways is displayed in Figure 4.5, in Section 4.2.2.

However, sCI + alcohol reactions are not merely a significant sink for tropospheric alcohols, but also are a significant source of AAAH in many different environments, such as the rainforests.[111] The bimolecular reactivity has been shown to be significant as the

reactions between sCIs and H_2O & $(H_2O)_2$ are significant sources of σ-hydroxy-hydroperoxide, which is directly involved in forest damage.[141,195,293,387-391] As this AAAH product is also a peroxide, it could also potentially cause this kind of boreal damage.[344]

AAAH breakdown is a long-term decomposition unlike the unimolecular decomposition of sCIs, which produce OH radicals much more swiftly. The Tadayon *et al.* study showed how high the barrier is to OH dissociation and a similar high barrier to thermal decomposition to produce H_2O + an ester.[344] Much like AAAH, the VHP product has also been shown to produce OH during decomposition.[185,392-396] These AAAH and VHP decomposition pathways constitute a primary reason for this study.[10] The VHP channel derived from sCIs + H_2O & $(H_2O)_2$ reactions requires the treatment of quantum tunnelling to account for the full VHP yields, therefore this treatment is included here. A comparison of the k_{UNI} of various sCIs with both simple and more complex methods of calculating tunnelling factors is carried out in section 3.5.

4.1.2 The sCI and alcohols Involved in this Study

The standard computational procedure in identifying the reaction potential energy surface (PES), the Eckart tunnelling-correction, collision limits (k_{COLL}) and dipole-capture moment limits ($k_{d\text{-}d}$) of each reaction is outlined in method section.[286,294,300,309,314,315,318,320,397,398] This study, unlike the previous study of alkene ozonolysis in Chapter 3, determines rate constants (k_{TST}) by using the open source software named the Kinetic and Statistical Thermodynamical Package (KiSThelP) as opposed to the Master Equation Solver for Multi-Energy Well Reactions (MESMER).[318,329] The method for KiSThelP can be found in Method Section 2.4. Unlike content in chapters 3, 5 & 6, rate constants are calculated using conventional transition state theory (k_{TST}) at standard temperature and pressure unless stated otherwise.

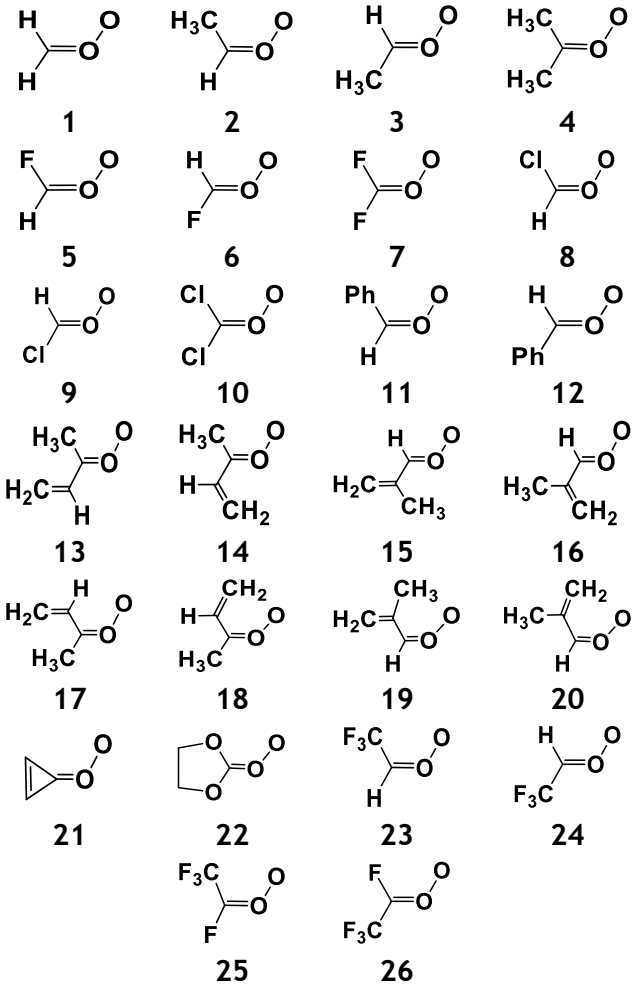

*Figure 4.3: sCIs studied labelled as **sCIs 1-26***

sCIs 1—26, displayed in Figure 4.3, are investigated in this study to observe the reactivity of sCIs with atmospheric alcohol, MeOH. Other tropospheric alcohols, EtOH and iPrOH, are investigated for their reactions with **sCIs 1**, **11** & **12**. These sCIs have different sources: **sCIs 1—4** are derived from the simplest atmospheric alkene, such as ethene, propene and

butene, which can be common in rural environments, but are quite abundant in urban anthropogenic VOC emissions.[399] Halogenated **sCIs 5—10** & **23—26** are the product of the ozonolysis of a new generation of hydrofluoroolefin refrigerants, such as CF_3CFCH_2, *E*-$CF_3CH{=}CHCl$ & *E*-$CF_3CH{=}CHF$. The study of the halogenated sCIs, *syn*-/*anti*-FCHOO, *syn*-/*anti*-ClCHOO, CF_2OO and CCl_2OO, labelled as **sCIs 5—10**, are studied to see the effect of strong electronegative substituent groups. Further analysis of HFOs and their ozonolysis is found in Section 3.7. Folic emissions are a major source of conjugated sCIs, such as **sCIs 11** & **12** (*syn*-/*anti*-PhCHOO), which are generated from the ozonolysis of styrene ($PhCH{=}CH_2$).[400] Isoprene, is the most globally abundant alkene and is the source of conjugated **sCIs 13—20**.[22] **sCIs 13—20** are produced in significant yields so are therefore quite common in the forested, pristine environments, where isoprene is emitted.

sCI 21, cyclopropenone oxide, is also included in this study to observe what effect sCI internal steric tension has on reactivity. The non-halogenated cyclic 1,3-dioxolane-2-carbonyl oxide (**sCI 22**) is studied because it has both cyclic strain and has a strong electronegative group. Both **sCIs 21** & **22** are examined for computational reasons, as they are not naturally occurring sCIs. Although not in the original study, the MeOH reactions with *syn*- & *anti*-CF_3CHOO and *syn*- & *anti*-CF_3CFOO were undertaken in section 5.7.2 in the study of heteroatom tuning in HFO-sCIs and these results have been detailed. These sCIs are referred to as **sCIs 23—26**.

4.2 Reactions of sCI + Alcohol: An Overview

4.2.1 Overview of the sCI 1 + MeOH Reactions

CH_2OO, referred to as **sCI 1** in this study, is chosen for investigation because it is simple, abundant in the troposphere and has been extensively studied in the literature. **sCI 1** has previously been studied in part because of this chemical simplicity but also because it is suitable to produce and measure experimentally. **sCI 1** has also been extensively used as an archetype sCI, for example in examining the effectiveness of **sCI 1** as a tropospheric sink for CO_2, hydrochlorofluorocarbons (HCFCs) and alkanes.[273,274,372] Lastly, **sCI 1** is commonly examined because its abundance in the atmosphere makes it important to tropospheric modelling. The **sCI 1** + MeOH reaction is studied in greater detail than the other sCIs in this chapter. This includes: a comparison of different computational methods to calculate the PES of **sCI 1** + MeOH; and modelling the decomposition of the α-alkyloxyalkyl hydroperoxide (AAAH) product decomposition. Much like analysis seen later for reactions including MeOH reactions with **sCIs 2**, **3** & **4**, a comparison of the theoretical rate constant (k_{THEO}) with literature k_{EXP} values is also performed. This extensive analysis

of the **sCI 1** + MeOH reaction is for the purposes of validating the computational method used throughout this thesis.

sCI 1 treated as an archetype here too, because it has an advantage over many other sCIs in that a significant amount of experimental data already present in the literature for not just MeOH, but also reactions with the other two alcohols studied in this chapter: EtOH & iPrOH.[51,344] Other sCIs in this study do have experimental analyses in the literature, but they are either restricted to reactions only with methanol, such as **sCI 2**, **3** and **4**, or are too complex to run computationally in this study, such as $CH_3(CH_2)_{11}CHOO$ + MeOH & iPrOH.[51,386,401,402] For the reasons previously listed, determining the k_{TST} values for alcohol reactions with **sCI 1** are an appropriate case study to determine whether the method employed in this thesis is accurate and whether changing the alcohol $-R_3$ group impacts the reaction chemistry. **sCI 1** + EtOH & iPrOH reactions are analysed in section 4.2.4.

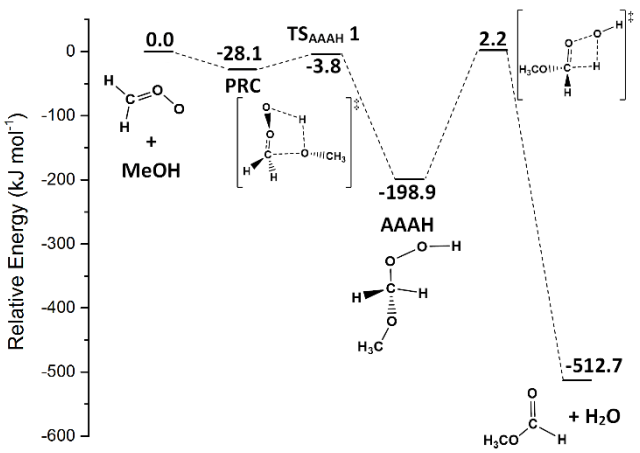

*Figure 4.4: PES of **sCI 1** + MeOH including AAAH decomposition, derived using computational method: DF-HF/DF-LCCSD(T)-F12/aug-cc-pVTZ //B3LYP/aug-cc-pVTZ. Energies are relative to raw reactants.*

Figure 4.4 displays the lowest energy pathway PES of the **sCI 1** + MeOH reaction, including both the AAAH formation (TS_{AAAH}) and an AAAH decomposition pathway (TS_{ESTER}). The TS_{AAAH} step is divided into two pathways, the low energy TS_{AAAH} 1 mechanism (-3.81 kJ mol^{-1}), which is submerged here compared to the raw reactants, and the higher energy TS_{AAAH} 2, which is positive going (+0.11 kJ mol^{-1}) compared to the raw reactants. These two barriers are dependent on the relative position of the CH_3 branch on MeOH, described further in Figure 4.5 in section 4.2.2. The **sCI 1** + MeOH reaction does not produce a VHP side channel (TS_{VHP}) and therefore the TS_{AAAH} step has no competing side reactions.

The conventional transition state theory k_{TST} (298 K) value for the **sCI 1** + MeOH reaction, 1.17×10^{-14} cm^3 s^{-1}, is lower than the literature experimental rates seen by Tadayon *et al.* (k_{EXP} [295 K, 90 Torr] = 1.4×10^{-13} cm^3 s^{-1}) and McGillen *et al.* (k_{EXP} [293 K, 10 Torr] = 1.04 ×

10^{-13} cm^3 s^{-1}). In this chapter, the Master Equation (k_{ME}) rate constants are used for all non-standard temperature rate constants because k_{ME} values are reliable and MESMER has a well-functioning user interface for obtaining k_{ME} values at many temperatures. Altering the computational conditions so they are in line with the experimental temperature used by McGillen *et al.* & Tadayon *et al.* (293 & 295 K), move both k_{ME} values to ~1.21 × 10^{-14} cm^3 s^{-1}. This is marginally closer to the literature experimental rates mentioned previously and the fact that the k_{ME} (293 K) calculated here is within one order of magnitude of the k_{EXP} values from the McGillen *et al.* study helps validate the computational method used in this study.

The structures, barrier heights and the k_{TST} of **sCI 1** + MeOH reaction are also calculated using *M062X/aug-cc-pVTZ* method, and compared to the standard B3LYP method used throughout this thesis. The M062X analysis of **sCI 1** + MeOH also displays one submerged TS_{AAAH} 1 (-7.34 kJ mol^{-1}) barrier and one positive TS_{AAAH} 2 (1.83 kJ mol^{-1}) barrier and the k_{TST} (4.1 × 10^{-14} cm^3 s^{-1}) was found to be similar to the k_{TST} of the B3LYP calculations. The reliability of these B3LYP calculations was also tested by comparing the rate constants and barrier heights to some computational analysis in the literature. A literature study of this reaction by Lin *et al.* produced two barriers: a lower energy TS_{AAAH} 1 barrier (-8.65 kJ mol^{-1}) and a higher energy but still submerged TS_{AAAH} 2 barrier (-4.26 kJ mol^{-1}). The k_{THEO} found was 1.42 × 10^{-13} cm^3 s^{-1}, which is only somewhat similar to those derived in this study and outside one order of magnitude of the B3LYP method.[402]

The AAAH decomposition channel, TS_{ESTER}, is explored for two reasons: to see if TS_{AAAH} is just the first part of a two-step reaction of AAAH formation and instantaneous decomposition, such as with the ozonolysis of alkenes (see Chapter 3) or the SO_2 reaction with sCIs (see Section 5.4); and to compare the calculations of the B3LYP computational method in this study with the calculations of literature work into the same reaction. The AAAH decomposition channel, TS_{ESTER}, is much higher energy (~2.2 kJ mol^{-1}) than the energy AAAH ground state energy (-198.9 kJ mol^{-1}) and creating a more stable intermediate product. A Tadayon *et al.* study of the **sCI 1** + MeOH reaction confirms this high TS_{ESTER} barrier (-0.8 kJ mol^{-1}) as well as a providing a high barrier to the unimolecular elimination of the OH to produce a methoxymethyl oxyl radical (-4.7 kJ mol^{-1}).[344] In the Tadayon *et al.* study, these high energy barriers to AAAH decomposition are also exhibited for **sCI 1** reactions with EtOH & iPrOH, for both the TS_{ESTER} barrier (-0.7 — +0.2 kJ mol^{-1}) and the OH radical escape (-5.3 — -4.1 kJ mol^{-1}).[344] This is supported by available experimental data, although somewhat minimal, showing that AAAHs are mostly broken down by further bimolecular reaction with OH radicals and they have long lifetimes (~2

days), compared to sCIs (~2 ms).[51,145,344,392-396,403] This theoretical and experimental confirmation that no instantaneous decomposition of AAAHs takes place confirms that the B3LYP method is accurate and that the AAAHs can be treated as the final product in these reactions, with further calculations of AAAH decomposition barriers not required. For the remainder of this chapter only the TS_{AAAH} and TS_{VHP} barriers will be calculated.

4.2.2 Overview of the sCI + ROH Potential Energy Surface (PES)

The sCI + alcohol reactions can have two different competing reaction pathways, as shown in Figure 4.5, but the VHP channel is only accessible to certain sCIs. In general, the sCI + alcohol reaction proceeds predominantly through a single pathway, the TS_{AAAH} channel.[51,344,401] In this case, the reactants form a pre-reaction complex (PRC), where a hydrogen bond is formed between the alcohol OH group and the terminal oxygen on the sCI. AAAH formation proceeds via the alcohol O-H bond breaking with the H atom moving towards the terminal O of the sCI, to form a new OH bond and the remaining R_3-O group forming a new bond to the central C of the sCI. This is referred to as a TS_{AAAH} barrier for the remainder of this study.

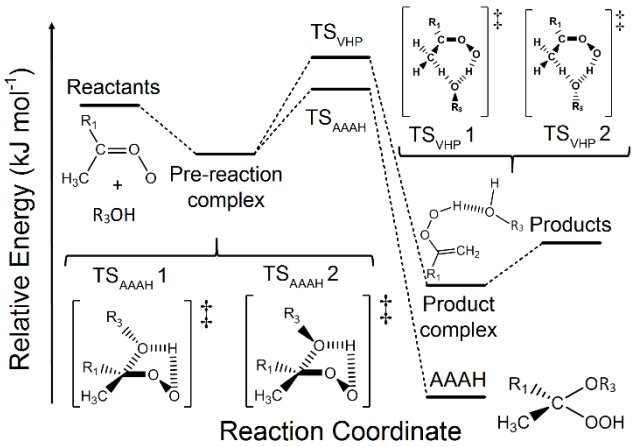

Figure 4.5: Standard PES for MeOH reactions with and sCI with a methyl group in the syn-position.

The second type of pathway identified, the VHP pathway or TS_{VHP}, proceeds via a simultaneous transfer of the H atom from the R_3O-H to the terminal O on the sCI, and the *syn*-CH_3 transfer an α-H atom to the O on the alcohol, to form the VHP. Similar to the unimolecular decomposition, referred to as the *1,4-alkyl-H-migration*, the 'catalysis' of this process by alcohol is also available in sCI reactions with formic acid, water and sulphuric acid.[182,195,293,404-407] This pathway is only accessible to sCIs, such as *syn*-CH_3CHOO, *syn*-EtCHOO and *syn*-iPrCHOO, which have at least one α-H on a *syn* substituent, facilitating the *1,4-alkyl-H-migration*. Figure 4.5 shows the reaction of an sCI with a *syn*-CH_3 group as it is the only substituent group used in this study that can access the TS_{VHP}

pathway. The sCIs analysed in this study that have access to this VHP pathway are *syn*-CH_3CHOO, $(CH_3)_2COO$, and the two distinct conformers of *syn*-$CH_3C(CH{=}CH_2)OO$.

However, the general reaction scheme is slightly more complex than these simplistic descriptions of TS_{AAAH} and TS_{VHP} because the exact energy of the transition state varies based on the O-R_3 position within the TS geometric structure. As shown in Figure 4.5, the structural changes between TS_{AAAH} 1 & 2, as well as between TS_{VHP} 1 & 2, are differentiated by the relative position of the O-R_3 branch, and this can lead to differences in barrier heights. There is increased conformational flexibility of the EtOH and iPrOH co-reactants over MeOH, particularly with respect to the alcohol's H-O-C-C dihedral angle. By altering that dihedral angle, numerous additional TSs can emerge from TS_{AAAH} 1 & 2 and TS_{VHP} 1 & 2. These additional TSs are referred to as *subchannels* in this study and they are labelled depending on which channel they originate from (e.g. **sCI 1** + MeOH produces 1 × TS_{AAAH} 1 channel but due to conformeric rotation **sCI 1** + EtOH produces 3 × TS_{AAAH} 1: TS_{AAAH} 1.1, TS_{AAAH} 1.2 and TS_{AAAH} 1.3). The differences in the height of the energy barrier between different TS conformers is largely due to changes in the degree of steric hinderance in the TS structures. The EtOH or iPrOH reactions with **sCIs 2**, **4**, **13** or **14** likely produces similarly complex potential energy surfaces, however no direct evidence for this is generated here, as only MeOH is investigated with **sCIs 2**, **4**, **13** or **14**.

Reaction data between MeOH and all **sCIs 1—26**, with additional information on the reactions of EtOH and/or iPrOH reactions with **sCIs 1**, **3**, **11** & **12**, are found in Table 4.1 including: carbonyl oxide moiety, transition state zero-point corrected energy ($\Delta E_{TS_{AAAH}1}$ & $\Delta E_{TS_{AAAH}2}$), and rate constants (k_{TST}). In Table 4.1, reactions between **sCIs 2**, **4**, **13** or **14** and MeOH possess two rate constants, an overall rate constant and a VHP rate constant. This data is used to infer the conjugative, hyper-conjugative, H-bonding or steric impacts sCI substitution on reactivity, in a fashion similar to that of alkenes in Chapter 3. Occasionally, it should be noted that k_{TST} values are too high to use or the reaction is barrierless, so the $k_{d\text{-}d}$ capture moment is employed instead. Full discussion of these results is found in Section 4.3—4.6.

*Table 4.1: Criegee intermediate number (**#sCI**); alcohol (ROH); ratio between OO and CO bond lengths on the carbonyl oxide moiety ($q=R_{OO}/R_{CO}$)*; energy barriers of and lowest TS barrier from each channel ($\Delta E_{TS_{AAAH}1}$ & $\Delta E_{TS_{AAAH}2}$); the combined total of rate constants of all reaction channels at 298.15 K (k_{TST}); contribution of tunnelling to channel [$\kappa_{contr.} = \sum(\Gamma \times \kappa)$];*

#sCI	ROH	q	$\Delta E_{TS_{AAAH}1}$ (kJ mol^{-1})	$\Delta E_{TS_{AAAH}2}$ (kJ mol^{-1})	k_{TST} (298.15 K) (cm^3 molec^{-1} s^{-1})	Average κ
	MeOH		-3.81	0.11	1.17×10^{-14}	1.10
1	EtOH	1.078	-7.42	-1.55	6.17×10^{-14}	1.09
	iPrOH		-4.51	-2.87	1.21×10^{-14}	1.10
2	MeOH	1.084	10.04	18.75	1.82×10^{-17}	1.20
			28.99	***27.19***	***1.09×10^{-18}***	***26.02***
3	MeOH	1.093	-17.73	-13.99	2.09×10^{-12}	1.17
4	MeOH	1.091	1.21	9.63	5.63×10^{-16}	1.39
			26.11	***25.32***	***5.81×10^{-18}***	***37.73***
5	MeOH	1.113	-13.02	-15.16	7.62×10^{-13}	1.07
6	MeOH	1.136	-32.22	-29.55	8.66×10^{-10} **	1.03
7	MeOH	1.164	>>$k_{d\text{-}d}$	-40.51	1.96×10^{-8} ***	1.00
8	MeOH	1.082	12.14	13.96	1.10×10^{-17}	1.13
9	MeOH	1.104	-21.07	-14.67	6.50×10^{-12}	1.10
10	MeOH	1.093	-3.60	1.39	2.40×10^{-15}	1.12
	MeOH		10.40	10.09	4.01×10^{-17}	1.35
11	EtOH	1.075	7.45	8.04	9.79×10^{-17}	1.33
	iPrOH		6.16	6.58	7.51×10^{-17}	1.36
	MeOH		-17.43	-10.91	1.72×10^{-12}	1.54
12	EtOH	1.084	-21.01	-12.35	6.51×10^{-12}	1.56
	iPrOH		-20.84	-16.01	2.48×10^{-12}	1.95
13	MeOH	1.065	14.66	23.25	4.04×10^{-18}	2.24
			36.41	***58.63***	***4.04×10^{-20}***	***70.80***
14	MeOH	1.075	7.31	18.66	3.66×10^{-17}	2.14
			32.63	***30.82***	***2.61×10^{-19}***	***36.85***
15	MeOH	1.078	-9.96	-8.67	1.61×10^{-13}	1.71
16	MeOH	1.079	-15.88	-7.37	5.10×10^{-13}	1.45
17	MeOH	1.067	0.79	2.26	1.19×10^{-15}	2.18
18	MeOH	1.069	8.44	13.25	3.95×10^{-17}	1.66
19	MeOH	1.076	3.55	4.62	3.75×10^{-16}	1.38
20	MeOH	1.065	13.42	19.79	4.81×10^{-18}	1.42
21	MeOH	1.186	-30.31	-26.67	3.59×10^{-10} **	1.46
22	MeOH	1.174	-44.31	-30.14	4.20×10^{-8} **	1.53
23	MeOH	1.064	5.80	11.67	9.43×10^{-17}	N.I.
24	MeOH	1.071	-9.41	-5.49	3.30×10^{-14}	N.I.
25	MeOH	1.114	>>$k_{d\text{-}d}$	-27.30	5.75×10^{-12} ***	N.I.
26	MeOH	1.101	-26.18	-26.39	3.31×10^{-11}	N.I.

*Notes: **VHP channels in bold and italics**.* N.I. is an abbreviation for *not included*.

** While q is generally the descriptor term for molecular charge, it is used throughout this chapter to describe the ratio between OO and CO bond lengths, as found in the study of sCI + H_2O reactions by Anglada et al.*[195,408]

*** Where $k_{TST} > k_{d\text{-}d}$, the rate constant used is the $k_{d\text{-}d}$ value. All $k_{d\text{-}d}$ values are found in Appendix Section 2.1.*

**** Where the TS_{AAAH} 1 is barrierless, the ">>$k_{d\text{-}d}$" symbol is displayed and the $k_{d\text{-}d}$ rate constant is used.*

4.3 Various Alcohols Reactions with Simplest sCIs

This section explains the changes in sCIs + alcohol reaction chemistry with respect to two different factors: alteration of the alcohol $-R_3$ group; and changes in the non-conjugated R_1 & R_2 substituent groups of sCIs. The impact of changing the alcohol $-R_3$ substituent group is measured by modelling individual sCI reactions with MeOH, EtOH & iPrOH. Alternatively, varying sCI $-R_1$ & $-R_2$ substituents, both with respect to composition and orientation, e.g. choice of *syn*- or *anti*-position, also effects reactivity. To see the impact of using heteroatomic groups such as F and Cl substituents, see Section 4.4, and to see the impact of using conjugated alkyl substituents, see Section 4.5.

4.3.1 Comparing the sCI 1 reactions with MeOH, EtOH & iPrOH

Experimental studies referenced above have investigated sCI + alcohol reactions with respect to alteration of the alcohol $-R_3$ group, using both direct and indirect measurements. These reactions include**: sCI 1** + MeOH, EtOH & iPrOH, in studies by McGillen *et al*. and Tadayon *et al*.; and $CH_3(CH_2)_{11}CHOO$ + MeOH & iPrOH by Tobias *et* Ziemann.[51,386,402] Therefore, **sCI 1** reactions with these alcohols can be used to benchmark the theoretical treatments herein. The computational procedures used can then be expanded to identify trends in reactivities for alcohol reactions with larger sCIs, such as *syn*- & *anti*-PhCHOO reaction with MeOH, EtOH & iPrOH, seen in Section 4.3.2.

Firstly, it is worth noting that sCI reactions with EtOH & iPrOH are increasingly complex because of rotation around the new H-O-C-C dihedral axis, produces multiple conformeric subchannels for both TS_{AAAH} 1 and TS_{AAAH} 2, whereas the H-O-C-H dihedral angle rotation for MeOH produces chemically identical TS subchannels. However, for simplicity, in PES figures like Figure 4.6 only the lowest energy pathways of these channels are displayed. The remaining TSs that have been computed are found in Appendix Section 2.3 and all contribute to the k_{TST} constant. The calculation of multiple subchannels is important because each TS can have a non-negligible influence on the k_{TST} of sCI + EtOH or iPrOH reactions.

The lowest energy barriers for **sCI 1** reactions with all three alcohols are submerged (Figure 4.6), but this is insufficient to explain the experimental observations by Tadayon *et al*.. If the most reactive pathway dictated the reactivity of the **sCI 1** + alcohol systems, this would give reactivity trends of k_{EtOH} [TS_{AAAH} 1.1] > k_{MeOH} [TS_{AAAH} 1] > k_{iPrOH} [TS_{AAAH} 1.1], with rate constants of 2.95×10^{-14}, 9.52×10^{-15} & 6.61×10^{-15} $cm^3\ s^{-1}$ respectively. This would follow the theoretical analysis by Tadayon *et al.*, which also gave a k_{THEO} trend of $k_{iPrOH} > k_{EtOH} > k_{MeOH}$. However, as this study includes multiple conformeric TSs, the

increased number of low energy TSs for the **sCI 1** + EtOH & iPrOH reactions alters this reactivity trend, and is more consistent with available experimental data.

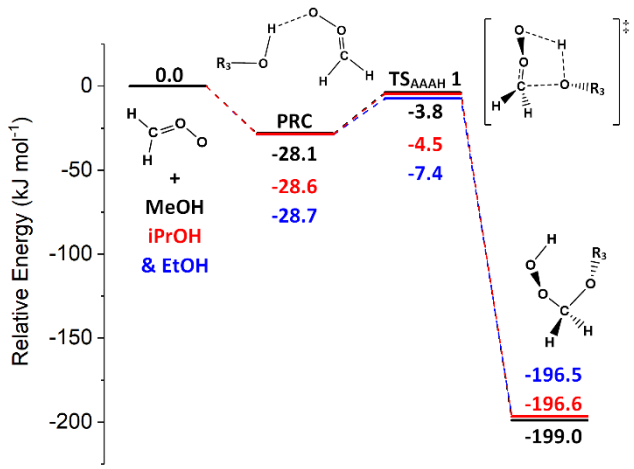

Figure 4.6: Comparison of lowest energy transition states of sCI 1 + MeOH, EtOH & iPrOH reactions. Energies are relative to raw reactants.

The inclusion of these subchannels is particularly important for the relative reactivity of MeOH & iPrOH, rather than that of EtOH as the overall k_{EtOH} (6.24×10^{-14} cm^3 s^{-1}) exceeds k_{MeOH} & k_{iPrOH} regardless of analysis methodology. On the other hand, the additional TS_{AAAH} subchannels promotes the k_{TST} of iPrOH (1.23×10^{-14} cm^3 s^{-1}) over that of MeOH (1.19×10^{-14} cm^3 s^{-1}), showing the importance of calculating all the rate coefficients for all TS subchannels.

The theoretical trend of $k_{EtOH} > k_{MeOH} > k_{iPrOH}$ is confirmed by the Tadayon *et al.* study, where, through the method of flash photolysis, the k_{EXP} values determined for **sCI 1** reactions with MeOH, EtOH and iPrOH (1.4×10^{-13}, 2.3×10^{-13} & 1.9×10^{-13} cm^3 s^{-1} at 295 K, 90 Torr) exhibits the same reactivity trend in k_{TST} values.[344] A study produced by McGillen *et al.* also shows the same patterns for **sCI 1** + MeOH & EtOH with k_{EXP} *(293 K, 9.99 Torr)* values of 1.04×10^{-13} & 1.16×10^{-13} cm^3 s^{-1}.[51]

Modifying the temperature conditions to match those of Tadayon *et al.* (295 K) gives rise to reactivities that are marginally more consistent with experiment: **sCI 1** + MeOH, EtOH & iPrOH (1.21×10^{-14}, 6.63×10^{-14} & 1.25×10^{-14} cm^3 s^{-1}). The k_{TST} (293 K) is also computed at conditions matching those of McGillen *et al.*, showing that **sCI 1** + MeOH & EtOH exhibit slightly larger k_{TST} values (1.21×10^{-14} & 6.68×10^{-12} cm^3 s^{-1}) than under standard conditions.[51]

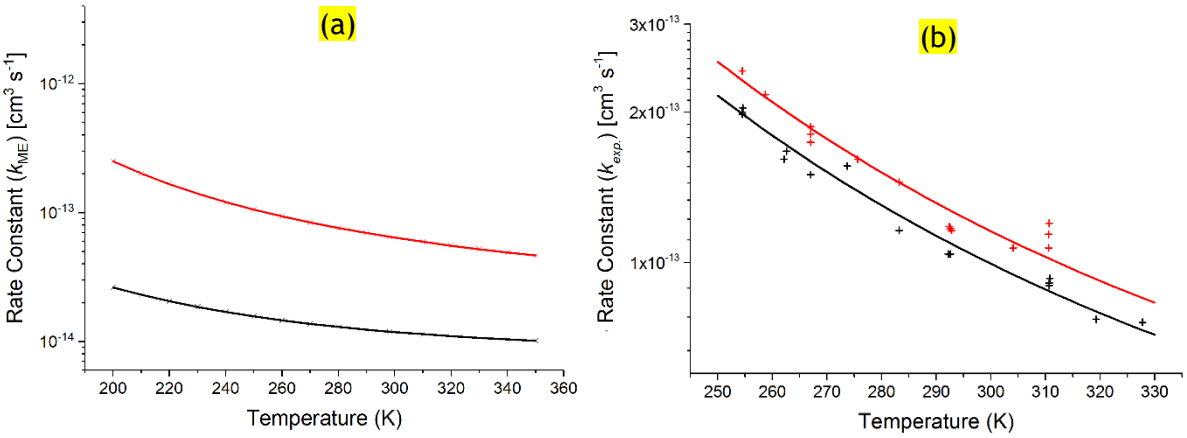

*Figure 4.7: Temperature dependences of sCI—alcohol reactions, **sCI1** + MeOH (black) and **sCI 1** + EtOH (red) at standard pressure, **Figure 4.7a**, on the left: displays the temperature dependences of the theoretical rate constants [k_{ME}] from this chapter; **Figure 4.7b**, seen on the right: the temperature dependences using experimental rate constants [k_{EXP}] for T= 250-330 K at p = 9.99 Torr, by McGillen et al.[51]*

The relationship between temperature change and the rate constant, referred to as 'temperature dependence', is an important attribute explored in this theoretical study. This theoretical temperature dependence is subsequently compared to similar experimental temperature dependences for the **sCI 1** + MeOH & EtOH reactions in the *McGillen et al.* study, demonstrating this is an efficient and accurate way of calculating the k_{THEO} values over various temperatures. As observed in Figure 4.7b, the *McGillen et al.* k_{EXP} temperature dependence is negative between atmospheric temperatures 250 — 330 K for both MeOH (in black) & EtOH (in red) reactions with **sCI 1**.[51] The theoretical temperature dependence for **sCI 1** + MeOH & EtOH displayed in Figure 4.7a is also one of a negative temperature dependence trend, in agreement with the k_{EXP} trends in the *McGillen et al.* study. These k_{TST} temperature dependencies, displayed for both **sCI 1** + MeOH & EtOH, are only on a marginal descent, which is consistent with both reactions having minimally submerged reaction barriers. This suggests the barrier is overestimated when compared to the steeper k_{EXP} trend. But by agreeing with the experimental temperature-dependence trends, the reliability of the computational method used in this thesis is established.

In a literature study by Lin *et al.* a similar theoretical investigation of the temperature-dependent rate coefficients of **sCI 1** + MeOH reactions between 273 and 373 K was carried out. The Lin *et al.* temperature dependence, at 760 Torr, was also found to have a negative slope in agreement with the trends in this thesis.[401] No study of the temperature dependence of **sCI 1** + iPrOH reaction and therefore only the one k_{EXP} value at 293 K mentioned earlier from the work of Tadayon *et al.* is available to compare to.

4.3.2 sCIs 11 & 12 reaction with MeOH, EtOH & iPrOH

The small changes in overall reactivity for **sCI 1** with MeOH, EtOH & iPrOH implies that altering the $-R_3$ alcohol substituent makes little difference to total reactivity. The most significant concern in applying this assumption for all sCI-alcohol reactions is that interaction between larger $-R_1$ & $-R_2$ substituents of an sCI and the $-R_3$ substituent of the alcohol is of an unknown/negligible energetic impact. This was explored to a small extent in reactions with the bulky sCI, $CH_3(CH_2)_{11}CHOO$, in the Tobias and Ziemann study, where the potential increase in steric blocking of the more bulky iPrOH seemed to have little energetic impact when compared to reactions with MeOH.[386] However, this single study, does not provide enough evidence to completely validate that altering the alcohol $-R_3$ substituent has little overall impact on sCI + alcohol reactivity or that only a subtle reactivity trend, $k_{EtOH} > k_{iPrOH} > k_{MeOH}$, is produced.

To survey this variation of steric bulk within the sCI + alcohol reaction, MeOH, EtOH and iPrOH are investigated reacting with one bulky *syn*-sCI, *syn*-PhCHOO (**sCI 11**), and one bulky *anti*-sCI, *anti*-PhCHOO (**sCI 12**). The sCIs, *syn*- & *anti*-PhCHOO are shorthand for *syn*- & *anti*-$(C_6H_5)CHOO$, where the aromatic C_6H_5 benzene group, referred to as a phenyl or Ph group, is bonded to the carbonyl oxide. Unlike the conjugated **sCIs 13—20**, little conjugative impact is demonstrated between the COO and the Ph groups. Using alcohol reactions with **sCIs 11** & **12**, this subsection will examine what impact the *syn*- and *anti*-positions of the Ph group have on reactivity. *Syn*- and *anti*-CH_3CHOO (**sCIs 2** & **3**) is one example where the two conformers are chemically distinct species have been spectroscopically identified.[141,142] Large k_{EXP} disparities between **sCIs 2** and **3** in bimolecular reactions with SO_2, H_2O and NO_2 particularly highlight this distinction between the *syn* & *anti* conformers.[141,142] This disparity between *syn*- and *anti*-sCIs in their bimolecular reactivity is also demonstrated for **sCIs 11** & **12** reactions with H_2O, in theoretical analysis by Bracco *et al.*.[409]

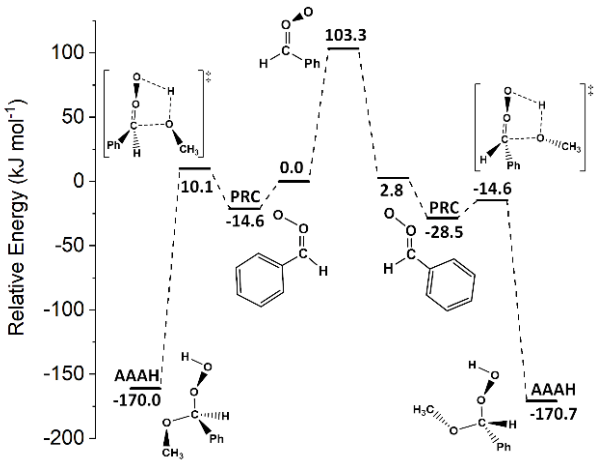

*Figure 4.8: PES of **sCI 11** (left) and **sCI 12** (right) + MeOH to AAAH, linked by the high TS to interconversion between **sCIs 11** & **12**. Energies are relative to raw **sCI 11** + MeOH.*
Note: In this thesis, the phenyl group for both syn- & anti-PhCHOO preferentially adopt an eclipsed conformation relative to the carbonyl oxide group when optimised, rather than staggered conformation. While a staggered conformation would reduce steric interactions between the Ph group and the carbonyl oxide, particularly with the terminal oxygen in the syn conformer, the conjugation between the Ph group and the carbonyl group in the eclipsed conformation may stabiles the sCI further. These eclipsed conformations are found to be the optimised geometries for syn- & anti-PhCHOO in various computational studies that examine their bimolecular chemistry reactivity with NH_3, SO_2 & H_2O.[181,409,410]

The significant disparity in bimolecular reactivity between MeOH reactions with **sCIs 11** & **12**, displayed in Figure 4.8, continues the pattern of higher reactivity for *anti* than *syn* conformers.[141,142,409] Whilst the PESs for sCI + MeOH reactions for **sCIs 11** & **12** is mostly similar to **sCI 1**, one minor difference is that **sCI 11** + MeOH has a TS_{AAAH} 2 barrier with a lower energy than TS_{AAAH} 1 (see structural TS_{AAAH} image for **sCI 11** + MeOH in Figure 4.8). This replication of the large divergences between *syn* and *anti* conformers continues with the large gap in k_{TST} between MeOH + **sCIs 11** & **12** (4.01×10^{-17} & 1.72×10^{-12} cm^3 s^{-1}).

MeOH, EtOH & iPrOH reactions with **sCIs 11** & **12** produce similar trends to their reactions with **sCI 1**, one of the small differences between k_{MeOH}, k_{EtOH} & k_{iPrOH}. **sCI 11** reactions exhibit the same reactivity order ($k_{EtOH} > k_{iPrOH} > k_{MeOH}$) to **sCI 1**, with k_{EtOH} being the most reactive (9.74×10^{-17} cm^3 $molec^{-1}$ s^{-1}) of the 3 × R_3OH co-reactants. The only change in trend is that while for **sCI 1** there is only a very small difference between k_{iPrOH} and k_{MeOH}, **sCI 11** exhibits a significantly larger gap between k_{iPrOH} (7.51×10^{-17} cm^3 s^{-1}) and k_{MeOH}. **sCI 12** also shows this $k_{EtOH} > k_{iPrOH} > k_{MeOH}$ pattern, with values of 6.51, 2.48 & 1.72×10^{-12} cm^3 s^{-1}, respectively. This gives this chapter a strong internal consistency, that while changes in the alcohol's R_3 group has little effect, changes to the sCI R_1 & R_2 group induce changes in reactivity by orders of magnitude. This is consistent with the idea that MeOH, EtOH and iPrOH may act as one taxonomic group when reacting with sCIs.

In contrast to R_3OH substitution, the reactions of **sCIs 11** & **12** with alcohols demonstrate that the composition of the R_1 & R_2 groups of the sCI make a significant difference to

reactivity and should be explored. Here, the shift between **sCIs 11** & **12**, the location of the —Ph group, causes a change in the rate constant of 10^4 — 10^5 cm^3 s^{-1}. The constancy of the higher reactivity of the *anti* conformers, such as with **sCI 12** and the literature studies of **sCIs 2** & **3** reactions with H_2O, $(H_2O)_2$ and SO_2, has produced several hypotheses to explain the phenomenon.[141,193,411,412] One such hypothesis is that there is steric blocking of the terminal oxygen reaction site by the —Ph group. As there is significant movement required in the *syn*-PhCHOO structure but not in the *anti*-PhCHOO structure for reactions with MeOH, this hypothesis may contribute to the difference in reactivity between **sCIs 11** & **12**. Whilst conjugative effects can stabilise or destabilise sCIs (see Section 4.5), the Ph substituents in the **sCIs 11** & **12** structures offer little conjugation with the COO group, and so this would appear to have little impact on overall reactivity. Hyper-conjugative effects could have a greater effect, but **sCIs 11** & **12** are lacking in the normally pre-requisite α-H atoms. There is also a hypothesis that the α-/ß-H atoms in the *syn*- position increases stability of the *syn*-sCI by having increased permanent dipole-induced dipole (referred to as *H-bonding*) interactions between α/ß-Hs with the terminal O. The phenyl group has 1 × ß-H atom, which could participate in *H-bonding* interactions. Both the hyper-conjugative and these *H-bonding* effects are explored further in Section 4.4.3, when comparing both *anti* and *syn*-CH_3 & CF_3 substituents. For an overall comparison of sCIs reactivity and the main causes for these changes in reactivity see Section 4.7.

4.3.3 Analysis of *syn*- and *anti*-CH_3CHOO (sCIs 2 & 3) Reactions with MeOH (+ EtOH)

As shown in chapter 3, ozonolysis of common atmospheric alkenes, such as propene, can produce both *syn* and *anti* conformers of CH_3CHOO, referred to in this study as **sCIs 2** and **3**. Much like **sCIs 11** & **12**, both **sCIs 2** & **3** act in isolation to each other, due to their high barrier to interconversion, and, as seen in Figure 4.9, have individual chemistries with MeOH. However, if Figure 4.9 is compared to Figure 4.8, **sCIs 2** & **3** have a larger ΔE difference between them (14.0 kJ mol^{-1}) than do **sCIs 11** & **12** (2.8 kJ mol^{-1}). This lower ΔE for **sCI 2** may be due to the stabilising effect of the *H-bonding* interactions of the α-H atoms on the *syn*-CH_3 substituent with the terminal O, whereas **sCIs 11** has no stabilising α-H atoms and the considerable size of the -Ph group may cause steric clashes with the terminal O atoms.

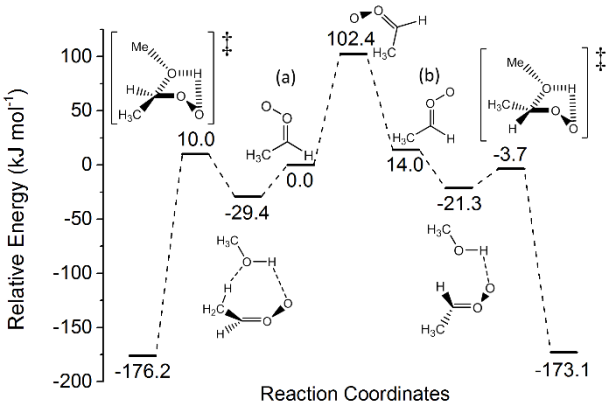

*Figure 4.9: PES of **sCI 2** and **sCI 3** + MeOH including interconversion barrier between sCI conformers. Energies are relative to raw reactants (**sCI 2** + MeOH).*
Note: In the syn-CH_3CHOO + MeOH pre-reaction complex includes a C-H---O intermolecular bond that is of note because it somewhat lowers the energy of the overall complex, compared to say the syn-CF_3CHOO + MeOH PRC energy (-16.1 kJ mol^{-1}). This is noteworthy, because the strength by which PRCs can be bound together is known to influence on the kinetics and tunneling of the reaction.[413] This C-H---O intermolecular bond is also notable because it aligns the PRC in the position that the VHP channel adopts, perhaps facilitating the reaction.

The **sCI 2** + MeOH reaction has a lower k_{TST} value (1.82×10^{-17} cm^3 s^{-1}) not only than the highly reactive **sCI 3** + MeOH (2.09×10^{-12}) but also than **sCI 1** + MeOH (1.17×10^{-14}), because of its TS_{AAAH} barrier is so high, as seen in Figure 4.9. The only experimental measurement of **sCI 2** + MeOH known to the author is a study by Lin *et al.*, which showed the rate constant was below the detection level of the equipment ($<2 \times 10^{-17}$ cm^3 s^{-1}), which is in line with the low reactivity shown in this thesis.[402]

Unlike **sCI 11**, due to the presence of α-H atoms in the *syn*-CH_3 position the **sCI 2** + MeOH reaction has access to the TS_{VHP} 1 and TS_{VHP} 2 channels, which can produce VHP products. The high barrier heights of TS_{VHP} 1 & 2 (29.0 & 27.2 kJ mol^{-1}) are partially circumvented by a high tunnelling rate, κ_{ECKART} (~ 25), increasing Γ_{VHP} from 0.008 to a small but significant 0.057. This TS_{VHP} pathway is discussed further in the appendix. This is comparable to a theoretical study by Anglada *et* Sole, where the **sCI 2** + H_2O & $(H_2O)_2$ reactions show similar TS_{VHP} reaction pathways, competing with the hydroxy hydroperoxide (TS_{HHP}) channel, an analogue of the TS_{AAAH} channel.[293] Whilst all the sCI + $(H_2O)_2$ reactions by Anglada *et* Sole have a very low Γ_{VHP} yield of <<0.01, **sCI 2** + H_2O (~0.508) is much more significant than that of **sCI 2** + MeOH.[293] Prior work into the **sCI 2** + MeOH reaction has not examined the competing VHP reaction channel in any detail.[401,402]

sCI 3 + MeOH, like **sCI 12**, is much more reactive than both **sCIs 1**, **2** & **11**, as shown in Figure 4.9, with a k_{TST} of ~2.09×10^{-12} cm^3 s^{-1}. This reaction in fact marginally exceeds the reactivity of **sCI 12** + MeOH, as the increased number of α-H atoms in the *anti*-CH_3 group increases the hyperconjugative impact of the substituent group, thereby destabilising the sCI. Of all the sCIs examined with purely hydrocarbon substituents, **sCI 3** is the most

reactive with MeOH. The k_{EXP} [295K, 250 Torr] measured by Lin *et al* for **sCI 3** + MeOH (5×10^{-12} cm^3 s^{-1}) is similar to the k_{TST} [295K] (2.03×10^{-12} cm^3 s^{-1}) derived in this chapter. **sCI 3** is the most reactive of the atmospherically prevalent sCIs (**sCIs 1—4** & **11—20**), a pattern observed in other studies.[93,195,273,293,372] Whilst most mono-substituted sCIs can be readily categorised as *syn* or *anti*, with this change being reflected in their reactivities, disubstituted sCIs can react very differently yet again, as shown in comparing MeOH reactions with **sCIs 1** & **4**.

4.3.4 Analysis of the MeOH + $(CH_3)_2COO$ Reaction

Experimental analysis of $(CH_3)_2COO$, **sCI 4**, ranges from unimolecular decomposition to reactions with many atmospheric species including H_2O, $(H_2O)_2$, NO_2 and SO_2.[119,184,388,412,414] The experimental rate constant of **sCI 4** + MeOH, derived by McGillen *et al.* (~ 10^{-14} cm^3 s^{-1}), diverges significantly in reactivity from the **sCI 1** + MeOH and **sCI 1** + EtOH reactions (~ 10^{-12} cm^3 s^{-1}), once again demonstrating that altering the sCI's R_1 and R_2 substituent groups seems more significant than altering the R_3-OH group.[51]

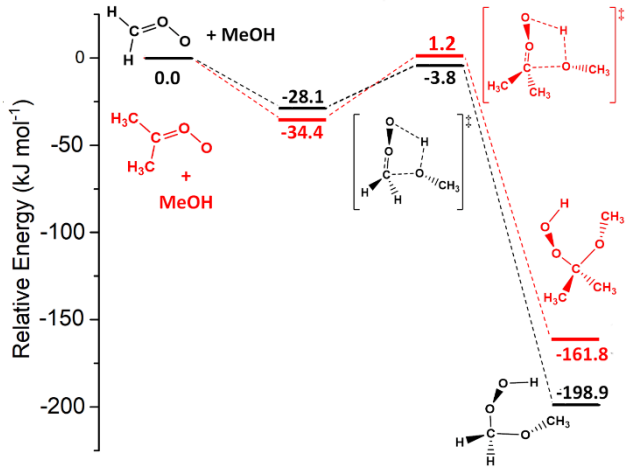

*Figure 4.10: Comparison of the lowest energy PES between MeOH + **sCI 1** (black) or **sCI 4** (red). Energies are relative to raw reactants.*

Figure 4.10, a comparison between sCI + MeOH reactions, displays a decreased reactivity for the disubstituted **sCI 4** compared with **sCI 1**. This reduction in reactivity is partially due to the additional steric bulkiness of the *syn*-CH_3 group, an effect that also reduces the reactivity of **sCI 2**. **sCI4** + MeOH has VHP channels similar to **sCI 2** (k_{TST} [VHP]~10^{-18} cm^3 molec.$^{-1}$ s^{-1}), but due to an increase in the k_{TST} [AAAH] of **sCI 4**, the Γ_{VHP} decreases to ~ 0.01. It seems that the *anti*-CH_3 group of **sCI 4** introduces an inductive effect with respect to both reaction channels, but this has a far greater impact on the AAAH channel. This combination of an inductive effect from the *anti*-CH_3 group and the reductive effect of the *syn*-CH_3 group gives rise to a middling k_{TST} (**sCI 4** + MeOH) ~ 5.63×10^{-16} cm^3 s^{-1}. This leads

to a pattern of $k_{sCI\,2} < k_{sCI\,4} < k_{sCI\,1} < k_{sCI\,3}$, similar to those seen in sCI reactions with H_2O, $(H_2O)_2$ and SO_2.[141,145,178,184,193,195,293,388,411,414]

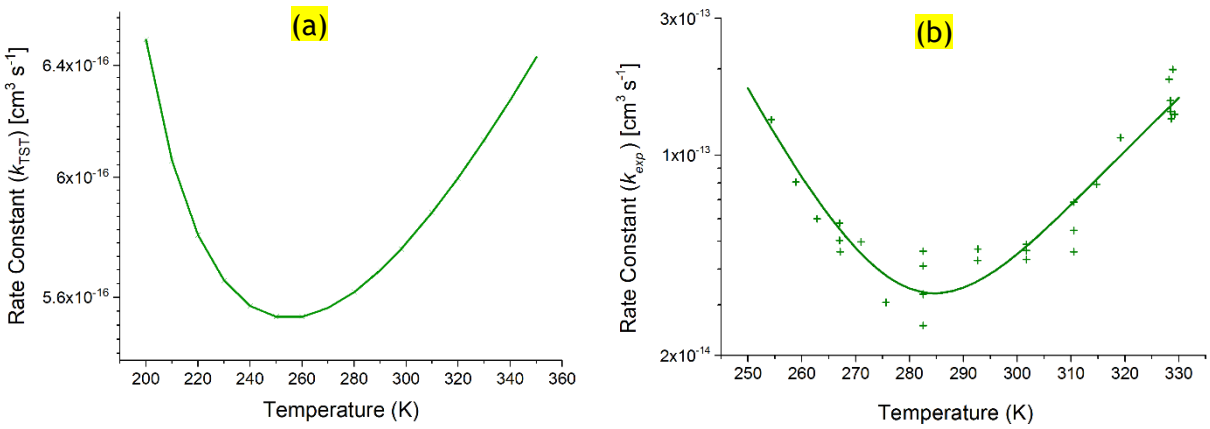

Figure 4.11: Comparing temperature dependence for the $(CH_3)_2COO$ + MeOH with theoretical rate constants [k_{TST}] under standard pressure from this thesis (Figure 4.11a); and experimentally determined rate constants [k_{EXP}] carried out by McGillen et al. between 250-330 K at p = 9.99 Torr (Figure 4.11b).[51]

While, the experimental analysis of **sCI 4** + MeOH by McGillen *et al.* gave a k_{EXP} *[292.2 K, 9.99 Torr]* ~ 4.32 × 10^{-14} cm^3 s^{-1}, not as similar to the temperature adjusted k_{TST} *[292 K, 9.99 Torr]* ~5.74 × 10^{-16} cm^3 s^{-1}, found here, the fact that the results in this chapter successfully mapped a similar temperature dependence (Figure 4.11) shows a significant degree of reliability to these calculations.[51] McGillen *et al.* found that **sCI 4** + MeOH exhibits an unusual mixed temperature dependence at ~10 Torr, which is replicated in the at standard temperature this chapter (for pressure adjusted results see Appendix Section 2.2). This mixed temperature dependence can be explained in the context that the more reactive **sCI 1** + MeOH exhibits a negative temperature dependence and the less reactive **sCI 2** + MeOH exhibits a positive computed temperature dependence.[51,402] As the reactivity of **sCI 4** sits in between the reactivities of **sCIs 1** & **2**, the temperature dependence for **sCI 4** + MeOH is a logical combination of the chemistries of **sCIs 1** & **2** + MeOH reactions. The minimum rate constant in this mixed temperature dependence does show differences in the results with the k_{EXP} profile minimum point at ~ 285 K, whereas the pressure adjusted k_{TST} minimum point is ~255 K.

From this standpoint **sCI 4** + MeOH, exhibits a similar process to other reactions in the literature such as the OH + MeOH reaction, which, also exhibits a u-shaped temperature dependence.[413] According to Shannon *et al.*, this reaction a negative temperature dependence prior to ~200 K, as the significant role of tunnelling and the frequency of forming stable intermolecular OH—MeOH PRC decreases with increased temperature.[413] But at high temperatures, this inverts to positive temperature dependence as the increased energy allows the reactants to overcome the low reaction barrier, which is also

seen for **sCI 4** + MeOH at higher temperatures.[413] As the role of tunneling is maximised at lower temperatures, also plays an important role in maintaining higher rate constants at lower temperatures within this mixed temperature dependence of **sCI 4** + MeOH reaction, although, unlike the OH + MeOH reaction studied by Shannon *et al.*, is not the sole reason for a mixed temperature dependence in this context.[413]

Figure 4.12 displays the temperature dependence at standard pressure of all reaction mechanisms (TS_{AAAH} 1, TS_{AAAH} 2, TS_{VHP} 1 & TS_{VHP} 2), compared to that of the full rate constant (in black). The breakdown of this temperature dependence shows that TS_{AAAH} 1 is the main contributor to the k_{TST} at most temperatures and exhibits the same mixed temperature dependence as the overall rate constant. TS_{VHP} 1 & TS_{VHP} 2 also exhibit mixed temperature dependences, whereas TS_{AAAH} 2 exhibits a positive temperature dependence.

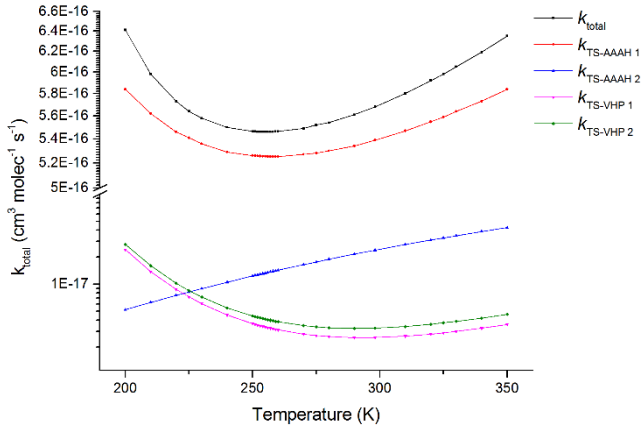

*Figure 4.12: Comparison of different TS temperature dependence with overall k_{TST} for **sCI 4** + MeOH.*

Therefore, this mixed temperature dependence seems to emerge from the nature of the reaction barrier. **sCI2** + MeOH has a high and positive TS_{AAAH} 1 reaction barrier meaning that more energy needs to be injected into the system to increase the reaction rate, whereas **sCI 1** + MeOH has a low and submerged TS_{AAAH} 1 barrier indicating that formation of the pre-reaction complex is the rate determining step. Accordingly, **sCI 1** + MeOH has a negative temperature dependence because, as temperatures increase, the weak intermolecular bond in the PRCs are more likely to dissociate, shortening the PRC lifetime, and reducing the number of PRCs that then undergo reaction to produce AAAHs. The mixed temperature dependence of **sCI 4** + MeOH emerges from a channel which has a reaction barrier very similar to the separated reactant energies, (~1.2 kJ mol^{-1}). This means that the rate determining step switches from the reversible formation of the pre-reaction complex, which decreases in probability as heat is added to the system; to the overcoming of the TS_{AAAH} 1 barrier, which increases as heat is added to the system.

4.4 Non-atmospherically prevalent sCIs reactions with MeOH

The ozonolysis of hydrofluoroolefins (HFOs), explained in Introduction Section 1.7 and explored in Section 3.7, have been shown to synthesise hydrofluoroolefin-derived sCIs (HFO-sCIs). These HFO-sCIs can be used to observe the effect of electronegative groups in the *syn* and/or *anti* positions of sCIs: *syn*- & *anti*-FCHOO, *syn*- & *anti*-ClCHOO, CF_2OO and CCl_2OO. Other sCIs studied in this section includes theoretical cyclic-sCIs (**sCIs 21** & **22**) to see the effect of steric tension and heterocycles on sCI reactivity. MeOH reactions with *syn*- & *anti*-CF_3CHOO and *syn*- & *anti*-CF_3CFOO (**sCIs 23—26**) are taken from the computational study of HFO-sCIs reaction with other atmospheric species, in chapter 5.

4.4.1 Fluorinated sCIs 5—7 Reactions With MeOH

One common theme seen for *syn*-FCHOO, *anti*-FCHOO and CF_2OO, referred to as **sCIs 5—7**, in Table 4.1, is that their reactions with MeOH produce larger k_{TST} values than all their **sCIs 2—4** counterparts. This may emerge from the electron-withdrawing —F substituent producing an electro-positive central C atom, increasing the zwitterionic character of the COO group. The **sCI 5** reaction with MeOH produces a large k_{TST} value (7.62×10^{-13} cm^3 s^{-1}), even though we have generally seen *syn* conformers show low reactivities. In fact, this reaction is the slowest of those for **sCIs 5—7**. The inductive impact of the *syn*-F group on **sCI 5** produces a reactivity exceeding the moderate reactivities of **sCIs 1** & **4**. **sCI 5**, and much like **sCI 11** has a lower energy TS_{AAAH} 2 barrier than TS_{AAAH} 1 (-15.16 & -13.02 kJ mol^{-1}), even though both pathways contribute significantly to the k_{TST}.

The electron-withdrawing *anti*-F substituent also increases the zwitterionic character of **sCI 6** further which means its reaction with MeOH has a larger k_{TST} value (8.66×10^{-10} cm^3 s^{-1}) than **sCI 5**, following the overarching theme that substituents in the *anti* position strengthen the reactivity compared to their *syn* counterparts. Difluorinated **sCI 7** is unusual, exceeding the reactivity of both mono-substituted sCIs, **sCIs 5** or **6**. Common disubstituted sCIs, like **sCIs 4**, **10**, **13**, **14**, **17** or **18**, have lower k_{TST} values than the *anti*-sCI equivalents. This is due to the reductive impact of the additional *syn* substituent in disubstituted sCIs. However, the high reactivity of **sCI 7** + MeOH shows the significant inductive input of the *syn*-F group.

Much like the other sCI + MeOH reactions, the **sCI 7** + MeOH reaction has 2 × TS_{AAAH} pathways, but the one-dimensional minimum energy pathway for the TS_{AAAH} 1 channel produces an asymptote between reactants and products, with no energy barrier. Unlike most barrierless rate determining steps in this thesis, the **sCI 7** + MeOH reaction has one barrierless TS_{AAAH} 1 channel and one channel with a low TS_{AAAH} 2 barrier (-40.5 kJ mol^{-1}),

that generate the same product. This phenomenon is only replicated for the **sCI 25** + MeOH reaction and this is expanded on further for both reactions in Appendix Section 2.6. The barrierless nature of TS_{AAAH} 1 for the **sCI 7** + MeOH reaction and the very large k_{TST} for **sCI 6** + MeOH reaction (8.66×10^{-10} cm^3 s^{-1}) means that the dipole-dipole capture limits (k_{d-d} = 7.23 & 7.07×10^{-10} cm^3 s^{-1}) are employed as the rate constants. Without the employment of k_{d-d} capture limits, the reactivity trend of k_{CF_2OO} > $k_{anti\text{-}FCHOO}$> $k_{syn\text{-}FCHOO}$, caused by the inductive effect of F substituents, seems to be consistent with those for sCIs reactions with H_2, CH_4 & H_2O.[195,273,274]

4.4.2 Chlorinated sCIs 8—10 + MeOH

Syn- & *anti*-ClCHOO and CCl_2OO, referred to as **sCIs 8—10**, react with MeOH to produce k_{TST} values more similar to the methylated sCIs (**sCIs 2—4**) than the fluorinated sCIs (**sCIs 5—7**). For example, the *syn*-Cl group on the **sCI 8** increase the biradical sCI character and therefore gives a low k_{MeOH} (1.10×10^{-17} cm^3 s^{-1}), very similar to that of **sCI 2** of (1.82×10^{-17} cm^3 s^{-1}). This could be due to Cl atoms being much less electronegative than F atoms, meaning that any inductive effect caused by the Cl substituent might be overcome by the reductive impact of being in the *syn* group. Also, unlike **sCI 5**, it has a $\Delta E_{TS_{AAAH}\,1}$ of 12.1 kJ mol^{-1} which is less than $\Delta E_{TS_{AAAH}\,2}$ of 14.0 kJ mol^{-1}, reversing the reactivity order of TS_{AAAH} barriers seen in **sCI 5**.

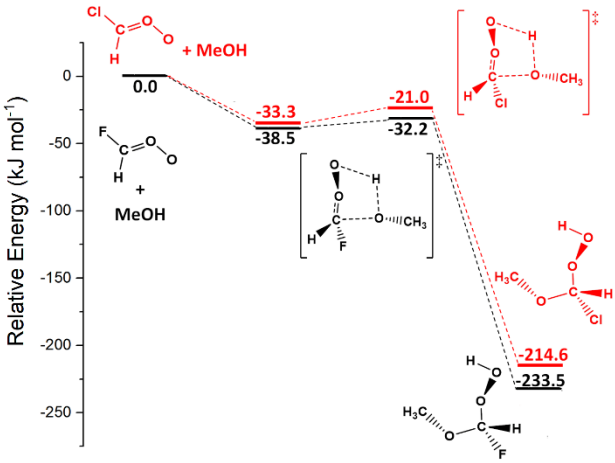

*Figure 4.13: A comparison of PES of fluorinated **sCI 6** (black) with chlorinated **sCI 9** (red). Energies are relative to raw reactants.*

The contrast between the small electron-withdrawing impact of the Cl compared to the large impact of the F group, is seen in Figure 4.13, where there is a higher ΔE barrier for chlorinated **sCI 9** compared to fluorinated **sCI 6**. This small electron-withdrawing impact of *anti*-Cl group may help give a larger k_{MeOH} for **sCI 9** (6.50×10^{-12} cm^3 s^{-1}) than the k_{MeOH} of the *anti* methylated **sCI 3** (2.09×10^{-12} cm^3 s^{-1}). Much like **sCI 4**, the combination of the

inductive contribution of the *anti*-Cl group and a reduction in reactivity from the *syn*-Cl group means that **sCI 10** produces a medium k_{MeOH} (2.40 × 10^{-15} cm^3 s^{-1}). The weak electronegative impact of the Cl substituent in the sCI + MeOH reaction leads to two different observations: that fluorinated sCIs reactivity significantly exceeds the reactivity of their chlorinated equivalents, and that the chlorinated reactivity trend is $k_{anti\text{-}ClCHOO}$ > k_{Cl_2COO} > $k_{syn\text{-}ClCHOO}$. Both these observations are also reflected in the reactivity of **sCIs 5—10** with CO_2, H_2 and CH_4.[273,274,372]

4.4.3 MeOH reactions with trifluoro-methylated sCIs (sCIs 23—26)

Reactions of *syn*- & *anti*-CF_3CHOO and *syn*- & *anti*-CF_3CFOO, referred to as **sCIs 23—26**, with MeOH provide several important insights, including the impact of the *H-bonding* interaction between α-H atoms and the terminal O atoms. This was seen in the MeOH + **sCIs 2** & **4** reactions where substituting the α-H atoms in the CH_3 substituent groups with -F atoms, forming **sCIs 23** & **24**, any potential *H-bonding* interaction is removed. In the same systems, any hyperconjugative effect caused by α-H atoms could also be investigated by their replacement with F atoms.

The impact of *H-bonding* interactions can be observed in Table 4.2, where the MeOH + **sCI 23** reaction exhibits a reduced ΔE for TS_{AAAH} 1 & 2 barriers compared to **sCI 2** + MeOH (10.04 & 18.75 kJ mol^{-1}). The stabilising impact of *H-bonding* interactions between *syn*-α-H atoms and the terminal O atom is observed in the fact that the *syn* conformer of CH_3CHOO (**sCI 2**), which has *syn*-α-H atoms, is 14.0 kJ mol^{-1} lower in energy than the *anti* conformer (**sCI 3**); whereas the **sCI 23**, where with repulsive *syn*-α-F atoms are present, is 3.4 kJ mol^{-1} higher in energy compared to its *anti* counterpart (**sCI 24**). The elimination of *H-bonding* stabilisation explains the comparably lower barrier and consequentially larger rate constant for **sCI 23** + MeOH reaction, in Table 4.2, compared to the *H-bonding* stabilised **sCI 2** + MeOH (k_{TST} = 1.82 × 10^{-17} cm^3 s^{-1}).

Table 4.2: Reaction between MeOH and selected Criegee intermediate by number (sCI #); ratio between OO and CO bond lengths on the carbonyl oxide moiety (q); zero-point corrected energies of TS_{AAAH} 1 ($\Delta E_{TS_{AAAH}\,1}$) and lowest TS_{AAAH} 2 ($\Delta E_{TS_{AAAH}\,2}$); the k_{ME} constant was obtained microcanonical rate method using MESMER software.

Reaction sCI + MeOH	sCI #	*q*	$\Delta E_{TS_{AAAH}\,1}$ (kJ mol^{-1})	$\Delta E_{TS_{AAAH}\,2}$ (kJ mol^{-1})	k_{ME} (298.15 K) (cm^3 s^{-1}) *
syn-CF_3CHOO + MeOH	23	1.064	5.80	11.67	9.43 × 10^{-17}
anti-CF_3CHOO + MeOH	24	1.071	-9.41	-5.49	3.30 × 10^{-14}
syn-CF_3CFOO + MeOH	25	1.114	>> $k_{d\text{-}d}$	-27.30	*5.50 × 10^{-10}* **
anti-CF_3CFOO + MeOH	26	1.101	-26.18	-26.39	3.31 × 10^{-11}

** k_{ME} value is used here because these reactions were obtained for another project in Chapter 5*
*** rate constant obtained using dipole-dipole capture limit due to a reaction channel being barrierless.*

An inductive impact of hyperconjugative α-H atoms in the *anti* position can be inferred from Table 4.2, when **sCI 24** + MeOH is compared against **sCI 3** + MeOH. **sCI 24** + MeOH is less reactive and provides a lower k_{THEO} than **sCI 3** + MeOH (2.09×10^{-12} cm^3 s^{-1}), implying that the removal of these hyperconjugative α-H atoms causes a reduction in reactivity. This consistently lower reactivity for **sCI 24**, compared to **sCI 3**, also reflected in the literature theoretical analyses of **sCI 3** & **sCI 24** reactions with CO_2 and H_2, indicates that these α-H atoms in the *anti* position have this hyper-conjugative inductive impact.[195,273,274] Whilst eliminating some of the *H-bonding* and hyper-conjugative interactions by substituting the α-H atoms with α-F atoms reduces the reactivity difference between **sCI 23** & **sCI 24**, it does not eliminate it completely. This implies there are additional significant steric or inductive factor(s) involved in *syn* or *anti* sCI substitution affecting the reactivity, not explained by *H-bonding* and hyperconjugative interactions.

Syn- & *anti*-CF_3CFOO, referred to as **sCIs 25** & **26**, are some of the most reactive sCIs in this study, with k_{MeOH} values either close to, or exceeding, the dipole-dipole capture limit. This is due to the high reactivity caused by the inductive -F substituent. Having bulky groups in the *syn*-position, such as with **sCIs 2**, **19**, **20** & **23**, usually produces lower k_{THEO} values, however the bulky *syn*-CF_3 group in **sCI 25** produces a larger k_{THEO} value than that of *anti*-CF_3 group, **sCI 26**. This is because with the —CF_3 group in the *syn*-position, the highly reactive —F substituent is in the *anti* position. This is the same phenomenon seen in the higher reactivity of the **sCI 6**, caused by the *anti*-F group, compared to the reductive impact of the *syn*-F group of **sCI 5**.

4.4.4 Cyclic disubstituted sCIs

sCIs 21 & **22** are both disubstituted sCIs, having essentially the same group in both R_1 and R_2 positions, but they are also both cyclic, making them unique in this study. To the author's knowledge, neither compound has been identified or studied experimentally, as they are used for exploratory purposes, and so they can be compared to previous theoretical analysis.[195] **sCI 21** has submerged TS_{AAAH} 1 & 2 barriers (~ -29 kJ mol^{-1}) when reacting with MeOH, giving rise to a large k_{TST} value in reaction with MeOH of (3.59×10^{-10} cm^3 s^{-1}). The cyclopropene segment of **sCI 21** compresses the atoms closer together within the structure the increasing repulsion between atoms and therefore to the total energy of the sCI. This structural feature, referred to as "torsional strain", makes this **sCI 21** + MeOH highly reactive, although the rate constant still does not exceed the dipole-dipole capture limit ($k_{d\text{-}d}$ ~1.14×10^{-9} cm^3 s^{-1}). This means that the effect of torsional strain on k_{TST} values is much smaller than the inductive impact of electron-withdrawing substituents, such as the F atoms in **sCIs 6**, **7**, **25** & **26**. This electron-withdrawing effect is

also observed in the higher reactivity in **sCI 22** + MeOH reaction, caused by the substituent's O atoms. The electronegative nature of the O atoms bonded to the COO group cause the same inductive increases in reactivity that have been observed before. This leads to a large k_{MeOH} (4.20×10^{-8} cm^3 s^{-1}) which exceeds both the $k_{d\text{-}d}$ (1.62×10^{-9} cm^3 s^{-1}) and the k_{MeOH} of the highly reactive, fluorinated **sCI 6** (8.66×10^{-10} cm^3 s^{-1}). This large k_{THEO} for **sCIs 21** & **22**, compared to the naturally occurring sCIs, is also reported by Anglada *et al.* in the study of sCI + H_2O reactions.[195]

4.5 MeOH reactions with Isoprene-Derived-sCIs (sCIs 13 — 20)

Isoprene is very prevalent in the atmosphere and roughly 10% of its decomposition arises via ozonolysis.[415-417] This means that isoprene derived sCIs are very atmospherically abundant, so exploring their reactivity with MeOH is important. Isoprene derived sCIs can be divided into two types: methyl vinyl ketone oxide and methacrolein oxide (MVKOO and MACROO). These unsaturated sCIs have significant barriers to internal interconversion due to the conjugated nature of the C=C-C=O-O functional group. These conformers can then be subdivided as *syn*- or *anti*- conformers and further as *trans*- and *cis*- isomers, depending on the dihedral angle between the C=C bond and the COO group. Examples can be seen of this in this chapter with **sCIs 13** & **17** classified as *syn* and *anti* conformers of each other, and **sCIs 15** & **16** as *trans*- and *cis*- isomers of each other. These 8 different sCIs are chemically distinct and their labels are in Figure 4.14 below. Some of these sCIs were synthesised and identified experimentally by Barber *et al.*[376] **sCI 1** is also an isoprene derived sCI, but its reaction with MeOH has already been explored.

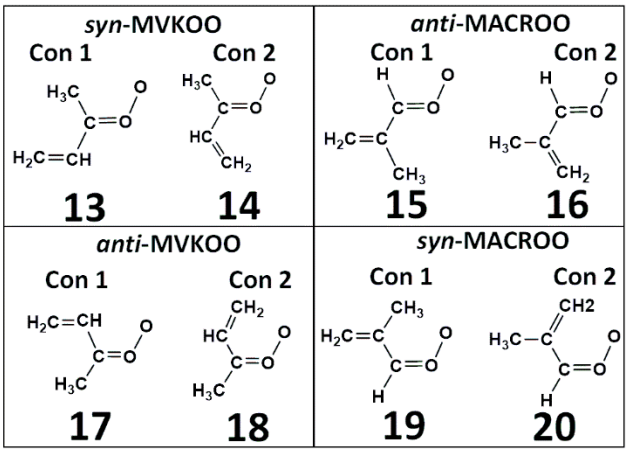

*Figure 4.14: Isoprene derived MVKOO and MACROO studied in this section, referred to as **sCIs 13—20**.*

4.5.1 MeOH reactions with sCIs 13—16: The Impact of unsaturated substituents in the *anti* position

As seen previously, bulky *syn*-CH_3 groups in **sCIs 13** & **14** restrict access to the COO group and stabilise the COO group, lowering the reactivity. This increased stabilisation of the COO group is caused by increased *H-bonding* interactions between *syn*-α-H atoms with the terminal O. As observed in Figure 4.15a, this *syn*-CH_3 stabilisation contributes to the high energy barriers and therefore the low k_{TST} values (4.04×10^{-18} & 3.66×10^{-17} $cm^3\ s^{-1}$). Also seen in Figure 4.15a, is that the *cis* orientation of **sCI 14** places the electron rich COO and $C{=}CH_2$ groups in close proximity, inducing a steric repulsion. This increases the energy for **sCI 14** (+ 6.6 kJ mol^{-1}). However, the structural movement of the sCI during the TS_{AAAH} 1 &

TS_{AAAH} 2 mechanisms involves the COO and C=CH_2 groups rotating away from each other, lowering the local repulsive forces and thereby the energy of TS_{AAAH} barriers. The reduced stability of **sCI 14** and the reduction of localised COO — C=CH_2 repulsion during the reaction mechanism may explain that $k_{sCI\ 13} < k_{sCI\ 14}$. Whilst MeOH reactions with **sCIs 13** & **14** have competing VHP side reactions, these have a small impact ($\Gamma_{VHP} < 0.01$) and are mainly explored in the appendix.

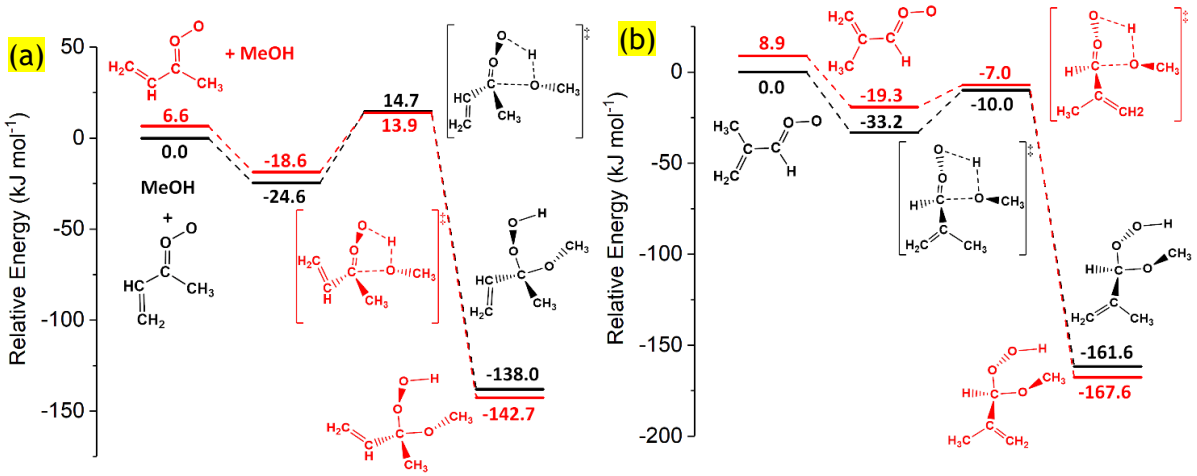

*Figure 4.15: Potential Energy Surfaces of MeOH + **sCI 13** (black) & **sCI 14** (red) (Figure 4.15a) reactions and MeOH + **sCI 15** (black) & **sCI 16** (red) reactions (Figure 4.15b). Energies in Figure 4.15a are relative to raw **sCI 13** + MeOH and Energies in Figure 4.15b are relative to raw **sCI 15** + MeOH.*

Because **sCIs 15** & **16** don't have bulky *syn*-CH_3 groups, they have a much higher reactivity than **sCIs 13** & **14**. The large k_{TST} values for MeOH + **sCIs 15** & **16** (1.61 & 5.10 × 10^{-13} cm^3 s^{-1}) follow the trend seen in MeOH + **sCIs 3** & **12**, where alkyl groups in the *anti* position causes an inductive impact on the COO group. Another area of commonality is that **sCIs 15** & **16** exhibit the same COO and C=CH_2 repulsion seen for **sCIs 13** & **14**, shown by the 8.9 kJ mol^{-1} higher energy of **sCI 16**. **sCI 16** also sees the two groups rotate away from each other through the H_2C=C-C=O dihedral rotation during the TS_{AAAH} 1 & TS_{AAAH} 2 reaction mechanisms. This is leads to a reduction in the barrier heights shown in Figure 4.15b. This seems to be a common factor for sCIs with conjugated unsaturated substituents.

In summary, the main reasons for the higher reactivity for **sCIs 15** & **16** are the inductive *anti*-alkyl groups and the reductive effect of *syn*-CH_3 stabilisation on **sCIs 13** & **14**. A unique trend observed here is that $k_{sCI\ 15} < k_{sCI\ 16}$ and $k_{sCI\ 13} < k_{sCI\ 14}$, caused by H_2C=C-C=O dihedral rotation within the TS_{AAAH} reaction mechanism removing *COO —C=CH_2* repulsion found in **sCIs 14** & **16**. This trend in reactivity $k_{sCI\ 13} < k_{sCI\ 14} << k_{sCI\ 15} < k_{sCI\ 16}$ is consistent with sCI + H_2O & $(H_2O)_2$ work by Anglada *et al.*[195,293]

4.5.2 MeOH reactions with sCIs 17—20: The Impact of unsaturated substituents in the *syn* position

Whereas the common attribute of **sCIs 13—16** was the unsaturated group in the *anti* position, **sCIs 17—20** have that unsaturated group in the *syn* position. Due to the steric hinderance caused by *syn* alkyl groups these sCIs have a lower range of k_{MeOH} values (10^{-18} — 10^{-15} cm^3 s^{-1}). Much like **sCIs 13—16**, the absolute k_{MeOH} value for each sCI is dependent of on whether the *anti* position also has an alkyl substituent and whether the unsaturated group is in the *cis*/*trans* orientation. However, the *cis*/*trans* orientation of the unsaturated group produces unusual trends in this reaction series, where the *cis* conformers, **sCIs 18** & **20**, are lower in energy than their *trans* conformer equivalents, **sCIs 17** & **19**, shown in Figure 4.16.

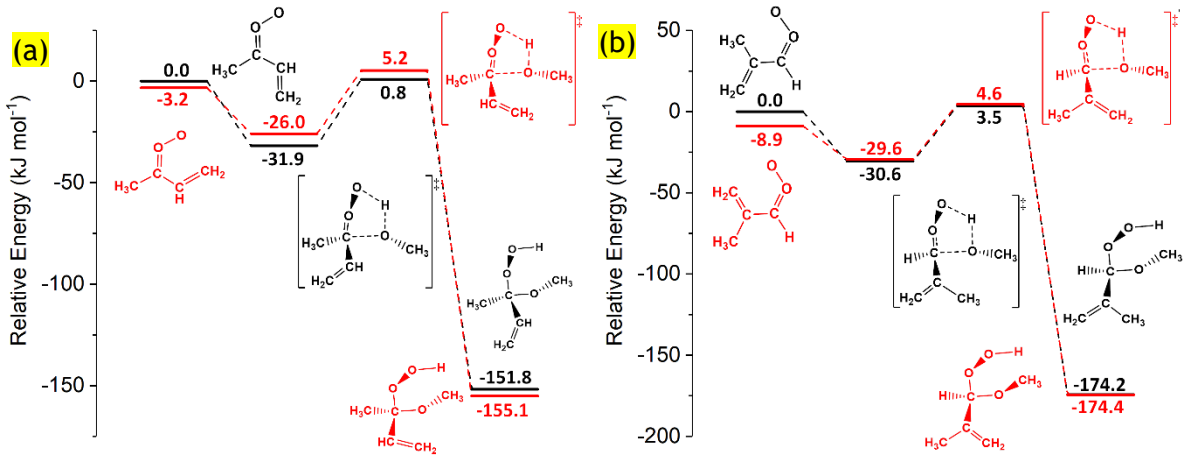

*Figure 4.16: MeOH + sCIs 17 (black) & 18 (red) (Figure 4.16a) reactions and MeOH + sCIs 19 (black) & 20(red) (Figure 4.16b) using only TS_{AAAH} pathways. Energies in Figure 4.16a are relative to raw **sCI 17** + MeOH and energies in Figure 4.16b are relative to raw **sCI 19** + MeOH.*

In **sCIs 18** & **20**, the *cis*-C=CH_2 group is *syn*- to the terminal oxygen of the sCI, which produces a circular structure with a set of overlapping orbitals that lowers the overall energy. This is in contrast to **sCIs 14** & **16**, which do not observe the same overlapping orbitals and the COO and C=CH_2 repulsion, increases the energy of the system. These environments for **sCIs 18** & **20**, also possess 1 pair of π-electrons from the *cis*-C=C bond, 1 pair from the C=O bond and one of the two pairs of π-electrons from the terminal oxygen. This produces the right shape and the right number of electrons (2n+2) required for an aromatic ring, but as the ring is incomplete, this is referred to as a pseudo-aromatic ring. This *pseudo-aromatic ring stabilisation* leads to **sCIs 18** & **20** having a comparably low energy compared to their **sCIs 17** & **19** counterparts (Figure 4.16).

This additional *pseudo-aromatic ring stabilisation* seen in **sCI 18** + MeOH, also leads to a increase in the relative TS_{AAAH} 1 barrier height of ~8 kJ mol^{-1}, as the H_2C=C-C=O dihedral

rotation within the reaction mechanism involves breaking **sCI 18**'s pseudo-aromaticity. This leads to a k_{TST} for **sCI 18** + MeOH significantly smaller (3.75×10^{-17} cm^3 s^{-1}) than that of **sCI 17** (1.19×10^{-15} cm^3 s^{-1}). This *pseudo-aromatic ring stabilisation* appears to have a similar but slightly larger effect for **sCI 20** + MeOH, giving rise to a smaller k_{TST} (4.81×10^{-18} cm^3 s^{-1}) than **sCI 19** (3.75×10^{-16} cm^3 s^{-1}). This pattern of $k_{sCI\ 18} < k_{sCI\ 17}$ and $k_{sCI\ 20} < k_{sCI\ 19}$ continues in the Anglada *et* Sole theoretical study of sCI + H_2O & $(H_2O)_2$ reactions, but differences in k_{TST} are less pronounced.[293]

One last trend seen in the Anglada *et* Sole study of **sCIs 17—20** + H_2O & $(H_2O)_2$, was that **sCIs 17** is more reactive than **sCI 19**, and **sCI 18** is more reactive than **sCI 20**, due to the inductive impact of the *anti*-CH_3 substituents of **sCIs 17** & **18**.[293] However, here it is observed that the reductive impact of the *pseudo-aromatic ring stabilisation* seems to be greater than that of the inductive impact from *anti*-CH_3 substituents.

4.5.3 Molecular Orbital Analysis of *Pseudo-Aromatic Ring Stabilisation*

The results from the molecular orbital (MO) analysis of both **sCIs 17—20** with their respective TS_{AAAH} structures, in this section, indicates that the orientation of the unsaturated >C=C< group with respect to the carbonyl oxide group causes this reduced reactivity for **sCIs 18** & **20**. The highest occupied molecular orbital (HOMO) of **sCIs 17** & **19**, displayed in Figure 4.17, has a significant portion of π-bonding character on both the carbonyl oxide and the >C=C< group. On the other hand, the second-highest occupied molecular orbital (HOMO-1) features instead has a significant portion of both σ-character on the central carbon atom and some $\pi*$-character located on the two oxygen atoms. However, in the π-bonding MOs for **sCIs 18** & **20**, there is an orbital overlap between the π-elements on the terminal oxygen and the >C=C< group, which then stabilises the overall structure and demotes this π-bonding HOMO to the HOMO-1 position.

Furthermore, the orbital with a σ-component is promoted from the HOMO-1 position in sCI **17** to the HOMO position in sCI **18**, without any significant increase in overall orbital energy (see Figure 4.17). This lack of an energy difference between the two σ-bonding MOs, and the large energy drop (10.2 kJ mol^{-1}) seen between the *trans*-orientated π-bonding MO in sCI **17** and the *cis*-orientated π-bonding MO in sCI **18** provides further evidence that it is the π-bonding overlap that stabilises the sCI **18** structure. This overlap in the *cis*-orientated π-orbitals also causes the π-bonding MO to drop in energy between **sCIs 19** & **20** (-24.2 kJ mol^{-1}), demoting the **sCI 19** HOMO to the HOMO-1 position in **sCI 20**.

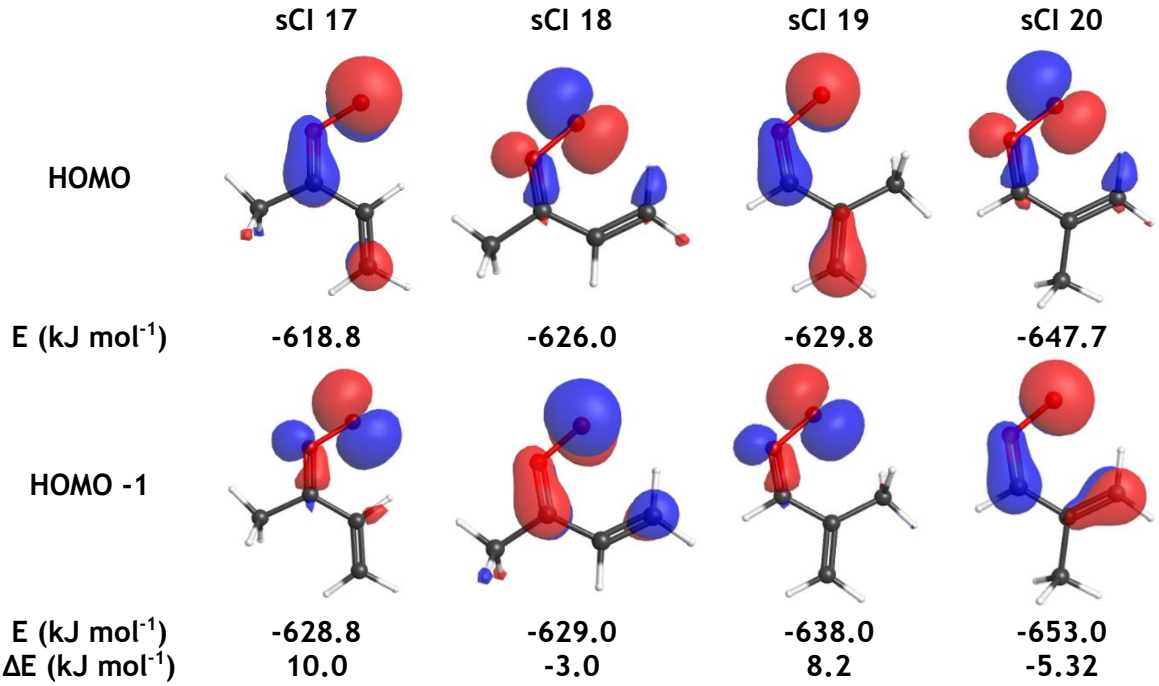

*Figure 4.17: The configurations and relative energies of the HOMO and HOMO-1 for **sCIs 17—20** displayed using the WebMO software.*

However, this lowering of the energy of π-bonding MOs in **sCIs 18** & **20** and the subsequent inversions of the HOMO and HOMO-1 structures, are not repeated for the TS_{AAAH} structures. **sCIs 17—20** all have similar HOMO configurations and HOMO-1 configurations for all TS_{AAAH} 1 structures (see Figure 4.18), which implies that the respective TS_{AAAH} 1 energies for **sCIs 17** & **19**, will be similar to that of **sCIs 18** & **20**, in absolute terms. The fact that the *cis*-orientated π-bonding MOs lower the energy in the **sCIs 18** & **20** reactants but not their TS_{AAAH} 1 structures largely explains why the k_{THEO} values for the *cis*-orientated **sCIs 18** & **20** + MeOH reactions are lower than that for **sCIs 17** & **19** + MeOH.

This π-orbital overlap is thought by the author to be favourable because the orientation of the >C=C< bond in the *syn*-group, combined with the carbonyl oxide group, form a pseudo-ring with the 2n+2 number of electrons that allows aromatic stabilisation. This reduction in reactivity for **sCIs 18** & **20**, caused by the *pseudo-aromatic ring stabilisation*, is only known to occur for reactions across the carbonyl oxide moiety, such as the TS_{AAAH} in sCI + MeOH reactions or TS_{HHP} in sCI + H_2O reactions. This study does not explore this effect on either the self-reaction of **sCIs 17** & **18**, or reaction across the space between the sCI terminal O and the *β*-carbon of the C=C group, referred to as a vinyl insertion by Yin *et* Takahashi.[418] For the full set of MeOH + **sCIs 13—20** reactions, the MO calculations and the images of the HOMO and HOMO-1, please see Appendix Section 2.5.

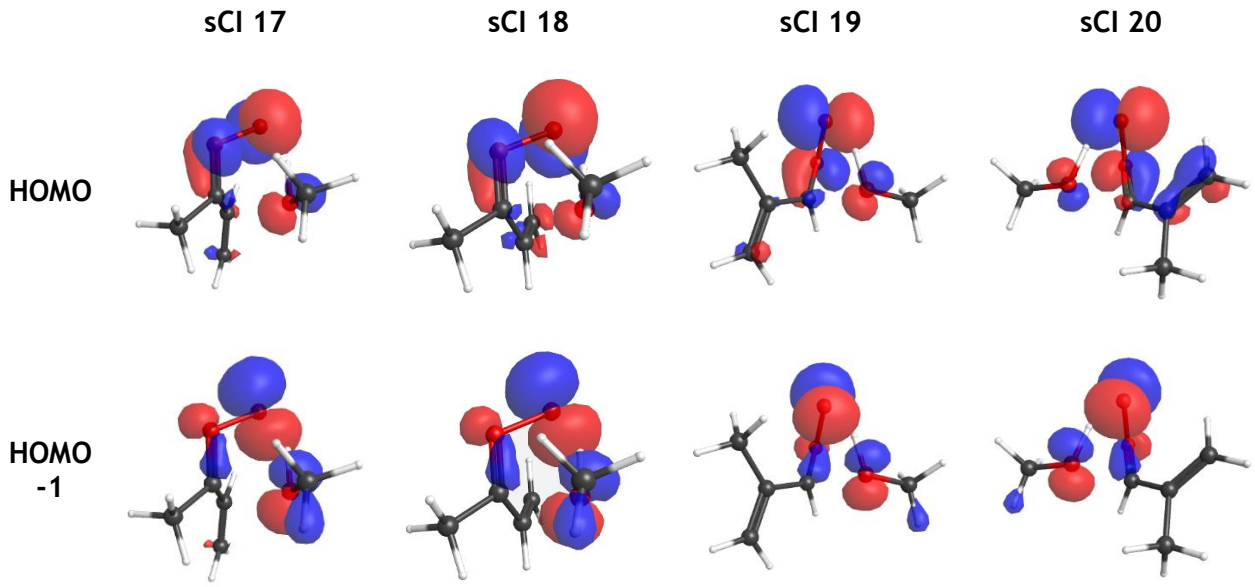

Figure 4.18: The configurations of the HOMO and HOMO-1 for MeOH + sCIs 17-20 TS_{AAAH} 1 structures displayed using the WebMO software.

One additional observation is that both π-bonding MO diagrams of **sCIs 17** & **18** in Figure 4.17, and the HOMO diagrams of the TS_{AAAH} 1 in Figure 4.18, show the sCI to have small electronic contributions from the α-H atoms in the *anti*-CH_3 substituents. This contribution by these α-H atoms provides some confirmation to the theory mentioned prior, that these α-H atoms exhibit a hyperconjugative effect on the carbonyl oxide group of the sCI. This hyperconjugative impact on **sCIs 17** & **18** appears to lower the energy of the TS barrier and produce a larger k_{TST} values for **sCIs 17** & **18** than **sCIs 19** & **20**, respectively.

4.6 The Effect of Eckart Tunnelling on sCI to Vinyl Hydroperoxide (VHP) Channels

A secondary competing reaction to AAAH formation for the reaction for sCIs with a *syn*-CH_3 group is referred to as MeOH—"catalysed" VHP formation, where the methanol promotes a 1,4-H transfer, or the VHP channel.[195] The only sCIs in this study which have accessible VHP pathways are **sCIs 2**, **4**, **13** & **14**, due to their *syn*-CH_3 group. The height of the TS_{VHP} classical barrier relative to the TS_{AAAH} barrier would usually exclude this channel as a viable reaction pathway worthy of study, but the impact of quantum tunnelling has made VHP channels more competitive in the similar sCI + H_2O reactions.[195,293,418]

Quantum tunnelling is a quantum-mechanical phenomenon, where the mechanism between reactant(s) and product(s) involves low mass atom motion. Those low mass atoms in the reactant can "tunnel" through the classical energy reaction barriers.[419] This facilitates the formation of the product and amplifies the impact of such pathways.[419] If applied to hydrogen atoms, this is referred to as H-tunnelling. To some extent, the impact

of H-tunnelling can be measured experimentally, by substituting the key H atoms with deuterium (^2H), and observing alterations in kinetic parameters (the kinetic isotope effect).[51] As tunnelling relies on "low mass atom motion", by doubling the mass of the H atoms, any impact of tunnelling, if present will reduce significantly. For example, Orr-Ewing and co-workers replaced key hydrogens with deuterium in the **sCI 4** + MeOH reaction and measured the impact of tunnelling by seeing the change in k_{EXP} at various temperatures.[51]

The impact of tunnelling on these channels, when investigated computationally, depends on the type of method used to derive the tunnelling constant and the type of movement involved in the reaction mechanism. The three types of tunnelling examined in this study are: Wigner factor (κ_{Wigner}), asymmetric Eckart tunnelling factor (κ_{Eckart}), and higher level *semiclassical on-the-fly instanton* factors. The methods for calculating these tunnelling factors are found in Method section 2.6. As the main movement in the VHP reaction mechanism involves the two *low-mass* H atoms in simultaneous motion, without significant movement elsewhere in the TS_{VHP} structure, tunnelling is expected to have a significant impact. In contrast, the TS_{AAAH} reaction mechanism has significant large atom movement, in particular of the larger central C atom in the sCI and O in the alcohol, which would significantly reduce tunnelling for this reaction.

The reduced impact of tunnelling on TS_{AAAH} channels is shown by the small range of κ_{Eckart} values for all TS_{AAAH} channels, ranging from 1 to 2.44. This is in contrast to both the highest κ_{Eckart} value for the TS_{VHP} channel in this chapter, ~95, and the highest κ_{Eckart} value sCI reactions + $(H_2O)_2$, ~100, in the Anglada *et* Sole study, both of which are greater an order of magnitude than the κ_{Eckart} for the TS_{AAAH} channels. This large disparity between κ_{Eckart} values is important in determining the significance of the VHP pathway. Therefore verifying the reliability of the κ_{Eckart} values is important. To do this, the following section involves both a comparative analysis of κ_{Eckart} values with other tunnelling methods and reviews the impact of both the κ_{Eckart} values and the VHP channel overall.

4.6.1 Application of Various Tunnelling Factors to Unimolecular Decomposition of sCIs 2 & 14

The *unimolecular* decomposition reaction of **sCIs 2** & **14** to a VHP, via *1,4-alkyl-H-migration*, seen in Figure 4.19, is used as a case study to compare the accuracy of the κ_{Eckart} factor with other types of tunnelling factors and their subsequent impact on the unimolecular rate constant (k_{UNI}). These reactions are selected as the case studies because: they involve a small intramolecular reaction, therefore lowering computational

cost of calculation; experimental analysis of this reaction is plentiful; due to the facile similarities between the unimolecular and bimolecular VHP formation mechanisms, the same tunnelling treatment can be applied.[182]

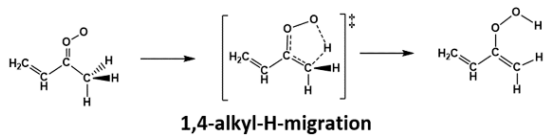

*Figure 4.19: Unimolecular reaction of **sCI 14** to produce a vinyl hydroperoxide.*

As mentioned earlier in this chapter, examination of the temperature dependence of various sCI + alcohol reactions has been performed, including on the **sCI 4** + MeOH reaction. This **sCI 4** + MeOH reaction involves significant contributions from the VHP pathway, and therefore the κ_{Eckart} constant, over a significant range of temperatures (200 — 350 K). To verify that the computed κ_{Eckart} constant is suitable for this purpose, a comparative analysis of these tunnelling constants on k_{UNI} of **sCIs 2** & **14** over a range of temperatures is carried out (Table 4.3).

*Table 4.3: A comparison tunnelling constants determined using the Wigner factor (κ_{Wigner}), asymmetric Eckart tunnelling factor (κ_{Eckart}), and semiclassical on-the-fly instanton methods for the unimolecular decomposition of **sCIs 2** & **14***

T (K)		sCI 2				sCI 14		
		κ_{Wigner}	κ_{ECKART}	instanton method DFT (N = 256)	instanton method CCSD(T) (N = 16)	κ_{Wigner}	κ_{ECKART}	instanton method DFT (N = 256)
160	κ	9.76	2.46×10^9	8.12×10^8	1.52×10^{10}	9.93	9.12×10^9	1.08×10^9
	k_{TST}	4.32×10^{-10}	0.109	0.0360	0.673	1.97×10^{-10}	0.01811	0.00214
260	κ	4.32	489.9	284.55	948.4	4.38	690.3	317.53
	k_{TST}	0.121	13.70	7.96	26.53	0.0167	2.63	1.21
360	κ	2.73	10.53	13.62	21.35	2.76	11.49	15.93
	k_{TST}	615.53	2374	3071	4814	139.24	579.66	803.65

The κ_{ECKART} values for **sCI 2** display a high degree of corroboration with the higher-level calculations across a range of temperatures, showing a higher accuracy than the simplistic κ_{Wigner}. As an example, the κ_{ECKART} value for **sCI 2** at 160K appears really quite accurate as it falls between the instanton tunnelling constants (~10^9-10^{10}), and leads to similar k_{UNI} values (~0.1 s^{-1}). The κ_{ECKART} values at 260 K also exhibit a similar consistency with κ_{ECKART} and k_{UNI} values falling between the two instanton tunnelling constants. Even while the κ_{ECKART} values at 360 K do not fall between the two instanton tunnelling values, it does produce a much better results than the simplistic κ_{Wigner}, which is inaccurate across all three temperatures.

In the tunnelling constants of the unimolecular decomposition of **sCI 14** there is a high degree of proximity between the κ_{ECKART} and the instanton method, showing the same level

of consistency seen on the tunnelling constants of **sCI 2**. All values of κ_{ECKART} for **sCIs 14** are found to be significantly within one order of magnitude tunnelling, even at higher temperatures. The most accurate κ_{ECKART}, compared to the instanton methods, are produced close to room temperature but there is a high degree of accuracy of κ_{Eckart} value across all temperatures measured for both **sCIs 2** & **14**.

To test the accuracy of the κ_{Eckart} values, they were also used to determine the theoretical k_{UNI} of **sCIs 2**, **4**, **13** & **14**, compared to the raw k_{UNI}, the Wigner corrected k_{UNI}, and the k_{EXP} (see Table 4.4). Of the 3 k_{UNI} values, the Eckart corrected k_{UNI} consistently demonstrated the greatest consistency with the k_{EXP} values.[182,376]

*Table 4.4: Evaluation of the unimolecular sCI-to-VHP reaction for **sCIs 2**, **4**, **13** & **14**, by comparing literature experimental rate constants (k_{EXP}), with the raw, Wigner, Eckart corrected rate constants (k_{THEO}; $k_{THEO}\,\kappa_{Wigner}$] & k_{THEO} [κ_{Eckart}])*

	sCI2	sCI4	sCI 13	sCI 14
k_{THEO} (s^{-1})	1.762	7.475	0.312	0.301
κ_{Wigner}	3.524	3.437	3.577	3.572
k_{THEO} [κ_{Wigner}] (s^{-1})	6.209	25.69	1.115	1.077
κ_{Eckart}	58.98	45.47	72.30	71.77
k_{THEO} [κ_{Eckart}] (s^{-1})	103.9	339.9	22.5	21.6
k_{EXP} (s^{-1})	136	478	33	50
ref	182	182	376	182

In summary, the κ_{ECKART} values corroborate well with the more in depth *semiclassical on-the-fly instanton* correction values and are much more accurate than the simplistic κ_{Wigner} correction. Comparisons with literature studies also shows that the Eckart-corrected k_{UNI} values are accurate in predicting experimental k_{UNI} values of **sCIs 2**, **4**, **13** & **14**. Each method has benefits and costs. For example, the *Wigner function* (κ_{Wigner}) requires very little input other than the imaginary frequency of the transition state and the temperature, giving it very little computational cost. The instanton methods are accurate but require significant computational power for small calculations and so scalability is difficult. On the other hand, the κ_{Eckart} correction is reliable has been used in various studies involving sCI bimolecular chemistry and requires a small amount of computational power, and so has been adopted as the tunnelling correction throughout this thesis. However it is found in appendix section 2.8 that the VHP channel has very little role, even with the impact of κ_{ECKART} functions.

4.7 Overall Analysis of Trends Using Taxonomic Classification

One of the purposes of this thesis was to aid in the classification of these sCIs into taxonomic groups by common characteristics, such as the carbonyl oxide moiety; *syn*/*anti* conformeric forms; or *cis*/*trans* orientation for unsaturated sCIs. In this section, the theoretical results from sCI + alcohol reactions will be compared by their possible taxonomic classification. Taxonomic classification of *sCIs* are the main focus of this section because, while a change reactivity does result from altering the alcohol -R_3 group (k_{MeOH} < k_{iPrOH} < k_{EtOH}), it results in relatively small changes in reactivity (< 10^1 cm^3 s^{-1}).

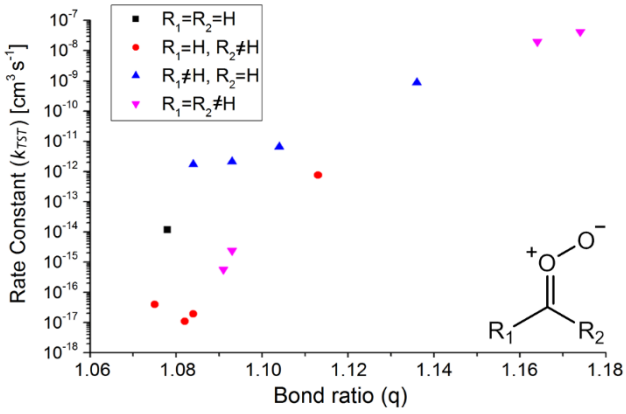

Figure 4.20: Relationship between OO and CO bond lengths as a measure of the carbonyl oxide moiety (q) and sCI + MeOH rate constant (k_{TST}). The plot demonstrates the correlation between q, an approximate measure of the zwitterionic character of the sCI, and rate constant.

On the other hand, altering the sCI substituent groups has been well documented to change the electronic character of the COO functional group and therefore the sCI reactivity. The electronic character of the COO moiety is well understood to be mixed between zwitterionic and biradical resonance structures and this can be represented by the R_{OO}/R_{CO} bond ratio (*q*) of the carbonyl oxide group. sCIs with greater biradical character leads to lower *q* values because the more saturated C-O bond lengthens and the corresponding greater electropositivity in the central O causes the O-O to shorten. Whereas, a more zwitterionic sCI moiety not only has a shorter C-O bond due to its more unsaturated nature, but the O-O bond subsequently lengthens. The greater C=O dipole seen in zwitterionic sCIs, makes the electropositive central C atom more vulnerable to attack by the alcohol's electronegative O leading to larger k_{TST} values, as seen in Figure 4.20.

As noted throughout the study *anti*-sCI reactivity (seen in blue) exceeds that of its *syn* equivalents (see in red). As disubstituted sCIs are affected by both the reductive impacts of *syn*-substituents and the inductive impacts of *anti*-substituents, they are grouped separately from either. However, **sCI 1**, or CH_2OO, is also grouped separately from all three sets because it uniquely has none of the inductive or reductive impacts of sCI

substitution. Throughout all four of these groups, Figure 4.20 shows a positive correlation between the k_{MeOH} values and a greater zwitterionic character of the sCI. One trend observed in this graph is that sCIs with greater electronegative substituents produce larger k_{TST} values, as they draw electron density away from the central C and therefore increase zwitterionic character. This is observed in the trend of $k_{(CH_3)_2COO} < k_{CCl_2OO} \ll k_{CF_2OO}$, although the particularly low $k_{(CH_3)_2COO}$ maybe due to the *H-bonding* effect caused by the presence of *syn*-α-H atoms.

For visual clarity, not all sCIs explored in this chapter are included in Figure 4.20, for example those with fluorinated *syn*-/*anti*-CH_3 groups. Whereas the hyperconjugative α-H atoms in the *anti*-CH_3 group destabilise the **sCI 3**, the α-F atoms in **sCIs 24** show no such hyperconjugation, reflected in the lower reactivity for **sCIs 24**. Conversely the α-F atoms had a destabilising impact in **sCI 23** and compared to the α-H atoms in **sCIs 2**, **4**, **13** & **14**. This is due to α-H atoms forming stabilising permanent dipole—induced dipole bonds with the terminal O, whereas the terminal O is repulsed by electronegative α-F atoms. The CF_3 groups in **sCIs 23** & **24** do follow the traditional pattern such that the *anti* conformer is more reactive, but they neutralise the extra attributes seen for CH_3 substituents, making this difference less pronounced. This may require a new taxonomic group for similar substituents, especially considering that the electronegative nature of a -CF_3 group may decrease the length of the C-O bond. By reversing the trend of increasing reactivity with *q* ratio, **sCIs 23** & **24** may lead to a more convoluted correlation between *q* and reactivity.

Another group that may require their own taxonomic classification would be sCIs with unsaturated substituents, explored prior in section 4.5, because the impact of the *cis*/*trans* orientation of the C=C bond reverses when in either the *syn*- or *anti*-position. This could potentially lead to 4 separate sCI taxonomic groups. Torsional strain caused by either cyclic constraints seen with **sCI 21**, or electronic repulsion, such as with **sCIs 25** & **26** can also contribute to an increased reactivity without increase in *q* ratio of the COO group. This distorts the trend in Figure 4.20 and may also require a new taxonomic classification.

4.8 Atmospheric implications

The relative local atmospheric impact of a particular reaction can be measured using the *Calculated effective first-order rate constant* (k_{eff}), which takes into account both the individual rate constant (k_{THEO}) and the local concentration of the co-reactant.[184,372] In this study, the relatively high atmospheric abundance of MeOH, EtOH & iPrOH (34.1, 176.3 & 44.2 ppbv) measured in San Paulo, Brazil, due to evaporation of vehicular biofuel, is used to calculate the k_{eff} value.[383] This higher abundance provides a greater understanding of localised atmospheric impact.

Table 4.5: Calculated effective first-order rate constant for sCIs with a Range of Tropospheric Constituents. $k_{EFF} = k \times$ [co-reactant]. [184,372]

CI	Co-reactant	[Co-reactant] (molec/cm^3)	k_{THEO} (cm^3 molec.$^{-1}$ s^{-1})	k_{eff} (th.) (s^{-1})	k_{exp} (cm^3 molec.$^{-1}$ s^{-1})	k_{eff} (ex.) (s^{-1})	References
1	MeOH	8.4×10^{11}	1.2×10^{-14}	0.0101	1.4×10^{-13}	0.12	This work [344]
	EtOH	4.3×10^{12}	6.2×10^{-14}	0.27	2.3×10^{-13}	0.99	This work [344]
	iPrOH	1.1×10^{12}	1.2×10^{-14}	0.013	1.9×10^{-13}	0.21	This work [344]
	H_2O	6.2×10^{17}	3.5×10^{-15}	2.2×10^{3}	1.3×10^{-15}	806	[136,144,420]
	$(H_2O)_2$	4.0×10^{14}	2.3×10^{-10}	9.3×10^{4}	7.5×10^{-12}	3.0×10^{3}	[144,184,420]
	O_3	6.0×10^{11}	4.0×10^{-13}	0.24	6.7×10^{-14}	0.040	[421-423]
	SO_2	8.7×10^{10}	5.1×10^{-10}	44.4	3.9×10^{-11}	3.4	[142,191,424]
	CO	5.1×10^{13}	2.0×10^{-21}	1.0×10^{-7}	Unknown	Unknown	[142,402]
	NO_2	7.0×10^{14}	4.4×10^{-12}	3.1×10^{3}	1.5×10^{-12}	1.1×10^{3}	[142,425]
	CO_2	1.0×10^{16}	3.5×10^{-19}	3.5×10^{-3}	$<10^{-17}$	<0.2	[372,426]
	HNO_3	1.1×10^{11}	5.1×10^{-10}	57	5.4×10^{-10}	60	[272,307,427]
	HCOOH	3.1×10^{11}	1.0×10^{-10}	31	1.1×10^{-10}	2.7	[428,429]
	CH_3COOH	3.9×10^{10}	Unknown	Unknown	1.3×10^{-10}	16	[428,430]
	HCl	3.2×10^{10}	4.1×10^{-11}	1.3	4.6×10^{-11}	1.5	[272,431]
2	MeOH	8.4×10^{11}	1.9×10^{-17}	1.6×10^{-5}	Unknown	Unknown	This work
	$(H_2O)_2$	4.0×10^{14}	1.4×10^{-12}	278	Unknown	Unknown	[144,184]
	SO_2	8.7×10^{10}	Unknown	Unknown	2.4×10^{-11}	2.1	[141]
	[Thermal decomposition]					166	[136]
	HCOOH	3.1×10^{11}	Unknown	Unknown	2.5×10^{-10}	78	[428]
	CH_3COOH	3.9×10^{10}	Unknown	Unknown	1.7×10^{-10}	6.7	[428]
3	MeOH	8.4×10^{11}	2.1×10^{-12}	1.8	5×10^{-12}	4.2	This work [402]
	$(H_2O)_2$	4.0×10^{14}	1.1×10^{-09}	4.2×10^{5}	4.4×10^{-11}	1.8×10^{4}	[144,184,411]
	SO_2	8.7×10^{10}	Unknown	Unknown	6.7×10^{-11}	5.8	[141]
	HCOOH	3.1×10^{11}	Unknown	Unknown	5.0×10^{-10}	160	[428]
	CH_3COOH	3.9×10^{10}	Unknown	Unknown	2.5×10^{-10}	9.9	[428]
4	MeOH	8.4×10^{11}	5.7×10^{-16}	4.7×10^{-4}	4.3×10^{-14}	0.036	This work [51]
	$(H_2O)_2$	4.0×10^{14}	7.0×10^{-13}	280	$<1.3 \times 10^{-13}$	<52	[144,184]
	SO_2	8.7×10^{10}	4.0×10^{-10}	34	1.3×10^{-11}	1.1	[184,308]
	HCOOH	3.1×10^{11}	Unknown	Unknown	3.1×10^{-10}	97	[320]
	CH_3COOH	3.9×10^{10}	Unknown	Unknown	3.1×10^{-10}	12	[320]
15	MeOH	1.7×10^{12}	1.6×10^{-13}	0.27	Unknown	Unknown	This work
	H_2O	6.2×10^{17}	2.9×10^{-15}	1.8×10^{3}	Unknown	Unknown	[144,184]
	$(H_2O)_2$	4.0×10^{14}	3.3×10^{-12}	1.3×10^{3}	Unknown	Unknown	[144,184]
16	MeOH	1.7×10^{12}	5.1×10^{-13}	0.87	Unknown	Unknown	This work
	H_2O	6.2×10^{17}	1.7×10^{-14}	1.1×10^{4}			
	$(H_2O)_2$	4.0×10^{14}	2.2×10^{-11}	8.8×10^{3}	Unknown	Unknown	[2,5]

[a] *Where available, computed rate constants [k_{eff}(th)] with experimental values [k_{eff}(ex)]. Tropospheric concentrations and experimental rate constants were taken from the references shown in the final column.*

[b] *Reaction rate constants based upon previously reported ΔG_{TS} all exceed the computed gas collision limit, and so only this collision limit is reported here.*

In Osaka, Japan, a typical urban environment, concentrations of MeOH, EtOH & iPrOH from biofuel use are very low (~5-10 ppbv).[383] This means that compared to other tropospheric pollutants such as SO_2/NO_2, sCI + alcohol reactions are overall less competitive, in most urban environments. A study by Khan *et al.* compared the ability of sCIs to act as a sink for common atmospheric species compared to OH radicals, a standard sink for many typical atmospheric species.[111] They suggest that whilst sCIs are significant sinks for some common gases, including formic acid and hydrochloric acid, OH radicals were far more reactive with alcohols under these atmospheric concentrations. The more localised alcohol abundances, such as that in San Paulo, Brazil are adopted for this study, to make **sCI 1** + alcohol reactions competitive with such as common tropospheric pollutants in Table 4.5, as O_3, CO and O_3.[111] Due to their prevalence of only naturally occurring sCIs are studied in this section.

While reactions between **sCI 1** and other atmospheric species, including O_3, HCl and CO_2, are less competitive than the reaction with MeOH, all sCI + alcohol reactions are overshadowed by H_2O & $(H_2O)_2$. The MeOH reaction with **sCI 2**, a common *syn*-sCI, has a low k_{TST}, not only relative to other sCIs, but compared to sCI unimolecular decomposition rates and sCI reaction with other common atmospheric species such as SO_2, HCOOH, H_2O & $(H_2O)_2$. This implies that many of the common *syn*-sCIs, such as **sCIs 19** & **20** would be similar, and have minimal impact on tropospheric alcohol concentrations. The MeOH + **sCI 4** reaction sees a similar comparatively low k_{EFF} implying that reactions with other alkyl disubstituted sCIs, such as **sCIs 13**, **14**, **17** & **18**, will also reflect a low atmospheric impact.

The MeOH reactions between *anti*-sCIs, such as **sCI 3** + MeOH, have larger k_{TST} and k_{EXP} values, making them more competitive not just with other minor atmospheric pollutants including SO_2 and organic acids, but to a limited extent H_2O & $(H_2O)_2$. This is also seen in the *anti*-sCIs, **sCIs 15** & **16**, which could be highly reactive with many atmospheric species such as SO_2 and NO_2 as well.[293] As there appears to be little literature research into the bimolecular chemistry of **sCIs 15** & **16**, this work could trigger further exploration of the computational or experimental bimolecular chemistries of these sCIs with other atmospheric toxins.

In this study, the impact of AAAHs produced by this reaction is not explored in great depth. However, due to the increased accuracy this study provides for reactions which are dominant sources for AAAH, it should be very helpful for atmospheric modelling purposes. Previous analysis, such as the study produced by Orr-Ewing and co-workers, have even emphasized that in rainforests sCI + alcohol reactions can contribute to ~30 Gg yr^{-1} of

AAAHs. This may also be reflected in urban biofuel rich environments, as one of the top sources of AAAHs in an urban environment: an area worthy of future exploration.

4.9 Further work

There are several areas this work could be expanded including: that the sCIs could be better classified into taxonomic groups and a general formula could be applied to other more complex sCIs + alcohol reactions. This could be similar to the analysis done for the ozonolysis of alkenes in Chapter 6 or in the structural-activity analysis done by McGillen *et al.*.[118,155] These taxonomic classifications could be applied to long chain sCIs like in the $CH_3(CH_2)_{11}CHOO$ + MeOH or iPrOH reactions studied by Tobias *et* Ziemann, or a long chain alcohol.[386] Other applications of the k_{TST} values from these sCI + alcohol reactions, or even the taxonomic classification, would be to fully apply these classifications in atmospheric models, providing greater insights than is possible from k_{eff} values alone.

Other sCIs could also be studied, such as those derived from methyl vinyl ketone (MVK) and methacrolein (MACR), which are both alkenes to have been found to be prevalent in the atmosphere, as isoprene ozonolysis byproducts.[182,355] Due to the rotation of the O=C-C=O dihedral bond, *syn*- & *anti*-$CH_3C(O)$-CHOO each have 2 conformeric forms, and both are produced from O_3 + MVK (shown in section 3.3.1). Ozonolysis of MACR also produces a similar sCIs, *syn*- & *anti*-OCH-$C(CH_3)$OO, both of which also have two conformers, due to O=C-C=O dihedral rotation.[355] This would contribute to knowledge about sCI taxonomic groups as these sCIs have aldehyde or ketone substituents.

There are also many other sCI + alcohol reactions that could be tested, targeting reactivity modifiers such as the effect of reducing the number of α-H atoms, with sCIs like *syn*- & *anti*-EtCHOO, iPrCHOO, tBuCHOO & CF_3CF_2CHOO. These would also be useful as they are products of the ozonolysis of important alkenes discussed in Chapter 2. Research could be undertaken to see if *pseudo-aromatic stabilisation effect*, seen for **sCIs 18** & **20**, is evident with other similar sCIs, like CH_2=CHCHOO reported by Yin *et* Takahashi.[418] For sCIs with this *pseudo-aromatic stabilisation effect*, the Yin *et* Takahashi study postulates a highly competitive side reaction with H_2O, *referred to as vinyl insertion*, that could be relevant for some sCI + alcohol reactions.[418] Other alcohols such as phenol or butanol could be included in an even more comprehensive analyses which may include sCI reactions with atmospheric species like NH_3, H_2S, HF, HCl & CH_3SH. The only sCI + CH_3SH reaction studied thus far is the reaction of **sCI 1**, by Li *et al.*, and so an expanded study may be warranted.[432]

4.10 Conclusion

Throughout these sCI + alcohol reactions it is observed that altering the sCI substituent groups alters the sCI + alcohol reaction rate constants by orders of magnitude. On the other hand, the rate constant variation across different alcohols does not exceed one order of magnitude, with the general trend ($k_{MeOH} < k_{iPrOH} < k_{EtOH}$). This means that the composition and the spatial orientation of the sCI substituents are used as the basis for a series of taxonomic groups to describe the sCI + alcohol reaction.

The first two taxonomic sCI groups, *anti*- & *syn*-sCIs, are based on the much larger k_{TST} values for *anti*-sCI reactions with MeOH compared to their analogous *syn* conformers, confirming the "monosubstituted" sCI reactivity trend already well-established in the literature. However, the higher reactivity of **sCI 3** + MeOH over **sCI 24** + MeOH infers that hyperconjugative α-H atoms in the *anti*-position amplifies this higher reactivity. In contrast, the α-H atoms in the *syn* position appear to have a small reductive effect on the **sCI 2** reactivity with MeOH compared with the fluorinated counterpart **sCI 23**.

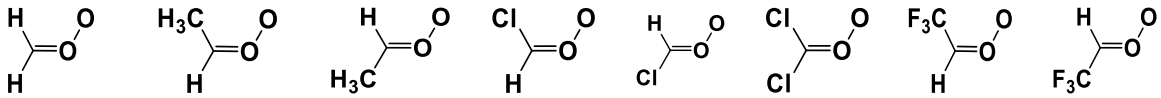

1 **2** **3** **8** **9** **10** **23** **24**

*Figure 4.21: Schematics of the structures of **sCIs 1, 2, 3, 8, 9, 10, 23** & **24**.*

A third viable taxonomic group, "disubstituted" sCIs, have both *anti*- & *syn*- groups of the sCI occupied, such as in **sCI 10**, and these disubstituted sCIs + MeOH reactions often have a k_{TST} value somewhere between the *anti*- & *syn*-sCIs, here **sCIs 8** & **9**. The disubstituted exception to this is **sCI 1**, which should reasonably be treated as a taxonomic group on its own. In this single case the —H substituents lack both inductive impact and steric hinderance to reaction.

sCIs which have at least one —F substituent or a 1,3-dioxolane substituent may also be grouped together, because regardless of the *anti*- or *syn*- positions of the group, these highly electronegative substituents increase the k_{TST} value of the sCI + alcohol reaction, often beyond the dipole-dipole capture limit.

Throughout these groups, the sCI reactivity broadly scales with the bond ratio in the carbonyl oxide group (R_{OO}/R_{CO}), a model of electronic character of the sCI, and this could be used as a modifier within a class to provide precise k_{TST} values. Such nuances in reaction rates would be important in the atmospheric modelling of cities such as Sao Paulo, where alcohols are abundant due to heavy biofuel emissions.[383] However this comprehensive model is also important in modelling sCI + alcohol reactions in biogenic

tropospheric simulations because the primary AAAH product, may be implicated with boreal damage in the rainforests.[111,141,195,293,344,387–391] In conclusion, the effect of sCI substituents on a variety of sCI + alcohol reactions has been comprehensively evaluated, an extended series of taxonomic sCIs groups has been correlated with the k_{TST} values, and that the data shown here may provide an ansatz for the chemical kinetic prediction of previously unknown sCI + alcohol systems.

5.0 Chapter 5: Bimolecular sinks of Criegee intermediates derived from Hydrofluoroolefins.

The aim of this chapter is to investigate the tropospheric bimolecular chemistry of a new range of stabilised Criegee intermediates (sCIs) derived from hydrofluoroolefin (HFO) breakdown, referred to as *HFO-sCIs*. To review the effect of the location and composition of the halogenated substituent groups seen in HFO-sCIs (—F or —CF_3 principally), this chapter features a computational chemistry analysis of HFO-sCI reactions with a significant range of common tropospheric trace gases, including: SO_2, H_2S and HCl. A comparative analysis of the trends in the computational rate constants (k_{THEO}) and product branching ratios (Γ_{THEO}) can be used to determine the impact of factors such as: the *syn* and/or *anti* position of the substituent(s); the CF_3 substituent compared to the more common -CH_3 group; and the effect of the co-reactants on sCI reactivity.

5.1 The Importance of Tropospheric Hydrofluoroolefins and Criegee intermediates derived from them.

Hydrofluoroolefins and hydrochlorofluoroolefins (referred generically HFOs in this chapter) provide an increasingly large market share of refrigerator coolants in the United States of America (USA), China and the European Union (EU) countries, due to tendency of previous generations of refrigerants to deplete the ozone layer and/or to contribute to anthropogenic climate change when emitted.[197–199] Using both the ozone depletion potential (ODP) and the 100-year global warming potential (GWP_{100}), a comparative analysis of the impact of some HFOs and their market competitors is displayed in Table 5.1.

Table 5.1: Comparison of CFCs, HFCs and HFOs as refrigerants in Global Warming Potential over 100 years (GWP_{100}); Ozone Depletion Potential (ODP); atmospheric lifetimes; and HFO-sCIs produced from ozonolysis.

Name	Structure	GWP_{100}	ODP	Lifetime (yr)	HFO-sCIs	*ref*
HFO-1234yf	$CF_3CF{=}CH_2$	4	0	10.5 days	CH_2OO	2,24,224
HCFO-1233zd	*E*-$ClCH{=}CHCF_3$	14	0.0005	26 days	*Syn-/Anti*-CF_3CFOO *Syn-/Anti*-ClCHOO	2,225,226
HFO-1234ze	*E*-$FCH{=}CHCF_3$	<1	0	16.4 days	*Syn-/Anti*-CF_3CHOO *Syn-/Anti*-FCHOO	2,24,227
CFC-11	$CFCl_3$	4660	1	45	*Syn-/Anti*-CF_3CHOO N/A	2,24
CFC-12	CCl_2F_2	10,200	0.82	100	N/A	2
HFC-134a	CH_2FCF_3	3710	0.0013	13.4	N/A	2,216
HFC-245fa	$CHF_2CH_2CF_3$	858	0	7.7	N/A	2,24

The shorter lifetimes and therefore the lower GWP_{100} of prototypical HFOs, like HFO-1234yf (CF_3CFCH_2) and HCFO-1233zd (*E*-CF3CHCHCl), is due to reactions with tropospheric

species such as NO_3 & OH radicals and O_3.[224,226,227,348] The ozonolysis of HFOs (seen in Figure 5.1) was found to result in the HFO derived stabilised Criegee intermediates (HFO-sCIs) in Table 5.1.

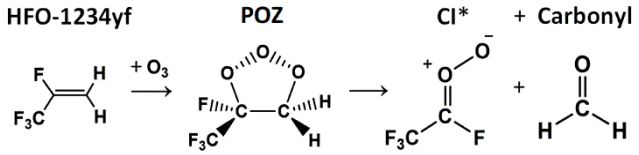

Figure 5.1: Ozonolysis of an example HFO (HFO-1234yf).

The HFO + O_3 reactions are important to this chapter because they form Criegee intermediates, which once collisionally stabilised, may react with other tropospheric species, such as the aldehyde/ketone co-product in Figure 5.1.[224,226,241] While the global abundance of other alkenes, like isoprene, are much higher than that of HFOs, the importance of local urban HFO abundance is demonstrated in environments like Beijing, where tropospheric HFO breakdown by OH radicals and O_3 produces a significant abundance of trifluoroacetic acid (TFA).[199,433-436] This increase in local TFA abundance is known to cause irritation to the respiratory tract, and, due to their common source, TFA is likely to co-locate and produce a significant atmospheric reaction with HFO-sCIs.[199]

HFO-1234yf, HFO-1233zd(*E*), and HFO-1234ze(*E*) produce several HFO-sCIs worth investigating: CH_2OO, FCHOO, ClCHOO, CF_3CHOO and CF_3CFOO. While *syn*- & *anti*-ClCHOO has been interrogated experimentally, to the author's knowledge, of those sCIs identified in Table 5.1, the only HFO-sCI with significant computational *and* experimental literature on its bimolecular chemistry is the exhaustively studied CH_2OO.[182,195,293,437-439] Some computational studies of reactions between *syn*- & *anti*-CF_3CHOO and certain atmospheric species, such as CO_2, H_2 and $CF_3CH{=}CH_2$ are in the literature, but the bimolecular analysis of *syn*- or *anti*-CF_3CFOO has yet to be conducted.[273,305,372] No further calculations of *syn*- & *anti*-FCHOO and *syn*- & *anti*-ClCHOO were investigated in this study, due to an already extensive computational literature.[93,273,274,372]

Figure 5.2 displays the HFO-sCIs interrogated within this thesis chapter, which includes CH_2OO, *syn*-/*anti*-CF_3CHOO and *syn*-/*anti*-CF_3CFOO, referred to using the nomenclature from Chapter 4, as **sCIs 1**, **23—26**. The exhaustive experimental and computational examination of **sCI 1** reactions can provide a point of reference, or *benchmark*, to: corroborate the accuracy of the computational approach, by comparing **sCI 1** trends in this study with literature trends; and help to integrate the analysis of **sCIs 23—26** reactions into literature patterns, which have no experimental point of comparison. This approach is analogous to that undertaken in previous chapters. There are also references to other sCI

reactions either described in Chapter 4 or in the experimental and theoretical literature, and these too are referenced as a comparative tool. These "reference sCIs", displayed in Figure 5.2, are *syn*- & *anti*-CH_3CHOO, $(CH_3)_2COO$, *syn*- & *anti*-FCHOO, CF_2OO and *anti*-PhCHOO (referred to as **sCIs 2—8** & **12**). Also displayed in Figure 5.2 are all co-reactants employed in this chapter.

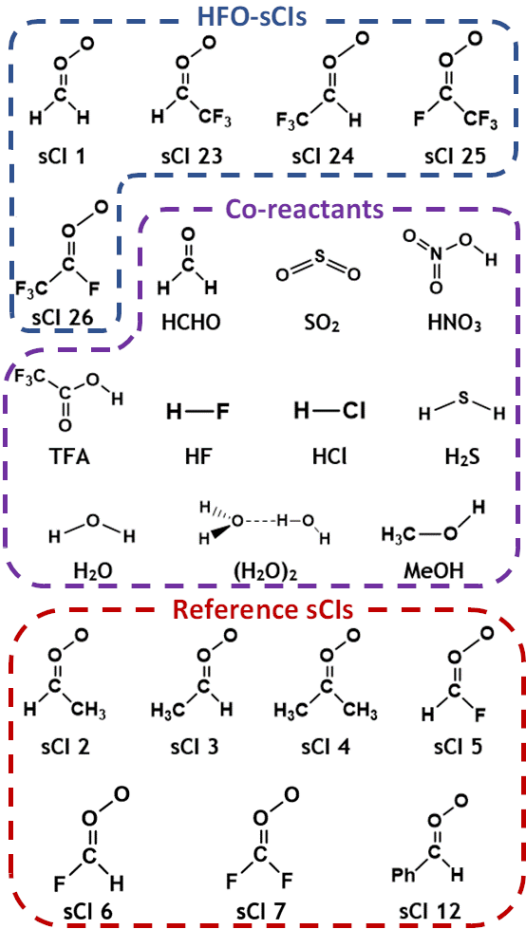

Figure 5.2: Geometric Structures of HFO-sCIs (sCIs 1, 23 — 26); co-reactants modelled in this chapter; and "reference sCIs" (sCIs referenced in this chapter from other chapters or other studies in the literature).

One of the reasons why H_2O monomer and dimer are selected as co-reactants is because water's global abundance (~0—40,000 ppm) means they are responsible for reacting with up to 95% of the *total global flux* of some atmospheric sCIs.[15,141,195,293,387,388,391] HCHO and TFA are selected because there is significant prospect of high local concentrations being co-located with HFO-sCIs, due to their common HFO source.[199,224]

Another group of co-reactants were targeted because the reactions with sCIs could cause a "disproportionate impact" in atmospheric studies, either by providing a competitive sink for that co-reactant or an important source for species harmful to humans or the environment. The competitive species are focused on those co-reactants identified by a study by Khan *et al*. where CH_2OO has similar or greater capacity than OH radicals, to

facilitate the depletion of those targeted co-reactants, such as the sCI reactions with HNO_3, HCl and H_2S.[111] Reactions that act as a competitive *source* for harmful species includes the sCI + SO_2 reaction, which produces SO_3, a source of aerosol nucleation.[191,440] Another example of a competitive source of harmful species is from the sCI + MeOH & H_2O reactions, which produce a large proportion of the global flux of the α-alkoxyalkylhydroperoxides (AAAH) and α-hydroxy-hydroperoxides (HHP). These are oxidising species that cause both forest damage and SOA formation.[141,195,293,387–391]

One last area of consideration in co-reactant targeting is that a Kumar *et al.* study has calculated that the sCI reactivity with H_2X (X=O, S, Se, and Te) increases with the size of the X atom, referred to as *heteroatom tuning* of the co-reactants.[441] In this chapter, the co-reactants with low mass heteroatoms, H_2O & HF, are compared with species which have the same structures but larger heteroatoms of the same periodic group, H_2S & HCl, to see if all the HFO-sCIs in this chapter replicate the co-reactant *heteroatom tuning* patterns observed in the Kumar *et al.* study.[441] The last reactions featured in this chapter, not yet mentioned above, are only examined because the HCHO + **sCIs 23** & **24** and **sCI 1** + CF_3CHO reactions are part of the same multistep potential energy surface (PES) and so the rate constants (k_{THEO}) and product branching ratios (Γ_{THEO}) of **sCI 1** + CF_3CHO can swiftly be determined, using the same MESMER input file. This is also the case for HCHO + **sCIs 25** & **26** and **sCI 1** + CF_3CFO which are part of the reaction chemistry of **sCI 1** + CF_3CFO.

5.2 Results of this study

Table 5.2 provides an overview of the results from this study.

*Table 5.2: Co-reactant and their chosen atmospheric concentration ([**co-reactant**]); Criegee Intermediate number [sCI]); computational master equation rate constant (k_{ME}); dipole-dipole capture limit ($k_{d\text{-}d}$);* literature experimental rate constant (k_{exp}); and calculated effective first-order rate constant ($k_{eff} = k_{THEO} \times$ [co-reactant]).*

[Co-reactant] (molec./cm^3)	sCI	k_{ME} (cm^3 s^{-1})	$k_{d\text{-}d}$ (cm^3 s^{-1})	k_{exp} (cm^3 s^{-1})	k_{eff} (s^{-1})
HCHO	1	**2.79×10^{-12}**	1.06×10^{-9}	-	5.60
	23	**2.69×10^{-13}**	8.04×10^{-10}	-	0.54
2.0×10^{12}	24	**2.49×10^{-12}**	6.46×10^{-10}	-	5.0
(Urban Heavy	25	» $k_{d\text{-}d}$	**7.20×10^{-10}**	-	1447
traffic) [442]	26	**1.66×10^{-11}**	7.07×10^{-10}	-	33.4
CF_3CHO	1	» $k_{d\text{-}d}$	6.50×10^{-10}	-	-
CF_3CFO	1	**1.98×10^{-12}**	3.34×10^{-10}	-	-
SO_2	1	» $k_{d\text{-}d}$	**7.25×10^{-10}**	3.80×10^{-11}	300
	23	**1.90×10^{-12}**	5.08×10^{-10}	-	0.79
4.1×10^{11}	24	» $k_{d\text{-}d}$	**4.08×10^{-10}**	-	169
(Beijing urban	25	» $k_{d\text{-}d}$	**4.51×10^{-10}**	-	186
area) [443]	26	» $k_{d\text{-}d}$	**4.42×10^{-10}**	-	183
HNO_3	1	8.22×10^{-9}	**8.45×10^{-10}**	5.1×10^{-10}	94
	23	**2.06×10^{-11}**	5.93×10^{-10}	-	2.3
1.1×10^{11}	24	**8.87×10^{-11}**	4.76×10^{-10}	-	9.8
(Houston,	25	9.25×10^{-8}	**5.26×10^{-10}**	-	58
Texas) [444]	26	**7.53×10^{-11}**	5.16×10^{-10}	-	8.4
TFA	1	» $k_{d\text{-}d}$	**7.54×10^{-10}**	3.50×10^{-10}	2.5×10^{-2}
	23	» $k_{d\text{-}d}$	**4.96×10^{-10}**	-	1.7×10^{-2}
3.3×10^{7}	24	» $k_{d\text{-}d}$	**3.98×10^{-10}**	-	1.3×10^{-2}
(Beijing higher	25	» $k_{d\text{-}d}$	**4.35×10^{-10}**	-	1.5×10^{-2}
emission areas)	26	» $k_{d\text{-}d}$	**4.27×10^{-10}**	-	1.4×10^{-2}
H_2O	1	**1.18×10^{-16}**	1.06×10^{-9}	*2.4×10^{-16}*	73
	23	**1.35×10^{-18}**	8.38×10^{-10}	-	0.83
6.2×10^{17}	24	**1.12×10^{-16}**	6.73×10^{-10}	-	70
(~80% humidity	25	**5.13×10^{-12}**	7.54×10^{-10}	-	3.2×10^{6}
Sao Paulo) [422,445]	26	**2.27×10^{-13}**	7.40×10^{-10}	-	1.4×10^{5}
$(H_2O)_2$	1	**3.28×10^{-12}**	1.07×10^{-9}	7.50×10^{-12}	2.9×10^{3}
	23	**2.71×10^{-12}**	7.99×10^{-10}	-	2.4×10^{3}
8.7×10^{14}	24	**3.74×10^{-12}**	6.42×10^{-10}	-	3.3×10^{3}
(~80% humidity	25	1.14×10^{-6}	**7.14×10^{-10}**	-	6.2×10^{5}
Sao Paulo) [422,445]	26	1.46×10^{-9}	**7.01×10^{-10}**	-	6.1×10^{5}
MeOH	1	**1.20×10^{-14}**	8.15×10^{-10}	1.1×10^{-13}	0.010
	23	**9.43×10^{-17}**	6.14×10^{-10}	-	7.9×10^{-5}
8.4×10^{11}	24	**3.30×10^{-14}**	4.93×10^{-10}	-	0.028
(Sao Paulo,	25	» $k_{d\text{-}d}$	**5.50×10^{-10}**	-	462
Brazil) [383]	26	**3.31×10^{-11}**	5.39×10^{-10}	-	28
H_2S	1	**7.06×10^{-15}**	5.68×10^{-10}	1.7×10^{-13}	0.052
	23	**1.96×10^{-16}**	4.26×10^{-10}	-	1.4×10^{-3}
1.2×10^{13}	24	**5.72×10^{-15}**	3.42×10^{-10}	-	0.042
(Industrial	25	**6.08×10^{-13}**	3.81×10^{-10}	-	4.5
landfill) [446]	26	**1.23×10^{-14}**	3.74×10^{-10}	-	0.091
HCl	1	**4.70×10^{-10}**	6.06×10^{-10}	4.1×10^{-11}	58
	23	**4.04×10^{-15}**	4.51×10^{-10}	-	5.0×10^{-3}
1.2×10^{11}	24	**7.28×10^{-11}**	3.62×10^{-10}	-	8.96
(Daytime	25	**1.64×10^{-10}**	4.03×10^{-10}	-	20
Los Angeles) [427]	26	**1.13×10^{-10}**	3.96×10^{-10}	-	14
HF	1	**3.32×10^{-13}**	8.15×10^{-10}	-	0.12
3.7×10^{11}	23	**6.67×10^{-18}**	6.14×10^{-10}	-	2.5×10^{-6}
(near Volcano	24	**2.86×10^{-15}**	4.93×10^{-10}	-	1.1×10^{-3}
vicinity	25	**1.19×10^{-11}**	5.50×10^{-10}	-	4.4
ambient T) [447]	26	**3.66×10^{-13}**	5.39×10^{-10}	-	0.14

** "» $k_{d\text{-}d}$" refers to barrierless reactions that yield no k_{ME} and that the $k_{d\text{-}d}$ should be used instead.*
*** In bold is the overall theoretical rate constant (k_{THEO}), which is the lowest between the k_{ME} & $k_{d\text{-}d}$ values.*

5.3 HFO-sCIs reactions with Formaldehyde (HCHO)

Formaldehyde, or HCHO, emissions are known to be carcinogenic, toxic if inhaled, and to cause other health problems (Section 1.5.6).[16,170,171] The literature abundance of HCHO varies significantly (usually between 1—171 μg/m^3) depending on the tropospheric environment (Appendix Section 3.3.1).[448] An examination of sCI reactions with HCHO is undertaken in this thesis because HCHO is a co-product of the ozonolysis of many alkenes (including HFO-1234yf) and it is important to understand natural sinks for pollutants like HCHO.

5.3.1 The sCI 1 + HCHO Reaction

sCI 1 + HCHO is used in Figure 5.3 to demonstrate the key stationary points of an sCI + HCHO reaction potential energy surface (PES): a single cycloaddition (TS_C) step, where the reactants form a heteroozonide ring (HOZ); and the intermediate product breakdown pathways (TS_D & TS_{FAc}), where the HOZ fragments into formic acid (FAc) and HCHO. The HOZ breakdown step can proceed via two mechanisms, either: through a high energy, 1-step channel or a lower energy, 2-step channel via hydroxymethyl formate (HAE), both shown in figure 5.3. The 1-step TS_{FAc} channel is in blue and the 2-step HAE channel, using TS_D and TS_{HAE}, is in red.

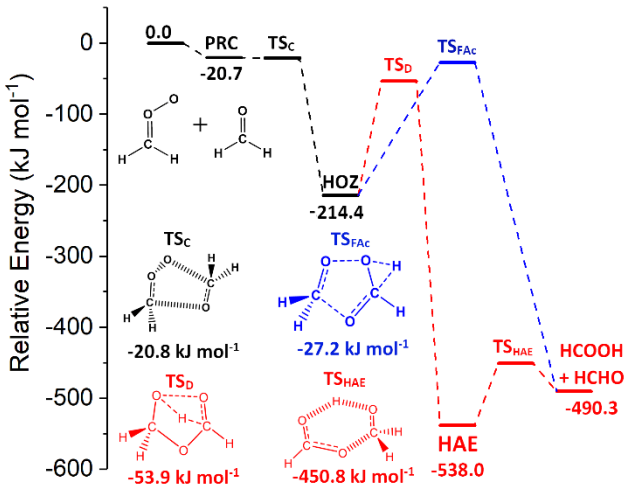

*Figure 5.3: The potential energy surface of **sCI 1** + HCHO displaying both HOZ fragmentations: a 1-step channel (in blue) and a lower energy, 2-step channel via a hydroxyalkyl ester (in red). Energies are relative to raw reactants.*

The low energy TS_C, displayed in Figure 5.3, is similar those calculated by the Jalan *et al.* and Ma Qiao *et al.* studies (-26.4 & -20.1 kJ mol^{-1}) respectively. Consequently, the k_{THEO} value from the Ma Qiao *et al.* study (~4.03 × 10^{-10} cm^3 s^{-1}) is similar to that reported in this chapter (k_{ME} = 2.79 × 10^{-11} cm^3 s^{-1}). Whilst there is no experimental rate constant (k_{EXP}) for **sCI 1** + HCHO, Taatjes *et al.*, Stone *et al.*, and Elsamra *et al.* all examined the similar

CH_2OO + CH_3CHO reaction and they measured similar k_{EXP} values (3.0×10^{-13} — 1.7×10^{-12} $cm^3\ s^{-1}$) to the k_{ME} of CH_2OO + HCHO calculated in this study.

HOZ fragmentation pathways were also calculated in the Jalan *et al.* and Ma Qiao *et al.* studies and some common patterns emerge, which correlate with the analysis in Figure 5.3. The studies produced by Jalan *et al.* and the Ma Qiao *et al.* display a much lower barrier to the HAE channel (-94.6 & -67.8 kJ mol^{-1}) compared to the TS_{FAc} channel (-40.2 & -38.5 kJ mol^{-1}) for HOZ decomposition. This energy disparity between the channels is continued in Figure 5.3 showing that this study agrees with the HOZ decomposition preferences in literature. The energy of the TS barrier between HAE and the HCOOH + HCHO final products, TS_{HAE}, in this study (-450.8 kJ mol^{-1}) is also displayed in both the Jalan *et al.* and Ma Qiao *et al.* studies (-459.8 & -444.3 kJ mol^{-1}). Because of this low TS_{HAE} barrier, compared to the high TS_D barrier, 100% conversion to the final products is assumed. In the decomposition of the HOZ pathway, the production of formic acid via HAE displays a higher branching ratio (Γ_{HAE} ~0.973) than the direct transfer channel (Γ_{FAc} ~0.027).

5.3.2 HCHO + sCIs 23 & 24 and CF_3CHO + sCI 1 Reactions

HCHO reactions with **sCIs 23** & **24** (the non-interchangeable *syn*- and *anti*-CF_3CHOO conformers respectively) also exhibit very similar 2-stage reaction surface, with a single cycloaddition (TS_C) step each to a joint HOZ, followed by HOZ fragmentation pathways. Therefore both HCHO reactions with **sCIs 23** & **24** occupy part of the same PES, a phenomenon also seen in the Ma Qiao *et al.* study with **sCI 12** + HCHO & **sCI 1** + PhCHO reactions.[181] The cycloaddition for **sCI 23** + HCHO produces a significantly higher TS_C barrier (-11.6 kJ mol^{-1}) than **sCI 24** + HCHO (-19.0 kJ mol^{-1}). This leads to a smaller k_{THEO} for **sCI 23** + HCHO compared to **sCI 24** (2.69×10^{-13} & 2.49×10^{-12} $cm^3\ s^{-1}$ respectively). As shown in Table 5.3, computational studies of sCI reactions with $CF_3CH{=}CH_2$, CO_2 and H_2 also show **sCI 24** reactions have lower energy barriers, and consequentially larger k_{THEO} values, than **sCI 23**.[273,305,441]

*Table 5.3: The energy barriers [ΔE_{TS}] and rate constants [k_{THEO}] for **sCIs 1—3** reactions HCHO, as well as various other co-reactants from other literature studies.*

		ΔE_{TS} [kJ mol^{-1}]				k_{THEO} [10^{-13} $cm^3\ s^{-1}$]	
sCI	#sCI	H_2	CO_2	HCHO	$CF_3CH{=}CH_2$	k_{HCHO}	$k_{CF_3CH=CH_2}$
CH_2OO	**1**	74.5	17.6	-20.8	-12.8	27.9	1.76
Syn-CF_3CHOO	**23**	-	32.6	-11.6	-13.8	2.69	77.9
Anti-CF_3CHOO	**24**	52.3	25.1	-19.0	-16.9	24.9	285
Reference		273	372	This study	305	This study	305

The *syn*- & *anti*-CF_3 groups induce similar trends to those seen previously, where **sCI 3** exhibits larger k_{EXP} values than **sCI 2** for reactions with H_2O, $(H_2O)_2$, SO_2 and MeOH.[55,141,402,420] One area of divergence with the other computational literature is that, unlike sCI reactions with $CF_3CH{=}CH_2$, CO_2 and H_2, **sCI 1** + HCHO has a lower energy TS barrier and larger k_{THEO} values than **sCI 24** (see Table 5.3).

Figure 5.4 shows that there are several other important differences between the HCHO + **sCIs 23** & **24** PES with that of the **sCI 1** + HCHO PES, including that the HOZ produced by HCHO + **sCIs 23** & **24** has multiple conformers that can interconvert over a small TS_{HOZ} barrier (~20 kJ mol^{-1}). The second difference is that, whereas **sCI 1** + HCHO is the only sCI source for its HOZ, the HOZ in figure 5.4 has three sCI sources, **sCI 23** + HCHO, **sCI 24** + HCHO and **sCI 1** + CF_3CHO. This means that each of these three sCI + aldehyde reactions can, via HOZ formation followed by use of a cyclo-reversion mechanism, interconvert to the other reactant pairs.

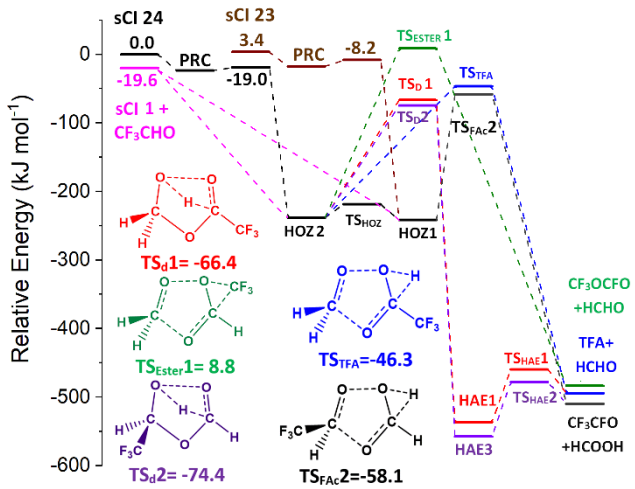

*Figure 5.4: The collective potential energy surface for **sCIs 23** & **24** + HCHO and **sCI 1** + CF_3CHO reactions with minima energy structures of each HOZ fragmentation displayed. Energies are relative to raw **sCI 24** + HCHO.*

Another major difference between the **sCIs 23** & **24** + HCHO reactions with **sCI 1** + HCHO is that due to the extra -CF_3 substituent group in **sCIs 23** & **24**, there are three additional HOZ decomposition pathways for these systems, and their mechanisms are displayed in Figure 5.4. These three extra reaction channels are: the TS_{ESTER} channel, which produces CF_3OCHO + HCHO; TS_{TFA} which produces a CF_3COOH (TFA) and HCHO, via a one-step mechanism; and TS_D 1, which produces TFA and HCHO, using a two-step mechanism that proceeds via a new HAE. For full molecular geometries of *all* stationary points in this reaction, see Appendix Section 8.2.

These three new mechanistic pathways are verified in the Jalan *et al.* computational study, where the **sCI 1** + CH_3CHO reaction produces an HOZ with an extra —CH_3 group.

Much like the extra —CF_3 group for **sCIs 23** & **24**, this extra CH_3 group opens up new channels that produce: HCHO + CH_3COOH, via either a one or two step mechanism; and HCHO + CH_3OCHO.[449] Ma Qiao *et al.* found that the extra —Ph substituent in **sCI 12** + HCHO, also opens up three new channels, that produce HCHO + PhCOOH or PhOCHO.[181]

There are two cycloaddition steps for **sCI 1** + CF_3CHO, which depend on the approach direction of the CF_3CHO. The -CF_3 substituent in the TS_C 3 points in the opposite direction to the terminal O and produces HOZ 1, whereas with TS_C 4 the -CF_3 group points in the same direction as the terminal O and produces HOZ 2. As noted in Figure 5.5, for **sCI 1** + CF_3CHO, both TS_C steps are barrierless and therefore the $k_{d\text{-}d}$ limit, (~6.50 × 10^{-10} cm^3 s^{-1}) becomes the k_{THEO} constant.[309,320] All barrierless channels are explored using a relaxed energy scan, explained further in Method Section 2.1, and found in Appendix Section 3.2.

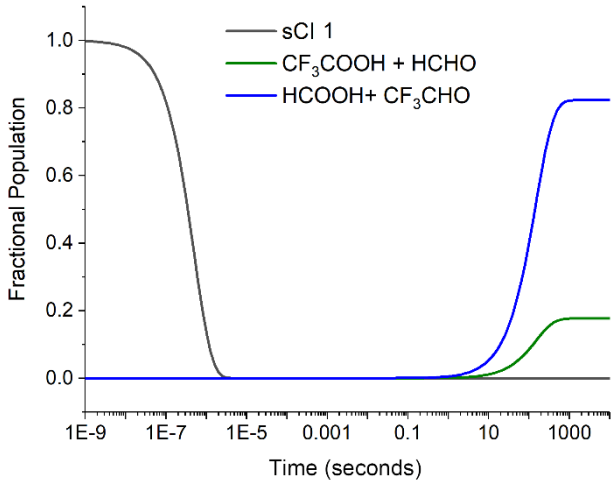

*Figure 5.5: Fractional Populations of reactants and products for the **sCI 1** + CF_3CHO reaction over time. For full details on the conditions of the reaction see Appendix Section 3.1.4. Excess CF_3CHO reagent concentration is ~1.0 × 10^{16} molec./cm^3.*

There is a significant yield of TFA, as shown in Figure 5.5, but of the two mechanistic pathways that produce TFA + HCHO, the two step HAE pathway produces a higher $\Gamma_{TS_{d1}}$ (~0.120) than the direct transfer pathway $\Gamma_{TS_{TFA}}$ (~ 0.019).[181] This is due to a lower barrier to the 2-step HAE channel (TS_D 1 ~-66.4 kJ mol^{-1}) than that of the direct transfer TS_{TFA} barrier (-46.3 kJ mol^{-1}) following the similar trends observed for the TS_D and TS_{FAc} pathways in the **sCI 1** + HCHO reaction. Many of the reactions here have multiple transition states (denoted as subchannels) which differ only subtly based on conformer choice, so for clarity only the lowest channel is shown. However, all channels have been computed and can be found in the Appendix Section 3.4. Interestingly though, for the reaction channels that produce TFA (TS_D and TS_{TFA}) there is only one reaction subchannel, as they emerge from HOZ decomposition via H-transfer from the -$CHCF_3$- section of the HOZ, which has only one hydrogen to transfer.

In contrast the two highest yield HOZ fragmentation pathways that produce CF_3CHO + HCOOH, TS_D 2 and TS_{FAc}, do have multiple subchannels. This is primarily because the TS_D 2 and TS_{FAc} pathways are accessed by H-transfer from the $-CH_2-$ section of the HOZ and these two H atoms are in chemically distinct environments. Both subchannels from the multistep fragmentation exhibit significant yields of CF_3CHO + HCOOH ($\Gamma_{TS_D\,2}$ ~0.398 & $\Gamma_{TS_D\,3}$ ~0.084). The direct transfer mechanism sees the same pattern of the TS_{FAc} 1 (-50.6 kJ mol^{-1}) having a higher energy than TS_{FAc} 2 (-58.1 kJ mol^{-1}), but they collectively produce a small product branching fraction (Γ_{THEO} ~ 0.064). For **sCI 1** + CF_3CHO, there was very little overall yield (<<0.01) for Γ_{ESTER}, $\Gamma_{\mathbf{sCI\ 23}+HCHO}$ and $\Gamma_{\mathbf{sCI\ 24}+HCHO}$.

Table 5.4: The full final product branching fractions of each sCI + aldehyde & ketone reaction.

Reaction sCI + HCHO	Final Product Branching Ratio Exit				
	$\Gamma_{sCI1+R_1CR_2O}$	$\Gamma_{HCHO+R_1CR_2OO}$	$\Gamma_{HCOOH+R_1CR_2O}$	$\Gamma_{TFA+HCHO}$	$\Gamma_{Ester+HCHO}$
sCI 23 + HCHO	0.993	7.40×10^{-5}	0.006	0.001	1.78×10^{-7}
sCI 24 + HCHO	0.991	3.92×10^{-6}	0.007	0.002	1.02×10^{-7}
sCI 25 + HCHO	0.843	9.40×10^{-9}	0.156	-	3.06×10^{-5}
sCI 26 + HCHO	0.842	8.13×10^{-9}	0.158	-	4.98×10^{-5}
sCI 1 + R_1CR_2O	$\Gamma_{HCHO+\,anti\text{-}R_1CR_2OO}$	$\Gamma_{HCHO+\,syn\text{-}R_1CR_2OO}$	$\Gamma_{HCOOH+R_1CR_2O}$	$\Gamma_{TFA+HCHO}$	$\Gamma_{Ester+HCHO}$
sCI 1 + CF_3CHO	1.47×10^{-6}	2.49×10^{-5}	0.823	0.177	2.14×10^{-8}
sCI 1 + CF_3CFO	3.10×10^{-14}	3.51×10^{-12}	~1.000	-	1.74×10^{-7}

In the computational analysis of HOZ decomposition, both the results of **sCI 1** + CH_3CHO by Jalan *et al.* and the results of **sCI 12** + HCHO by Ma Qiao *et al.* show similar trends to **sCI 1** + CF_3CHO in this work.[181,450] Firstly, the lowest energy barriers are for the two-part channels via the HAEs rather than the direct H-transfer channels. The second trend is the high yield of formic acid pathways, which are controlled by differences in barrier heights, in the **sCI 1** + CH_3CHO reaction ($\Delta E[TS_{FAc}] < \Delta E[TS_{CH_3COOH}] < \Delta E[TS_{CH_3OCHO}]$). Finally, the Jalan *et al.* and Ma Qiao *et al.* calculations of **sCI 1** + CH_3CHO and **sCI 12** + HCHO respectively, also exhibit very high barriers for the ester pathways (-13.8 & -33.9 kJ mol^{-1}).

Despite the fact that through a mutual HOZ intermediate product they are part of the same PES (see Figure 5.4), the calculated **sCI 1** + CF_3CHO reaction produces only very low branching ratios for the cyclo-reversion pathways to **sCI 23** + HCHO & **sCI 24** + HCHO. Given that the energy of the **sCI 1** + CF_3CHO reactants are ~20 kJ mol^{-1} below both **sCI 23** & **sCI 24** + HCHO their low $\Gamma_{\mathbf{sCI\ 23}+HCHO}$ and $\Gamma_{\mathbf{sCI\ 24}+HCHO}$ values were foreseeable. However, cyclo-reversion to **sCI 1** + CF_3CHO species from **sCIs 23** & **sCI 24** + HCHO has no TS barrier, unlike the other HOZ fragmentation channels and so the final product branching ratio of **sCI 1** + CF_3CHO (calculated using the reverse inverse Laplace transformation method described in Method Section 2.5) is likely to be noteworthy. Indeed, the **sCI 23** + HCHO

reaction produces an even larger $\Gamma_{sCI1+HCHO}$ value (~0.993) than might be expected considering the low barriers to the other HOZ fragmentation products: TS_D 1, TS_{TFA}, TS_D 2 & TS_{FAc}. On the other hand, the high $\Gamma_{sCI1+HCHO}$ values may be explained by the large k_{d-d} value (see Table 5.2 in Section 5.2), used as the pre-exponential factor in the reverse inverse Laplace transform, and also perhaps from the increased entropy gain during fragmentation.

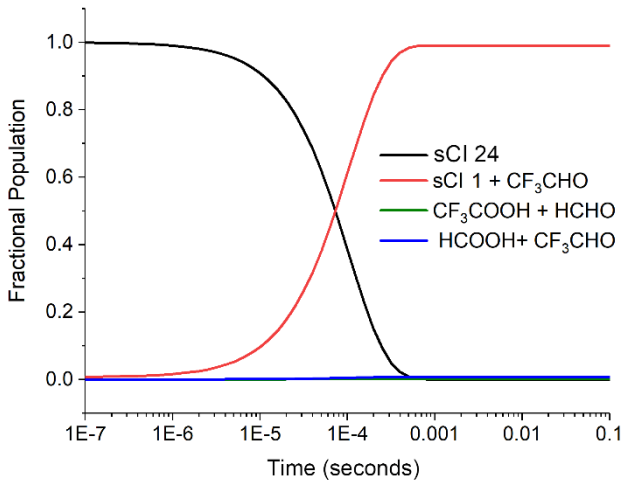

*Figure 5.6: Population fraction of reactants and products for the **sCI 24** + HCHO reaction over time. For full details on the conditions of the reaction see Appendix Section 3.1.4. Excess HCHO reagent concentration is ~1.0 × 10^{16} molec./cm^3.*

As shown in Figure 5.6, the fractional HOZ decomposition for **sCI 24** + HCHO is similar to that of **sCI 23** + HCHO. This is because, as the energy difference between of **sCIs 23** & **24** is very small (~3 kJ mol^{-1}) and so, aside from the different cycloaddition channels, the PES for the reaction is essentially the same. There are some slight changes of yields, where $\Gamma_{HCOOH + CF_3CHO}$ is ~0.0056, but this is still effectively negligible compared to $\Gamma_{sCI\ 1 + CF_3CHO}$ (~0.993). The most significant result from this HOZ fragmentation is the dominance of $\Gamma_{sCI\ 1 + CF_3CHO}$ (~0.99) for **sCIs 23** & **24** + HCHO compared to the dominance of $\Gamma_{HCOOH + CF_3CHO}$ (0.823) & $\Gamma_{TFA + HCHO}$ (0.177) for the **sCI 1** + CF_3CHO reaction.

5.3.3 HCHO + sCIs 25 & 26 and CF_3CFO + sCI 1 Reactions

Compared to **sCIs 1**, **23** & **24**, the reaction of **sCI 26** + HCHO has a significantly lower TS_C barrier and therefore produces a considerably larger k_{THEO} (1.67 × 10^{-11} cm^3 s^{-1}). However, Figure 5.7 shows that **sCI 25** + HCHO is so reactive that the reaction is barrierless and the k_{d-d} limit (~7.20 × 10^{-10} cm^3 s^{-1}) effectively becomes the k_{THEO} value. This is a notable observation as **sCI 25**, which has the more bulky -CF_3 group in the *syn* position, has a larger k_{THEO} than **sCI 26**, which has the -CF_3 in the *anti* position. This reverses the trend observed both in the literature and other parts of this thesis, where sCIs with bulky *syn*

groups have reduced k_{EXP} and k_{THEO}, compared to their *anti* counterparts, for example in the cases of both CH_3CHOO and CF_3CHOO.[141,193,273,305,372,402] However, while these *syn*-CH_3 & *syn*-CF_3 groups, may act to reduce COO moiety, the additional —F groups in **sCI 25** explains the increase in reactivity of the COO group, as seen with the computational chemistry of the reactive and highly fluorinated **sCI 7** reactions with CO_2, MeOH and CH_4.[93,274,372] While there is also an increase in COO reactivity caused by the *syn*-F group, it is a more marginal increase than caused by an *anti*-F group, as shown in the **sCIs 5** & **6** + MeOH reactions in Section 4.4. This may explain why **sCI 25**, which has an *anti*-F substituent, is more reactive than **sCI 26**, which has an *syn*-F substituent.[93,274,372]

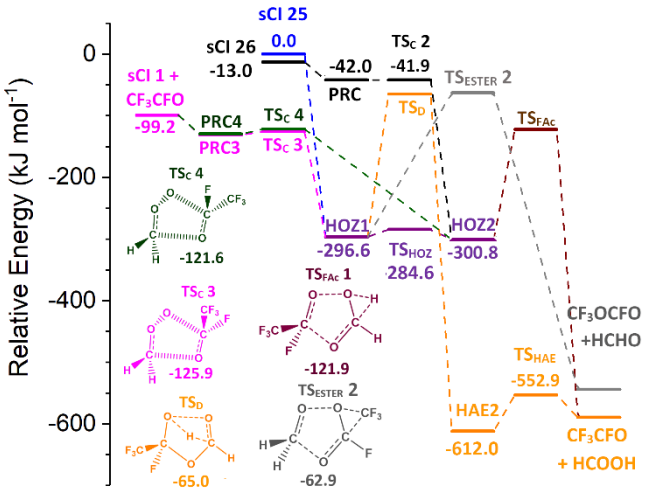

*Figure 5.7: Full PES of the **sCIs 25** & **26** + HCHO and **sCI1** + CF_3CFO reaction. Energies are relative to raw **sCI 25** + HCHO.*

The cycloaddition reactions of **sCIs 25** & **26** + HCHO and **sCI 1** + CF_3CFO produce the same short-lived HOZ intermediate generating a unified PES, as shown in Figure 5.7. Similar to the phenomenon seen for **sCIs 23** & **24** + HCHO, each cycloaddition pathway can also provide a cyclo-reversion HOZ fragmentation mechanism. One key difference with **sCIs 23** & **24** is that the >CH-CF_3 section of the HOZ is instead a >CF-CF_3 section, which means that all pathways that produce TFA (TS_D 1 and TS_{TFA}) become unavailable. These HOZs still breakdown to produce CF_3CFO + HCOOH, via TS_D and TS_{FA} 1 & 2, and they produce CF_3OCFO + HCHO, TS_{ESTER} 1 & 2.

While **sCI 1** + CF_3CFO is not barrierless, the TS_C 3 & 4 structures have low energy barriers (-26.7 & -22.4 kJ mol^{-1}) and generate large k_{THEO} (1.98×10^{-12} cm^3 s^{-1}). **sCI 1** + CF_3CFO not only supports the lowest energy barriers in the HOZ fragmentation pathways, but it is around ~100 kJ mol^{-1} lower in energy than **sCIs 25** & **26** + HCHO. This leads to significant disparity between the high Γ_{CI1+CF_3CFO} values for the **sCIs 25** & **26** + HCHO (0.842 & 0.833) and the low $\Gamma_{CI25+HCHO}$ and $\Gamma_{CI26+HCHO}$ values (<0.001) for the **sCI 1** + CF_3CFO.

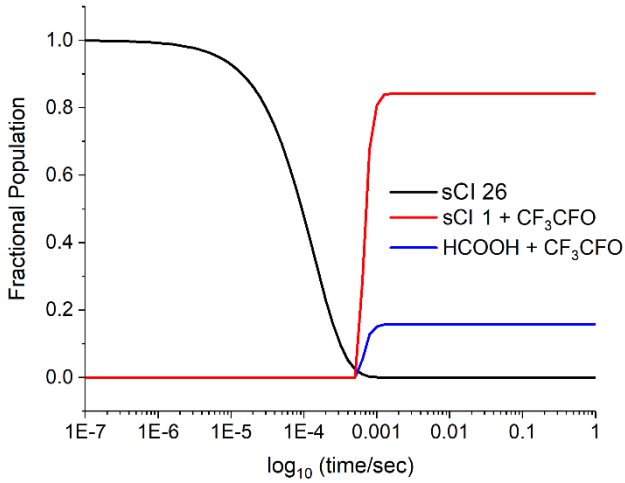

*Figure 5.8: Population fraction of reactants and products over time for the **sCI 26** + HCHO reaction. For full details on the conditions of the reaction see Appendix Section 3.1.4. Excess HCHO reagent concentration is ~1.0 × 10^{16} molec./cm^3.*

Figure 5.8 shows that the 1-step TS_{FAc} barriers (-121.9 & -104.3 kJ mol^{-1}) are in fact lower than that of the two-step HAE pathway (-65.0 kJ mol^{-1}), a change from the HCHO + **sCIs 1**, **23** & **24** reactions. The 1-step TS_{FAc} pathway is very important because although it has modest product fragmentation fraction (~0.16) in the **sCIs 25** & **26** + HCHO reactions, in the **sCI 1** + CF_3CFO reactions the Γ_{FAc} value dominates (>0.999). While **sCI 25** + HCHO have unusually low TS_{Ester} barriers (-62.9 & -51.5 kJ mol^{-1}), the Γ_{Ester} is still very low (≪0.001).)

5.3.4 Overview of HFO-sCI + HCHO reactions

In conclusion, **sCI 1** trends in reactivity observed here are consistent with any prior literature available. For example, *anti*-CF_3CHOO is observed as being more reactive than its *syn*-conformer, and sCIs with -F groups have the largest k_{THEO} values. Overall, this means that the HFO-sCIs + HCHO reaction produce the following trends: k_{THEO} (**sCI 23**) < k_{THEO} (**sCI 24**) < k_{THEO} (**sCI 1**) < k_{THEO} (**sCI 26**) < $k_{d\text{-}d}$ (**sCI 25**). The trend seen for sCI + aldehyde reactivity are as follows: k_{THEO} (**CF_3CFO**) < k_{THEO} (**HCHO**) < k_{THEO} (**CF_3CHO**).

HOZ decomposition of **sCI 23—26** + HCHO produce quite complex patterns compared to **sCI 1** + HCHO, the PES being unified with that of the **sCI 1** + CF_3CHO/CF_3CFO reactions. Two consistencies across all reactions are that that pathways that produce esters have negligible branching fractions and *all* HOZ fragmentation pathways produce an aldehyde co-product. While there is complexity in the analysis of these PESs, some general trends remain significantly similar across the **sCI 23—26** + HCHO reactions, with the dominant pathways yielding **sCI 1** + CF_3CHO/CF_3CFO and the smaller secondary channels produce either TFA (if pathways are accessible) or HCOOH. HOZ fragmentation of **sCI 1** + CF_3CHO/CF_3CFO does not lead to sCIs formation, instead generating formic acid and TFA.

5.4 HFO-sCIs reactions with Sulphur Dioxide (SO_2)

The sCI + SO_2 reaction is studied due to its significant prominence in the literature, which is due to the dominant final product of the reaction being SO_3. SO_3 is a source of organosulphates and is involved in the formation and growth of secondary organic aerosol (SOA) nuclei.[191,440,451] This process of SO_3 promoting nucleation is of considerable importance because these aerosols are an airborne solid, liquid or multiphase suspension of particulate matter, which can seriously affect climate temperatures, through absorbing or scattering solar radiation (depending on the aerosol type), and can gravely harm human health, by causing serious respiratory problems and premature death.[19,73-75,452] Another major atmospheric role that sCI + SO_2 reactions provide is an effective gaseous sCI sink. Depletion by SO_2 is thought to cause ~1% loss of **sCI 2** in rural Europe to ~22% loss of "*syn*-CH_3-*anti*-(*trans*-CH_2=CH)–COO" in boreal forest.[453]

5.4.1 The sCI 1 + SO_2 Reaction

As in the case of HCHO as a co-reactant, the **sCI 1** + SO_2 reaction undergoes a cycloaddition step (TS_{EXO} & TS_{ENDO}) to produce a heteroozonide. To prevent confusion with the sCI + HCHO reaction, these particular cyclic ozonides are referred to as secondary ozonides (SOZ). Figure 5.9 displays the cycloaddition steps. TS_{EXO} & TS_{ENDO} lead to the formation of the diastereomeric *exo*- and *endo*-SOZ conformers, referred to as SOZs 1 & 2. The rate-determining cycloaddition steps for **sCI 1** + SO_2 proceed through TS_{EXO} and TS_{ENDO} channels, which are both barrierless, which means that the appropriate rate constant for this reaction is the $k_{d\text{-}d}$ value (7.25×10^{-10} cm^3 s^{-1}). This leads to a small overestimate of the k_{EXP} values reported in literature for **sCI 1** + SO_2 ($3.3—4.1 \times 10^{-11}$ cm^3 s^{-1}), although the theoretical analysis of Kuwata *et al.* also displays the reaction as barrierless.[145,178,191,440,454,455]

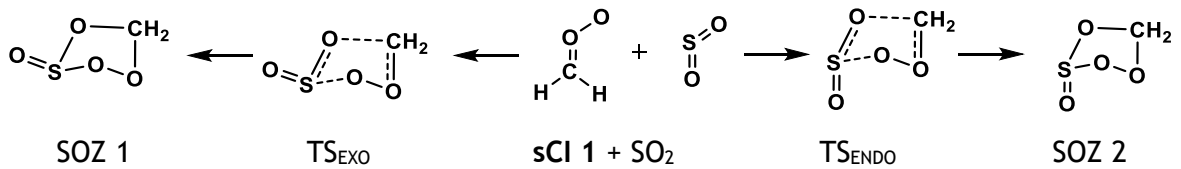

*Figure 5.9: Cycloaddition Step of **sCI 1** + SO_2 reaction*

Both the SOZs that are formed in the **sCI 1** + SO_2 reaction can transition to each other via a low pseudo-rotation barrier, TS_{SOZ}, shown in Figure 5.10, meaning they can freely interconvert. However, one important observation of this reaction in a study by Kuwata *et al.* is that interconversion of the SOZ conformers via the inversion of the S atom requires

>180 kJ mol^{-1} excess energy, which is far greater than both cyclo-reversion (via TS_{EXO} & TS_{ENDO}) and SOZ fragmentation pathways.[191]

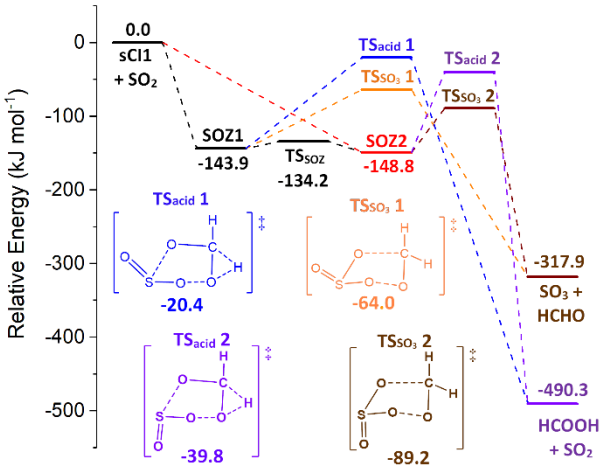

*Figure 5.10: The potential energy surface of **sCI 1** + SO_2 with SOZ fragmentation mechanisms displayed. Energies are relative to raw reactants.*

In this study, the two types of SOZ decomposition pathways calculated for the **sCI 1** + SO_2 reaction, TS_{SO_3} or TS_{acid}, both of which are single step mechanisms (see Figure 5.10). This is different to the sCI + HCHO reactions, which have multistep HAE channels. Of the SOZ decomposition final products, SO_3 + HCHO, produced via TS_{SO_3} 1 & 2, dominates with a yield of Γ_{SO_3} ~0.966 with a subordinate yield of HCOOH + SO_2, produced via TS_{acid} 1 & 2 (Γ_{acid} ~0.034). This is a similar Γ_{SO_3} dominance that was shown in the Kuwett *et al.* study for **sCI 1** + SO_2 (Γ_{SO_3} ~ 0.973—0.984).[191]

An extended study of the SO_2 reactions with **sCIs 1** & **4** by Kuwata *et al.* is amongst the most comprehensive computational studies examined in the literature and it explores numerous major and minor SOZ fragmentation pathways. Many pathways are like those displayed in figure 5.10, but one SOZ fragmentation pathway includes a homolytic O-O bond fission to produce a 1,5-(bis)oxy diradical intermediate product. While this 1,5-(bis)oxy diradical intermediate further fragments to generate important products, such as SOCO rings, sulphurous anhydrides or 1,3-(bis)oxy diradicals, the Kuwata *et al.* study showed that these pathways had a minor contribution to the **sCI 1** + SO_2 branching ratios. These 1,5-(bis)oxy diradical pathways are not explored here for **sCIs 1** & **23**—**26** + SO_2 based on this observation of negligible branching.[191]

5.4.2 SO_2 Cycloaddition of sCIs 23 & 24

Unlike the barrierless cycloaddition processes of **sCIs 1** & **24**—**26** + SO_2 reactions, **sCI 23** + SO_2 has real TS_{EXO} and TS_{ENDO} barriers linked with reactants and products through complete

one-dimensional IRC profiles (see Appendix Section 8.3). The existence of TS_{EXO} and TS_{ENDO} structures seen for **sCI 23** + SO_2 provides assurance that sCI + SO_2 reactions proceed via two cycloaddition channels (as shown in Figure 5.9), which had previously only been implied by asymptotic minimum energy pathway calculations.

Based on the indication that the *exo*- and *endo*- pathways are barrierless for SO_2 reactions with **sCI 1** & **24—26** it is assumed that both pathways are exploited equally and the ratio of *exo*-SOZ 1:*endo*-SOZ 2 produced is very close to 1:1. But as **sCI 23** + SO_2 is not barrierless, the yield of the different SOZs depends on the proportion of the k_{THEO} that occurs via TS_{exo} (0.307) or TS_{endo} (0.693) respectively. Also, as **sCI 23** + SO_2 uniquely has cycloaddition energy barriers (~18 kJ mol^{-1}), this reaction generates the lowest total k_{THEO} value (~1.90×10^{-12} cm^3 s^{-1}) of all sCI + SO_2 reactions in this study. On the other hand, the rate constant of **sCI 24** + SO_2, like **sCI 1**, is limited by the $k_{d\text{-}d}$ value (4.08×10^{-10} cm^3 s^{-1}) because of the barrierless rate-determining step. This follows the pattern observed in the reactions of HCHO, as well as the k_{THEO} analysis for CO_2, H_2 and CF_3CHCH_2, all of which suggest that **sCI 23** is much less reactive than of the **sCIs 1** & **24**.[273,305,372] Similar and analogous **sCIs 2** & **3** (*syn*- & *anti*-CH_3CHOO) exhibit the same pattern with the **sCI 2** having a lower k_{EXP} with SO_2, than the **sCIs 1** & **3**.[141,193,454]

When the R_1 & R_2 groups in an sCI are identical, sCI + SO_2 reactions such as **sCI 1** + SO_2 (seen previously in Figure 5.10), or **sCI 4** ($(CH_3)_2COO$) + SO_2 in the Kuwata *et al*. study, the *endo*- and *exo*-SOZs interconvert freely. However, in the Kuwata *et al*. study it is also noted that the SO_2 reactions with **sCIs 2** & **3** produces stereochemically distinct SOZ conformers, due to the very high barrier to S inversion.[191] This continues for CF_3CHOO as **sCI 23** can react with SO_2 to produce both *exo* and *endo* SOZ conformers, but these cannot interconvert without cyclo-reversion back to the **sCI 23** and SO_2. This is also true for **sCI 24** + SO_2, which produces *endo and exo* conformers, SOZs 3 & 4. The *pseudo*-rotation barrier, TS_{SOZ}, can facilitate interconversion from SOZ 1 to SOZ 3 through TS_{SOZ} 1, and SOZ 2 to SOZ 4 through TS_{SOZ} 2. This SOZ interconversion is shown in Figure 5.11 and this same phenomenon is also observed for **sCIs 25** & **26**.

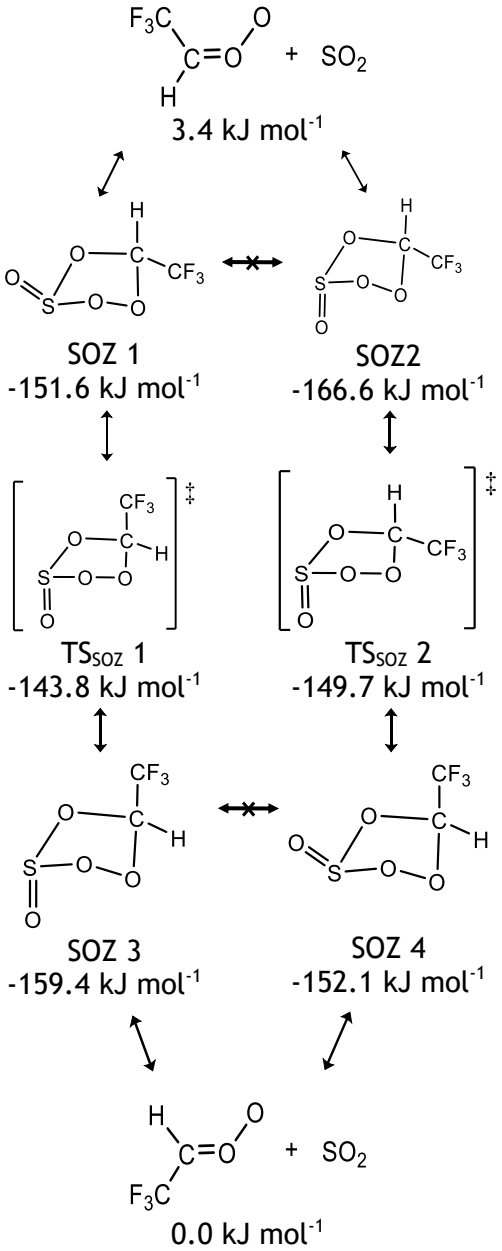

*Figure 5.11: Structures and Relative Energies of Secondary Ozonides Formed by SO_2 + **sCIs 23** & **24** Reactions. Energies are relative to raw **sCI 24** + SO_2.*

The fact that SOZ 1&3 are stereochemically distinct from SOZ 2&4 is further reflected in the fragmentation mechanisms, which are also stereochemically different. This is seen in Figure 5.12, with TS_{SO_3} 2, TS_{acid} 1 & TS_{Ester} 1 only accessible from SOZs 1&3 and TS_{SO_3} 1, TS_{acid} 2 & TS_{Ester} 2 are only accessible from SOZs 2&4. This contrasts with **sCI 1**+ SO_2, which is an example where all intermediate product conformers have access to all transition states in that system, as all the intermediate products readily interconvert.

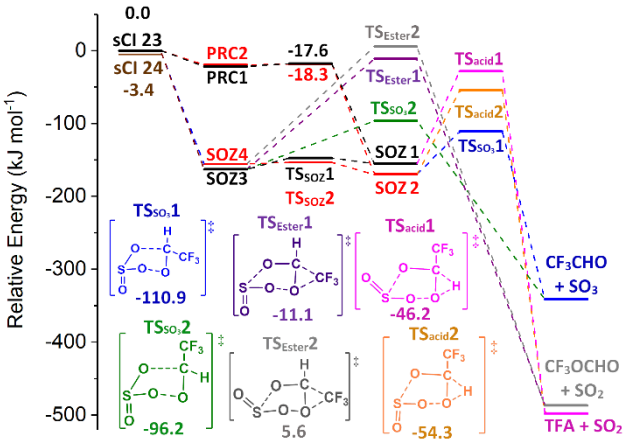

*Figure 5.12: PES of **sCIs 23** & **24** + SO_2 featuring lowest energy SOZ breakdown mechanisms. Energies are relative to raw **sCI 23** + SO_2.*

This type of non-interchangeable, stereochemically-distinct SOZ conformer and fragmentation phenomena is likely to extend to other sCI reactions too. For example, reactions between mono-substituted carbonyl molecule, such as CH_3CHO, and monosubstituted sCI, such as **sCI 23** & **24**, are also likely to produce stereochemically distinct non-interchangeable HOZs, depending on the relative orientation of the reactants.[191,425,453]

*Table 5.5: Overall product branching fractions for SO_2 reactions with of **sCIs 23—26** (for full details on use of $k_{d\text{-}d}$ values as the pre-exponential conditions of reactions see Appendix Section 3.1.4).*

Reaction sCI + SO_2	sCI #	Final Product Branching Ratio Exit $\Gamma_{SO_3 + aldehyde}$	$\Gamma_{SO_2 + acid}$	$\Gamma_{SO_2 + Ester}$	$\Gamma_{SO_2 + other\ CI}$
$CH_2OO + SO_2$	1	0.968	0.032	N/A	N/A
syn-$CF_3CHOO + SO_2$	23	0.9922	0.0019	<0.0001	SO_2 + **CI3**: 0.0059
anti-$CF_3CHOO + SO_2$	24	0.9973	0.0027	<0.0001	SO_2 + **CI2**: <0.0001
syn-$CF_3CFOO + SO_2$	25	0.9860	N/A	0.0090	SO_2 + **CI5**: 0.0050
anti-$CF_3CFOO + SO_2$	26	0.9955	N/A	0.0045	SO_2 + **CI4**: <0.0001

With a high $\Gamma_{SO_3+CF_3CHO}$ (~0.996—0.997), a low yield of acid (Γ_{SO_2+TFA} ~0.002—0.003) and negligible ester yield, **sCIs 23** & **24** + SO_2 reactions produce similar branching ratios to **sCI 1** + SO_2 (see Table 5.5). In contrast to the high yields of CI pathways from HCHO reactions with **sCIs 23** & **24** (>0.80) in section 5.3, the cyclo-reversion yields for **sCIs 23** & **24** + SO_2 are small ($\Gamma_{SO_2 + other\ CI}$ <0.006).)

5.4.3 SO_2 cycloaddition of sCI 25 & 26

Reactions of SO_2 + **sCIs 25** & **26,** whilst similar to **sCI 23** & **24,** have several crucial differences including that the *exo*- and the *endo*- cycloaddition channels for *both* sCI conformers are barrierless (see in Figure 5.13). Therefore, all k_{ME} values exceed the dipole—dipole capture limits ($k_{d\text{-}d}$ ~4.51 & 4.42 × 10^{-10} cm^3 s^{-1}). While there is little

experimental precedence, the large k_{THEO} values for **sCIs 25** & **26** + SO_2 that result from using the $k_{d\text{-}d}$ values are similar to k_{EXP} values for other sCI + SO_2 reactions (~10^{-11} — 10^{-10} cm^3 s^{-1}). [141,184,193,414] The high reactivity of **sCIs 25** & **26** + SO_2 corroborates with the large k_{THEO} values of **sCIs 25** & **26** + HCHO reactions.

SOZ fragmentation for **sCIs 25** & **26** forms only TS_{SO_3} & TS_{Ester} as there are no H-atoms in the right location on the SOZ structure for TS_{acid} to take place. As with **sCIs 23** & **24**, the cycloaddition produces two sets of non-interchangeable SOZs and therefore both SOZ channels exhibit at least 1 TS_{SO_3} and TS_{Ester} decomposition pathway. Despite the divergent TS_{SO_3} & TS_{Ester} barriers (see figure 5.13), the breakdown of SOZ1/3 and SOZ2/4 have similar $\Gamma_{SO_3+CF_3CFO}$ values (0.987 & 0.995).

The TS_{Ester} barriers are low in energy (-83.9 & -69.3 kJ mol^{-1}) compared to those of **sCI 23** + SO_2 (-11.1 & 5.63 kJ mol^{-1}). These lower TS_{Ester} energy barriers give rise to more competitive, if still small, $\Gamma_{SO_2+Ester}$ values for SO_2 + **sCI 25** (~0.009) and SO_2 + **sCI 26** (~0.004) compared to that of the SO_2 + **sCIs 23** & **24** reactions (<0.001). **sCI 26** is 13.0 kJ mol^{-1} lower in energy than **sCI 25** but otherwise the PES are very similar and therefore the SOZ fragmentation branching ratio of the dominant TS_{SO_3} pathway for **sCI 25** + SO_2 ($\Gamma_{SO_3+CF_3CFO}$ ~0.991) and **sCI 26** + SO_2 ($\Gamma_{SO_3+CF_3CFO}$ ~0.996) are also comparable.

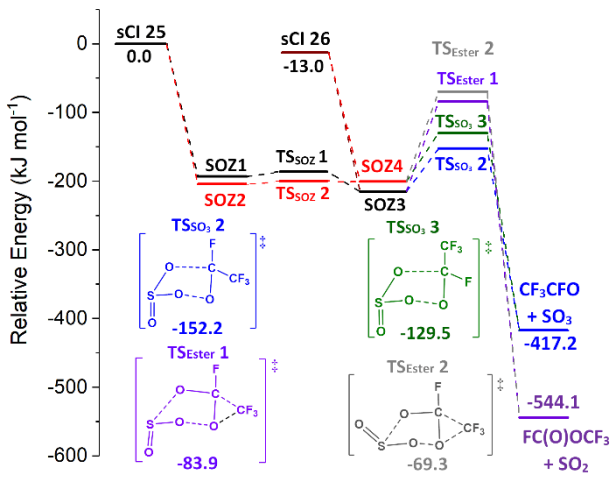

*Figure 5.13: PES of **sCIs 25** & **26** + SO_2 featuring lowest energy SOZ breakdown mechanisms. Energies are relative to raw **sCI 25** + SO_2.*

As with the **sCIs 23** & **24** + SO_2 reactions, the cyclo-reversion channels for the **sCIs 25** & **26** + SO_2 reactions do not contribute significantly to the SOZ fragmentation branching ratios ($\Gamma_{SO_2 + \text{other CI}}$ <0.01) with $\Gamma_{SO_3 + \text{aldehyde}}$ so heavily dominant. The theoretical analysis of SOZ decomposition for **sCI 4** + SO_2, produced by Kuwata *et al.*, is the closest analogous system in the literature. Both show a similar $\Gamma_{SO_3+ R_1CR_2O}$ (0.962) dominance over that of $\Gamma_{SO_2+R_1OC(O)R_2}$ (0.025).[191]

5.4.4 Summary

In summary, the SO_2 + HFO-sCI reactions follow similar 2 stage PES structures observed for HCHO + HFO-sCI, not-withstanding that the SO_2 reactions do not undergo significant SOZ fragmentation via cyclo-reversion. As with sCI + HCHO reactions, **sCI 23** + SO_2 exhibits the lowest k_{THEO} value, of the sCI + SO_2 reactions in this chapter. However, as the rate determining steps for SO_2 reaction with **sCIs 1**, **24**, **25** & **26** are barrierless, they resist the trend seen sCI + HCHO reactions and instead adopt very similar $k_{d\text{-}d}$ values as rate constants. SO_3 + R_1CR_2O is the dominant set of products (Γ > 90%) for all SOZ decomposition pathways, with branching contributions of pathways following this trend: $\Gamma_{SO_3+ R_1CR_2O} \gg \Gamma_{SO_2+ R_1C(O)OH} > \Gamma_{SO_2+R_1OC(O)R_2}$.

5.5 HFO-sCI Reactions with Organic and Inorganic Acids

Both organic acids, such as TFA and carboxylic acids, and inorganic acids, including HNO_3 and HCl, have significant abundance in a wide variety of tropospheric environments, as shown in Appendix Section 3.3.[240,272,305,427,444,447,456] Khan *et al.*, have found sCIs to be competitive with OH radicals as bimolecular sinks for many of these acids, including TFA and HNO_3.[111] A computational analysis of **sCIs 1 & 23—26** reactions with example organic and inorganic acids, TFA and HNO_3, was completed and is analysed further in this section. Given the importance of sCI depletion to tropospheric acids, these reactions may make significant contributions to atmospheric models.

5.5.1 HFO-sCIs Reactions with Nitric Acid

The primary reaction mechanism of the sCI + HNO_3 reaction, a "1,4-insertion", is shown in Figure 5.14 and it leads to the formation of nitrooxyalkyl hydroperoxide (NAHP) product.

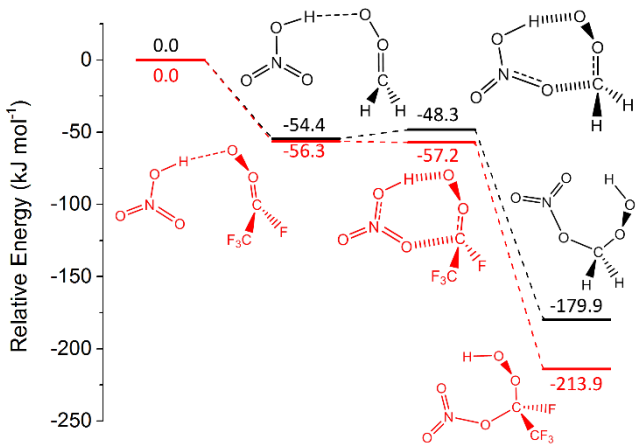

*Figure 5.14: The potential energy surface of HNO_3 with **sCI 1** and **sCI 25**. Energies are relative to raw reactants.*

Previous computational analysis of the **sCI 1** + HNO_3 reaction, seen in the Raghunath *et al.* and Veercken studies, show two significant observations: a competing reaction "1,2-insertion" that also produces nitrooxyalkyl hydroperoxide (NAHP), and the identification of NAHP fragmentation pathways.[307,431] However, the 1,2-insertion has not been explored in this thesis because the Veercken study shows it is over ~30 kJ mol^{-1} higher in energy than the equivalent 1,4-insertion, shown in Figure 5.14. The *secondary* NAHP fragmentation pathways analysed by Raghunath *et al.* and Veercken do not appear to contribute to the understanding of HNO_3 or sCI depletion, the focus of this study. Also, unlike the intermediate products of sCI + HCHO or SO_2 reactions, this NAHP fragmentation occurs over significantly longer time and so is beyond the scope of this study.[307,431]

None of the HNO_3 + sCI reactions are barrierless, but the barrier height varies significantly depending on the sCI, ($\Delta E_{TS_{sCI\ 23}}$ = -29.1 kJ mol^{-1}, $\Delta E_{TS_{sCI\ 24}}$ = -35.9 kJ mol^{-1}, $\Delta E_{TS_{sCI\ 1}}$ = -48.3 kJ mol^{-1}, $\Delta E_{TS_{sCI\ 26}}$ = -52.5 kJ mol^{-1} & $\Delta E_{TS_{sCI\ 25}}$ = -57.2 kJ mol^{-1}). The trend in reactivity indicated by these barrier heights reflect the HFO-sCI reactivity seen in previous sections ($k_{sCI\ 23}$ < $k_{sCI\ 24}$ < $k_{sCI\ 1}$ < $k_{sCI\ 26}$ < $k_{sCI\ 25}$). However, given the high reactivity of the **sCI 1** + HNO_3 reaction, shown in the large k_{ME} value (8.21 × 10^{-9} cm^3 s^{-1}), the $k_{d\text{-}d}$ limit (8.45 × 10^{-10} cm^3 s^{-1}) is used as the rate constant. The use of the $k_{d\text{-}d}$ value is validated by it producing a rate far closer to the k_{EXP} [295 K] value (5.4 × 10^{-10} cm^3 s^{-1}) reported in the Foreman *et al.* study.

Whilst **sCI 25** + HNO_3 has the largest k_{ME} value (9.25 × 10^{-8} cm^3 s^{-1}), following the trend seen for the other **sCIs 23—26** reactions, the $k_{d\text{-}d}$ limit (5.26 × 10^{-10} cm^3 s^{-1}) reduces the rate constant to below that of the usually less reactive **sCI 1** + HNO_3. One noteworthy anomalous result is the unusually large k_{THEO} value (8.87 × 10^{-11} cm^3 s^{-1}) for **sCI 24** + HNO_3. The medium reactivity of **sCI 24** usually leads greater rate constants than its *syn* equivalent, as shown by the k_{THEO} value of the **sCI 23** + HNO_3 (2.06 × 10^{-11} cm^3 s^{-1}), but here it also exceeds the k_{THEO} value of the HNO_3 reaction with **sCI 26** (k_{THEO} ~7.57 × 10^{-11} cm^3 s^{-1}), a usually very reactive sCI.

5.5.2 HFO-sCIs Reactions with Trifluoroacetic Acid (TFA)

The TFA reactions with **sCIs 1** & **23—26** all proceed via a barrierless mechanism, similar to that of HNO_3, to produce hydroperoxy esters (HPE). Figure 5.15 displays and confirms the barrierless nature for TFA + **sCI 25**. All **sCIs 1** & **23—26** + TFA are shown to be barrierless through similar calculations of each MEP in Appendix Section 8.5.

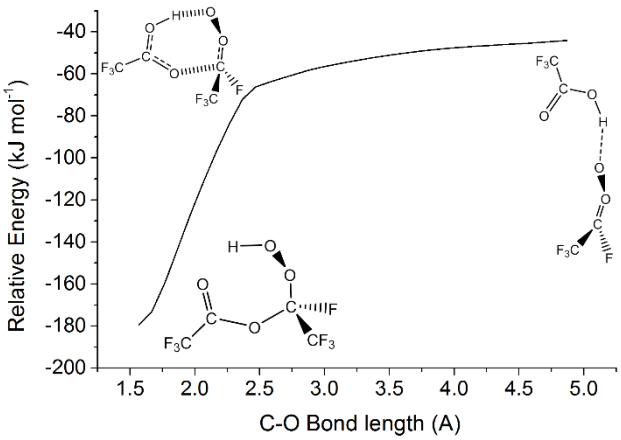

*Figure 5.15: The barrierless minimum energy pathway for **sCI 25** + TFA reaction. Energies are relative to raw reactants.*

As all TFA reactions with HFO-sCI are barrierless, their calculated rate constants exceed $k_{d\text{-}d}$ values (3.98 – 7.54 × 10^{-10} cm^3 s^{-1}). The k_{EXP} for TFA reactions with both **sCI 1** (3.4 × 10^{-10} cm^3 s^{-1}) and the usually much less reactive **sCI 4** (6.1 × 10^{-10} cm^3 s^{-1}) are both quite close to their $k_{d\text{-}d}$ limits (7.54 & 7.57 × 10^{-10} cm^3 s^{-1} respectively).[309] This provides experimental verification that the TFA + sCI reactions are very energetic and therefore that the $k_{d\text{-}d}$ limit calculation is a reliable method for computing their rate constants.[309]

5.6 sCI Reactions with Water Monomer and Dimer

The sCI + H_2O & $(H_2O)_2$ reaction is a dominant loss mechanism for many tropospheric sCIs, due to their large k_{EXP} values and the high abundance of H_2O & $(H_2O)_2$ in the troposphere.[111,293] Significant fractions of these reactions produce α-hydroxy-hydroperoxides (HHP), compounds implicated in forest damage and associated with generating important secondary products like H_2O_2, organic acids and aldehydes.[132,389,390,457–461] sCIs with available α-H atoms in the *syn* position (e.g. **sCIs 2** & **4**) can undergo a 1,4-H transfer to produce a vinyl hydroperoxide (VHP).[93,195,293] This VHP formation can be catalysed during reactions with H_2O, $(H_2O)_2$, H_2SO_4, HCOOH & MeOH. Despite VHP formation being competitive with HHP formation in many sCI + H_2O reactions, this analysis of HFO-sCI + H_2O & $(H_2O)_2$ reactions focuses exclusively on HHP formation, as **sCIs 1** & **23—26** lack the necessary *syn*-α-H atoms required to exhibit VHP channels.

5.6.1 H_2O reaction with sCIs 1 & 23—26

The **sCIs 1** & **23—26** + H_2O systems react via the TS_{HHP} 1 or TS_{HHP} 2 channels, depending on the orientation of the non-reactive O-H bond (see Figure 5.16), producing readily interchangeable conformers of the same HHP. Much like the reactions with HNO_3 & TFA, further breakdown of the HHP product occurs over such lengthy timescales (~2 days) that exploration of HHP breakdown is excluded from this study.[392,462] The lowest energy TS_{HHP} structure depends on the sCI involved (as observed in Figure 5.16). Unusually for the two *syn*-conformer, **sCIs 23** & **25**, TS_{HHP} 2 has the lower energy, whereas TS_{HHP} 1 has the lowest TS barrier energy for **sCIs 1**, **24** & **26**.

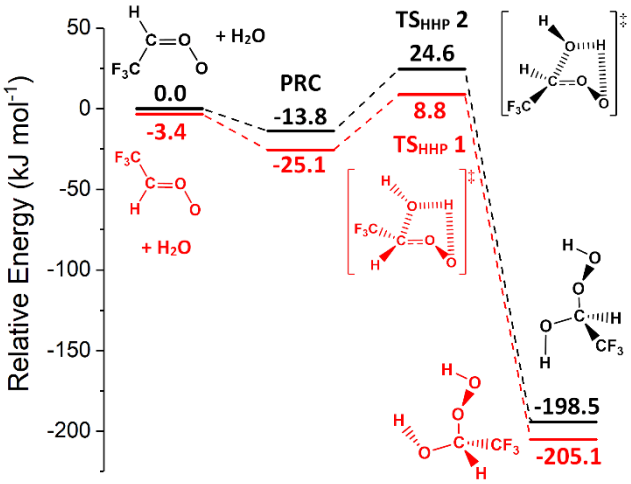

*Figure 5.16: The potential energy surface of the **sCI 23** (in black) & **sCI 24** (in red) reactions with H_2O. Energies are relative to raw **sCI 23** + H_2O.*

The computed reaction of H_2O with **sCI 1** is consistent with prior experimental and theoretical studies. The TS barrier calculated for this chapter is not submerged (14.3 kJ mol^{-1}) and is similar, albeit a little higher than those calculated by Anglada and Solé (6.3 or 9.3 kJ mol^{-1} depending on the method used) for the same reaction.[293] The energy barrier for this chapter produces a k_{ME} (1.18 × 10^{-16} cm^3 s^{-1}) which is within range of k_{EXP} values (0.25 – 13 × 10^{-16} cm^3 s^{-1}), and is particularly close to the value of Sheps *et al.* (k_{EXP} [293 K, 50 Torr] = 2.4 × 10^{-16} cm^3 s^{-1}). [55,178,387,463,464] The k_{ME} value is in agreement with literature studies suggesting that the **sCI 1** reaction has a lower k_{EXP} with H_2O than with HNO_3, SO_2 or TFA.[145,178,272,309,440,454,455,465] Throughout this chapter, the k_{THEO} values for all HFO-sCI + H_2O reactions are all lower than those for equivalent HFO-sCI reactions with HCHO, SO_2 and HNO_3.

The calculations of H_2O reactions with **sCIs 1**, **23** & **24** extends the reactivity trends of this chapter such that the rate constant ordering follows the pattern: $k_{sCI\ 23} < k_{sCI\ 24} \leq k_{sCI\ 1}$. This is also somewhat consistent with previous literature studies of sCI reactions with CH_4, H_2 & $CF_3CH{=}CH_2$, where **sCI 24** is more reactive than **sCI 23**.[273,305,372] One extra observation worth noting is that **sCIs 25** & **26** have a negative temperature dependence, 200 K < T < 400 K, whereas **sCIs 1**, **23**, **24** + H_2O all have a positive temperature dependence. The breakdown of k_{ME} by temperature can be observed in the Appendix Section 3.1.

It is also worth considering if fluorination of a *syn*-/*anti*-CH_3 group, has a significant impact on the sCI + H_2O reaction kinetics, by comparing H_2O + **sCIs 23** & **24** from this chapter with H_2O + **sCIs 2** & **3** (*syn*- & *anti*-CH_3CHOO) from the Anglada *et al.* studies.[195,293] The significant impact of fluorinating methyl groups is shown in the energy differentials between *syn* & *anti* conformers, with H_2O + **sCIs 2** & **3** seeing much larger disparities between their TS_{HHP} 1 barriers (22.34 & -5.02 kJ mol^{-1} respectively), whereas H_2O + **sCIs 23**

& **24** a see only a small differential in barrier heights (25.70 & 12.20 kJ mol^{-1} respectively).[195,293] One major cause of this change is that the destabilising effect of a hyperconjugative *anti*-CH_3 substituent appears to be mitigated by fluorination, reflected by the drop in k_{THEO} between **sCI 3** + H_2O (1.35 × 10^{-13} cm^3 s^{-1}) and **sCI 24** + H_2O (1.12 × 10^{-16} cm^3 s^{-1}).[141,193,388,411] The hyperconjugative effect of having α-H atoms in the *anti*-CH_3 substituent may explain this large gap in reactivity between **sCIs 3** & **24**. A further examination of fluorination on *syn* & *anti*-CH_3 groups is explored for sCI + alcohol reactions, in Section 4.4.

An additional -F substituent in CF_3CFOO conformers, compared to CF_3CHOO, increases the overall k_{ME} value regardless of whether it is an *anti*-F group or a *syn*-F group, such as with **sCIs 25** & **26** respectively (k_{H_2O} ~ 62.1 & 2.3 × 10^{-13} cm^3 s^{-1}). The enhancing effect that both *syn* & *anti*-F substituents have on sCI reactivity, is also seen in an Anglada *et al*. study where the **sCI 8** + H_2O reaction produces a very large k_{THEO} value (4.65 × 10^{-9} cm^3 s^{-1}).[195] This k_{TST} value for **sCI 8** + H_2O does exceed the $k_{d\text{-}d}$ limit determined using the CF_2OO and H_2O structures in this thesis (7.07 × 10^{-10} cm^3 s^{-1}) but the trend is still clear. sCI + H_2O reactions yield lower k_{THEO} values compared to HFO-sCIs reactions with HCHO, SO_2, TFA or HNO_3, even with the -F substituent in **sCIs 25** & **26**.

5.6.2 Reactions between $(H_2O)_2$ with sCIs 1 & 23—26

The mechanism for the sCI + $(H_2O)_2$ reaction is very similar to the monomer equivalent, except that the non-reacting H_2O molecule in the dimer acts to catalyse HHP formation, as shown in Figure 5.17. There are four subchannels for this reaction which depend on the direction of the non-reactive hydrogen atoms, as seen in the case of the monomer reaction. However, in this instance the difference between the four pathways is <5 kJ mol^{-1}. Due to this small energy disparity between channels, the $(H_2O)_2$ + **sCIs 1, 23, 24, 25** & **26** all show a reasonably even contribution to k_{ME} from all sub-pathways (referred to as $TS_{(H_2O)_2}$ 1-4). Details of all the $TS_{(H_2O)_2}$ barriers found in the Appendix Section 3.4.

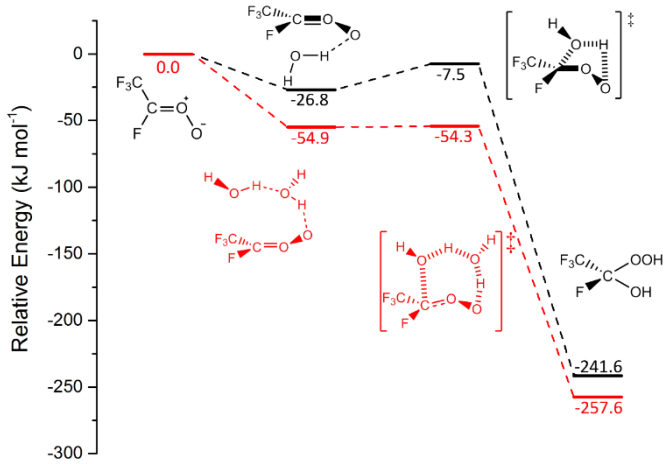

*Figure 5.17: The lowest energy potential energy surface barriers for **sCI 26** reactions with H_2O and $(H_2O)_2$. Energies are relative to raw reactants.*

The small energy difference in barriers seen between subchannels is also borne out in the computational analysis of the **sCI 1** + $(H_2O)_2$ reaction by Anglada and Solé. In that study the $TS_{(H_2O)_2}$ barrier heights range between -35.5 to -30.8 kJ mol^{-1} or -31.4 to -26.3 kJ mol^{-1} depending on the choice of theoretical method.[293] The range of $TS_{(H_2O)_2}$ barrier heights for the **sCI 1** + $(H_2O)_2$ reaction (-27.1 to -21.9 kJ mol^{-1}) generated for this chapter are similar but slightly larger to those seen in the Anglada and Solé study. Despite the divergence in barrier heights with the Anglada and Solé study, the k_{ME} of the **sCI 1** + $(H_2O)_2$ reaction calculated for this chapter (3.28×10^{-12} cm^3 s^{-1}) is very similar to the range of k_{EXP} values reported in the literature ($4.0 - 8.2 \times 10^{-12}$ cm^3 s^{-1}).[55,387,424,466-468]

The $(H_2O)_2$ reactions with **sCI 23—26** exhibit some noteworthy results including that **sCI 23** + $(H_2O)_2$ has the lowest k_{ME} value (2.71×10^{-12} cm^3 s^{-1}). However, the k_{ME} of **sCI 24** + $(H_2O)_2$ is greater (3.74×10^{-12} cm^3 s^{-1}) than that of the **sCI 1** equivalent, reversing the trend seen for HNO_3, H_2O and HCHO. The k_{ME} values of **sCIs 25** & **26** reactions with $(H_2O)_2$ would overwhelmingly surpass **sCI 24**, but the $k_{d\text{-}d}$ (~7×10^{-10} cm^3 s^{-1}) restrains the size of those k_{THEO} values. This means that the k_{THEO} disparity between the H_2O and $(H_2O)_2$ observed with **sCIs 25** & **26** ($10^2 - 10^3$ cm^3 s^{-1}), is significantly smaller than that of **sCIs 1**, **23** & **24** ($10^4 - 10^6$ cm^3 s^{-1}). This has significant atmospheric implications, discussed in Section 5.8.

5.7 Impact of Heteroatom Tuning on sCIs Reactions with H-X (X = F, Cl, OMe, SH and OH)

Within the literature, there is a theoretical study by Kumar and Francisco, which uses a series of "H_2X" co-reactants (where X = O, S, Se or Te) to explore sCI reaction chemistry with respect to trends in co-reactant reactivity. It was found that if the central "X" atomic element of "H_2X" was substituted with an element further down Gr16 on the

periodic table, then the k_{THEO} value increased.[441] The process of substituting a single atom in a co-reactant with another element further up or down the same group on the periodic table, and the effect on bimolecular sCI reactions, is called *heteroatom tuning* of the co-reactant. As *heteroatom tuning* effects were observed in computational studies of H_2X reactions with four different sCIs (**sCIs 1**—**4**), it might be the basis of a new taxonomic grouping.

In previous studies of both ozonolysis of alkenes and sCI chemistry, common patterns, centered on alkene or sCI structure, have been observed in experimental and theoretical literature and they have been used as the basis of taxonomic groupings. In studies by McGillen *et al.* and Vereecken *et al.*, these larger taxonomic groups of alkenes and sCIs are used as part of a model to predict the rate constants of alkene ozonolysis or unimolecular decay of sCIs. The application of such models can be observed when a large group of organic peroxy radicals are often treated as the same "RO_2" molecule for the purposes of atmospheric simulations modelling, such as *AtChem 2*.[469]

These taxonomy-based methods, if applied to sCIs, are mainly used on the basis of the sCI structure (e.g. *syn*- or *anti*-sCI), or the type of substituents (e.g. halogenated), not on features of a co-reactants. However, the *heteroatom tuning* study by Kumar and Francisco is limited in scope and has been extended greatly herein through computations of HFO-sCIs reactions with both Gr16 centred co-reactants (H_2O, MeOH & H_2S) and Gr17 centred co-reactants (HF & HCl).[441] Whilst this studying of various sinks for significant tropospheric gases, such as H_2O, HCl, MeOH & H_2S, are important, the trends observed in this section could provide the core of a new taxonomy-based method of determining sCI bimolecular chemistry using the co-reactant. If applied, these models could reduce cost required to run the large number and variety of sCI reactions in atmospheric simulations.[118,182,335]

5.7.1 sCI Reactions with Hydrogen Sulphide (H_2S)

H_2S is a common tropospheric gas, mostly abundant in localised regions that produce geothermal power or have volcanic activity, but it is toxic and so removal by sCIs would be beneficial to human health.[2,81,89,470] sCI + H_2S reactions have two TS channels and these both produce the same hydrosulphide alkyl hydroperoxide.

The benchmark reaction, **sCI 1** + H_2S sees a drop in energy for the lowest TS reaction barrier (4.3 kJ mol^{-1}) compared to **sCI 1** + H_2O (14.3 kJ mol^{-1}), which is consistent with the prior study by Kumar and Francisco.[441] The changes in relative energies yield a k_{ME} for **sCI 1** + H_2S (7.06×10^{-15} cm^3 s^{-1}), higher than **sCI 1** + H_2O (1.18×10^{-16} cm^3 s^{-1}). This is a similar trend as observed in k_{EXP} values for the H_2S (1.7×10^{-13} cm^3 s^{-1}) and H_2O (0.25 – 13 × 10^{-16}

cm^3 s^{-1}) reactions.[55,178,387,463,464,471] Both k_{ME} and k_{EXP} yield a difference of ~10^2 cm^3 s^{-1} upon heterosubstitution, in line with the Kumar and Francisco study.[441] In fact the Kumar and Francisco computational study shows that the further down Gr16 the H_2X central atom is, the lower the sCI + H_2X reaction barrier.[441] This disparity is suggested to be due to the weaker covalent hydrogen bond of H_2S, evident in the increased S-H vs. O-H bond length.[441]

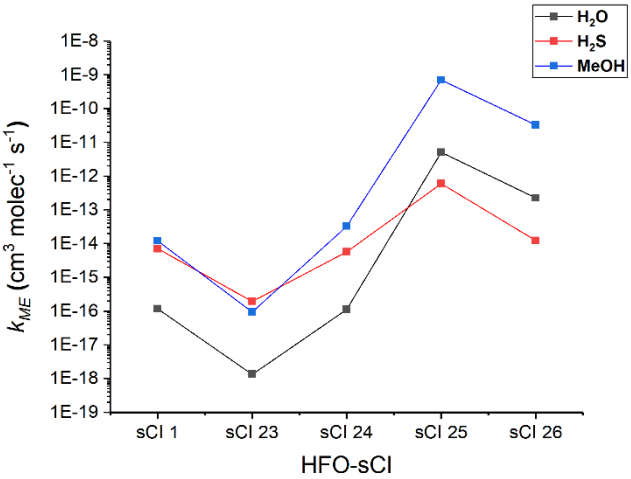

*Figure 5.18: A comparison of the impact that heteroatom tuning of the Gr16 centred co-reactant (identity in the legend) has on the bimolecular rate constant (k_{ME}) of different HFO-sCI reaction. Of note in this figure is the large increase in reactivity for **sCIs 25** & **26** + H_2O and MeOH that is **not** observed in H_2S reactions.*

The impact of heteroatom tuning can be observed in the low barriers for **sCIs 23** & **24** + H_2S (9.9 & 1.7 kJ mol^{-1}) compared to their H_2O equivalents (24.6 & 12.2 kJ mol^{-1}). As observed in Figure 5.18, **sCIs 23** & **24** have larger k_{H_2S} values (1.96 & 57.2 × 10^{-16} cm^3 s^{-1}) than k_{H_2O} values, a continuation of the pattern seen for **sCI 1** + H_2X. This higher reactivity for sCI + H_2S reactions continues the observations of Kumar and Francisco, which reported lower reaction barriers for **sCIs 2** & **3** + H_2S (10.5 & -20.9 kJ mol^{-1}) compared to H_2O equivalent reactions (22.6 & -7.5 kJ mol^{-1}).[441] Despite the impact of heteroatom tuning, sCI + H_2S reactions continue much of the reactivity trend ($k_{sCI\ 23} < k_{sCI\ 24} < k_{sCI\ 1}$) seen for much of this study.

While the addition of CF_3 or CH_3 substituent groups seems to have little effect on the high reactivity of sCI + H_2S reactions, the addition of the -F substituent groups seen in **sCIs 25** & **26**, appears to induce stagnation in the reactivity of the sCI + H_2S reaction. The k_{ME} of **sCIs 25** & **26** reactions with H_2S (60.8 & 1.23 × 10^{-14} cm^3 s^{-1}) sees only a marginal increase due to the introduction of the -F substituent, whereas with most other bimolecular sCI reactions in this study, such as with **sCIs 25** & **26** + H_2O (k_{ME} ~51.3 & 2.27 × 10^{-13} cm^3 s^{-1}), the increase in k_{ME} is large. While there are overall increases for both k_{H_2O} and k_{H_2S} values, Figure 5.18 shows that the -F substituent leads to k_{H_2O} exceeding k_{H_2S} for both **sCIs 25** &

26, an inversion of the trend seen for **sCIs 1**, **23** & **24**. However, this trend inversion, where $k_{H_2S} < k_{H_2O}$ for **sCIs 25** & **26** reactions is unlikely to be caused by any increases in steric bulk because the additional -F group is quite small. Also, despite the greater steric bulk of **sCI 4** than **sCIs 25** & **26**, the Kumar and Francisco computational analysis of the **sCI 4** reaction shows that there is a higher energy barrier for reaction with H_2O (17.6 kJ mol^{-1}) than that of reaction with H_2S (2.9 kJ mol^{-1}).[441]

Similar to the other reactions in this study, **sCI 25** has the largest k_{ME} of the H_2S reactions, with a change in k_{ME} between **sCI 1** and **sCI 25** less than one order of magnitude. This is quite low compared to other reactions with other tropospheric co-reactants, for example the case of H_2O where the change is ca. three orders of magnitude. This is an indicator that the heteroatom tuning trend, namely that the rate constant for sCI + H_2X increases with the size of the "X" atom, observed for **sCIs 1**, **23** & **24** here, as well as for **sCIs 2—4** in the Kumar and Francisco study, may not apply to **sCIs 25** & **26** reactions with H_2X.

5.7.2 sCI Reactions With Methanol (MeOH)

The theoretical trends seen for sCI + H_2O & H_2S reactions (such as $k_{H_2S} > k_{H_2O}$ for **sCIs 1**, **23** & **24** and $k_{H_2O} > k_{H_2S}$ for **sCIs 25** & **26**) are well explored in the previous section, but it is not yet entirely clear what gives rise to this rate tuning, for example whether these observations are caused by tuning of electronic factors alone or whether steric interactions play a more important role. The MeOH reactions with **sCIs 1** & **23—26** proceed via the same type of hydrogen abstraction reaction mechanism as sCI + H_2O/H_2S (Chapter 4) but these additional sCI + MeOH reactions provide is additional steric bulk in the co-reactant with minimal changes in electronic co-reactant character.

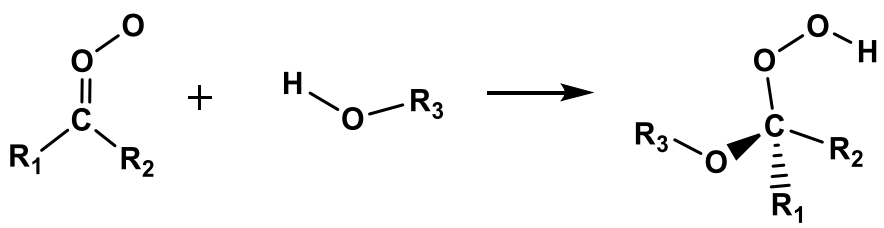

Figure 5.19: Formation of AAAHs from the sCI + alcohol reaction

Much like the sCI + H_2O reactions, the sCI + MeOH reactions proceed through a transition state to produce an α-alkoxyalkylhydroperoxides, AAAH (seen in Figure 5.19), an oxidising species implicated in forest damage and SOA formation.[141,195,293,387-391] The submerged barrier of the **sCI 1** + MeOH reaction (-3.8 kJ mol^{-1}) contrasts with the emergent barrier of the **sCI 1** + H_2O reaction (14.3 kJ mol^{-1}) leading to a significantly higher **sCI 1** + MeOH k_{ME} value (1.20×10^{-14} cm^3 s^{-1}) compared to the H_2O reaction (1.18×10^{-16} cm^3 s^{-1}). As seen in

Figure 5.18, this gap between the k_{H_2O} and k_{MeOH} constants of ~10^2 cm^3 s^{-1} is consistent across all **sCIs 1, 23—26** and the stagnation seen for H_2S + **sCIs 25** & **26** reactions are not observed for the **sCIs 25** & **26** + MeOH reactions. In general, the sCI + MeOH reaction exhibits the same reactivity trend that has been observed for most of this chapter: $k_{sCI\ 23} < k_{sCI\ 24} < k_{sCI\ 1} < k_{sCI\ 26} < k_{sCI\ 25}$. As there is no mitigation in the reactivity of **sCIs 25** & **26** in their reaction with MeOH, it appears that the interaction between the new -F substituent in **sCIs 25** & **26** and the large sulphur atom in H_2S in the reaction is responsible for stagnation of k_{ME} values.

Table 5.6: Reaction between MeOH and HFO-sCIs number; ratio between OO and CO bond lengths on the carbonyl oxide moiety (q); Energy barrier of TS_{AAAH} 1 and lowest TS_{AAAH} 2; total rate constant (k_{THEO}).

Reaction sCI + MeOH	sCI #	*q*	TS_{AAAH} 1 (kJ mol^{-1})	TS_{AAAH} 2 (kJ mol^{-1})	k_{THEO} (298.15 K) (cm^3 s^{-1}) *
CH_2OO + MeOH	1	1.078	-3.82	0.10	1.20×10^{-14}
syn-CF_3CHOO + MeOH	23	1.064	5.80	11.67	9.43×10^{-17}
anti-CF_3CHOO + MeOH	24	1.071	-9.41	-5.49	3.30×10^{-14}
syn-CF_3CFOO + MeOH	25	1.114	$\gg k_{d\text{-}d}$	-27.30	5.50×10^{-10} **
anti-CF_3CFOO + MeOH	26	1.101	-26.18	-26.39	3.31×10^{-11}

** the k_{THEO} constant was obtained using the microcanonical rate (k_{ME}) method using MESMER software.*
*** rate constant was obtained using dipole-dipole capture limit due to a reaction channel being barrierless.*

By integrating the computational analysis of MeOH reactions in this chapter, with **sCIs 2** & **3** + MeOH found in the extended analysis of sCI + MeOH reactions in Chapter 4, comparative effects of fluorination of a methyl substituent group can be observed. The MeOH + **sCIs 3** & **24** reactions both have higher reactivities than MeOH + **sCIs 2** & **23** reactions, but the k_{MeOH} of **sCI 24** (3.30×10^{-14} cm^3 s^{-1}) is significantly lower than the k_{MeOH} of **sCI 3** (2.09×10^{-12} cm^3 s^{-1}). This is perhaps due to the increased hyper-conjugative effects of having the 3 × α-H atoms on the *anti*-CH_3 group, which is consistent with the comparative analysis of the k_{THEO} values of H_2O + **sCIs 3** & **24**, as noted in Section 5.6.1. Another observation in Section 5.6.1 is that, while the additional stabilising *H-bonding* interaction between α-H atoms on a *syn*-CH_3 group and the terminal oxygen lowers the k_{H_2O} constant for **sCI 2**, the repulsion between the α-F atoms on a *syn*-CF_3 group and the terminal O destabilises **sCI 23** and increases the k_{H_2O} constant. The stabilising effect of the α-H atoms in **sCI 2** means that it generates a lower k_{MeOH} value (1.82×10^{-17} cm^3 s^{-1}) than **sCI 23** + MeOH does (9.43×10^{-17} cm^3 s^{-1}). This is explored further in the sCI + alcohol study in Section 4.4.3 and for a full analysis of sCI + alcohol reactions, see Chapter 4.

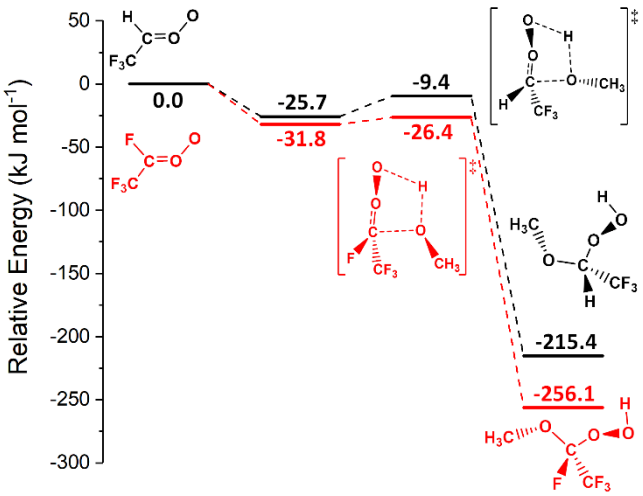

*Figure 5.20: The lowest energy potential energy surface barriers for **sCIs 24** & **26** reactions with MeOH. Energies are relative to raw reactants.*

However, the main observation from this analysis of **sCIs 1, 23—26** + MeOH continues to be that the "stagnation" of reactivity seen in H_2S reactions with **sCIs 25** & **26**, is likely caused by the -F substituent group on the sCI interacting with the large sulphur atom in H_2S.

5.7.3 Reactions with HF & HCl with HFO-sCIs

According to computational analysis in studies by Chhantyal-Pun *et al.* and Foreman *et al.*, both sCI + NH_3 and sCI + HCl reactions also proceed via similar H-X bond abstraction mechanisms to the sCI + H_2X reactions studied in Section 5.7.1.[272,325] This means that a heteroatom tuning analysis could be undertaken by substituting the central X atom with other elements from the same periodic group to analyse in either sCI + XH_3 (XH_3 = NH_3 & PH_3) or sCI + HX (XH = HF & HCl) reactions. It is worth noting at this point that HCl can have high tropospheric concentrations, most significantly in atmospheric environments near large bodies of salt water. In these areas, tropospheric modelling suggests that HCl reactions with sCIs are competitive with OH radicals as a sink for HCl gas.[111,427] While there are significant emissions of HF from volcanic eruptions and geothermal emissions, little computational or experimental chemistry has been undertaken for the reactions between sCIs and HF.[447] In this section, analysis of the sCI + HF & HCl reactions undertaken by the author is compared against the heteroatom tuning trends in sCI + H_2X to see if these trends hold, are amplified or dissipate for the sCI + HX reactions.

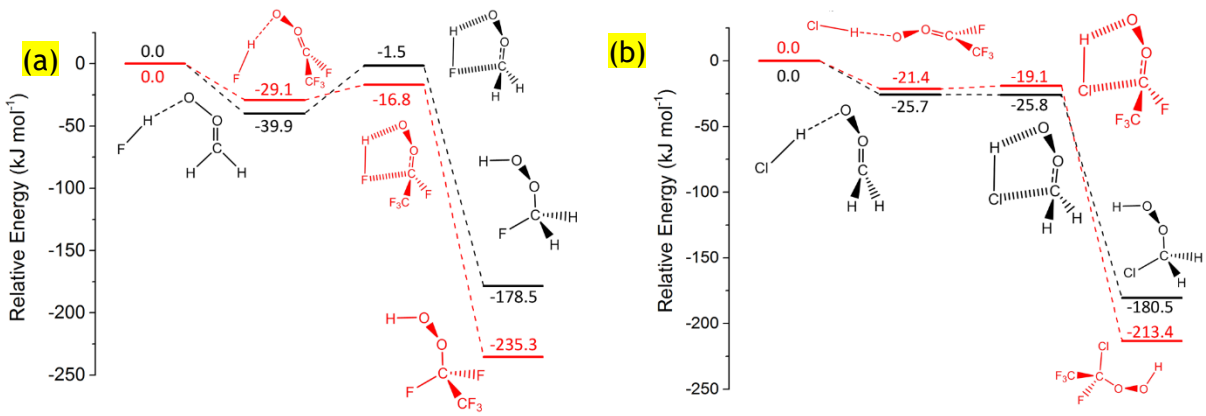

*Figure 5.21: Comparison of the potential energy surfaces of **sCI 1** and **sCI 25** with H-F (on the left, referred to as Figure 5.21a) and HCl (on the right, referred to as Figure 5.21b). Energies are relative to raw reactants.*

The sCI + HF reaction has some notable differences with its analogue sCI + H_2O reaction, including exhibiting no subchannels. **sCI 1** + HF (3.32×10^{-13} cm^3 s^{-1}) also has a significantly larger k_{ME} than that of **sCI 1** + H_2O (1.18×10^{-16} cm^3 s^{-1}). The k_{ME} of **sCI 24** + HF (2.86×10^{-15} cm^3 s^{-1}) is larger than that of **sCI 23** (6.67×10^{-18} cm^3 s^{-1}), with a much greater difference in k_{HF} values (~5×10^3 cm^3 s^{-1}) than that seen for k_{H_2O} (~1×10^2 cm^3 s^{-1}). Overall, the reactivity trend observed for HFO-sCIs + HF, $k_{sCI\ 23} < k_{sCI\ 24} < k_{sCI\ 1} < k_{sCI\ 26} < k_{sCI\ 25}$, is exactly the same as that of H_2O, but HFO-sCI + HF reactions are marginally more reactive than with H_2O.

Much like the changes in reactivity between H_2S and H_2O, **sCIs 1, 23—26** + HCl all see overall increases in reactivity over HF. **sCI 1** + HCl has a very low TS energy, shown in Figure 5.21a, and consequentially its large k_{ME} (4.70×10^{-10} cm^3 s^{-1}) are reasonably consistent with literature values e.g. k_{EXP} ~4.6×10^{-11} cm^3 s^{-1}.[272] One important observation of **sCI 1** + HF & HCl is that as the heteroatom of the H-X co-reactant increases in size, the k_{ME} of the reaction with **sCI 1** increases. A similar heteroatom tuning trend that is seen in the increase in k_{ME} value moving from **sCI 1** + H_2O to **sCI 1** + H_2S.

The enhanced reactivity of this heteroatom tuning is also evident in the reactions of **sCIs 23** & **24**. These sCIs have an increase in reactivity from HF to HCl of k_{ME} (~10^3 — 10^4 cm^3 s^{-1}). This is larger than the reactivity change moving between H_2O and H_2S (~10^1 — 10^2 cm^3 s^{-1}), with full results in Table 5.2 in section 5.2. However, as in Figure 5.21b, changes in sCI substituent (i.e. between -CF_3 and -F), now have limited impact. In fact, the k_{ME} of HCl + **sCI 1** exceeds both that of HCl + **sCI 25** (1.64×10^{-10} cm^3 s^{-1}) and **sCI 26** (1.13×10^{-10} cm^3 s^{-1}) for the only time in this chapter.

To the author's knowledge there is no experimental or theoretical data in the literature on **sCIs 23—26** reactions with HF or HCl but there is a computational study of HCl reactions with **sCIs 2** & **3** by Cabezas and Endo.[472] The data in the Cabezas and Endo study

does exhibit some similar trends to the data garnered here, but the potential energy surfaces of **sCIs 1** & **23—26** + HCl calculated for this chapter are refined using a higher level of theory, so such comparisons are limited in scope. The brief comparative analysis to the Cabezas and Endo study is therefore on Appendix Section 3.6.

5.7.4 Overview of Heteroatom Tuning on HFO-sCI + H-X reactions

The heteroatom tuning reported in this sCI — H-X abstraction analysis identifies several key properties, some of which already exist in the literature, and others that do not. The first characteristic is that all their primary reaction mechanisms proceed via the same hydrogen abstraction. The second characteristic is that the more polar co-reactants e.g. those with -F & -Cl produce a larger k_{ME} than their Gr16 counterparts -OH & -SH.

One significant heteroatom tuning trend is that, in reactions with **sCIs 1 & 23—24**, the co-reactants with the larger heteroatoms, such as H_2S and HCl, produced larger k_{ME} values than those with the small heteroatoms, like H_2O and HF. This agrees with heteroatom tuning trends identified by the Kumar and Francisco computational study, where H_2S produced larger rate constants than H_2O in reactions with **sCI 1—4**. Much of these theoretical observation, such as the k_{THEO} values, found for **sCI 1** reactions with H_2O, H_2S & HCl have been experimentally and theoretically confirmed.[55,178,195,272,387,441,463,464,471] Reactivity trends with **sCI 1** and Group 14 compounds (XH_4) have also been investigated, and show increased k_{TST} [**sCI 1** + SiH_4] over that of CH_4, again consistent with the observations made here.[273] To the best of the authors knowledge there are no comparisons of sCIs reactions with both PH_3 and NH_3.

5.8 Atmospheric impact of HFO-sCI reactions

As HFOs proliferate into widespread use in refrigerators, insulation and vehicle cooling systems (as is happening in China, the EU and the USA), HFO-sCIs are naturally becoming more abundant. As this occurs, they may start to compete as bimolecular sinks for tropospheric species on a more global level.[197,198] This thesis assists in classifying and understanding the tropospheric chemistry of HFO-sCIs, with the ultimate goal of dividing them into taxonomic groups for inclusion in atmospheric models. It is also important to identify deviations in reactivity trends e.g. the higher reactivity of a *syn*-conformer, **sCI 25**, over an *anti*-conformer, **sCI 26**; or the fact that during heteroatom sCI + H_2X or HX reactions the most reactive sCIs, **sCIs 25** & **26**, stagnate or reduce the reactivity when reacting with H_2S or HCl. These discrepancies are vital to understand, because

atmospheric models that do not include such subtleties in reaction kinetics may not prove reliable in calculating pollution levels, where HFO concentrations are very high.

Table 5.7: Calculated effective first-order rate constant (k_{eff}) values for HFO-sCI + co-reactant reactions in this chapter (derived from Table 5.2)

Co-reactant	k_{eff} (s^{-1})				
	CH_2OO **sCI 1**	*syn*-CF_3CHOO **sCI 23**	*anti*-CF_3CHOO **sCI 24**	*syn*-CF_3CFOO **sCI 25**	*anti*-CF_3CFOO **sCI 26**
HCHO	5.6	0.54	5.0	1447	33.4
SO_2	300	0.79	169	186	183
HNO_3	94	2.3	9.8	58	8.4
TFA	2.5×10^{-2}	1.7×10^{-2}	1.3×10^{-2}	1.2×10^{-2}	1.2×10^{-2}
H_2O	73	0.83	70	3.2×10^{6}	1.4×10^{5}
$(H_2O)_2$	2.9×10^{3}	2.4×10^{3}	3.3×10^{3}	6.2×10^{5}	6.1×10^{5}
MeOH	0.010	7.9×10^{-5}	0.028	462	28
H_2S	0.085	1.4×10^{-3}	0.042	4.5	0.091
HCl	58	5.0×10^{-3}	8.96	20	14
HF	0.12	2.5×10^{-6}	1.1×10^{-3}	4.4	0.14

Contrasting the effectiveness of $(H_2O)_2$ as an sCI sink with that of H_2O is particularly noteworthy when comparing **sCIs 1**, **23** & **24** with **sCIs 25—26**. For example, **sCI 23** has a 10^6 cm^3 s^{-1} larger $k_{(H_2O)_2}$ than k_{H_2O}, which negates the increased natural abundance of H_2O (6.2×10^{17} molec. cm^{-3}) over $(H_2O)_2$ (8.7×10^{14} molec./cm^3). This gives **sCI 23** that k_{eff} ($(H_2O)_2$) is around 10^3 s^{-1} higher than k_{eff} (H_2O), which is standard for most sCIs in comparing the impact of H_2O and $(H_2O)_2$. In more straightforward terms, this means that because k_{eff} ($(H_2O)_2$) > k_{eff} (H_2O), tropospheric removal of **sCI 23** is more likely to occur through reaction with water dimer than with water monomer. **sCI 1** and **sCI 24** also exhibit larger k_{eff} ($(H_2O)_2$) than k_{eff} (H_2O) varying between 10^1—10^3 s^{-1}. The high theoretical impact of the $k_{(H_2O)_2}$ value on **sCIs 1**, **23** & **24** depletion compared with the still high but lower theoretical impact of k_{H_2O} is reflecting the same observation in the experimental analysis of **sCI 1** and **sCI 3** reactions with water (a larger k_{EXP} $((H_2O)_2)$ ~10^{-12}—10^{-11} cm^3 s^{-1} compared to the k_{EXP} (H_2O) ~10^{-16}—10^{-14} cm^3 s^{-1}). This is borne out in the computational study by Anglada and Solé, where **sCIs 1—4** all have a 10^4—10^6 cm^3 s^{-1} greater $k_{(H_2O)_2}$ than k_{H_2O}.[293] **sCIs 1, 23** & **24** + $(H_2O)_2$ all have a greater than k_{eff} (H_2O). (see Appendix Section 3.3).

Unlike reactions with the sCIs mentioned above, **sCIs 25** & **26** + $(H_2O)_2$ reactions exceed the dipole-dipole capture limit, $k_{d\text{-}d}$, which provides an upper limit to the k_{eff}. Correspondingly, sCI reactions with H_2O approach, but crucially are *not* constrained by $k_{d\text{-}d}$. Therefore, k_{H_2O} for **sCIs 25** & **26** is much more similar to the $k_{(H_2O)_2}$, and thus the higher abundance of H_2O over $(H_2O)_2$ leads to the unusual result that k_{eff} (H_2O) is significantly greater than k_{eff} ($(H_2O)_2$) for **sCIs 25** & **26**.

Reactions between sCIs and $H_2O/(H_2O)_2$ have been shown to be a significant tropospheric source of α-hydroxy-hydroperoxides. Due to the larger k_{ME} of these HFO-sCIs with H_2O, and the high abundance of water vapour, these reactions may be a significant source of fluorinated α-hydroxy-hydroperoxides.

Some sCI reactions like sCI + SO_2 and HNO_3 reactions do produce large k_{eff} values (1—300 s^{-1}), which is expected as sCIs compete with OH radicals (the atmospheric detergent) in the depletion of tropospheric SO_2 and HNO_3 species. But these reactions are still not very prominent sCI depletion pathways, as the large k_{eff} values for the **sCIs 1**, **23**—**26** + H_2O or $(H_2O)_2$ reactions (10^3—10^6 s^{-1}) are so much higher. The atmospheric importance of the rate $k_{d\text{-}d}$ limit is shown in the **sCI 25** + HCHO reaction, which, despite more reactive than the **sCI 25** + H_2O or $(H_2O)_2$ reactions, still has a significantly lower k_{eff} value (~1447 s^{-1}), due to the constraint to the rate constant provided by the $k_{d\text{-}d}$ value.

The overall effectiveness of these co-reactants as sCI sinks varies with co-reactant choice. The k_{eff} (SO_2) of **sCIs 1, 23** & **24** are comparable with the k_{eff} (H_2O), & k_{eff} ($(H_2O)_2$), more so than **sCIs 25** & **26**. This means that the reaction with SO_2 is competitive with water and water dimer as a tropospheric sink for **sCIs 1, 23** & **24**. This high tropospheric abundance H_2O and $(H_2O)_2$ and the steep increase in k_{ME}, which is not large enough to reach the $k_{d\text{-}d}$ values, also leads to the same observation for HFO-sCI reactions with TFA & HNO_3. This sharp increase in the k_{eff} across **sCIs 25** & **26** + H_2O and $(H_2O)_2$, means that the k_{eff} of the less reactive **sCIs 1, 23 & 24** + TFA & HNO_3 produce more competitive k_{eff} values, because the $k_{d\text{-}d}$ provides a key restraint for most of the highly reactive sCI reactions with TFA & HNO_3. This stagnation in k_{eff} values is not repeated across **sCIs 1**, **23**—**26** for reactions with HF and MeOH and the k_{eff} scales with reactivity of the sCI, but due to the low abundance of tropospheric HF and MeOH, their k_{eff} values are not too competitive, relative to the comparable reactions with H_2O and $(H_2O)_2$. The **sCIs 1**, **23** & **24** reactions involving HCl and H_2S have increased k_{ME} compared to HF and H_2O, leading to a significant convergence of k_{eff} for all **sCIs 1**, **23** & **24** reactions, including HCl, H_2S, H_2O & $(H_2O)_2$ as co-reactants. The plateau in k_{ME} reached by **sCIs 25** & **26** causes a significant drop in magnitude of their k_{eff} values. Regardless of these nuances, the computed k_{eff} values still suggest that H_2O and $(H_2O)_2$ are the dominant bimolecular sink for **sCIs 1** & **23—26**.

For atmospheric models, an important observation is that reactions of SO_2 with **sCIs 23—26** have very high reaction k_{THEO} constants and are > 90% efficiency in R_1CR_2O + SO_3 production. These reactions therefore act as a significant producer of atmospheric H_2SO_4 and aerosols.[187-190] sCI + SO_2 reactions also contribute a small amount to atmospheric budgets of HCOOH, for **sCI 1,** or TFA, for **sCIs 23** and **24**.

HCHO is a ubiquitous chemical gas in building and other urban environments. It is a by-product of the ozonolysis of many HFOs (and other alkenes), so in areas of high alkene or HFO emission, the computed k_{eff} may underestimate the importance of these reactions with respect to tropospheric composition.[224,241,351] Reactions between HFO-sCIs & HCHO give sizeably varying product distributions based on the sCI. **sCI 1** + HCHO predominantly leads to the production of HCOOH (>99%), assuming 100% conversion of HAE to HCHO + HCOOH. **sCIs 23** & **24** + HCHO yield non-negligible amounts of the cyclo-reversion products CF_3CHO + **sCI 1**, which should be significant as it contributes to total populations of sCIs and of course forms a smaller, more reactive sCI in the process. These reactions also generate other atmospheric species, such as TFA, HCOOH & CF_3CHO. **sCIs 25** & **26** + HCHO product distribution is dominated by CF_3CFO + **sCI 1** with a small yield of HCOOH & CF_3CHO. During the HCHO reactions with **sCIs 25** & **26**, there is a significant drop in energy (~100 kJ mol^{-1}) between reactants and products of the cyclo-reversion pathway (**sCI 1** + CF_3CFO), which means the products may have high internal energy. The large **CI 1** + CF_3CFO yield (~0.9) with high levels internal energy, may lead to a large yield of *hot* CIs and a subsequent increase in the OH yield, similar to that seen in the ozonolysis of alkenes.

Comparing reactions of **sCI 1** with HCHO, CF_3CHO and CF_3CFO, the rate constants are relatively similar. **sCI 1** reactions with CF_3CHO and CF_3CFO may be significant in more local environments as both reactants produced as ozonolysis by-products and CF_3CHO and CF_3CFO are not common on a planetary level.[224,367] Although HCHO is common in the atmosphere and CF_3CHO & CF_3CFO are not, their relatively similar rate constants with **sCI 1** indicates that aldehydes and ketones may provide a taxonomic class of reactions too, at least with respect to deriving rate constants. Compared with **sCIs 23—26** + HCHO, the reactions of **sCI 1** with CF_3CHO and CF_3CFO yield very little cyclo-reverted sCI product and instead produce greater quantities of TFA & HCOOH. These **sCIs 1, 23—26** reactions with HCHO (and CF_3CHO and CF_3CFO) may be important, less because they provide vital sinks for sCIs or pollutant co-reactants, but because of what species the HOZ intermediate fragmentation produces.

Small but significant yields of TFA & HCHO also emerge from reactions of **sCIs 23** & **24** with HCHO, but are unlikely to be as important in this regards due to the high yield of the **sCI 1** + CF_3CHO cyclo-reversion pathway. In contrast the **sCI 1** + CF_3CHO reaction may yield significant amounts of TFA & HCHO products. It has been shown that HFOs, such as HFO-1234yf, produce significant amounts of atmospheric TFA and this work is in clear agreement, demonstrating that reactions of **sCIs 23** & **24** with HCHO and SO_2 give non-

negligible yields of TFA.[224,240] With this in mind, reactions of TFA and **sCIs 23—26**, formed from the decomposition of the same HFOs, may be of greater tropospheric significance than previously assumed. The computational analysis of TFA reactions with **sCIs 1** & **23—26** in this chapter adds to evidence that the sCI reaction with carboxylic acids are a barrierless or close to barrierless reaction series, found in much of the experimental and computational literature.[309,320] This means that the sCI reaction with carboxylic acids can be added to a taxonomic class of barrierless sCI reactions.

5.9 Further work of HFO-sCI reactions

Perhaps the most important future work to come from this chapter is the creation of formal taxonomic classes, creating groups of like-reactions or similar sCIs. These taxonomic groups could then be added into atmospheric models, such as *AtChem 2.0*, to determine the impact of these sCI bimolecular reactions compared to other sinks for trace atmospheric species, such as reaction with OH radicals. As shown in chapter 4, there is very little variation in k_{THEO} constants between sCIs with MeOH, EtOH and iPrOH, so this would be an example of a good taxonomic group, albeit somewhat small. Identifying similar reactivity groups from this chapter and ensuring there are few deviations from predicted reactivity is key. This work is already underway.

HFO-sCIs have been experimentally investigated, predominantly focusing on *syn*-/*anti*-FCHOO, CF_2OO, *syn*-/*anti*-ClCHOO and CCl_2OO (**sCIs 5—10**). This study has expanded upon this research and focused on the HFO-sCIs with limited prior knowledge, such as *syn*-/*anti*-CF_3CHOO & *syn*-/*anti*-CF_3CFOO (**sCIs 23—26**). However, the breadth of this study could be expanded further. Several other halogenated alkenes are already in commercial circulation and have been shown to react with O_3. Many of these HFOs are both used in both industrial practices but also in fine chemical synthesis, including $CH_2{=}CHCH_2Cl$, $CH_2{=}CHCH_2Br$ & $CH_2{=}CHCH_2I$. CFC replacements also include HFO-1345fz & $(CF_3)_2C{=}CH_2$.[241,335,473-475] Ozonolysis of these HFOs could generate HFO-sCIs including $(CF_3)_2COO$, $ClCH_2$-CHOO, $BrCH_2$-CHOO, ICH_2-CHOO, CF_3CF_2-CHOO from HFO-1345fz and CH_3-CClOO or Et-CClOO.[241] If a study on these other HFO-sCIs, which are not studied in this thesis, is undertaken, it would be beneficial to identify which of the HFOs just mentioned would be most frequently emitted into the atmosphere to identify which of those CIs would have the most impact.

This study could also be extended to other important atmospheric co-reactants such as aldehydes and ketones, for example CH_3CHO and $(CH_3)_2CO$, which have been observed experimentally in reaction with CH_2OO.[428] Taxonomic classification of these sCI + aldehyde & ketone reactions, and reactions like them that react via cyclic ozonide intermediate

products, could be explored further for rate constants and product branching ratios but this maybe much more complex as they often produce non-interchangeable HOZ/SOZ sets (similar to those seen for SO_2 reactions with **sCIs 23—26**). This effect has minimal impact on SOZ decomposition trends for SO_2 reactions with **sCIs 23—26**. It should be highlighted that this initial observation does not eliminate the possibility of altering the SOZ decomposition trends of other sCI reactions with SO_2, or indeed with aldehydes or ketones. The simplest example of sCIs reacting with aldehydes to produce non-interchangeable HOZ/SOZ sets is **sCIs 2** & **3** with CH_3CHO. These cycloaddition reactions could be extended towards the creation of a structure-activity relationship (SAR) for such systems.

Other atmospheric co-reactant species that could extend this study include other common acids such as HCOOH, CH_3COOH and pyruvic acid. sCI reactions with many of these extended species are predicted to be competitive with OH radicals.[108,177,178,428]

Another possible area of extension to this work could be to further alter the heteroatom doped co-reactants. For example, a Kumar and Francisco study investigates reactions of **sCIs 1—4** with H_2Se & H_2Te, and showed that as one progresses down Gr16, the reaction barrier is reduced. Similar trends could be investigated through the computation of sCI reaction potential energy surfaces with HBr & HI. Investigation of Gr15 co-reactants such as NH_3 and PH_3, is also an option, with the latter of course being a perfect example of a reactant which is much easier to work with *in silico*.

In this chapter, to see if the heteroatom tuning study of sCI + H_2X reaction was due to changes in the X atom (X= O or S) was caused by additional bulk, the **sCIs 1** & **23—26** + H_2O was compared to the equivalent reaction with the bulkier CH_3OH. Any extension of this heteroatom tuning study to involve such reactions as the sCI + H_2X (H_2S, H_2Se & H_2Te) or sCI + XH_3 (NH_3 & PH_3), could also include sCI reactions with the bulkier CH_3NH_2 & CH_3SH, to see if steric bulk are a cause of these trends.[325,432]

5.10 Conclusion

The general bimolecular reactivity for HFO-sCIs follows a single predictable trend based on halogen substitution patterns. The least reactive of the sCIs examined was **sCI 23**, the major influence here being the reductive *syn*-CF_3 group, without any hyperconjugative α-H atoms in the substituent to promote reactivity, such as in the *syn*-CH_3 group seen in **sCI 2**. Both **sCIs 25** & **26** have very high reactivity due to their —F substituents, which strongly inductively promote reactivity, with the *syn*-orientated **sCI 25** being the most reactive HFO-sCI studied here. In general, having a halogen directly bonded to the carbonyl oxide

moiety heavily promotes reactivity, and as seen in previous chapters, substitution in the *anti*- position is more favourable.

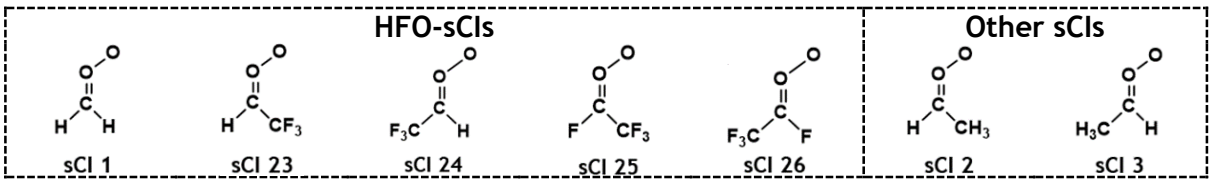

*Figure 5.22: Schematics of the structures of **sCIs 1—3, 23—26**.*

HFO reactions which have the greatest atmospheric impact analysed in this chapter are those with H_2O and $(H_2O)_2$, not only because water is so tropospherically abundant but also because **sCIs 25** & **26** are so reactive that reaction with H_2O monomer approaches the dipole capture limit, a feature not observed in many other systems.[111,293] It is important to evaluate the sCI + H_2O & $(H_2O)_2$ reactions in atmospheric models because any increased yields of the HHP product may deteriorate greenery near areas of high HFO emissions, as HHPs have been implicated with biogenic damage.[111,141,195,293,344,387–391]

The highly energetic HFO-sCI + SO_2 reactions examined in this chapter are also atmospherically important because they may provide a valuable sink for HFO-sCIs in urban areas. Additionally, the reaction favours reaction channels that convert SO_2 to SO_3, a species associated with nucleation of noxious aerosols.[191,440,451] **sCIs 23—26** + SO_2 reactions all produce multiple non-interchangeable "SOZ" intermediate products, which have not previously been investigates. However, the investigation of these **sCIs 23—26** + SO_2 reactions found that these non-interchangeable SOZs did not significantly alter the final product yields, an outcome that may be replicated for the similar **sCIs 2** & **3** + SO_2 reactions.[191]

The unusually low reactivity of **sCIs 25** & **26** in reaction with H_2S and HCl (compared to **sCIs 1**, **23** & **24**), seems to be contrary to previous reactivity trends and makes a strict taxonomic classification difficult. This is important as accurately and effectively modelling the decay of H_2S & HCl, via reaction with a variety of sCIs, is beneficial in simulating certain local tropospheric environments, such as coastal cities, where HCl is pervasive, and volcanic areas, where the toxic H_2S gas is known to cause human fatalities.[1,2,81,89,427,470]

Despite these slight issues, the overall taxonomic classification established in the sCI + alcohol study in Chapter 4 can be applied to these HFO-sCIs, and is perhaps the most rigorous option without further investigation. **sCI 23** & **sCI 24** would be categorised in the *syn*-CI and *anti*-sCI groups, respectively. Despite **sCIs 25** & **26** having unusually low reactivity with H_2S & HCl, they are categorised together in the "electronegative substituent" taxonomic group because for most reactions analysed, the inductive —F

substituents cause a high reactivity similar to that of other fluorinated sCIs species. In conclusion, the bimolecular HFO-sCI reactions in this chapter are important to the literature as a whole because: these HFO-sCIs may rapidly deplete many tropospheric pollutants; the **sCIs 23** & **24** reactions further validate the theory that removing hyperconjugative α-H atoms from substituents affects sCI chemistry; and it provides evidence that even the most unusual sCIs, such as **sCIs 25** & **26**, can fit into a wider sCI taxonomic classification system.

6.0 Modelling the Ozonolysis of Alkenes With Lengthy Alkyl Substituents

The objective of this chapter is to find a viable model to determine the ozonolysis chemistry of lengthy, flexible alkenes. This model should involve incorporation of previously calculated ozonolysis trends from Chapter 3, the new steric interactions that the lengthy alkyl chain will trigger and a mechanism to incorporate a few full computational calculations as a corrective technique. The efficacy of the model will be verified by calculating the theoretical rate constant (k_{THEO}) and product branching fraction (Γ_{THEO}) values for an example reaction: O_3 + *Z*-2-hexene (referred to as Alkene **19**). The principal task of these models must be to calculate the relative Gibbs free energy (ΔG) of all transition states (TSs) in the reaction, which is vital in determining the k_{THEO} and Γ_{THEO} values. Also considered in this chapter are the role of all minima; ΔG_{298K} trends observed in Chapter 3 for previous O_3 + alkene reactions; and the impact of rotational and geometric changes on TS energies. To determine the effectiveness of any models, they are first applied to some of the smaller O_3 + alkene systems, seen in Chapter 3. Furthermore, the accuracy of these models for O_3 + *Z*-2-hexene are further validated against the known experimental data and a couple of purposefully calculated trial TS structures from the O_3 + *Z*-2-hexene system. Not only are results of this ozonolysis chemistry of *Z*-2-hexene of interest when examining local environments where *Z*-2-hexene is abundant like Los Angeles, but the application of this model to a wide variety of other lengthy alkenes will likely increase the atmospheric impact of the work in this chapter.

6.1 Introduction

The ozonolysis of alkenes with lengthy alkyl substituents, such as the —nPr group in *Z*-2-hexene (referred to as Alkene **19** in Figure 6.1), have many more stationary points on the potential energy surface (PES) than the O_3 + alkene reactions examined in Chapter 3. The large number of transition states (TS) structures is induced by the conformational flexibility of the long —nPr substituents in Alkene **19.** The heavy computational cost this would induce makes generating a new theoretical model that is not reliant upon explicit computation of every stationary point extremely beneficial.

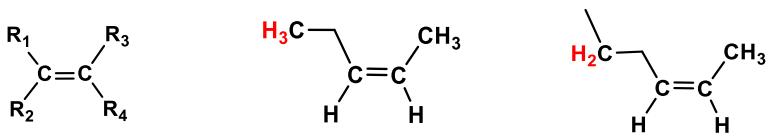

*Figure 6.1: Schematic of Standard Alkene, Alkene **16** & Alkene **19** with β-H atoms highlighted in Red.*

The model derived here must include the capacity to generate the theoretical rate constants (k_{THEO}), to determine the speed of the alkene depletion, and product branching

ratios (Γ_{THEO}) and to simulate in what ratio each Criegee intermediate (CI) is generated. Epoxide pathways do not feature in this chapter as both theoretical analysis in Section 3.8 and experimental analysis conclusively demonstrates that the pathway has negligible impact for aliphatic mono-alkenes.[121,341,342]

Here the author also focuses on whether the decline in ß-H atoms between the —Et substituent in Alkene **16** and the —nPr group in Alkene **19** (ß-H atoms are in red in Figure 6.1) has a significant impact on the ozonolysis k_{THEO} & Γ_{THEO} values. Theoretical studies on the ozonolysis of similarly long alkenes are sparing, however experimental analysis of O_3 + Alkene **19** and other analogous alkenes in the literature can be used to confirm trends relating to substituent ß-H atoms (see Section 6.8 for more details).[10,360]

6.1.1 The Atmospheric Abundance of *Z*-2-hexene and Other Lengthy Alkenes

Alkenes with long conformationally-flexible substituents, such as 1-pentene and 1-hexene, are abundant in both megacities (~5 × 10^9 molec./cm^3) and rural areas (~1 × 10^8 molec./cm^3).[182,476] These lengthy alkenes have been found to contribute significantly to local VOC populations, such as the noteworthy emission rate (~25 kt yr^{-1}) of 1-pentene in the Yangtze River Delta region in China, largely generated by heavy chemical industry in the region.[477] The ozonolysis of these lengthy alkenes is found to be important to human health the Yangtze River Delta region, where alkenes like 1-pentene, along with many other volatile organic compounds have high ozone formation potential.[477] These urban environments also provide other major sources of ozone which induce alkene ozonolysis, such as use of petrol in personal automotive vehicles.

These lengthy alkenes are found to be prevalent in the gas-phase in several other different environments around the globe. The low but still significant atmospheric concentrations of 1-pentene (0.14 — 2.75 ppb), *E*-2-hexene (0.13 — 2.31 ppb) and *Alkene **19*** (0.05 — 1.04 ppb) in cities like Los Angeles emphasises the importance of deriving a model to understand their ozonolysis.[478] Alkene **19** is also found in diesel-powered medium duty truck gas emissions, at 100 µg km^{-1}, along with *E*-2-hexene (160 µg km^{-1}).[479] See appendix section 4.1.4, for some small details known about their the ozonolysis chemistry. Other important lengthy alkenes are part of the annual non-methane VOC flux (~10^{14} g/yr) of which ~11% are monoterpenes, such as α- and ß- pinene, and ~44% are isoprene.[480]

6.1.2 Theoretical Importance of Analysis of the Ozonolysis of Lengthy Alkenes

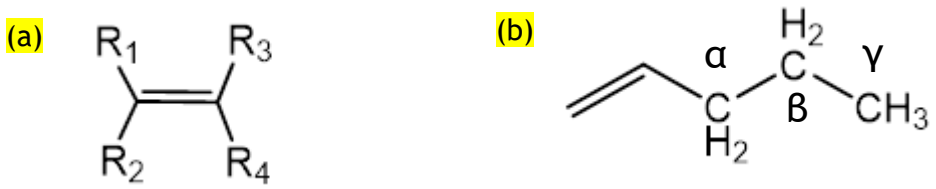

Figure 6.2: Comparison of Alkene substituent positions (Figure 6.2a); and α, β & γ branching positions (Figure 6.2b).

One of the trends identified in Chapter 3 was that —CH_3 substituents induced an increase in ozonolysis reaction rates in alkenes, by the >C=C< bond forming a hyperconjugative relationship with any α-H atoms (see Figure 6.2 for positions of hydrogen analogues labelled using Greek letters: α, β, γ …). Furthermore, when these —CH_3 substituents were themselves augmented with peripheral methyl groups into —Et, —iPr & —tBu substituents, the consequential decrease in α-H atoms in general induced a reducing effect on reactivity It is quite probable that β-H atoms have a hyperconjugative relationship with the >C=C< bond and therefore when β-H atoms are replaced, similar trends in reactivity are observed. However, when an —Et substituent is expanded into an —nPr group (seen in Figure 6.3), alkenes such as 1-pentene, *E*-2-hexene, Alkene **19** and 2-methyl-2-hexene, are highly conformationally flexible, so the additional steric interactions caused by this —nPr flexibility may also inhibit the reaction site.

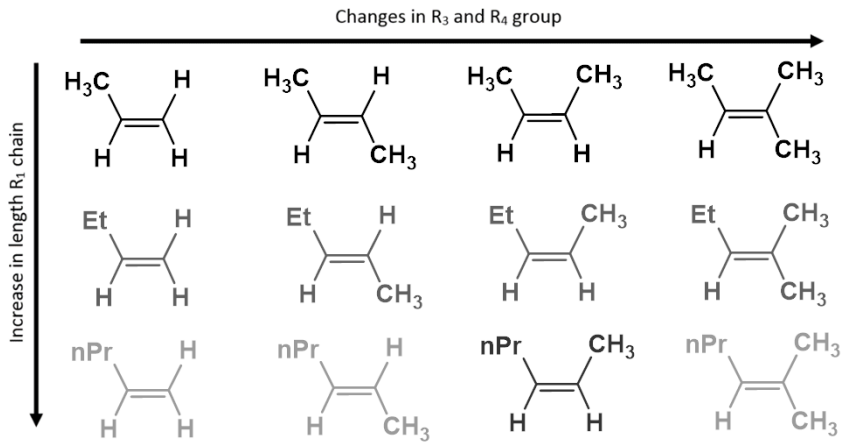

Figure 6.3: Alkenes of analysis categorised in columns by increasing length of the R_1 substituent and in rows by the changes in R_3 and R_4 substituents.

This conformeric flexibility means that any ozonolysis study would require calculating the geometries of a large number of stationary points, generating a very high computational cost (see Section 6.2). To manage this array of stationary points, the author has instead designed a series of models designed to calculate the k_{THEO} and Γ_{THEO} values for these reactions reliably and efficiently without explicitly computing each stationary point.

Determining the ozonolysis chemistry of alkenes with —nPr substituents is preferred over isobutyl or neopentyl groups because the computational cost scales with molecular size and in this testing phase for these models, many computational calculations are still required. In Chapter 3 it was determined that reductions in numbers of α-H atoms when moving from a —CH_3 substituent into an —Et group had a temporary inductive effect (further reductions in α-H atoms however usually led to declines in k_{THEO} values) and so increased the rate of the reaction. Alkenes with —nPr substituents are of great interest because if the reduction in the number of ß-H atoms has a similar temporary inductive effect, then these alkenes are likely to have larger ozonolysis k_{THEO} value than equivalent alkenes with isobutyl or neopentyl groups.

The ozonolysis of Alkene **16** has both the inductive effect of having *Z*-orientated substituents and the significant steric repulsion between the —Et and —CH_3 groups, causing a large degree of electronic and steric complexity in transition states (TSs).

The higher ozonolysis k_{THEO} value calculated for the *Z*-orientated Alkene **16** (2.8×10^{-15} cm^3 s^{-1}) compared to Alkenes **2** & **15** (3.2×10^{-17} & 1.1×10^{-15} cm^3 s^{-1}) suggests that the *Z*-orientated Alkene **19** may have a higher ozonolysis k_{THEO} value than 1-pentene & *E*-2-hexene. In cities like Los Angeles, 1-pentene (0.14 — 2.75 ppb) and *E*-2-hexene (0.13 — 2.31 ppb) are slightly more abundant than Alkene **19** (0.05 — 1.04 ppb), however the O_3 + Alkene **19** reaction is likely to have greater impact due to this larger k_{THEO} value.[478] The abundance and therefore the impact of 2-methyl-2-hexene is unknown.

This analysis of O_3 + alkenes with —nPr substituents is important because the only reference made to substituent ß-H atoms in Chapter 3 is a comparison between the ozonolysis of 1-butene to that of 3,3,4,4,4-tetrafluoro-1-butene. The changes in k_{THEO} and Γ_{THEO} values caused by the fluorination of the Et substituent may be due to the impact of reducing the number of ß-H atoms, as well as the number of α-H atoms. Unfortunately, this is convoluted by the impact of haloalkyl substituents on the >C=C< bond. The work in this chapter may help deconvolute these effects.

To the author's knowledge no computational analysis of O_3 + Alkene **19** exists, and experimental analysis provides only k_{EXP} values with no references to product branching ratios (Γ_{EXP}) or OH yields.[10,162,365] Even if Γ_{EXP} values for CI yields are measured, they may be less reliable due to the difficulty of differentiating between *syn*- & *anti*-CIs, as well as the short-lived nature of hot CIs.[10,182–185]

6.2 Conformational Flexible Alkenes: A Computational Overview

The two-stage ozonolysis of Alkene **19** is similar to that of the *Z*- orientated Alkenes **16** & **18**, with a cycloaddition (TS_{OZO}) step that produces a group of short-lived intermediate products, primary ozonides (POZs), followed by a POZ fragmentation step. As seen in Figure 6.4, the number of TSs grows with the length of the alkyl substituent, due to increasing conformational flexibility in the alkene.

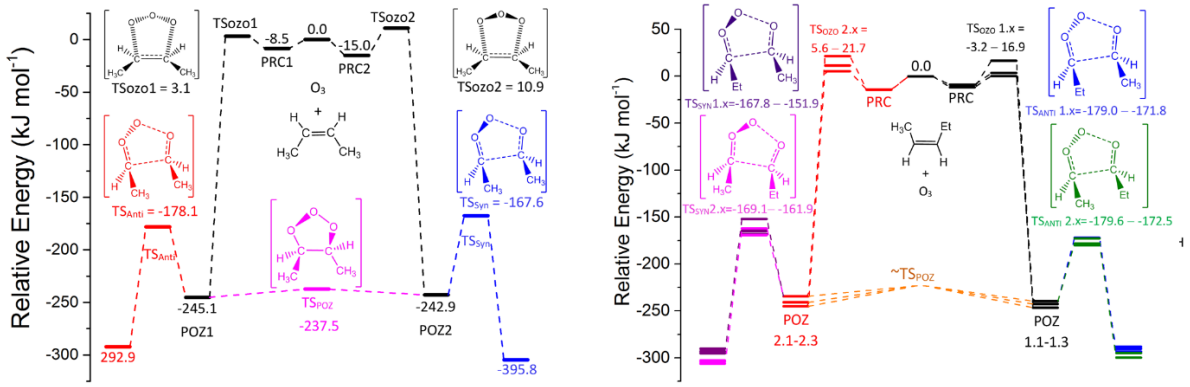

*Figure 6.4: Potential energy surface of O_3 reactions with Alkene **18** (left) and Alkene **16** (right). Subchannels vary in energy depending on the orientation of the —Et group. Energies are relative to raw reactants*

Also shown in Figure 6.4, the TS_{OZO} barriers always proceed via 1,3-cycloaddition but the energy of the two cycloaddition structures (TS_{OZO} 1 & 2) varies depending on the orientation of the O_3. The increased confirmational flexibility of O_3 + Alkene **16** produces two sets of TS_{OZO} channels (TS_{OZO} 1.1—1.3 & TS_{OZO} 2.1—2.3) that depend on the orientation of the —Et group. The computational cost of calculating this number of TS_{OZO} structures for O_3 + Alkene **19** is further magnified, as seen in Figure 6.5, as the conformational flexibility the new —nPr substituent in the $—R_1$ position generates triple the number of TS_{OZO} structures (TS_{OZO} 1.1—1.9 & TS_{OZO} 2.1—2.9).

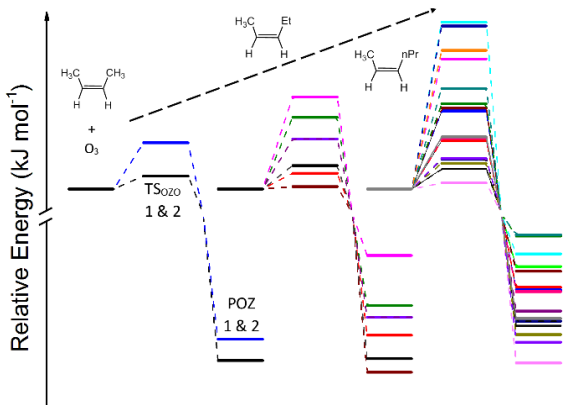

*Figure 6.5: Approximated number of TS_{OZO} and POZ structures from the Potential Energy Surfaces of Ozonolyses of Alkene **16** (Z-$CH_3CHCHCH_3$), Alkene **18** (Z-$EtCHCHCH_3$) & Alkene **19** (Z-$nPrCHCHCH_3$).*

The number of POZ conformers in O_3 + Alkene **19** is also tripled as well as the number of POZ isomerisation (TS_{POZ}) structures. All the POZ conformers produced from each TS_{OZO} structure freely interconvert (Appendix Section 1.6.2) and so determining these TS_{POZ} structures is unnecessary.

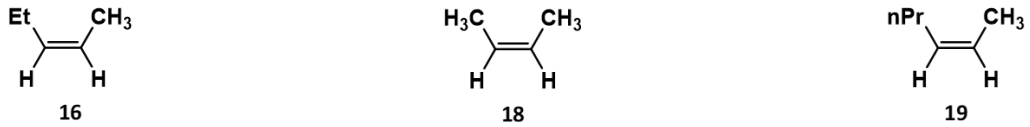

*Figure 6.6: Schematic of the Chemical Structures of Alkenes **16**, **18** & **19**.*

Unlike TS_{OZO} channels, the swift POZ fragmentation mechanisms generate different products through different channels, labelled according to the name or orientation of the CI product. The small size and symmetry of the Alkene **18** (as seen in Figure 6.6) means that POZ fragmentation only produces *anti*- & *syn*-CH_3CHOO (and a CH_3CHO co-product), via a TS_{ANTI} and TS_{SYN} respectively. Alkene **16** has a longer —Et group in the —R_1 position making the Alkene more flexible and breaking the symmetry seen for Alkene **18**. This produces a large number of TS structures during the ozonolysis, which are grouped by channels that produce identical CIs: *anti*- & *syn*-EtCHOO, via TS_{ANTI} 1.1—1.3 and TS_{SYN} 1.1—1.3; and *anti*- & *syn*-CH_3CHOO, via TS_{ANTI} 2.1—2.3 and TS_{SYN} 2.1—2.3. The CIs mentioned here are featured in Figure 6.7.

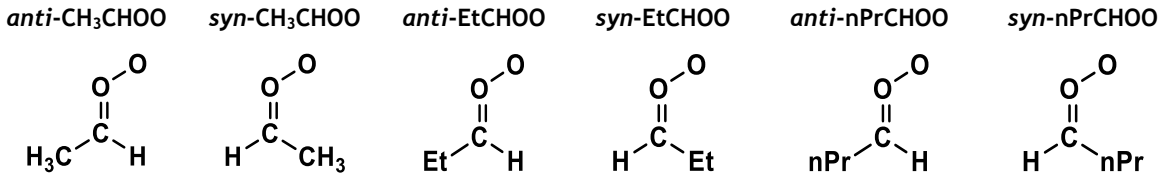

*Figure 6.7: Different Structures of some of the CIs produced in the ozonolysis of Alkenes **16** & **19**.*

This increase in conformational flexibility from Alkene **18** to Alkene **16** increases in the number of TS structure to be optimised from 3 to 18, which increases computational cost significantly. As this conformational flexibility increases for Alkene **19** the number of cycloaddition TSs increases to two sets of nine TS_{OZO} structures (TS_{OZO} 1.1—1.9 & TS_{OZO} 2.1—2.9) loosely represented in Figure 6.8. The POZ fragmentation process for O_3 + Alkene **19** is also more complex than for O_3 + Alkene **16** with each channel (also broadly displayed in Figure 6.8) containing 9 TS structures. These channels in ozonolysis of Alkene **19** are: TS_{ANTI} 1.1—1.9 & TS_{SYN} 1.1—1.9 which produce *anti*- & *syn*-nPrCHOO (and a CH_3CHO co-product) and TS_{ANTI} 2.1—2.9 & TS_{SYN} 2.1—2.9 which produces *anti*- & *syn*-CH_3CHOO (and an nPrCHO co-product).

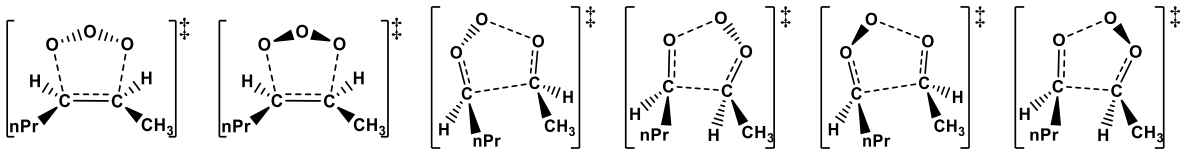

*Figure 6.8: Different TS Structures from in the ozonolysis of Alkene **19**.*

The —nPr substituent increases the number of TSs for O_3 + Alkene **19** to 54 structures, but this increase in computational cost would be compounded by the increase in size of the molecular structure. This issue of a very large number of TS structures effects the ozonolysis of 1-pentene, *E*-2-hexene, 2-methyl-2-hexene amongst many others. The logical consequence to this predicament is to produce a predictive model, that determines the ozonolysis chemistry of these lengthy alkenes without identifying and computing every stationary point on the reaction potential energy surface. To see previous method see other methods see Appendix section 4.1.3

6.3 Free Energy-Structural Projection (FESP) Model 1 Methodology

The theoretical relative Gibbs free energy (ΔG_{THEO}) of the TS structure is a thermodynamic value that characterizes the relationship between a TS, the k_{THEO} values (see Equation 6.1) and the comparative product Γ_{THEO} values at a specified temperature. It is therefore the aim of the models that are derived herein to determine the ΔG_{THEO} for all TS structure on the PES on the O_3 + Alkene **19** reaction.

$$k_{TST} = \boldsymbol{\kappa} \frac{RT}{P_0} \frac{k_B T}{h} \, e^{-(\Delta G_{TS})/RT} \qquad \textit{Equation 6.1}$$

All the minima on the O_3 + Alkene **19** PES must also be determined, which includes: 4 alkene conformers, 18 POZs, and 18 different conformeric structures for the CI and aldehyde products. However, these minima have a far lower computational cost to optimise compared to the TS structures. For this reason, all minima identified above are geometrically optimised, with harmonic frequencies identified and molecular energies calculated using the computational methods described in Method Section 2.1. No pre-reaction or post-reaction complexes are optimised during this analysis. The POZ structures and Gibbs free energies obtained for all POZ structures for O_3 + Alkene **19** are shown in Figure 6.9.

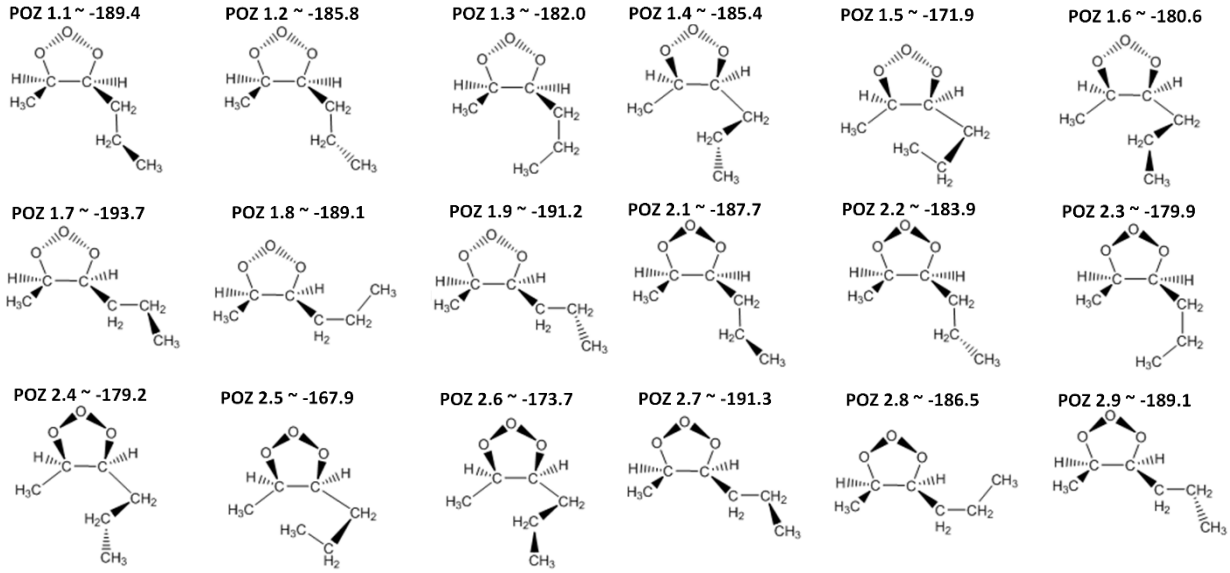

*Figure 6.9: Structure and Gibbs free energy, ΔG_{THEO}, (in kJ mol^{-1}) of all the Primary ozonide (POZ) conformers for O_3 + Alkene **19** (Z-2-hexene). Gibbs Free energy values in kJ mol^{-1}.*

Although there are 36 different TS structures in the O_3 + Alkene **19** reaction (TS_{ANTI} 1.1—1.9, TS_{SYN} 1.1—1.9, TS_{ANTI} 2.1—2.9 & TS_{SYN} 2.1—2.9), previous studies of the very similar O_3 + Alkene **16** reaction shows that many of the POZs are associated with one TS_{OZO} structure and two fragmentation structures (for example: TS_{OZO} 1.1 → POZ 1.1 → TS_{ANTI} 1.1 & TS_{ANTI} 2.1). Although technically the POZs can freely interconvert and behave as one POZ during reaction, and resulting TS structures have common electronic and steric features with the geometries of the possible POZ conformers (see Figure 6.10), producing commonalities between the ΔG_{THEO} values of the POZ and the TS.

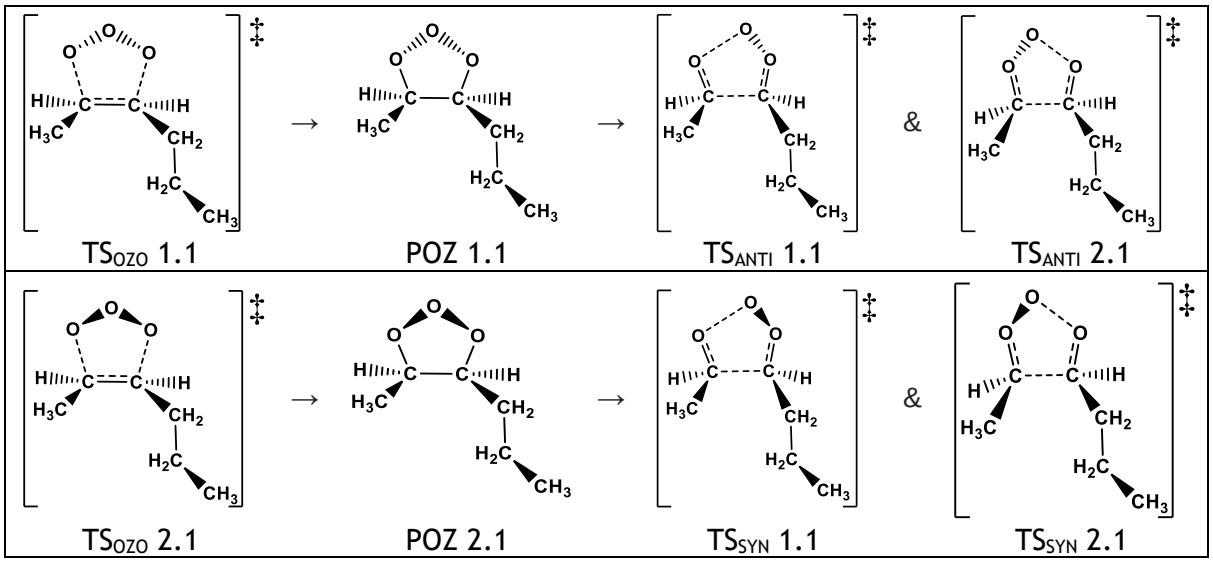

*Figure 6.10: General Structures of Example POZs from O_3 + Alkene **19** and their common structural features with their related TS structures. Gibbs Free energy values in kJ mol^{-1}.*

These commonalities between geometric features and ΔG_{THEO} values of the POZ and the TS structures have been investigated in reactions taken from Chapter 3, and this has been

used to produce a Free Energy-Structural Projection (FESP) model. Once tested this FESP model is used to project relative a Gibbs Free Energy value for each TS structure (ΔG_{PROJ} [TS]) on the PES of the O_3 + Alkene **16** reaction. The fine tuning and verification process during the analysis of the results from this basic FESP model led to the creation of three different final approaches (FESP models 1—3) outlined individually in Sections 6.3—6.7. These FESP models are then compared to existing experimental data and to the McGillen *et al*. SAR model in Section 6.8.[118]

6.3.1 Determining the Relative Gibbs Free Energy Value.

Throughout this thesis, it is apparent that alkenes with similar chemical structures or similar chemical moieties (for example those that it might be helpful to group as a taxonomic class), also display very similar reaction rates: or at very least reaction rates which change in a uniform and predictable way. Most importantly, this predictable change is observed in the ΔG_{THEO} values, and in the energy differences for the TS barrier heights are relative POZ conformer energies (an observation discussed in much greater depth in Sections 6.3.2—6.3.3). Therefore, changes in stationary point ΔG_{THEO} values between O_3 + Alkene **16** can readily be used to predict ΔG_{THEO} values for the ozonolysis of an Alkene with a longer $-R_1$ substituent, like Alkene **19.**

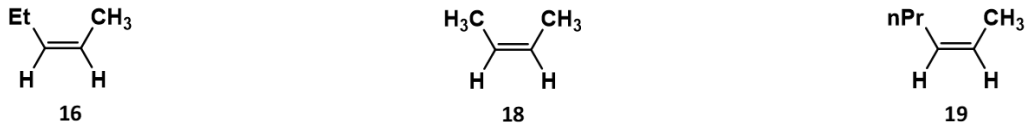

*Figure 6.11: Schematic of the Chemical Structures of Alkenes **16**, **18** & **19**.*

The general FESP model can be applied to the ozonolysis of any alkene where one is interested in extending an $-R_1$ substituent e.g. from Me to Et, and where the PES of the shorter chain alkene is well established.

Ideally, the model should allow the extension of properties for the reaction of O_3 + Alkene **16** to the O_3 + Alkene **19** reaction. The theory of FESP model 1 is that steric and electronic differences in the analogous TS structures of O_3 + Alkene **19**, compared to that of O_3 + Alkene **16**, can be accounted for by the differences in the ΔG_{THEO} value of the POZ. That means that if the ΔG_{THEO} value of a POZ conformer (POZ 1.1) rises or falls, the ΔG_{THEO} value of the TS barriers associated with that POZ (TS_{OZO} 1.1, TS_{ANTI} 1.1 & TS_{ANTI} 2.1) rise or fall by a similar ΔG_{THEO} value. As seen in Equation 6.2, the difference between the ΔG_{THEO} value of a POZ and its related TS structure (both of the same O_3 + Alkene reaction) is referred to as the "ΔG_{TS-POZ}" value, which is a critical numerical component in the FESP models.

$$\Delta G_{TS-POZ} = \Delta G_{THEO}\,[TS] - \Delta G_{THEO}\,[POZ] \qquad \textit{Equation 6.2}$$

To apply this to an actual system from Chapter 3, the ΔG_{TS-POZ} values have been extracted from all example TS structures associated with the POZ 1.1 of O_3 + Alkene **16**:

*Table 6.1: Structures and Relative Gibbs Free energy (ΔG_{THEO}) values for POZ 1.1 and each of its related TS structures (TS_{OZO} 1.1, TS_{ANTI} 1.1 & TS_{ANTI} 2.1) of the O_3 + Alkene **16** reaction; and the Gibbs free energy differences between the POZ and the related TS structures (ΔG_{TS-POZ}). Gibbs Free energy values in kJ mol^{-1}.*

Label	TS_{OZO} 1.1	POZ 1.1	TS_{ANTI} 1.1	TS_{ANTI} 2.1
Structure	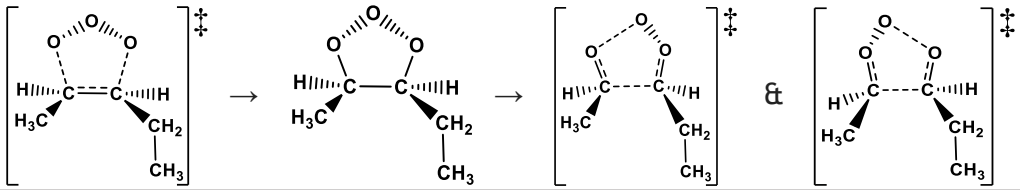			
ΔG_{THEO}	49.57	-190.47	-125.47	-121.30
ΔG_{TS-POZ}	240.04	N/A	65.00	69.16

These ΔG_{TS-POZ} values are important because, as the changes in ΔG_{THEO} values caused by the longer $-R_1$ substituent applies to both the POZ and TS structures, that means the ΔG_{TS-POZ} value of, for example, TS_{OZO} 1.1 of O_3 + Alkene **19** (see Table 6.1) are very similar to that of the analogous TS_{OZO} 1.1 of O_3 + Alkene **16**. This implies that the ΔG_{THEO} value of the TS barrier for O_3 + Alkene **19** may not need to be calculated computationally. Instead, a total of the ΔG_{THEO} value of the POZ for O_3 + Alkene **19** and the ΔG_{TS-POZ} value of the analogous TS barrier in the O_3 + Alkene **16** reaction produces a *projected* Gibbs free energy (ΔG_{PROJ}) of the TS barrier for O_3 + Alkene **19**, as shown in Equation 6.3.

$$\Delta G_{PROJ}\,[TS]\ (\text{Alkene } \mathbf{19}) = \Delta G_{THEO}\,[POZ]\ (\text{Alkene } \mathbf{19}) + \Delta G_{TS-POZ}\ (\text{Alkene } \mathbf{16}) \qquad \textit{Equation 6.3}$$

Examples of applying this FESP principle are illustrated in Figure 6.12, which displays the ΔG_{PROJ} values of TS_{OZO} 1.1, TS_{ANTI} 1.1 & TS_{ANTI} 2.1 for O_3 + Alkene **19** obtained using the computationally obtained ΔG_{THEO} value of POZ 1.1 for O_3 + Alkene **19** and the ΔG_{TS-POZ} values for TS_{OZO} 1.1, TS_{ANTI} 1.1 & TS_{ANTI} 2.1 of O_3 + Alkene **16** (extracted from Table 6.1).

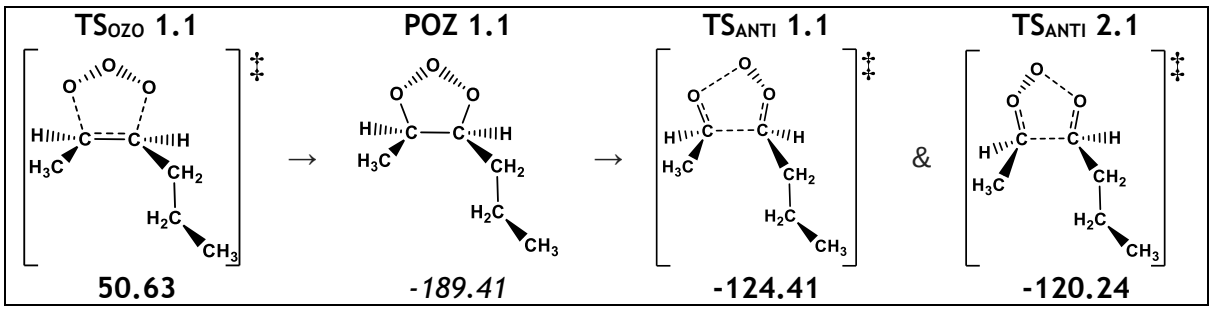

*Figure 6.12: Computational Relative Gibbs Free energy (ΔG_{THEO}) value for POZ 1.1 and Projected Relative Gibbs Free energy (ΔG_{PROJ}) of the related TS structures (TS_{OZO} 1.1, TS_{ANTI} 1.1 & TS_{ANTI} 2.1) for O_3 + Alkene **19**. Gibbs Free energy values in kJ mol^{-1}.*

An adapted version of the notation given in Equations 6.2 & 6.3 for Gibbs Free energy, where the ΔG_{TS-POZ}, ΔG_{THEO}, or ΔG_{PROJ} labels include the TS or POZ described in square

parentheses (e.g. ΔG_{TS-POZ} [TS_{OZO} 1.1]), is applied throughout this chapter. The basis of FESP Models 1—3, is that the ΔG_{TS-POZ} values for these analogous TS structure remain similar across the ozonolysis of comparable alkenes, such as Alkenes **16**, **18** & **19**.

6.3.2 Applying FESP Model to MESMER.

Two further challenges in determining the k_{THEO} or Γ_{THEO} values using the MESMER software (see Section 1.8.4 / Section 2.5) are requirements to provide a *zero-point corrected energy* (ΔE_{THEO}) and a vibronic frequencies file for each structure. Thus far, only the ΔG_{PROJ} values for each O_3 + Alkene **19** TS have been determined. However, at this stage one can use the full O_3 + Alkene **16** MESMER input file to determine the k_{THEO} or Γ_{THEO} values for the O_3 + Alkene **19** reaction, with just minor modifications described below. The k_{PROJ} & Γ_{PROJ} notation are used purely for FESP model 1, and other notation is used for other FESP models.

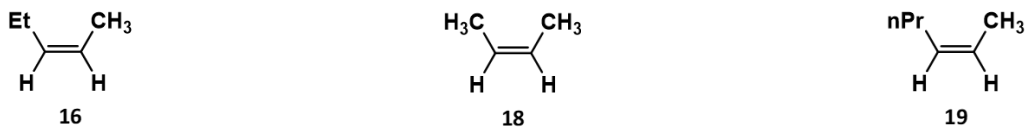

*Figure 6.13: Schematic of the Chemical Structures of Alkenes **16**, **18** & **19**.*

The segment of this new adapted O_3 + Alkene **19** MESMER file that describes a TS structure is derived from the analogous TS structure in the O_3 + Alkene **16** MESMER file with the only critical difference being a new adjusted energy barrier (ΔE_{PROJ}). Each TS structure in O_3 + Alkene **16** (e.g. TS_{OZO} 1.1) is emulated by using three TS structures for O_3 + Alkene **19** (e.g. TS_{OZO} 1.1—1.3), which means that each O_3 + Alkene **16** TS structure is placed into triplicate in the O_3 + Alkene **19** MESMER file. While the key minima structures for O_3 + Alkene **19** have been fully computationally determined, the O_3 + Alkene **16** POZ structures are used in the O_3 + Alkene **19** MESMER file, with an adjusted ΔE_{PROJ} value used for the POZ too, as the same number of atoms must be maintained throughout the MESMER file. The pre- & post-reaction complexes are left unchanged in the input file.

To generate these newly adjusted ΔE_{PROJ} values for stationary points of O_3 + Alkene **19**, the difference between the ΔG_{THEO} value and the ΔE_{THEO} value of the analogous stationary point for O_3 + Alkene **16** is required. This "Δ_{ADJ}" value is obtained using Equation 6.4:

$$\Delta_{ADJ} \text{ (Alkene } \mathbf{16}\text{)} = \Delta G_{THEO} \text{ (Alkene } \mathbf{16}\text{)} - \Delta E_{THEO} \text{ (Alkene } \mathbf{16}\text{)} \qquad \textit{Equation 6.4}$$

This Δ_{ADJ} value is then used to convert the ΔG_{PROJ} value for O_3 + Alkene **19** to a ΔE_{PROJ} value, as seen in Equation 6.5, that can be placed into the O_3 + Alkene **19** MESMER file.

$$\Delta E_{ADJ} \text{ (Alkene } \mathbf{19}) = \Delta G_{PROJ} \text{ (Alkene } \mathbf{19}) - \Delta_{ADJ} \text{ (Alkene } \mathbf{16}) \qquad \textit{Equation 6.5}$$

The ΔE_{ADJ} values for POZ structures for O_3 + Alkene **19**, are obtained using their already calculated ΔG_{THEO} values instead. To avoid ambiguities, Table 6.2 shows an example where Δ_{ADJ} values calculated for the POZ 1.1 & TS_{ANTI} 1.1 structures of O_3 + Alkene **16**, are used to determine the ΔE_{PROJ} values for POZ 1.1 & TS_{ANTI} 1.1 structures of O_3 + Alkene **19** (using Equations 6.4 & 6.5).

*Table 6.2: Visual representation of the calculation of adjusted energy barriers (ΔE_{PROJ}) values for POZ 1.1 & TS_{ANTI} 1.1 structures from O_3 + Alkene **19**, using all numerical values from O_3 + Alkene **16** for all the components in Equations 6.4 & 6.5. *Note: The ΔG_{PROJ} given here for POZ 1.1 is a full calculated ΔG_{THEO} value. Gibbs Free energy values in kJ mol^{-1}.*

Reaction	O_3 + Alkene **16**		**Reaction**	O_3 + Alkene **19**	
Label	POZ 1.1	TS_{ANTI} 1.1	**Label**	POZ 1.1	TS_{ANTI} 1.1
Structure	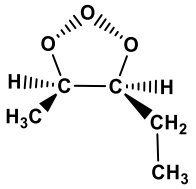	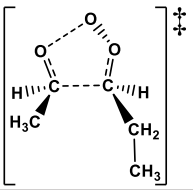	**Structure**	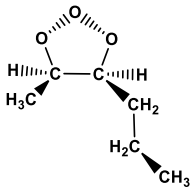	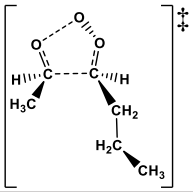
ΔG_{THEO}	-190.5	-125.5	ΔG_{PROJ}	-189.4 *	-124.4
ΔE_{THEO}	-242.5	-177.9	Δ_{ADJ}	52.0	52.4
Δ_{ADJ}	52.0	52.4	ΔE_{ADJ}	-241.4	-176.8

The concept here is that the difference in ozonolysis chemistry between Alkenes **16** & **19** can be accounted for by the ΔE_{ADJ} values created in this adjusted MESMER file. In Section 6.4 the use of these adjusted MESMER files, referred to as the MESMER Projection Technique, is validated by comparing the k_{PROJ} & Γ_{PROJ} values to the k_{THEO} & Γ_{THEO} values of a variety of O_3 + alkene reactions from Chapter 3. To avoid ambiguities, MESMER projection technique does not involve calculating the ΔG_{PROJ} values. It simply the process of using the ΔG_{PROJ} values to produce k_{PROJ} & Γ_{PROJ}. Validating that this MESMER Projection Technique is important, as it is used in all FESP models thus affecting all k_{PROJ} & Γ_{PROJ}.

The free interconversion between POZ conformers means that a single POZ can be used in calculating Γ_{THEO}, thereby reducing computational cost. This is the same notion of POZ interconversion which was validated and applied to O_3 + alkene reactions in Chapter 3. Incorporated into every k_{PROJ} and Γ_{PROJ} values are Eckart factors (κ_{ECKART}) for tunnelling, taken from the imaginary frequency of the smaller alkene TS (e.g. the imaginary frequency used for TS_{OZO} 1.1, 1.2 & 1.3 for O_3 + Alkene **19** is that of TS_{OZO} 1.1 for O_3 + Alkene **16**, -139.20 cm^{-1}). Both the canonical rate constants (k_{CAN}) can then be calculated for O_3 + Alkene **19** using FESP models 1—3, and can be found in Appendix Section 4.5.

6.4 Validation of the Accuracy of FESP Model 1

6.4.1 Validation of the MESMER projection technique

To trial the MESMER Projection Technique, the ozonolysis chemistries of a variety of Alkenes with —Et substituents, Alkenes **2**, **7**, **15** & **16**, are determined using adjusted MESMER files from the equivalent Alkenes with —CH_3 substituents, Alkenes **1**, **6**, **17** & **18**, (Figure 6.14). In the first instance, ΔG_{PROJ} values rather than ΔG_{THEO} (determined in Chapter 3) are used to determine ΔE_{ADJ}. If the any changes in chemistry by extending the alkyl chain are accounted for solely in this new ΔE_{ADJ} value then the test rate constant (k_{TEST}) and test product branching fractions (Γ_{TEST}) should be in agreement with the explicitly computed values. (The use of the k_{TEST} and Γ_{TEST} labels to display the testing of *MESMER projection technique* is to differentiate these values from those of the fully projected FESP model 1.)

R_1 substituent	Monosubstituted	*E*-isomer	*Z*-isomer	Trisubstituted
—CH_3	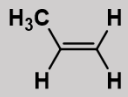 **1**	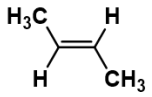 **17**	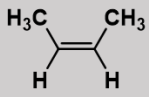 **18**	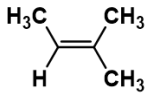 **6**
—Et	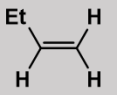 **2**	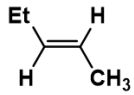 **15**	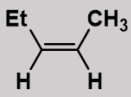 **16**	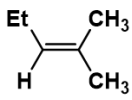 **7**

*Figure 6.14: Schematic of Alkenes **1**, **2**, **6**, **7** & **15—18** categorised by chemical structure.*

The first reaction where this MESMER Projection Technique is trialled is O_3 + Alkene **2** (1-butene) using the input file from O_3 + Alkene **1** (propene). Figure 6.15 shows that POZ fragmentation pathways for O_3 + Alkene **2** are analogous to those of O_3 + Alkene **1** with the TS_{FO} channels producing CH_2OO + R_1CHO and the TS_{ANTI} & TS_{SYN} channels producing *anti-/syn*-R_1CHOO + HCHO. As these analogous transition states are similar in terms of structural and electronic chemistry, applying these ΔE_{ADJ} values from O_3 + Alkene **2** to the analogous TS structures in the O_3 + Alkene **1** MESMER file should account for the lengthening of the —R_1 group.

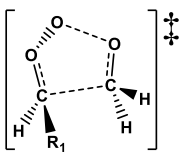
TS_{ANTI} or TS_{ANTI} 1—3

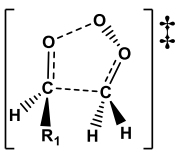
TS_{FO} 1 or TS_{FO} 1.1—1.3

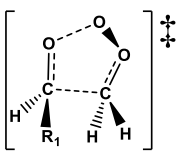
TS_{FO} 2 or TS_{FO} 2.1—2.3

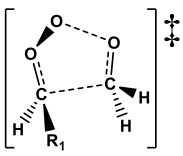
TS_{SYN} or TS_{SYN} 1—3

*Figure 6.15: Different POZ fragmentation channels by their general TS structures for O_3 + Alkenes **1** & **2**. The TS_{FO} 1 & 2 produce formaldehyde oxide or CH_2OO and TS_{ANTI} & TS_{SYN} channels produce anti-/syn-R_1CHOO.*

Table 6.3 displays the comparison between the full computational treatment and the use of *MESMER projection technique* on the O_3 + 1-butene reaction.

*Table 6.3: The MESMER projection technique rate constants and product branching fractions for O_3 + Alkene **2** (k_{TEST} & Γ_{TEST}) and the computational rate constants and product branching fractions for O_3 + Alkene **2** from Chapter 3 (k_{THEO} & Γ_{THEO}) subdivided by subchannel (.1, .2 & .3) and aggregate across the channel (Σ); the gap between the k_{TEST} & k_{THEO} values [$\delta k_{TEST} = k_{TEST} - k_{THEO}$]; and the Γ_{TEST} & Γ_{THEO} values [$\delta\Gamma = \Gamma_{TEST} - \Gamma_{THEO}$].*

Channel	k_{TEST} [10^{-18} cm^3 s^{-1}]				k_{THEO} [10^{-18} cm^3 s^{-1}]				δk_{TEST}
	(.1)	(.2)	(.3)	**Σ**	(.1)	(.2)	(.3)	**Σ**	
TS_{OZO} 1	27.7	18.8	34.4	**80.9**	27.7	19.0	34.1	**80.8**	0.1
TS_{OZO} 2	5.1	1.6	15.5	**22.3**	5.10	1.65	15.2	**21.9**	0.4
Total	103.1				102.7				
Channel	Γ_{TEST}				Γ_{THEO}				$\delta\Gamma_{TEST}$
	(.1)	(.2)	(.3)	**Σ**	(.1)	(.2)	(.3)	**Σ**	
Γ_{CH_2OO} **(1)**	0.064	0.059	0.069	**0.193**	0.068	0.058	0.073	**0.199**	-0.006
Γ_{CH_2OO} **(2)**	0.052	0.054	0.062	**0.169**	0.057	0.051	0.065	**0.173**	-0.004
$\Gamma_{anti\text{-}CH_3CHOO}$	0.133	0.124	0.178	**0.434**	0.130	0.108	0.188	**0.427**	0.007
$\Gamma_{syn\text{-}CH_3CHOO}$	0.087	0.017	0.100	**0.202**	0.082	0.019	0.099	**0.201**	0.001

The high degree of accuracy for the *MESMER projection technique* is shown such that the k_{TEST} value deviates by <1% of the explicit k_{THEO} value. The Γ_{TEST} deviates slightly for each pathway but the lack of deviation in the overall branching fractions (<0.01) shows that the *MESMER projection technique* provides good consistency with calculations from Chapter 3. The deviation factors "δk_{TEST}" & $\delta\Gamma_{TEST}$ are determined using Equations 6.6—6.7.

$$\delta k_{TEST} = k_{TEST} - k_{THEO} \qquad \text{Equation 6.6}$$

$$\delta\Gamma_{TEST} = \Gamma_{TEST} - \Gamma_{THEO} \qquad \text{Equation 6.7}$$

Similarly good results are found when expanding this test to the systems of *E*- & *Z*-pentene and 2-methyl-2-pentene (to full results see Appendix Section 4.2.2) further validating this *MESMER projection technique*.

While the *MESMER projection technique* produces reliable k_{THEO} and Γ_{THEO} values from explicit ΔG_{THEO} values, the accuracy of the FESP model which uses ΔG_{PROJ} values has yet to be determined. This is explored in the following subsections, by trialling FESP model 1 on O_3 + Alkenes **2**, **7**, **15** & **16** (1-butene, *E*- & *Z*-pentene and 2-methyl-2-pentene), where the k_{PROJ} and Γ_{PROJ} can be compared directly against computational k_{THEO} and Γ_{THEO} produced in Chapter 3. If FESP model 1 produces reliable k_{PROJ} & Γ_{PROJ} values for the O_3 + alkene systems in Chapter 3, it will be trustworthy enough to use on O_3 + Alkene **19**.

6.4.2 The Accuracy of FESP Model 1 Using the Ozonolysis of 1-Butene

O_3 + Alkene **2** provides the first FESP test case as it is the simplest alkene with an —Et substituent. ΔG_{TS-POZ} values are taken from analogous TS structures and adjusted MESMER files for O_3 + Alkene **1**.

*Figure 6.16: Schematic of the chemical structures of Alkenes **1** & **2**.*

The ΔG_{PROJ} values produced for the TS structures of O_3 + Alkene **2** were found to be very similar to the explicitly computed ΔG_{THEO} values calculated in Chapter 3, with all but two structures showing < 2 kJ mol^{-1} divergence in Gibbs free energy ($\delta\Delta G_{PROJ}$). Table 6.4 displays the differences in ΔG_{PROJ} & ΔG_{THEO} values for some key TS structures, but the full table of ΔG_{PROJ}, ΔG_{THEO} & $\delta\Delta G_{PROJ}$ values of O_3 + Alkene **2**, is on Appendix Section 4.2.4.

*Table 6.4: Projections values of the lowest energy TS structures of O_3 + Alkene **2**; relative theoretical Gibbs free energy [ΔG_{THEO}]; projected relative Gibbs Free energy using FESP model 1 [ΔG_{PROJ}] (obtained from the ΔG_{THEO} of the POZ conformer for O_3 + Alkene **2** and the ΔG_{TS-POZ} for Alkene **1**); and the difference between projected and the relative Gibbs free energy of the TS structure [$\delta\Delta G_{PROJ} = \Delta G_{THEO} - \Delta G_{PROJ}$]. Gibbs Free energy values in kJ mol^{-1}.*

Label	TS_{OZO} 1.3	TS_{ANTI} 3	TS_{FO}1.3	TS_{FO} 2.2
Structure	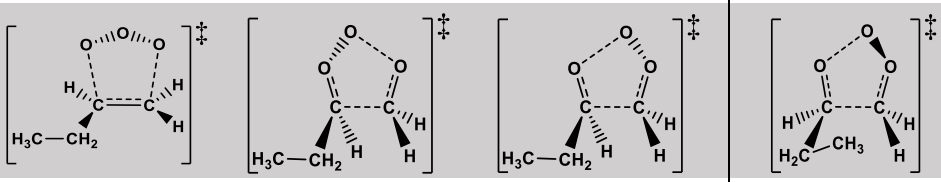			
ΔG_{THEO}	56.4	-115.4	-109.2	-106.7
ΔG_{PROJ}	56.3	-115.1	-108.9	-102.7
$\delta\Delta G_{PROJ}$	**0.1**	**-0.3**	**-0.3**	**-4.0**
CI product	N/A	*anti*-EtCHOO	CH_2OO	CH_2OO
Label	**TS_{OZO} 2.3**	**TS_{FO}2.3**	**TS_{SYN} 3**	**TS_{SYN} 2**
Structure	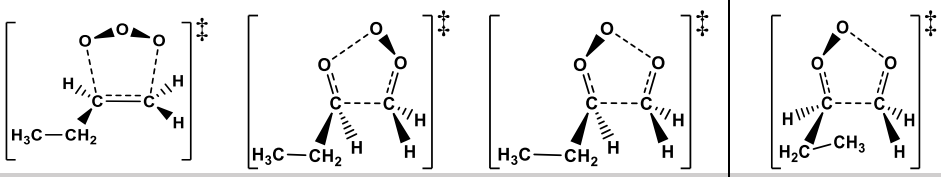			
ΔG_{THEO}	58.4	-107.6	-113.4	-100.9
ΔG_{PROJ}	59.4	-107.6	-113.8	-108.8
$\delta\Delta G_{PROJ}$	**-1.0**	**0.0**	**0.4**	**7.9**
CI product	N/A	CH_2OO	*syn*-EtCHOO	*syn*-EtCHOO

The two TS barriers that do see a > 2 kJ mol^{-1} $\delta\Delta G_{PROJ}$, the TS_{FA} 2.2 and TS_{SYN} 2 pathways, are also displayed in Table 6.4. These divergences occur for TS structures that emerge from POZ 2.2, the highest energy POZ structure. In both the TS_{FA} 2.2 and TS_{SYN} 2 structures the orientation of the —Et group and the central oxygen in the 1,2,3 trioxolane segment of

the POZ are in close proximity, implying that steric interaction between these components of the structure may cause increased discrepancy. This steric interaction drives a desire for an updated FESP model 2, in Section 6.6.

The full breakdown of both the k_{PROJ} & Γ_{PROJ} values resulting from these ΔG_{PROJ} values are displayed with the k_{THEO} & Γ_{THEO} values in Table 6.5. This comparison shows that FESP model 1 provides an accurate representation of O_3 + Alkene **2**.

*Table 6.5: The rate constants and product branching fractions for O_3 + Alkene **2** using the* FESP model 1 *(k_{PROJ} & Γ_{PROJ})* and *the full computational analysis from Chapter 3 (k_{THEO} & Γ_{THEO}) subdivided by subchannel (.1, .2 & .3) and aggregate across the channel (Σ); difference between the k_{PROJ} & k_{THEO} values [$\delta k_{TEST} = k_{PROJ} - k_{THEO}$]; difference between the Γ_{PROJ} & Γ_{THEO} values for each channel [$\delta\Gamma = \Gamma_{PROJ} - \Gamma_{THEO}$].*

Alkene 2	k_{PROJ} [10^{-18} cm^3 s^{-1}]				k_{THEO} [10^{-18} cm^3 s^{-1}]				δk_{PROJ}
Channel	(.1)	(.2)	(.3)	**Σ**	(.1)	(.2)	(.3)	**Σ**	
TS_{OZO} 1	22.6	12.7	36.3	**71.6**	27.7	19.0	34.1	**80.8**	-9.2
TS_{OZO} 2	5.09	1.36	10.2	**16.6**	5.10	1.65	15.2	**21.9**	-5.3
Total	88.2				102.7				-14.5
Channel	Γ_{PROJ}				Γ_{THEO}				$\Delta\Gamma_{PROJ}$
	(.1)	(.2)	(.3)	**Σ**	(.1)	(.2)	(.3)	**Σ**	
Γ_{CH_2OO} **(1)**	0.060	0.050	0.069	**0.179**	0.068	0.058	0.073	**0.199**	-0.020
Γ_{CH_2OO} **(2)**	0.054	0.035	0.067	**0.156**	0.057	0.051	0.065	**0.173**	-0.017
$\Gamma_{anti\text{-}CH_3CHOO}$	0.142	0.119	0.164	**0.427**	0.130	0.108	0.188	**0.427**	-0.002
$\Gamma_{syn\text{-}CH_3CHOO}$	0.083	0.055	0.102	**0.240**	0.082	0.019	0.099	**0.201**	0.039

The very small difference between the k_{PROJ} value for O_3 + Alkene **2** (8.82×10^{-17} cm^3 s^{-1}) and the k_{THEO} constant (1.03×10^{-16} cm^3 s^{-1}) appears to be mainly attributed to subtle changes across all TS_{OZO} structures, rather than a substantial inaccuracy in any single TS_{OZO} structure. This also appears to be the case for the Γ_{PROJ} values, which are within ~2% of the Γ_{THEO} values. The main Γ_{PROJ} deviations can be observed with TS_{FO} 2.2 and TS_{SYN} 2, which have the largest deviations for individual subchannels (0.016—0.036). This is ultimately insignificant in this case, as TS_{FO} 2.2 and TS_{SYN} 2 both have high ΔG_{PROJ} & ΔG_{THEO} barriers. Critically, the Γ_{THEO} and Γ_{PROJ} values exhibit the same product branching preferences: $\Gamma_{anti\text{-}CH_3CHOO} > \Gamma_{syn\text{-}CH_3CHOO} > \Gamma_{CH_2OO}$ (1) > Γ_{CH_2OO} (2). Deviations between the k_{THEO} & Γ_{THEO} and k_{PROJ} & Γ_{PROJ} values are minor, providing additional evidence that FESP model 1 is reliable and that ΔG_{PROJ} values can be used as a fair and accurate representation of the ΔG_{THEO}. The Accuracy of FESP Model 1 is explored in some detail for the Ozonolysis of Alkenes **15**, **16** & **7** in Appendix Sections 4.2.5—4.2.7. Broadly, however the k_{PROJ} & Γ_{PROJ} values for O_3 + Alkenes **15**, **16** & **7** are similar to their k_{THEO} & Γ_{THEO} values determined in Chapter 3, provides more evidence that FESP model 1 is quite accurate.

6.4.3 Summary

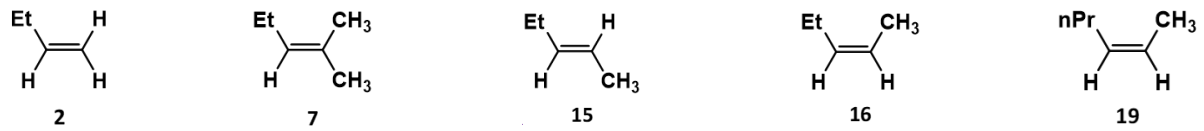

*Figure 6.17: Schematic of the chemical structures of Alkenes **2**, **7**, **15**, **16** & **19**.*

It has been demonstrated that the MESMER projection technique is a reliable way of producing k_{PROJ} & Γ_{PROJ} values for alkene ozonolysis reactions. The FESP Model 1 produces k_{PROJ} & Γ_{PROJ} values similar to the explicitly computed k_{THEO} & Γ_{THEO} values for all O_3 reactions with Alkenes **2**, **7**, **15** & **16**. The FESP Model 1 results even shows the same reactivity trend across this set of alkenes (Alkene **2** < Alkene **15** < Alkene **16** < Alkene **7**). However, changes in the steric interactions between different structural moieties are not always accounted for in the FESP Model 1. This is mainly where rotations and distortions move the —Et substituent within the projected system, and other structural movements are well accounted for within ΔG_{TS-POZ}. Overall, FESP Model 1 provides a reliable and accurate provisional model to determine the ozonolysis chemistry of Alkene **19**, however further iterations of the model are generated to include the impact structural rotations that induce steric energy changes impacting k_{PROJ} or Γ_{THEO}.

6.5 Applying FESP Model 1 to the Ozonolysis of *Z*-2-hexene

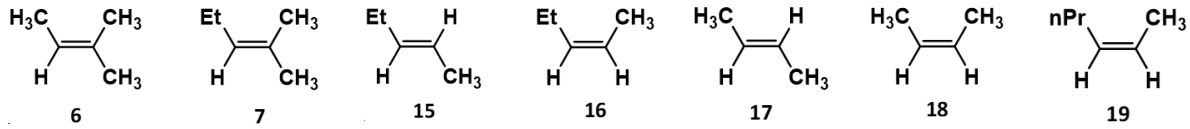

*Figure 6.18: Schematic of the chemical structures of Alkenes **6**, **7** & **15—19**.*

As Alkene **19** has an —nPr substituent in the $—R_1$ position, the MESMER input files and the $\Delta G_{TS—POZ}$ [TS] values are obtained from the equivalent alkene with an —Et substituent in the $—R_1$ position, O_3 + Alkene **16**. Use of FESP model 1 for other —nPr substituted alkenes, such as 1-pentene, *E*-2-hexene, and 2-methyl-2-hexene, would also use the MESMER input files and the $\Delta G_{TS—POZ}$ [TS] values from the equivalent —Et substituted alkenes (Alkenes **2**, **7** & **15**). A general schematic of O_3 + Alkene **19** is displayed in Figure 6.19 and the large number of TS structures in the reaction are grouped by "channel".

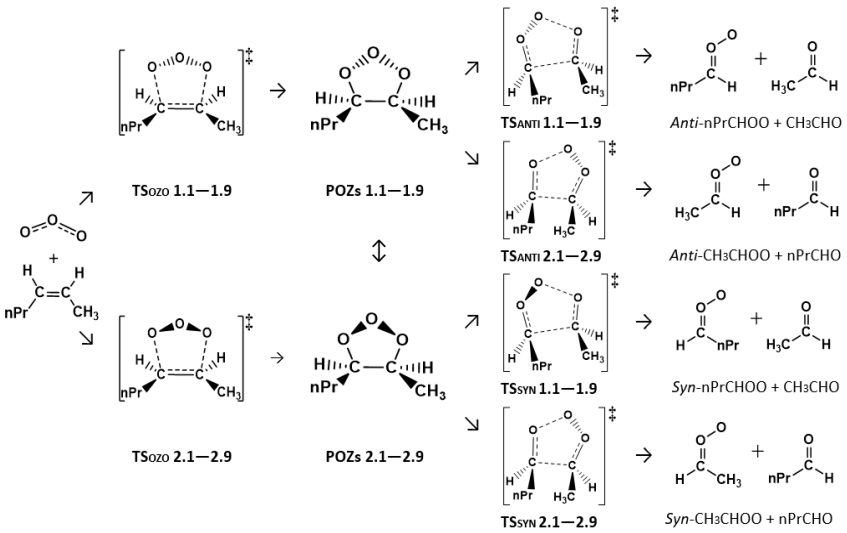

*Figure 6.19: General Schematic of the O_3 + Alkene **19** reaction.*

The ΔG_{PROJ} values for each of these TS structures are displayed in Table 6.6, having been calculated using the ΔG_{THEO} values for the POZ conformers and the $\Delta G_{TS—POZ}$ values from the analogous TS structures in the O_3 + Alkene **16** reaction from Chapter 3.

*Table 6.6: Projected Gibbs Free Energy (ΔG_{PROJ}) values for transition states of O_3 + Alkene **19** (Z-2-hexene) calculated using FESP Model 1 involving the: the relative theoretical Gibbs free energy [ΔG_{THEO}] of the POZ; and the ΔG_{THEO} difference between the analogous TS and POZ structures for the O_3 + Alkene **16** reaction (ΔG_{TS-POZ} [TS]): ΔG_{PROJ} [TS] = ΔG_{THEO} [POZ] + ΔG_{TS-POZ} [TS]. Gibbs Free energy values in kJ mol^{-1}.*

POZ (Alkene 19)		TS (Alkene 16)		TS (Alkene 19)		POZ (Alkene 19)		TS (Alkene 16)		TS (Alkene 19)	
Label	ΔG_{THEO}	Label	ΔG_{TS-POZ}	Label	ΔG_{PROJ}	Label	ΔG_{THEO}	Label	ΔG_{TS-POZ}	Label	ΔG_{PROJ}
		TS_{OZO} 1.1	240.04	**TS_{OZO} 1.1**	**50.63**			TS_{OZO} 2.1	246.49	**TS_{OZO} 2.1**	**58.76**
POZ 1.1	-189.41	TS_{ANTI} 1.1	65.00	**TS_{ANTI} 1.1**	**-124.41**	POZ2.1	-187.73	TS_{SYN} 1.1	72.62	**TS_{SYN} 1.1**	**-115.11**
		TS_{ANTI} 2.1	69.16	**TS_{ANTI} 2.1**	**-120.24**			TS_{SYN} 2.1	76.84	**TS_{SYN} 2.1**	**-110.89**
		TS_{OZO} 1.1	240.04	**TS_{OZO} 1.2**	**54.25**			TS_{OZO} 2.1	246.49	**TS_{OZO} 2.2**	**62.58**
POZ1.2	-185.79	TS_{ANTI} 1.1	65.00	**TS_{ANTI} 1.2**	**-120.79**	POZ2.2	-183.91	TS_{SYN} 1.1	72.62	**TS_{SYN} 1.2**	**-111.29**
		TS_{ANTI} 2.1	69.16	**TS_{ANTI} 2.2**	**-116.62**			TS_{SYN} 2.1	76.84	**TS_{SYN} 2.2**	**-107.07**
		TS_{OZO} 1.1	240.04	**TS_{OZO} 1.3**	**58.05**			TS_{OZO} 2.1	246.49	**TS_{OZO} 2.3**	**66.59**
POZ1.3	-181.99	TS_{ANTI} 1.1	65.00	**TS_{ANTI} 1.3**	**-116.99**	POZ2.3	-179.90	TS_{SYN} 1.1	72.62	**TS_{SYN} 1.3**	**-107.28**
		TS_{ANTI} 2.1	69.16	**TS_{ANTI} 2.3**	**-112.82**			TS_{SYN} 2.1	76.84	**TS_{SYN} 2.3**	**-103.06**
		TS_{OZO} 1.2	249.19	**TS_{OZO} 1.4**	**63.82**			TS_{OZO} 2.2	251.71	**TS_{OZO} 2.4**	**72.53**
POZ1.4	-185.37	TS_{ANTI} 1.2	68.02	**TS_{ANTI} 1.4**	**-117.35**	POZ2.4	-179.18	TS_{SYN} 1.2	82.97	**TS_{SYN} 1.1**	**-107.03**
		TS_{ANTI} 2.2	61.22	**TS_{ANTI} 2.4**	**-124.15**			TS_{SYN} 2.2	72.15	**TS_{SYN} 2.1**	**-96.21**
		TS_{OZO} 1.2	249.19	**TS_{OZO} 1.5**	**77.33**			TS_{OZO} 2.2	251.71	**TS_{OZO} 2.5**	**83.84**
POZ1.5	-171.86	TS_{ANTI} 1.2	68.02	**TS_{ANTI} 1.5**	**-103.84**	POZ2.5	-167.87	TS_{SYN} 1.2	82.97	**TS_{SYN} 1.5**	**-95.72**
		TS_{ANTI} 2.2	61.22	**TS_{ANTI} 2.5**	**-110.64**			TS_{SYN} 2.2	72.15	**TS_{SYN} 2.5**	**-84.90**
		TS_{OZO} 1.2	249.19	**TS_{OZO} 1.6**	**68.63**			TS_{OZO} 2.2	251.71	**TS_{OZO} 2.6**	**78.06**
POZ1.6	-180.55	TS_{ANTI} 1.2	68.02	**TS_{ANTI} 1.6**	**-112.53**	POZ2.6	-173.65	TS_{SYN} 1.2	82.97	**TS_{SYN} 1.6**	**-101.50**
		TS_{ANTI} 2.2	61.22	**TS_{ANTI} 2.6**	**-119.33**			TS_{SYN} 2.2	72.15	**TS_{SYN} 2.6**	**-90.68**
		TS_{OZO} 1.3	241.16	**TS_{OZO} 1.7**	**47.43**			TS_{OZO} 2.3	245.63	**TS_{OZO} 2.7**	**54.38**
POZ1.7	-193.73	TS_{ANTI} 1.3	67.43	**TS_{ANTI} 1.7**	**-126.30**	POZ2.7	-191.26	TS_{SYN} 1.3	77.92	**TS_{SYN} 1.7**	**-114.76**
		TS_{ANTI} 2.3	67.02	**TS_{ANTI} 2.7**	**-126.71**			TS_{SYN} 2.3	76.50	**TS_{SYN} 2.7**	**-113.34**
		TS_{OZO} 1.3	241.16	**TS_{OZO} 1.8**	**52.08**			TS_{OZO} 2.3	245.63	**TS_{OZO} 2.8**	**59.12**
POZ1.8	-189.08	TS_{ANTI} 1.3	67.43	**TS_{ANTI} 1.8**	**-121.64**	POZ2.8	-186.51	TS_{SYN} 1.3	77.92	**TS_{SYN} 1.8**	**-112.64**
		TS_{ANTI} 2.3	67.02	**TS_{ANTI} 2.8**	**-122.06**			TS_{SYN} 2.3	76.50	**TS_{SYN} 2.8**	**-111.22**
		TS_{OZO} 1.3	241.16	**TS_{OZO} 1.9**	**50.01**			TS_{OZO} 2.3	245.63	**TS_{OZO} 2.9**	**56.50**
POZ1.9	-191.15	TS_{ANTI} 1.3	67.43	**TS_{ANTI} 1.9**	**-123.72**	POZ2.9	-189.13	TS_{SYN} 1.3	77.92	**TS_{SYN} 1.9**	**-110.02**
		TS_{ANTI} 2.3	67.02	**TS_{ANTI} 2.9**	**-124.13**			TS_{SYN} 2.3	76.50	**TS_{SYN} 2.9**	**-108.60**

As the O_3 + Alkene **19** model calculations are partially built from the O_3 + Alkene **16** system it is not unexpected that the k_{PROJ} value for O_3 + Alkene **19**, displayed in Table 6.7, is similar to the k_{THEO} value of O_3 + Alkene **16** (~2.84 × 10^{-15} cm^3 s^{-1}), albeit slightly smaller. Given the range of k_{EXP} values found for both O_3 + Alkene **19** (1.05—1.44 × 10^{-16} cm^3 s^{-1}) and O_3 + Alkene **16** reactions (1.27—1.29 × 10^{-16} cm^3 s^{-1}) this is consistent with experimental literature.[10,360]

Table 6.7: The rate constant (k_{PROJ}) [× 10^{-17} cm^3 s^{-1}] and product branching Criegee intermediate fractions (Γ_{PROJ}) for O_3 + Alkene 19 calculated using FESP model 1 by overall channel (TS_{OZO} 1 and TS_{OZO} 2) and subchannel (.1, .2, .3 …) and overall percentage k_{PROJ} per ozonolysis pathway; POZ breakdown branching fraction analysed per subchannel and total yield of respective.

	k_{PROJ} (TS) [× 10^{-17} cm^3 s^{-1}]									
Channel	.1	.2	.3	.4	.5	.6	.7	.8	.9	%
TS_{OZO} 1	34.79	8.10	1.74	0.138	*<0.001*	0.019	123.0	18.8	44.4	94.4%
TS_{OZO} 2	1.33	0.28	0.057	0.005	<0.001	<0.001	7.73	1.14	3.27	5.6%
Overall					247.8					100%
Γ_{PROJ}	.1	.2	.3	.4	.5	.6	.7	.8	.9	Total
$\Gamma_{anti\text{-}nPrCHOO}$	0.080	0.043	0.022	0.026	0.002	0.011	0.128	0.058	0.083	0.455
$\Gamma_{syn\text{-}nPrCHOO}$	0.006	0.003	0.001	<0.001	<0.001	<0.001	0.010	0.004	0.007	0.031
$\Gamma_{anti\text{-}CH_3CHOO}$	0.042	0.023	0.011	0.077	0.007	0.034	0.126	0.057	0.082	0.459
$\Gamma_{syn\text{-}CH_3CHOO}$	0.012	0.006	0.003	0.003	<0.001	<0.001	0.014	0.006	0.009	0.055

This k_{PROJ} value for O_3 + Alkene **19** is dominated by reaction via the TS_{OZO} 1.7 subchannels, with significant contributions from the TS_{OZO} 1.1, 1.8 & 1.9 mechanisms. The large contributions to the k_{PROJ} values from a variety of TS_{OZO} mechanisms demonstrates the importance of identifying all TS structures on the PES of O_3 + Alkene **19**. However, all of the TS_{OZO} 2.1—2.9 have k_{PROJ} values < 1 × 10^{-16} cm^3 s^{-1}, continuing the trend observed in Chapter 3, that reaction via TS_{OZO} 1 structures dominate the overall of k_{PROJ} value (94.2%). One important observation is that the steric bulk of the long —nPr substituent has little overall effect on the k_{PROJ} value, except in a subset of cases where the —nPr substituent experiences significant steric clashes with the remaining moiety at the TS geometry. This steric interaction is seen in the TS_{OZO} 1.4—1.6 & TS_{OZO} 2.4—2.6 structures, which have just a small contribution to the overall k_{PROJ} values.

The Γ_{PROJ} values for O_3 + Alkene **19** shows similar results to those from O_3 + Alkene **16**. While all TS_{ANTI} 1.1—1.9 contribute to the total reactive yield, TS_{ANTI} 1.1, 1.7 & 1.9 dominate the overall $\Gamma_{anti\text{-}nPrCHOO}$ branching fraction (~0.455). All TS_{ANTI} 2.1—2.9 mechanisms have small contributions to the overall $\Gamma_{anti\text{-}CH_3CHOO}$ (~0.459) but the majority of this is concentrated in three subchannels: TS_{ANTI} 2.4, 2.7 and 2.9 (Γ_{THEO} ~ 0.077, 0.126 & 0.082). The correspondingly small $\Gamma_{syn\text{-}CH_3CHOO}$ value (0.055) and the $\Gamma_{syn\text{-}nPrCHOO}$ value (0.031) shows that *anti*-CIs is favoured over *syn*-CIs, especially for the ozonolysis of Z-orientated alkenes, consistent with the results of previous chapters. The branching preference for CIs with larger numbers of α-H atoms, seen in Chapter 3, continues for O_3 + Alkene **19** with the

higher overall Γ_{THEO} for CH_3CHOO (0.514) compared to nPrCHOO (0.486). However, this CH_3CHOO preference is smaller than that seen for O_3 + Alkene **16** (0.544).

Despite the fact that the ΔG_{PROJ} values omit rotational and steric distortion, FESP model 1 produces a k_{PROJ} value similar to that seen in the literature and Γ_{PROJ} results similar to analogous alkenes in Chapter 3. This implies that, while the model still needs further work on incorporating the rotational and steric distortions (covered in FESP model 2), FESP Model 1 is a reliable framework in which to determine the ozonolysis k_{PROJ} & Γ_{PROJ} values for alkenes with lengthy alkyl substituents.

6.6 FESP Model 2: Applying Hindered-Internal-Rotation and Steric Factors

To produce a fully accurate set of k_{PROJ} & Γ_{PROJ} results for O_3 + Alkene **19**, the FESP model must consider steric and rotational interactions within the TS structures, that have been show previously to cause deviations in FESP models from explicitly computed TS energies.

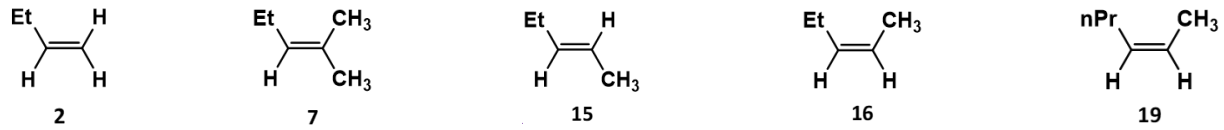

*Figure 6.20: Schematic of the chemical structures of Alkenes **2**, **7**, **15**, **16** & **19**.*

These steric deviations cause inconsistencies primarily between the ΔG_{PROJ} & ΔG_{THEO} values. These deviations are cross-examined in the next section and used to identify a common set of environment dependent factors that alter the ΔG_{THEO} values. FESP model 1 relies not on producing physical structures of the TS but on the hypothesis that a reliable ΔG_{PROJ} [TS] value can be calculated by using: the ΔG_{THEO} value of the related POZ; and the difference in ΔG_{THEO} values between the analogous TS & POZ structures, the ΔG_{TS-POZ} value, of an analogous alkene with a shortened alkyl group. However, the structural motion involved in the transition between the POZ and the TS geometries are known to cause the ΔG_{THEO} & ΔG_{PROJ} values to diverge for O_3 + Alkene **16**, and it is anticipated that a similar effect may occur for O_3 + Alkene **19**. For the purposes of describing rotations and distortions with the O_3 + alkene reaction, Figure 6.21 labels the C atoms for *E*- & *Z*-2-pentene $^1C - {}^5C$ by standard UPAC nomenclature.

*Figure 6.21: Alkenes **15** & **16** with the Carbon atoms $^1C - {}^5C$ by standard UPAC nomenclature.*

The author has deduced that observed changes between the ΔG_{PROJ} & ΔG_{THEO} values in O_3 + Alkenes **2**, **7**, **15** & **16** reactions can be linked to a common group of steric factors, namely whether the two mutually repelling sites are converging or diverging in the shift between the POZ and the TS geometries (example of this in Figure 6.22). If these common rotational or steric factors can be quantified, they can be identified in all reactions and numerical corrections applied, for example in the case of O_3 + Alkene **19**. FESP model 2 uses the framework of FESP model 1 as a foundation, but then applies these quantified

common numerical factors on a TS-by-TS basis, so that steric changes are taken into consideration.

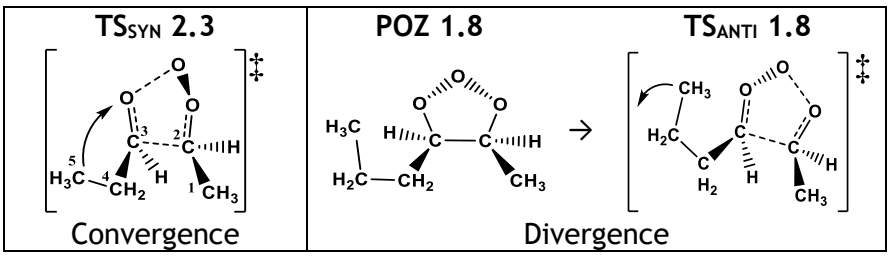

*Figure 6.22: Examples of Hindered-Internal-Rotation in O_3 + Alkene **15** and the use of that steric factor in O_3 + Alkene **19**.*

The discrepancies in the TS structure that cause these δΔG divergences fall into two factors: *hindered-internal-rotation* (Δ_{ROT}) and underlying steric repulsion (Δ_{STERIC}). The *hindered-internal-rotation* factor is induced during both the cycloaddition and POZ fragmentation in all R_1—R_4 substituents. Ethyl group rotation around the C—R bond, seen as a the ^5C-^4C-^3C-^2C dihedral angle in Figure 6.22, swings the —Et group towards (see TS_{SYN} 2.3) or away from (see TS_{SYN} 1.3) other segments of structure. The Δ_{STERIC} factors emerge from one of these underlying structural changes between the POZ and the TS geometries. Such steric induced geometric changes are not required if the ethyl group is replaced by a smaller substituent, for example -Me or -H. This shift in structure incidentally pulls the —Et group away or pushes it towards another part of the TS structure. During both Δ_{STERIC} or Δ_{ROT} movements, the —Et group either converges or diverges with another structural moiety, and therefore causes changes in the degree of mutual repulsion, which in turn increases or decreases the ΔG_{THEO}. Numerical correction factors in can be found in Appendix Section 4.2.9.

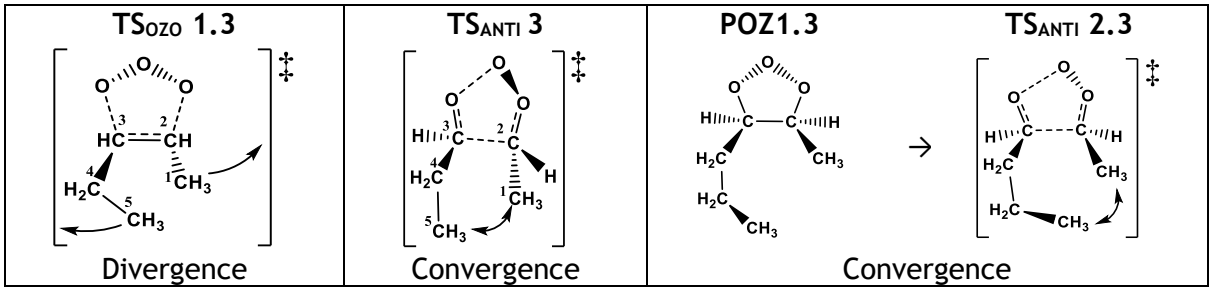

*Figure 6.23: Underlying steric factor in O_3 + Alkene 15 and the use of that steric factor in O_3 + Alkene **19**.*

The quantified Δ_{STERIC} and Δ_{ROT} factors are obtained from the average difference between the ΔG_{THEO} & ΔG_{PROJ} values (Equation 6.8). The Δ_{STERIC} and Δ_{ROT} factors for O_3 + Alkenes **2**, **7**, **15** & **16** are only examined if their $\delta\Delta G_{PROJ}$ values are non-negligible ($\delta\Delta G_{PROJ}$ < -2 kJ mol^{-1} or > 2 kJ mol^{-1}).

$$\delta\Delta G_{PROJ} = \Delta G_{THEO} - \Delta G_{PROJ} \qquad \textit{Equation 6.8}$$

Only O_3 + Alkenes **15** & **16** feature in the figures in this section as all Δ_{STERIC} and Δ_{ROT} are found in at least one TS structure in these reactions and it simplifies labelling and descriptions throughout.

6.6.1 The Hindered-Internal-Rotational (Δ_{ROT}) Factors

As the first convergent hindered internal rotations derived here is for the O_3 + Alkene **15** reaction, where, as seen in Table 6.8, the distortions of the for TS_{ANTI} 2.2 structure rotates the —Et substituent towards the central oxygen of the 1,2,3-trioxolane segment of the structure. This convergence generates greater steric repulsions between these two segments and therefore raises the overall energy of TS_{ANTI} 2.2. The reverse effect also transpires in the O_3 + Alkene **15** reaction, as the rotation in the TS_{SYN} 2.2 structure causes the —Et substituent to diverge with the central oxygen, reducing the steric repulsion and lowering the overall energy of the structure.

*Table 6.8: Structures of TS_{ANTI} 2.2 & TS_{SYN} 2.2 from O_3 + Alkene **15** and TS_{ANTI} 2.2 & TS_{SYN} 2.2 from O_3 + Alkene **16** and the degree of divergence [$\delta\Delta G_{PROJ} = \Delta G_{THEO} - \Delta G_{PROJ}$] measured using the relative theoretical Gibbs free energy [ΔG_{THEO}]: and the model 1 projected Gibbs free energy (ΔG_{PROJ}); and the nomenclature and Δ_{ROT} factor obtained. Gibbs Free energy values in kJ mol^{-1}.*

Alkene	15		16	
TS Label	TS_{SYN} 2.2	TS_{ANTI} 2.2	TS_{ANTI} 2.2	TS_{OZO} 1.2
Structure	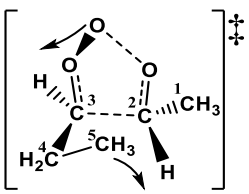	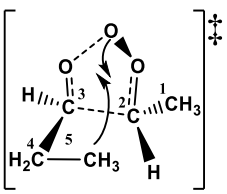	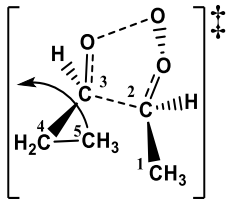	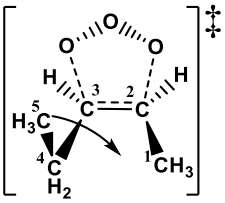
ΔG_{THEO}	-111.4	-121.9	-125.7	62.3
ΔG_{PROJ}	-120.4	-118.6	-119.6	55.0
$\delta\Delta G_{PROJ}$	9.0	-3.3	-6.1	7.3
Δ_{ROT} Factor	Δ_{DIV} (—Et,^{c}O,—H)	Δ_{CON} (—Et,^{c}O,—H)	Δ_{DIV} (—Et,^{t}O,—CH_3)	Δ_{CON} (—Et,^{t}O,—CH_3)
Average	-8.4 ± 0.5	3.7 ± 0.3	-6.6 ± 1.9	6.3 ± 1.0

These specific movements are not unique to the O_3 + Alkene **15** reaction because, as seen previously in Section 6.4.2, these same pair of hindered internal rotations occur in the O_3 + Alkene **2** reactions for similar TS structures. This set of hindered internal rotation (Δ_{ROT}) factors (referred to as the **Δ_{DIV} (—Et,^{c}O,—H)** and **Δ_{CON} (—Et,^{c}O,—H)** factors) are paired together because they involve the same segments of the structure converging or diverging. To quantify the energetic component, found in Table 6.8 for each of these factors all similar distortions across all O_3 + Alkenes **2**, **7**, **15** & **16** reaction were identified, and separate average energetic deviation were produced for the convergent and divergent factors. While many of the other Δ_{ROT} & Δ_{STERIC} factors discussed in this section also feature for the O_3 + Alkenes **2** & **7** reactions, for the sake of simplicity, the author only describes

these factors herein with reference to the O_3 + Alkenes **15** & **16** reactions (for the other TS structures where these distortions take place see Appendix Section 4.2.9).

The second type of hindered internal rotation identified here can be seen clearly for TS_{OZO} 1.2 in the O_3 + Alkene **16** reaction (see Table 6.8), where the rotating —Et substituent can be seen converging with *E* orientated —CH_3 substituent. This raises the energy of the structure too, but this alkyl—alkyl steric interaction is distinguished from later such interactions because of the proximity of the —Et substituent to the terminal oxygen of the 1,2,3-trioxolane segment. The divergence version of this hindered internal rotation is that seen for TS_{ANTI} 2.2 in O_3 + Alkene **16**, where the —Et substituent in a similar environment instead rotationally diverges from the —CH_3 substituent, causing a drop in energy. These factors are referred to as: **Δ_{CON} (—Et,^{t}O,—CH_3)** & **Δ_{DIV} (—Et,^{t}O,—CH_3)**.

A third type of hindered internal rotation is noted from the TS_{OZO} 2.2 in the O_3 + Alkene **16** reaction, also centres on the —Et substituent rotationally converging with the —CH_3 substituent. However, the forward-facing central oxygen in the 1, 2, 3-trioxolane segment provides an additional hindrance (or "steric trap") in this rotation making this distortion and the increase in energy associated with it a separate factor. This convergence is paired with a similar *steric trap* divergence seen for TS_{SYN} 2.2, where the —Et substituent rotates away from the —CH_3 group and the central oxygen, causing a drop in energy. The average energy deviations these **Δ_{CON} (—Et,^{c}O,—CH_3)** & **Δ_{DIV} (—Et,^{c}O,—CH_3)** factors are both found in Table 6.9.

*Table 6.9: Structures of TS_{SYN} 2.2, TS_{OZO} 2.2, TS_{SYN} 1.2 & TS_{SYN} 2.3 from O_3 + Alkene **16** and the degree of divergence [$\delta\Delta G_{PROJ} = \Delta G_{THEO} - \Delta G_{PROJ}$] measured using the relative theoretical Gibbs free energy [ΔG_{THEO}]: and the model 1 projected Gibbs free energy (ΔG_{PROJ}); and the nomenclature and average value internal Δ_{ROT} factor obtained. Gibbs Free energy values in kJ mol^{-1}.*

Alkene	**16**		**16**	
TS Label	**TS_{SYN} 2.2**	**TS_{OZO} 2.2**	**TS_{SYN} 1.2**	**TS_{SYN} 2.3**
Structure	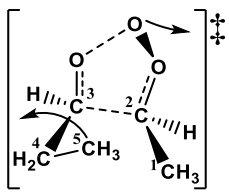	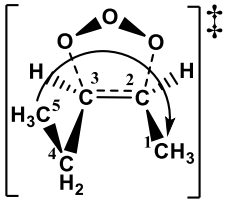	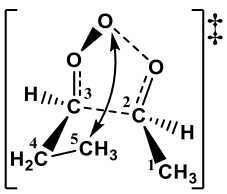	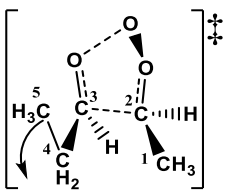
ΔG_{THEO}	-109.0	70.5	-98.2	-116.44
ΔG_{PROJ}	-102.7	67.1	-102.7	-114.43
$\delta\Delta G_{PROJ}$	**-6.4**	**3.4**	**4.5**	**-2.0**
Δ_{ROT} Factor	**Δ_{DIV} (—Et,^{c}O,—CH_3)**	**Δ_{CON} (—Et,^{c}O,—CH_3)**	**Δ_{CON} (*syn*—Et,^{c}O,—CH_3)**	**$\Delta_{DIV}/\Delta_{CON}$ (—Et,^{t}O)**
Average	-5.4 ± 1.0	3.2 ± 0.1	4.9 ± 0.5	±2.4 ± 0.4

The distortions of the —Et substituent seen for TS_{SYN} 1.2 for O_3 + Alkene **16** involves a rotation into similar environment to the previously described *steric trap* (i.e. an upward

facing —Et substituent converging with the central oxygen atom and the —CH_3 substituent). However, the production of *syn*-EtCHOO in TS_{SYN} 1.2 generates a concurrent rotation that shifts the central oxygen atom much closer to the —Et substituent raising the energy of the system further, as seen in Table 6.9. This unique combination of converging factors that generates this **Δ_{CON} (*syn*—Et,^{c}O,—CH_3)** factor means no divergence equivalent is observed or required.

The last internal rotation of note in Table 6.9 is seen for TS_{SYN} 2.3 in O_3 + Alkene **16**, which involves a simple divergence of the —Et group from the terminal oxygen in the 1, 2, 3-trioxolane. As no comparable convergent distortion was observed across O_3 reactions with Alkenes **2**, **7**, **15** & **16**, the resultant quantified energetic factor for this divergence (**Δ_{DIV} (—Et,—^{t}O)**) is also used for the convergent equivalent factor (**Δ_{CON} (—Et,—^{t}O)**).

Although these Δ_{ROT} factors, were not automatically applied by FESP Model 1 for O_3 + Alkenes **2**, **7**, **15** & **16**, they were intrinsically applied to O_3 + Alkene **19** because they were part of the explicitly computed model for O_3 + Alkene **16**, which was used as the template. This meant that "internally-hindered-rotational" adjustments were not required to be accounted for separately. However, during O_3 + Alkene **19**, the lengthy —nPr substituent interacts with many parts of the TS structure and so these adjustments are applied as steric factors.

6.6.2 The Steric (Δ_{STERIC}) Factors

Δ_{STERIC} factors arise from an underlying structural change in POZ and the TS geometries from the template alkene ozonolysis reaction. This increase in alkyl chain length between the template and the new system (such as the change from —Et to —nPr) causes a steric repulsion with additional structural moieties. Mainly, Δ_{STERIC} factors cause discrepancies between ΔG_{PROJ} & ΔG_{THEO} values, as can be seen in both the TS_{OZO} 1.1 & the TS_{ANTI} 1.1 structures from O_3 + Alkene **15**, observed in Table 6.10.

*Table 6.10: Structures of TS_{OZO} 1.1, POZ 1.1 & TS_{ANTI} 1.1 from O_3 + Alkene **15** and the degree of divergence [$\delta\Delta G_{PROJ} = \Delta G_{THEO} - \Delta G_{PROJ}$] measured using the relative theoretical Gibbs free energy [ΔG_{THEO}]: and the model 1 projected Gibbs free energy (ΔG_{PROJ}); and the nomenclature Δ_{STERIC} factor obtained. Gibbs Free energy values in kJ mol^{-1}.*

Alkene	**16**		
TS Label	**TS_{OZO} 1.1**	**POZ 1.1**	**TS_{ANTI} 1.1**
Structure	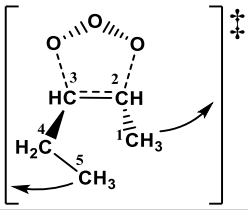	→ 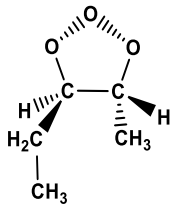 →	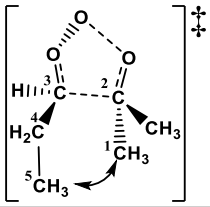
ΔG_{THEO}	47.8	-194.8	-113.9
ΔG_{PROJ}	52.8	-	-120.8
$\delta\Delta G_{PROJ}$	-4.9	-	6.9
Δ_{ROT} Factor	**Δ_{DIV} (—Et,—CH_3)**	-	**Δ_{CON} (—Et,— CH_3)**
Average	-4.0 ± 1.2	-	5.4 ± 1.5

The —Et and —CH_3 substituents in the TS_{ANTI} 1.1 structure are in much closer proximity than that seen in POZ 1.1, which causes the energy of the system to increase, a factor that FESP model 1 has not taken into account. Conversely, the structural shift involved between the POZ 1.1 and the TS_{OZO} 1.1 structures shifts the —Et and —CH_3 substituents apart, therefore reducing steric interaction and lowering the energy. These contrasting converging and diverging alkyl—alkyl interactions are the basis of a set of quantified Δ_{STERIC} factors (**Δ_{DIV} (—Et,—CH_3)** & **Δ_{CON} (—Et,—CH_3)**) seen in Figure 6.24, alongside the other factors listed in Section 6.6.1.

Hindered-internal-rotations can be applied as steric factors, therefore in the following section they are just referred to collectively as Δ_{STERIC} factors. The accuracy of FESP model 1 was examined in Section 6.4 using comparative calculations of the ozonolysis of Alkenes **2**, **7**, **15** & **16**, but the trialling of FESP model 2 calculations of these reactions in the same way would serve little purpose. This is because the cornerstone of FESP model 2, was the FESP model 1 comparison of O_3 + Alkenes **2**, **7**, **15** & **16** and so a FESP model 2 calculation of these systems would not add anything. All these Δ_{STERIC} and Δ_{ROT} factors with structural examples can be seen in Figure 6.24.

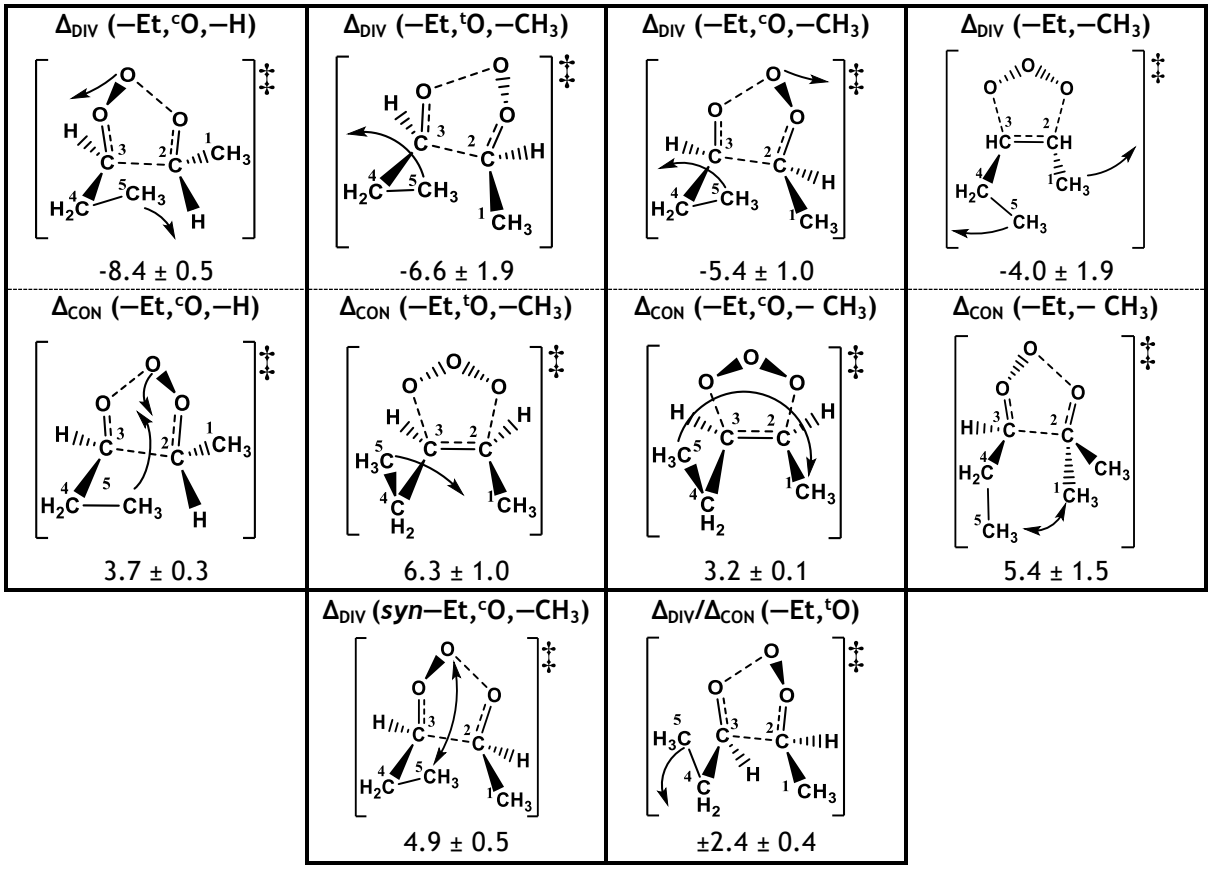

Figure 6.24: Summary of converging (Δ_{CON}) and diverging (Δ_{DIV}) steric and rotational factors labels with an example structure of each factor and the quantified numerical factor (kJ mol^{-1}).

6.6.3 Applying FESP model 2 to the Ozonolysis of *Z*-2-hexene

The additional feature of FESP model 2, which makes it distinct from the previous FESP model, is the treatment of anticipated geometric shifts between the POZ and TS structures that are likely to cause convergence or a divergence between the —nPr group and other segments of the structures. Where such shifts take place, the appropriate steric factor is applied to produce a modified "ΔG_{STERIC}" energy using Equation 6.9.

$$\Delta G_{STERIC}\,[TS] = \Delta G_{PROJ}\,[TS] + \Delta_{STERIC} = \Delta G_{THEO}\,[POZ] + \Delta G_{TS-POZ}\,[TS] + \Delta_{STERIC} \qquad \textit{Equation 6.9}$$

There is no full computational PES analysis of O_3 + Alkene **19**, and so potential changes in steric interactions are gleaned by anticipated POZ-to-TS geometric shifts. These POZ-to-TS shifts in O_3 + Alkene **19** were estimated by examining each POZ and comparing it to the analogous POZ & TS structure in the O_3 + Alkene **16** reaction. Once a convergence between the —nPr group and other segments of the POZ is isolated, the type of interaction is taking place (e.g. an alkyl—alkyl interaction) and what environment this movement is

transpiring in (e.g. the proximity to the 1, 2, 3-trioxolane segment) is identified. A suitable steric factor from Figure 6.24 is applied to produce the ΔG_{STERIC} energy.

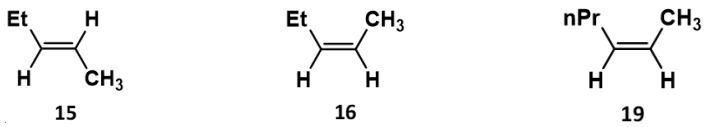

*Figure 6.25: Schematic of the chemical structures of Alkenes **15**, **16** & **19**.*

An example where this steric factor is applied is seen when contrasting the structures of POZ 1.3 and the anticipated TS_{ANTI} 2.3 seen in Figure 6.26, where the resultant structural shift produces a new steric convergence between the —nPr and the —CH_3 substituents, and so a steric factor is most likely warranted. As this steric interaction involves only an alkyl—alkyl convergence, an appropriate steric factor from Figure 6.24 is the **Δ_{CON} (—Et,—CH_3)** factor, which is derived from a similar *alkyl—alkyl* interaction. This contrasts with the anticipated TS_{ANTI} 2.1 structure sees no new steric interactions involving the —nPr substituent (also seen in Figure 6.26) and so no steric factor is applied.

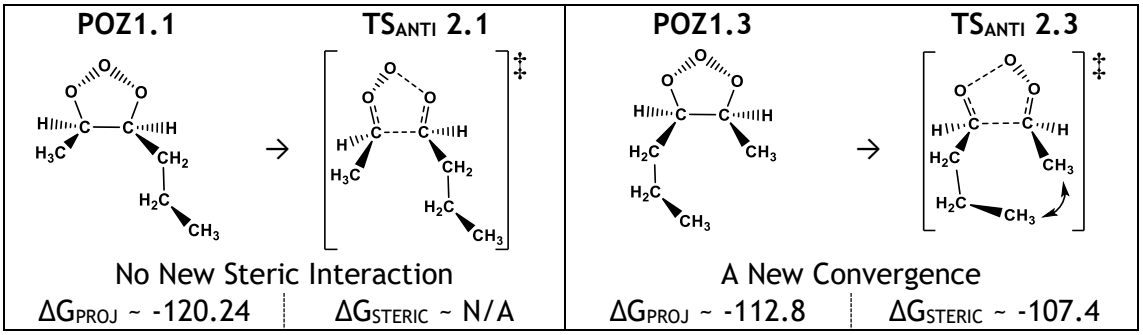

Figure 6.26: The estimated geometric shifts for POZ 1.1 → TS_{ANTI} 2.1 and POZ 1.3 → TS_{ANTI} 2.3 for O_3 + Alkene 19 and the new steric interactions that are produced from this shift; and projected and sterically adjusted Gibbs free energy (ΔG_{PROJ} & ΔG_{STERIC}) values for TS_{ANTI} 2.1 & TS_{ANTI} 2.3. Gibbs Free energy values in kJ mol^{-1}.

One crucial factor involved in analysing these steric interactions is that the length and flexibility of the —nPr substituent means that it can have steric repulsions with the alkyl segment of the POZ ring, which was not possible for the shorter —Et substituent. In the estimated structural POZ 1.2 → TS_{ANTI} 2.2 shift (seen in Figure 6.27) the —nPr substituent diverges with the alkyl section of the POZ. In FESP model 2, this alkyl—alkyl interaction is energetically equivalent to the interactions seen with between alkyl substituents (such as those seen for O_3 + Alkene **15** in Figure 6.27) and therefore the alkyl—alkyl divergence steric factor, **Δ_{DIV} (—Et,—CH_3)**, is applied to TS_{ANTI} 2.2, as well.

O_3 + Alkene 15		O_3 + Alkene 19	
TS_{OZO} 1.3	TS_{ANTI} 3	POZ1.2	TS_{ANTI} 2.2
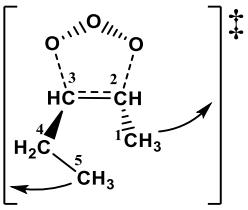	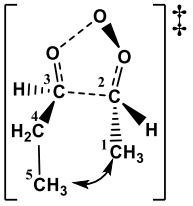	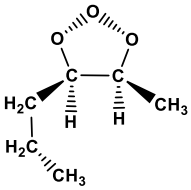 →	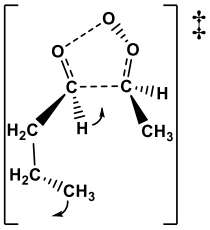
Divergence	Convergence	A New Divergence	
Δ_{DIV} (—Et,—CH_3) = -4.0	Δ_{CON} (—Et,—CH_3) = 5.4	ΔG_{PROJ} ~ -116.6	ΔG_{STERIC} ~ -120.4

Figure 6.27: Structural examples of Δ_{STERIC} factors that are applied for alkyl—alkyl interaction; the estimated geometric shifts and ΔG_{PROJ} & ΔG_{STERIC} values for TS_{ANTI} 2.2 for O_3 + Alkene 19. Gibbs Free energy values in kJ mol^{-1}.

The second set of important steric factors concerns the structural movement affecting the proximity of the —nPr substituent to the terminal oxygen in the 1,2,3-trioxolane group, such as those seen in the movement from POZ 2.8 to TS_{SYN} 1.8 or TS_{SYN} 2.8. The geometric shift in the TS_{SYN} 1.8 sees the —nPr substituent converging with this terminal oxygen, in contrast to TS_{SYN} 2.8, which sees a divergence between these two groups (see structures in Table 6.11). The equivalent convergent and divergent "alkyl—terminal oxygen" steric factors (**Δ_{CON} (—Et,^{t}O)** and **Δ_{DIV} (—Et,^{t}O)**) are therefore applied to TS_{SYN} 1.8 & TS_{SYN} 2.8, respectively in FESP model 2.

Table 6.11: Structural examples of Δ_{STERIC} factors that are applied for alkyl—terminal oxygen interaction; the estimated geometric shifts and ΔG_{PROJ} & ΔG_{STERIC} values for TS_{SYN} 1.8 & 2.8 for O_3 + Alkene 19. Gibbs Free energy values in kJ mol^{-1}.

O_3 + Alkene 16	O_3 + Alkene 19		
TS_{SYN} 2.3	POZ 2.8	TS_{SYN} 1.8	TS_{SYN} 2.8
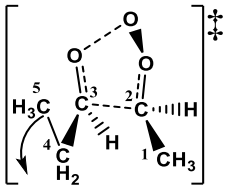	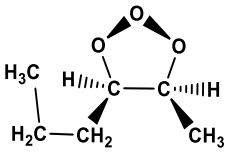 →	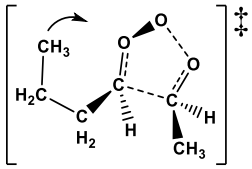	& 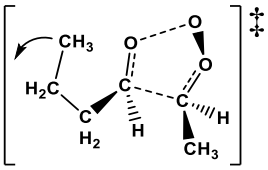
Divergence	-	Convergence	Divergence
Δ_{CON} (—Et,^{t}O) = 2.4	ΔG_{PROJ}	-108.6	-110.0
Δ_{DIV} (—Et,^{t}O) = -2.4	ΔG_{STERIC}	-106.2	-112.4

The two sets of factors listed in Tables 6.9 & 6.10 are applied to alkyl—alkyl and the alkyl—terminal oxygen interactions across most TS structures involved in the FESP model 2 calculations for the O_3 + Alkene **19** reaction, but there are an array of other factors applied to other TS structures in this reaction too. The results of using these other factors are displayed in the sterically adjusted results in Table 6.12, but these TS barrier heights are so high that increasing or decreasing their energy with these steric alterations shows only limited impact. This is particularly true with respect to generating the FESP model 2

rate constant (k_{STERIC}) and product branching ratios (Γ_{STERIC}). A brief description of the application of these steric factors is included in Appendix Section 4.2.10 instead.

Table 6.12: Production of steric corrected relative Gibbs Free energy (ΔG_{STERIC}) for FESP model 2, using the steric correction (Δ_{STERIC}) factors and the projected relative Gibbs Free energy (ΔG_{PROJ}) from FESP model 1 [$\Delta G_{STERIC} = \Delta G_{PROJ} + \Delta_{STERIC}$]. Note: the ΔG_{PROJ} values are used in FESP model 2 if there is no steric factor for that TS. Gibbs Free energy values in kJ mol^{-1}.

Δ_{STERIC} Factor: Δ_{DIV} (—Et,—CH_3) ~ -4.0			Δ_{STERIC} Factor: Δ_{CON} (—Et,—CH_3) ~ 5.4		
TS Label	**ΔG_{PROJ}**	**ΔG_{STERIC}**	**TS Label**	**ΔG_{PROJ}**	**ΔG_{STERIC}**
TS_{OZO} 1.2	54.3	50.3	TS_{OZO} 1.3	58.1	63.5
TS_{OZO} 2.2	62.6	58.6	TS_{OZO} 2.3	66.6	72.0
TS_{ANTI} 1.2	-120.8	-124.8	TS_{ANTI} 1.3	-117.0	-111.6
TS_{ANTI} 1.9	-123.7	-127.7	TS_{ANTI} 1.5	-103.8	-98.4
TS_{ANTI} 2.2	-116.6	-120.6	TS_{ANTI} 2.3	-112.8	-107.4
TS_{ANTI} 2.5	-110.6	-114.6	TS_{SYN} 1.3	-103.1	-97.7
TS_{ANTI} 2.9	-124.1	-128.1	TS_{SYN} 2.5	-95.7	-90.3
TS_{SYN} 1.2	-107.1	-111.1			
TS_{SYN} 1.9	-111.2	-115.2			
Δ_{STERIC} Factor: Δ_{CON} (—Et,^{t}O) ~ 2.4			**Δ_{STERIC} Factor: Δ_{DIV} (—Et,^{t}O) ~ -2.4**		
TS Label	**ΔG_{PROJ}**	**ΔG_{STERIC}**	**TS Label**	**ΔG_{PROJ}**	**ΔG_{STERIC}**
TS_{OZO} 1.6	68.6	71.0	TS_{ANTI} 1.6	-112.5	-114.9
TS_{OZO} 1.8	52.1	54.5	TS_{ANTI} 1.8	-121.6	-124.0
TS_{OZO} 2.6	78.0	80.4	TS_{ANTI} 2.8	-122.0	-124.4
TS_{OZO} 2.8	59.1	61.5	TS_{SYN} 2.8	-110.0	-112.4
TS_{ANTI} 2.6	-119.3	-116.9	**Δ_{STERIC} Factor: Δ_{DIV} (*syn*—Et,^{c}O,—CH_3) ~ 4.92**		
TS_{SYN} 1.8	-108.6	-106.2	**TS Label**	**ΔG_{PROJ}**	**ΔG_{STERIC}**
TS_{SYN} 2.6	-101.5	-99.1	TS_{SYN} 1.6	-90.7	-85.8
Δ_{STERIC} Factor: Δ_{CON} (—Et,^{c}O,—CH_3) ~ 3.2			**Δ_{STERIC} Factor: Δ_{CON} (—Et,^{t}O,—CH_3) ~ 6.3**		
TS Label	**ΔG_{PROJ}**	**ΔG_{STERIC}**	**TS Label**	**ΔG_{PROJ}**	**ΔG_{STERIC}**
TS_{OZO} 2.5	83.8	87.0	TS_{OZO} 1.5	77.3	83.6
TS_{SYN} 1.5	-84.9	-81.7			

Most of these steric changes seen in Table 6.12, lead to some minor changes in the overall PES, when applied to O_3 + Alkene **19**. However, small reductions in ΔG_{STERIC} values for key TS barriers, such as TS_{OZO} 1.2, may have some impact on the overall ozonolysis chemistry of Alkene **19**, explored subsequently.

6.6.4 The Ozonolysis Chemistry of Alkene 19 Using FESP Model 2

The ozonolysis chemistry of Alkene **19**, fully calculated using FESP model 2, is very similar to that seen for FESP model 1, illustrated in the similarity between the k_{STERIC} rate constant, seen in Table 6.13, compared to the FESP model 1 rate constant (2.47×10^{-15} cm^3 s^{-1}). This is probably because steric interactions increase barrier heights, and as FESP model 2 adjusts primarily TS structures already likely to be high in energy. This is confirmed by the fact that it is only a few key structures, TS_{OZO} 1.2 and TS_{OZO} 2.2, that are almost entirely responsible for this mild increase in this sterically adjusted rate constant: an important detail that may be crucial if FESP model 2 is applied to more bulky alkenes.

*Table 6.13: The rate constant (k_{STERIC}) [× 10^{-17} cm^3 s^{-1}] and product branching ratios of Criegee intermediates (Γ_{STERIC}) for O_3 + Alkene **19** using FESP model 2 by overall channel (TS_{OZO} 1 and TS_{OZO} 2) and subchannel (.1, .2, .3 …) and overall percentage k_{ME} per ozonolysis pathway; POZ breakdown branching fraction analysed per subchannel and total yield of respective. Note: TS_{OZO} 1.5 was not being calculated by MESMER so the k_{TST} was used instead.*

	k_{STERIC} (TS) [× 10^{-17} cm^3 s^{-1}]									
Channel	.1	.2	.3	.4	.5	.6	.7	.8	.9	%
TS_{OZO} 1	34.8	40.2	0.201	0.138	<0.001	0.002	126.0	*7.30*	44.4	94.5%
TS_{OZO} 2	1.33	1.41	0.006	0.005	<0.001	<0.001	7.73	0.437	3.27	5.5%
Overall					267.2					100%
Γ_{STERIC}	.1	.2	.3	.4	.5	.6	.7	.8	.9	Total
$\Gamma_{anti\text{-}nPrCHOO}$	0.063	0.066	0.007	0.022	<0.001	0.014	0.100	0.069	0.124	**0.466**
$\Gamma_{syn\text{-}nPrCHOO}$	0.005	0.005	<0.001	<0.001	<0.001	<0.001	0.008	0.002	0.012	**0.033**
$\Gamma_{anti\text{-}CH_3CHOO}$	0.034	0.036	0.004	0.060	0.013	0.019	0.097	0.067	0.121	**0.452**
$\Gamma_{syn\text{-}CH_3CHOO}$	0.010	0.005	0.003	0.003	<0.001	<0.001	0.011	0.008	0.008	**0.049**

The overall product branching fractions for O_3 + Alkene **19**, displayed in Table 6.13, show that *anti*-CIs dominate (~0.939), which is generally consistent with the FESP model 1 results. The results here do show a slight increase in dominance of *anti*-nPrCHOO yield, mainly due to drops in the TS_{ANTI} 1.2 & TS_{ANTI} 1.9 barriers, but there is very little overall change for the *anti*-CH_3CHOO yield. FESP model 2 does produce minor reductions in the branching fractions for *syn*-nPrCHOO & *syn*-CH_3CHOO. Overall, the CI ratio of nPrCHOO:CH_3CHOO is still close to level (0.499:0.501), with a small increase in nPrCHOO yield compared to FESP model 1.

These small but significant changes between FESP models 1 & 2 results demonstrates that steric interactions provide an ample contribution from the ozonolysis chemistry of Alkene **19**. Also, the fact that small changes in a couple of TS barrier heights altered the overall rate constant by an adequate amount shows that these steric adjustments may be critical especially when considering the ozonolysis of alkenes with more bulky alkyl groups.

6.7 The Empirical Corrected FESP Model 3

To determine the accuracy of these modelling techniques for the ozonolysis of lengthy alkenes, the computational relative Gibbs free energies of two trial TS structures from the O_3 + Alkene **19** reaction, are compared to those obtained from FESP models 1 & 2. This comparison also allows the author to determine the effectiveness of using steric factors to account for geometric distortions and whether any corrective factors need to be applied.

6.7.1 The Derivation of an Empirical Correction (Δ_{EMP}) Factor

The two TS structures that were selected to computationally examine from the O_3 + Alkene **19** potential energy surface were TS_{ANTI} 1.8 & TS_{SYN} 1.8 because they likely contain

steric factors that need application to this new system comparative to the template, Alkene **16**. While FESP model 1 was partially validated using previous computational analysis from Chapter 3, the application of these derived steric factors have yet to be empirically verified. Also, the TS_{ANTI} 1.8 & TS_{SYN} 1.8 structures have low enough energies to produce substantial product yields, whereas many of the other TS structures that have steric factors applied, such as TS_{SYN} 1.5 & 1.6, either have such high energy they become of negligible importance or they have complex structures that would be more difficult to optimise.

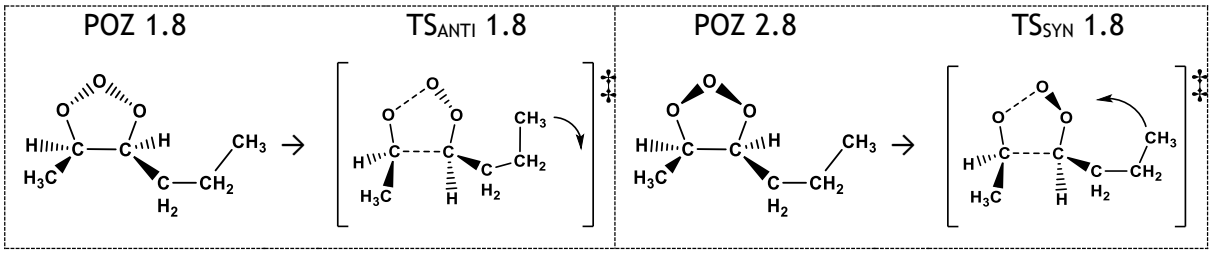

Figure 6.28: Representation of the anticipated movements involved in changed structures from POZ to TS on the PES of O_3 + Z-2-hexene

One key factor is selecting these stationary points to optimise is because whereas the TS_{ANTI} 1.8 distortions involves a divergence between the —nPr substituent from the terminal oxygen in the trioxolane, the TS_{SYN} 1.8 movements involve the opposite convergence with the same segments. This allows the author to analyse whether a full set of steric factors, **Δ_{DIV} (—Et,^{t}O)** & **Δ_{CON} (—Et,^{t}O)**, are reliable. The validation of the **Δ_{CON} (—Et,^{t}O)** factor is of particular importance as well, thus far it has only been inferred from calculations of similar effects (see Section 6.6.1), but could be verified further here. This verification of the steric factors applied was used across a wide range of different TS structures in FESP model 2 calculations of the ozonolysis of Alkene **19**.

Table 6.14: A comparison of the different models of cis-2-hexene using relative Gibbs free energies of: Transition States (TS); FESP Model 1 (ΔG_{PROJ}); FESP Model 2 (ΔG_{STERIC}); Computational calculation (ΔG_{THEO}); deviation of model 1 ($\delta\Delta G_{PROJ} = \Delta G_{THEO} - \Delta G_{PROJ}$) and model 2 ($\delta\Delta G_{STERIC} = \Delta G_{THEO} - \Delta G_{STERIC}$) from the theoretical value; empirical constant derived from average FESP model 2 deviation (Δ_{EMP}).

	(kJ mol^{-1})					
TS	**ΔG_{PROJ}**	**ΔG_{STERIC}**	**ΔG_{THEO}**	**$\delta\Delta G_{PROJ}$**	**$\delta\Delta G_{STERIC}$**	**Δ_{EMP}**
TS_{ANTI} 1.8	-121.6	-124.0	-126.4	-4.75	-2.38	-2.59
TS_{SYN} 1.8	-108.6	-106.2	-109.0	-0.42	-2.79	
Difference	13.0	17.8	17.4			

As displayed in Table 6.14, the computational relative Gibbs free energies for TS_{ANTI} 1.8 & TS_{SYN} 1.8 deviate by <5 kJ mol^{-1} from those calculated by FESP models 1 & 2 meaning both models show a sufficient level of accuracy. However, FESP model 2 is more reliable because its relative Gibbs free energies deviate from the computational energies by a common factor, whereas FESP model 1 has deviations that are much more dispersed. This

is crucial because it is often the distance between energy barriers, not their absolute values, that are important when determining the product branching fractions.

This validation of using steric factors to treat the Gibbs free energy deviations of these sterically inhibited TS structures complements the validation of the use of the ΔG_{PROJ} values for TS structures without new steric interactions seen in Section 6.4 and clearly demonstrates the applicability of the FESP model over a wide range of TS structures. However, while the FESP model 2 values are good approximations, the common Gibbs Free energy offset of both TS_{ANTI} 1.8 & TS_{SYN} 1.8 implies that a general deviation in these geometries may be occurring across all sterically adjusted TS structures. To solve this, "FESP model 3" uses an empirical correction (Δ_{EMP} = -2.59), derived from the average deviation between ΔG_{STERIC} values in Table 6.14, to calculate an empirically corrected "ΔG_{EMP} [TS]" value in Equation 6.10:

$$\Delta G_{EMP}\,[TS] = \Delta G_{PROJ} + \Delta_{STERIC} + \Delta_{EMP} \qquad \textit{Equation 6.10}$$

This Δ_{EMP} correction is applied only to structures that have a Δ_{STERIC} factor incorporated into them in FESP model 2 and the ΔG_{PROJ} value is used for all other TS mechanisms. All ΔG_{EMP} values for such TS structures using FESP model 3 are displayed in Table 6.15.

*Table 6.15: The empirically-corrected relative Gibbs Free energy (ΔG_{EMP}) values of the sterically corrected TS structures for O_3 + Alkene **19** calculated from the empirical correction (Δ_{EMP} ~ -2.6 kJ mol^{-1}) factor and the sterically corrected relative Gibbs Free energy (ΔG_{STERIC}) values [$\Delta G_{EMP} = \Delta G_{STERIC} + \Delta_{EMP}$]. ΔG_{EMP} values are only calculated from those TS structures that have been sterically corrected. The ΔG_{STERIC} values of these TSs are found in Table 6.12, in section 6.6.3. Gibbs Free energy values in kJ mol^{-1}.*

TS_{OZO} structures	ΔG_{EMP} value (kJ mol^{-1})	TS_{ANTI} structures	ΔG_{EMP} value (kJ mol^{-1})	TS_{SYN} structures	ΔG_{EMP} value (kJ mol^{-1})
TS_{OZO} 1.2	47.7	TS_{ANTI} 1.2	-127.4	TS_{SYN} 1.2	-113.6
TS_{OZO} 1.3	60.8	TS_{ANTI} 1.3	-114.2	TS_{SYN} 1.3	-100.3
TS_{OZO} 1.5	81.1	TS_{ANTI} 1.5	-101.1	TS_{SYN} 1.5	-84.3
TS_{OZO} 1.6	68.4	TS_{ANTI} 1.6	-117.5	TS_{SYN} 1.6	-88.4
TS_{OZO} 1.8	51.9	TS_{ANTI} 1.8	-126.6	TS_{SYN} 1.8	-108.8
TS_{OZO} 2.2	56.0	TS_{ANTI} 1.9	-130.3	TS_{SYN} 1.9	-117.8
TS_{OZO} 2.3	69.4	TS_{ANTI} 2.2	-123.2	TS_{SYN} 2.5	-92.9
TS_{OZO} 2.5	84.5	TS_{ANTI} 2.3	-110.0	TS_{SYN} 2.6	-101.7
TS_{OZO} 2.6	77.8	TS_{ANTI} 2.5	-117.2	TS_{SYN} 2.8	-115.0
TS_{OZO} 2.8	58.9	TS_{ANTI} 2.6	-119.6		
		TS_{ANTI} 2.8	-127.0		
		TS_{ANTI} 2.9	-130.7		

6.7.2 Analysing the Ozonolysis of Alkene 19 using the FESP Model 3

The ozonolysis chemistry of Alkene **19** derived using of FESP model 3, in terms of both the rate constant (k_{EMP}) and the branching fraction (Γ_{EMP}), is in agreement with many of the equivalent results from both FESP model 1 and FESP model 2. The k_{EMP} rate constant,

shown in Table 6.16, is somewhat larger than the rate constants from FESP model 1 (2.5 × 10^{-15} cm^3 s^{-1}) and FESP model 2 (2.7 × 10^{-15} cm^3 s^{-1}). However, as applying the empirical correction factor leads to a reduction in the critical TS_{OZO} 1.2 & TS_{OZO} 1.8 barriers, a rate constant determined using FESP model 3 is anticipated to be larger.

Table 6.16: MESMER application to ozonolysis of Z-2-hexene (alkene 19) using model 3: Empirically corrected rate constants, k_{EMP} (TS) [cm^3 molec.$^{-1}$ s^{-1}], by overall channel (TS_{OZO} 1 and TS_{OZO} 2), subchannel (TS .1, TS .2, etc.) and overall percentage k_{EMP} per ozonolysis pathway; POZ breakdown branching fraction analysed per subchannel and total yield of respective CI (Γ_{EMP}).
Note: TS_{OZO} 1.5 & 1.8 was not being calculated by MESMER so the k_{TST} was used instead.

	k_{EMP} (TS) [× 10^{-17} cm^3 s^{-1}]									
Channel	.1	.2	.3	.4	.5	.6	.7	.8	.9	%
TS_{OZO} 1	34.8	114.0	0.566	0.138	<0.001	0.021	126.0	20.8	44.4	95.1%
TS_{OZO} 2	1.33	4.03	0.018	0.005	<0.001	<0.001	7.73	1.25	3.27	4.9%
Overall					358.4					100%
Γ_{EMP}	.1	.2	.3	.4	.5	.6	.7	.8	.9	Total
$\Gamma_{anti\text{-}nPrCHOO}$	0.048	0.080	0.007	0.015	<0.001	0.015	0.077	0.082	0.155	**0.480**
$\Gamma_{syn\text{-}nPrCHOO}$	0.003	0.005	<0.001	<0.001	<0.001	<0.001	0.005	0.002	0.012	**0.028**
$\Gamma_{anti\text{-}CH_3CHOO}$	0.024	0.041	0.004	0.046	0.013	0.020	0.076	0.081	0.153	**0.456**
$\Gamma_{syn\text{-}CH_3CHOO}$	0.007	0.003	0.002	0.002	<0.001	<0.001	0.007	0.008	0.005	**0.034**

Much like with the differences in branching fractions between FESP models 1 and 2, the overall Γ_{EMP} distribution from FESP model 3, shown in Table 6.16, sees a marginal increase with *anti*-nPrCHOO yields, whereas the *anti*-CH_3CHOO yields remaining steady. The resultant Γ_{EMP} value, shown in Table 6.16, for *syn*-nPrCHOO & *syn*-CH_3CHOO remain small across all three FESP models. This CI ratio of nPrCHOO:CH_3CHOO for FESP model 3 are close to even (0.508:0.492), similar to that across equivalent FESP models 1 & 2 results.

FESP model 3 results of O_3 + Alkene **19** were also calculated using the computational relative Gibbs free energies and imaginary frequencies for the TS_{ANTI} 1.8 & TS_{SYN} 1.8 structures (used to determine the Eckart function) calculated previously. This change has negligible impact and so is included in Appendix Section 4.4.1.

6.7.3 Summary

All three FESP models show similar reactivity of O_3 + Alkene **19**, with the largest rate constant being exhibited for FESP model 3 and the branching ratio altering very little across all models. This consistency of results throughout all three FESP models and the significant accuracy in these models in predicting the ΔG_{THEO} values for TS_{ANTI} 1.8 and TS_{SYN} 1.8 (shown in Figure 6.29), implies that these models are reliable in producing the ozonolysis chemistry of these lengthy alkenes. As the models increase in complexity, the accuracy of the models likely increases, however FESP model 2 may have the broadest

applicability as it does not require an empirical correction derived from *ab initio* TS state calculations.

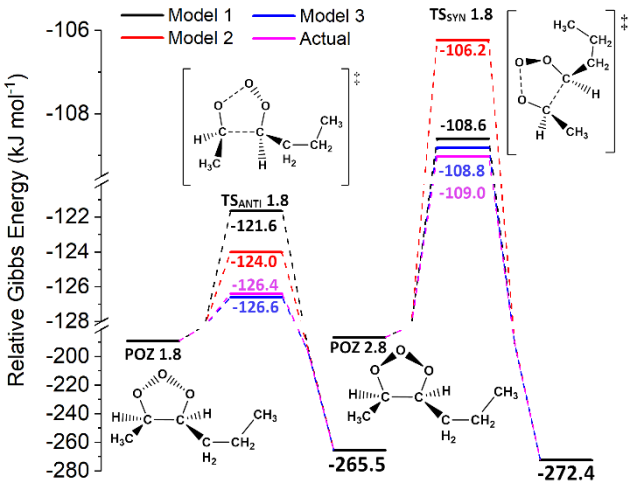

Figure 6.29: Comparison of Model's 1 (black), 2 (red) and 3 (blue) projections of TS_{ANTI} 1.8 & TS_{SYN} 1.8 compared with the computational analysis (magenta) to see the accuracy of each model. Energy is relative to the raw reactants.

6.8 Comparing the FESP Models 1—3 Calculations of the Ozonolysis Chemistry of Alkene 19.

In this section, the rate constants and product branching fractions calculated using FESP models 1—3 for the O_3 + Alkene **19** reaction are reviewed in the context of previously identified ozonolysis chemistry trends, to examine the accuracy of these FESP models in greater depth. This includes comparisons with both the theoretical trends obtained for alkene ozonolysis chemistry in Chapter 3, and the experimental trends identified in the literature. The verification that the ozonolysis chemistry produced by the FESP models is an accurate representation is crucial, because then a FESP model could then be applied to examine other alkenes with lengthy substituents, such as those in Figure 6.30. Furthermore, if the results of the O_3 + Alkene **19** reaction are accurate they could be built into tropospheric simulations of urban environments, such as Los Angeles.

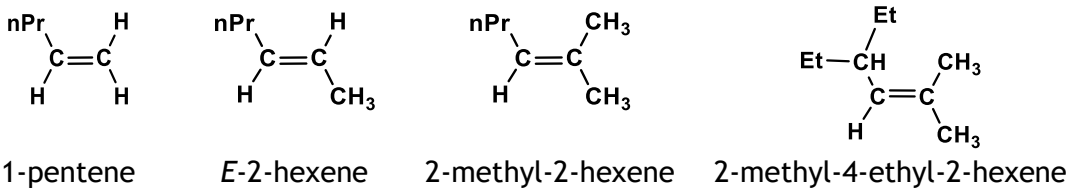

Figure 6.30: Schematic of the chemical structures of Alkenes with lengthy substituent groups.

One of the main reactivity trends identified in Chapter 3 was a continued inductive effect of lengthening of the —R_1 substituent, from a —CH_3 group in Alkenes **1**, **6**, **17** & **18**, to an —Et group, in Alkenes **2**, **7**, **15** & **16**. This is important for the work in this chapter because the further lengthening of the —R_1 substituent from a —Et group in Alkene **16** to an —nPr group in Alkenes **19** could very well produce a similar inductive effect.

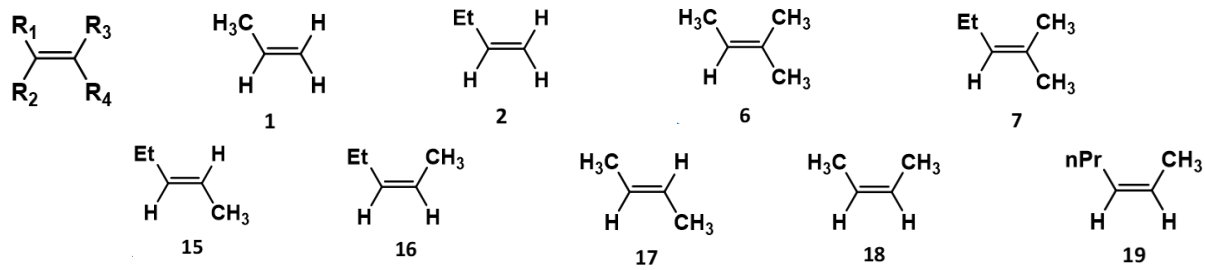

*Figure 6.31: Schematic of General Alkene and Alkenes **1**, **2**, **6**, **7** & **15—19**.*

If there is no inductive change between Alkenes **16** & **19,** then O_3 + Alkene **19** is likely only to show an equal or lower rate constant, as the increase in steric bulk of the —nPr substituent will impede access to the >C=C< reaction site. The structure-activity relationship model derived by McGillen and co-workers shows a decline in the ozonolysis k_{SAR} constant between Alkene **16** (~1.81 × 10^{-16} cm^3 s^{-1}) and Alkene **19** (~1.40 × 10^{-16} cm^3 s^{-}

[1]) precisely because the SAR model applies only the steric considerations, when differentiating between Alkenes **16** & **19**. However, while the overall range of rate constants calculated by FESP models is broad (see Table 6.17), FESP model 3, the most fine-tuned of the FESP models, shows an increase in the overall k_{EMP} constant (~3.58 × 10^{-15} cm^3 s^{-1}) compared to the k_{THEO} value for Alkene **16** (~2.84 × 10^{-15} cm^3 s^{-1}).

Table 6.17: Comparison of ozonolysis chemistry of a variety alkenes: literature experimental rate constants (k_{EXP}); theoretical rate constants (k_{THEO}); experimental product branching ratios (Γ_{EXP}); theoretical product branching ratios (Γ_{THEO}) Note: this Table also contains the rate constants from the structure-activity relationship model by McGillen et al. and the rate constants (k_{PROJ}, k_{STERIC} & k_{EMP}) and the product branching fractions (Γ_{PROJ}, Γ_{STERIC} & Γ_{EMP}) from FESP models 1—3.[118]

Alkenes	Rate constant (× 10^{-18} cm^3 s^{-1})		R_1CR_2OO:R_3CR_4OO		ref
	k_{EXP}	k_{THEO}	Γ_{EXP}	Γ_{THEO}	
Alkene **1**	9.9-10.1	32.4	0.65:0.35	0.73:0.27	166,349,352
Alkene **2**	9.65-10.9	103	0.62:0.38	0.63:0.37	352,353
1-pentene	10.0-10.6	-	0.51:0.49	-	156
1-hexene	9.0-11.5	-	0.50:0.50	-	156
1-heptene	9.2-12	-	0.50:0.50	-	156
1-octene	10.1-14	-	0.50:0.50	-	156
1-decene	9.3-11.1	-	0.52:0.48	-	156
Alkene **17**	127.8—190	361	1.00 (0.50:0.50)		10,360
Alkene **15**	*159.2-315*	1127	-	0.39:0.61	10,360
E-2-hexene	153-157	-	-	-	10,360
Alkene **18**	121.5—125	1175	1.00 (0.50:0.50)		10
Alkene **16**	k_{EXP} ~ 127-128.27	2835	-	0.43:0.57	10
	k_{SAR} ~ 181		-	-	118
Alkene **19**	k_{EXP} ~ 105-144	k_{PROJ} ~ 2479	Γ_{PROJ}	0.486:0.514	10
		k_{STERIC} ~ 2672	Γ_{STERIC}	0.499:0.501	
	k_{SAR} ~ 140	k_{EMP} ~ 3584	Γ_{EMP}	0.508:0.492	118
Alkene **6**	386-797	4336	0.32:0.68	0.30:0.70	10,162,365
Alkene **7**	406-454	5114	-	0.34:0.76	10,360

This theoretical rate constant for O_3 + Alkene **19** compared to that of O_3 + Alkene **16** gives evidence to the hypothesis that the three ß-H atoms may have a small hyperconjugative impact on the >C=C< bond. One of the observations in Chapter 3 was that the decline in substituent α-H atoms between —CH_3 substituent in Alkenes **1**, **6**, **17** & **18**, to an —Et group, in Alkenes **2**, **7**, **15** & **16**, could have contributed to the larger rate constants in the —Et substituted alkenes. The similar decrease in the number of substituent ß-H atoms between the —Et group in Alkene **16** compared to the —nPr group in Alkene **19** may in a similar way be responsible for the larger k_{EMP} constant for O_3 + Alkene **19**.

When comparing the literature results for the ozonolysis of Alkenes **16** & **19**, the upper limits for the ozonolysis rate constant for k_{EXP} value for O_3 + Alkene **19** is in agreement with this higher reactivity for Alkene **19**.[10,360] On top of this, the ozonolysis of 1-pentene and *E*-2-hexene, which also have —nPr substituents, also seem to demonstrate marginally larger k_{EXP} values.[10,156,360] However, the range and degree of uncertainty for these rate constants makes comparing the trends in k_{EXP} values and the trends in theoretically

obtained rate constants challenging. Nevertheless, as the literature k_{EXP} values for the ozonolysis of Alkenes **16** & **19** are quite similar (see Table 6.17), the fact that the k_{EMP} value for O_3 + Alkene **19** and the k_{THEO} value for O_3 + Alkene **16** are also in close proximity shows that FESP model 3 is relatively accurate.

If the computational trends in Chapter 3 hold for FESP model 3, the *Z*-orientated Alkene **19** would have a higher ozonolysis rate constant than monosubstituted, 1-pentene, the *E*-orientated 2-hexene isomer but a lower ozonolysis rate constant than the trisubstituted 2-methyl-2-hexene. However, a comparison with these other —nPr substituted equivalent alkenes is not yet possible, as FESP model 3 has yet to be applied to O_3 reactions with these other alkenes. Despite this, the fact that the k_{EMP} value for O_3 + *Z*-orientated Alkene **19** is higher than the k_{THEO} values for the monosubstituted Alkene **2** and the *E*-orientated Alkene **15**, but lower than the k_{THEO} value of the trisubstituted Alkene **7**, underscores the dependability of FESP model 3 (Table 6.17).

To the author's knowledge, no analysis of the Γ_{EXP} values for O_3 + Alkene **19** exists in the literature however certain trends can be extracted from the ozonolysis of other lengthy alkenes, although these literature studies do not distinguish between *syn*- & *anti*-CIs. One such literature trend for O_3 + mono-substituted alkenes, seen in Table 6.17, is that as the —R_1 substituent length increases, the yield for R_1CHOO moves in a stepwise manner from highly favoured for CH_3CHOO towards more evenly distributed for EtCHOO and finally to an nPrCHOO group. This trend is reflected in this thesis when comparing the R_1CHOO:CH_3CHOO ratios for O_3 + Alkenes **16** & **19**, where the EtCHOO:CH_3CHOO for O_3 + Alkene **16** (0.43:0.57) favoured the CH_3CHOO yield but shifts towards an even distribution for the EtCHOO:CH_3CHOO for O_3 + Alkenes **19** (0.51:0.49). As no experimental OH yield or Γ_{EXP} values for CIs for O_3 + Alkenes **19** are known to the author, this is the strongest way of validating the Γ_{EMP} values from FESP model 3 available to the author.

As noted in previous sections, the overall POZ fragmentation branching fractions do not vary significantly between FESP models and so for comparative purposes the Γ_{EMP} values generated by the finely tuned FESP model 3 for O_3 + Alkenes **19** are used. The dominance of *anti*-sCIs, shown with the high Γ_{EMP} values for *anti*-nPrCHOO (0.480) and *anti*-CH_3CHOO (0.457), is a continuation of the high computational yields of *anti*-CH_3CHOO (0.872) for the *Z*-orientated Alkene **18** and of *anti*-CH_3CHOO (0.510) & *anti*-EtCHOO (0.395) for the *Z*-orientated Alkene **16**. The fact that the FESP model results obtained for O_3 + Alkenes **19** continues the trends first observed in Chapter 3, further underscores the reliable results of these FESP models.

One additional observation from comparing the ozonolysis chemistries of Alkenes **16** & **19** is that the decline of substituent ß-H atoms appears to have little or no effect on the Γ_{EMP} values for *syn*-CIs. The only known effect of this change in substituent is an increased preference for *anti*-nPrCHOO, but the link to substituent ß-H atoms has yet to be established. Overall, the impact of this decrease in substituent ß-H atoms, has little effect except a mild increase in the rate constant and a slightly larger preference for *anti*-nPrCHOO over *anti*-EtCHOO. However, the effect of the decline in the number of substituent ß-H atoms on this CI yield is not known exactly as the ozonolysis of only one alkene with an —nPr substituent has been analysed using FESP model 3.

6.9 Atmospheric implications

One important observation in the literature is that lengthening the $-R_1$ substituent beyond an —nPr group to an n-butyl or an n-pentyl group has negligible effect on the ozonolysis chemistry of an alkene (see Table 6.17 in Section 6.8 or references for exact examples).[10,118,156] This is because the additional alkyl groups to the carbon chain are too distant from the >C=C< bond or the POZ structure to have steric or inductive implications on the reactivity of the alkene.[10,118,156] This increases the overall importance of these FESP models because then the ozonolysis chemistry of these longer alkenes can be effectively modelled, without any additional computational cost. So, this means that this FESP model can be used to categorise various important atmospheric alkenes together into taxonomic groups and reducing the computational cost of calculating the ozonolysis k_{THEO} and Γ_{THEO} values.

The ozonolysis of 2-methyl-2-hexene, identified as a very suitable candidate for further investigation earlier in this chapter, could be used in a manner from which to derive a new taxonomic group Figure 6.32. This taxonomic group would include alkenes with an aliphatic substituent group of 3 or more carbon chains and some acyclic monoterpenes. While it was not identified earlier as an atmospherically abundant alkene, an investigation of O_3 + 2-methyl-2-hexene as a template with FESP model 2 and/or 3 could provide useful input for an atmospheric model by removing the computational cost of calculating the ozonolysis chemistry of some acyclic monoterpenes. These acyclic monoterpenes could include ß-Myrcene, which can represent up to 10% of BVOC emissions from *P. ponderosa (A), 0.19* % of BVOC emissions *from P. ponderosa (B) and contributes significantly to indoor environments through emissions from cleaning and air conditioning products*.[481,482] Other acyclic monoterpenes include α-farnesene, which is emitted from manzanita, white fir, Ceanothus shrubs, and ponderosa pine, and ß-farnesene, which is emitted from sliver birch and cut and dry ponderosa pine.[243,483]

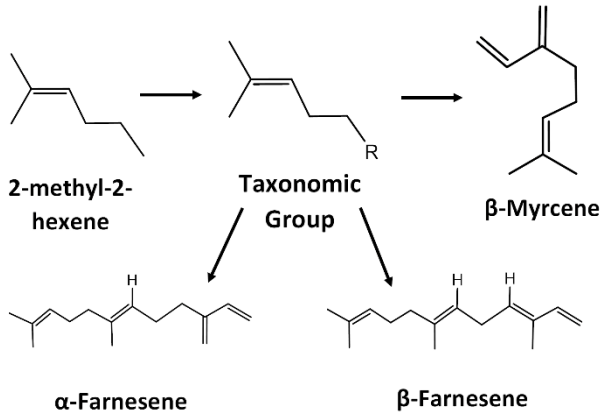

Figure 6.32: Applying 2-methyl-2-hexene using model to extended natural alkenes in taxonomic group [$(CH_3)_2C{=}CHCH_2CH_2R$]

The difficulties of applying this model to these acyclic monoterpenes is the multiple unsaturated bonds, which cause problems in two ways. Firstly, the additional double bonds may have an overall effect of the *R* group's impact on the C=C bond chemistry. The second effect is that having multiple C=C bonds produce several different competing reaction pathways. However, *Deng et al.*, have already done some analysis of this type of challenge and have observed that the $(CH_3)_2$**C=C**HCH_2CH_2R bond dominates ozonolysis reaction of ß-Myrcene.[484] The analysis of both the ozonolysis k_{EMP} and Γ_{EMP} of each of these alkenes will be quite significant in indoor conditions, local environmental models and global models.[482]

When considering the tropospheric implications of modelling O_3 + Alkene **19**, the medium size k_{THEO} value is similar to the literature k_{EXP} value, but this k_{EXP} value provides a more reliable input to an atmospheric model. The main contribution provided by this direct study of O_3 + Alkene **19**, not supplied by the literature, is the observation of the high Γ_{EMP} values for *anti*-nPrCHOO (0.480) & *anti*-CH_3CHOO (0.457) values. CIs that have high Γ_{EMP} yields can break down pollutants, either by direct bimolecular reaction or through producing OH radicals, in the areas where there are significant localised *Z*-2-hexene concentrations (identified in Section 6.1). The smaller $\Gamma_{syn\text{-nPrCHOO}}$ (0.028) & $\Gamma_{syn\text{-CH3CHOO}}$ (0.034) values, whilst less significant are still at non-negligible levels and so knowledge of their yield is important. Reactions that produce *anti*-nPrCHOO and *syn*-nPrCHOO may warrant further exploration for their tropospheric bimolecular reactivity.

6.10 Further Work for FESP Modelling

There are many alkene ozonolysis reactions that FESP modelling could be applied to, however, the ozonolysis of the —nPr substituted 1-pentene, *E*-2-hexene, 2-methyl-2-hexene, naturally spring from the work based in this Chapter. This is because FESP

modelling is purpose built for a system involving an —nPr substituents and was validated using the ozonolysis reactions of their —Et substituted equivalent alkenes, Alkene **2**, **15** & **7** respectively (see Figure 6.33 for a structural comparison).

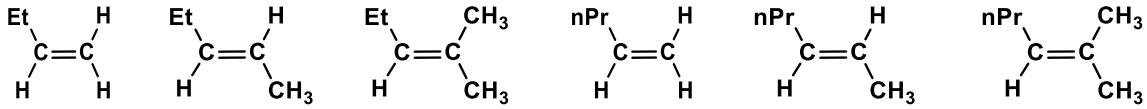

Alkene **2** | Alkene **15** | Alkene **7** | 1-pentene | *E*-2-hexene | 2-methyl-2-hexene

*Figure 6.33: Schematic Alkenes **2**, **7** & **15** and 1-pentene, E-2-hexene, 2-methyl-2-hexene*

Another group of ozonolysis reactions which emerge as natural extensions of this chapter are alkenes: Z-$(CH_3)_2$**CH**$CH_2CH{=}CHCH_3$ (1 × ß-H atoms) and Z-$(CH_3)_3CCH_2CH{=}CHCH_3$ (0 × ß-H atoms). This is because, when contrasted with Alkenes **16** & **19** (their —Et and —nPr substituted equivalents), a comparative investigation of the effect of substituent ß-H atoms has on ozonolysis chemistry can be completed, similar to that seen for substituent α-H atoms in Chapter 3. The third group of reactions would require significant fine-tuning of the FESP model as they would involve alkenes with bulkier alkyl groups or other functional groups, such as enal, enone, haloalkyl & alkene groups.

The last group to which the FESP model could be applied is the two-step reactions of sCIs with atmospheric species, such as HCHO and SO_2 seen in Sections 5.3 & 5.4. As shown from the work in this thesis, sCIs with lengthy conformerically flexible alkyl substituents, such as *anti*-& *syn*-nPrCHOO, are generated in significant yields from the ozonolysis of lengthy alkenes. When these HCHO and SO_2 reactions involve sCIs with lengthy conformerically flexible alkyl groups, much like with the ozonolysis of conformationally flexible alkenes, the number intermediate products and TS structures increase dramatically. This degree of complexity is precisely what this FESP model is designed to manage.

6.11 Conclusion

One of the most important outcomes of the development of these three different FESP models is that the common chemistry within the alkene taxonomic groups, derived in Chapter 3, is used to successfully project the chemistry of a new system, O_3 + Alkene **19.** The final projection model, FESP 3, provides accurate reaction rates and branching fractions, at minimal computational cost. This new method of predicting the ozonolysis chemistry of alkenes with lengthy substituents has been finely tuned to manage and incorporate a variety of fine steric interactions. While a small empirical corrective factor has to be applied, the calculations of individual TS structures provided evidence that the steric interactions and the resultant energetic changes are forecast effectively by FESP model 3.

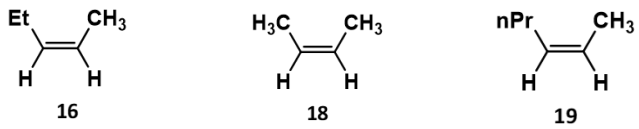

*Figure 6.34: Schematic of the chemical structures of Alkenes **16**, **18** & **19**.*

Using this new predictive model, it is suggested that tropospheric depletion of Alkene **19** via ozonolysis is expected to be more common than that of similar alkenes (1-pentene or *E*-2-hexene) due to the high ozonolysis k_{EMP} value for Alkene **19**.[478] Alkene **19** is estimated to fit well with the "*Z*-alkene" taxonomic group from Chapter 3 because it has: a *Z*-orientation, a similarly high reactivity, and the sizeable branching preference for *anti*-CIs over *syn*-CIs. The *anti*-nPrCHOO & *anti*-CH_3CHOO products are known to have higher bimolecular reactivity but lower unimolecular decay rates than their *syn* counterparts.[182] Therefore, in atmospheric simulations of urban areas where large O_3 and Alkene **19** abundances overlap, like Los Angeles, the bimolecular *anti*-sCI reactions are likely to be increasingly important in local atmospheric simulations.[478]

In summary, with the fine-tuned FESP model 3, the author has constructed a model whereby an alkene ozonolysis reaction with a large number of TS structures can be analysed simply and effectively. As the FESP models draw on both the theory that alkenes within the same taxonomic groups have similar ozonolysis chemistry (formulated in Chapter 3), the accuracy and reliability of the FESP results for O_3 + Alkene **19** validates that classification system. This model fills an important gap in the literature because alkenes with extremely lengthy alkyl groups, such as *Z*-2-octene, can now be analysed using FESP model 3, just like Alkene **19** has been interrogated here. As the ozonolysis chemistry of small and inflexible alkenes can be determined using explicit computational approaches and the ozonolysis of alkenes with flexible medium and large alkyl groups can be analysed using FESP models, a comprehensive system for determining the ozonolysis chemistry of most tropospheric alkenes has now been determined.

7.0 Bibliography

(1) Carfora, A.; Campobasso, C. P.; Cassandro, P.; La Sala, F.; Maiellaro, A.; Perna, A.; Petrella, R.; Borriello, R. Fatal Inhalation of Volcanic Gases in Three Tourists of a Geothermal Area. *Forensic Science International* **2019**, *297*, e1–e7. https://doi.org/10.1016/j.forsciint.2019.01.044.

(2) Fifth Assessment Report - Climate Change 2013 http://www.ipcc.ch/report/ar5/wg1/ (accessed 2018 -08 -26).

(3) West, J. B. Joseph Black, Carbon Dioxide, Latent Heat, and the Beginnings of the Discovery of the Respiratory Gases. *American Journal of Physiology-Lung Cellular and Molecular Physiology* **2014**, *306* (12), L1057–L1063. https://doi.org/10.1152/ajplung.00020.2014.

(4) Cavendish, H. Three Papers, Containing Experiments on Factitious Air, by the Hon. Henry Cavendish, F. R. S. *Philosophical Transactions of the Royal Society of London Series I* **1766**, *56*, 141–184.

(5) Priestley, J. An Account of Further Discoveries in Air. *Philosophical Transactions (1683-1775)* **1775**, *65*, 384–394.

(6) Antoine-Laurent de Lavoisier, *Opuscules physiques et chimiques*; Deterville, 1801.

(7) Sir William Ramsay. *The Gases of the Atmosphere: The History of Their Discovery*; Macmillan and Company limited, 1905.

(8) Schoenbein, C. F. On the Odour Accompanying Electricity, and on the Probability of Its Dependence on the Presence of a New Substance; **1840**, *17*, 293–294. https://doi.org/10.1098/rspl.1837.0114.

(9) Schönbein, C. F. On the Production of Ozone by Chemical Means. *Philosophical Magazine* **1844**, *24*, 466–467. https://doi.org/10.1098/rspl.1843.0014.

(10) Calvert, J. G.; Orlando, J. J.; Stockwell, W. R.; Wallington, T. J. *The Mechanisms of Reactions Influencing Atmospheric Ozone*; Oxford University Press, 2015.

(11) UV absorbance DNA quantitation | BMG LABTECH https://www.bmglabtech.com/uv-absorbance-dna-quantitation/ (accessed 2020 -11 -14).

(12) Molina, M. J.; Rowland, F. S. Stratospheric Sink for Chlorofluoromethanes: Chlorine Atom-Catalysed Destruction of Ozone. *Nature* **1974**, *249* (5460), 810–812. https://doi.org/10.1038/249810a0.

(13) Yagura, T.; Makita, K.; Yamamoto, H.; Menck, C. F. M.; Schuch, A. P. Biological Sensors for Solar Ultraviolet Radiation. *Sensors* **2011**, *11* (4), 4277–4294. https://doi.org/10.3390/s110404277.

(14) Langematz, U. Stratospheric Ozone: Down and up through the Anthropocene. *ChemTexts* **2019**, *5* (2), 8. https://doi.org/10.1007/s40828-019-0082-7.

(15) Holloway, A. M.; Wayne, R. P. *Atmospheric Chemistry*; Royal Society of Chemistry, 2010.

(16) Tiwary, A.; Williams, I. *Air Pollution: Measurement, Modelling and Mitigation, Fourth Edition*; CRC Press, 2018.

(17) Material Safety Data Sheet for Ozone https://ozonesolutions.com/blog/material-safety-data-sheet-for-ozone/ (accessed 2020 -11 -14).

(18) Air quality in Europe 2019 — European Environment Agency https://www.eea.europa.eu/publications/air-quality-in-europe-2019 (accessed 2020 -11 -14).

(19) US EPA, O. Benefits and Costs of the Clean Air Act 1990-2020. Report Documents and Graphics https://www.epa.gov/clean-air-act-overview/benefits-and-costs-clean-air-act-1990-2020-report-documents-and-graphics (accessed 2020 -07 -20).

(20) Hallquist, M.; Munthe, J.; Hu, M.; Wang, T.; Chan, C. K.; Gao, J.; Boman, J.; Guo, S.; Hallquist, Å. M.; Mellqvist, J.; Moldanova, J.; Pathak, R. K.; Pettersson, J. B.; Pleijel, H.; Simpson, D.; Thynell, M. Photochemical Smog in China: Scientific

Challenges and Implications for Air-Quality Policies. *Natl Sci Rev* **2016**, *3* (4), 401–403. https://doi.org/10.1093/nsr/nww080.
(21) Nguyen, T. B.; Tyndall, G. S.; Crounse, J. D.; Teng, A. P.; Bates, K. H.; Schwantes, R. H.; Coggon, M. M.; Zhang, L.; Feiner, P.; Milller, D. O.; Skog, K. M.; Rivera-Rios, J. C.; Dorris, M.; Olson, K. F.; Koss, A.; Wild, R. J.; Brown, S. S.; Goldstein, A. H.; Gouw, J. A. de; Brune, W. H.; Keutsch, F. N.; Seinfeld, J. H.; Wennberg, P. O. Atmospheric Fates of Criegee Intermediates in the Ozonolysis of Isoprene. *Phys. Chem. Chem. Phys.* **2016**, *18* (15), 10241–10254. https://doi.org/10.1039/C6CP00053C.
(22) H. Khan M. Anwar; Morris William C.; Galloway Matthew; A. Shallcross Beth M.; Percival Carl J.; Shallcross Dudley E. An Estimation of the Levels of Stabilized Criegee Intermediates in the UK Urban and Rural Atmosphere Using the Steady-State Approximation and the Potential Effects of These Intermediates on Tropospheric Oxidation Cycles. *International Journal of Chemical Kinetics* **2017**, *49* (8), 611–621. https://doi.org/10.1002/kin.21101.
(23) Monks, P. S. Gas-Phase Radical Chemistry in the Troposphere. *Chem. Soc. Rev.* **2005**, *34* (5), 376–395. https://doi.org/10.1039/B307982C.
(24) Wallington, T. J.; Sulbaek Andersen, M. P.; Nielsen, O. J. Atmospheric Chemistry of Short-Chain Haloolefins: Photochemical Ozone Creation Potentials (POCPs), Global Warming Potentials (GWPs), and Ozone Depletion Potentials (ODPs). *Chemosphere* **2015**, *129*, 135–141. https://doi.org/10.1016/j.chemosphere.2014.06.092.
(25) Nguyen, T. L.; Lee, H.; Matthews, D. A.; McCarthy, M. C.; Stanton, J. F. Stabilization of the Simplest Criegee Intermediate from the Reaction between Ozone and Ethylene: A High-Level Quantum Chemical and Kinetic Analysis of Ozonolysis. *J. Phys. Chem. A* **2015**, *119* (22), 5524–5533. https://doi.org/10.1021/acs.jpca.5b02088.
(26) Mohanakumar, K. *Stratosphere Troposphere Interactions: An Introduction*; Springer Science & Business Media, 2008.
(27) Buis, A. The Atmosphere: Getting a Handle on Carbon Dioxide *NASA's Jet Propulsion Team*. https://climate.nasa.gov/news/2915/the-atmosphere-getting-a-handle-on-carbon-dioxide (accessed 2020-07-24).
(28) Nowamooz, A.; Lemieux, J.-M.; Molson, J.; Therrien, R. Numerical Investigation of Methane and Formation Fluid Leakage along the Casing of a Decommissioned Shale Gas Well. *Water Resources Research* **2015**, *51* (6), 4592–4622. https://doi.org/10.1002/2014WR016146.
(29) Walter, K. M.; Smith, L. C.; Stuart Chapin, F. Methane Bubbling from Northern Lakes: Present and Future Contributions to the Global Methane Budget. *Philosophical Transactions of the Royal Society A: Mathematical, Physical and Engineering Sciences* **2007**, *365* (1856), 1657–1676. https://doi.org/10.1098/rsta.2007.2036.
(30) Bosch, C. Process of Producing Ammonia. US990191A, April 18, 1911.
(31) Ertl, G. Zum Mechanismus Der Ammoniak-Synthese. *Nachrichten aus Chemie, Technik und Laboratorium* **1983**, *31* (3), 178–182. https://doi.org/10.1002/nadc.19830310307.
(32) Flavell-While, Claudia, Fritz Haber and Carl Bosch – Feed the World *The Chemical Engineer* https://www.thechemicalengineer.com/features/cewctw-fritz-haber-and-carl-bosch-feed-the-world/ (accessed 2020-07-19).
(33) Hoffman, B. M.; Lukoyanov, D.; Dean, D. R.; Seefeldt, L. C. Nitrogenase: A Draft Mechanism. *Acc Chem Res* **2013**, *46* (2), 587–595. https://doi.org/10.1021/ar300267m.
(34) Ji, B.; Yang, K.; Zhu, L.; Jiang, Y.; Wang, H.; Zhou, J.; Zhang, H. Aerobic Denitrification: A Review of Important Advances of the Last 30 Years. *Biotechnol Bioproc E* **2015**, *20* (4), 643–651. https://doi.org/10.1007/s12257-015-0009-0.

(35) Wang, F.; Cao, Y.; Zhou, J. Thermodynamic Analysis of High-Temperature Helium Heated Fuel Reforming for Hydrogen Production. *International Journal of Energy Research* **2015**, *39* (3), 418–432. https://doi.org/10.1002/er.3263.
(36) Ogden, J. M. Prospects for Building a Hydrogen Energy Infrastructure. *Annu. Rev. Energy. Environ.* **1999**, *24* (1), 227–279. https://doi.org/10.1146/annurev.energy.24.1.227.
(37) Stocker, T. F.; Qin, D.; Plattner, G.-K.; Tignor, M. M. B.; Allen, S. K.; Boschung, J.; Nauels, A.; Xia, Y.; Bex, V.; Midgley, P. M. Working Group I Contribution to the Fifth Assessment Report of the Intergovernmental Panel on Climate Change. 14.
(38) Watson, J. D.; Crick, F. H. C. Molecular Structure of Nucleic Acids: A Structure for Deoxyribose Nucleic Acid. *Nature* **1953**, *171* (4356), 737–738. https://doi.org/10.1038/171737a0.
(39) Gupta, R. S.; Mukhtar, T.; Singh, B. Evolutionary Relationships among Photosynthetic Prokaryotes (Heliobacterium Chlorum, Chloroflexus Aurantiacus, Cyanobacteria, Chlorobium Tepidum and Proteobacteria): Implications Regarding the Origin of Photosynthesis. *Molecular Microbiology* **1999**, *32* (5), 893–906. https://doi.org/10.1046/j.1365-2958.1999.01417.x.
(40) El-Sharkawy, M.; Hesketh, J. Photosynthesis among Species in Relation to Characteristics of Leaf Anatomy and CO_2 Diffusion Resistance. *Crop Science* **1965**, *5* (6), 517. https://doi.org/10.2135/cropsci1965.0011183X000500060010x.
(41) Schmidt-Rohr, K. Oxygen Is the High-Energy Molecule Powering Complex Multicellular Life: Fundamental Corrections to Traditional Bioenergetics. *ACS Omega* **2020**, *5* (5), 2221–2233. https://doi.org/10.1021/acsomega.9b03352.
(42) Callendar, G. S. The Artificial Production of Carbon Dioxide and Its Influence on Temperature. *Quarterly Journal of the Royal Meteorological Society* **1938**, *64* (275), 223–240. https://doi.org/10.1002/qj.49706427503.
(43) NASA, NOAA Analyses Reveal 2019 Second Warmest Year on Record https://climate.nasa.gov/news/2945/nasa-noaa-analyses-reveal-2019-second-warmest-year-on-record (accessed 2020 -07 -24).
(44) Effects of Low-Level Inhalation Exposure to Carbon Dioxide in Indoor Environments: A Short Review on Human Health and Psychomotor Performance. *Environment International* **2018**, *121*, 51–56. https://doi.org/10.1016/j.envint.2018.08.059.
(45) Thermodynamics of the Carbon Dioxide System in the Oceans. *Geochimica et Cosmochimica Acta* **1995**, *59* (4), 661–677. https://doi.org/10.1016/0016-7037(94)00354-O.
(46) Anthony, K. R. N.; Kline, D. I.; Diaz-Pulido, G.; Dove, S.; Hoegh-Guldberg, O. Ocean Acidification Causes Bleaching and Productivity Loss in Coral Reef Builders. *Proc Natl Acad Sci U.S.A* **2008**, *105* (45), 17442–17446. https://doi.org/10.1038/nature04095.
(47) Gattuso, J.-P.; Hansson, L. *Ocean Acidification*; OUP Oxford, 2011.
(48) Orr, J.C.; Fabry, V. J.; Yool, A. Anthropogenic ocean acidification over the twenty-first century and its impact on calcifying organisms *Nature* **2009**, *161* (3), 449–459. https://doi.org/10.1007/s00442-009-1400-3.
(49) Limm, E. B.; Simonin, K. A.; Bothman, A. G.; Dawson, T. E. Foliar Water Uptake: A Common Water Acquisition Strategy for Plants of the Redwood Forest. *Oecologia* **2009**, *161* (3), 449–459. https://doi.org/10.1007/s00442-009-1400-3.
(50) B, A. W. Absorption of Water by the Leaves of Plants. *Nature* **1878**, *19* (478), 183–183. https://doi.org/10.1038/019183a0.
(51) McGillen, M. R.; Curchod, B. F. E.; Chhantyal-Pun, R.; Beames, J. M.; Watson, N.; Khan, M. A. H.; McMahon, L.; Shallcross, D. E.; Orr-Ewing, A. J. Criegee Intermediate–Alcohol Reactions, A Potential Source of Functionalized Hydroperoxides in the Atmosphere. *ACS Earth Space Chem.* **2017**, *1* (10), 664–672. https://doi.org/10.1021/acsearthspacechem.7b00108.

(52) Ung, A. Y.-M.; Back, R. A. The Photolysis of Water Vapor and Reactions of Hydroxyl Radicals. *Can. J. Chem.* **1964**, *42* (4), 753–763. https://doi.org/10.1139/v64-114.
(53) Chu, L.; Anastaio, C. Formation of Hydroxyl Radical from the Photolysis of Frozen Hydrogen Peroxide *The Journal of Physical Chemistry A.* **2005**, *109* (28), 6264–6271 https://doi.org/10.1021/jp051415f
(54) Vione, D.; Falletti, G.; Maurino, V.; Minero, C.; Pelizzetti, E.; Malandrino, M.; Ajassa, R.; Olariu, R.-I.; Arsene, C. Sources and Sinks of Hydroxyl Radicals upon Irradiation of Natural Water Samples. *Environ. Sci. Technol.* **2006**, *40* (12), 3775–3781. https://doi.org/10.1021/es052206b.
(55) Sheps, L.; Rotavera, B.; J. Eskola, A.; L. Osborn, D.; A. Taatjes, C.; Au, K.; E. Shallcross, D.; H. Khan, M. A.; J. Percival, C. The Reaction of Criegee Intermediate CH_2OO with Water Dimer: Primary Products and Atmospheric Impact. *Physical Chemistry Chemical Physics* **2017**, *19* (33), 21970–21979. https://doi.org/10.1039/C7CP03265J.
(56) Andrady, A. L. Microplastics in the Marine Environment. *Marine Pollution Bulletin* **2011**, *62* (8), 1596–1605. https://doi.org/10.1016/j.marpolbul.2011.05.030.
(57) Smith, M.; Love, D. C.; Rochman, C. M.; Neff, R. A. Microplastics in Seafood and the Implications for Human Health. *Curr Envir Health Rpt* **2018**, *5* (3), 375–386. https://doi.org/10.1007/s40572-018-0206-z.
(58) Van Cauwenberghe, L.; Janssen, C. R. Microplastics in Bivalves Cultured for Human Consumption. *Environmental Pollution* **2014**, *193*, 65–70. https://doi.org/10.1016/j.envpol.2014.06.010.
(59) Qin, L.-Q.; Wang, X.-P.; Li, W.; Tong, X.; Tong, W.-J. The Minerals and Heavy Metals in Cow's Milk from China and Japan. *Journal of Health Science* **2009**, *55* (2), 300–305. https://doi.org/10.1248/jhs.55.300.
(60) Leone, I. A. The Effects of Atmospheric Pollution on Vegetation. *Environmental Pollution and Toxicology* **1980**.
(61) Schuur, E. A. G.; Bockheim, J.; Canadell, J. G.; Euskirchen, E.; Field, C. B.; Goryachkin, S. V.; Hagemann, S.; Kuhry, P.; Lafleur, P. M.; Lee, H.; Mazhitova, G.; Nelson, F. E.; Rinke, A.; Romanovsky, V. E.; Shiklomanov, N.; Tarnocai, C.; Venevsky, S.; Vogel, J. G.; Zimov, S. A. Vulnerability of Permafrost Carbon to Climate Change: Implications for the Global Carbon Cycle. *BioScience* **2008**, *58* (8), 701–714. https://doi.org/10.1641/B580807.
(62) Lu, X.; Yao, T.; Li, Y.; Fung, J. C. H.; Lau, A. K. H. Source Apportionment and Health Effect of NOx over the Pearl River Delta Region in Southern China. *Environmental Pollution* **2016**, *212*, 135–146. https://doi.org/10.1016/j.envpol.2016.01.056.
(63) Cao, J.; Yang, C.; Li, J.; Chen, R.; Chen, B.; Gu, D.; Kan, H. Association between Long-Term Exposure to Outdoor Air Pollution and Mortality in China: A Cohort Study. *Journal of Hazardous Materials* **2011**, *186* (2), 1594–1600. https://doi.org/10.1016/j.jhazmat.2010.12.036.
(64) Chaloulakou, A.; Mavroidis, I.; Gavriil, I. Compliance with the Annual NO_2 Air Quality Standard in Athens. Required NO_x Levels and Expected Health Implications. *Atmospheric Environment* **2008**, *42* (3), 454–465. https://doi.org/10.1016/j.atmosenv.2007.09.067.
(65) Nafstad Per; Håheim Lise Lund; Wisløff Torbjørn; Gram Frederick; Oftedal Bente; Holme Ingar; Hjermann Ingvar; Leren Paul. Urban Air Pollution and Mortality in a Cohort of Norwegian Men. *Environmental Health Perspectives* **2004**, *112* (5), 610–615. https://doi.org/10.1289/ehp.6684.
(66) Aj, C.; Mt, K.; Aj, F.; St, H. Exposure to Nitrogen Dioxide (NO_2) and Respiratory Disease Risk. *Rev Environ Health* **1998**, *13* (1–2), 73–90.
(67) NO_x control technologies for Euro 6 diesel passenger cars | International Council on Clean Transportation https://theicct.org/publications/nox-control-technologies-euro-6-diesel-passenger-cars (accessed 2020 -07 -20).

(68) Schiermeier, Q. The Science behind the Volkswagen Emissions Scandal. *Nature News*. https://doi.org/10.1038/nature.2015.18426.
(69) Volkswagen Says 11 Million Cars Worldwide Are Affected in Diesel Deception - The New York Times https://www.nytimes.com/2015/09/23/business/international/volkswagen-diesel-car-scandal.html (accessed 2020 -07 -20).
(70) Chossière, G. P.; Malina, R.; Ashok, A.; Dedoussi, I. C.; Eastham, S. D.; Speth, R. L.; Barrett, S. R. H. Public Health Impacts of Excess NO_x Emissions from Volkswagen Diesel Passenger Vehicles in Germany. *Environ. Res. Lett.* **2017**, *12* (3), 034014. https://doi.org/10.1088/1748-9326/aa5987.
(71) Barrett, S. R. H.; Speth, R. L.; Eastham, S. D.; Dedoussi, I. C.; Ashok, A.; Malina, R.; Keith, D. W. Impact of the Volkswagen Emissions Control Defeat Device on US Public Health. *Environ. Res. Lett.* **2015**, *10* (11), 114005. https://doi.org/10.1088/1748-9326/10/11/114005.
(72) Grennfelt, P.; Engleryd, A.; Forsius, M.; Hov, Ø.; Rodhe, H.; Cowling, E. Acid Rain and Air Pollution: 50 Years of Progress in Environmental Science and Policy. *Ambio* **2020**, *49* (4), 849–864. https://doi.org/10.1007/s13280-019-01244-4.
(73) Huang, D.; Xu, J.; Zhang, S. Valuing the Health Risks of Particulate Air Pollution in the Pearl River Delta, China. *Environmental Science & Policy* **2012**, *15* (1), 38–47. https://doi.org/10.1016/j.envsci.2011.09.007.
(74) Wang, J.; Wang, S.; Voorhees, A. S.; Zhao, B.; Jang, C.; Jiang, J.; Fu, J. S.; Ding, D.; Zhu, Y.; Hao, J. Assessment of Short-Term PM2.5-Related Mortality Due to Different Emission Sources in the Yangtze River Delta, China. *Atmospheric Environment* **2015**, *123*, 440–448. https://doi.org/10.1016/j.atmosenv.2015.05.060.
(75) Baek, J.; Hu, Y.; Odman, M. T.; Russell, A. G. Modeling Secondary Organic Aerosol in CMAQ Using Multigenerational Oxidation of Semi-Volatile Organic Compounds. *Journal of Geophysical Research: Atmospheres* **2011**, *116* (D22). https://doi.org/10.1029/2011JD015911.
(76) CDC Tobacco Free. Tobacco-Related Mortality https://www.cdc.gov/tobacco/data_statistics/fact_sheets/health_effects/tobacco_related_mortality/index.htm (accessed 2020 -07 -20).
(77) Braun, M.; Koger, F.; Klingelhöfer, D.; Müller, R.; Groneberg, D. A. Particulate Matter Emissions of Four Different Cigarette Types of One Popular Brand: Influence of Tobacco Strength and Additives. *Int J Environ Res Public Health* **2019**, *16* (2). https://doi.org/10.3390/ijerph16020263.
(78) Kant, N.; Müller, R.; Braun, M.; Gerber, A.; Groneberg, D. Particulate Matter in Second-Hand Smoke Emitted from Different Cigarette Sizes and Types of the Brand Vogue Mainly Smoked by Women. *Int J Environ Res Public Health* **2016**, *13* (8). https://doi.org/10.3390/ijerph13080799.
(79) Ambient (outdoor) air pollution https://www.who.int/news-room/fact-sheets/detail/ambient-(outdoor)-air-quality-and-health (accessed 2020 -01 -12).
(80) Saunois, M.; Bousquet, P.; Poulter, B.; Peregon, A.; Ciais, P.; Canadell, J. G.; Dlugokencky, E. J.; Etiope, G.; Bastviken, D.; Houweling, S.; Janssens-Maenhout, G.; Tubiello, F. N.; Castaldi, S.; Jackson, R. B.; Alexe, M.; Arora, V. K.; Beerling, D. J.; Bergamaschi, P.; Blake, D. R.; Brailsford, G.; Brovkin, V.; Bruhwiler, L.; Crevoisier, C.; Crill, P.; Covey, K.; Curry, C.; Frankenberg, C.; Gedney, N.; Höglund-Isaksson, L.; Ishizawa, M.; Ito, A.; Joos, F.; Kim, H.-S.; Kleinen, T.; Krummel, P.; Lamarque, J.-F.; Langenfelds, R.; Locatelli, R.; Machida, T.; Maksyutov, S.; McDonald, K. C.; Marshall, J.; Melton, J. R.; Morino, I.; Naik, V.; O'Doherty, S.; Parmentier, F.-J. W.; Patra, P. K.; Peng, C.; Peng, S.; Peters, G. P.; Pison, I.; Prigent, C.; Prinn, R.; Ramonet, M.; Riley, W. J.; Saito, M.; Santini, M.; Schroeder, R.; Simpson, I. J.; Spahni, R.; Steele, P.; Takizawa, A.; Thornton, B. F.; Tian, H.; Tohjima, Y.; Viovy, N.; Voulgarakis, A.; van Weele, M.; van der Werf, G.

R.; Weiss, R.; Wiedinmyer, C.; Wilton, D. J.; Wiltshire, A.; Worthy, D.; Wunch, D.; Xu, X.; Yoshida, Y.; Zhang, B.; Zhang, Z.; Zhu, Q. The Global Methane Budget 2000–2012. *Earth Syst. Sci. Data* **2016**, *8* (2), 697–751. https://doi.org/10.5194/essd-8-697-2016.

(81) Sindelarova, K.; Granier, C.; Bouarar, I.; Guenther, A.; Tilmes, S.; Stavrakou, T.; Müller, J.-F.; Kuhn, U.; Stefani, P.; Knorr, W. Global Data Set of Biogenic VOC Emissions Calculated by the MEGAN Model over the Last 30 Years. *Atmospheric Chemistry and Physics* **2014**, *14* (17), 9317–9341. https://doi.org/10.5194/acp-14-9317-2014.

(82) Mather, T. A. Volcanoes and the Environment: Lessons for Understanding Earth's Past and Future from Studies of Present-Day Volcanic Emissions. *Journal of Volcanology and Geothermal Research* **2015**, *304*, 160–179. https://doi.org/10.1016/j.jvolgeores.2015.08.016.

(83) Carn, S. A.; Fioletov, V. E.; McLinden, C. A.; Li, C.; Krotkov, N. A. A Decade of Global Volcanic SO_2 Emissions Measured from Space. *Scientific Reports* **2017**, *7* (1), 44095. https://doi.org/10.1038/srep44095.

(84) Eisinger, M.; Burrows, J. P. Tropospheric Sulfur Dioxide Observed by the ERS-2 GOME Instrument. *Geophysical Research Letters* **1998**, *25* (22), 4177–4180. https://doi.org/10.1029/1998GL900128.

(85) Carn, S. A.; Krotkov, N. A.; Yang, K.; Krueger, A. J. Measuring Global Volcanic Degassing with the Ozone Monitoring Instrument (OMI). *Geological Society, London, Special Publications* **2013**, *380* (1), 229–257. https://doi.org/10.1144/SP380.12.

(86) Theys, N.; Roozendael, M. V.; Dils, B.; Hendrick, F.; Hao, N.; Mazière, M. D. First Satellite Detection of Volcanic Bromine Monoxide Emission after the Kasatochi Eruption. *Geophysical Research Letters* **2009**, *36* (3). https://doi.org/10.1029/2008GL036552.

(87) Theys, N.; Smedt, I. D.; Roozendael, M. V.; Froidevaux, L.; Clarisse, L.; Hendrick, F. First Satellite Detection of Volcanic OClO after the Eruption of Puyehue-Cordón Caulle. *Geophysical Research Letters* **2014**, *41* (2), 667–672. https://doi.org/10.1002/2013GL058416.

(88) Carn, S. A.; Krueger, A. J.; Arellano, S.; Krotkov, N. A.; Yang, K. Daily Monitoring of Ecuadorian Volcanic Degassing from Space. *Journal of Volcanology and Geothermal Research* **2008**, *176* (1), 141–150. https://doi.org/10.1016/j.jvolgeores.2008.01.029.

(89) Chou, C. H. S. J.; Organization, W. H.; Safety, I. P. on C. *Hydrogen Sulfide : Human Health Aspects*; World Health Organization, 2003.

(90) Clarisse, L.; R'Honi, Y.; Coheur, P.; Hurtmans, D.; Clerbaux, C. Thermal infrared nadir observations of 24 atmospheric gases *Geophys. Res. Lett.* **2011**, *38* (10), L10802- https://doi.org/10.1029/2011GL047271

(91) Yokelson, R. J.; Christian, T. J.; Karl, T. G.; Guenther, A. The Tropical Forest and Fire Emissions Experiment: Laboratory Fire Measurements and Synthesis of Campaign Data. *Atmospheric Chemistry and Physics* **2008**, *8* (13), 3509–3527. https://doi.org/10.5194/acp-8-3509-2008.

(92) Keene, W. C.; Khalil, M. A. K.; Erickson, D. J.; McCulloch, A.; Graedel, T. E.; Lobert, J. M.; Aucott, M. L.; Gong, S. L.; Harper, D. B.; Kleiman, G.; Midgley, P.; Moore, R. M.; Seuzaret, C.; Sturges, W. T.; Benkovitz, C. M.; Koropalov, V.; Barrie, L. A.; Li, Y. F. Composite Global Emissions of Reactive Chlorine from Anthropogenic and Natural Sources: Reactive Chlorine Emissions Inventory. *Journal of Geophysical Research: Atmospheres* **1999**, *104* (D7), 8429–8440. https://doi.org/10.1029/1998JD100084.

(93) Watson, N. A. I.; Black, J. A.; Stonelake, T. M.; Knowles, P. J.; Beames, J. M. An Extended Computational Study of Criegee Intermediate–Alcohol Reactions. *J. Phys. Chem. A* **2018**. https://doi.org/10.1021/acs.jpca.8b09349.

(94) Atkins, P.; Paula, J. de; Friedman, R. *Physical Chemistry: Quanta, Matter, and Change*; OUP Oxford, 2013.
(95) Aroeira, G. J. R.; Abbott, A. S.; Elliott, S. N.; Turney, J. M.; Schaefer, H. F. The Addition of Methanol to Criegee Intermediates. *Phys. Chem. Chem. Phys.* **2019**, *21* (32), 17760–17771. https://doi.org/10.1039/C9CP03480C.
(96) Ritchie, G. *Atmospheric Chemistry: From The Surface To The Stratosphere*; World Scientific Publishing Company, 2017.
(97) Ochterski, J. W. Thermochemistry in Gaussian. *Gaussian Inc* **2000**, *1*, 19.
(98) Ochterski, J. W. Vibrational Analysis in Gaussian. *help@ gaussian. com* **1999**.
(99) Frisch, M. J.; Trucks, G. W.; Schlegel, H. B.; Scuseria, G. E.; Robb, M. A.; Cheeseman, J. R.; Scalmani, G.; Barone, V.; Mennucci, B.; Petersson, G. A. Gaussian 09 Manual. *Gaussian, Inc*.
(100) Clapeyron, É. Mémoire Sur La Puissance Motrice de La Chaleur. *Journal de l'École polytechnique* **1834**, *14*, 153–190.
(101) Melosh, H. J. Atmospheric Impact Processes. *Advances in Space Research* **1991**, *11* (6), 87–93. https://doi.org/10.1016/0273-1177(91)90235-C.
(102) Hunten, D. M. The Escape of Light Gases from Planetary Atmospheres. *J. Atmos. Sci.* **1973**, *30* (8), 1481–1494. https://doi.org/10.1175/1520-0469(1973)030<1481:TEOLGF>2.0.CO;2.
(103) Greenfield, S. M. Rain Scavenging of Radioactive Particulate Matter from the Atmosphere. *Journal of Atmospheric Sciences* **1957**, *14*, 115–125. https://doi.org/10.1175/1520-0469(1957)014<0115:RSORPM>2.0.CO;2.
(104) Cherrier, G.; Belut, E.; Gerardin, F.; Tanière, A.; Rimbert, N. Aerosol Particles Scavenging by a Droplet: Microphysical Modeling in the Greenfield Gap. *Atmospheric Environment* **2017**, *166*, 519–530. https://doi.org/10.1016/j.atmosenv.2017.07.052.
(105) Kumar, M.; Zhong, J.; Francisco, J. S.; Zeng, X. C. Criegee Intermediate-Hydrogen Sulfide Chemistry at the Air/Water Interface *Chem Sci* **2017**, *8* (8), 5385–5391. https://doi.org/10.1039/c7sc01797a.
(106) Osborne, M. presented as part of the slides for Lecture 9 of Atmospheric Evolution and Structure, University of Sussex, January, 2014.
(107) Atkinson, R.; Baulch, D. L.; Cox, R. A.; Crowley, J. N.; Hampson, R. F.; Hynes, R. G.; Jenkin, M. E.; Rossi, M. J.; Troe, J. Evaluated Kinetic and Photochemical Data for Atmospheric Chemistry: Volume I - Gas Phase Reactions of O_x, HO_x, NO_x and SO_x Species. *Atmospheric Chemistry and Physics* **2004**, *4* (6), 1461–1738. https://doi.org/10.5194/acp-4-1461-2004.
(108) Atkinson, R.; Baulch, D. L.; Cox, R. A.; Hampson, R. F.; Kerr, J. A.; Rossi, M. J.; Troe, J. Evaluated Kinetic, Photochemical and Heterogeneous Data for Atmospheric Chemistry: Supplement V. IUPAC Subcommittee on Gas Kinetic Data Evaluation for Atmospheric Chemistry. *Journal of Physical and Chemical Reference Data* **1997**, *26* (3), 521–1011. https://doi.org/10.1063/1.556011.
(109) Calvert, J. G. *The Mechanisms of Atmospheric Oxidation of the Alkenes*; Oxford University Press, 2000.
(110) Geyer, A.; Bächmann, K.; Hofzumahaus, A.; Holland, F.; Konrad, S.; Klüpfel, T.; Pätz, H.-W.; Perner, D.; Mihelcic, D.; Schäfer, H.-J.; Volz-Thomas, A.; Platt, U. Nighttime Formation of Peroxy and Hydroxyl Radicals during the BERLIOZ Campaign: Observations and Modeling Studies. *Journal of Geophysical Research: Atmospheres* **2003**, *108* (D4). https://doi.org/10.1029/2001JD000656.
(111) H. Khan, M. A.; J. Percival, C.; L. Caravan, R.; A. Taatjes, C.; E. Shallcross, D. Criegee Intermediates and Their Impacts on the Troposphere. *Environmental Science: Processes & Impacts* **2018**. https://doi.org/10.1039/C7EM00585G.
(112) Na, K.; Song, C.; Cocker, D. R. Formation of Secondary Organic Aerosol from the Reaction of Styrene with Ozone in the Presence and Absence of Ammonia and

Water. *Atmospheric Environment* **2006**, *40* (10), 1889–1900. https://doi.org/10.1016/j.atmosenv.2005.10.063.
(113) Razumovskii, S. D. Comparison of Reaction Rates for Ozone-Alkene and Ozone-Alkane Systems in the Gas Phase and in Solution. *Russ Chem Bull* **1995**, *44* (12), 2287–2288. https://doi.org/10.1007/BF00713595.
(114) Atkinson, R.; Carter, W. P. L. Kinetics and Mechanisms of the Gas-Phase Reactions of Ozone with Organic Compounds under Atmospheric Conditions. *Chem. Rev.* **1984**, *84* (5), 437–470. https://doi.org/10.1021/cr00063a002.
(115) Criegee, R.; Wenner, G. Die Ozonisierung Des 9,10-Oktalins. *Justus Liebigs Annalen der Chemie* **1949**, *564* (1), 9–15. https://doi.org/10.1002/jlac.19495640103.
(116) Criegee, R. Mechanism of Ozonolysis. *Angewandte Chemie International Edition in English* **1975**, *14* (11), 745–752. https://doi.org/10.1002/anie.197507451.
(117) Alcock, W. G.; Mile, B. Pre-Zwitterion Intermediates in the Liquid-Phase Ozonolysis of Alkenes. *J. Chem. Soc., Chem. Commun.* **1976**, No. 1, 5–6. https://doi.org/10.1039/C39760000005.
(118) R. McGillen, M.; J. Carey, T.; T. Archibald, A.; C. Wenger, J.; E. Shallcross, D.; J. Percival, C. Structure–Activity Relationship (SAR) for the Gas-Phase Ozonolysis of Aliphatic Alkenes and Dialkenes. *Physical Chemistry Chemical Physics* **2008**, *10* (13), 1757–1768. https://doi.org/10.1039/B715394E.
(119) Berndt, T.; Jokinen, T.; Mauldin, R. L.; Petäjä, T.; Herrmann, H.; Junninen, H.; Paasonen, P.; Worsnop D. R.;, and Sipilä, M. Gas-Phase Ozonolysis of Selected Olefins: The Yield of Stabilized Criegee Intermediate and the Reactivity toward SO_2 *The Journal of Physical Chemistry Letters* **2012**, *3* (19), 2892–2896 https://doi.org/10.1021/jz301158u
(120) Mayorov, A. V.; Krisyuk, B. E.; Sokolova, N. Kinetics and Mechanisms of the First Step of Ozonolysis of Trans-Isoprene. *Computational and Theoretical Chemistry* **2020**, *1186*, 112904. https://doi.org/10.1016/j.comptc.2020.112904.
(121) Li, Y.; Liu, H.; Huang, X.; Li, Z.; Sun, Y.; Sun, C. Theoretical Study for Ozonolysis of 1,3-Butadiene. *Journal of Molecular Structure: THEOCHEM* **2010**, *945* (1), 120–128. https://doi.org/10.1016/j.theochem.2010.01.021.
(122) Almatarneh, M. H.; Elayan, I. A.; Poirier, R. A.; Altarawneh, M. The Ozonolysis of Cyclic Monoterpenes: A Computational Review. *Can. J. Chem.* **2017**, *96* (3), 281–292. https://doi.org/10.1139/cjc-2017-0587.
(123) Johnson, D.; Marston, G. The Gas-Phase Ozonolysis of Unsaturated Volatile Organic Compounds in the Troposphere. *Chem. Soc. Rev.* **2008**, *37* (4), 699–716. https://doi.org/10.1039/B704260B.
(124) Newland, M. J.; Nelson, B. S.; Muñoz, A.; Ródenas, M.; Vera, T.; Tárrega, J.; Rickard, A. R. Trends in Stabilisation of Criegee Intermediates from Alkene Ozonolysis. *Phys. Chem. Chem. Phys.* **2020**, *22* (24), 13698–13706. https://doi.org/10.1039/D0CP00897D.
(125) Liang, Z.; Wei, T.; Xie, J.; Li, H.; Liu, H. Direct Conversion of Terminal Alkenes to Aldehydes via Ozonolysis Reaction in Rotating Zigzag Bed. *J IRAN CHEM SOC* **2020**, *17* (9), 2379–2384. https://doi.org/10.1007/s13738-020-01933-y.
(126) Neeb, P.; Horie, O.; Moortgat, G. K. The Ethene−Ozone Reaction in the Gas Phase. *J. Phys. Chem. A* **1998**, *102* (34), 6778–6785. https://doi.org/10.1021/jp981264z.
(127) Martinez, R. I.; Herron, J. T. Stopped-Flow Studies of the Mechanisms of Ozone-Alkene Reactions in the Gas Phase: Trans-2-Butene. *J. Phys. Chem.* **1988**, *92* (16), 4644–4648. https://doi.org/10.1021/j100327a017.
(128) Niki, H.; Maker, P. D.; Savage, C. M.; Breitenbach, L. P.; Hurley, M. D. FTIR Spectroscopic Study of the Mechanism for the Gas-Phase Reaction between Ozone and Tetramethylethylene. *J. Phys. Chem.* **1987**, *91* (4), 941–946. https://doi.org/10.1021/j100288a035.
(129) Cremer, D.; Gauss, J.; Kraka, E.; Stanton, J. F.; Bartlett, R. J. A CCSD (T) Investigation of Carbonyl Oxide and Dioxirane. Equilibrium Geometries, Dipole

Moments, Infrared Spectra, Heats of Formation and Isomerization Energies. *Chemical Physics Letters* **1993**, *209* (5), 547–556. https://doi.org/10.1016/0009-2614(93)80131-8.
(130) Gutbrod, R.; Schindler, R. N.; Kraka, E.; Cremer, D. Formation of OH Radicals in the Gas Phase Ozonolysis of Alkenes: The Unexpected Role of Carbonyl Oxides. *Chemical Physics Letters* **1996**, *252* (3), 221–229. https://doi.org/10.1016/0009-2614(96)00126-1.
(131) Gutbrod, R.; Kraka, E.; Schindler, R. N.; Cremer, D. Kinetic and Theoretical Investigation of the Gas-Phase Ozonolysis of Isoprene: Carbonyl Oxides as an Important Source for OH Radicals in the Atmosphere. *J. Am. Chem. Soc.* **1997**, *119* (31), 7330–7342. https://doi.org/10.1021/ja970050c.
(132) Horie, O.; Moortgat, G. K. Gas-Phase Ozonolysis of Alkenes. Recent Advances in Mechanistic Investigations. *Acc. Chem. Res.* **1998**, *31* (7), 387–396. https://doi.org/10.1021/ar9702740.
(133) Horie, O.; Moortgat, G. K. Decomposition Pathways of the Excited Criegee Intermediates in the Ozonolysis of Simple Alkenes. *Atmospheric Environment. Part A. General Topics* **1991**, *25* (9), 1881–1896. https://doi.org/10.1016/0960-1686(91)90271-8.
(134) Su, F.; Calvert, J. G.; Shaw, J. H. A FTIR Spectroscopic Study of the Ozone-Ethene Reaction Mechanism in Oxygen-Rich Mixtures. *The Journal of Physical Chemistry* **1980**, *84* (3), 239–246. https://doi.org/10.1021/j100440a003.
(135) Atkinson, R. Gas-Phase Tropospheric Chemistry of Volatile Organic Compounds: 1. Alkanes and Alkenes. *Journal of Physical and Chemical Reference Data* **1997**, *26* (2), 215–290. https://doi.org/10.1063/1.556012.
(136) Fang, Y.; Liu, F.; Barber, V. P.; Klippenstein, S. J.; McCoy, A. B.; Lester, M. I. Communication: Real Time Observation of Unimolecular Decay of Criegee Intermediates to OH Radical Products. *The Journal of Chemical Physics* **2016**, *144* (6), 061102. https://doi.org/10.1063/1.4941768.
(137) Novelli, A.; Vereecken, L.; Lelieveld, J.; Harder, H. Direct Observation of OH Formation from Stabilised Criegee Intermediates. *Phys. Chem. Chem. Phys.* **2014**, *16* (37), 19941–19951. https://doi.org/10.1039/C4CP02719A.
(138) Harrison, R. M.; Yin, J.; Tilling, R. M.; Cai, X.; Seakins, P. W.; Hopkins, J. R.; Lansley, D. L.; Lewis, A. C.; Hunter, M. C.; Heard, D. E.; Carpenter, L. J.; Creasey, D. J.; Lee, J. D.; Pilling, M. J.; Carslaw, N.; Emmerson, K. M.; Redington, A.; Derwent, R. G.; Ryall, D.; Mills, G.; Penkett, S. A. Measurement and Modelling of Air Pollution and Atmospheric Chemistry in the U.K. West Midlands Conurbation: Overview of the PUMA Consortium Project. *Science of The Total Environment* **2006**, *360* (1), 5–25. https://doi.org/10.1016/j.scitotenv.2005.08.053.
(139) Su, Y.-T.; Huang, Y.-H.; Witek, H. A.; Lee, Y.-P. Infrared Absorption Spectrum of the Simplest Criegee Intermediate CH_2OO. *Science* **2013**, *340* (6129), 174–176. https://doi.org/10.1126/science.1234369.
(140) Lin, J. J.-M.; Chao, W. Structure-Dependent Reactivity of Criegee Intermediates Studied with Spectroscopic Methods. *Chem. Soc. Rev.* **2017**, *46* (24), 7483–7497. https://doi.org/10.1039/C7CS00336F.
(141) Taatjes, C. A.; Welz, O.; Eskola, A. J.; Savee, J. D.; Scheer, A. M.; Shallcross, D. E.; Rotavera, B.; Lee, E. P. F.; Dyke, J. M.; Mok, D. K. W.; Osborn, D. L.; Percival, C. J. Direct Measurements of Conformer-Dependent Reactivity of the Criegee Intermediate CH_3CHOO. *Science* **2013**, *340* (6129), 177–180. https://doi.org/10.1126/science.1234689.
(142) Lin, H.-Y.; Huang, Y.-H.; Wang, X.; Bowman, J. M.; Nishimura, Y.; Witek, H. A.; Lee, Y.-P. Infrared Identification of the Criegee Intermediates *Syn*- and *Anti*-CH_3CHOO, and Their Distinct Conformation-Dependent Reactivity. *Nature Communications* **2015**, *6*, 7012. https://doi.org/10.1038/ncomms8012.

(143) Womack, C. C.; Martin-Drumel, M.-A.; Brown, G. G.; Field, R. W.; McCarthy, M. C. Observation of the Simplest Criegee Intermediate CH_2OO in the Gas-Phase Ozonolysis of Ethylene. *Science Advances* **2015**, *1* (2), e1400105. https://doi.org/10.1126/sciadv.1400105.
(144) Taatjes, C. A.; Meloni, G.; Selby, T. M.; Trevitt, A. J.; Osborn, D. L.; Percival, C. J.; Shallcross, D. E. Direct Observation of the Gas-Phase Criegee Intermediate (CH2OO). *J. Am. Chem. Soc.* **2008**, *130* (36), 11883–11885. https://doi.org/10.1021/ja804165q.
(145) Welz, O.; Savee, J. D.; Osborn, D. L.; Vasu, S. S.; Percival, C. J.; Shallcross, D. E.; Taatjes, C. A. Direct Kinetic Measurements of Criegee Intermediate (CH_2OO) Formed by Reaction of CH_2I with O_2. *Science* **2012**, *335* (6065), 204–207. https://doi.org/10.1126/science.1213229.
(146) Huang, H.; Eskola, A. J.; Taatjes, C. A. Pressure-Dependent I-Atom Yield in the Reaction of CH_2I with O_2 Shows a Remarkable Apparent Third-Body Efficiency for O_2. *J. Phys. Chem. Lett.* **2012**, *3* (22), 3399–3403. https://doi.org/10.1021/jz301585c.
(147) SDS of Diiodomethane, Safety Data Sheets, CAS 75-11-6 https://www.chemblink.com/MSDS/75-11-6_MSDS.htm (accessed 2020 -11 -22).
(148) Smith, M. C.; Ting, W.-L.; Chang, C.-H.; Takahashi, K.; Boering, K. A.; Lin, J. J.-M. UV Absorption Spectrum of the C2 Criegee Intermediate CH_3CHOO. *J. Chem. Phys.* **2014**, *141* (7), 074302. https://doi.org/10.1063/1.4892582.
(149) Smith, M. C.; Chao, W.; Takahashi, K.; Boering, K. A.; Lin, J. J.-M. Unimolecular Decomposition Rate of the Criegee Intermediate $(CH_3)_2COO$ Measured Directly with UV Absorption Spectroscopy. *J. Phys. Chem. A* **2016**, *120* (27), 4789–4798. https://doi.org/10.1021/acs.jpca.5b12124.
(150) Goldan, P. D.; Kuster, W. C.; Fehsenfeld, F. C.; Montzka, S. A. The Observation of a C5 Alcohol Emission in a North American Pine Forest. *Geophysical Research Letters* **1993**, *20* (11), 1039–1042. https://doi.org/10.1029/93GL00247.
(151) PubChem. Limonene https://pubchem.ncbi.nlm.nih.gov/compound/22311 (accessed 2020 -03 -30).
(152) Alpha-Pinene - an overview | ScienceDirect Topics https://www-sciencedirect-com.abc.cardiff.ac.uk/topics/agricultural-and-biological-sciences/alpha-pinene (accessed 2020 -03 -30).
(153) Zebib, B.; Beyrouthy, M. E.; Safi, C.; Merah, O. Chemical Composition of the Essential Oil of Satureja Myrtifolia (Boiss. & Hohen.) from Lebanon. *Journal of Essential Oil Bearing Plants* **2015**, *18* (1), 248–254. https://doi.org/10.1080/0972060X.2014.890075.
(154) Sommariva, R.; Cox, S.; Martin, C.; Borońska, K.; Young, J.; Jimack, P. K.; Pilling, M. J.; Matthaios, V. N.; Nelson, B. S.; Newland, M. J.; Panagi, M.; Bloss, W. J.; Monks, P. S.; Rickard, A. R. AtChem (Version 1), an Open-Source Box Model for the Master Chemical Mechanism. *Geoscientific Model Development* **2020**, *13* (1), 169–183. https://doi.org/10.5194/gmd-13-169-2020.
(155) McGillen, M. R.; Archibald, A. T.; Carey, T.; Leather, K. E.; Shallcross, D. E.; Wenger, J. C.; Percival, C. J. Structure–Activity Relationship (SAR) for the Prediction of Gas-Phase Ozonolysis Rate Coefficients: An Extension towards Heteroatomic Unsaturated Species. *Phys. Chem. Chem. Phys.* **2011**, *13* (7), 2842–2849. https://doi.org/10.1039/C0CP01732A.
(156) Atkinson, Roger.; Tuazon, E. C.; Aschmann, S. M. Products of the Gas-Phase Reactions of O_3 with Alkenes. *Environ. Sci. Technol.* **1995**, *29* (7), 1860–1866. https://doi.org/10.1021/es00007a025.
(157) McGillen, M. R.; Ghalaieny, M.; Percival, C. J. Determination of Gas-Phase Ozonolysis Rate Coefficients of C8–14 Terminal Alkenes at Elevated Temperatures Using the Relative Rate Method. *Phys. Chem. Chem. Phys.* **2011**, *13* (23), 10965–10969. https://doi.org/10.1039/C0CP02643C.

(158) Li, M.; Liu, Y.; Wang, L. Gas-Phase Ozonolysis of Furans, Methylfurans, and Dimethylfurans in the Atmosphere. *Phys. Chem. Chem. Phys.* **2018**, *20* (38), 24735–24743. https://doi.org/10.1039/C8CP04947E.
(159) Alvarado, A.; Tuazon, E. C.; Aschmann, S. M.; Atkinson, R.; Arey, J. Products of the Gas-Phase Reactions of O(^{3}P) Atoms and O_3 with α-Pinene and 1,2-Dimethyl-1-Cyclohexene. *Journal of Geophysical Research: Atmospheres* **1998**, *103* (D19), 25541–25551. https://doi.org/10.1029/98JD00524.
(160) Liu, F.; Beames, J. M.; Green, A. M.; Lester, M. I. UV Spectroscopic Characterization of Dimethyl- and Ethyl-Substituted Carbonyl Oxides. *J. Phys. Chem. A* **2014**, *118* (12), 2298–2306. https://doi.org/10.1021/jp412726z.
(161) Atkinson, R.; Aschmann, S. M. Hydroxyl Radical Production from the Gas-Phase Reactions of Ozone with a Series of Alkenes under Atmospheric Conditions. *Environ. Sci. Technol.* **1993**, *27* (7), 1357–1363. https://doi.org/10.1021/es00044a010.
(162) Orzechowska, G. E.; Paulson, S. E. Production of OH Radicals from the Reactions of C4–C6 Internal Alkenes and Styrenes with Ozone in the Gas Phase. *Atmospheric Environment* **2002**, *36* (3), 571–581. https://doi.org/10.1016/S1352-2310(01)00445-9.
(163) Kroll, J. H.; Donahue, N. M.; Cee, V. J.; Demerjian, K. L.; Anderson, J. G. Gas-Phase Ozonolysis of Alkenes: Formation of OH from Anti Carbonyl Oxides. *J. Am. Chem. Soc.* **2002**, *124* (29), 8518–8519. https://doi.org/10.1021/ja0266060.
(164) Atkinson, R.; Aschmann, S. M.; Arey, J.; Shorees, B. Formation of OH Radicals in the Gas Phase Reactions of O_3 with a Series of Terpenes. *Journal of Geophysical Research: Atmospheres* **1992**, *97* (D5), 6065–6073. https://doi.org/10.1029/92JD00062.
(165) Horie, O.; Neeb, P.; Moortgat, G. K. The Reactions of the Criegee Intermediate CH3 CHOO in the Gas-Phase Ozonolysis of 2-Butene Isomers. *International Journal of Chemical Kinetics* **1997**, *29* (6), 461–468. https://doi.org/10.1002/(SICI)1097-4601(1997)29:6<461::AID-KIN8>3.0.CO;2-S.
(166) Tuazon, E. C.; Aschmann, S. M.; Arey, J.; Atkinson, R. Products of the Gas-Phase Reactions of O3 with a Series of Methyl-Substituted Ethenes. *Environ. Sci. Technol.* **1997**, *31* (10), 3004–3009. https://doi.org/10.1021/es970258y.
(167) Horie, O.; Neeb, P.; Moortgat, G. K. Ozonolysis of trans- and cis-2-butenes in low parts-per-million concentration ranges. *International Journal of Chemical Kinetics* **1994**, *26* (11), 1075–1094. https://doi.org/10.1002/kin.550261104.
(168) Nazaroff, W. W.; Weschler, C. J. Cleaning Products and Air Fresheners: Exposure to Primary and Secondary Air Pollutants. *Atmospheric Environment* **2004**, *38* (18), 2841–2865. https://doi.org/10.1016/j.atmosenv.2004.02.040.
(169) Calogirou, A.; Larsen, B. R.; Kotzias, D. Gas-Phase Terpene Oxidation Products: A Review. *Atmospheric Environment* **1999**, *33* (9), 1423–1439. https://doi.org/10.1016/S1352-2310(98)00277-5.
(170) Zhu, L.; Jacob, D. J.; Keutsch, F. N.; Mickley, L. J.; Scheffe, R.; Strum, M.; González Abad, G.; Chance, K.; Yang, K.; Rappenglück, B.; Millet, D. B.; Baasandorj, M.; Jaeglé, L.; Shah, V. Formaldehyde (HCHO) As a Hazardous Air Pollutant: Mapping Surface Air Concentrations from Satellite and Inferring Cancer Risks in the United States. *Environ. Sci. Technol.* **2017**, *51* (10), 5650–5657. https://doi.org/10.1021/acs.est.7b01356.
(171) Salamanca, J. C.; Meehan-Atrash, J.; Vreeke, S.; Escobedo, J. O.; Peyton, D. H.; Strongin, R. M. E-Cigarettes Can Emit Formaldehyde at High Levels under Conditions That Have Been Reported to Be Non-Averse to Users. *Sci Rep* **2018**, *8*. https://doi.org/10.1038/s41598-018-25907-6.
(172) US EPA, O. 2011 National Air Toxics Assessment https://www.epa.gov/national-air-toxics-assessment/2011-national-air-toxics-assessment (accessed 2020 -11 -21).

(173) Millet, D. B.; Guenther, A.; Siegel, D. A.; Nelson, N. B.; Singh, H. B.; Gouw, J. A. de; Warneke, C.; Williams, J.; Eerdekens, G.; Sinha, V.; Karl, T.; Flocke, F.; Apel, E.; Riemer, D. D.; Palmer, P. I.; Barkley, M. Global Atmospheric Budget of Acetaldehyde: 3-D Model Analysis and Constraints from in-Situ and Satellite Observations. *Atmospheric Chemistry and Physics* **2010**, *10* (7), 3405–3425. https://doi.org/10.5194/acp-10-3405-2010.
(174) Heard, D. E.; Carpenter, L. J.; Creasey, D. J.; Hopkins, J. R.; Lee, J. D.; Lewis, A. C.; Pilling, M. J.; Seakins, P. W.; Carslaw, N.; Emmerson, K. M. High Levels of the Hydroxyl Radical in the Winter Urban Troposphere. *Geophysical Research Letters* **2004**, *31* (18). https://doi.org/10.1029/2004GL020544.
(175) Savage, N. CageCapture: Designing a Molecule to Filter out Pollutants. *Nature* **2020**. https://doi.org/10.1038/d41586-020-01797-5.
(176) Yang, D. S.; Pennisi, S. V.; Son, K.-C.; Kays, S. J. Screening Indoor Plants for Volatile Organic Pollutant Removal Efficiency. *HortScience* **2009**, *44* (5), 1377–1381. https://doi.org/10.21273/HORTSCI.44.5.1377.
(177) A. Taatjes, C.; Welz, O.; J. Eskola, A.; D. Savee, J.; L. Osborn, D.; F. Lee, E. P.; M. Dyke, J.; K. Mok, D. W.; E. Shallcross, D.; J. Percival, C. Direct Measurement of Criegee Intermediate (CH 2 OO) Reactions with Acetone , Acetaldehyde , and Hexafluoroacetone. *Physical Chemistry Chemical Physics* **2012**, *14* (30), 10391–10400. https://doi.org/10.1039/C2CP40294G.
(178) Stone, D.; Blitz, M.; Daubney, L.; M. Howes, N. U.; Seakins, P. Kinetics of CH_2OO Reactions with SO_2, NO_2, NO, H_2O and CH_3CHO as a Function of Pressure. *Physical Chemistry Chemical Physics* **2014**, *16* (3), 1139–1149. https://doi.org/10.1039/C3CP54391A.
(179) Elsamra, R. M. I.; Jalan, A.; Buras, Z. J.; Middaugh, J. E.; Green, W. H. Temperature- and Pressure-Dependent Kinetics of CH_2OO + CH_3COCH_3 and CH_2OO + CH_3CHO: Direct Measurements and Theoretical Analysis. *International Journal of Chemical Kinetics* **2016**, *48* (8), 474–488. https://doi.org/10.1002/kin.21007.
(180) Fenske, J. D.; Hasson, A. S.; Ho, A. W.; Paulson, S. E. Measurement of Absolute Unimolecular and Bimolecular Rate Constants for CH3CHOO Generated by the Trans-2-Butene Reaction with Ozone in the Gas Phase. *J. Phys. Chem. A* **2000**, *104* (44), 9921–9932. https://doi.org/10.1021/jp0016636.
(181) Ma Qiao; Lin Xiaoxiao; Yang Chengqiang; Long Bo; Gai Yanbo; Zhang Weijun. The Influences of Ammonia on Aerosol Formation in the Ozonolysis of Styrene: Roles of Criegee Intermediate Reactions. *Royal Society Open Science* **2018**, *5* (5), 172171. https://doi.org/10.1098/rsos.172171.
(182) Vereecken, L.; Novelli, A.; Taraborrelli, D. Unimolecular Decay Strongly Limits the Atmospheric Impact of Criegee Intermediates. *Phys Chem Chem Phys* **2017**, *19* (47), 31599–31612. https://doi.org/10.1039/c7cp05541b.
(183) J. Newland, M.; R. Rickard, A.; S. Alam, M.; Vereecken, L.; Muñoz, A.; Ródenas, M.; J. Bloss, W. Kinetics of Stabilised Criegee Intermediates Derived from Alkene Ozonolysis: Reactions with SO_2, H_2O and Decomposition under Boundary Layer Conditions. *Physical Chemistry Chemical Physics* **2015**, *17* (6), 4076–4088. https://doi.org/10.1039/C4CP04186K.
(184) Huang, H.-L.; Chao, W.; Lin, J. J.-M. Kinetics of a Criegee Intermediate That Would Survive High Humidity and May Oxidize Atmospheric SO_2. *PNAS* **2015**, *112* (35), 10857–10862. https://doi.org/10.1073/pnas.1513149112.
(185) Olzmann, M.; Kraka, E.; Cremer, D.; Gutbrod, R.; Andersson, S. Energetics, Kinetics, and Product Distributions of the Reactions of Ozone with Ethene and 2,3-Dimethyl-2-Butene. *J. Phys. Chem. A* **1997**, *101* (49), 9421–9429. https://doi.org/10.1021/jp971663e.
(186) Novelli, A.; Hens, K.; Ernest, C. T.; Martinez, M.; Nolscher, A.; Sinha, V.; Paasonen, P.; Petaja, T.; Sipila, M.; Elste, T.; Kubistin, D. Estimating the Atmospheric Concentration of Criegee Intermediates and Their Possible

Interference in a FAGE-LIF Instrument. *Faculty of Science, Medicine and Health - Papers* **2017**, 7807–7826. https://doi.org/10.5194/acp-17-7807-2017.
(187) Mauldin Iii, R. L.; Berndt, T.; Sipilä, M.; Paasonen, P.; Petäjä, T.; Kim, S.; Kurtén, T.; Stratmann, F.; Kerminen, V.-M.; Kulmala, M. A New Atmospherically Relevant Oxidant of Sulphur Dioxide. *Nature* **2012**, *488* (7410), 193–196. https://doi.org/10.1038/nature11278.
(188) Cox, R. A.; Penkett, S. A. Oxidation of Atmospheric SO_2 by Products of the Ozone–Olefin Reaction. *Nature* **1971**, *230* (5292), 321–322. https://doi.org/10.1038/230321a0.
(189) Jang, M.; Czoschke, N. M.; Lee, S.; Kamens, R. M. Heterogeneous Atmospheric Aerosol Production by Acid-Catalyzed Particle-Phase Reactions. *Science* **2002**, *298* (5594), 814–817. https://doi.org/10.1126/science.1075798.
(190) Boy, M.; Mogensen, D.; Smolander, S.; Zhou, L.; Nieminen, T.; Paasonen, P.; Plass-Dülmer, C.; Sipilä, M.; Petäjä, T.; Mauldin, L.; Berresheim, H.; Kulmala, M. Oxidation of SO_2 by Stabilized Criegee Intermediate (SCI) Radicals as a Crucial Source for Atmospheric Sulfuric Acid Concentrations. *Atmospheric Chemistry and Physics* **2013**, *13* (7), 3865–3879. https://doi.org/10.5194/acp-13-3865-2013.
(191) Kuwata, K. T.; Guinn, E. J.; Hermes, M. R.; Fernandez, J. A.; Mathison, J. M.; Huang, K. A Computational Re-Examination of the Criegee Intermediate–Sulfur Dioxide Reaction. *J. Phys. Chem. A* **2015**, *119* (41), 10316–10335. https://doi.org/10.1021/acs.jpca.5b06565.
(192) Menzel, D. B.; Keller, Do. A.; Leung, K.-H. Covalent Reactions in the Toxicity of SO_2 and Sulfite. In *Biological Reactive Intermediates III: Mechanisms of Action in Animal Models and Human Disease*; Kocsis, J. J., Jollow, D. J., Witmer, C. M., Nelson, J. O., Snyder, R., Eds.; Advances in Experimental Medicine and Biology; Springer US: Boston, MA, 1986; pp 477–492. https://doi.org/10.1007/978-1-4684-5134-4_46.
(193) Sheps, L.; Scully, A. M.; Au, K. UV Absorption Probing of the Conformer-Dependent Reactivity of a Criegee Intermediate CH_3CHOO. *Phys. Chem. Chem. Phys.* **2014**, *16* (48), 26701–26706. https://doi.org/10.1039/C4CP04408H.
(194) Chao, W.; Lin, Y.-H.; Yin, C.; Lin, W.-H.; Takahashi, K.; Lin, J. J.-M. Temperature and Isotope Effects in the Reaction of CH_3CHOO with Methanol. *Phys. Chem. Chem. Phys.* **2019**, *21* (25), 13633–13640. https://doi.org/10.1039/C9CP02534K.
(195) Anglada, J. M.; González, J.; Torrent-Sucarrat, M. Effects of the Substituents on the Reactivity of Carbonyl Oxides. A Theoretical Study on the Reaction of Substituted Carbonyl Oxides with Water. *Phys. Chem. Chem. Phys.* **2011**, *13* (28), 13034–13045. https://doi.org/10.1039/C1CP20872A.
(196) Zeng, Z.; Altarawneh, M.; Oluwoye, I.; Glarborg, P.; Dlugogorski, B. Z. Inhibition and Promotion of Pyrolysis by Hydrogen Sulfide (H_2S) and Sulfanyl Radical (SH). *J. Phys. Chem. A* **2016**, *120* (45), 8941–8948. https://doi.org/10.1021/acs.jpca.6b09357.
(197) US EPA, O. Refrigerant Transition & Environmental Impacts https://www.epa.gov/mvac/refrigerant-transition-environmental-impacts (accessed 2019 -01 -09).
(198) European Commission - PRESS RELEASES - Press release - Refrigerants used in mobile air condition systems (MAC) - State of play http://europa.eu/rapid/press-release_MEMO-14-50_en.htm (accessed 2019 -01 -09).
(199) Zhang, B.; Zhai, Z.; Zhang, J. Distribution of Trifluoroacetic Acid in Gas and Particulate Phases in Beijing from 2013 to 2016. *Science of The Total Environment* **2018**, *634*, 471–477. https://doi.org/10.1016/j.scitotenv.2018.03.384.
(200) Onwude, D. I.; Hashim, N.; Janius, R. B.; Nawi, N. M.; Abdan, K. Modeling the Thin-Layer Drying of Fruits and Vegetables: A Review. *Comprehensive Reviews in Food Science and Food Safety* **2016**, *15* (3), 599–618. https://doi.org/10.1111/1541-4337.12196.

(201) Onwude, D. I.; Hashim, N.; Chen, G. Recent Advances of Novel Thermal Combined Hot Air Drying of Agricultural Crops. *Trends in Food Science & Technology* **2016**, *57*, 132–145. https://doi.org/10.1016/j.tifs.2016.09.012.
(202) Intake, I.; Henney, J. E.; Taylor, C. L.; Boon, C. S. *Preservation and Physical Property Roles of Sodium in Foods*; National Academies Press (US), 2010.
(203) CULLEN, W. *Of the Cold Produced by Evaporating Fluids, and of Some Other Means of Producing Cold.*; 1782.
(204) Smith, E. C. Pioneers of Refrigeration*. *Nature* **1943**, *151* (3832), 412–413. https://doi.org/10.1038/151412a0.
(205) Improvement in Apparatus for Freezing Liquids. US30201A, October 2, 1860.
(206) Carre, F. P. E. Improvement in Ice-Machines. USRE5287E, February 18, 1873.
(207) Woods, R. J. H. Breed, Culture, and Economy: The New Zealand Frozen Meat Trade, 1880–1914. *Agricultural History Review* **2012**, *60* (2), 288–308.
(208) National income and expenditure of the United Kingdom, 1870–1952 https://www.researchgate.net/publication/227577343_National_income_and_expenditure_of_the_United_Kingdom_1870-1952 (accessed 2020 -08 -06).
(209) Calm, J. M. The next Generation of Refrigerants – Historical Review, Considerations, and Outlook. *International Journal of Refrigeration* **2008**, *31* (7), 1123–1133. https://doi.org/10.1016/j.ijrefrig.2008.01.013.
(210) Edelmann, F. T. The Life and Legacy of Thomas Midgley Jr. *Papers and Proceedings of the Royal Society of Tasmania* **2016**, *150*, 45–49. https://doi.org/10.26749/rstpp.150.1.45.
(211) Anderson, J. G.; Brune, W. H.; Proffitt, M. H. Ozone Destruction by Chlorine Radicals within the Antarctic Vortex: The Spatial and Temporal Evolution of ClO-O_3 Anticorrelation Based on in Situ ER-2 Data. *Journal of Geophysical Research: Atmospheres* **1989**, *94* (D9), 11465–11479. https://doi.org/10.1029/JD094iD09p11465.
(212) US EPA, O. Updating Ozone Calculations and Emissions Profiles for Use in the Atmospheric and Health Effects Framework Model https://www.epa.gov/ozone-layer-protection/updating-ozone-calculations-and-emissions-profiles-use-atmospheric-and-health (accessed 2020 -08 -07).
(213) The Montreal Protocol https://web.archive.org/web/20130602153542/http://ozone.unep.org/new_site/en/montreal_protocol.php (accessed 2020 -05 -04).
(214) Velders, G. J. M.; Andersen, S. O.; Daniel, J. S.; Fahey, D. W.; McFarland, M. The Importance of the Montreal Protocol in Protecting Climate. *PNAS* **2007**, *104* (12), 4814–4819. https://doi.org/10.1073/pnas.0610328104.
(215) McKenzie, R.; Bernhard, G.; Liley, B.; Disterhoft, P.; Rhodes, S.; Bais, A.; Morgenstern, O.; Newman, P.; Oman, L.; Brogniez, C.; Simic, S. Success of Montreal Protocol Demonstrated by Comparing High-Quality UV Measurements with "World Avoided" Calculations from Two Chemistry-Climate Models. *Sci Rep* **2019**, *9* (1), 1–13. https://doi.org/10.1038/s41598-019-48625-z.
(216) Hurwitz, M. M.; Fleming, E. L.; Newman, P. A.; Li, F.; Mlawer, E.; Cady-Pereira, K.; Bailey, R. Ozone Depletion by Hydrofluorocarbons. *Geophysical Research Letters* **2015**, *42* (20), 8686–8692. https://doi.org/10.1002/2015GL065856.
(217) Rigby, M.; Park, S.; Saito, T.; Western, L. M.; Redington, A. L.; Fang, X.; Henne, S.; Manning, A. J.; Prinn, R. G.; Dutton, G. S.; Fraser, P. J.; Ganesan, A. L.; Hall, B. D.; Harth, C. M.; Kim, J.; Kim, K.-R.; Krummel, P. B.; Lee, T.; Li, S.; Liang, Q.; Lunt, M. F.; Montzka, S. A.; Mühle, J.; O'Doherty, S.; Park, M.-K.; Reimann, S.; Salameh, P. K.; Simmonds, P.; Tunnicliffe, R. L.; Weiss, R. F.; Yokouchi, Y.; Young, D. Increase in CFC-11 Emissions from Eastern China Based on Atmospheric Observations. *Nature* **2019**, *569* (7757), 546–550. https://doi.org/10.1038/s41586-019-1193-4.

(218) Strahan, S. E.; Douglass, A. R. Decline in Antarctic Ozone Depletion and Lower Stratospheric Chlorine Determined From Aura Microwave Limb Sounder Observations. *Geophysical Research Letters* **2018**, *45* (1), 382–390. https://doi.org/10.1002/2017GL074830.
(219) Christmas, M. J.; Dimitratos, Y. N. Process for the Manufacture of Chlorodifluoromethane. EP1868973A1, December 26, 2007.
(220) Producing Process for Synthesizing 1, 1, 1, 2-Tetrafluoroethane by Liquid Phase-Gas Phase Method. CN101648846A, February 17, 2010.
(221) Pu, J.; Xu, H.; Yao, B.; Yu, Y.; Jiang, Y.; Ma, Q.; Chen, L. Estimate of Hydrofluorocarbon Emissions for 2012–16 in the Yangtze River Delta, China. *Adv. Atmos. Sci.* **2020**, *37* (6), 576–585. https://doi.org/10.1007/s00376-020-9242-3.
(222) Environment, U. N. Cooling Emissions and Policy Synthesis Report http://www.unenvironment.org/resources/report/cooling-emissions-and-policy-synthesis-report (accessed 2020 -08 -07).
(223) Xiang, B.; Patra, P. K.; Montzka, S. A.; Miller, S. M.; Elkins, J. W.; Moore, F. L.; Atlas, E. L.; Miller, B. R.; Weiss, R. F.; Prinn, R. G.; Wofsy, S. C. Global Emissions of Refrigerants HCFC-22 and HFC-134a: Unforeseen Seasonal Contributions. *PNAS* **2014**, *111* (49), 17379–17384. https://doi.org/10.1073/pnas.1417372111.
(224) Paul, S.; Deka, R. C.; Gour, N. K. Kinetics, Mechanism, and Global Warming Potentials of HFO-1234yf Initiated by O_3 Molecules and NO_3 Radicals: Insights from Quantum Study. *Environmental Science and Pollution Research* **2018**, *25* (26), 26144–26156. https://doi.org/10.1007/s11356-018-2633-7.
(225) Orkin, V. L.; Martynova, L. E.; Kurylo, M. J. Photochemical Properties of Trans-1-Chloro-3,3,3-Trifluoropropene (Trans-CHCl═CHCF$_3$): OH Reaction Rate Constant, UV and IR Absorption Spectra, Global Warming Potential, and Ozone Depletion Potential. *J. Phys. Chem. A* **2014**, *118* (28), 5263–5271. https://doi.org/10.1021/jp5018949.
(226) Rao, P. K.; Gejji, S. P. Atmospheric Degradation of HCFO-1233zd(E) Initiated by OH Radical, Cl Atom and O_3 Molecule: Kinetics, Reaction Mechanisms and Implications. *Journal of Fluorine Chemistry* **2018**, *211*, 180–193. https://doi.org/10.1016/j.jfluchem.2018.05.001.
(227) Antiñolo, M.; Bravo, I.; Jiménez, E.; Ballesteros, B.; Albaladejo, J. Atmospheric Chemistry of E- and Z-CF$_3$CH═CHF (HFO-1234ze): OH Reaction Kinetics as a Function of Temperature and UV and IR Absorption Cross Sections. *J. Phys. Chem. A* **2017**, *121* (43), 8322–8331. https://doi.org/10.1021/acs.jpca.7b06174.
(228) Kigali Amendment to the Montreal Protocol https://treaties.un.org/Pages/ViewDetails.aspx?src=IND&mtdsg_no=XXVII-2-f&chapter=27&clang=_en (accessed 2020 -05 -04).
(229) Luecken, D. J.; Waterland, R. L.; Papasavva, S.; Taddonio, K. N.; Hutzell, W. T.; Rugh, J. P.; Andersen, S. O. Ozone and TFA Impacts in North America from Degradation of 2,3,3,3-Tetrafluoropropene (HFO-1234yf), A Potential Greenhouse Gas Replacement. *Environ. Sci. Technol.* **2010**, *44* (1), 343–348. https://doi.org/10.1021/es902481f.
(230) Navarro-Esbrí, J.; Amat-Albuixech, M.; Molés, F.; Mateu-Royo, C.; Mota-Babiloni, A.; Collado, R. HCFO-1224yd(Z) as HFC-245fa Drop-in Alternative in Low Temperature ORC Systems: Experimental Analysis in a Waste Heat Recovery Real Facility. *Energy* **2020**, *193*, 116701. https://doi.org/10.1016/j.energy.2019.116701.
(231) Court ruling could imperil Chemours' most profitable product https://www.delawareonline.com/story/news/2017/08/09/court-ruling-could-imperil-chemours-most-profitable-product/551967001/ (accessed 2020 -08 -07).
(232) Navarro-Esbrí, J.; Molés, F.; Peris, B.; Mota-Babiloni, A.; Kontomaris, K. Experimental Study of an Organic Rankine Cycle with HFO-1336mzz-Z as a Low Global Warming Potential Working Fluid for Micro-Scale Low Temperature

Applications. *Energy* **2017**, *133*, 79–89. https://doi.org/10.1016/j.energy.2017.05.092.
(233) Molés, F.; Navarro-Esbrí, J.; Peris, B.; Mota-Babiloni, A.; Barragán-Cervera, Á.; Kontomaris, K. (Kostas). Low GWP Alternatives to HFC-245fa in Organic Rankine Cycles for Low Temperature Heat Recovery: HCFO-1233zd-E and HFO-1336mzz-Z. *Applied Thermal Engineering* **2014**, *71* (1), 204–212. https://doi.org/10.1016/j.applthermaleng.2014.06.055.
(234) Mateu-Royo, C.; Navarro-Esbrí, J.; Mota-Babiloni, A.; Amat-Albuixech, M.; Molés, F. Thermodynamic Analysis of Low GWP Alternatives to HFC-245fa in High-Temperature Heat Pumps: HCFO-1224yd(Z), HCFO-1233zd(E) and HFO-1336mzz(Z). *Applied Thermal Engineering* **2019**, *152*, 762–777. https://doi.org/10.1016/j.applthermaleng.2019.02.047.
(235) Molés, F.; Navarro-Esbrí, J.; Peris, B.; Mota-Babiloni, A.; Barragán-Cervera, Á.; Kontomaris, K. (Kostas). Thermo-Economic Evaluation of Low Global Warming Potential Alternatives to HFC-245fa in Organic Rankine Cycles. *Energy Procedia* **2017**, *142*, 1199–1205. https://doi.org/10.1016/j.egypro.2017.12.381.
(236) Singh, R. R.; Pham, H. T.; Wilson, D. P.; Thomas, R. H. Azeotrope-like Compositions of Tetrafluoropropene and Trifluoroiodomethane. US6969701B2, November 29, 2005.
(237) Orkin, V. L.; Huie, R. E.; Kurylo, M. J. Rate Constants for the Reactions of OH with HFC-245cb ($CH_3CF_2CF_3$) and Some Fluoroalkenes (CH_2CHCF_3, CH_2CFCF_3, CF_2CFCF_3, and CF_2CF_2). *J. Phys. Chem. A* **1997**, *101* (48), 9118–9124. https://doi.org/10.1021/jp971994r.
(238) Papadimitriou, V. C.; Talukdar, R. K.; Portmann, R. W.; Ravishankara, A. R.; Burkholder, J. B. $CF_3CF{=}CH_2$ and (Z)-$CF_3CF{=}CHF$: Temperature Dependent OH Rate Coefficients and Global Warming Potentials. *Phys Chem Chem Phys* **2008**, *10* (6), 808–820. https://doi.org/10.1039/b714382f.
(239) Andersen, M. P. S.; Nilsson, E. J. K.; Nielsen, O. J.; Johnson, M. S.; Hurley, M. D.; Wallington, T. J. Atmospheric Chemistry of Trans-$CF_3CHCHCl$: Kinetics of the Gas-Phase Reactions with Cl Atoms, OH Radicals, and O3. *Journal of Photochemistry and Photobiology A: Chemistry* **2008**, *199* (1), 92–97. https://doi.org/10.1016/j.jphotochem.2008.05.013.
(240) Wang, Z.; Wang, Y.; Li, J.; Henne, S.; Zhang, B.; Hu, J.; Zhang, J. Impacts of the Degradation of 2,3,3,3-Tetrafluoropropene into Trifluoroacetic Acid from Its Application in Automobile Air Conditioners in China, the United States, and Europe. *Environ. Sci. Technol.* **2018**, *52* (5), 2819–2826. https://doi.org/10.1021/acs.est.7b05960.
(241) Rao, P. K.; Gejji, S. P. Molecular Insights for the HFO-1345fz +X (X = Cl, O_3 or NO_3) Reaction and Fate of Alkoxy Radicals Initiated by Cl: DFT Investigations. *Journal of Fluorine Chemistry* **2017**, *204*, 65–75. https://doi.org/10.1016/j.jfluchem.2017.08.015.
(242) Chuong, B.; Stevens, P. S. Kinetic Study of the OH + Isoprene and OH + Ethylene Reactions between 2 and 6 Torr and over the Temperature Range 300−423 K. *J. Phys. Chem. A* **2000**, *104* (22), 5230–5237. https://doi.org/10.1021/jp993613a.
(243) Kim, D.; Stevens, P. S.; Hites, R. A. Rate Constants for the Gas-Phase Reactions of OH and O_3 with ß-Ocimene, ß-Myrcene, and α- and ß-Farnesene as a Function of Temperature. *J. Phys. Chem. A* **2011**, *115* (4), 500–506. https://doi.org/10.1021/jp111173s.
(244) Grant, G. H.; Richards, W. G. *Computational Chemistry*; Oxford University Press, 1995.
(245) Herwig, R. Computational Modeling of Drug Response with Applications to Neuroscience. *Dialogues Clin Neurosci* **2014**, *16* (4), 465–477.

(246) Lin, X.; Li, X.; Lin, X. A Review on Applications of Computational Methods in Drug Screening and Design. *Molecules* **2020**, *25* (6). https://doi.org/10.3390/molecules25061375.
(247) Vogiatzis, K. D.; Polynski, M. V.; Kirkland, J. K.; Townsend, J.; Hashemi, A.; Liu, C.; Pidko, E. A. Computational Approach to Molecular Catalysis by 3d Transition Metals: Challenges and Opportunities. *Chem. Rev.* **2019**, *119* (4), 2453–2523. https://doi.org/10.1021/acs.chemrev.8b00361.
(248) Quesne, M. G.; Silveri, F.; de Leeuw, N. H.; Catlow, C. R. A. Advances in Sustainable Catalysis: A Computational Perspective. *Front. Chem.* **2019**, *7*. https://doi.org/10.3389/fchem.2019.00182.
(249) Skyner, R. E.; McDonagh, J. L.; Groom, C. R.; Mourik, T. van; Mitchell, J. B. O. A Review of Methods for the Calculation of Solution Free Energies and the Modelling of Systems in Solution. *Phys. Chem. Chem. Phys.* **2015**, *17* (9), 6174–6191. https://doi.org/10.1039/C5CP00288E.
(250) Orozco, M.; Luque, F. J. Theoretical Methods for the Description of the Solvent Effect in Biomolecular Systems. *Chem. Rev.* **2000**, *100* (11), 4187–4226. https://doi.org/10.1021/cr990052a.
(251) De Broglie, L. Waves and Quanta. *Nature* **1923**, *112* (2815), 540–540. https://doi.org/10.1038/112540a0.
(252) Lewars, E. G. *Computational Chemistry: Introduction to the Theory and Applications of Molecular and Quantum Mechanics*; Springer Science & Business Media, 2010.
(253) Sinanoğlu, O.; Tuan, D. F. Many-Electron Theory of Atoms and Molecules. III. Effect of Correlation on Orbitals. *J. Chem. Phys.* **1963**, *38* (7), 1740–1748. https://doi.org/10.1063/1.1776948.
(254) Sinanoğlu, O. Many-Electron Theory of Atoms, Molecules and Their Interactions. In *Advances in Chemical Physics*; John Wiley & Sons, Ltd, 1964; pp 315–412. https://doi.org/10.1002/9780470143520.ch7.
(255) 11.1: Gaussian Basis Sets https://chem.libretexts.org/Courses/University_of_California_Davis/UCD_Chem_110B%3A_Physical_Chemistry_II/Text/11%3A_Computational_Quantum_Chemistry/11.1%3A_Gaussian_Basis_Sets (accessed 2020 -12 -21).
(256) Boys, S. F.; Egerton, A. C. Electronic Wave Functions - I. A General Method of Calculation for the Stationary States of Any Molecular System. *Proceedings of the Royal Society of London. Series A. Mathematical and Physical Sciences* **1950**, *200* (1063), 542–554. https://doi.org/10.1098/rspa.1950.0036.
(257) Pye, C. C.; Mercer, C. J. On the Least-Squares Fitting of Slater-Type Orbitals with Gaussians: Reproduction of the STO-NG Fits Using Microsoft Excel and Maple. *J. Chem. Educ.* **2012**, *89* (11), 1405–1410. https://doi.org/10.1021/ed300032f.
(258) 11.2: Gaussian Basis Sets https://chem.libretexts.org/Courses/Pacific_Union_College/Quantum_Chemistry/11%3A_Computational_Quantum_Chemistry/11.02%3A_Gaussian_Basis_Sets (accessed 2020 -12 -04).
(259) Weigend, F.; Ahlrichs, R. Balanced Basis Sets of Split Valence, Triple Zeta Valence and Quadruple Zeta Valence Quality for H to Rn: Design and Assessment of Accuracy. *Phys. Chem. Chem. Phys.* **2005**, *7* (18), 3297–3305. https://doi.org/10.1039/B508541A.
(260) Schäfer, A.; Huber, C.; Ahlrichs, R. Fully Optimized Contracted Gaussian Basis Sets of Triple Zeta Valence Quality for Atoms Li to Kr. *J. Chem. Phys.* **1994**, *100* (8), 5829–5835. https://doi.org/10.1063/1.467146.
(261) Weigend, F.; Furche, F.; Ahlrichs, R. Gaussian Basis Sets of Quadruple Zeta Valence Quality for Atoms H–Kr. *J. Chem. Phys.* **2003**, *119* (24), 12753–12762. https://doi.org/10.1063/1.1627293.

(262) Jensen, F. Polarization Consistent Basis Sets: Principles. *J. Chem. Phys.* **2001**, *115* (20), 9113–9125. https://doi.org/10.1063/1.1413524.
(263) Jensen, F. Polarization Consistent Basis Sets. II. Estimating the Kohn–Sham Basis Set Limit. *J. Chem. Phys.* **2002**, *116* (17), 7372–7379. https://doi.org/10.1063/1.1465405.
(264) Schäfer, A.; Horn, H.; Ahlrichs, R. Fully Optimized Contracted Gaussian Basis Sets for Atoms Li to Kr. *J. Chem. Phys.* **1992**, *97* (4), 2571–2577. https://doi.org/10.1063/1.463096.
(265) 11.3: Extended Basis Sets https://chem.libretexts.org/Bookshelves/Physical_and_Theoretical_Chemistry_Textbook_Maps/Map%3A_Physical_Chemistry_(McQuarrie_and_Simon)/11%3A_Computational_Quantum_Chemistry/11.03%3A_Extended_Basis_Sets (accessed 2020 -12 - 23).
(266) Kupka, T.; Lim, C. Polarization-Consistent versus Correlation-Consistent Basis Sets in Predicting Molecular and Spectroscopic Properties. *J. Phys. Chem. A* **2007**, *111* (10), 1927–1932. https://doi.org/10.1021/jp065008v.
(267) Feller, D.; Peterson, K. A.; Crawford, T. D. Sources of Error in Electronic Structure Calculations on Small Chemical Systems. *J Chem Phys* **2006**, *124* (5), 054107. https://doi.org/10.1063/1.2137323.
(268) Woon, D. E.; Dunning, T. H. Gaussian Basis Sets for Use in Correlated Molecular Calculations. V. Core-valence Basis Sets for Boron through Neon. *J. Chem. Phys.* **1995**, *103* (11), 4572–4585. https://doi.org/10.1063/1.470645.
(269) Peterson, K. A.; Dunning, T. H. Accurate Correlation Consistent Basis Sets for Molecular Core–Valence Correlation Effects: The Second Row Atoms Al–Ar, and the First Row Atoms B–Ne Revisited. *J. Chem. Phys.* **2002**, *117* (23), 10548–10560. https://doi.org/10.1063/1.1520138.
(270) Comeau, D. C.; Zellmer, R. J.; Shavitt, I. The Location and Characterization of Stationary Points on Molecular Potential Energy Surfaces. In *Geometrical Derivatives of Energy Surfaces and Molecular Properties*; Jørgensen, P., Simons, J., Eds.; NATO ASI Series; Springer Netherlands: Dordrecht, 1986; pp 243–251. https://doi.org/10.1007/978-94-009-4584-5_19.
(271) Bernhard Schlegel, H. Estimating the Hessian for Gradient-Type Geometry Optimizations. *Theoret. Chim. Acta* **1984**, *66* (5), 333–340. https://doi.org/10.1007/BF00554788.
(272) Foreman, E. S.; Kapnas, K. M.; Murray, C. Reactions between Criegee Intermediates and the Inorganic Acids HCl and HNO_3: Kinetics and Atmospheric Implications. *Angewandte Chemie International Edition* **2016**, *55* (35), 10419–10422. https://doi.org/10.1002/anie.201604662.
(273) Kumar, M.; Francisco, J. S. H–X (X = H, CH_3, CH_2F, CHF_2, CF_3, and SiH_3) Bond Activation by Criegee Intermediates: A Theoretical Perspective. *J. Phys. Chem. A* **2017**, *121* (49), 9421–9428. https://doi.org/10.1021/acs.jpca.7b10535.
(274) Xu, K.; Wang, W.; Wei, W.; Feng, W.; Sun, Q.; Li, P. Insights into the Reaction Mechanism of Criegee Intermediate CH_2OO with Methane and Implications for the Formation of Methanol. *J. Phys. Chem. A* **2017**, *121* (38), 7236–7245. https://doi.org/10.1021/acs.jpca.7b05858.
(275) Spellmeyer, D. *Annual Reports in Computational Chemistry*; Elsevier, 2006.
(276) Localizability of Dynamic Electron Correlation. *Chemical Physics Letters* **1983**, *100* (2), 151–154. https://doi.org/10.1016/0009-2614(83)80703-9.
(277) Pulay, P.; Saebø, S. Orbital-Invariant Formulation and Second-Order Gradient Evaluation in Møller-Plesset Perturbation Theory. *Theoret. Chim. Acta* **1986**, *69* (5), 357–368. https://doi.org/10.1007/BF00526697.
(278) Li, W.; Piecuch, P.; Gour, J. R.; Li, S. Local Correlation Calculations Using Standard and Renormalized Coupled-Cluster Approaches. *J. Chem. Phys.* **2009**, *131* (11), 114109. https://doi.org/10.1063/1.3218842.

(279) Polly, R.; Werner *, H.-J.; Manby, F. R.; Knowles, P. J. Fast Hartree–Fock Theory Using Local Density Fitting Approximations. *Molecular Physics* **2004**, *102* (21–22), 2311–2321. https://doi.org/10.1080/0026897042000274801.
(280) Jung, Y.; Sodt, A.; Gill, P. M. W.; Head-Gordon, M. Auxiliary Basis Expansions for Large-Scale Electronic Structure Calculations. *PNAS* **2005**, *102* (19), 6692–6697. https://doi.org/10.1073/pnas.0408475102.
(281) Werner, H.-J.; Pflüger, K. Chapter 4 On the Selection of Domains and Orbital Pairs in Local Correlation Treatments. In *Annual Reports in Computational Chemistry*; Spellmeyer, D. C., Ed.; Elsevier, 2006; Vol. 2, pp 53–80. https://doi.org/10.1016/S1574-1400(06)02004-4.
(282) Weigend, F. A Fully Direct RI-HF Algorithm: Implementation, Optimised Auxiliary Basis Sets, Demonstration of Accuracy and Efficiency. *Phys. Chem. Chem. Phys.* **2002**, *4* (18), 4285–4291. https://doi.org/10.1039/B204199P.
(283) Aquilante, F.; Lindh, R.; Pedersen, T. B. Unbiased Auxiliary Basis Sets for Accurate Two-Electron Integral Approximations. *The Journal of Chemical Physics* **2007**, *127* (11), 114107. https://doi.org/10.1063/1.2777146.
(284) Loibl, S.; Manby, F. R.; Schütz, M. Density Fitted, Local Hartree–Fock Treatment of NMR Chemical Shifts Using London Atomic Orbitals. *Molecular Physics* **2010**, *108* (3–4), 477–485. https://doi.org/10.1080/00268970903580133.
(285) Adler, T. B.; Knizia, G.; Werner, H.-J. A Simple and Efficient CCSD(T)-F12 Approximation. *J. Chem. Phys.* **2007**, *127* (22), 221106. https://doi.org/10.1063/1.2817618.
(286) Adler, T. B.; Werner, H.-J. An Explicitly Correlated Local Coupled Cluster Method for Calculations of Large Molecules Close to the Basis Set Limit. *The Journal of Chemical Physics* **2011**, *135* (14), 144117. https://doi.org/10.1063/1.3647565.
(287) Adler, T. B.; Werner, H.-J.; Manby, F. R. Local Explicitly Correlated Second-Order Perturbation Theory for the Accurate Treatment of Large Molecules. *J. Chem. Phys.* **2009**, *130* (5), 054106. https://doi.org/10.1063/1.3040174.
(288) Knizia, G.; Adler, T. B.; Werner, H.-J. Simplified CCSD(T)-F12 Methods: Theory and Benchmarks. *J. Chem. Phys.* **2009**, *130* (5), 054104. https://doi.org/10.1063/1.3054300.
(289) Werner, H.-J.; Knowles, P. J.; Manby, F. R.; Black, J. A.; Doll, K.; Heßelmann, A.; Kats, D.; Köhn, A.; Korona, T.; Kreplin, D. A.; Ma, Q.; MillerIII, T. F.; Mitrushchenkov, A.; Peterson, K. A.; Polyak, I.; Rauhut, G.; Sibaev, M. The Molpro Quantum Chemistry Package. *The Journal of Chemical Physics* **2020**, *152* (14), 144107. https://doi.org/10.1063/5.0005081.
(290) Hohenberg, P.; Kohn, W. Inhomogeneous Electron Gas. *Phys. Rev.* **1964**, *136* (3B), B864–B871. https://doi.org/10.1103/PhysRev.136.B864.
(291) Kohn, W.; Sham, L. J. Self-Consistent Equations Including Exchange and Correlation Effects. *Phys. Rev.* **1965**, *140* (4A), A1133–A1138. https://doi.org/10.1103/PhysRev.140.A1133.
(292) Web of Science [v.5.34] - Web of Science Core Collection Result Analysis https://wcs-webofknowledge-com.abc.cardiff.ac.uk/RA/analyze.do?product=WOS&SID=F3m9qr8Rks9sPxdgKfI&field=PY_PublicationYear_PublicationYear_en&yearSort=true (accessed 2020 -08 -16).
(293) Anglada, J. M.; Solé, A. Impact of the Water Dimer on the Atmospheric Reactivity of Carbonyl Oxides. *Phys. Chem. Chem. Phys.* **2016**, *18* (26), 17698–17712. https://doi.org/10.1039/C6CP02531E.
(294) Becke, A. D. Density-functional Thermochemistry. III. The Role of Exact Exchange. *The Journal of Chemical Physics* **1993**, *98* (7), 5648–5652. https://doi.org/10.1063/1.464913.
(295) Sousa, S. F.; Fernandes, P. A.; Ramos, M. J. General Performance of Density Functionals. *J. Phys. Chem. A* **2007**, *111* (42), 10439–10452. https://doi.org/10.1021/jp0734474.

(296) Car, null; Parrinello, null. Unified Approach for Molecular Dynamics and Density-Functional Theory. *Phys. Rev. Lett.* **1985**, *55* (22), 2471–2474. https://doi.org/10.1103/PhysRevLett.55.2471.
(297) Harris, J.; Jones, R. O. The Surface Energy of a Bounded Electron Gas. *J. Phys. F: Met. Phys.* **1974**, *4* (8), 1170–1186. https://doi.org/10.1088/0305-4608/4/8/013.
(298) Poater, J.; Duran, M.; Solà, M. Parametrization of the Becke3-LYP Hybrid Functional for a Series of Small Molecules Using Quantum Molecular Similarity Techniques. *Journal of Computational Chemistry* **2001**, *22* (14), 1666–1678. https://doi.org/10.1002/jcc.1122.
(299) Becke, A. D. Density-Functional Exchange-Energy Approximation with Correct Asymptotic Behavior. *Phys. Rev. A* **1988**, *38* (6), 3098–3100. https://doi.org/10.1103/PhysRevA.38.3098.
(300) Lee, C.; Yang, W.; Parr, R. G. Development of the Colle-Salvetti Correlation-Energy Formula into a Functional of the Electron Density. *Physical Review B* **1988**, *37* (2), 785–789. https://doi.org/10.1103/PhysRevB.37.785.
(301) Zhao, Y.; Truhlar, D. G. The M06 Suite of Density Functionals for Main Group Thermochemistry, Thermochemical Kinetics, Noncovalent Interactions, Excited States, and Transition Elements: Two New Functionals and Systematic Testing of Four M06-Class Functionals and 12 Other Functionals. *Theor Chem Account* **2008**, *120* (1), 215–241. https://doi.org/10.1007/s00214-007-0310-x.
(302) Lynch, B. J.; Fast, P. L.; Harris, M.; Truhlar, D. G. Adiabatic Connection for Kinetics. *J. Phys. Chem. A* **2000**, *104* (21), 4811–4815. https://doi.org/10.1021/jp000497z.
(303) P. Misiewicz, J.; N. Elliott, S.; B. Moore, K.; F. Schaefer, H. Re-Examining Ammonia Addition to the Criegee Intermediate: Converging to Chemical Accuracy. *Physical Chemistry Chemical Physics* **2018**, *20* (11), 7479–7491. https://doi.org/10.1039/C7CP08582F.
(304) Almatarneh, M. H.; Elayan, I. A.; Altarawneh, M.; Hollett, J. W. A Computational Study of the Ozonolysis of Sabinene. *Theor Chem Acc* **2019**, *138* (2), 30. https://doi.org/10.1007/s00214-019-2420-7.
(305) Vereecken, L.; Harder, H.; Novelli, A. The Reactions of Criegee Intermediates with Alkenes, Ozone, and Carbonyl Oxides. *Physical Chemistry Chemical Physics* **2014**, *16* (9), 4039. https://doi.org/10.1039/c3cp54514h.
(306) Zhang, D.; Zhang, R. Ozonolysis of α-Pinene and β-Pinene: Kinetics and Mechanism. *J. Chem. Phys.* **2005**, *122* (11), 114308. https://doi.org/10.1063/1.1862616.
(307) Raghunath, P.; Lee, Y.-P.; Lin, M. C. Computational Chemical Kinetics for the Reaction of Criegee Intermediate CH_2OO with HNO_3 and Its Catalytic Conversion to OH and HCO. *J. Phys. Chem. A* **2017**, *121* (20), 3871–3878. https://doi.org/10.1021/acs.jpca.7b02196.
(308) Kurtén, T.; Lane, J. R.; Jørgensen, S.; Kjaergaard, H. G. A Computational Study of the Oxidation of SO_2 to SO_3 by Gas-Phase Organic Oxidants. *J. Phys. Chem. A* **2011**, *115* (31), 8669–8681. https://doi.org/10.1021/jp203907d.
(309) Chhantyal-Pun, R.; McGillen, M. R.; Beames, J. M.; Khan, M. A. H.; Percival, C. J.; Shallcross, D. E.; Orr-Ewing, A. J. Temperature-Dependence of the Rates of Reaction of Trifluoroacetic Acid with Criegee Intermediates. *Angewandte Chemie International Edition* **2017**, *56* (31), 9044–9047. https://doi.org/10.1002/anie.201703700.
(310) M. J. Frisch, G. W. Trucks, H. B. Schlegel, G. E. Scuseria, M. A. Robb, J. R. Cheeseman, G. Scalmani, V. Barone, G. A. Petersson, H. Nakatsuji, X. Li, M. Caricato, A. Marenich, J. Bloino, B. G. Janesko, R. Gomperts, B. Mennucci, H. P. Hratchian, J. V. Ortiz, A. F. Izmaylov, J. L. Sonnenberg, D. Williams-Young, F. Ding, F. Lipparini, F. Egidi, J. Goings, B. Peng, A. Petrone, T. Henderson, D. Ranasinghe, V. G. Zakrzewski, J. Gao, N. Rega, G. Zheng, W. Liang, M. Hada, M. Ehara, K. Toyota, R. Fukuda, J. Hasegawa, M. Ishida, T. Nakajima, Y. Honda, O.

Kitao, H. Nakai, T. Vreven, K. Throssell, J. A. Montgomery, Jr., J. E. Peralta, F. Ogliaro, M. Bearpark, J. J. Heyd, E. Brothers, K. N. Kudin, V. N. Staroverov, T. Keith, R. Kobayashi, J. Normand, K. Raghavachari, A. Rendell, J. C. Burant, S. S. Iyengar, J. Tomasi, M. Cossi, J. M. Millam, M. Klene, C. Adamo, R. Cammi, J. W. Ochterski, R. L. Martin, K. Morokuma, O. Farkas, J. B. Foresman, and D. J. Fox,. *Gaussian 09, Revision A.02*; Gaussian, Inc: Wallingford CT, 2016.

(311) Kim, K.; Jordan, K. D. Comparison of Density Functional and MP2 Calculations on the Water Monomer and Dimer. *J. Phys. Chem.* **1994**, *98* (40), 10089–10094. https://doi.org/10.1021/j100091a024.

(312) Ab Initio Calculation of Vibrational Absorption and Circular Dichroism Spectra Using Density Functional Force Fields | The Journal of Physical Chemistry https://pubs-acs-org.abc.cardiff.ac.uk/doi/10.1021/j100096a001 (accessed 2020 -07 -16).

(313) Zhao, Y.; Truhlar, D. G. Density Functional for Spectroscopy: No Long-Range Self-Interaction Error, Good Performance for Rydberg and Charge-Transfer States, and Better Performance on Average than B3LYP for Ground States. *J. Phys. Chem. A* **2006**, *110* (49), 13126–13130. https://doi.org/10.1021/jp066479k.

(314) Kendall, R. A.; Dunning, T. H.; Harrison, R. J. Electron Affinities of the First-row Atoms Revisited. Systematic Basis Sets and Wave Functions. *The Journal of Chemical Physics* **1992**, *96* (9), 6796–6806. https://doi.org/10.1063/1.462569.

(315) Dunning, T. H. Gaussian Basis Sets for Use in Correlated Molecular Calculations. I. The Atoms Boron through Neon and Hydrogen. *The Journal of Chemical Physics* **1989**, *90* (2), 1007–1023. https://doi.org/10.1063/1.456153.

(316) Peng, C.; Schlegel, H. B. Combining Synchronous Transit and Quasi-Newton Methods to Find Transition States. *Israel Journal of Chemistry* **1993**, *33* (4), 449–454. https://doi.org/10.1002/ijch.199300051.

(317) Frisch, M. J. GAUSSIAN09. *http://www.gaussian.com/*.

(318) Werner, H.-J.; Knowles, P. J.; Knizia, G.; Manby, F. R.; Schütz, M. Molpro: A General-Purpose Quantum Chemistry Program Package: Molpro. *Wiley Interdisciplinary Reviews: Computational Molecular Science* **2012**, *2* (2), 242–253. https://doi.org/10.1002/wcms.82.

(319) Zhao, Q.; Liu, F.; Wang, W.; Li, C.; Lü, J.; Wang, W. Reactions between Hydroxyl-Substituted Alkylperoxy Radicals and Criegee Intermediates: Correlations of the Electronic Characteristics of Methyl Substituents and the Reactivity. *Phys. Chem. Chem. Phys.* **2017**, *19* (23), 15073–15083. https://doi.org/10.1039/C7CP00869D.

(320) Chhantyal-Pun, R.; Rotavera, B.; McGillen, M. R.; Khan, M. A. H.; Eskola, A. J.; Caravan, R. L.; Blacker, L.; Tew, D. P.; Osborn, D. L.; Percival, C. J.; Taatjes, C. A.; Shallcross, D. E.; Orr-Ewing, A. J. Criegee Intermediate Reactions with Carboxylic Acids: A Potential Source of Secondary Organic Aerosol in the Atmosphere. *ACS Earth Space Chem.* **2018**, *2* (8), 833–842. https://doi.org/10.1021/acsearthspacechem.8b00069.

(321) Glowacki, D. R.; Liang, C.-H.; Morley, C.; Pilling, M. J.; Robertson, S. H. MESMER: An Open-Source Master Equation Solver for Multi-Energy Well Reactions. *J. Phys. Chem. A* **2012**, *116* (38), 9545–9560. https://doi.org/10.1021/jp3051033.

(322) Carr, S. A.; Glowacki, D. R.; Liang, C.-H.; Baeza-Romero, M. T.; Blitz, M. A.; Pilling, M. J.; Seakins, P. W. Experimental and Modeling Studies of the Pressure and Temperature Dependences of the Kinetics and the OH Yields in the Acetyl + O2 Reaction. *J. Phys. Chem. A* **2011**, *115* (6), 1069–1085. https://doi.org/10.1021/jp1099199.

(323) McKee, K. W.; Blitz, M. A.; Cleary, P. A.; Glowacki, D. R.; Pilling, M. J.; Seakins, P. W.; Wang, L. Experimental and Master Equation Study of the Kinetics of OH + C2H2: Temperature Dependence of the Limiting High Pressure and Pressure Dependent Rate Coefficients. *J. Phys. Chem. A* **2007**, *111* (19), 4043–4055. https://doi.org/10.1021/jp067594y.

(324) Goldsmith, C. F.; Klippenstein, S. J.; Green, W. H. Theoretical Rate Coefficients for Allyl+HO2 and Allyloxy Decomposition. *Proceedings of the Combustion Institute* **2011**, *33* (1), 273–282. https://doi.org/10.1016/j.proci.2010.05.054.
(325) Chhantyal-Pun, R.; Shannon, R.; Tew, D. P.; Caravan, R. L.; Duchi, M.; Wong, C.; Ingham, A.; Feldman, C.; McGillen, M. R.; Khan, M. A. H. H.; Antonov, I. O.; Rotavera, B.; Ramasesha, K.; Osborn, D. L.; Taatjes, C. A.; Percival, C.; Shallcross, D. E.; Orr-Ewing, A. Experimental and Computational Studies of Criegee Intermediate Reactions with NH3 and CH3NH2. *Phys. Chem. Chem. Phys.* **2019**. https://doi.org/10.1039/C8CP06810K.
(326) Blitz, M. A.; Talbi, D.; Seakins, P. W.; Smith, I. W. M. Rate Constants and Branching Ratios for the Reaction of CH Radicals with NH_3: A Combined Experimental and Theoretical Study. *J. Phys. Chem. A* **2012**, *116* (24), 5877–5885. https://doi.org/10.1021/jp209383t.
(327) Peltola, J.; Seal, P.; Inkilä, A.; Eskola, A. Time-Resolved, Broadband UV-Absorption Spectrometry Measurements of Criegee Intermediate Kinetics Using a New Photolytic Precursor: Unimolecular Decomposition of CH_2OO and Its Reaction with Formic Acid. *Phys. Chem. Chem. Phys.* **2020**, *22* (21), 11797–11808. https://doi.org/10.1039/D0CP00302F.
(328) Wigner, E. Concerning the excess of potential barriers in chemical reactions. *Z. Phys. Chem. B-Chem. Elem. Aufbau. Mater.* **1932**, *19* (2/3), 203–216.
(329) Canneaux, S.; Bohr, F.; Henon, E. KiSThelP: A Program to Predict Thermodynamic Properties and Rate Constants from Quantum Chemistry Results. *J Comput Chem* **2014**, *35* (1), 82–93. https://doi.org/10.1002/jcc.23470.
(330) Habershon, S.; Manolopoulos, D. E.; Markland, T. E.; Miller, T. F. Ring-Polymer Molecular Dynamics: Quantum Effects in Chemical Dynamics from Classical Trajectories in an Extended Phase Space. *Annual Review of Physical Chemistry* **2013**, *64* (1), 387–413. https://doi.org/10.1146/annurev-physchem-040412-110122.
(331) Beyer, A. N.; Richardson, J. O.; Knowles, P. J.; Rommel, J.; Althorpe, S. C. Quantum Tunneling Rates of Gas-Phase Reactions from On-the-Fly Instanton Calculations. *J. Phys. Chem. Lett.* **2016**, *7* (21), 4374–4379. https://doi.org/10.1021/acs.jpclett.6b02115.
(332) Richardson, J. O. Derivation of Instanton Rate Theory from First Principles. *The Journal of Chemical Physics* **2016**, *144* (11), 114106. https://doi.org/10.1063/1.4943866.
(333) Richardson, J. O.; Althorpe, S. C. Ring-Polymer Molecular Dynamics Rate-Theory in the Deep-Tunneling Regime: Connection with Semiclassical Instanton Theory. *The Journal of Chemical Physics* **2009**, *131* (21), 214106. https://doi.org/10.1063/1.3267318.
(334) Richardson, J. O.; Althorpe, S. C. Ring-Polymer Instanton Method for Calculating Tunneling Splittings. *The Journal of Chemical Physics* **2011**, *134* (5), 054109. https://doi.org/10.1063/1.3530589.
(335) Leather, K. E.; McGillen, M. R.; Percival, C. J. Temperature-Dependent Ozonolysis Kinetics of Selected Alkenes in the Gas Phase: An Experimental and Structure–Activity Relationship (SAR) Study. *Phys. Chem. Chem. Phys.* **2010**, *12* (12), 2935–2943. https://doi.org/10.1039/B919731A.
(336) Loudon, M.; Parise, J. *Organic Chemistry*; Macmillan Learning, 2015.
(337) Rhew, R. C.; Deventer, M. J.; Turnipseed, A. A.; Warneke, C.; Ortega, J.; Shen, S.; Martinez, L.; Koss, A.; Lerner, B. M.; Gilman, J. B.; Smith, J. N.; Guenther, A. B.; Gouw, J. A. de. Ethene, Propene, Butene and Isoprene Emissions from a Ponderosa Pine Forest Measured by Relaxed Eddy Accumulation. *Atmospheric Chemistry and Physics* **2017**, *17* (21), 13417–13438. https://doi.org/10.5194/acp-17-13417-2017.
(338) Kazil, J.; McKeen, S.; Kim, S.-W.; Ahmadov, R.; Grell, G. A.; Talukdar, R. K.; Ravishankara, A. R. Deposition and Rainwater Concentrations of Trifluoroacetic

Acid in the United States from the Use of HFO-1234yf. *Journal of Geophysical Research: Atmospheres* **2014**, *119* (24), 14,059-14,079. https://doi.org/10.1002/2014JD022058.
(339) Reimann, S.; Lewis, A. C. Anthropogenic VOCs. In *Volatile Organic Compounds in the Atmosphere*; John Wiley & Sons, Ltd, 2007; pp 33–81. https://doi.org/10.1002/9780470988657.ch2.
(340) San José, R.; Stohl, A.; Karatzas, K.; Bohler, T.; James, P.; Pérez, J. L. A Modelling Study of an Extraordinary Night Time Ozone Episode over Madrid Domain. *Environmental Modelling & Software* **2005**, *20* (5), 587–593. https://doi.org/10.1016/j.envsoft.2004.03.009.
(341) Atkinson, R.; Aschmann, S. M.; Arey, J.; Tuazon, E. C. Formation Yields of Epoxides and O(3P) Atoms from the Gas-Phase Reactions of O_3 with a Series of Alkenes. *International Journal of Chemical Kinetics* **1994**, *26* (9), 945–950. https://doi.org/10.1002/kin.550260908.
(342) Atkinson, R.; Arey, J.; Aschmann, S. M.; Tuazon, E. C. Formation of $O(^3P)$ Atoms and Epoxides from the Gas- Phase Reaction of O_3 with Isoprene. *Res Chem Intermed* **1994**, *20* (3), 385–394. https://doi.org/10.1163/156856794X00388.
(343) Cremer, D. Theoretical Determination of Molecular Structure and Conformation. III. The Pseudorotation Surface of 1,2,3-trioxolane and 1,2,4-trioxolane. *J. Chem. Phys.* **1979**, *70* (4), 1898–1910. https://doi.org/10.1063/1.437669.
(344) Tadayon, S. V.; Foreman, E. S.; Murray, C. Kinetics of the Reactions between the Criegee Intermediate CH2OO and Alcohols. *J. Phys. Chem. A* **2018**, *122* (1), 258–268. https://doi.org/10.1021/acs.jpca.7b09773.
(345) Percival, C. J.; Welz, O.; Eskola, A. J.; Savee, J. D.; Osborn, D. L.; Topping, D. O.; Lowe, D.; Utembe, S. R.; Bacak, A.; McFiggans, G.; Cooke, M. C.; Xiao, P.; Archibald†, A. T.; Jenkin, M. E.; Derwent, R. G.; Riipinen, I.; Mok, D. W. K.; Lee, E. P. F.; Dyke, J. M.; Taatjes, C. A.; Shallcross, D. E. Regional and Global Impacts of Criegee Intermediates on Atmospheric Sulphuric Acid Concentrations and First Steps of Aerosol Formation. *Faraday Discuss.* **2013**, *165* (0), 45–73. https://doi.org/10.1039/C3FD00048F.
(346) ICSC 0814 - MESITYL OXIDE https://www.ilo.org/dyn/icsc/showcard.display?p_lang=en&p_card_id=0814&p_version=2 (accessed 2021 -02 -11).
(347) Vollmer, M. K.; Reimann, S.; Hill, M.; Brunner, D. First Observations of the Fourth Generation Synthetic Halocarbons HFC-1234yf, HFC-1234ze(E), and HCFC-1233zd(E) in the Atmosphere. *Environ. Sci. Technol.* **2015**, *49* (5), 2703–2708. https://doi.org/10.1021/es505123x.
(348) Nielsen, O. J.; Javadi, M. S.; Sulbaek Andersen, M. P.; Hurley, M. D.; Wallington, T. J.; Singh, R. Atmospheric Chemistry of CF_3CFCH_2: Kinetics and Mechanisms of Gas-Phase Reactions with Cl Atoms, OH Radicals, and O_3. *Chemical Physics Letters* **2007**, *439* (1), 18–22. https://doi.org/10.1016/j.cplett.2007.03.053.
(349) Jia, L.; Xu, Y.; Ge, M.; Du, L.; Wang, G.; Zhuang, G. Kinetic Study of the Gas-Phase Ozonolysis of Propylene. *Acta Physico-Chimica Sinica* **2006**, *22* (10), 1260–1266. https://doi.org/10.1016/S1872-1508(06)60060-0.
(350) Rickard, A. R.; Johnson, D.; McGill, C. D.; Marston, G. OH Yields in the Gas-Phase Reactions of Ozone with Alkenes. *J. Phys. Chem. A* **1999**, *103* (38), 7656–7664. https://doi.org/10.1021/jp9916992.
(351) Qi, B.; Yang, B.; Wang, Z.; Yang, H.; Liu, L. Production of Radicals in the Ozonolysis of Propene in Air. *Sci. China Ser. B-Chem.* **2009**, *52* (3), 356–361. https://doi.org/10.1007/s11426-008-0132-2.
(352) Grosjean, E.; Grosjean, D. Gas Phase Reaction of Alkenes with Ozone: Formation Yields of Primary Carbonyls and Biradicals. *Environ. Sci. Technol.* **1997**, *31* (8), 2421–2427. https://doi.org/10.1021/es970075b.

(353) Shi, Y.; Xu, Y.; Jia, L. Arrhenius Parameters for the Gas-Phase Reactions of O3 with Two Butenes and Two Methyl-Substituted Butenes over the Temperature Range of 295-351 K. *International Journal of Chemical Kinetics* **2011**, *43* (5), 238–246. https://doi.org/10.1002/kin.20553.
(354) Grosjean, E.; Grosjean, D. Rate Constants for the Gas-phase Reaction of C5—C10 Alkenes with Ozone. *International Journal of Chemical Kinetics* **1995**, *27* (11), 1045–1054. https://doi.org/10.1002/kin.550271102.
(355) Ren, Y.; Grosselin, B.; Daële, V.; Mellouki, A. Investigation of the Reaction of Ozone with Isoprene, Methacrolein and Methyl Vinyl Ketone Using the HELIOS Chamber. *Faraday Discuss.* **2017**, *200* (0), 289–311. https://doi.org/10.1039/C7FD00014F.
(356) Sato, K.; Klotz, B.; Taketsugu, T.; Takayanagi, T. Kinetic Measurements for the Reactions of Ozone with Crotonaldehyde and Its Methyl Derivatives and Calculations of Transition-State Theory. *Physical Chemistry Chemical Physics* **2004**, *6* (15), 3969–3976. https://doi.org/10.1039/B402496F.
(357) Soto, A.; Ballesteros, B.; Jiménez, E.; Antiñolo, M.; Martínez, E.; Albaladejo, J. Kinetic and Mechanistic Study of the Gas-Phase Reaction of $C_xF_{2x+1}CH{=}CH_2$ (X=1, 2, 3, 4 and 6) with O_3 under Atmospheric Conditions. *Chemosphere* **2018**, *201*, 318–327. https://doi.org/10.1016/j.chemosphere.2018.02.183.
(358) Andersen, M. P. S.; Nielsen, O. J.; Toft, A.; Nakayama, T.; Matsumi, Y.; Waterland, R. L.; Buck, R. C.; Hurley, M. D.; Wallington, T. J. Atmospheric Chemistry of $C_xF_{2x+1}CHCH_2$ (X=1, 2, 4, 6, and 8): Kinetics of Gas-Phase Reactions with Cl Atoms, OH Radicals, and O_3. *Journal of Photochemistry and Photobiology A: Chemistry* **2005**, *176* (1), 124–128. https://doi.org/10.1016/j.jphotochem.2005.06.015.
(359) Søndergaard, R.; Nielsen, O. J.; Hurley, M. D.; Wallington, T. J.; Singh, R. Atmospheric Chemistry of Trans-CF_3CHCHF: Kinetics of the Gas-Phase Reactions with Cl Atoms, OH Radicals, and O_3. *Chemical Physics Letters* **2007**, *443* (4), 199–204. https://doi.org/10.1016/j.cplett.2007.06.084.
(360) Avzianova, E. V.; Ariya, P. A. Temperature-Dependent Kinetic Study for Ozonolysis of Selected Tropospheric Alkenes. *International Journal of Chemical Kinetics* **2002**, *34* (12), 678–684. https://doi.org/10.1002/kin.10093.
(361) Paulson, S. E.; Chung, M. Y.; Hasson, A. S. OH Radical Formation from the Gas-Phase Reaction of Ozone with Terminal Alkenes and the Relationship between Structure and Mechanism. *J. Phys. Chem. A* **1999**, *103* (41), 8125–8138. https://doi.org/10.1021/jp991995e.
(362) Wegener, R.; Brauers, T.; Koppmann, R.; Bares, S. R.; Rohrer, F.; Tillmann, R.; Wahner, A.; Hansel, A.; Wisthaler, A. Simulation Chamber Investigation of the Reactions of Ozone with Short-Chained Alkenes. *Journal of Geophysical Research: Atmospheres* **2007**, *112* (D13). https://doi.org/10.1029/2006JD007531.
(363) Grosjean, D.; Williams, E. L.; Grosjean, E. Atmospheric Chemistry of Isoprene and of Its Carbonyl Products. *Environ. Sci. Technol.* **1993**, *27* (5), 830–840. https://doi.org/10.1021/es00042a004.
(364) Paulson, S. E.; Chung, M.; Sen, A. D.; Orzechowska, G. Measurement of OH Radical Formation from the Reaction of Ozone with Several Biogenic Alkenes. *Journal of Geophysical Research: Atmospheres* **1998**, *103* (D19), 25533–25539. https://doi.org/10.1029/98JD01951.
(365) McGill, C. D.; Rickard, A. R.; Johnson, D.; Marston, G. Product Yields in the Reactions of Ozone with *Z*-but-2-ene, *E*-but-2-ene and 2-Methylbut-2-Ene. *Chemosphere* **1999**, *38* (6), 1205–1212. https://doi.org/10.1016/S0045-6535(98)00512-8.
(366) Neeb Peter; Horie Osamu; Moortgat Geert K. Gas-phase Ozonolysis of Ethene in the Presence of Hydroxylic Compounds. *International Journal of Chemical Kinetics*

1999, *28* (10), 721–730. https://doi.org/10.1002/(SICI)1097-4601(1996)28:10<721::AID-KIN2>3.0.CO;2-P.
(367) Andersen, M. P. S.; Sølling, T. I.; Andersen, L. L.; Volkova, A.; Hovanessian, D.; Britzman, C.; Nielsen, O. J.; Wallington, T. J. Atmospheric Chemistry of (Z)-CF3CHCHCl: Products and Mechanisms of the Cl Atom, OH Radical and O_3 Reactions, and Role of (E)–(Z) Isomerization. *Phys. Chem. Chem. Phys.* **2018**, *20* (44), 27949–27958. https://doi.org/10.1039/C8CP04903C.
(368) Donahue, N. M.; Kroll, J. H.; Anderson, J. G.; Demerjian, K. L. Direct Observation of OH Production from the Ozonolysis of Olefins. *Geophysical Research Letters* **1998**, *25* (1), 59–62. https://doi.org/10.1029/97GL53560.
(369) Natural refrigerant air-conditioning in trains and buses http://www.r744.com/articles/1483/natural_refrigerant_air-conditioning_in_trains_and_buses_br (accessed 2019 -01 -16).
(370) Park, H. R.; Valcárcel, J.; SanRoman, S. M. Low GWP Refrigerant for Buses and Trains Air Conditioning. 4.
(371) Honeywell Starts up HFO Refrigerants Plant in Louisiana - Chemical Engineering.
(372) Kumar, M.; Francisco, J. S. Reactions of Criegee Intermediates with Non-Water Greenhouse Gases: Implications for Metal Free Chemical Fixation of Carbon Dioxide. *J. Phys. Chem. Lett.* **2017**, *8* (17), 4206–4213. https://doi.org/10.1021/acs.jpclett.7b01762.
(373) Kula, J. Safer Ozonolysis Reactions: A Compilation of Laboratory Experience. *Chem. Health Saf.* **1999**, *6* (6), 21–22. https://doi.org/10.1021/acs.chas.8b06607.
(374) Hida, T.; Kikuchi, J.; Kakinuma, M.; Nogusa, H. Risk Assessment and Safety Evaluation Study for Ozonolysis of ß-Pinene: Raw Material of a Novel Prostaglandin D2 Receptor Antagonist S-5751. *Org. Process Res. Dev.* **2010**, *14* (6), 1485–1489. https://doi.org/10.1021/op100065d.
(375) Porterfield, J. P.; Eibenberger, S.; Patterson, D.; McCarthy, M. C. The Ozonolysis of Isoprene in a Cryogenic Buffer Gas Cell by High Resolution Microwave Spectroscopy. *Phys. Chem. Chem. Phys.* **2018**, *20* (24), 16828–16834. https://doi.org/10.1039/C8CP02055H.
(376) Barber, V. P.; Pandit, S.; Green, A. M.; Trongsiriwat, N.; Walsh, P. J.; Klippenstein, S. J.; Lester, M. I. Four-Carbon Criegee Intermediate from Isoprene Ozonolysis: Methyl Vinyl Ketone Oxide Synthesis, Infrared Spectrum, and OH Production. *J. Am. Chem. Soc.* **2018**, *140* (34), 10866–10880. https://doi.org/10.1021/jacs.8b06010.
(377) Vansco, M. F.; Marchetti, B.; Trongsiriwat, N.; Bhagde, T.; Wang, G.; Walsh, P. J.; Klippenstein, S. J.; Lester, M. I. Synthesis, Electronic Spectroscopy, and Photochemistry of Methacrolein Oxide: A Four-Carbon Unsaturated Criegee Intermediate from Isoprene Ozonolysis. *J. Am. Chem. Soc.* **2019**, *141* (38), 15058–15069. https://doi.org/10.1021/jacs.9b05193.
(378) Zhang, D.; Zhang, R. Mechanism of OH Formation from Ozonolysis of Isoprene: A Quantum-Chemical Study. *J. Am. Chem. Soc.* **2002**, *124* (11), 2692–2703. https://doi.org/10.1021/ja011518l.
(379) Kuo, M.-T.; Weber, I.; Fittschen, C.; Lin, J. J.-M. Kinetics of Dimethyl Sulfide (DMS) Reactions with Isoprene-Derived Criegee Intermediates Studied with Direct UV Absorption. *Atmospheric Chemistry and Physics Discussions* **2020**, 1–16. https://doi.org/10.5194/acp-2020-326.
(380) Warneke, C.; Holzinger, R.; Hansel, A.; Jordan, A.; Lindinger, W.; Pöschl, U.; Williams, J.; Hoor, P.; Fischer, H.; Crutzen, P. J.; Scheeren, H. A.; Lelieveld, J. Isoprene and Its Oxidation Products Methyl Vinyl Ketone, Methacrolein, and Isoprene Related Peroxides Measured Online over the Tropical Rain Forest of Surinam in March 1998. *Journal of Atmospheric Chemistry* **2001**, *38* (2), 167–185. https://doi.org/10.1023/A:1006326802432.

(381) Berndt, T.; Mentler, B.; Scholz, W.; Fischer, L.; Herrmann, H.; Kulmala, M.; Hansel, A. Accretion Product Formation from Ozonolysis and OH Radical Reaction of α-Pinene: Mechanistic Insight and the Influence of Isoprene and Ethylene. *Environ. Sci. Technol.* **2018**, *52* (19), 11069–11077. https://doi.org/10.1021/acs.est.8b02210.
(382) Zhao, Y.; Zhang, R.; Wang, H.; He, M.; Sun, X.; Zhang, Q.; Wang, W.; Ru, M. Mechanism of Atmospheric Ozonolysis of Sabinene: A DFT Study. *Journal of Molecular Structure: THEOCHEM* **2010**, *942* (1), 32–37. https://doi.org/10.1016/j.theochem.2009.11.029.
(383) Nguyen, H. T.-H.; Takenaka, N.; Bandow, H.; Maeda, Y.; de Oliva, S. T.; Botelho, M. M. f.; Tavares, T. M. Atmospheric Alcohols and Aldehydes Concentrations Measured in Osaka, Japan and in Sao Paulo, Brazil. *Atmospheric Environment* **2001**, *35* (18), 3075–3083. https://doi.org/10.1016/S1352-2310(01)00136-4.
(384) Alvim, D. S.; Gatti, L. V.; Corrêa, S. M.; Chiquetto, J. B.; de Souza Rossatti, C.; Pretto, A.; Santos, M. H. dos; Yamazaki, A.; Orlando, J. P.; Santos, G. M. Main Ozone-Forming VOCs in the City of Sao Paulo: Observations, Modelling and Impacts. *Air Qual Atmos Health* **2017**, *10* (4), 421–435. https://doi.org/10.1007/s11869-016-0429-9.
(385) Neeb, P.; Horie, O.; Moortgat, G. Gas-Phase Ozonolysis of Ethene in the Presence of Hydroxylic Compounds. *International Journal of Chemical Kinetics - INT J CHEM KINET* **1996**, *28*, 721–730. https://doi.org/10.1002/(SICI)1097-4601(1996)28:103.0.CO;2-P.
(386) Tobias, H. J.; Ziemann, P. J. Kinetics of the Gas-Phase Reactions of Alcohols, Aldehydes, Carboxylic Acids, and Water with the C13 Stabilized Criegee Intermediate Formed from Ozonolysis of 1-Tetradecene. *J. Phys. Chem. A* **2001**, *105* (25), 6129–6135. https://doi.org/10.1021/jp004631r.
(387) Chao, W.; Hsieh, J.-T.; Chang, C.-H.; Lin, J. J.-M. Direct Kinetic Measurement of the Reaction of the Simplest Criegee Intermediate with Water Vapor. *Science* **2015**, *347* (6223), 751–754. https://doi.org/10.1126/science.1261549.
(388) Newland, M. J.; Rickard, A. R.; Vereecken, L.; Muñoz, A.; Ródenas, M.; Bloss, W. J. Atmospheric Isoprene Ozonolysis: Impacts of Stabilised Criegee Intermediate Reactions with SO_2, H_2O and Dimethyl Sulfide. *Atmospheric Chemistry and Physics* **2015**, *15* (16), 9521–9536. https://doi.org/10.5194/acp-15-9521-2015.
(389) Becker, K. H.; Brockmann, K. J.; Bechara, J. Production of Hydrogen Peroxide in Forest Air by Reaction of Ozone with Terpenes. *Nature* **1990**, *346* (6281), 256–258. https://doi.org/10.1038/346256a0.
(390) Gäb, S.; Hellpointner, E.; Turner, W. V.; Koŕte, F. Hydroxymethyl Hydroperoxide and Bis(Hydroxymethyl) Peroxide from Gas-Phase Ozonolysis of Naturally Occurring Alkenes. *Nature* **1985**, *316* (6028), 535–536. https://doi.org/10.1038/316535a0.
(391) Atmospheric Chemistry of Criegee Intermediates: Unimolecular Reactions and Reactions with Water - Journal of the American Chemical Society (ACS Publications) https://pubs.acs.org/doi/abs/10.1021/jacs.6b08655?source=chemport (accessed 2019 -01 -16).
(392) Bauerle, S.; Moortgat, G. K. Absorption Cross-Sections of HOCH2OOH Vapor between 205 and 360 Nm at 298 K. *Chemical Physics Letters* **1999**, *309* (1), 43–48. https://doi.org/10.1016/S0009-2614(99)00652-1.
(393) Baasandorj, M.; Papanastasiou, D. K.; Talukdar, R. K.; Hasson, A. S.; Burkholder, J. B. $(CH_3)_3COOH$ (Tert-Butyl Hydroperoxide): OH Reaction Rate Coefficients between 206 and 375 K and the OH Photolysis Quantum Yield at 248 Nm. *Phys. Chem. Chem. Phys.* **2010**, *12* (38), 12101–12111. https://doi.org/10.1039/C0CP00463D.
(394) Anastasi, C.; Smith, I. W. M.; Parkes, D. A. Flash Photolysis Study of the Spectra of CH_3O_2 and $C(CH_3)_3O_2$ Radicals and the Kinetics of Their Mutual Reactions and with

NO. *J. Chem. Soc., Faraday Trans. 1* **1978**, *74* (0), 1693–1701. https://doi.org/10.1039/F19787401693.
(395) Blitz, M. A.; Heard, D. E.; Pilling, M. J. Wavelength Dependent Photodissociation of CH_3OOH: Quantum Yields for CH_3O and OH, and Measurement of the OH+CH_3OOH Rate Coefficient. *Journal of Photochemistry and Photobiology A: Chemistry* **2005**, *176* (1), 107–113. https://doi.org/10.1016/j.jphotochem.2005.09.017.
(396) Vaghjiani, G. L.; Ravishankara, A. R. Kinetics and Mechanism of Hydroxyl Radical Reaction with Methyl Hydroperoxide. *J. Phys. Chem.* **1989**, *93* (5), 1948–1959. https://doi.org/10.1021/j100342a050.
(397) Gonzalez, Carlos.; Schlegel, H. Bernhard. Reaction Path Following in Mass-Weighted Internal Coordinates. *J. Phys. Chem.* **1990**, *94* (14), 5523–5527. https://doi.org/10.1021/j100377a021.
(398) Ishida, K.; Morokuma, K.; Komornicki, A. The Intrinsic Reaction Coordinate. An *ab initio* Calculation for HNC→HCN and $H^- + CH_4 \rightarrow CH_4 + H^-$. *The Journal of Chemical Physics* **1977**, *66* (5), 2153–2156. https://doi.org/10.1063/1.434152.
(399) Borbon, A.; Gilman, J. B.; Kuster, W. C.; Grand, N.; Chevaillier, S.; Colomb, A.; Dolgorouky, C.; Gros, V.; Lopez, M.; Sarda-Esteve, R.; Holloway, J.; Stutz, J.; Petetin, H.; McKeen, S.; Beekmann, M.; Warneke, C.; Parrish, D. D.; de Gouw, J. A. Emission Ratios of Anthropogenic Volatile Organic Compounds in Northern Mid-Latitude Megacities: Observations versus Emission Inventories in Los Angeles and Paris: VOC EMISSION RATIOS IN MODERN MEGACITIES. *Journal of Geophysical Research: Atmospheres* **2013**, *118* (4), 2041–2057. https://doi.org/10.1002/jgrd.50059.
(400) Tuazon, E. C.; Arey, J.; Atkinson, R.; Aschmann, S. M. Gas-Phase Reactions of 2-Vinylpyridine and Styrene with Hydroxyl and NO_3 Radicals and Ozone. *Environ. Sci. Technol.* **1993**, *27* (9), 1832–1841. https://doi.org/10.1021/es00046a011.
(401) Lin, Y.-H.; Yin, C.; Lin, W.-H.; Li, Y.-L.; Takahashi, K.; Lin, J. J.-M. Criegee Intermediate Reaction with Alcohol Is Enhanced by a Single Water Molecule. *J. Phys. Chem. Lett.* **2018**, *9* (24), 7040–7044. https://doi.org/10.1021/acs.jpclett.8b03349.
(402) Lin, Y.-H.; Takahashi, K.; Lin, J. J.-M. Reactivity of Criegee Intermediates toward Carbon Dioxide. *J. Phys. Chem. Lett.* **2018**, *9* (1), 184–188. https://doi.org/10.1021/acs.jpclett.7b03154.
(403) Report on the IGAC/SPARC Chemistry-Climate Model Initiative (CCMI) 2013 Science Workshop https://www.researchgate.net/publication/259904110_Report_on_the_IGACSPARC_Chemistry-Climate_Model_Initiatve_CCMI_2013_Science_Workshop (accessed 2020 -09 -25).
(404) Kumar, M.; Busch, D. H.; Subramaniam, B.; Thompson, W. H. Barrierless Tautomerization of Criegee Intermediates via Acid Catalysis. *Phys. Chem. Chem. Phys.* **2014**, *16* (42), 22968–22973. https://doi.org/10.1039/C4CP03065F.
(405) Liu, F.; Fang, Y.; Kumar, M.; Thompson, W. H.; Lester, M. I. Direct Observation of Vinyl Hydroperoxide. *Phys. Chem. Chem. Phys.* **2015**, *17* (32), 20490–20494. https://doi.org/10.1039/C5CP02917A.
(406) Cabezas, C.; Endo, Y. Observation of Hydroperoxyethyl Formate from the Reaction between the Methyl Criegee Intermediate and Formic Acid. *Phys. Chem. Chem. Phys.* **2020**, *22* (2), 446–454. https://doi.org/10.1039/C9CP05030B.
(407) Sarrami, F.; Mackenzie-Rae, F. A.; Karton, A. A Computational Investigation of the Sulphuric Acid-Catalysed 1,4-Hydrogen Transfer in Higher Criegee Intermediates. *International Journal of Quantum Chemistry 0* (0), e25599. https://doi.org/10.1002/qua.25599.
(408) Todeschini, R.; Consonni, V. *Handbook of Molecular Descriptors*; John Wiley & Sons, 2008.

(409) Bracco, L. L. B.; Tucceri, M. E.; Escalona, A.; Díaz-de-Mera, Y.; Aranda, A.; Rodríguez, A. M.; Rodríguez, D. New Particle Formation from the Reactions of Ozone with Indene and Styrene. *Phys. Chem. Chem. Phys.* **2019**, *21* (21), 11214–11225. https://doi.org/10.1039/C9CP00912D.
(410) Du, B.; Zhang, W. Theoretical Insight into the Reaction Mechanism and Kinetics for the Criegee Intermediate of Anti-PhCHOO with SO_2. *Molecules* **2020**, *25* (13), 3041. https://doi.org/10.3390/molecules25133041.
(411) Lin, L.-C.; Chao, W.; Chang, C.-H.; Takahashi, K.; Lin, J. J.-M. Temperature Dependence of the Reaction of Anti-CH_3CHOO with Water Vapor. *Phys. Chem. Chem. Phys.* **2016**, *18* (40), 28189–28197. https://doi.org/10.1039/C6CP05171E.
(412) B. Ryzhkov, A.; A. Ariya, P. A Theoretical Study of the Reactions of Parent and Substituted Criegee Intermediates with Water and the Water Dimer. *Physical Chemistry Chemical Physics* **2004**, *6* (21), 5042–5050. https://doi.org/10.1039/B408414D.
(413) Shannon, R. J.; Blitz, M. A.; Goddard, A.; Heard, D. E. Accelerated Chemistry in the Reaction between the Hydroxyl Radical and Methanol at Interstellar Temperatures Facilitated by Tunnelling. *Nature Chem* **2013**, *5* (9), 745–749. https://doi.org/10.1038/nchem.1692.
(414) Chhantyal-Pun, R.; Welz, O.; Savee, J. D.; Eskola, A. J.; Lee, E. P. F.; Blacker, L.; Hill, H. R.; Ashcroft, M.; Khan, M. A. H.; Lloyd-Jones, G. C.; Evans, L.; Rotavera, B.; Huang, H.; Osborn, D. L.; Mok, D. K. W.; Dyke, J. M.; Shallcross, D. E.; Percival, C. J.; Orr-Ewing, A. J.; Taatjes, C. A. Direct Measurements of Unimolecular and Bimolecular Reaction Kinetics of the Criegee Intermediate (CH3)2COO. *J. Phys. Chem. A* **2017**, *121* (1), 4–15. https://doi.org/10.1021/acs.jpca.6b07810.
(415) Kumar, M.; Shee, J.; Rudshteyn, B.; Reichman, D. R.; Friesner, R. A.; Miller, C. E.; Francisco, J. S. Multiple Stable Isoprene–Ozone Complexes Reveal Complex Entrance Channel Dynamics in the Isoprene + Ozone Reaction. *J. Am. Chem. Soc.* **2020**, *142* (24), 10806–10813. https://doi.org/10.1021/jacs.0c02360.
(416) Isidorov, V. A. *Organic Chemistry of the Earth's Atmosphere*; Springer-Verlag: Berlin Heidelberg, 1990.
(417) Atkinson, R.; Baulch, D. L.; Cox, R. A.; Crowley, J. N.; Hampson, R. F.; Hynes, R. G.; Jenkin, M. E.; Rossi, M. J.; Troe, J.; IUPAC Subcommittee. Evaluated Kinetic and Photochemical Data for Atmospheric Chemistry: Volume II - Gas Phase Reactions of Organic Species. *Atmospheric Chemistry and Physics* **2006**, *6* (11), 3625–4055. https://doi.org/10.5194/acp-6-3625-2006.
(418) Yin, C.; Takahashi, K. Effect of Unsaturated Substituents in the Reaction of Criegee Intermediates with Water Vapor. *Phys. Chem. Chem. Phys.* **2018**, *20* (30), 20217–20227. https://doi.org/10.1039/C8CP02064G.
(419) Meisner, J.; Kästner, J. Atom Tunneling in Chemistry. *Angewandte Chemie International Edition* **2016**, *55* (18), 5400–5413. https://doi.org/10.1002/anie.201511028.
(420) Lin, L.-C.; Chang, H.-T.; Chang, C.-H.; Chao, W.; Smith, M. C.; Chang, C.-H.; Lin, J. J.-M.; Takahashi, K. Competition between H_2O and $(H_2O)_2$ Reactions with CH_2OO/CH_3CHOO. *Phys. Chem. Chem. Phys.* **2016**, *18* (6), 4557–4568. https://doi.org/10.1039/C5CP06446E.
(421) Vereecken, L.; Rickard, A. R.; Newland, M. J.; Bloss, W. J. Theoretical Study of the Reactions of Criegee Intermediates with Ozone, Alkylhydroperoxides, and Carbon Monoxide. *Phys. Chem. Chem. Phys.* **2015**, *17* (37), 23847–23858. https://doi.org/10.1039/C5CP03862F.
(422) Bravo, M. A.; Son, J.; de Freitas, C. U.; Gouveia, N.; Bell, M. L. Air Pollution and Mortality in São Paulo, Brazil: Effects of Multiple Pollutants and Analysis of Susceptible Populations. *Journal of Exposure Science and Environmental Epidemiology* **2016**, *26* (2), 150–161. https://doi.org/10.1038/jes.2014.90.

(423) Chang, Y.-P.; Chang, H.-H.; Lin, J. J.-M. Kinetics of the Simplest Criegee Intermediate Reaction with Ozone Studied by Mid-Infrared Quantum Cascade Laser Spectrometer. 17.
(424) Liu, Y.; Liu, F.; Liu, S.; Dai, D.; Dong, W.; Yang, X. A Kinetic Study of the CH2OO Criegee Intermediate Reaction with SO_2, $(H_2O)_2$, CH_2I_2 and I Atoms Using OH Laser Induced Fluorescence. *Physical Chemistry Chemical Physics* **2017**, *19* (31), 20786–20794. https://doi.org/10.1039/C7CP04336H.
(425) Vereecken L.; Nguyen H. M. T. Theoretical Study of the Reaction of Carbonyl Oxide with Nitrogen Dioxide: $CH_2OO + NO_2$. *International Journal of Chemical Kinetics* **2017**, *49* (10), 752–760. https://doi.org/10.1002/kin.21112.
(426) US Department of Commerce, N. ESRL Global Monitoring Division - Global Greenhouse Gas Reference Network https://www.esrl.noaa.gov/gmd/ccgg/trends/ (accessed 2018 -03 -31).
(427) Crisp, T. A.; Lerner, B. M.; Williams, E. J.; Quinn, P. K.; Bates, T. S.; Bertram, T. H. Observations of Gas Phase Hydrochloric Acid in the Polluted Marine Boundary Layer. *Journal of Geophysical Research: Atmospheres* **2014**, *119* (11), 6897–6915. https://doi.org/10.1002/2013JD020992.
(428) Welz, O.; Eskola, A. J.; Sheps, L.; Rotavera, B.; Savee, J. D.; Scheer, A. M.; Osborn, D. L.; Lowe, D.; Murray Booth, A.; Xiao, P.; Anwar H. Khan, M.; Percival, C. J.; Shallcross, D. E.; Taatjes, C. A. Rate Coefficients of C1 and C2 Criegee Intermediate Reactions with Formic and Acetic Acid Near the Collision Limit: Direct Kinetics Measurements and Atmospheric Implications. *Angewandte Chemie International Edition* **2014**, *53* (18), 4547–4550. https://doi.org/10.1002/anie.201400964.
(429) Bannan, T. J.; Booth, A. M.; Breton, M. L.; Bacak, A.; Muller, J. B. A.; Leather, K. E.; Khan, M. A. H.; Lee, J. D.; Dunmore, R. E.; Hopkins, J. R.; Fleming, Z. L.; Sheps, L.; Taatjes, C. A.; Shallcross, D. E.; Percival, C. J. Seasonality of Formic Acid (HCOOH) in London during the ClearfLo Campaign. *Journal of Geophysical Research: Atmospheres* **2017**, *122* (22), 12,488-12,498. https://doi.org/10.1002/2017JD027064.
(430) Khan, M. A. H.; Lyons, K.; Chhantyal-Pun, R.; McGillen, M. R.; Caravan, R. L.; Taatjes, C. A.; Orr-Ewing, A. J.; Percival, C. J.; Shallcross, D. E. Investigating the Tropospheric Chemistry of Acetic Acid Using the Global 3-D Chemistry Transport Model, STOCHEM-CRI. *Journal of Geophysical Research: Atmospheres* **2018**, *123* (11), 6267–6281. https://doi.org/10.1029/2018JD028529.
(431) Vereecken, L. The Reaction of Criegee Intermediates with Acids and Enols. *Phys. Chem. Chem. Phys.* **2017**, *19* (42), 28630–28640. https://doi.org/10.1039/C7CP05132H.
(432) Li, Y.-L.; Lin, Y.-H.; Yin, C.; Takahashi, K.; Chiang, C.-Y.; Chang, Y.-P.; Lin, J. J.-M. Temperature-Dependent Rate Coefficient for the Reaction of CH_3SH with the Simplest Criegee Intermediate. *J. Phys. Chem. A* **2019**. https://doi.org/10.1021/acs.jpca.8b12553.
(433) Russell, M. H.; Hoogeweg, G.; Webster, E. M.; Ellis, D. A.; Waterland, R. L.; Hoke, R. A. TFA from HFO-1234yf: Accumulation and Aquatic Risk in Terminal Water Bodies. *Environmental Toxicology and Chemistry* **2012**, *31* (9), 1957–1965. https://doi.org/10.1002/etc.1925.
(434) Wu, J.; Martin, J. W.; Zhai, Z.; Lu, K.; Li, L.; Fang, X.; Jin, H.; Hu, J.; Zhang, J. Airborne Trifluoroacetic Acid and Its Fraction from the Degradation of HFC-134a in Beijing, China. *Environ. Sci. Technol.* **2014**, *48* (7), 3675–3681. https://doi.org/10.1021/es4050264.
(435) Zhai, Z.; Wu, J.; Hu, X.; Li, L.; Guo, J.; Zhang, B.; Hu, J.; Zhang, J. A 17-Fold Increase of Trifluoroacetic Acid in Landscape Waters of Beijing, China during the Last Decade. *Chemosphere* **2015**, *129*, 110–117. https://doi.org/10.1016/j.chemosphere.2014.09.033.

(436) Kazil, J.; McKeen, S. A.; Kim, S.; Ahmadov, R.; Grell, G. A.; Talukdar, R. K.; Ravishankara, A. R. WRF/Chem Study of Dry and Wet Deposition of Trifluoroacetic Acid Produced from the Atmospheric Degradation of a Few Short-Lived HFCs. *AGU Fall Meeting Abstracts* **2011**, *44*, A44C-08.
(437) Kumar, M.; Busch, D. H.; Subramaniam, B.; Thompson, W. H. Criegee Intermediate Reaction with CO: Mechanism, Barriers, Conformer-Dependence, and Implications for Ozonolysis Chemistry. *J. Phys. Chem. A* **2014**, *118* (10), 1887–1894. https://doi.org/10.1021/jp500258h.
(438) Jalan, A.; Allen, J. W.; and Green, W. H. Chemically activated formation of organic acids in reactions of the Criegee intermediate with aldehydes and ketones - *Physical Chemistry Chemical Physics* **2013**, 15, 16841-16852.
(439) Cabezas, C.; Guillemin, J.-C.; Endo, Y. Fourier-Transform Microwave Spectroscopy of a Halogen Substituted Criegee Intermediate ClCHOO. *The Journal of Chemical Physics* **2016**, *145* (18), 184304. https://doi.org/10.1063/1.4967250.
(440) Chhantyal-Pun, R.; Davey, A.; E. Shallcross, D.; J. Percival, C.; J. Orr-Ewing, A. A Kinetic Study of the CH_2OO Criegee Intermediate Self-Reaction, Reaction with SO_2 and Unimolecular Reaction Using Cavity Ring-down Spectroscopy. *Physical Chemistry Chemical Physics* **2015**, *17* (5), 3617–3626. https://doi.org/10.1039/C4CP04198D.
(441) Kumar, M.; Francisco, J. S. Heteroatom Tuning of Bimolecular Criegee Reactions and Its Implications. *Angewandte Chemie International Edition* **2016**, *55* (43), 13432–13435. https://doi.org/10.1002/anie.201604848.
(442) Air quality guidelines for Europe https://www.euro.who.int/en/publications/abstracts/air-quality-guidelines-for-europe (accessed 2021 -01 -22).
(443) Characteristics and Recent Trends of Sulfur Dioxide at Urban, Rural, and Background Sites in North China: Effectiveness of Control Measures. *Journal of Environmental Sciences* **2012**, *24* (1), 34–49. https://doi.org/10.1016/S1001-0742(11)60727-4.
(444) Leong, Y. J.; Rutter, A. P.; Wong, H. Y.; Gutierrez, C. V.; Junaid, M.; Scheuer, E.; Gong, L.; Lewicki, R.; Dibb, J. E.; Tittel, F. K.; Griffin, R. J. Impact of Environmental Variables on the Reduction of Nitric Acid by Proxies for Volatile Organic Compounds Emitted by Motor Vehicles. *Atmospheric Pollution Research* **2016**, *7* (2), 221–227. https://doi.org/10.1016/j.apr.2015.09.006.
(445) Anglada, J. M.; Hoffman, G. J.; Slipchenko, L. V.; M.Costa, M.; Ruiz-López, M. F.; Francisco, J. S. Atmospheric Significance of Water Clusters and Ozone–Water Complexes. *J. Phys. Chem. A* **2013**, *117* (40), 10381–10396. https://doi.org/10.1021/jp407282c.
(446) Levels, N. R. C. (US) C. on A. E. G. *Hydrogen Sulfide Acute Exposure Guideline Levels*; National Academies Press (US), 2010.
(447) Cheng, M.-D. Atmospheric Chemistry of Hydrogen Fluoride. *J Atmos Chem* **2018**, *75* (1), 1–16. https://doi.org/10.1007/s10874-017-9359-7.
(448) Raw, G. J.; Coward, S. K. D.; Brown, V. M.; Crump, D. R. Exposure to Air Pollutants in English Homes. *Journal of Exposure Science & Environmental Epidemiology* **2004**, *14* (1), S85–S94. https://doi.org/10.1038/sj.jea.7500363.
(449) Jalan, A.; Allen, J. W.; Green, W. H. Chemically activated formation of organic acids in reactions of the Criegee intermediate with aldehydes and ketones - *Physical Chemistry Chemical Physics* **2013**, 15, 16841-16852 https://doi.org/10.1039/C3CP52598H.
(450) Jalan, A.; Allen, J. W.; Green, W. H. Chemically Activated Formation of Organic Acids in Reactions of the Criegee Intermediate with Aldehydes and Ketones. *Phys. Chem. Chem. Phys.* **2013**, *15* (39), 16841–16852. https://doi.org/10.1039/C3CP52598H.

(451) Hallquist, M.; Wenger, J. C.; Baltensperger, U.; Rudich, Y.; Simpson, D.; Claeys, M.; Dommen, J.; Donahue, N. M.; George, C.; Goldstein, A. H.; Hamilton, J. F.; Herrmann, H.; Hoffmann, T.; Iinuma, Y.; Jang, M.; Jenkin, M. E.; Jimenez, J. L.; Kiendler-Scharr, A.; Maenhaut, W.; McFiggans, G.; Mentel, T. F.; Monod, A.; Prévôt, A. S. H.; Seinfeld, J. H.; Surratt, J. D.; Szmigielski, R.; Wildt, J. The Formation, Properties and Impact of Secondary Organic Aerosol: Current and Emerging Issues. *Atmospheric Chemistry and Physics* **2009**, *9* (14), 5155–5236. https://doi.org/10.5194/acp-9-5155-2009.
(452) The Role of Aerosol in Climate Change, the Environment, and Human Health. *Atmospheric and Oceanic Science Letters*.
(453) Vereecken, L.; Harder, H.; Novelli, A. The Reaction of Criegee Intermediates with NO, RO_2, and SO_2, and Their Fate in the Atmosphere. *Phys. Chem. Chem. Phys.* **2012**, *14* (42), 14682–14695. https://doi.org/10.1039/C2CP42300F.
(454) Sheps, L. Absolute Ultraviolet Absorption Spectrum of a Criegee Intermediate CH2OO. *J. Phys. Chem. Lett.* **2013**, *4* (24), 4201–4205. https://doi.org/10.1021/jz402191w.
(455) Liu, Y.; Bayes, K. D.; Sander, S. P. Measuring Rate Constants for Reactions of the Simplest Criegee Intermediate (CH_2OO) by Monitoring the OH Radical. *J. Phys. Chem. A* **2014**, *118* (4), 741–747. https://doi.org/10.1021/jp407058b.
(456) Sanhueza, E. Hydrochloric Acid from Chlorocarbons: A Significant Global Source of Background Rain Acidity. *Tellus B* **2001**, *53* (2), 122–132. https://doi.org/10.1034/j.1600-0889.2001.d01-11.x.
(457) Neeb, P.; Sauer, F.; Horie, O.; Moortgat, G. K. Formation of Hydroxymethyl Hydroperoxide and Formic Acid in Alkene Ozonolysis in the Presence of Water Vapour. *Atmospheric Environment* **1997**, *31* (10), 1417–1423. https://doi.org/10.1016/S1352-2310(96)00322-6.
(458) Sauer, F.; Schäfer, C.; Neeb, P.; Horie, O.; Moortgat, G. K. Formation of Hydrogen Peroxide in the Ozonolysis of Isoprene and Simple Alkenes under Humid Conditions. *Atmospheric Environment* **1999**, *33* (2), 229–241. https://doi.org/10.1016/S1352-2310(98)00152-6.
(459) Crehuet, R.; Anglada, J. M.; Bofill, J. M. Tropospheric Formation of Hydroxymethyl Hydroperoxide, Formic Acid, H_2O_2, and OH from Carbonyl Oxide in the Presence of Water Vapor: A Theoretical Study of the Reaction Mechanism. *Chemistry – A European Journal* **2001**, *7* (10), 2227–2235. https://doi.org/10.1002/1521-3765(20010518)7:10<2227::AID-CHEM2227>3.0.CO;2-O.
(460) Jiménez, E.; González, S.; Cazaunau, M.; Chen, H.; Ballesteros, B.; Daële, V.; Albaladejo, J.; Mellouki, A. Atmospheric Degradation Initiated by OH Radicals of the Potential Foam Expansion Agent, $CF_3(CF_2)_2CH{=}CH_2$ (HFC-1447fz): Kinetics and Formation of Gaseous Products and Secondary Organic Aerosols. *Environmental Science and Technology* **2016**, *50* (3), 1234–1242. https://doi.org/10.1021/acs.est.5b04379.
(461) Aplincourt, P.; Anglada, J. M. Theoretical Studies on Isoprene Ozonolysis under Tropospheric Conditions. 1. Reaction of Substituted Carbonyl Oxides with Water. *J. Phys. Chem. A* **2003**, *107* (30), 5798–5811. https://doi.org/10.1021/jp026868o.
(462) Fry, J. L.; Matthews, J.; Lane, J. R.; Roehl, C. M.; Sinha, A.; Kjaergaard, H. G.; Wennberg, P. O. OH-Stretch Vibrational Spectroscopy of Hydroxymethyl Hydroperoxide. *J. Phys. Chem. A* **2006**, *110* (22), 7072–7079. https://doi.org/10.1021/jp0612127.
(463) Ouyang, B.; W. McLeod, M.; L. Jones, R.; J. Bloss, W. NO_3 Radical Production from the Reaction between the Criegee Intermediate CH_2OO and NO_2. *Physical Chemistry Chemical Physics* **2013**, *15* (40), 17070–17075. https://doi.org/10.1039/C3CP53024H.
(464) Berndt, T.; Kaethner, R.; Voigtländer, J.; Stratmann, F.; Pfeifle, M.; Reichle, P.; Sipilä, M.; Kulmala, M.; Olzmann, M. Kinetics of the Unimolecular Reaction of

CH2OO and the Bimolecular Reactions with the Water Monomer, Acetaldehyde and Acetone under Atmospheric Conditions. *Phys. Chem. Chem. Phys.* **2015**, *17* (30), 19862–19873. https://doi.org/10.1039/C5CP02224J.
(465) Direct Probing of Criegee Intermediates from Gas-Phase Ozonolysis Using Chemical Ionization Mass Spectrometry *Journal of the American Chemical Society* **2017**, 139, 38, 13387–13392 https://doi.org/10.1021/jacs.7b05849.
(466) Smith, M. C.; Chang, C.-H.; Chao, W.; Lin, L.-C.; Takahashi, K.; Boering, K. A.; Lin, J. J.-M. Strong Negative Temperature Dependence of the Simplest Criegee Intermediate CH_2OO Reaction with Water Dimer. *J. Phys. Chem. Lett.* **2015**, *6* (14), 2708–2713. https://doi.org/10.1021/acs.jpclett.5b01109.
(467) Lewis, T. R.; Blitz, M. A.; Heard, D. E.; Seakins, P. W. Direct Evidence for a Substantive Reaction between the Criegee Intermediate, CH_2OO, and the Water Vapour Dimer. *Phys. Chem. Chem. Phys.* **2015**, *17* (7), 4859–4863. https://doi.org/10.1039/C4CP04750H.
(468) Yajima, R.; Sakamoto, Y.; Inomata, S.; Hirokawa, J. Relative Reactivity Measurements of Stabilized CH_2OO, Produced by Ethene Ozonolysis, Toward Acetic Acid and Water Vapor Using Chemical Ionization Mass Spectrometry. *J. Phys. Chem. A* **2017**, *121* (34), 6440–6449. https://doi.org/10.1021/acs.jpca.7b05065.
(469) Sommariva, R.; Cox, S.; Martin, C.; Borońska, K.; Young, J.; Jimack, P.; Pilling, M. J.; Matthaios, V. N.; Newland, M. J.; Panagi, M.; Bloss, W. J.; Monks, P. S.; Rickard, A. R. AtChem, an Open Source Box-Model for the Master Chemical Mechanism. *Geoscientific Model Development Discussions* **2019**, 1–27. https://doi.org/10.5194/gmd-2019-192.
(470) Doujaiji, B.; Al-Tawfiq, J. A. Hydrogen Sulfide Exposure in an Adult Male. *Ann Saudi Med* **2010**, *30* (1), 76–80. https://doi.org/10.4103/0256-4947.59379.
(471) Smith, M. C.; Chao, W.; Kumar, M.; Francisco, J. S.; Takahashi, K.; Lin, J. J.-M. Temperature-Dependent Rate Coefficients for the Reaction of CH_2OO with Hydrogen Sulfide. *J. Phys. Chem. A* **2017**, *121* (5), 938–945. https://doi.org/10.1021/acs.jpca.6b12303.
(472) Cabezas, C.; Endo, Y. The Reaction between the Methyl Criegee Intermediate and Hydrogen Chloride: An FTMW Spectroscopic Study. *Phys. Chem. Chem. Phys.* **2018**, *20* (35), 22569–22575. https://doi.org/10.1039/C8CP04171G.
(473) Murphy, P. M. The Chemistry and Utility of Hexafluoroisobutylene (HFIB) and Hexafluoroisobutylene Oxide (HFIBO). *Journal of Fluorine Chemistry* **2013**, *156*, 345–362. https://doi.org/10.1016/j.jfluchem.2013.07.015.
(474) Gai, Y.; Ge, M.; Wang, W. Kinetic Studies of O3 Reactions with 3-Bromopropene and 3-Iodopropene in the Temperature Range 288–328 K. *Atmospheric Environment* **2009**, *43* (22), 3467–3471. https://doi.org/10.1016/j.atmosenv.2009.04.038.
(475) Zhang, Q.; Chen, Y.; Tong, S.; Ge, M.; Shenolikar, J.; Johnson, M. S.; Wang, Y.; Tsona, N. T.; Mellouki, A.; Du, L. Atmospheric Oxidation of Selected Chlorinated Alkenes by O3, OH, NO3 and Cl. *Atmospheric Environment* **2017**, *170*, 12–21. https://doi.org/10.1016/j.atmosenv.2017.09.031.
(476) Velasco, E.; Lamb, B.; Westberg, H.; Allwine, E.; Sosa, G.; Arriaga-Colina, J. L.; Jobson, B. T.; Alexander, M. L.; Prazeller, P.; Knighton, W. B.; Rogers, T. M.; Grutter, M.; Herndon, S. C.; Kolb, C. E.; Zavala, M.; de Foy, B.; Volkamer, R.; Molina, L. T.; Molina, M. J. Distribution, Magnitudes, Reactivities, Ratios and Diurnal Patterns of Volatile Organic Compounds in the Valley of Mexico during the MCMA 2002 & 2003 Field Campaigns. *Atmospheric Chemistry and Physics* **2007**, *7* (2), 329–353. https://doi.org/10.5194/acp-7-329-2007.
(477) Huang, C.; Chen, C. H.; Li, L.; Cheng, Z.; Wang, H. L.; Huang, H. Y.; Streets, D. G.; Wang, Y. J.; Zhang, G. F.; Chen, Y. R. Emission Inventory of Anthropogenic Air Pollutants and VOC Species in the Yangtze River Delta Region, China. *Atmospheric Chemistry and Physics* **2011**, *11* (9), 4105–4120. https://doi.org/10.5194/acp-11-4105-2011.

(478) North, G. R.; Pyle, J. A.; Zhang, F. *Encyclopedia of Atmospheric Sciences*; Elsevier, 2014.
(479) Schauer, J. J.; Kleeman, M. J.; Cass, G. R.; Simoneit, B. R. T. Measurement of Emissions from Air Pollution Sources. 2. C1 through C30 Organic Compounds from Medium Duty Diesel Trucks. *Environ. Sci. Technol.* **1999**, *33* (10), 1578–1587. https://doi.org/10.1021/es980081n.
(480) Guenther, A.; Hewitt, C. N.; Erickson, D.; Fall, R.; Geron, C.; Graedel, T.; Harley, P.; Klinger, L.; Lerdau, M.; Mckay, W. A.; Pierce, T.; Scholes, B.; Steinbrecher, R.; Tallamraju, R.; Taylor, J.; Zimmerman, P. A Global Model of Natural Volatile Organic Compound Emissions. *Journal of Geophysical Research: Atmospheres* **1995**, *100* (D5), 8873–8892. https://doi.org/10.1029/94JD02950.
(481) Helmig, D.; Daly, R. W.; Milford, J.; Guenther, A. Seasonal Trends of Biogenic Terpene Emissions. *Chemosphere* **2013**, *93* (1), 35–46. https://doi.org/10.1016/j.chemosphere.2013.04.058.
(482) Huang, Y.; Ho, S. S. H.; Ho, K. F.; Lee, S. C.; Gao, Y.; Cheng, Y.; Chan, C. S. Characterization of Biogenic Volatile Organic Compounds (BVOCs) in Cleaning Reagents and Air Fresheners in Hong Kong. *Atmospheric Environment* **2011**, *45* (34), 6191–6196. https://doi.org/10.1016/j.atmosenv.2011.08.012.
(483) Goldstein, A. H.; McKay, M.; Kurpius, M. R.; Schade, G. W.; Lee, A.; Holzinger, R.; Rasmussen, R. A. Forest Thinning Experiment Confirms Ozone Deposition to Forest Canopy Is Dominated by Reaction with Biogenic VOCs. *Geophysical Research Letters* **2004**, *31* (22). https://doi.org/10.1029/2004GL021259.
(484) Deng, P.; Wang, L.; Wang, L. Mechanism of Gas-Phase Ozonolysis of ß-Myrcene in the Atmosphere. *J. Phys. Chem. A* **2018**, *122* (11), 3013–3020. https://doi.org/10.1021/acs.jpca.8b00983.